

Czech Technical University in Prague
Faculty of Electrical Engineering
Department of Physics



Ion Deflectometry in Z-pinch plasmas

Doctoral thesis

Ing. Vojtěch Munzar

Ph.D. programme: P2612 Electrical Engineering and Information Technology

Branch of study: 1701V011 Plasmas Physics

Supervisor: prof. Ing. Daniel Klír, Ph.D.

Supervisor Specialist: Ing. Karel Řezáč, Ph.D.

Prague, January 2023

Abstract

Dynamics of z-pinch is strongly influenced by the distribution of conductive currents and B-fields. However, the B-field measurement in the high energy density plasmas is, in practice, a very challenging task because the high temperatures and densities limit the applicability of classical diagnostic methods. Ion deflectometry is a relatively novel diagnostic method originally developed for EM field measurements in laser plasmas. It is based on the deflection of diagnostic ion beams in these fields that is proportional to the path integral of the studied fields. It does not rely on the plasma background and can measure EM fields in nearly vacuum environments with good spatial resolution. Despite several successful experiments, ion deflectometry's development in z-pinch has stopped because only a few z-pinch facilities had access to the powerful laser-pulse systems required for backlighting the fields by multi-MeV ions. Based on the results of our three selected papers, we described in this thesis the development of an alternative deflectometry method employing a more accessible ion source. First, we evaluated the contemporary deflectometry experiments in laser and z-pinch plasmas and explored the basic principles of ion deflectometry in order to extend its applicability in the z-pinch. A numerical code simulating the movements and deflections of ion beams in various B-fields was developed. We used these simulations to investigate the formation of the characteristic ion images and evaluated two basic configurations of ion deflectometry, where the probing beams enter the z-pinch radially or along its axis. Then, we focused on investigating multi-MeV deuterium beams, which were accelerated after the current disruption on the GIT-12 device but have also been observed at other z-pinch devices. By numerical reproduction of our experimental deuteron images obtained on GIT-12, we estimated the spatial distribution and the maximum divergence of the deuteron sources for multiple energies. In addition, we have made the measurements of the maximum values of the path integrals of the B-fields. After diagnosing these deuteron beams and their sources, we developed a unique way to employ them for the deflectometry measurements. As a result, we have made the first-ever measurements of the B-fields using the z-pinch-driven deuteron source for the backlighting. To record the deuteron deflections, a deflectometry grid was placed into the electrode gap without suppressing the deuteron source or destroying the imploding plasma. These measurements evaluated the total currents and 2D (xy) distributions of the path-integrated B-fields for several shots. Our experimental setup permitted the crucial approximation of the deuteron trajectories allowing to measure the averaged B-fields analytically and directly from the experimental data. Finally, we used our numerical code and the side-on SXR image of the imploding z-pinch to obtain a 2D (rz) tomographic map of the z-pinch B-fields. Surprisingly, these results showed that a significant part of the current flows beyond the hot dense z-pinch region.

Keywords: Magnetic fields, z-pinch, plasma, ion deflectometry, radiography, ion acceleration, B-field diagnostics

Abstrakt

Dynamika z-pinčů je silně ovlivněna rozložením jejich proudů a magnetických polí. Měření těchto polí v plazmatu s vysokou hustotou energie je však v praxi velmi náročný úkol, protože vysoké teploty a hustoty omezují použitelnost klasických diagnostických metod. Iontová deflektometrie je poměrně nová diagnostická metoda, která byla původně vyvinuta pro měření EM polí v laserovém plazmatu. Je založena na deflexích diagnostických iontových svazků v těchto polích, které jsou úměrné dráhovému integrálu zkoumaných polí. Tato metoda není závislá na plazmatu v pozadí a může měřit EM pole v téměř vakuovém prostředí a přitom s dobrým prostorovým rozlišením. Navzdory několika úspěšným experimentům s použitím této diagnostiky se vývoj iontové deflektometrie v z-pinčích zastavil, protože jen několik z-pinčových zařízení má přístup k výkonným laserovým pulzním systémům potřebným pro podsvícení magnetického pole ionty o energii několika MeV. Na základě výsledků našich tří vybraných článků jsme v této práci popsali vývoj alternativní metody deflektometrie využívající dostupnější zdroj iontů. Nejprve jsme vyhodnotili současné deflektometrické experimenty v laserovém a z-pinch plazmatu a prozkoumali základní principy iontové deflektometrie s cílem rozšířit její použitelnost v z-pinčích. Byl vyvinut numerický kód simulující pohyby a výchylky iontových svazků v různých magnetických polích. Pomocí těchto simulací jsme zkoumali vznik charakteristických iontových snímků a vyhodnotili dvě základní konfigurace iontové deflektometrie, kde sondující svazky vstupují do z-pinče radiálně nebo podél jeho osy. Poté jsme se zaměřili na zkoumání deuteriových svazků s energiemi v řádu MeVů, které byly urychleny po přerušení proudu na zařízení GIT-12, ale byly pozorovány i na jiných z-pinčových zařízeních. Numerickou reprodukcí našich experimentálních deuteronových snímků získaných na zařízení GIT-12 jsme určili prostorové rozložení a maximální divergenci deuteronových zdrojů pro více energií. Navíc jsme provedli měření maximálních hodnot dráhových integrálů magnetických polí. Po diagnostice těchto deuteronových svazků a jejich zdrojů jsme vyvinuli unikátní způsob jejich využití pro deflektometrická měření. Díky tomu jsme provedli vůbec první měření magnetických polí s využitím z-pinčem vytvořeného zdroje deuteronů pro jejich podsvícení. Pro záznam výchylek deuteronů byla mezi elektrody umístěna deflektometrická mřížka, aniž by došlo k potlačení zdroje deuteronů nebo zničení implodujícího plazmatu. Při těchto měřeních jsme pro několik shotů určili celkové proudy a plošné rozložení magnetických polí integrovaných podél dráhy deuteronů. Naše experimentální uspořádání umožnilo klíčovou aproximaci trajektorií deuteronů, která umožňuje měřit zprůměrovaná B-pole analyticky a přímo z experimentálních dat. Nakonec jsme použili náš numerický kód a boční rentgenový snímek implodujícího z-pinče k získání průřezové mapy magnetických polí. Tyto výsledky překvapivě ukázaly, že významná část proudu teče až za horkou a hustou oblastí z-pinče.

Klíčová slova: Magnetická pole, z-pinč, plasma, iontová deflektometrie, radiografie, urychlování iontů, diagnostika pro měření magnetických polí

Acknowledgements

I would like to express gratitude to my supervisor prof. Daniel Klír for his support, patience, and guidance through the adventurous journey of my Ph.D. studies. In particular, I would like to thank him for his fair criticisms and the heated discussions leading to substantial improvements in my research and this thesis. Also, I would like to thank my supervisor Dr. Karel Řezáč for his understanding attitude, his help with my numerical code, the technical and administrative issues.

My sincere thanks go to my collaborators in our research group for conducting experimental measurements and making very friendly atmosphere with the high “positive” energy density at our workplace. I would also like to thank my colleagues in the Department of Physics.

I greatly appreciate the work of the team at the GIT-12 facility in Tomsk, who enabled our “small” research group to perform experiments on the “large” MA pulsed-power device and thus achieve unique results and discoveries.

I would like to gratefully acknowledge the financial support provided by the GACR projects GA19-02545S “Current disruption and magnetic energy dissipation during acceleration of electrons and ions in z-pinch plasmas” and GA23-04679S “The study of z-pinch physics with novel diagnostic methods using fast ions”, in addition to the SGS project and SGS22/161/OHK3/3T/13: “Electric Discharges III: experimental research, modeling and applications”.

Finally, I would like to thank my family for their incredible support and patience, even though they may not have fully understood the scientific passion that kept me going.

Contents

Abstract	iii
Acknowledgements	vii
1 Introduction	1
1.1 Motivation and the goal of the thesis	1
1.2 Structure of the thesis	2
1.3 Comparison of laser-driven and z-pinch HED plasmas	2
1.4 Z-pinch	4
1.4.1 Equilibrium z-pinch	6
1.4.2 Instabilities	8
1.5 Applications of the fast z-pinches	11
1.5.1 Neutron-diagnosed subcritical experiments	11
1.5.2 Material and surface studies	12
1.5.3 Astrophysical jets and shocks	14
1.5.4 Magnetic reconnections	14
1.5.5 Equation of state, conductivity measurements	16
1.6 Classical diagnostic methods for B-field measurement in z-pinches	16
2 Measuring of EM fields using ion deflections	19
2.1 Characterization of the ion radiography/deflectometry method	20
2.2 Typical proton sources for the deflectometry measurements	20
2.2.1 TNSA-based broadband proton source	21
2.2.2 Fusion-based monoenergetic proton source	21
2.3 Ion detectors for ion deflectometry	23
2.3.1 Solid-state nuclear track detectors CR-39	23
2.3.2 Radiochromic films (RCFs)	24
2.4 Analysis of the ion deflections	28
2.4.1 Electric deflections	30
2.4.2 Magnetic deflections	32
2.4.3 Paraxial approximation	34
2.5 Proton radiography/deflectometry experiments in HED plasmas	39
2.5.1 Proton imaging of laser-produced plasmas	39
2.5.2 Proton deflectometry in z-pinch plasmas	44
3 Feasibility of proton deflectometry in z-pinches	49
3.1 Development of our ion-tracking numerical code	49
3.2 Selected results of our paper Munzar et al., IEEE (2018) with additional comments	50
3.2.1 Radial deflectometry of the azimuthal B-fields	51
3.2.2 Axial deflectometry of the azimuthal B-fields	58
3.2.3 Radial-axial deflectometry of the azimuthal B-fields	65

4	Characterization of MeV ion sources in z-pinches	67
4.1	Hybrid gas-puff z-pinch driven by the GIT-12 generator	68
4.2	Ion diagnostics on GIT-12	70
4.3	Experimental observations made with ion diagnostics on GIT-12	72
4.3.1	Characteristic radial lines captured by the beam-profile detector	72
4.3.2	Characteristic rings captured by the pinhole cameras	74
4.4	Investigation of the origin of the ring structures observed by the pinhole camera	77
4.5	Selected results of our paper Klir et al., PPCF (2020) with additional comments	81
4.5.1	Ion multi-pinhole images	81
4.5.2	Ion three-pinhole images	85
4.5.3	Ion pinhole images on the HAWK generator at the Naval Research Laboratory	88
4.6	Ring formation in ion pinhole images dominated by the distribution of azimuthal B-fields	90
5	Z-pinch-driven ion deflectometry measurements	99
5.1	Development of the z-pinch-driven ion deflectometry in z-pinches	100
5.2	Larmor orbit approximation	105
5.3	Analysis of the synthetic deflectograms of characteristic B-fields profiles	110
5.4	Experimental results of our paper Munzar et al., POP (2021) with additional comments	113
5.4.1	Estimation of the enclosed pinch current from the D-grid edge's displacement	115
5.4.2	Mapping xy profiles of the azimuthal B-fields employing the Larmor orbit approximation	116
5.4.3	Mapping rz profile of the azimuthal B-fields in the shot 2420 using numerical simulations	117
6	Thesis summary and future prospects	125
6.1	Summary	125
6.2	Future prospects	128
A	Own contributions of the author	131
B	Source codes of our numerical simulations	133
B.1	Models of the azimuthal magnetic fields	133
B.2	3D B-fields of the sloped z-pinch	136
B.3	Boris Pusher	137
B.4	Grid filter	139
C	Publications in Impacted Journals	143
	Publications related to this thesis	143
	Other publications	144
D	List of presentations	147
D.1	International conference	147
D.1.1	Oral presentations	147
D.1.2	Poster presentations	148
D.2	Student conferences	148
D.2.1	Oral presentations	148
D.3	Seminars at foreign institutions	149
E	List of international internships	151

F	List of international experimental campaigns	153
G	Selected papers	155
G.1	Article: Munzar et al., IEEE Trans. Plasma Sci. (2018)	155
G.2	Article: Klir et al., PPCF (2020)	166
G.3	Article: Munzar et al., POP (2021)	180
	Bibliography	219

Chapter 1

Introduction

1.1 Motivation and the goal of the thesis

High energy-density (HED) plasmas with high densities and temperatures represent extreme and exciting environments found in numerous places in the Universe but they do not occur naturally on Earth. These extreme conditions can be reproduced in the laboratory using powerful lasers or pulsed-power electric generators. HED plasmas are investigated for fundamental understanding of physical phenomena and various applications. Strong B-fields and electric currents, which may arise in these plasmas, have an important role in the plasma's dynamics.

So-called z-pinchs are one of the simplest forms of HED plasma. They are driven by strong electric kA-MA currents flowing along the z-axis (hence, the letter “z” in their name). The designation of a “pinch” originates from a strong radial magnetic force created by the axial currents and their azimuthal B-fields, which compresses plasmas and results in high plasma densities and temperatures. Even though topologies of currents and B-fields are essential in the formation and motion of z-pinch's hot plasmas, B-field measurements in z-pinchs are difficult due to the limitations of the classical diagnostic methods in the HED plasma environment. With the dawn of this millennium, a new diagnostic method, called ion deflectometry or ion radiography, was invented to diagnose laser-generated HED plasma, which is now commonly and successfully performed experimentally. There has been an effort to introduce this method into the z-pinchs. However, dedicated experiments and analysis achieved only partial successes while still requiring a powerful laser-pulse system unavailable in most z-pinch facilities.

This thesis aims to develop an alternative to the ion deflectometry method capable of measuring the B-field distributions in typical MA z-pinchs without the necessity of the laser-driven ion source. The core of this thesis is the results of three papers published in the peer-view journals, which reflect a journey of evolution this alternative diagnostic method. The selected papers are complemented by comments and additional analysis and results from the subsequent research to put them into perspective. This thesis guides us through the development of the ion deflectometry method, from reviewing the most important proton radiography experiments in the laser-produced and z-pinch plasmas to deriving the general equations for ion deflections

in magnetic fields and analyzing fundamental deflectometry configurations until finding the ion source produced within the z-pinch during its evolution and capable of ion imaging the z-pinch plasmas, and finally performing the first-ever ion deflectometry B-fields measurements providing the 2D (rz) topological map of local B-fields and other results.

1.2 Structure of the thesis

We have divided this thesis into five chapters. In the introduction (Chap. 1), we characterize the high-energy-density (HED) plasmas, then focus on the z-pinches and summarize their applications. In Chapter 2, we report the current state of the ion deflectometry technique for measurements of electric and magnetic fields in laser-generated plasmas. We discuss conventional sources of ion backlighting and ion detectors. Furthermore, we derive generalized equations for the ion deflections in perpendicular electric and magnetic fields. Afterward, we describe a theoretical analysis of ion deflectometry in the classical setup using the paraxial approximation. At the end of the chapter, we review the most interesting phenomena investigated by ion (proton) radiography in the laser-produced plasma experiments and evaluate its development in the z-pinches. In Chapter 3, we present the results published in our first selected paper [1] and introduce our own numerical ion-tracking code. Using this code, we investigate possibilities of proton deflectometry in z-pinch plasmas arranged in two fundamental experimental setups with the laser-driven ion (proton) source. The following chapters present our results published in two selected papers focused on our experiments with the hybrid gas-puff z-pinch GIT-12. In Chapter 4, we use ion pinhole diagnostics to characterize a z-pinch-driven source of MeV deuterons. Using experimental ion images and our simulations, we study the spatial distribution and the divergence of this deuteron source. These results are published in our paper [2]. Despite having sufficient energy and divergence, we find that deuteron beams accelerated in the z-pinch plasmas cannot be employed in the classical setup for the ion deflectometry B-field measurements. However, Chapter 5 related to our paper [3] describes the steps from the proposal of an alternative experimental setup to the first deflectometry measurements of z-pinch B-fields using the z-pinch-driven ion (deuteron) backlighter. The experimental ion images (deflectograms) provide information about the magnitude of enclosed currents flowing through the z-pinch, spatial distribution of averaged, and, in one experiment, even local azimuthal B-fields.

Since we desire to transfer the ion deflectometry from the laser-generated plasmas to z-pinches, the following section briefly compares both in the context of high-energy-density plasmas.

1.3 Comparison of laser-driven and z-pinch HED plasmas

HED plasmas are characterized by high densities and temperatures resulting in energy densities above 100 kJ/cm^3 , which correspond to pressures of $>1 \text{ Mbar}$ [4]–[6]. Fig. 1.1) puts HED plasmas

(blue regions) into the wider context of other plasmas according to their temperatures and particle densities. Interestingly, a boundary of the HED plasma is not a straight line. At lower densities, the boundary is horizontal because the plasma is dominated by radiation (more than collisional) processes, and thus, the pressure is set mainly by the plasma temperature T . With the increase of the plasma density, the thermal pressure becomes comparable with the radiation pressure, and the HED-plasma boundary slopes downwards. In extremely dense plasmas, plasma particles become strongly coupled, and the Fermi pressure of degenerate electron gas becomes significant. Thus, the boundary of HED plasmas in Fig. 1.1 falls vertically (green line) into the region of high-density condensed matter. The HED plasma is bounded from above by a relativistic limit (orange line) of the kinetic energy of plasma particles.

HED plasmas occur in the stellar interiors, brown or white dwarfs, galactic nuclei, accretion disks of black holes, and supernovae. These astrophysical objects are out of our earthly reach, but we can investigate some of their properties by reproducing temporarily-comparable HED plasmas in the laboratory. In addition, HED-plasma devices can produce a so-called Warm Dense Matter (WDM) coupled with many exciting processes, for example, inside the giant planets. WDM is usually excluded from the HED plasma definition and, in Fig. 1.1, is situated between condensed matter and HED plasmas because its temperatures are in terms of eV.

To produce HED laboratory plasmas, we must accumulate energy for an extended period of time and then quickly deliver it into a small spatial domain of the plasma. Since we cannot continuously supply the plasma volume with a high-energy flow, laboratory HED plasma experiments are short-lived, and we refer to them as *shots*. This thesis discusses two ways to achieve HED plasmas: intense lasers and electric pulsed-power generators, with a focus on the latter.

In the case of lasers, energy is pumped into the active laser medium through electron excitation and then quickly released by the stimulated emission of light. When photons from an intense laser pulse are focused onto a very small area (in terms of hundreds of μm^2), HED plasmas are created via the interaction of the laser with a target. Densities of laser-produced plasmas can reach up to extreme densities of a solid-state matter ($n_e \sim 10^{31} \text{ m}^{-3}$) and temperatures in terms of keV. The duration of the laser-produced plasma corresponds to the duration of the driving laser pulse and is in terms of hundreds of ns up to a few ps. The short pulse duration allows achieving the high power delivered into the plasma (up to a few PW). The PW-power fs-pulse lasers can efficiently accelerate ions (protons, most commonly) up to energies of tens of MeV by non-linear interactions with a target via Target Normal Sheath Acceleration (TNSA) mechanism [7], [8]. Laser-driven ion acceleration offers broad possibilities for applications [9], [10]. Laser-accelerated ions have been proposed for the fast ignition in the inertial confinement fusion (ICF) [11], [12]; hadron therapy for cancer treatment (recent tests and the state-of-the-art review in [13]–[15]); isochoric heating to achieve Warm-Dense-Matter states for studies of fundamental material properties, such as the equation of state (EOS), the material opacity or conductivity [16]–[18]; and finally, the proton deflectometry/radiography measurements (see Subsec. 2.5.1), coupled with the topic of this thesis. For ion imaging, the main advantages of lasers are their high flexibility and reproducibility. Moreover, utilizing multiple beamlets allows simultaneous

production and diagnosis of various plasmas phenomena. The main disadvantages of laser systems are the high cost and the low efficiency of light conversion.

In the case of pulsed-power generators, the electric energy is collected by capacitor banks and then quickly delivered (in ~ 100 ns – a few μ s) into an experimental load (gaseous or solid), creating HED plasma with typical spatial scales in terms of cm. As a result, a high (kA–MA) electric current starts to flow through the plasma while creating strong B-fields. Currents and B-fields together generate a magnetic Lorentz force $\mathbf{J} \times \mathbf{B}$, which implodes and compresses the plasma up to high densities ($n_e \sim 10^{26}$ m $^{-3}$) and pressures (~ 1 GBar), and creates a pinch. Because the “pinching” force acts towards the plasma, the *pinches* are magnetically confined current filaments. If the pinch current flows in one dominant direction, which we couple with the z -axis, we refer to these plasmas as z -*pinches*. The z -pinches share some advantages with laser plasmas, namely, the high control of input parameters and good reproducibility of the HED plasmas in the experiment. Compared to lasers, the pulsed-power generators are less expensive and can deliver more energy into the plasma with larger volumes and a longer duration. In contrast with lasers, the z -pinch devices excel in converting the electric energy into the plasma’s internal energy (up to $\sim 40\%$ [19]). Moreover, z -pinches with a high atomic number Z_i (e.g., created from metal wires) are powerful (350 TW power, 2.8 MJ radiated energy) and the most efficient X-ray radiators ($\sim 15\%$ [20], [21]). Z -pinches with the deuterium load are also efficient sources of neutrons (up to 6×10^7 neutrons per Joule of plasma energy [22], [23]). The disruption of the z -pinch can produce fast ions [24]–[27] and relativistic electrons [28]–[30]. Fig. 1.1 puts laser-produced and z -pinch plasmas in the context of other plasmas according to their temperature and plasma densities.

1.4 Z-pinch

The z -pinches are an exciting type of HED plasmas common in nature. They are observed in bead lightnings [37], solar winds [38], collimated astrophysical jets from active galactic nuclei [39], [40], and other magnetized filamentary structures. The z -pinches have been studied for decades for their conceptual simplicity. In the laboratory, they occur in various configurations, such as wire arrays or plasma foci. However, in all of them, a current density J_z oriented along the z -axis of a cylindrical plasma column generates azimuthal B-fields B_φ . The currents $\mathbf{J}_z = (0, 0, J_z)$ and azimuthal B-fields $\mathbf{B}_\varphi = (0, B_\varphi, 0)$ together¹ produce a magnetic Lorentz force with a density $\mathbf{f}_r = \mathbf{J}_z \times \mathbf{B}_\varphi$ acting radially inwards on the plasma (illustrated in Fig. 1.2). For general interacting \mathbf{J} and \mathbf{B} , their cross product $\mathbf{J} \times \mathbf{B}$ is often referred to as the “J-cross-B” force. Through this force, the stored electric energy is transformed into the kinetic energy of the

¹The coexistence of the current density J and the associated B-fields B at the same point may not be apparent. For example, an infinitely thin planar current layer would not be pushed by the $\mathbf{J} \times \mathbf{B}$ force because the magnetic field B is zero where the currents flow. Therefore, the finite thickness of the current layer is principally required so that current J in the given place interacts with B-fields generated by currents flowing through surrounding plasmas. Alternatively, the current-layer plane must be azimuthally closed so that the current J in a given layer element interacts with B-fields created in elements on the opposite side of the layer.

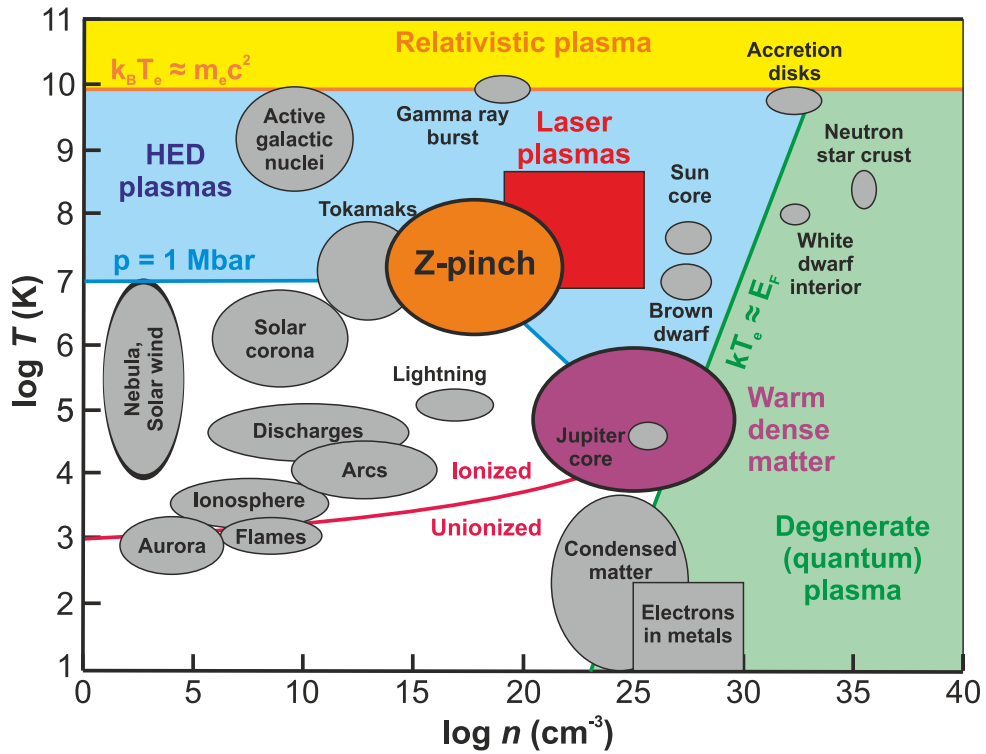


Figure 1.1: Temperatures and plasma densities of various types of plasmas. High-energy density plasmas are in a blue area. The graph has been compiled from [31]–[36].

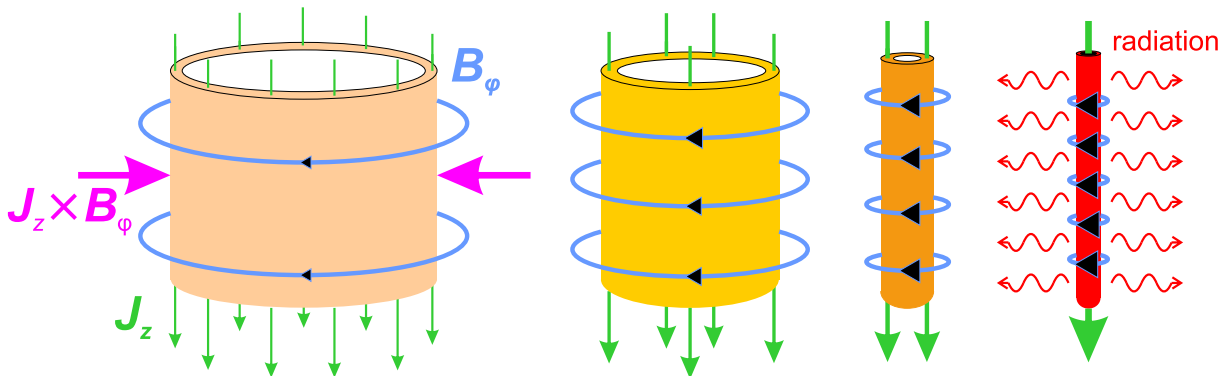


Figure 1.2: A “pinch effect”: Axial currents J_z flowing through the axis of a cylindrical plasma load create azimuthal B-fields B_ϕ . Together, they produce the radial “pinching” $\mathbf{J} \times \mathbf{B}$ force, which implodes and compresses the plasma. Through its implosion, the z-pinch transforms the electric energy into the kinetic energy of the implosion and then into the plasma’s internal energy. The compressed and magnetized load reaches high temperatures and densities and creates a z-pinch. Highly magnetized and high-energy-density environments and radiation (soft x-rays and fast particles) are prominent features of the z-pinch.

implosion, compressing and heating the plasma to high densities n and temperatures T . Ions and electrons travel together with the same velocity due to the quasineutrality, which results in the non-equal temperatures of electrons ($T_e \approx 0.1 - 1$ keV) and ions ($T_i \approx 1 - 100$ keV) in the compressed hot plasma.

Due to the compression, the thermal (kinetic) pressure $p = nk_bT$, where k_b is the Boltzmann constant, begins to rise. It acts against the compressing effect of the pinching $\mathbf{J}_z \times \mathbf{B}_\varphi$ force and tends to expand the plasma. The relation between the pressure gradient ∇p and the $\mathbf{J}_z \times \mathbf{B}_\varphi$ force determines the dynamics of the z-pinch plasma by the motion equation

$$\rho_m \frac{d^2 \mathbf{r}}{dt^2} = -\nabla p + \mathbf{J}_z \times \mathbf{B}_\varphi, \quad (1.1)$$

where ρ_m is the volumetric mass density of the plasma. Several other terms may appear in Eq. (1.1), such as plasma viscosity and the plasma accretion, but we assume them to be negligible compared to the pressure and the magnetic Lorentz force. If we assume a φz -symmetry ($\partial/\partial\varphi = \partial/\partial z = 0$) we can rewrite Eq. (1.1) into

$$\rho_m(r)\ddot{r}(r) = -\frac{\partial p(r)}{\partial r} + J_z(r)B_\varphi(r). \quad (1.2)$$

Using Ampers's law

$$\mu_0 J_z = (\nabla \times \mathbf{B}_\varphi)_z = \frac{1}{r} \frac{\partial(rB_\varphi)}{\partial r}, \quad (1.3)$$

where μ_0 is the permeability, we obtain an equation for the radial motion of the z-pinch

$$\rho_m(r)\ddot{r}(r) = -\frac{\partial}{\partial r} \left(p(r) + \frac{B_\varphi^2(r)}{2\mu_0} \right) - \frac{B_\varphi^2(r)}{\mu_0 r}. \quad (1.4)$$

The $B_\varphi^2/(\mu_0 r)$ term on the right-hand side (RHS) of Eq. (1.4) represents the magnetic tension, which acts radially inwards to straighten the curvature of the magnetic lines. The first term on the RHS of Eq. (1.4) represents a sum of gradients of the kinetic (thermal) $p = nk_bT$ and magnetic pressure $p_M = B_\varphi^2/(2\mu_0)$. The plasma confinement is often described by a pressure ratio called the plasma beta $\beta = p/p_M$. For $\beta < 1$, the magnetic pressure p_M exceeds the kinetic pressure p , and the plasma is compressed and strongly magnetized. For $\beta > 1$, the plasma is insufficiently confined, and the plasma tends to expand.

The magnetic and thermal forces can maintain hot dense plasmas in the equilibrium state if the forces are balanced out. Thus, we now investigate the equilibrium z-pinch and its stability.

1.4.1 Equilibrium z-pinch

In the case of the equilibrium z-pinch, the left-hand side of Eq. (1.4) is zero ($d^2r/dt^2 = 0$) resulting in an equation

$$0 = \frac{\partial}{\partial r} \left(p(r) + \frac{B_\varphi^2(r)}{2\mu_0} \right) + \frac{B_\varphi^2(r)}{\mu_0 r}. \quad (1.5)$$

Then, for the pressure gradient, we get

$$\frac{\partial p(r)}{\partial r} = -\frac{1}{2\mu_0 r^2} \frac{\partial r^2 B_\varphi^2(r)}{\partial r}. \quad (1.6)$$

If we write $B_\varphi(r)$ in terms of the electric current $I(r) = \int_0^r 2\pi r' J_z(r') dr'$ enclosed within the radius r and use Amper's law in the following form

$$B_\varphi(r) = \frac{\mu_0 I(r)}{2\pi r}, \quad (1.7)$$

we can simplify Eq. (1.6) and find the relation between the enclosed current $I(r)$ and the kinetic pressure $p(r)$

$$-\pi r^2 \frac{\partial p(r)}{\partial r} = \frac{\mu_0}{8\pi} \frac{\partial I^2(r)}{\partial r}. \quad (1.8)$$

Eq. (1.8) shows that the distribution of the plasma pressure $p(r)$ in the equilibrium z-pinch depends on the profile of the enclosed current $\partial I(r)$, which is coupled with the spatial distribution of the current density $J_z(r)$ and the azimuthal B-fields $B_\varphi(r)$. Note that the enclosed current $I(r)$ in Eq. (1.8) is integrated over the z-pinch cross-section within the radius r and so it represents local currents $J_z(r)$ only indirectly. Moreover, $I(r)$ is a monotonically increasing function as long as currents $J_z(r)$ do not change the axial orientation along the radius, and it remains a constant when there are no currents $J_z(r)$. It means that the function $\partial I^2(r)/\partial r$ is always positive, and it follows from Eq. (1.8) that the pressure of the equilibrium z-pinch must be monotonically decreasing with the radius ($\partial p/\partial r < 0$).

In order to solve Eq. (1.8) for the distribution of the enclosed current $I(r)$, it is reasonable to define a similar integrated quantity coupled with the pressure $p(r)$. Therefore, we introduce a quantity $\widehat{U} = \int_0^r 2\pi r' p(r') dr'$, corresponding to the linear density of the thermal energy U . If we integrate Eq. (1.8) by parts ("per-partes"), we find an equilibrium equation for a cross-section of the z-pinch at a given radius r

$$\widehat{U}(r) - \frac{r}{2} \frac{\partial \widehat{U}(r)}{\partial r} = \frac{\mu_0}{8\pi} I^2(r), \quad (1.9)$$

where $(r/2)\partial\widehat{U}(r)/\partial r$ corresponds to the antiderivative $[\pi(r')^2 p(r')]_0^r = \pi r^2 p(r)$. To evaluate the equilibrium of the whole cross-section of the z-pinch, we must take a radius r to its outer boundary, given by a *pinch radius* R_p , where $p(r = R_p) \rightarrow 0$ and $J_z(r = R_p) \rightarrow 0$. Accordingly, the second term on the left-hand side (LHS) of Eq. (1.9) goes to zero. The total linear energy density becomes $\widehat{U}_p = \widehat{U}(R_p) = \int_0^{R_p} 2\pi r' p(r') dr'$. Then, we obtain the famous relation of the Bennett equilibrium for the z-pinch [41]

$$\widehat{U}_p = (1 + \overline{Z}_i) \widehat{N}_i k_b T_B = \frac{\mu_0}{8\pi} I_p^2 \quad (1.10)$$

where $I_p = I(R_p)$ is the total current flowing through the z-pinch, \overline{Z}_i is the averaged ion charge, and \widehat{N}_i is the ion linear number density. The quantity T_B , called the Bennett temperature, is

the temperature of the z-pinch weighted over the plasma density

$$T_B = \frac{\int_0^{R_p} 2\pi r (n_i k_b T_i + n_e k_b T_e) dr}{\int_0^{R_p} 2\pi r (n_i k_b + n_e k_b) dr}, \quad (1.11)$$

where e and i subscripts denote the electron and ion components of plasma. The plasma pressure is given by a sum of its electron and ion components $p = p_e + p_i = n_e k_b T_e + n_i k_b T_i$. If the plasma is isothermal ($T_e = T_i$), the weighted temperature T_B equals the average plasma temperature ($T_B = \overline{T_e} = \overline{T_i}$). It follows from Eq. (1.10) that the z-pinch temperature grows with the total current flowing through the z-pinch. Therefore, both the profile and magnitude of the currents are important for maintaining the hot plasmas of the z-pinch.

In practice, the Bennett equilibrium usually occurs only for a short time, if ever, because the z-pinch is usually unstable due to magneto-hydrodynamic (MHD) instabilities. In the next section, we introduce the most important ones.

1.4.2 Instabilities

To study the instabilities of the equilibrium z-pinch, we analyze perturbations of its surface. From the equilibrium equation $\nabla p = -\mathbf{J}_z \times \mathbf{B}_\varphi$, it follows that currents \mathbf{J}_z and magnetic fields \mathbf{B}_φ are perpendicular to the pressure gradient. It means that these currents flow through surfaces of the constant pressure, which are identical to the magnetic surfaces of the constant B-fields. Let a function $\psi(r, \varphi, z, t)$ represent physical quantities constant over these surfaces. We assume that the instability is a small linear-wave perturbation $\psi_1(r)$ of the symmetrical stationary function $\psi_0(r)$. Therefore, $\psi(r, \varphi, z, t) = \psi_0(r) + \psi_1(r, \varphi, z, t)$. Then, we separate the radial perturbation $\psi_r(r)$ and write

$$\psi_1(r, \varphi, z, t) = \psi_r(r) e^{i(k_\varphi \varphi + k_z z - \omega t)}, \quad (1.12)$$

where k_φ and k_z are azimuthal and axial wavenumbers, respectively, ω is the angular wave frequency, and $\Gamma = \text{Im}(\omega)$ is the growth rate of the instability. Because the plasma surface is azimuthally enclosed, the perturbation ψ_1 must be periodical with respect to the azimuthal angle φ [$\psi_1(r, \varphi + 2\pi, z, t) = \psi_1(r, \varphi, z, t)$]. Therefore, $e^{ik_\varphi 2\pi} = 1$, and we can substitute the azimuthal wave number k_φ with a mode number m . Fig. 1.3 illustrates the most important instability modes: an axisymmetrical $m = 0$ instability, called the *sausage* instability, and an asymmetrical $m = 1$ instability called the *kink* instability. In the case of the $m = 0$ instability, the local increase of magnetic pressure causes a symmetrical constriction of the plasma and the creation of the plasma neck. The plasma in this neck is pushed out along the z-axis, which can lead to breaking the z-pinch column. In the case of the $m = 1$ instability, the magnetic pressure builds up in one side of the z-pinch column and elongates the z-pinch sideways.

The z-pinch is unstable if $\text{Im}(\omega) > 0$. Then, the growth rate of the MHD instabilities Γ is proportional to v_A/R_p [43], where R_p is the pinch radius and v_A is a so-called Alfvén velocity $v_A(R_p) = B_\varphi(R_p)/\sqrt{\rho_m \mu_0}$. The Alfvén velocity v_A characterizes the typical rate of the

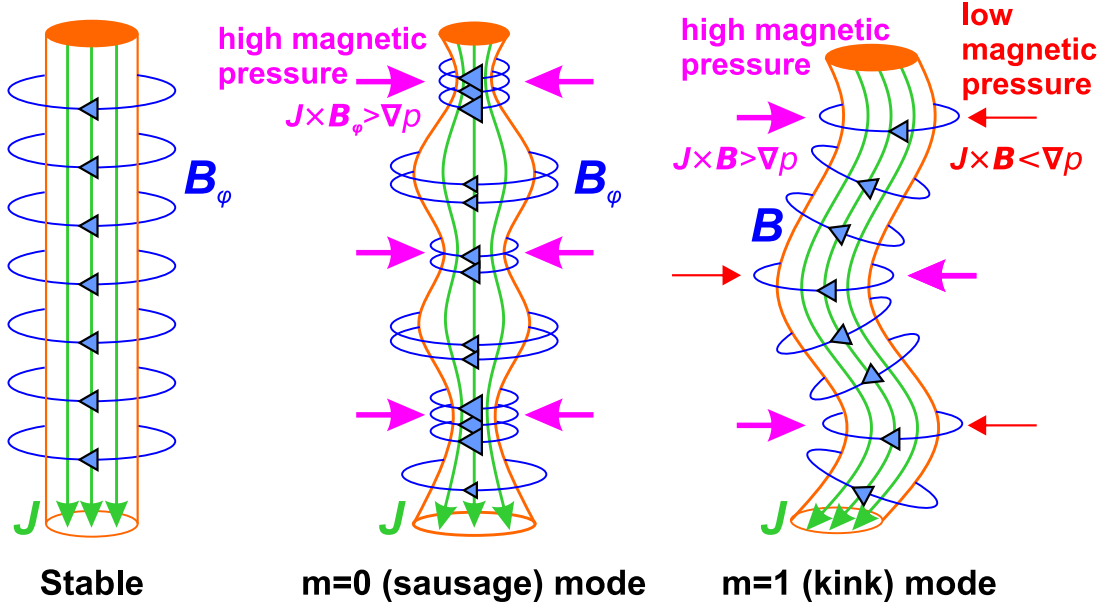


Figure 1.3: Comparison of the stable z-pinch and its two MHD instabilities, the sausage ($m = 0$) and kink ($m = 1$) modes, produced due to the local imbalance between the magnetic and the plasma pressure. [42]

magnetized plasma's dynamics, and the pinch radius R_p the typical spatial scale.

Now, we discuss the conditions of the z-pinch stability, when $\text{Im}(\omega) < 0$. The z-pinch is $m = 0$ stable, if the pressure profile satisfies the Kadomtsev's condition for any r [43]–[45]

$$-\frac{d \ln p(r)}{d \ln r} = -\frac{r}{p(r)} \frac{dp(r)}{dr} < \frac{4\gamma}{2 + \gamma\beta(r)}, \quad (1.13)$$

where γ is the heat capacity ratio and $\beta(r) = 2\mu_0 p(r)/B_\phi^2(r)$ is the plasma beta. It follows from Eq. (1.13) that the pressure in the stable z-pinch must decrease gradually. In the infinity, $\beta \xrightarrow{r \rightarrow +\infty} 0$, so the pressure must decrease slower than $r^{-2\gamma}$. In the isentropic process, we get $p(r) \propto \rho_m^{-\gamma}$, and thus, the mass density is required to decrease slower than r^{-2} , which is not comparable with the finite line mass condition. Therefore, the condition (1.13) is met only if the density ρ_m does not fall to zero (in the so-called gas-embedded z-pinch) or the temperature $T(r)$ grows so fast that the pressure $p(r)$ decreases slower with the radius r than the density $\rho_m(r)$ (strong skin-effect) [45]. However, the tailoring of the profile distribution cannot stabilize the kink instability.

For $m \geq 1$ stability, the B-field profile must satisfy the following condition [46]

$$\frac{r^2}{B_\phi(r)} \frac{d}{dr} \left(\frac{B_\phi(r)}{r} \right) < \frac{m^2 - 4}{2}. \quad (1.14)$$

If the current-density profile grows as $J_z(r) \propto r^{n_J}$, the stability condition in Eq. (1.14) can be written using the current-density polynomial exponent $n_J \geq 1$ as follows [47]

$$m^2 \geq 2n_J + 4 \quad (1.15)$$

Eq. (1.15) shows that any z-pinch with the non-singular current density is $m = 1$ unstable. By employing the conductive wall around the z-pinch, the plasma displacement can produce the feedback control of magnetic fields via the induction of Eddy currents in the wall, which can negate the perturbation of the $m = 1$ instability to a certain extent. However, the conductive wall must be very close to the plasma, which is usually impractical.

The z-pinch stability of all modes can be improved by embedding strong external axial B-fields B_z into the plasma [48], [49]. The additional magnetic pressure $B_z^2/2\mu_0$ inside the z-pinch, together with the thermal pressure p , help to balance the compressing magnetic pressure $B_\phi^2/2\mu_0$. Hence, they can stabilize the z-pinch and mitigate the instabilities to a certain extent. On the other hand, at the price of better stability, the axial B-fields B_z slow down the implosion velocity [48] of the current sheath due to higher magnetic pressure inside the plasma, which results in lower thermal pressures during the stagnation. To summarize this analysis, we conclude that, in realistic cases, the equilibrium z-pinch is always unstable at least for $m = 0$ and $m = 1$.

However, MHD instabilities may occur even during the implosion and complicate the energy transport. The most important dynamic instability is the magnetic Rayleigh-Taylor (MRT) instability. It occurs when the vacuum-plasma interface with the considerable mass density gradient $\nabla\rho_m$ is accelerated into the vacuum magnetic fields B_0 (magneto-fluid), which is parallel to the interface. In the z-pinch, the acceleration \mathbf{g} is produced by the inward $\mathbf{J} \times \mathbf{B}$ force but the plasma experiences the outwards acceleration $\mathbf{a} = -\mathbf{g}$ in its laboratory reference frame due to the inertial force. The MRT instability condition $\mathbf{a}\nabla\rho_m < 0$ infers that the outer surface of the plasma layer is MRT unstable during the accelerated implosion. The dispersion relation of the MRT instability is $\omega_{MRT}^2 = |\mathbf{g}|k - 2(\mathbf{k} \cdot \mathbf{B}_0)^2/(\mu_0\rho_m)$, where the k is the instability wave number. The MRT instability is mitigated by the density profile tailoring or embedding of the axial B-fields [50].

The stability of the equilibrium z-pinch is important, for example, for achieving thermonuclear plasmas. Without sufficient stability, z-pinch have not been as yet capable of reaching the necessary conditions for thermonuclear fusion with positive energy gain. However, there are still a few specialized z-pinch devices focused on the production and confinement of hot thermonuclear plasmas. They employ either magnetized liner preheated by a laser pulse in a concept of Magnetized Liner Inertial Fusion (MagLIF) [19], [51]–[53], or the stabilization of the z-pinch using a shear-flow plasma [54]–[56].

Interestingly, the inherent instability of z-pinch is beneficial for various applications which use rapid z-pinch disruptions to generate intense bursts of ions, electrons, neutrons, x-rays, or gamma rays. To that end, the z-pinch devices are designed to produce a fast implosion of the plasma bringing high currents close to the axis, followed by rapid dissipation of the stored magnetic energy into ion and electron beams accelerated by induced electric fields. Since the implosion plays a vital role in the energy transfer, we refer to these z-pinch as “fast” or “dynamic” [57].

1.5 Applications of the fast z-pinches

The applications of the fast z-pinches exploit either the extreme environments of magnetized HED plasmas (e.g., heat fluxes, soft x-ray thermal radiation, strong magnetic fields) or products of the z-pinch disruptions (e.g., fast ion and electron beams, beam-target neutrons and hard x-ray bremsstrahlung).

The fast dissipation of z-pinch's B-fields induces strong transient E-fields that accelerate ion and electron beams to high energies. When the accelerated electrons hit the anode or another metal part of the vessel, they produce hard X-ray (HXR) bremsstrahlung emission. In the case of the deuterium load, accelerated ions can produce fusion neutrons when they collide with surrounding z-pinch plasma (i.e., a beam target). The beam-target neutrons predominantly contribute to the z-pinch's high neutron yield. The number of thermonuclear neutrons originating from the magnetically confined HED plasmas is usually negligible, which was noted by Kurchatov in 1956 [58]. The exceptions represent specialized thermonuclear-fusion-focused experiments (e.g., MagLIF).

In particular, the dense plasma focus (DPF) is a common type of z-pinch device exhibiting reliable and very high neutron yields per shot with high repeatability. It can be used as a relatively cheap external source of multi-MeV neutrons. Its schematic is illustrated in Fig. 1.4. After applying high voltage to the coaxial electrodes, an electric discharge occurs close to the insulator separating the electrodes. The $\mathbf{J} \times \mathbf{B}$ force driven by the pulsed-power generator accelerates a current sheath axially along coaxial electrodes. During the axial acceleration, the drive current increases, and the current sheath ionizes and heats the gas, filling the electrode system. After the current sheath reaches the end of the central electrode, it is pulled out axially by the continuing axial acceleration. An axial current density J_z created by elongation of the current layer generates a strong radial component of $\mathbf{J} \times \mathbf{B}$ force pushing the plasma radially. The current layer implodes until it collides with itself in the on-axis region. It leads to the plasma compression, which we call a plasma focus.

In another common type of the z-pinch, the experimental load is in the form of one or multiple metal wires with a few to a few tens of micrometers in diameter arranged in an array. Hence we call it a wire array. When the electric current is driven through these wires, the wires start to ablate and generate metal plasma with the high atomic number Z_i . Due to the $\mathbf{J} \times \mathbf{B}$ force, the plasma implodes towards the axis and creates a dense z-pinch strongly radiating in the soft x-ray region.

In the following two subsections, we demonstrate how beam-target-fusion neutrons and accelerated ions and electrons are used for industrial applications by pulsed-power z-pinch devices.

1.5.1 Neutron-diagnosed subcritical experiments

Studying plutonium, highly enriched uranium, and other special nuclear material (SNM) under conditions encountered in a nuclear weapon is essential for the safety of the stockpiled nuclear arsenal. To that extent, subcritical amounts of weapon-relevant SNM can be repeatedly exposed

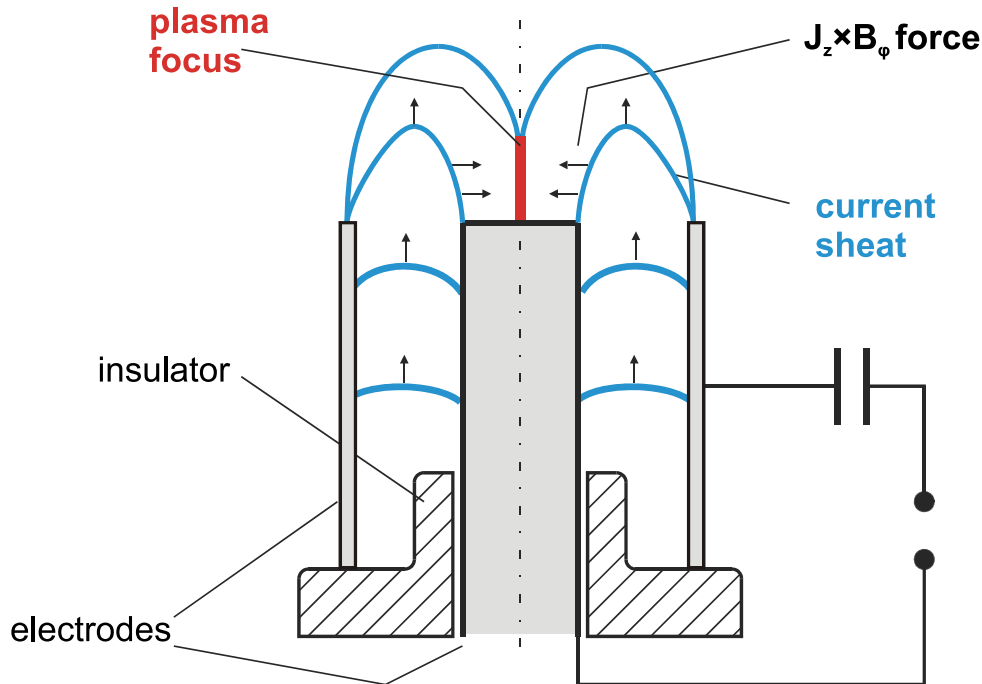


Figure 1.4: Schematics of the plasma focus configuration

to a short neutron burst from the dense plasma focus, which initiates multiple fission events without the need for the actual nuclear explosion [59]–[61]. Each fission event generates prompt gamma rays proportional to the related time-dependent neutron population. The sample is diagnosed by a time-of-flight detector array located far enough to separate gamma and neutron emissions. A characteristic decay curve is determined by measuring fission gamma rays as a function of time after an external neutron initiates the chain. In this way, neutron-diagnosed subcritical experiments (NDSEs) investigate the neutron transport and multiplication within a subcritical SNM undergoing dynamic compression.

1.5.2 Material and surface studies

The first wall of the future thermonuclear-fusion power-plant reactors must withstand significant thermal and radiation heat loads during transient events, such as plasma disruptions (PD), vertical displacement events (VDE), or edge localized modes (ELMs). The plasma focus devices can temporarily produce such extreme conditions. Thus, they can be employed for surface-damage testing of materials, that is, tungsten and CFC (carbon fiber composites), designed for the plasma-facing components (PFC) [62]–[64]. Besides testing the materials, the z-pinch plasmas can process them to improve their characteristics. [66], [67]. In the past years, the plasma foci have been widely used for the deposition of thin films, which cannot be obtained using other conventional techniques employing low-temperature plasmas. The film composition depends on the choice of the working gas and the material of an ablated anode or a target sample irradiated by ions [68], or electrons [69], [70] accelerated during the z-pinch disruption (see Fig. 1.6). Due to the freedom of this choice, dense plasma foci can produce thin films from various materials,

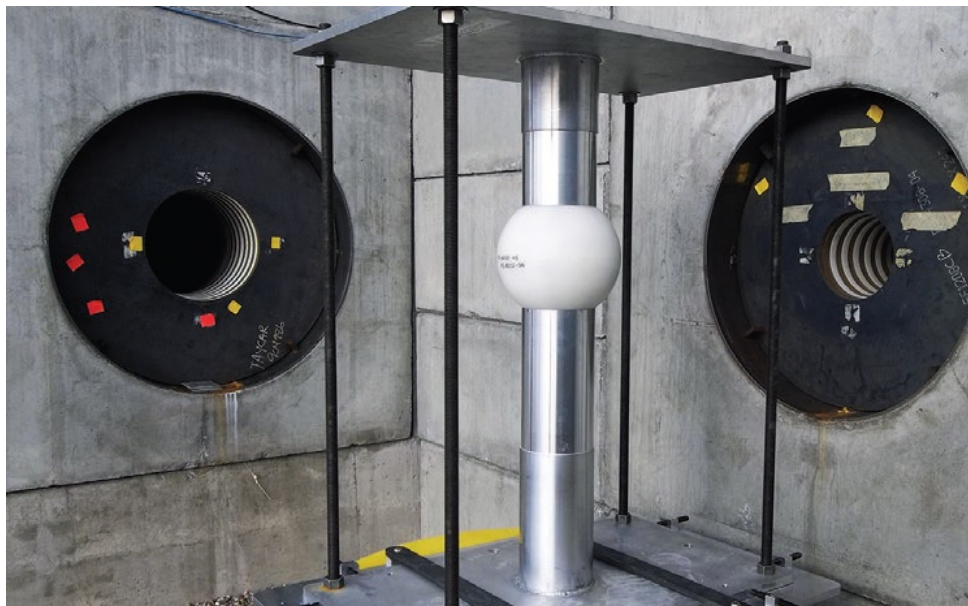


Figure 1.5: Photography of the NSDE test object, placed in the intersections of the line of sight of the dense plasma focus neutron pulse (tunnel on the right) and the line of sight of the gamma-ray detectors (tunnel on the left) [60].

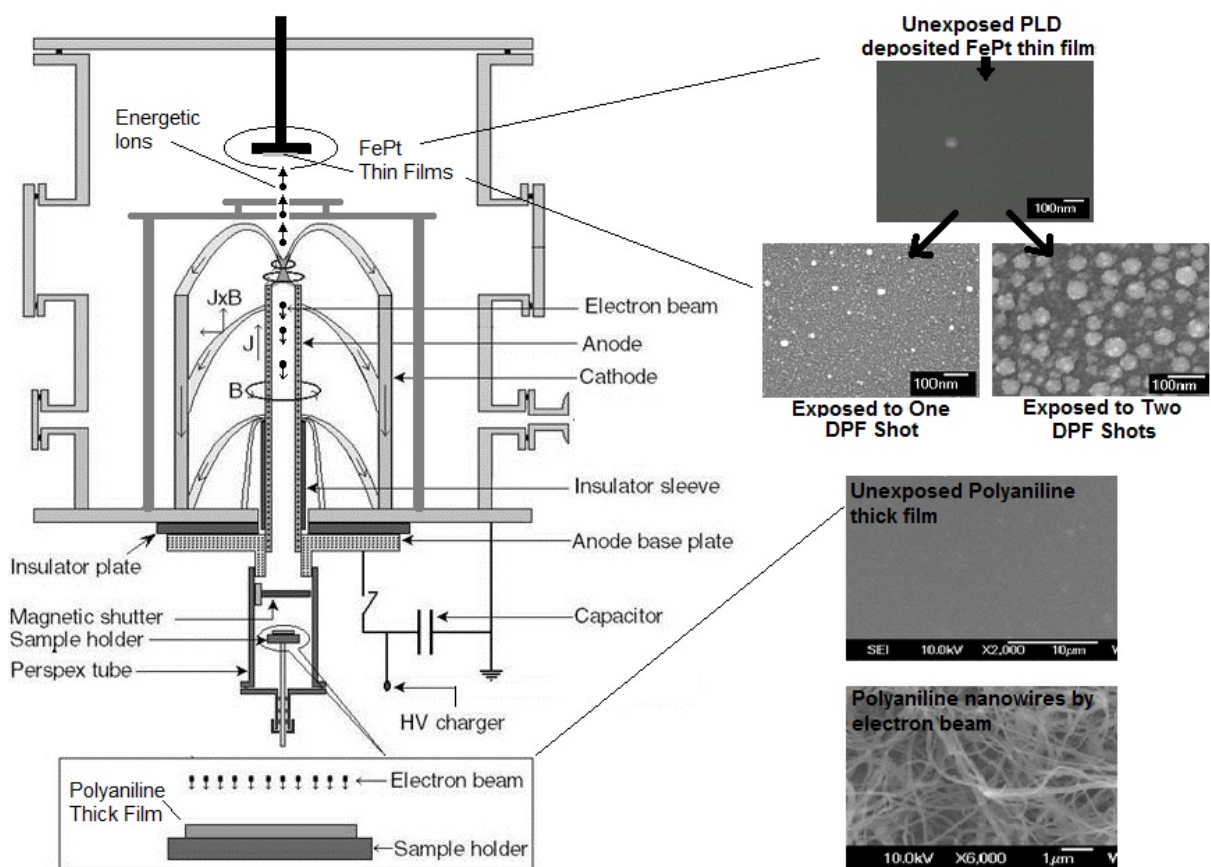


Figure 1.6: The schematic of DPF material processing/synthesis facility [65].

such as molybdenum nitride [71], magnesium aluminate [72], zinc oxide [73], titanium carbide [74], tungsten nitride [75], titanium nitride [76], [77], alumina-zirconia ceramic [78], amorphous carbon nitride [79], hafnium oxide [80], and others. Other examples of the plasma nanotechnology experiments employing z-pinch plasmas can be found in the reviews [65], [81], [82]. The plasma foci have also tested as efficient X-ray sources for material radiography (e.g., [83]–[86]).

The z-pinch can reproduce various phenomena in astrophysics, such as astrophysical jets and outflows, shock waves, magnetic reconnections, or conditions in the interiors of the giant planets. The comprehensive review of the contemporary astrophysics-relevant z-pinch experiments can be found in [87], [88].

1.5.3 Astrophysical jets and shocks

Collimated jets can be produced in active galactic nuclei (AGN), young stellar objects (YSO), or planetary nebulae (PNs). Since they are observed at distances much longer than their traversal dimensions, these jets must be collimated and stable. The origin of the stability and collimation of these jets is still being investigated. The conical wire arrays and dense plasma foci can generate comparable and astrophysical relevant jets [89]–[91]. In the case of the magnetically-dominated astrophysical jets, the collimation and the stability of the jets are attributed to the toroidal and poloidal B-fields [92], [93]. The toroidal fields probably originate from the differential rotation in the accretion disk or between the disk and the central star. The structure of these can be described by a model of so-called *magnetic towers*, which involves the presence of the magnetic cavity with dominating toroidal magnetic fields. Fig. 1.7 presents *radial wire arrays*, another type of the z-pinch, which can reproduce the magnetic tower jets in the laboratory [25], [94], [95].

Moreover, astrophysical shock waves have been investigated by the interaction of the z-pinch-driven jets with the medium [96], [97] or with each other [98]. Relevant radiative shocks have also been studied by the interaction of so-called the *inverse z-pinch* [99] with the surrounding gas. The inverse z-pinch effect (see Fig. 1.8a) occurs when the experimental load is driven by the return currents instead of the central ones. Then the direction of the $\mathbf{J} \times \mathbf{B}$ force accelerates the load outwards, in contrast to the classical imploding z-pinch.

1.5.4 Magnetic reconnections

Magnetic reconnection affects the dynamics of many astrophysical systems (for example, during the creation of stellar and solar flares). It occurs when the magnetic lines reconnect inside the plasma and release the magnetic energy into the surroundings as the thermal and kinetic energy of plasma flows and accelerates particles. However, the underlying processes of observed magnetic reconnections are still poorly understood. Inverse cylindrical wire arrays can produce fast-expanding magnetized plasma flows. When the plasmas of two neighboring cylindrical wire arrays merge, their magnetic fields reconnect (see Fig. 1.8) and can be investigated in the

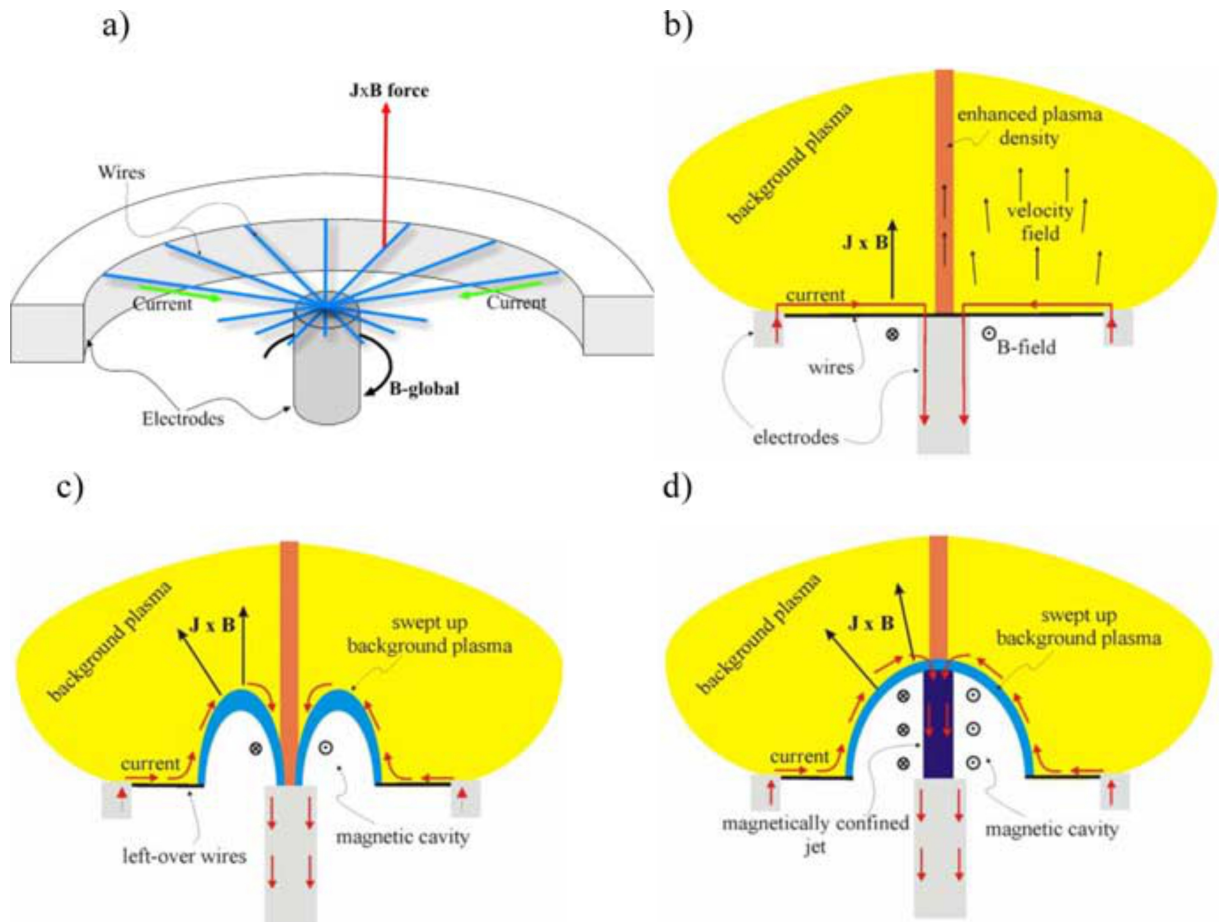


Figure 1.7: (a) Schematic of radial wire array experiments investigating magnetic tower jets. Currents flow radially through fine metallic wires from the outer to and along the central electrode. As a result, toroidal B-fields are created below the wires. (b) The currents ablate wires into the background plasma, which is accelerated axially from the array by the $\mathbf{J} \times \mathbf{B}$. During the ablation, the current paths remain close to the wires due to the resistive diffusion. (c) When the wire array is fully ablated, the currents create a magnetic cavity. It evolves (d) into a magnetic tower jet driven along the array's axis by the pressure of the toroidal B-field [94].

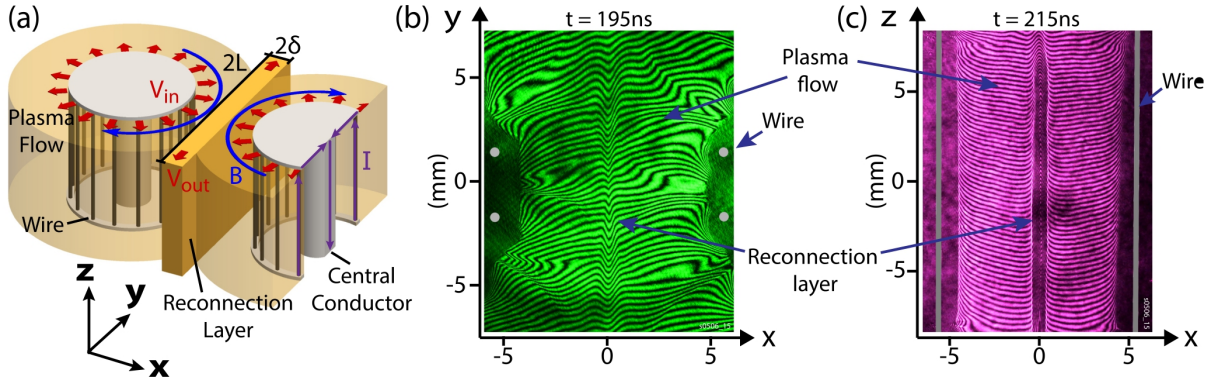


Figure 1.8: (a) Experimental setup of the inverse z-pinch. The current is applied to two parallel wire arrays. The $\mathbf{J} \times \mathbf{B}$ force at the outer side of the current sheath is inverted compared to the classical z-pinch and pushes the plasma radially outwards (i.e., the inverse pinch effect). Colliding magnetized plasma flows create a reconnection layer. The directions of the current (purple), plasma flows (red), and the embedded B-fields (blue) are shown. Interferometry (b) side-view and (c) top-view images of the interaction region display the formation of the reconnection layer [100].

laboratory [100]–[102].

1.5.5 Equation of state, conductivity measurements

Extreme pressures inside the cores of the giant planets can be reproduced by the impact of a so-called *flyer plate* [103], accelerated by the intense magnetic fields via the inverse pinch effect [104]. During the almost isentropic compression of the flyer plate, we can examine the equation of state (EOS) [105]–[108] or electrical conductivity [109] and thus validate the numerical models. Bright x-ray flashes generated by the z-pinch can be utilized for the opacity measurements, which are essential for the stellar interior processes [110]–[112].

All applications of the z-pinch require understanding the behavior of the current sheath and the evolution of the pinching $\mathbf{J} \times \mathbf{B}$ force. Therefore, the distribution of the axial currents \mathbf{J}_z and the azimuthal B-fields \mathbf{B}_φ are essential. However, they are difficult to be measured experimentally. In the next section, we briefly review the traditional B-field measurements technique, and then, in Chap. 2, we introduce and analyze a relatively new diagnostic method and the topic of this thesis, ion deflectometry.

1.6 Classical diagnostic methods for B-field measurement in z-pinch

Magnetic fields play a crucial role in the behavior of HED plasmas. In z-pinch discharges, the spatial distributions of B-fields and currents are essential for the dynamics of imploding plasmas and energy coupling to the plasma. Complex dynamics of the imploding plasma are investi-

gated using numerical models. However, these models' experimental verifications are needed, making the experimental B-field measurements very valuable. There are several traditional diagnostic methods for measuring the magnetic fields in z-pinch plasmas, namely *a)* Faraday rotation, *b)* B-dot probes, and *c)* Zeeman broadening. However, measuring the spatial distribution of B-fields is complicated due to various limitations, which are discussed in following paragraphs.

In the first method, the Faraday rotation, a plane of polarization of an electromagnetic wave rotates while propagating parallelly to B-fields B_{\parallel} through the plasma. A rotation angle θ_F is proportional to the path integral $\theta_F \propto \int n_e(s)B_{\parallel}(s)ds$, where $n_e(s)$ and $B_{\parallel}(s)$ are the electron density and the parallel B-fields at each point s along the path, respectively. Due to the necessity of a non-negligible electron density, this method cannot be used in near-vacuum environments. Moreover, a proper determination of an averaged B-field requires detailed knowledge of the local electron density profile $n_e(s)$. Simultaneous interferometric measurements can obtain the density profile, but they bring an additional source of error. In order to measure B-fields in surroundings with defined parameters, a magneto-optical fiber with the known length and density can be inserted into the plasma [113], [114]. B-fields diffused into the fiber represent the local B-fields in the plasma near it. When the fiber is irradiated by a diagnostic laser beam, the diffused B-fields rotate the polarization plane in the material with the given density and are measured. However, this fiber probe must not be invasive to the measured plasmas, so it cannot be placed into the hot core plasmas of the z-pinch. In addition, the density of the studied plasma must be lower than the critical density for EM wave propagation. However, using ultraviolet laser diagnostics at the wavelength of 266 nm [113], it has been possible to study plasmas up to densities of $\sim 10^{22} \text{ cm}^{-3}$.

The B-dot probe measures the temporal derivative of the B-fields by a small coil inserted into the plasma. In localized high-temperature and high-density plasmas of the z-pinch, these probes may be intrusive and cannot survive long. Thus, they are usually used to study B-fields at peripheral regions of the z-pinch plasma. Measurements of B-fields in hot dense plasmas close to the z-pinch axis are indirect. They require estimating the B-field evolution or extrapolation via numerical simulations [93], [115]. Therefore, a *micro-B-dot probe* has been developed at Cornell [116], [117] to minimize the influence of the inserted coil. However, a set of multiple B-dot probes is needed to measure the B-field distribution making this method more perturbative.

Using the Zeeman effect, the splitting of the emission lines in the presence of the external B-fields, we can measure the line shift $\Delta\lambda$ and estimate the magnetic strength B . The wavelength displacement of the spectrum line is

$$\Delta\lambda = \frac{e}{4\pi m_e c} g^* \lambda_0 B, \quad (1.16)$$

where e and m_e are the electron charge and mass, g^* is the Lande g-factor for the transition, λ_0 is the original wavelength, c is the speed of light. High temperatures and high densities of the

plasma complicate the Zeeman measurements since they cause Stark and Doppler broadenings smearing out the fine structure of the Zeeman splitting. However, even though these broadenings change the shape of the spectral lines (from the Dirac to the Voigt function), the peak position remains relatively unaffected. Therefore, spectral measurements employing two polarizations of fine-structure components can rely only on the line positions rather than their widths. Since these measurements require magnetic fields parallel (the longitudinal Zeeman effect) to the line of sight, the B-field measurements until recently were possible only at the outermost radius of the plasma column (the pinch radius) [118]–[120].

Nevertheless, to measure the B-field's spatial distribution of the z-pinch, we can utilize the fact that, in the imploding z-pinch plasma with the considerable atomic number Z_i , the degree of the ionization changes with the radius r . Recent experiments in z-pinch oxygen plasmas [121], [122] measured the spatial distribution of azimuthal B-fields in several points. They exploited the naturally occurring charge-state radial distribution and simultaneously recorded Zeeman-shifted spectral lines emitted from the different charge states. Nonetheless, only a few particular lines of sight coupled with the ionization change are suitable for the measurements. Therefore, the more detailed spatial distribution of the magnetic field, especially in low-Z plasma (e.g., hydrogen or deuterium), remains problematic.

An alternative method of B-field measurements in hot dense plasmas, called *ion radiography* (or *ion deflectometry*), has become widespread in the laser-plasma community during the last two decades. Its employment in the z-pinch is limited to the few pulsed-power facilities with access to intense lasers capable of producing multi-MeV probe ions. This thesis aims to further develop the ion deflectometry in the z-pinch and find an alternative source of ion backlighting.

The next Chapter review the current employment of this diagnostic technique in laser plasmas. We describe charged particle (proton) sources and detectors commonly used in deflectometry experiments. The theoretical background of this diagnostic is usually adapted to the needs of the laser-plasma experiments. Therefore, we derive the generalized deflection equations for the broader employment of ion deflectometry. Finally, we review contemporary radiography/deflectometry measurements of electric and magnetic (EM) fields in laser-produced and z-pinch plasmas.

Chapter 2

Measuring of EM fields using ion deflections

The ion radiography (or *ion deflectometry*) relies on measuring ion deflections in either electric or magnetic fields. Fig. 2.1 illustrates a classical experimental setup for the ion radiography/deflectometry. A small (point-like) source fires laminar ion beams into the interaction region. In this region, electric \mathcal{E} or magnetic \mathbf{B} fields deflect ion trajectories via the Lorentz force. Total ion deflections are proportional to the path integral of the fields, i.e., $\|\int_0^{\mathcal{L}} \mathcal{E} dL\|$ for electric fields and $\|\int_0^{\mathcal{L}} \mathbf{B} \times d\mathbf{L}\|$ for magnetic fields, where \mathcal{L} is the total length of the ion trajectory in the interaction region (in the deflecting fields), and $d\mathbf{L}$ is its path element. After leaving the interaction region, the ion beams irradiate the detector. The recorded ion image is distorted due to the ion deflections and, in this way, manifests the spatial distribution of path-integrated fields.

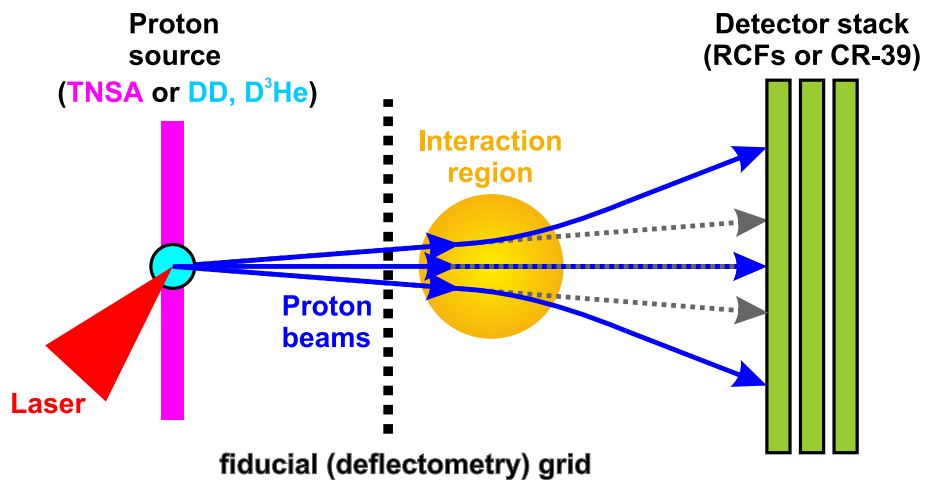


Figure 2.1: Schematic of the experimental setup for the proton radiography/deflectometry experiments

2.1 Characterization of the ion radiography/deflectometry method

Supposing the studied fields and the ion backlighting are reliably reproducible, we can acquire the ion beam's initial undistorted image from a reference shot without any fields. We can evaluate ion displacements, reflecting ion deflections and strengths of path-integrated fields, by comparing the distorted image of deflected ion beams with the undistorted (reference) ion image. Then, the spatial resolution of the measurements is set by the ion source size and the quality (sampling) of the image analysis. When we cannot determine the initial profile of the ion beam, we cannot retrieve the reference ion image. Then, a fiducial element (usually a regular grid) is implemented into the experimental setup and placed between the ion source and the interaction region. The distorted fiducial shadow in the detected ion image manifests the displacements of ions near the edges of the fiducial features. Since the spatial scales of the fiducial elements are usually larger than the size of the ion source, the fiducial structure determines the spatial resolution of the ion deflectometry. In the past, the designation “ion radiography” was used instead of “ion deflectometry” for measurements where the plasma density might influence diagnostic beams and the beam-plasma interaction needed to be evaluated. However, in contemporary papers, both designations are used interchangeably regardless of the importance of the beam-plasma scattering. In laser-driven plasmas the predominant term is “radiography”; in z-pinch plasmas, it is “deflectometry”.

Like in the Faraday rotation method, deflectometry measurements provide only path integrals of the fields. To retrieve actual fields from the path integrals, we must obtain additional information about the topology of the interaction region (e.g., the spatial scales of the fields by other independent measurements). Unless we can utilize some assumption of deflected ion trajectories, this technique usually relies on numerical ray-tracing (particle-tracking) simulations capable of reproducing the experimental ion images. Unlike the Faraday rotation method, the ion deflectometry requires no particles in the interaction region for its application. Thus, it can be employed even for measurements of vacuum EM fields. Moreover, this diagnostic does not need information about the spatial distribution of the plasma density along the ion paths because the interaction of the probe beams with the plasma is usually assumed negligible due to the high beam energy.

The employment of ion deflectometry demands specific ion sources for efficient backlighting. In the next section, we introduce two proton sources most commonly used in contemporary deflectometry measurements in laser-produced plasmas.

2.2 Typical proton sources for the deflectometry measurements

The ion-source size in the typical experimental setup (Fig. 2.1) must be small so that emitted ion rays do not cross. Then, the ion beam is laminar, and we can identify ion positions in the initial (reference) image. If the studied fields are time-varying, the ion emission duration must be short compared to the typical time scales of the fields. In this condition, probing ions can

take a “snapshot” of transient fields even in dynamic HED plasmas. However, measurements of highly fluctuating fields are limited by ion inertia. Moreover, for ion deflectometry, the beam energy must be high enough to prevent interaction between ions and background particles in the interaction region. For example, beam scattering and stopping would reduce the spatial resolution or influence the magnitudes of ion deflections, respectively. The required ion energies for typical laser-generated and z-pinch plasmas densities are in terms of MeV per nucleon.

Given these criteria, the most common diagnostic beams of charged particles with sufficient energy laminarity are multi-MeV proton beams generated by the interaction of a high-intensity laser with a foil target via Target Normal Sheath Acceleration (TNSA) [7], [123]–[125] or with an exploding pusher (a gas-filled capsule) via fusion reactions (namely, $D(d, p)T$ and $D(^3\text{He}, p)^4\text{He}$) [126]–[129].

2.2.1 TNSA-based broadband proton source

The laser-driven ion acceleration mechanism, called Target Normal Sheath Acceleration (TNSA), is an attractive and extensively studied process due to its diverse applications in science or medicine [8]. TNSA is essential for deflectometry measurements since it provides a suitable source of multi-MeV diagnostic protons. TNSA requires a short (fs), intense ($I_L \geq 10^{18}$ W/cm²), high-power (\sim PW) but low-energy (\sim J) laser pulse. Fig. 2.2 illustrates the TNSA mechanism. When the laser pulse irradiates a thin solid target, its strong electric fields accelerate electrons in the under-dense plasma (the preplasma) created by a ns prepulse (the pedestal) at the front (irradiated) side of the target. The electrons are accelerated up to relativistic energies. When they propagate through and exit the target, they create strong TV/m (MV/ μm) space-charge E-fields at the rear side of the target capable of accelerating ions (primarily protons originating from the surface impurities). Accelerated ions have energies of a few MeV/nucleon with a broad spectrum. To date, the highest proton energy achieved via TNSA is about 100 MeV [130]. These ion beams are highly laminar and seemingly emanate from a small ($\approx \mu\text{m}$) virtual source at the front side of the target. Therefore, the size of the virtual ion source determines the spatial resolution of the ion deflectometry instead of the actual source at the rear side.

2.2.2 Fusion-based monoenergetic proton source

The diagnostic multi-MeV protons can be achieved using lasers with lower intensities ($I_L \sim 10^{15}$ W/cm²), longer pulses (\sim ns), lower power (\sim TW) but higher pulse energies (\sim kJ) than are necessary for the TNSA mechanism. Such a laser pulse can drive an implosion of the spherical glass shell filled with D₂ or D³He gas leading to the generation of multi-MeV proton beams via fusion reactions



and



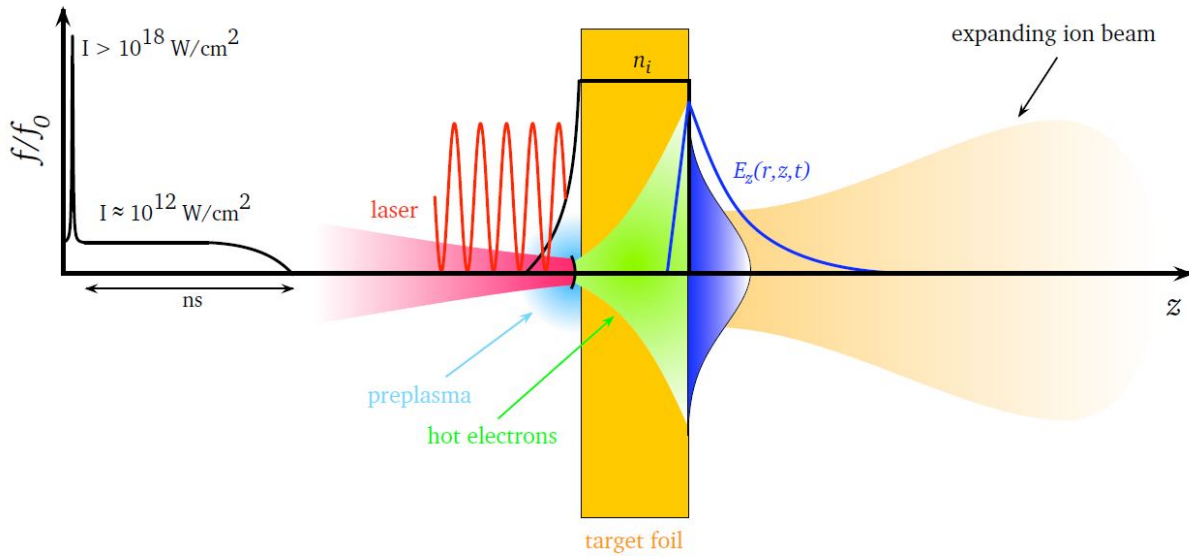


Figure 2.2: The schematic of the Target Normal Sheath Acceleration (TNSA) mechanism used for the generation multi-MeV proton beams [131].

These plasma implosions, known as “exploding pushers” [132]–[134], are similar to those in direct-drive inertial confinement fusion (ICF). The incident laser pulse causes rapid heating and a subsequent explosion of the target shell. The explosion produces a shock wave, which compresses and heats the gaseous fuel, turning it into hot dense and plasma. The fundamental difference between exploding pushers and ICF capsules is that the former are not designed to achieve to thermonuclear conditions or the ignition. The exploding pushers have a lower density of gaseous fuel (D_2 or D^3He) and a larger capsule radius than the ICF capsules. As a result, they produce a faster implosion, leading to the decoupling of ions with the electrons in the plasma and creating a population of suprathermal ions due to the kinetic processes [133], [135]. As a result, MeV protons are produced through fusion but not thermonuclear reactions. The exploding pushers are highly isotropic short-pulse proton sources with an nearly monoenergetic proton spectrum with two discrete energies of 3 and 14.7 MeV. Due to the small size of the localized proton source ($\approx \mu\text{m}$), the proton beams are highly laminar. Therefore, the exploding pushers have been utilized as proton backlighters for various ion deflectometry experiments [136]–[140]. The proton beams with well-defined discrete energy are highly beneficial for evaluating the stopping power of ions in the plasmas or E-fields’ influence on proton energy during beam deflection [141]–[143]. Proton imaging at two discrete energies allows capturing studied fields in two specific moments due to different times of flight of probing protons.

Furthermore, the ion deflectometry requires specific ion diagnostics capable of capturing high-fluence multi-MeV ion emissions and producing high-resolution ion images. The following section reviews the most common ion detectors used in laser-produced plasma measurements.

2.3 Ion detectors for ion deflectometry

The ion deflectometry manifests the spatial distribution of the path-integrated fields by capturing images of the deflected ion beams. The ion images are obtained using various detectors such as: image plates [144], micro-channel plates [145], scintillators [146], CR-39 detectors [147], or radiochromic films (RCFs) [148]. Tab. 2.1 compares the properties of these detectors. We will focus on RCFs and CR-39 detectors because they are widely used for ion imaging of EM fields in hot plasmas since they have an excellent spatial resolution in terms of μm and are insensitive to EMP pulses.

Table 2.1: Table of ion detectors commonly used for laser-driven ion diagnostics and measurements [8]. Sensitivity: L: light, UV: ultraviolet, x: x-rays, e-: electrons; the notation ‘●’ marks the sensitivity and ‘—’ the insensitivity.

	Spatial resolution	Time resolution	Treatment/display time	Single-particle sensitivity	Dynamic range (DR)	Sensitivity			Features/refs
						L	UV, x	e-	
Solid-state nuclear track detectors, e.g. CR-39 (allyl diglycol carbonate), etc	~ a few to a few tens of μm (pit size, depends on the ion kind and energy and etching time)	No	A few hours (etching, scanning, pit counting)	Yes	$\sim 10^2$ – 10^6 (background $\sim 10^2$ – 10^4 cm^{-2} , saturation $\sim 10^6$ – 10^8 cm^{-2})	—	—	—	(1) Sensitive to ions only ^a , single particles
Radiochromic film (RCF)	~3–10 μm (film, scanner)	No	Several minutes (scanning)	No	$\sim 10^2$ – 10^3 (e.g. 10 – 10^4 Gy)	—	●	●	(2) Self-developing
Imaging plate	Sub-100 μm (scanner)	No	Several minutes (scanning)	No	$\sim 10^5$	—	●	●	(3) Reusable, high DR
Activation	Sub-mm (contact radiography)	No	Tens of minutes–a few hours (decay time)	No	Very high ($>10^5$)	—	—	—	(4) Very high DR
Micro-channel plate (MCP)+phosphor screen + CCD	~several 10 s of μm (imaging system)	~a few 100 ps (MCP gate time)	~a few seconds (CCD readout)	Yes	$\sim 10^3$	—	●	●	(5) Online, single particles
Scintillator + gated I-CCD or EM-CCD	~several 100 μm (multiple scattering, imaging system)	~a few 100 ps (scintillation time)	~a few seconds (CCD readout)	No	$\sim 10^3$	●	●	●	(6) Online, stackable in depth

2.3.1 Solid-state nuclear track detectors CR-39

Solid-state nuclear track detectors CR-39 are made from a solid plastic thermosetting polymer [poly-allyl-diglycol-carbonate (PADC); $\text{C}_{12}\text{H}_{18}\text{O}_7$]. The abbreviation CR-39 stands for the 39th formula of this plastic developed in a project of the Columbia Resin company during the World War II. They are commonly manufactured for eyeglass lenses but can also be used as dosimeters for particle radiation [149]–[152]. In past years, CR-39s have characterized emissions of laser-produced [153] and fusion-based [147] proton beams and become standard detectors in proton radiography/deflectometry.

Ion detection using CR-39s is based on the fact that incident ions break polymeric bonds in the detector material and leave trails of the damaged polymer along their paths, so-called

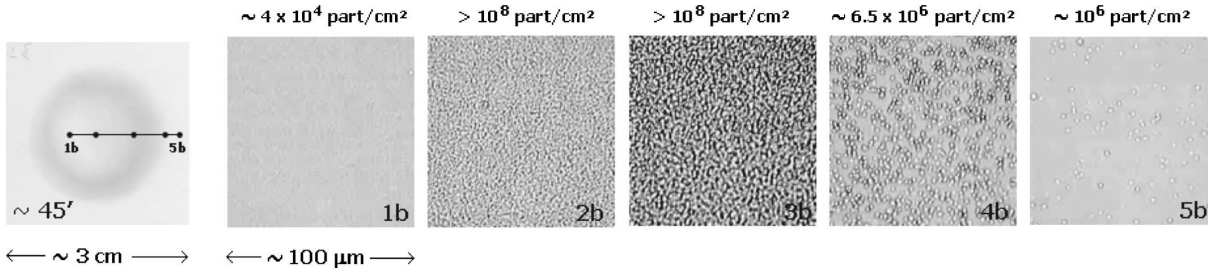


Figure 2.3: Saturation of CR-39 detectors when the number of detected tracks does not corresponds to the actual ion fluence due to the overexposing or overetching. A CR-39 detector shows the image of the laser-accelerated proton beam with a visible artifact white circle in its center. Microscope scans in various parts of the proton image reveal the density of the etched tracks corresponding to the proton fluence. Although the beam irradiance is the highest in the center of the circle, the number of tracks recognized by microscope analysis is the lowest and falsely indicates low proton fluence [157].

latent tracks. The amount of the dealt damage is proportional to the stopping power dE/dx , where x corresponds to the direction of penetrating ions. The length of the tracks corresponds to the stopping range of ions. The latent tracks are made visible by etching in a KOH or NaOH solution (usually etched in a ≈ 6 -mol/l solution for a few hours at $70 - 90^\circ\text{C}$). Because the etching rate of the latent tracks (damaged material) V_t is higher than the etching rate of the bulk (undamaged) material V_b , the etching process produces conical pits in ion impact points. The density of etched tracks corresponds to the ion fluence. The spatial resolution is given by the $\approx \mu\text{m}$ -size of the etched pits. The energy and species of the detected ions are acquired by precise measurements of the pit depth and diameter using an optical microscope.

The distinct advantage of CR-39s for employment in the HED plasma experiments is that they are practically insensitive to electron or electromagnetic radiation. Moreover, the ion detection efficiency can be very high [154], [155] depending on the ion species and energy (almost 100%, for the normal incidence of $6 - 8$ MeV protons). Besides ions, CR-39s can detect neutrons by producing recoil protons due to neutron interaction with the CR-39 material. These recoil protons then produce latent tracks. However, the detection efficiency of MeV neutrons is low ($\approx 10^{-4}$) [156].

A significant disadvantage of CR-39s is the necessity of their rather complicated processing after the exposure, namely the etching and microscope inspection techniques. Moreover, a saturation of CR-39s can occur in high-ion-flux experiments causing the overlapping tracks, which complicates their distinction. The saturation regime is associated with the appearance of the artifact patterns in the detector (see Fig. 2.3), which makes CR-39s less reliable than radiochromic films (RCFs).

2.3.2 Radiochromic films (RCFs)

Radiochromic films (RCFs) are commonly used in dosimetry [159]–[161]. They are often used in laser-plasma experiments for the detection of ion beams. There are several types of RCF

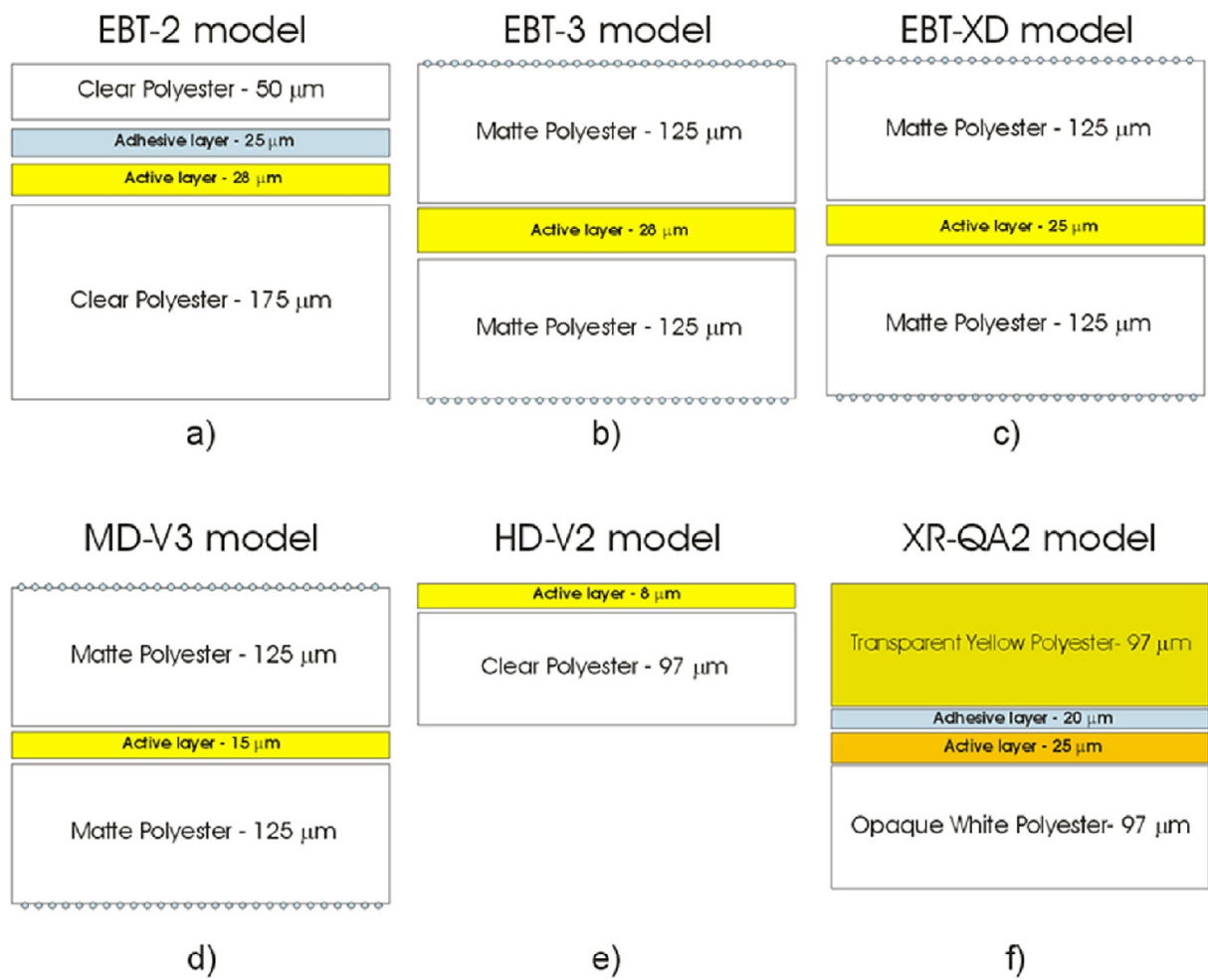


Figure 2.4: Diagram of the structures and layer thickness of common RCF detectors [158].

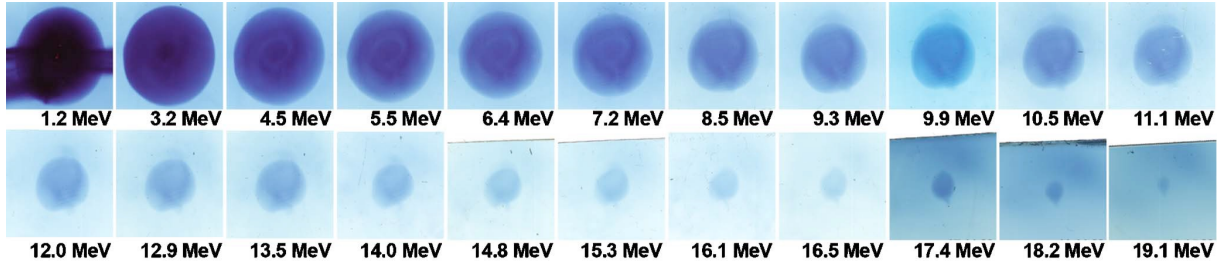


Figure 2.5: Laser-driven proton beam recorded by a RCF stack (nineteen films of type HD-810 and three MD-55 films) of the TRIDENT experiment. Each layer corresponds to the minimum energy of detected protons [162].

(see Fig. 2.4), but all contain an active layer and, usually, at least one supporting substrate layer. The active layer of the RCF contains a monomer, which darkens after exposure to the ionizing radiation due to the induced polymerization (see Fig. 2.5). The coloration of the RCF influences its local transmissivity $\mathcal{T} = I_{\lambda}/I_{\lambda_0}$, where I_{λ_0} and I_{λ} are intensities of the light transmitted through the RCF before and after the irradiation. The detector response to the irradiation is characterized by a so-called optical density $OD = -\log_{10}(\mathcal{T})$, which is non-linearly proportional to the exposed dose (see Fig. 2.6a). Therefore, to analyze RCFs, calibration curves are established via reference exposure of the RCF by a known dose of ion beams.

A major advantage of RCFs is that they are self-developing and provide qualitative results shortly after irradiation, but quantitative results, including calibration, after a few days depending on the RCF type. The theoretical limit of the spatial resolution is the dimension of each “activated” molecule in the film. In practice, the spatial resolution of the data set is limited by the sampling rate (typically in $\approx \mu\text{m}$) set of a film scanning [159]. The disadvantage of RCFs is that they are primarily sensitive to the deposited dose, i.e., not only to ions but also to UV radiation, X-rays, and electrons. Therefore, it is crucial to determine that the recorded signal in an RCF detector originates from ion emission. UV and X-ray photons generated by the z-pinch plasma or its disruption have longer mean free paths than the RCF thickness. Thus, their detection probability is low. Electrons traveling with ions in the accelerated beam to equalize their electric potential can be separated from ions using the magnet due to the low electron inertia. In addition, electrons usually create a diffusive halo signal, which can usually be distinguished from the structured ion image.

In contrast to CR-39s with typical thicknesses between 0.3 - 1.2 mm, RCFs are thin with thicknesses between 50 - 250 μm , and a single film usually does not absorb the whole spectrum of the multi-MeV ion emission. Therefore, RCFs are usually employed in a stack consisting of multiple layers of RCFs interlaced with absorbers. The stacked RCFs can record images of broadband ion emission (see Fig. 2.5) due to tailoring the ion stopping range in the detector. The ion stopping power in the RCF is inversely proportional to the ion velocity, which decreases with the ion penetration depth. Thus, the slowed down ions interact more with the material and the ion absorption in the matter for the given ion energy is characterized by a Bragg curve.

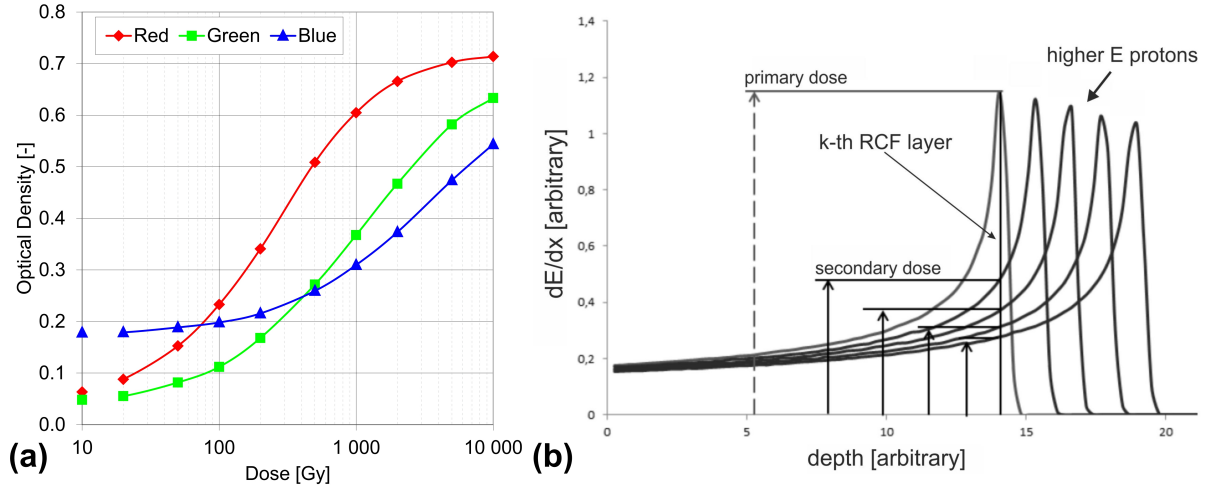


Figure 2.6: (a) Response curves for red, green, and blue components of the HD-V2 detector dye's color to the exposed dose. These curves are crucial for the RCF calibration and ion-energy unfolding of the RCF stack. (b) The energy deposited in a specific layer of RCF in the stack, primarily comprised of protons of stopping range equal or close to the RCF depth in the stack. Secondary and smaller contributions are from protons of higher energy stopped deeper in the stack [163].

Fig. 2.6b shows that an ion absorption peak is situated near the end of the ion path (range). Here, the ion velocity becomes low and ions interact strongly with the material. Accordingly, the position of this peak and the ion range depends on the energy of incoming ions. The first layers of the RCF beam are able to slow down and detect low-energy ions with high efficiency, while most high-energy ions are able to pass through. These first layers act as filters for others because they slow down ions with higher energies, which are captured by layers further in the stack.

Therefore, each layer of RCF is associated with a certain energy threshold of detected ions, which dominantly contribute to the final image. Ions with lower energies cannot reach the given layer. The contribution of ions with higher energies in this layer is small but can be non-negligible (see Fig. 2.6b). Therefore, the analysis of RCFs may require an energy unfolding of individual ion images, which removes contributions of higher ion energies layer-by-layer using the calibration curves. The ion energy thresholds for the individual RCFs with a given thickness are usually acquired using a numerical model called Stopping and Range of Ions in Matter (SRIM) [164], [165]. The energy resolution of the ion images is vital for measuring ion deflections and estimating the strengths of deflecting fields. Moreover, the RCF stack can provide temporal resolution of these fields if the ion emission is short compared to the ion time-of-flight (TOF) because ions with different energies reach the fields at different times.

After describing the experimental setup for ion deflectometry and its components, the following section analyzes the theoretical background of ion deflections in electric and magnetic fields.

2.4 Analysis of the ion deflections

The ion deflectometry is based on detecting ion beams, which are deflected from their initial (undeflected) direction by either electric \mathcal{E} or magnetic fields \mathbf{B} . We will consider only electric and magnetic fields perpendicular to the undeflected ion beams. Parallel electric fields would increase the beam energy but do not cause deflection, and parallel magnetic fields would not affect ions at all. Laser and z-pinch plasmas can often be assumed azimuthally symmetrical ($\partial/\partial\varphi = 0$). We will use this symmetry in our analysis, we assign the z -axis to an axis of the ion emission and consider only ion deflections by radial E-fields \mathcal{E}_r or azimuthal B-fields \mathbf{B}_φ . In addition, we assume that ion energies are non-relativistic.

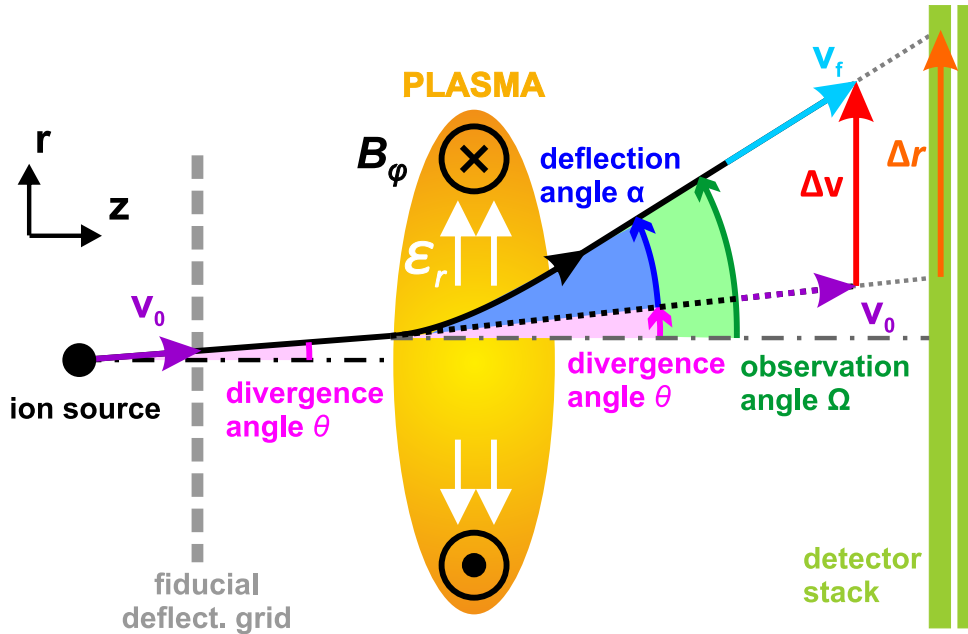


Figure 2.7: A schematic of a typical deflectometry setup for radial E-field \mathcal{E}_r or azimuthal B-field \mathbf{B}_φ measurements. These fields deflect ions and cause ion displacements $\Delta\mathbf{r}$ measured in the detector plane. The ion deflections alter the ion velocity vector \mathbf{v} from an initial ion velocity \mathbf{v}_0 to a (final) deflected ion velocity \mathbf{v}_f . The velocity change is characterized by a displacement velocity vector $\Delta\mathbf{v} = \mathbf{v}_f - \mathbf{v}_0$. An angular ion deflection is characterized by the deflection angle α from the initial ion divergence half-angle θ to the final observation angle Ω .

In a typical deflectometry setup (see Fig. 2.7), probe ions are emitted along the z -axis from a point-like source with an initial velocity \mathbf{v}_0 and travel towards the interaction region. The initial ion direction is given by an initial *divergence half-angle* θ . A fiducial deflectometry grid (a *D-grid*) can be employed in the experimental setup between the ion source and the studied EM-field region. The D-grid imprints its shadow into the ion emission marking the initial ion positions. Afterward, ions continue into the interaction plasma region. As ions travel through this region, local EM fields deflect their trajectories and alter their velocity vectors \mathbf{v} according to the ion motion equation

$$m_i \frac{d\mathbf{v}}{dt} = Q (\mathcal{E}_r + \mathbf{v} \times \mathbf{B}_\varphi), \quad (2.1)$$

where Q and m_i are ion charge and mass, respectively. After deflected ion beams leave the

interaction region, their altered and final velocity vector \mathbf{v}_f makes an *observation angle* Ω with the z -axis. Ion deflections cause a distortion of the ion beam profile, which is recorded by the detector and manifests the strengths of deflecting fields. We refer to the recorded images of distorted ion beams as ion *deflectograms* or *radiographs*. In the case the D-grid is employed, we evaluate ion deflections from distortions of the D-grid shadow in the recorded ion image. If the D-grid is not employed, we must acquire an initial (undistorted) ion image of the ion beam and evaluate how it differs from the distorted ion image.

We can characterize the total ion deflections by a *deflection angle* α between vectors \mathbf{v}_f and \mathbf{v}_0 as

$$\alpha = \Omega - \theta. \quad (2.2)$$

The orientation of the angles θ and Ω is important for ion deflections, which can be focusing or defocusing. For example, suppose that an ion is deflected in the opposite radial direction to which it has been emitted. In that case, the angle θ has opposite direction to Ω and increases the deflection angle (i.e., $|\alpha| = |\Omega| + |\theta|$). We define the magnitude of the deflection angle α only for values from interval $[-\pi, \pi]$. Therefore, the maximal ion deflection is by a half-turn ($\alpha = \pi$). In radial electric fields, larger deflection angles are not possible. In azimuthal B-fields, larger deflection angles are possible but their measurements are inherently ambiguous. For $|\alpha| > \pi$, we cannot decide whether the deflection angle is between \mathbf{v}_f and \mathbf{v}_0 or it is its complementary angle. Specifically, the ion deflection in magnetic fields by a multiple of an angle 2π is equivalent to the deflection angle $\alpha = 0$ because the 2π -rotation returns the velocity vector \mathbf{v} to its initial state.

Alternatively, we can describe the net ion deflection using a velocity change, defined by a displacement velocity vector $\Delta\mathbf{v} = \mathbf{v}_f - \mathbf{v}_0$ (see Fig. 2.7). The displacement velocity vector is proportional to the time integral of the deflection fields:

$$\Delta\mathbf{v} = \frac{Q}{m_i} \int_0^\tau (\mathcal{E}_r + \mathbf{v} \times \mathbf{B}_\varphi) dt, \quad (2.3)$$

where τ is the duration of the ion deflections in the interaction region. Eq. (2.3) demonstrates an inherent integral nature of the ion deflectometry, which can only measure the integrated fields. Deflectometry experiments aim to find the displacement velocity $\Delta\mathbf{v}$ by estimating \mathbf{v}_f , or the deflection angle α by estimating Ω . The quantities \mathbf{v}_0 and θ are usually set by known ion positions in the D-grid plane or by undeflected ion positions in the detector plane.

In practice, estimating the exact direction of ions incoming to the detector (given by the vector \mathbf{v}_f or the angle Ω) is often difficult. Then, we can only measure displacements of deflected ions $\Delta\mathbf{r}$ in the detector plane (see Fig. 2.7). The ion displacements $\Delta\mathbf{r}$ are proportional to a double integral of the measured fields over time:

$$\Delta\mathbf{r} = \frac{Q}{m_i} \int_0^\tau \left(\int_0^t (\mathcal{E}_r + \mathbf{v} \times \mathbf{B}_\varphi) dt' \right) dt. \quad (2.4)$$

In general, Eq. (2.4) is solved using numerical simulations tracking deflected ion trajectories. In specific situations, we can use some approximations, simplifying one of the integrals

and, thus, providing information about the integrated fields. Contemporary laser-plasma experiments of the proton radiography are commonly designed to allow a paraxial approximation (see Subsec. 2.4.3).

However, for performing ion deflectometry in z-pinch plasmas, we cannot expect conditions similar to laser plasmas, and thus, we derive general relations for ion deflections. Separately for radial E-fields and azimuthal B-fields, the following sections find the analytical relations (deflection equations) between the integrated fields and the deflection angle α or the velocity shift $\Delta \mathbf{v} = (\Delta v_r, 0, \Delta v_z)$. These deflection equations help us understand the principles of ion deflectometry.

2.4.1 Electric deflections

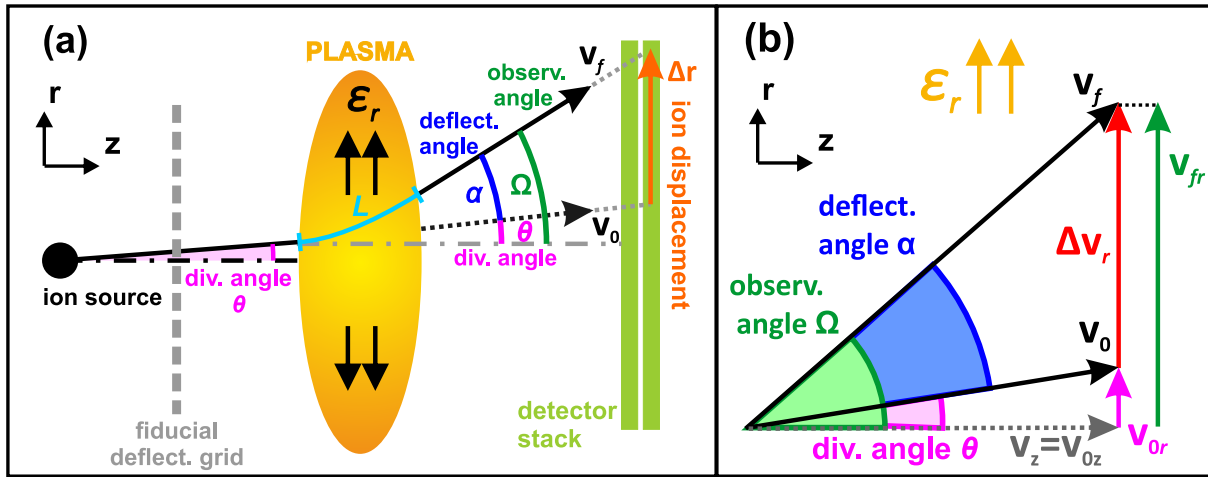


Figure 2.8: (a) Experimental setup of the ion deflectometry measurements of radial electric fields \mathcal{E}_r . (b) Schematics of the rotation and elongation of the ion velocity vector \mathbf{v} due to ion deflections in lateral (radial) electric fields.

Let us consider a deflectometry setup (Fig. 2.8a) for measurements of solely radial and static electric fields $\mathcal{E}_r = (\mathcal{E}_r, 0, 0)$. Due to the radial E-field direction, ion velocity's axial component v_z , perpendicular to the deflecting field, remains unaffected ($v_z = v_{0z}$), and the axial ion velocity shift is zero ($\Delta v_z = 0$). Thus, we consider only a radial component $\Delta v_r = v_{fr} - v_{0r}$ of the velocity shift $\Delta \mathbf{v} = \mathbf{v}_f - \mathbf{v}_0$ (see Fig. 2.8b). Then, we reduce Eq. (2.3) into

$$\Delta v_r = v_{fr} - v_{0r} = \frac{Q}{m_i} \int_0^\tau \mathcal{E}_r dt, \quad (2.5)$$

where v_{0r} and v_{fr} are radial components of \mathbf{v}_0 and \mathbf{v}_f , respectively. Fig. 2.8b shows that the radial components v_{0r} and v_{fr} are coupled with the initial and final ion directions. Therefore, they can be described by the divergence and observation angles θ and Ω , respectively, as follows

$$v_{0r} = v_z \tan \theta = v_0 \cos \theta \tan \theta \quad (2.6)$$

and

$$v_{fr} = v_z \tan \Omega = v_0 \cos \theta \tan \Omega \quad (2.7)$$

where we replaced the axial ion velocity $v_z = v_0 \cos \theta$. By subtraction of Eq. (2.6) from Eq. (2.7), we acquire a relation for a radial velocity shift

$$\Delta v_r = v_0 \frac{\sin(\Omega - \theta)}{\cos \Omega} = v_0 \frac{\sin \alpha}{\cos \Omega}, \quad (2.8)$$

where we used the sum formula $\tan \Omega - \tan \theta = \sin(\Omega - \theta)/(\cos \Omega \cos \theta)$ and the definition of the deflection angle $\alpha = \Omega - \theta$.

After modifying the left-hand side (LHS) of Eq. (2.5), we examine its right-hand side (RHS). Instead of integrating over the duration of ion deflections $\tau = \int_0^\tau dt$, which is difficult to estimate, it is convenient to integrate over the ion path length $\mathcal{L} = \int_0^\tau v dt$, which can be coupled to the spatial scales of the interaction region. Therefore, we rewrite RHS of Eq. (2.5) as follows

$$\frac{Q}{m_i} \int_0^\tau \mathcal{E}_r \frac{v dt}{v} = \frac{Q}{m_i v_0} \int_0^\mathcal{L} \mathcal{E}_r dL, \quad (2.9)$$

where $dL = v dt$ is the ion path element. To simplify the path integral in Eq. (2.9), we assumed electric fields change the direction of the ion velocity but do not significantly change its magnitude ($v \approx v_0$). Combining Eq. (2.8) with Eq. (2.9), we finally obtain a deflection equation for the path integral of the radial E-fields $\int_0^\mathcal{L} \mathcal{E}_r dL$:

$$\frac{\sin \alpha}{\cos \Omega} = \frac{Q}{m_i v_0^2} \int_0^\mathcal{L} \mathcal{E}_r dL = \frac{Q}{2E_0} \int_0^\mathcal{L} \mathcal{E}_r dL, \quad (2.10)$$

where $E_0 = m_i v_0^2/2$ is the initial energy of ion beams. Eq. (2.10) is valid only for $0 \leq |\Omega| < \pi/2$, which is in agreement with the setup in Fig. 2.8a. We exclude the particular case of the observation angle $|\Omega| = \pi/2$ because, in that case, deflected ions cannot be detected. The path-integrated E-fields in Eq. (2.10) are coupled to a weighted average of the actual E-fields $\overline{\mathcal{E}}_r = (\int_0^\mathcal{L} \mathcal{E}_r dL)/\mathcal{L}$ mapped by probing ions along their paths.

When the observation angle Ω is unknown, solving Eq. (2.10) requires a specific experimental setup. When the ion source is placed far from the plasma or the size of the E-field region is small compared to the source's size, the initial divergence θ becomes negligible ($\theta \approx 0$) and the initial ion velocity \mathbf{v}_0 is nearly axial. Then, we can approximate $\cos \Omega \approx \cos(\Omega - \theta) = \cos \alpha$ in Eq. (2.10) and, thus, obtain the deflection equation for path-integrated radial E-fields:

$$\tan(\alpha) = \frac{\Delta v_r}{v_0} = \frac{Q}{2E_0} \int_0^\mathcal{L} \mathcal{E}_r dL, \quad (2.11)$$

It is worth noting that the electric ion deflection is inversely proportional to the first power of the initial beam energy E_0 ($\tan(\alpha) \propto 1/E_0$). This dependence can distinguish electric and magnetic ion deflections.

2.4.2 Magnetic deflections

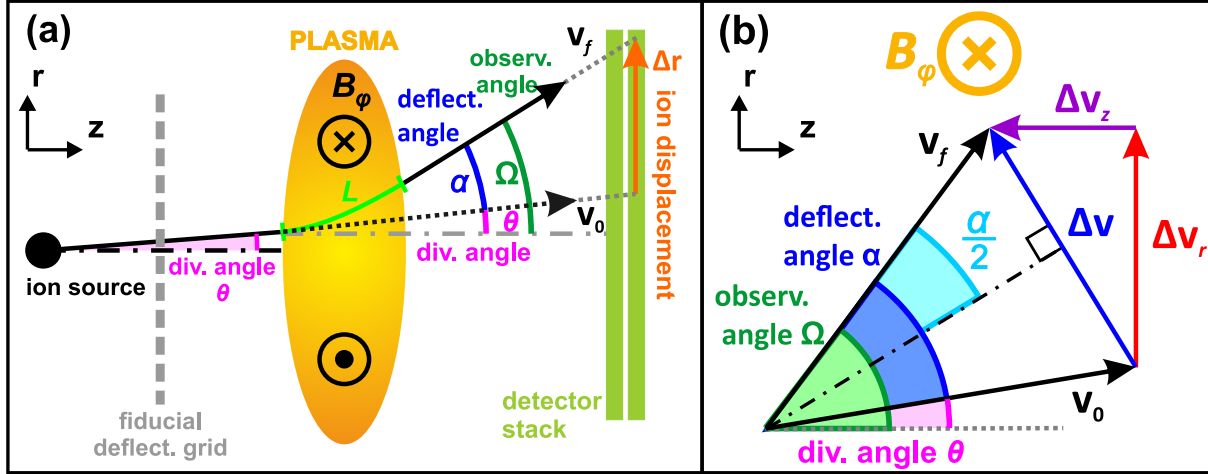


Figure 2.9: (a) Experimental setup of the ion deflectometry measurements of azimuthal B-fields \mathbf{B}_ϕ . (b) Schematics of the rotation of the ion velocity vector \mathbf{v} due to ion deflections in perpendicular magnetic fields.

Now, we investigate ion deflections in static azimuthal B-fields $\mathbf{B}_\phi = (0, B_\phi, 0)$ and assume no E-fields ($\mathcal{E} = 0$). Fig. 2.9a shows a typical experimental setup for B-field measurements. A relative orientation of the azimuthal B-fields to the beam direction is usually designed to defocus (disperse) incoming ions. Focused ions cross each other, which would, in the classical setup (Fig. 2.9a), lead to a non-injective projection of deflected ions onto the detector plane and the ambiguity of the results. It is worth noting that the defocused ions can cross each other if the profile of their deflections has a negative radial gradient (ion deflections are stronger closer to the z -axis, e.g., due to the radially decreasing B-fields) and its magnitude reaches a critical limit (see Subsec. 2.4.3 and Subsec. 3.2.2).

From Eq. (2.3), we can obtain a relation between the change in ion velocity $\Delta \mathbf{v} = \mathbf{v}_f - \mathbf{v}_0$ and the path-integrated B-fields $\int_0^{\mathcal{L}} \mathbf{B}_\phi \times d\mathbf{L}$:

$$\Delta \mathbf{v} = \frac{Q}{m_i} \int_0^{\mathcal{L}} \mathbf{v} \times \mathbf{B}_\phi dt = \frac{Q}{m_i} \int_0^{\mathcal{L}} d\mathbf{L} \times \mathbf{B}_\phi = -\frac{Q}{m_i} \int_0^{\mathcal{L}} \mathbf{B}_\phi \times d\mathbf{L}, \quad (2.12)$$

where $d\mathbf{L} = \mathbf{v} dt$ is the ion path element vector and $\mathcal{L} = \int_0^{\mathcal{T}} v dt$ is the total length of the ion path. During the magnetic ion deflections, the magnitude of ion velocities remains constant ($v \equiv \|\mathbf{v}_f\| = \|\mathbf{v}_0\|$) and their vectors \mathbf{v} only rotate in the rz plane. A schematic in Fig. 2.9b demonstrates how we can describe the rotation of the ion velocity vector, that is, the ion deflection, in magnetic fields. Bisecting the ion deflection angle α and the opposite side Δv of the triangle in Fig. 2.9b, we create a right triangle with an angle $\alpha/2$ allowing us to find the general

deflection equation for azimuthal B-fields¹:

$$\left| \sin\left(\frac{\alpha}{2}\right) \right| = \frac{\|\Delta\mathbf{v}\|}{2v} = \frac{Q}{2m_i v} \left\| \int_0^{\mathcal{L}} \mathbf{B}_\varphi \times d\mathbf{L} \right\| = \frac{Q}{2\sqrt{2m_i E}} \left\| \int_0^{\mathcal{L}} \mathbf{B}_\varphi \times d\mathbf{L} \right\| \quad (2.13)$$

In contrast to the ion deflections in electric fields, magnetic deflections are inversely proportional to the square root of the beam energy E [$\sin(\alpha/2) \propto 1/\sqrt{E}$], which is kept constant [$E(t) = E_0$]. Eq. (2.13) is vital for the on deflectometry in B-fields because it is generally valid for magnetic deflections with arbitrary magnitudes up to $|\alpha| = \pi$. This limit agrees with our definition of the deflection angle magnitude and prevents the ambiguity of the ion deflectometry for $\alpha > \pi$, represented in Eq. (2.13) by a periodicity of the sine function. Note that in Eq. (2.13), there is an absolute value of the path integral and not the path integral of an absolute value. In this way, Eq. (2.13) takes into account for consecutive deflections with the alternating orientation, which may cancel each other out.

The path-integrated B-fields $\int_0^{\mathcal{L}} \mathbf{B}_\varphi \times d\mathbf{L}$ are coupled to a weighted average of the actual B-fields $\overline{B_\varphi} = (\int_0^{\mathcal{L}} \mathbf{B}_\varphi \times d\mathbf{L})/\mathcal{L}$ mapped by probing ions along their paths. To further understand the meaning of the path-integrated B-fields $\int_0^{\mathcal{L}} \mathbf{B}_\varphi \times d\mathbf{L}$, we modify them as follows

$$\frac{Q}{\sqrt{2m_i E}} \int_0^{\mathcal{L}} \mathbf{B}_\varphi \times d\mathbf{L} = \int_0^{\mathcal{L}} \frac{\mathbf{e}_\varphi \times d\mathbf{L}}{R_L} \quad (2.14)$$

where $\mathbf{e}_\varphi = \mathbf{B}_\varphi/B_\varphi$. The numerator of the fraction on the RHS of Eq. (2.14) indicates the direction of ion deflections in the rz plane. The denominator is an ion Larmor radius (a ion gyroradius) $R_L = \sqrt{2m_i E}/(QB_\varphi)$ coupled with a local curvature of the ion trajectory κ_B ($R_L = 1/\kappa_B$). Therefore, the path-integrated B-fields $\int_0^{\mathcal{L}} \mathbf{B}_\varphi \times d\mathbf{L}$ describe not only the net ion deflection, given by $\Delta\mathbf{v} = \mathbf{v}_f - \mathbf{v}_0$, but also the total curvature of the ion trajectories $\int_0^{\mathcal{L}} \kappa_B dL/\mathcal{L}$.

In addition to the general deflection equation [i.e., Eq. (2.13)], we can derive similar equations for components of path-integrated B-fields. In the cylindrical coordinates (r, φ, z) , we obtain $\int_0^{\mathcal{L}} \mathbf{B}_\varphi \times d\mathbf{L} = (\int_0^Z B_\varphi dz, 0, -\int_0^{\mathcal{R}} B_\varphi dr)$, where $\mathcal{R} = \int_0^{\mathcal{T}} v_r dt$ and $Z = \int_0^{\mathcal{T}} v_z dt$. Using again the schematic in Fig. 2.9b, we find that

$$\Delta v_r = v_{fr} - v_{0r} = v(\sin \Omega - \sin \theta) = -\frac{Q}{m_i} \left(\int_0^{\mathcal{L}} \mathbf{B}_\varphi \times d\mathbf{L} \right)_r = -\frac{Q}{m_i} \int_0^Z B_\varphi dz \quad (2.15)$$

and

$$\Delta v_z = v_{fz} - v_{0z} = v(\cos \Omega - \cos \theta) = -\frac{Q}{m_i} \left(\int_0^{\mathcal{L}} \mathbf{B}_\varphi \times d\mathbf{L} \right)_z = \frac{Q}{m_i} \int_0^{\mathcal{R}} B_\varphi dr, \quad (2.16)$$

where we described the components of \mathbf{v}_f and \mathbf{v}_0 using the observation and divergence angles Ω and θ , respectively.

¹Interestingly, the bisection of the deflection angle α producing two right triangles is also used by the Boris algorithm [166] for numerical calculation of charge particle movement in B-fields. The right triangles are utilized by this algorithm to perform a discretized ion rotation using a vector triple product of the ion velocity and B-field vectors.

In practice, the deflectometry setups are usually designed to set at least one of the angles θ and Ω small. In that case, the other angle is equal in magnitude to the deflection angle α because $|\alpha| = |\Omega - \theta|$. Then, we can rewrite Eq. (2.15) and Eq. (2.16) only using the deflection angle α

$$|\sin \alpha| = \frac{|\Delta v_r|}{v} = \frac{Q}{mv} \left| \int_0^Z B_\varphi dz \right| = \frac{Q}{\sqrt{2m_i E}} \left| \int_0^Z B_\varphi dz \right| \quad (2.17)$$

and

$$1 - \cos \alpha = \frac{|\Delta v_z|}{v} = \frac{Q}{mv} \left| \int_0^{\mathcal{R}} B_\varphi dr \right| = \frac{Q}{\sqrt{2m_i E}} \left| \int_0^{\mathcal{R}} B_\varphi dr \right|, \quad (2.18)$$

respectively.

In the typical experimental setup, shown in Fig. 2.9a, we can use Eq. (2.17) for $\int_0^Z B_\varphi dz$ instead of general Eq. (2.13) for $\int_0^{\mathcal{L}} \mathbf{B}_\varphi \times d\mathbf{L}$ because the used ion detector records only radial (lateral) ion beam displacements Δr corresponding to Δv_r . Measuring the B-fields along the z -axis allows to estimate the axial length of the ion path Z (see Fig. 2.9a) and calculate the averaged B-fields $\overline{B_\varphi} = \int_0^Z B_\varphi dz / Z$. Interestingly, a product $\overline{B_\varphi} Z$ is analogous to a magnetic field-radius product $\overline{B_z} \mathcal{R}$ studied for quantitative measurements of the plasma-fuel stabilization by axial B-fields B_z in the Magnetic Liner Inertial Fusion (MagLIF) experiment [167].

Estimating the path-integrated electric or magnetic fields using ion deflectometry usually requires numerical Monte-Carlo simulations calculating trajectories of test charged particles sent into proposed fields. The estimated fields are found by adjusting their profile (a forward fit) to produce a synthetic image matching the experimental data. However, given by a range of mapped simulation parameters, it is possible that forward ion-tracking simulations can only find some of possible solutions for deflecting field profiles. Nevertheless, the path-integrated fields in many laser-plasma experiments can be recovered from experimental images using direct image analysis. In specific cases, the B-field recovery analysis has even an analytical solution. It is possible due to the specific properties of the laser-produced plasmas allowing the *paraxial approximation*.

2.4.3 Paraxial approximation

Kugland *et al.* [168] introduced an analytical approach to processing the proton images via the *paraxial approximation*, which calculates spatial distributions of the path-integrated fields from D-grid displacements or distorted proton-fluence features recorded by the detector.

The configuration in Fig. 2.10 illustrates prerequisites for the paraxial approximation in the azimuthal B-field measurements. Suppose the interaction B-field region is spherical with a diameter of $2a$ and there are no proton deflections outside it. In the laser-plasma experiments, we assume that the region's size $2a$ is small compared to the distances of the proton source l_S ($2a \ll l_S$) and the detector l_D ($a \ll l_D$). The essential assumption of the paraxial approximation is that the proton deflections are minimal ($\alpha \ll 1$). Then, we can linearize the electric and

magnetic deflection equations [Eq. (2.11) and Eq. (2.17)] using $\tan \alpha \approx \alpha \propto \int \mathcal{E}_r dL$ and $\sin \alpha \approx \alpha \propto \int B_\varphi dz$, respectively. To manifest distortions of the captured ion beam image, we place the detector at a considerable distance producing a high magnification ($l_S \ll l_D$).

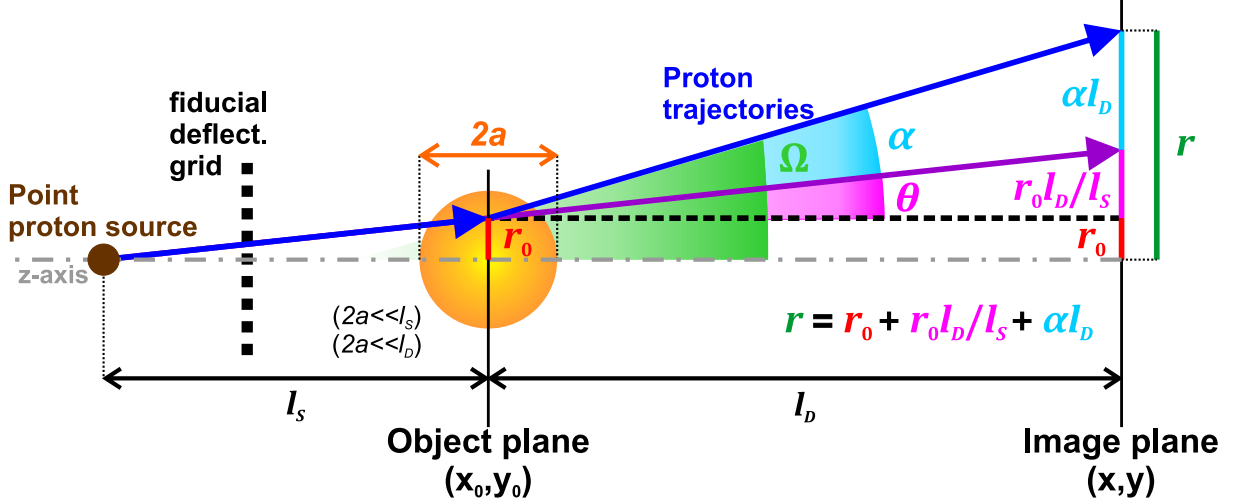


Figure 2.10: Experimental setup of proton radiography experiments demonstrates the geometry and the requirements for the paraxial approximation and the B-field inversion from the proton radiographs.

As a result of these assumptions, we can view proton deflections in this setup as instant rotations of proton beams in the interaction region localized into to an *object plane*. Accordingly, proton trajectories become connections of two line segments because proton beams travel freely before and after their instant deflection (see Fig. 2.10). Moreover, due to the high magnification and small size of the interaction region, the proton displacements due to magnetic deflections inside the plasma are negligible compared to ballistical displacements of proton beams in the detector plane ($\alpha a \ll \alpha l_D$), referred to as an *image plane*.

Now, we derive the paraxial approximation for deflections in azimuthal B-fields. For radial electric fields, the derivation is analogous. For better clarity, we assume axisymmetry ($\partial/\partial\varphi = 0$) and consider only radial (lateral) and axial (longitudinal) coordinates. The initial proton positions in the object plane (e.g., in the moment of deflection) are r_0 and z_0 . Since B-fields are projected onto this plane, the spatial distribution of path-integrated B-fields is characterized by $\alpha(r_0) \propto \int B_\varphi dz$. By examining the illustrative proton trajectory in Fig. 2.10, we find the final radial position of deflected proton beams in the detector (image) plane is given by

$$r = r_0 + \frac{r_0}{l_S} l_D + \alpha(r_0) l_D \approx \frac{l_D}{l_S} \left(r_0 + \alpha(r_0) l_S \right). \quad (2.19)$$

Due to the high magnification ($l_D \gg l_S$), we neglect the first term in Eq. (2.19) equal to the initial radial position of the proton ray r_0 . The second term relates to a projected image of undeflected proton beams. The last term is coupled with the proton displacements in B-fields inside the plasmas projected onto the image plane. In other words, a surface element $dS_0(r_0)$ of

the proton image in the object plane is mapped to the surface element $dS(r)$ in the image plane. Assuming axisymmetric deflections, we describe the surface transformation using an absolute value of a Jacobian determinant

$$\left| \frac{dS(r)}{dS_0(r_0)} \right| = \frac{2\pi r}{2\pi r_0} \frac{\partial r}{\partial r_0} = \frac{r}{r_0} \frac{\partial r}{\partial r_0}, \quad (2.20)$$

The surface element dS of distorted proton image contains information about the local proton deflections due to B-fields in the surface element dS_0 . Therefore, we substitute Eq. (2.19) into (2.20) and obtain

$$dS = \frac{r}{r_0} \frac{\partial r}{\partial r_0} dS_0 = \frac{r}{r_0} \frac{l_D}{l_S} \left(1 + l_S \frac{\partial \alpha}{\partial r_0} \right) dS_0 \approx \frac{l_D^2}{l_S^2} \left(1 + l_S \frac{\partial \alpha}{\partial r_0} \right) dS_0, \quad (2.21)$$

where we use $r/r_0 \approx l_D/l_S$. Protons spreading out from dS_0 into dS produce a modulated proton intensity (fluence) in the detector $\mathcal{I}(r)$ compared to the initial ambient proton beam's profile $\mathcal{I}_0(r_0)$. Since proton fluence modulation $\mathcal{I}/\mathcal{I}_0$ is inversely proportional to dS/dS_0 , we use Eq. (2.21) to find

$$\frac{\mathcal{I}(r)}{\mathcal{I}_0(r_0)} = \frac{dS_0}{dS} = \frac{l_S^2}{l_D^2} \frac{1}{1 + l_S(\partial\alpha/\partial r_0)} \approx \frac{l_S^2}{l_D^2} \left(1 - l_S \frac{\partial \alpha}{\partial r_0} \right). \quad (2.22)$$

Eq. (2.22) demonstrates that the modulation of the proton image $\mathcal{I}/\mathcal{I}_0$ is linearly proportional to a spatial derivative (gradient) of proton deflections $\partial\alpha/\partial r_0$, which we assume to be small ($|\partial\alpha/\partial r_0| \ll 1$). This assumption is essential for the image analysis using the paraxial approximation. Although our goal is to estimate path-integrated B-fields $\int B_\varphi dz$, it is beneficial to substitute them by path-integrated magnetic vector potential $\int A_z dz$. Accordingly, the deflection gradient $\partial\alpha/\partial r_0$ turns into

$$\frac{\partial \alpha}{\partial r_0} = \frac{Q}{\sqrt{2m_i E}} \frac{\partial}{\partial r_0} \int B_\varphi dz = -\frac{Q}{\sqrt{2m_i E}} \frac{\partial^2}{\partial r_0^2} \int A_z dz = \frac{\partial^2 \Phi}{\partial r_0^2}, \quad (2.23)$$

where Φ is a deflection potential given by $\Phi = -Q/(\sqrt{2m_i E}) \int A_z(r_0, z_0) dz_0$. Substituting Eq. (2.23) into Eq. (2.22), we obtain the Kugland inversion equation [168]

$$\frac{\partial^2 \Phi}{\partial r_0^2} = \frac{1}{l_S} \left(1 - \frac{l_D^2}{l_S^2} \frac{\mathcal{I}}{\mathcal{I}_0} \right). \quad (2.24)$$

If we do not assume the axisymmetry, Eq. (2.24) takes a general form of a Poisson's equation [168]

$$\nabla_{\perp 0}^2 \Phi(x_0, y_0) = 4\pi \mathcal{P}(x_0, y_0) \quad (2.25)$$

where $\nabla_{\perp 0}^2$ is a Laplace operator for the lateral coordinates (x_0, y_0) in the object plane, and \mathcal{P} is a source term, coupled with the proton fluence (intensity) \mathcal{I} of the radiograph. In addition to the magnetic deflections, Eq. (2.25) applies also for electric deflections with a corresponding potential $\Phi_{\mathcal{E}}(x_0, y_0) = (Q/2E) \int \phi_{\mathcal{E}}(x_0, y_0) dz_0$, where $\phi_{\mathcal{E}}(x_0, y_0)$ is a scalar electric potential. Eq. (2.25)

is a special case of an elliptic Monge–Ampère equation [169]. This type of differential equation enables retrieval of the path-integrated potential Φ and, subsequently, the path-integrated field [170].

For solving Eq. (2.25) and proton radiography in general, individual proton rays must not cross each other. Although in the setup, illustrated in Fig. 2.10, protons diverge, they still can intersect if there is a significant difference between deflections of individual neighboring proton beams. In other words, the B-field recovery fails when the deflection gradients $\partial\alpha/\partial r_0$, connected to the image distortions $\mathcal{I}/\mathcal{I}_0$ and contrast, are too strong. To qualitatively evaluate the deflection gradients, we introduce a so-called *contrast parameter* given by

$$\mu = l_S \frac{\alpha}{a}. \quad (2.26)$$

The contrast parameter μ approximates the deflection gradient $\partial\alpha/\partial r_0$ on the RHS of Eq. (2.22) and describes the deflection angles α of proton deflections over the characteristic spatial scale of the interaction region a ($\partial\alpha/\partial r_0 \approx \alpha/a$). According to value of μ , we classify four regimes of the image analysis using the paraxial approximation. These regimes are demonstrated in Fig. 2.11, where proton beams map toroidal B-fields.

If $\mu \ll 1$ (Fig. 2.11a), deflection gradients and image distortions are weak, and so, the proton beams do not cross each other. In this so-called *linear regime*, there is a linear relation between the deflection gradient and image distortion (see Eq. (2.22)). Moreover, the Poisson’s equation [Eq. (2.25)] is accurate and has an unambiguous solution. In simple cases of B-field distributions, we can find this solution analytically [168].

If $\mu \lesssim 1$ (Fig. 2.11b), the proton imaging gets into a so-called *non-linear injective regime*. Although Poisson’s equation is no longer accurate, the relation between the deflection potential Φ and the intensity profile \mathcal{I} is still injective and has an unambiguous numerical solution. Therefore, the field inversion from the proton image is commonly performed by many available solvers (namely, PRaLine [171], PROBLEM [172], PRNS [173], PRADICAMENT [174], and *fast-invert-shadowgraphy* [170] using the Voronoi-diagram method). For the most complex systems, neural network training has been employed for the proton radiography [175].

If μ reaches a critical limit $\mu_C \approx 1$ ($\mu \approx \mu_C$), a so-called *caustic regime* occurs (Fig. 2.11c). In this regime, some of the proton beamlets become so deflected that they start to cross each other, and typical *caustic* high-proton-fluence structures appear in the radiographs (see Fig. 2.11). In this regime, the inversion problem is not well-posed, and the image analysis provides multiple solutions. However, reconstruction algorithms are usually close to the correct solution if the proton source is almost perfectly point-sized.

If $\mu > \mu_C$ (Fig. 2.11d), the caustics become branched because crossing proton rays create two high-fluence structures. Without the knowledge of their origin, these structures can be falsely attributed to less deflected not crossing proton beams. Therefore, the numerical reconstruction algorithms provide significantly inaccurate results. The branched caustic regime occurs, for example, during the reconstruction of strong and stochastic fields, such as B-fields generated

by Weibel instability. Usually, these fields have an unpredictable and complicated distribution. Thus, their reconstruction from experimental proton images can be very difficult. Therefore, proton imaging of these B-fields is still subject of the contemporary research [172], [176]–[179].

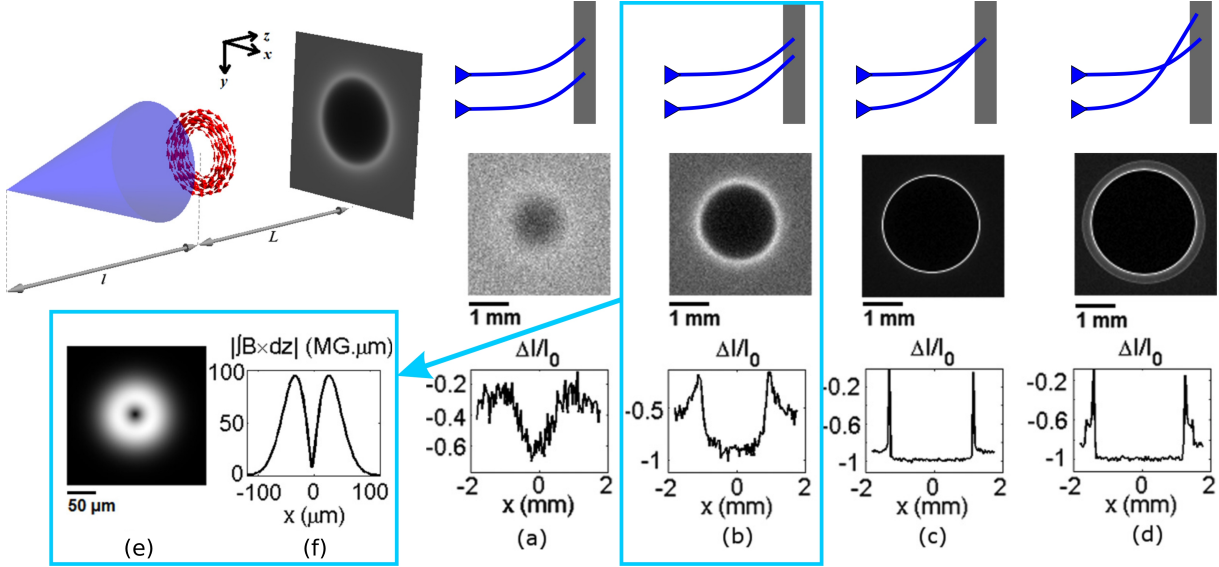


Figure 2.11: In a test configuration, proton beams are fired into toroidal B-fields with different strengths. Deflections of proton beams in these fields lead to the intensity modulation $\Delta\mathcal{I}/\mathcal{I}_0$ of the synthetic radiographs. The proton fluence profile along lateral cross-section in synthetic images demonstrate contrast regimes of proton deflectometry: (a) small intensity modulation - *linear regime* ($\mu \ll 1$), (b) large intensity modulation - *non-linear regime* ($\mu < 1$), (c) proton rays cross each other and caustics are formed - *caustic regime* ($\mu \approx \mu_C \sim 1$), and (d) proton rays overcross and the caustics become branched - *branched caustic regime* ($\mu > \mu_C$). (e) A profile of the path-integrated B-fields retrieved from the proton image (b). (f) The lateral 1D cross-section of the reconstructed B-fields. Note that brighter colors indicate higher protons and path-integrated B-field magnitudes. The figure has been compiled from two figures in [170].

The contrast parameter highlights the general requirement of small deflection angles α for ion deflectometry measurements. Accordingly, the experiments in the linear regime are the most beneficial for the B-field recovery. Moreover, this regime is significant for the physical interpretation of the data, which is possible with the naked eye without any analysis. According to Eq. (2.22), the modulated proton intensity of the radiographs \mathcal{I} in this regime depends linearly on the deflection angle gradient $\partial\alpha/\partial r_0$. Therefore, according to Eq. (2.23), it is also linearly proportional to the gradient of the path-integrated B-field $\partial(\int B_\varphi dz)/\partial r_0$, which we can couple to the path-integrated current density $\int J_z dz$. It means that the distribution of the distortions manifests the current density distribution and the radiograph somehow shows where the current flows. In the case of the toroidal B-fields in Fig. 2.11, it flows near the central axis of the toroid, which in the proton image creates a high-fluence ring structure. The reconstruction of the path-integrated fields from the experimental proton images has been successfully utilized in numerous experiments with laser-produced plasmas [174], [180]–[184].

In the following section (Sec. 2.5), we review the state-of-the-art deflectometry and radiog-

raphy/deflectometry experiments in laser-produced and z-pinch plasmas.

2.5 Proton radiography/deflectometry experiments in HED plasmas

The ion radiography/deflectometry allows measurements of the spatial distribution of transient electric and magnetic fields in the laser-produced plasmas. Most current experiments employ laser-accelerated protons. Subsec. 2.5.1 shows results from several interesting proton radiography measurements. A few proton deflectometry experiments have also been performed in z-pinch-like B-fields. However, the development of the ion deflectometry measurements in z-pinch-like B-fields has stopped since they required a short-pulse high-intensity laser for the proton probe production. Already performed experiments are discussed in Subsec. 2.5.2.

2.5.1 Proton imaging of laser-produced plasmas

Proton beams accelerated via TNSA (Subsec. 2.2.1) have a wide range of possible applications. Therefore, this proton accelerating mechanism is widely investigated and optimized to achieve the highest energies (reaching up to 100 MeV [130]). To better understand the phenomena concerning the TNSA mechanism, the related laser-target interactions have been probed by TNSA-driven protons [7], [185]–[188]. The broad energy spectrum of these protons allowed multi-frame snapshots of the evolving E-fields (see Fig. 2.12) created by fast electrons ejected from the rear side of the target.

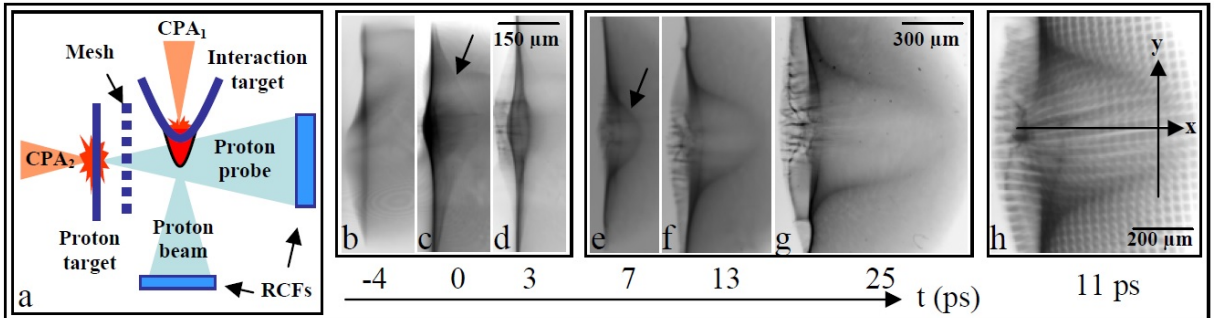


Figure 2.12: Side-on proton probing of the Target-Normal-Sheath-Acceleration (TNSA) electric fields generated by fs laser pulses [185], [186].

The TNSA mechanism leads to an ultra-short ionisation pulse generated inside the target due to the prompt escape of relativistic electrons from the target. In addition to E-field measurements, TNSA-driven protons have been able to capture (with a μm -spatial and ps-temporal resolution) a propagation of this pulse along the surface of a metallic wire attached to the target (see Fig. 2.13). Interestingly, the dominating deflections were caused by propagating electric fields, meaning that magnetic fields were negligible. The amplitude of the deflecting E-fields was

a few GV/m. The uniqueness of these measurements lied in the measured speed of propagating E-fields, which was close to the speed of light [189], [190].

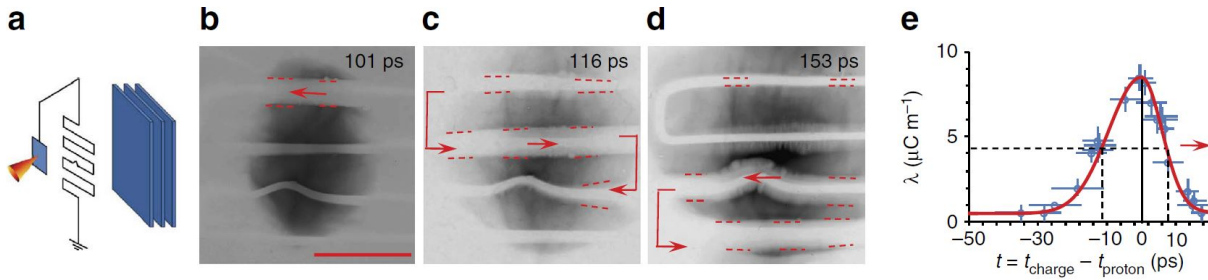


Figure 2.13: Proton imaging of the propagation of the ionisation pulse created by proton accelerating laser-target interaction [189].

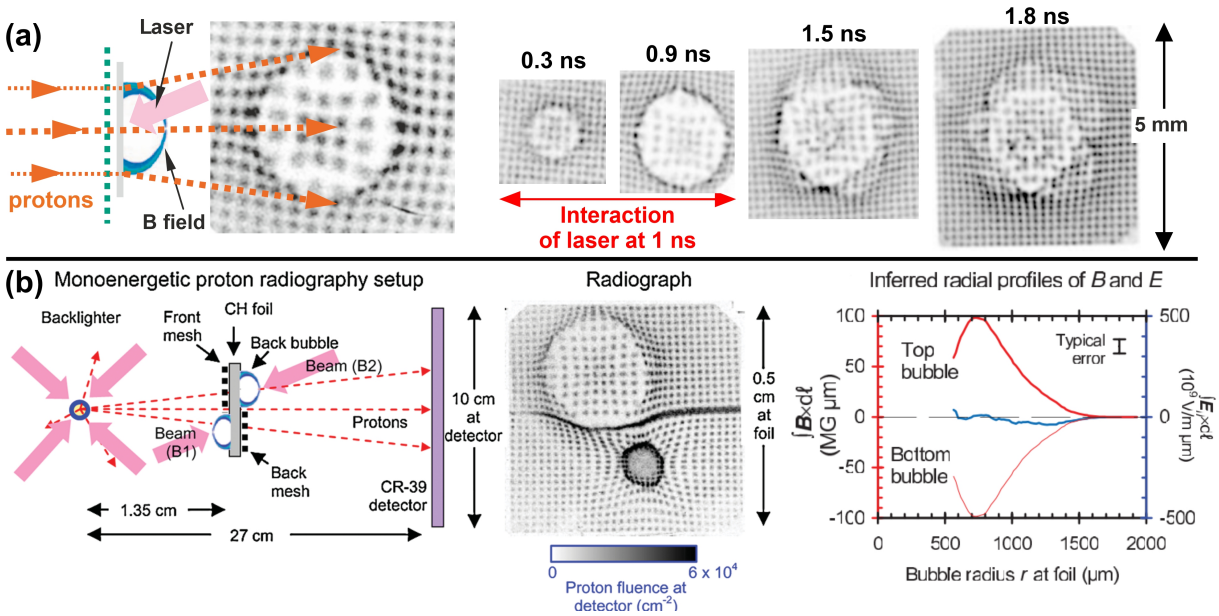


Figure 2.14: (a) Laser-driven plasma plumes (bubbles) were investigated by proton radiography with strong self-generated EM fields. [191] (b) To determine whether radial electric or azimuthal magnetic fields were predominantly present in these plasmas, two plasma plumes were created on the opposing sides of the target foil. From the experimental radiographs and measured path-integrals of acting fields, proton radiography proved the existence of strong MGauss azimuthal magnetic fields in these plasmas [142].

Fig. 2.14a shows laser-produced plasma plumes (bubbles), which are widely examined in the laser community due to strong self-generated EM fields. Proton radiography has been utilized to determine the nature of these EM fields [186], [191], [192]. In theory, both radial electric and azimuthal magnetic fields could cause proton deflections resulting in proton images displayed in Fig. 2.14a. However, these two types of fields can be distinguished by the change in the relative orientation of the incoming proton beams with respect to these fields. Accordingly, in experiments illustrated in Fig. 2.14b, two plasma bubbles have been produced at the front and the rear side of the single target by two independent ns laser beams. The contrasting character

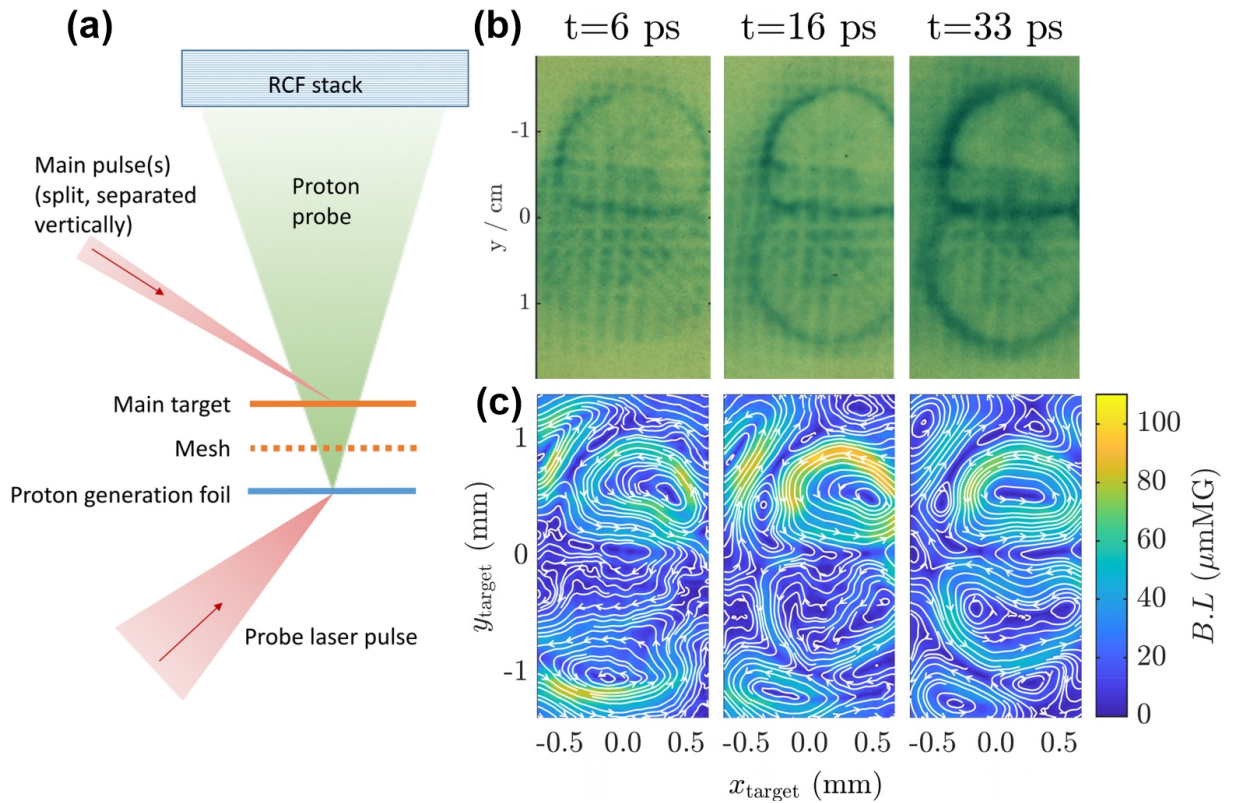


Figure 2.15: (a) Experimental setup and the (b) experimental proton radiographs revealing the azimuthal self-generated B-fields in the experiments with the plasma plumes created by laser-target interactions. (c) A numerical algorithm for image analysis identifies modulations of proton fluence in the experimental image and reconstructs distributions of path-integrated B-fields [181].

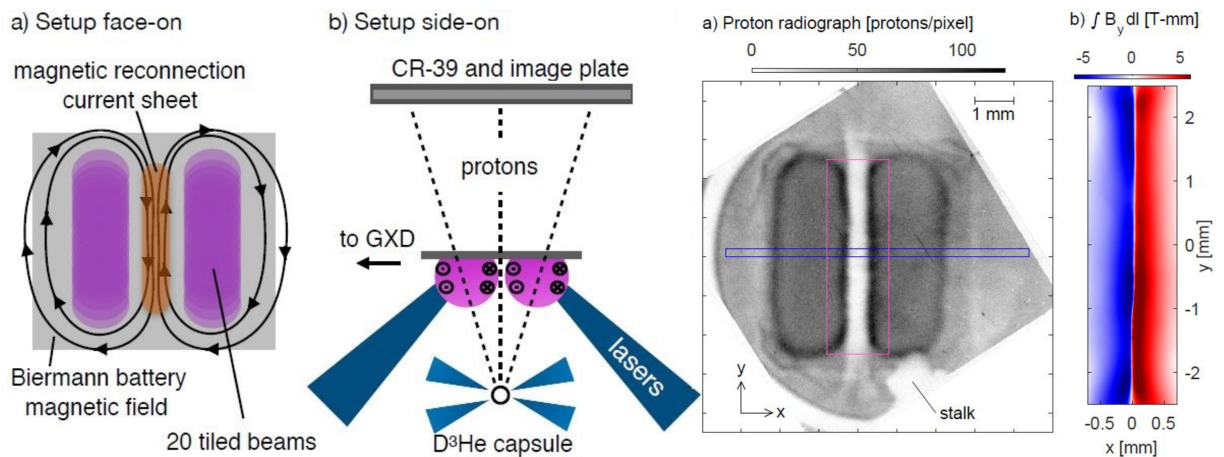


Figure 2.16: The experimental setup and the experimental proton image of two colliding plasma bubbles, which accommodate fastly reconnecting self-generated azimuthal B-fields and produce plasma jets. The path-integrated B-fields are estimated near the border between the bubbles [174].

of the proton deflections in these bubbles (see Fig. 2.14b) showed that the dominating proton deflecting force originated in the strong azimuthal B-fields. Deflections of axial proton beams caused by radial electric field would not change the direction. Fig. 2.15 presents azimuthal B-fields of two colliding plasma bubbles [181] reconstructed using the PROBLEM code (developed by Bott *et al.* in [172]) based on the paraxial approximation of the proton trajectories (see Subsec. 2.4.3).

Azimuthal B-fields in these plasma bubbles attracted much attention in the laser community because their strengths are typically in MGauss (hundreds of Tesla). These B-fields were measured and studied in various experiments using proton deflections [141], [142], [191]–[197]. Such strong self-generated B-fields \mathbf{B}_φ are caused by a so-called Biermann battery mechanism ($\partial\mathbf{B}_\varphi/\partial t \propto \nabla T_e \times \nabla n_e$), when non-parallel gradients of temperature ∇T_e and density ∇n_e are generated in the plasma by the interaction ns laser pulse with a foil target. In addition, proton imaging of two colliding plasma bubbles with frozen-in azimuthal B-fields allowed investigation of the magnetic reconnections [138], [174], [181], [182], [198]–[204] (see Fig. 2.16) and plasma jets [129], [205] (see Fig. 2.17), both relevant to the astrophysical objects.

Moreover, strong MGauss vacuum B-fields has been generated by laser-driven capacitor coils and then diagnosed by laser-produced protons [206]–[215]. Intriguing current filamentary structures produced by the Weibel instability (Fig. 2.18) due to the anisotropic electron velocity distribution are investigated via the proton radiography in the experiments with two colliding plasmas [216]–[222].

In experiments where the electric and magnetic fields are both present, the proton radiography can estimate the ratio of their strengths; for example, in the implosions of the directly-driven ICF capsules [126], [137], [139], [140], [191], [225]–[227] and the plasma flows inside irradiated hohlraums [136], [228], [229] (see Fig. 2.19). Recently, the proton radiography has been developed and demonstrated on National Ignition Facility (NIF) [230], [231]. Moreover, this diagnostic method allowed to study of EM fields present in collisionless shocks [223], [232]–[242]. In astrophysics, comparable shock waves are generated during the propagation of a supernova remnant blast shell into the interstellar medium and they are supposedly the dominant source of galactic high energy cosmic rays.

Besides protons, relativistic electrons have also been used for radiography of electric and magnetic fields [224], [243]–[246]. Fig. 2.20 demonstrates mapping transient magnetic fields associated with the electron thermal Weibel instability of a plasma wake traveling almost at the speed of light [224].

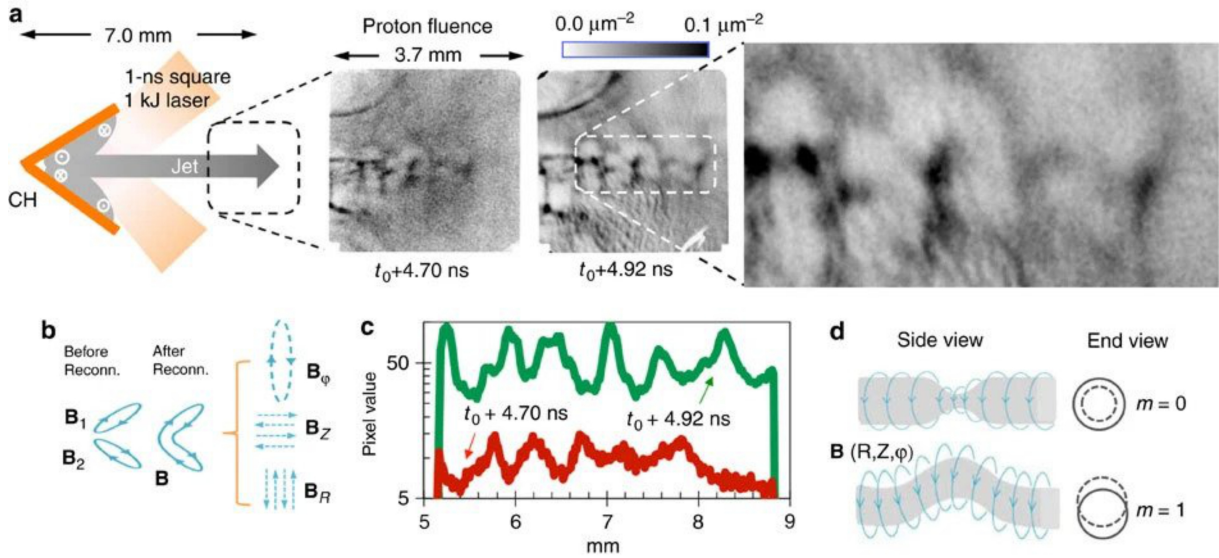


Figure 2.17: Scaled laboratory experiments explain the kink behaviour of the Crab Nebula jet. Interaction of the laser beam with the cone-shaped target forced two plasma plumes to collide and produce a plasma jet. Side-on proton radiographs of the frozen-in toroidal B-fields were mapped at two moments corresponding to two proton energies, i.e., ~ 3.3 and ~ 15 MeV. (b) Self-generated azimuthal B-fields (B_1 and B_2) associated with the two plasma plumes reconnect with each other. (c) Periodical fluctuations of the proton fluence in the direction of the jet has been contributed to (d) the current instabilities ($m = 0$ and $m = 1$) driven by these B-fields [129].

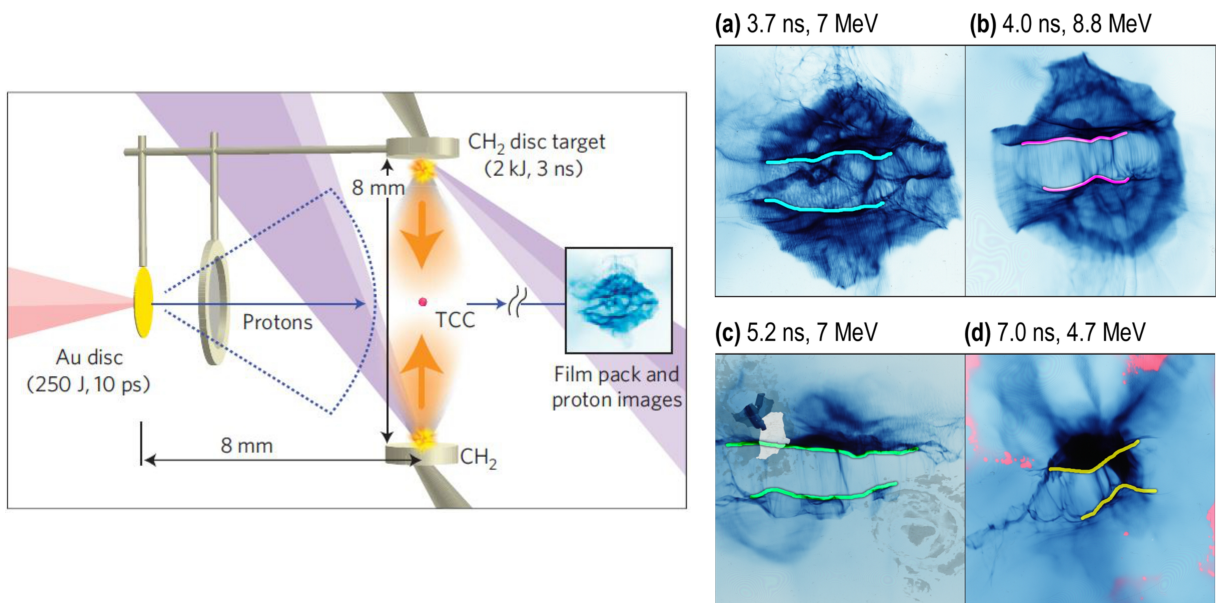


Figure 2.18: Experimental setup and obtained data of experiments studying self-generated filamentary structures in laser-produced counter-streaming plasmas. (a-d) The proton radiographs show horizontal bands of caustics over proton energies from 7 to 15 MeV, recorded by RCFs in various times of a single shot [180], [223].

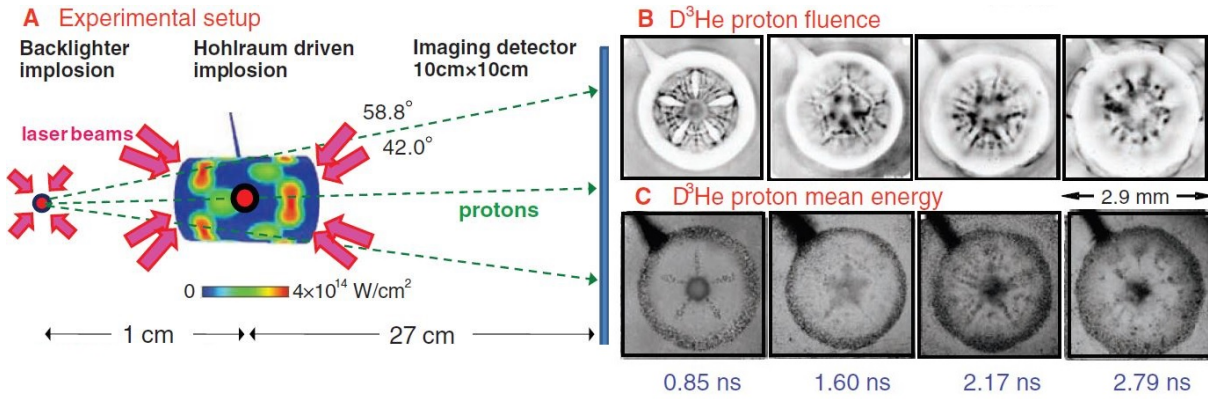


Figure 2.19: Proton radiography of electric fields created in ICF hohlraum-driven implosions [136].

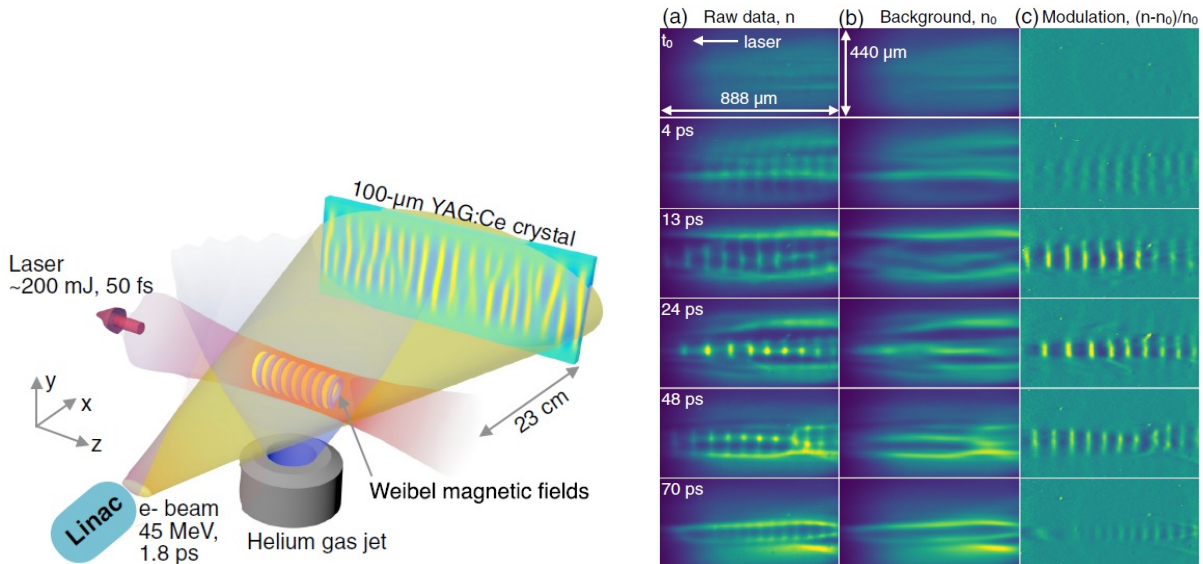


Figure 2.20: Experimental setup and the experimental electron radiographs of Weibel magnetic fields produced in the laser-produced plasma wakes. Ultrashort (1.8 ps), relativistic (45 MeV) electron bunches were produced by a linear accelerator [224].

2.5.2 Proton deflectometry in z-pinch plasmas

In z-pinch plasmas, there were only a few proton deflectometry measurements. They all employed laser-accelerated protons, which mapped the azimuthal B-fields radially. In 2012, dynamic electric fields and kA return currents were investigated in laser-driven z-pinch plasmas created by irradiating a sloped boron wire by a ns laser pulse at the OMEGA laser facility in Rochester, New York, USA [247]. Fig. 2.21a shows the experimental setup. Here, the wire target was driven by the electric potential produced by the laser interaction and then probed by fusion-based protons generated by an implosion of a thin-glass capsule, the exploding pusher (Subsec. 2.2.2), filled with equimolar D³He gas. Fig. 2.21b displays the energy spectrum of diagnostic proton beams. An energy upshift of ≈ 0.5 MeV has been observed in these interactions due to capsule charging [147], [248]. Therefore, the accelerated protons have almost discrete energy of ≈ 3.5

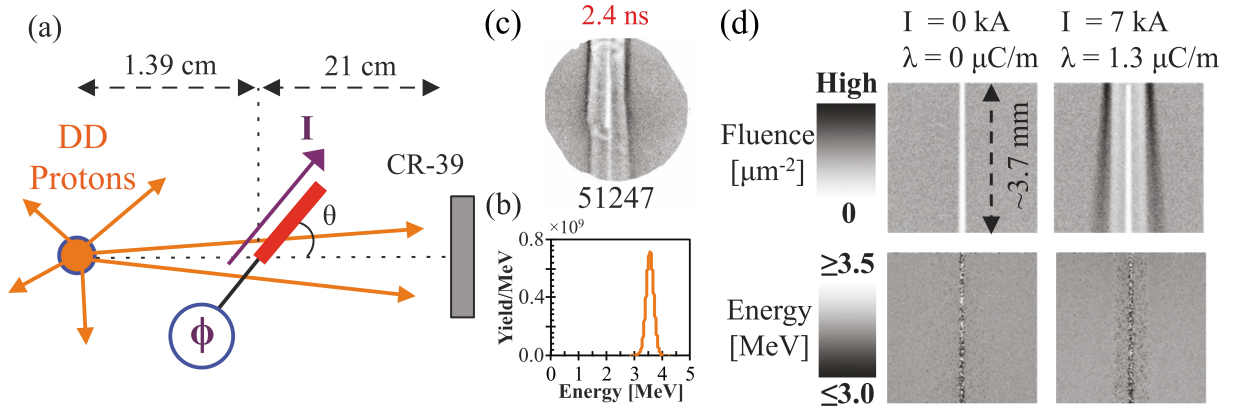


Figure 2.21: (a) Experimental setup of the first-ever proton deflectometry of the laser-driven z-pinch at OMEGA facility in Rochester, NY, USA. (b) The energy spectrum of probing protons was nearly monoenergetic with the mean energy of 3.5 MeV. (c) An experimental proton image displayed two symmetric sets of high-fluence structures (darker color shades) coupled with two types of deflecting fields, namely, radial electric and azimuthal magnetic fields. Production of (d) synthetic proton images comparable with the experimental data using the Geant4 framework allowed estimating the linear charge density λ and the currents I [195], [249].

MeV.

The experimental proton deflectograms (see an example in Fig. 2.21c), captured by CR-39 detectors, reveal two pairs of sloped high-fluence structures coupled with two types of deflecting fields. After irradiating the target, a hot electron population was generated by the laser-target interaction. When electrons escaped the target, they created a residual positive electric charge coupled with dynamic electric fields directed radially outwards from the target. In addition, return currents began to flow around the wire through the plasma, produced by ohmic ablation of the supporting stalk. These currents generated azimuthal magnetic fields deflecting protons. Therefore, there existed two separate regions of radial electric and azimuthal magnetic fields. Fig. 2.21d shows synthetic proton deflectograms obtained by simulating proton trajectories in the given configuration using the Geant4 framework. Reproducing the proton deflectograms in several comparable experiments allowed estimation of the linear charge density λ and dynamic currents I , which reached up to 1.3 $\mu\text{C}/\text{m}$ and 7 kA, respectively.

In 2014, the feasibility of the laser-driven proton deflectometry was investigated at ZEBRA, the MA pulsed-power z-pinch device at the Nevada Terawatt Facility (NTF) in Reno, NV, USA [250]. It was the only ion deflectometry experiment performed on any pulsed-power device. Fig. 2.22a shows the experimental configuration where proton beams were accelerated by laser-induced TNSA mechanism and proton images were recorded by RCF detectors. The resistive MHD code Gorgon and the hybrid PIC (particle-in-cell) code called Large Scale Plasma (LSP) were used to simulate the magnetic fields, calculate corresponding proton trajectories, and produce the synthetic proton images.

In the first experiments (see Fig. 2.22), there was no plasma, and a short-circuit load pro-

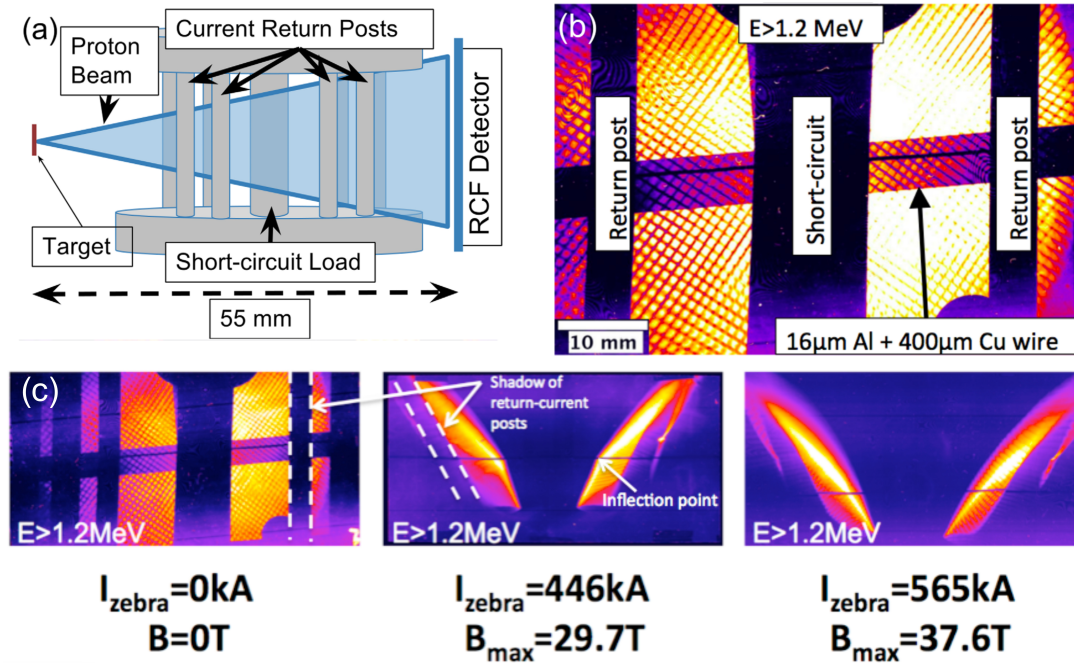


Figure 2.22: (a) Experimental setup of the z-pinch assembly at the Nevada Terawatt Facility (NTF) for proton deflectometry of vacuum z-pinch-like B-fields. (b) An experimental deflectogram of zero B-fields in a reference shot is compared to (c) proton images of non-zero azimuthal B-fields [250]. The RCF images are shown in false color, where the brighter colors represent higher proton fluence.

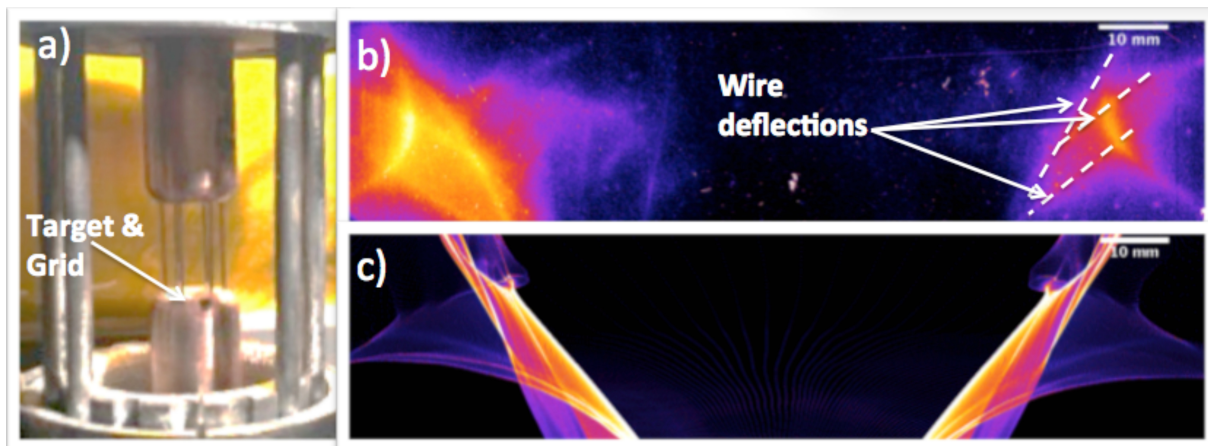


Figure 2.23: (a) Configuration of the proton deflectometry experiments with the wire-array load [249]; (b) experimental and (c) synthetic proton deflection images reveal sloped structures of high proton fluence, similarly to the experiments with vacuum azimuthal B-fields shown in Fig. 2.22.

duced azimuthal B-fields. The cylindrical region of the vacuum B-fields was delimited by current return posts, visible in the deflectogram of the reference shot without any fields shown in Fig. 2.22b. Fig. 2.22c compares the reference proton image with the experimental proton deflection images for two used currents $I = 446$ kA and $I = 565$ kA. The energy of the recorded protons is >1.2 MeV. The experimental data showed again sloped high proton-fluence structures created by the proton deflections distorting the proton image. These sloped structures have proven to be

characteristic of the azimuthal-B-field measurements using radially emitted probing protons (the radial proton deflectometry). Numerical proton-tracking simulations found that the inclination angle of these structures correlated to total currents and maximum magnetic fields. Although the deflectometry grid has been employed, its shadow was drastically distorted due to strong proton deflections and merged with the radial structures.

Fig. 2.23 presents the first successful B-field measurements in z-pinch plasmas performed with a cylindrical wire-array load. The experimental and corresponding synthetic deflectograms agreed and again displayed the characteristic sloped structures. Further deflectometry experiments with other loads, including a hybrid X-pinch and a radial foil load configuration, have been performed on NTF and assessed in the report [249]. However, to our knowledge, no other paper than [250] has been published.

The proton deflectometry has also been considered for the largest pulsed-power z-pinch device

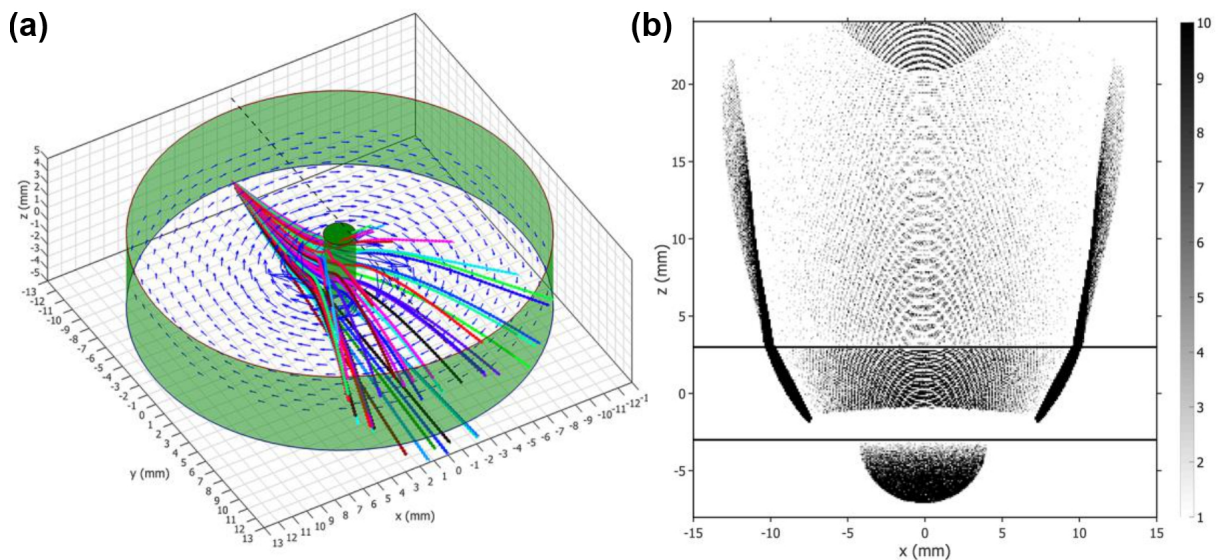


Figure 2.24: (a) Experimental setup and (b) synthetic proton deflectogram evaluated for possible employment of the proton deflectometry on the Z-machine. A volume of the probed B-fields was delimited vertically by the electrodes (vertical black lines in the synthetic deflectogram) and horizontally by return current rods. Because the assumed current of a liner was 20 MA, the required proton energy was 4.5 GeV. The numerical model of the simulation allowed test protons to pass through the boundaries of the B-field region to reveal a complete deflectogram of the deflected proton beam. [251].

in the world, the *Z-machine* [251] (see Fig. 2.24). Numerical simulations (see Fig. 2.24a) showed that probe protons must have energies of 4.5 GeV to radially transverse the external azimuthal B-fields and map the 20-MA imploding z-pinch liner. Proton beams with these extreme energies are so far unachievable. Therefore, the proton deflectometry was suggested for measurements of peripheral B-fields and the total z-pinch current estimation of the Z-machine, but this would still necessitate at least 30-MeV protons. However, numerical simulations of 4.5-GeV protons still provided useful information about the deflectometry in z-pinches. The numerical model assumed that electrodes are transparent to reveal a complete deflectogram of the deflected proton

beam (see Fig. 2.24b).

After the first experiments published in the papers [247] and [250], the development of proton deflectometry in z-pinch plasmas stopped, and the characteristic sloped structures were not further investigated. However, we were convinced that the broader employment of this technique in z-pinch plasmas was possible and that it could provide invaluable knowledge about the azimuthal B-fields and, in general, z-pinch-plasma physics. Thus, motivated by the rapidly growing proton deflectometry diagnostic and its influential results in laser-produced plasmas, we decided to build on the results from [247] and [250], and continue investigating the feasibility of the proton deflectometry in z-pinch plasmas with a focus on azimuthal B-fields.

Chapter 3

Feasibility of proton deflectometry in z-pinch

To analyze proton deflectometry in z-pinch, we have developed a numerical code as a testing platform for evaluating various configurations and examining the previous results of z-pinch deflectometry.

3.1 Development of our ion-tracking numerical code

Our numerical code has been written in Python and extensively utilizes Numpy, Scipy, and Matplotlib packages. Numba, a 'Just-In-Time' (JIT) compiler, optimizes code performance by translating a subset of Python and Numpy routines to fast machine code. The outputs of this code are synthetic ion images, produced using Monte Carlo simulations, and many related parameters, such as path-integrated fields. In the numeric model, the synthetic ion source emits $10^6 - 10^9$ monoenergetic test particles into a uniform emission cone with the divergence half-angle θ . The model neglects interactions of probing charge particles with the surroundings and between themselves. It assumes that B-field variations in time are short compared to the ion emission duration. The model allows B-fields to evolve in time, but for each individual test particle, the B-fields are treated as quasi-static. The ion movement is powered by the Boris Pusher (see App. B.3), which is widely used for the motion of charged particles in B-fields. The Boris algorithm rotates ion velocity vectors while conserving their magnitude and, thus, the ion energy. In this and the following chapters, the presented thesis will provide and comment results obtained using three generations of our numerical code and were published in our three selected papers [1]–[3].

3.2 Selected results of our paper Munzar et al., IEEE (2018) with additional comments

Our first paper [1] evaluates the feasibility of proton deflectometry in z-pinch. Its results have been acquired using our first generation of our ion-tracking code. The paper takes particular interest in (1) the general form of the magnetic deflection equation, (2) the formation of the sloped structures appearing in the experimental data, (3) required properties of the ion source for B-field measurements, and (4) comparison and evaluation of two experimental configurations, i.e., with radially and axially propagating ion beams. We published our results in Special Issue on Z-pinch Plasmas of *IEEE Transactions on Plasma Sciences* [1]. The paper in its entirety is included in the Appendix (App. G.1).

At the beginning of our paper, we introduce our numerical model and then discuss the path-integral $\mathbf{B}_\varphi \times d\mathbf{L}$ coupled with the deflection angle α . In laser-produced plasma experiments, the proton deflections are assumed to be very small ($\alpha \ll 1$) and allow the paraxial approximation (see Subsec. 2.4.3). Therefore, deflection equations connecting the path-integrated fields $\int \mathbf{B}_\varphi \times d\mathbf{L}$ to the deflection angle α are presented by many laser-plasma-community papers in linearized or simplified forms. Our paper derives a generalized magnetic deflection equation [i.e., Eq. (2.13)], which holds for arbitrary deflection angle from the defined interval $[-\pi, \pi]$. We point out that ion deflectometry can only provide the path integral of the studied fields. Thus, given value of the integral $\int \mathbf{B}_\varphi \times d\mathbf{L}$ can be produced by a class of equivalent proton trajectories. The paper refers to the value of this path integral of B-fields as the “ B_L parameter”. However, in years following the publication of our paper, a designation “path-integrated B-fields” has been established among the laser-generated plasma community. That is why we have adopted this designation as well.

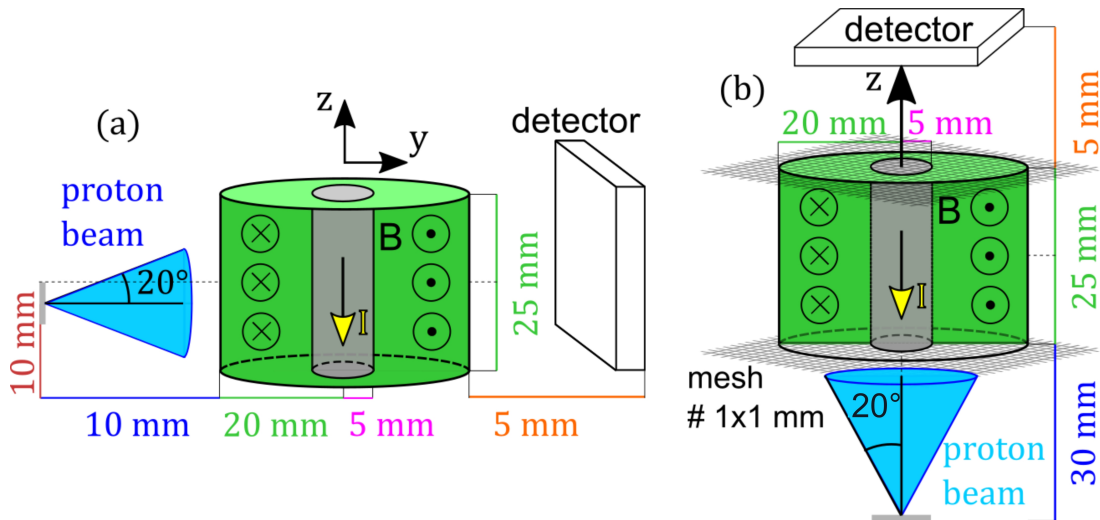


Figure 3.1: Experimental setups of (a) the radial and (b) axial ion deflectometry of azimuthal z-pinch B-fields. The schematics are not to scale.

After finding the general deflection equation, we use our numerical simulations to analyze synthetic deflectograms in two fundamental experimental configurations, illustrated in Fig. 3.1. These setups essentially differ in the direction of the proton beam relative to the z-pinch current. In the radial configuration (see Fig. 3.1a), proton beams are fired radially toward azimuthal z-pinch B-fields. It has been employed for deflectometry measurements in both z-pinch experiments on OMEGA [247] and ZEBRA [250] (Sec. 2.5.2). Based on the results of these experiments, we assume that, for realistic z-pinch currents, the D-grid shadow in proton images will be smeared. Therefore, we exclude the D-grid from the setup and examine only proton fluence in the experimental data. We refer to this configuration as *radial deflectometry*. In the axial configuration, protons are fired axially along the z-pinch axis. In this case, we employ the D-grid to manifest proton deflections and call this technique an *axial deflectometry*. This configuration resembles the typical setup of common measurements of azimuthal MGauss B-fields generated in laser-produced plasma plumes via the Biermann battery (see Fig. 2.14).

In both configurations, proton beams probe the same experimental load in a setup corresponding to the experiments on ZEBRA at the Nevada Terawatt Facility (NTF), (cf. Fig. 2.22), which represents as a characteristic high-impedance z-pinch device with the MA current and the 100-ns rise time. The backlighter in our model is a point-like proton source producing uniform laminar beams. The interaction region is delimited radially by virtual return-current current conductors arranged at a radius $R_B = 20$ mm and axially by two virtual electrodes separated by a 25-mm gap. The simulated experimental load is a 5-mm radius cylindrical z-pinch (the gray region in Fig. 3.1) with the electric current I flowing in the negative direction of the z-axis and creating static azimuthal B-fields. For each experimental setup, we examine whether synthetic deflectograms can distinguish the B-field distribution inside the z-pinch. To that end, we evaluate: (a) the skin current profile when the current flows only through a surface of the z-pinch and B-fields are zero inside the z-pinch, which we refer to as *hollow*; and (b) the constant-current-density profile where azimuthal B-fields grow linearly with the radius inside the z-pinch, which we refer to as *full*. Outside the z-pinch (green regions in Fig. 3.1), there are no currents, and thus, the vacuum B-fields have the $1/r$ -distribution.

In the following Subsection, we focus on the radial deflectometry and corresponding synthetic proton images.

3.2.1 Radial deflectometry of the azimuthal B-fields

In the radial deflectometry setup (Fig. 3.1a), the backlighter emits proton beams radially into z-pinch's azimuthal B-fields. The proton detector recording radial displacements of deflected proton beams is located on the other side of the z-pinch than the proton source. This configuration has been chosen in both measurements of z-pinch-like azimuthal B-fields at the Omega and NTF facilities [247], [250]. In these experiments, proton images [see Fig. 2.21b and Fig. 2.23b] revealed sloped structures with higher proton fluence. It has been shown that the slope angle of these structures for a given beam energy E is attributed to the total z-pinch current I . However,

the origin of the structures has been explained in neither of these papers [247], [250]. Therefore, we use our simulations in the setup shown in Fig. 3.1a to investigate the formation of synthetic deflectograms and find the origin of these structures.

To evaluate the employment of proton deflectometry in typical MA z-pinches, we examine azimuthal B-fields created by z-pinch currents of 0.7, 1.0, and 1.3 MA flowing within the 5-mm radius R_p . In the same setup, experiments at NTF employed 1.2-MeV protons to map only a 446-kA z-pinch. Magnetic deflections grow with the B-field magnitude and, hence, the current's first power ($B_\varphi \approx I$) but the proton energy's square root (see Eq. (2.17)). Thus, we can produce comparable data with the results at NTF if we employ proton beams with the 10-MeV energy since $(1.3 \text{ MA}/0.446 \text{ MA})^2 \cdot 1.2 \text{ MeV} \approx 10 \text{ MeV}$.

Fig. 3.2 compares the results of our simulations for two current density profiles of the mapped z-pinch. In blue, it is a “hollow” Z-pinch with skin currents, and in red, it is the “full” z-pinch with the constant current density. Because the experimental setup is azimuthally symmetrical, we compare only halves of the synthetic deflectograms for each B-field profile. In this configuration, we choose the divergence half-angle θ of proton beams equal to 20° . In all images and both B-field distributions, the sloped structures appear in the synthetic data (Fig. 3.2) and are similar to the ones observed in experiment (Fig. 2.22c). These structures delimit an area of low proton fluence in the center of the deflectogram. The lower-fluence area and the slope angle of the structures increase with increasing z-pinch current I . However, the particular profile of the current density (and the B-field) has only minimal impact on the shape of the deflectograms and the sloped structures. It affects the synthetic deflectograms (see Fig. 3.2) only in the area adjacent to the sloped structures closer to the z-axis. In the proton fluence of the “hollow” z-pinch deflectograms, there is a shadow near the inner side of the slope structure. In the case of the “full” z-pinch, there is no shadow, and the sloped structures are more pronounced. Nonetheless, such minor differences can be hard to notice experimentally.

Fig. 3.3 provides additional information about the sloped structures by comparing the cross-sectional proton fluence and calculated path-integrated B-fields corresponding to the proton signal along the dotted line in the synthetic deflectograms (in Fig. 3.2). This analysis shows that the sloped structures' high proton fluence correlates with the path-integrated B-field's maximum. Therefore, the sloped structures are produced by the most deflected protons. Interestingly, for 1.3-MA current, the path-integrated B-field distribution is no longer an injective function of the radial position in the detector plane. This area of the synthetic deflectograms indicates two possible values of the path-integrated B-fields and, thus, two possible deflection angles α of the captured protons. Moreover, in the case of the constant-current-density profile of the 1.3-MA z-pinch (the red graphs), the area of the sloped structure has two peaks in the recorded proton fluence. In other words, the sloped structure is branched (see Fig. 3.2c). Further analysis of the sloped structures is complicated because the realistic deflectograms in Fig. 3.2 display only a small portion of the deflected ion beam due to non-transparent electrodes.

To investigate how the sloped structures are formed, we modify our numerical model. Now,

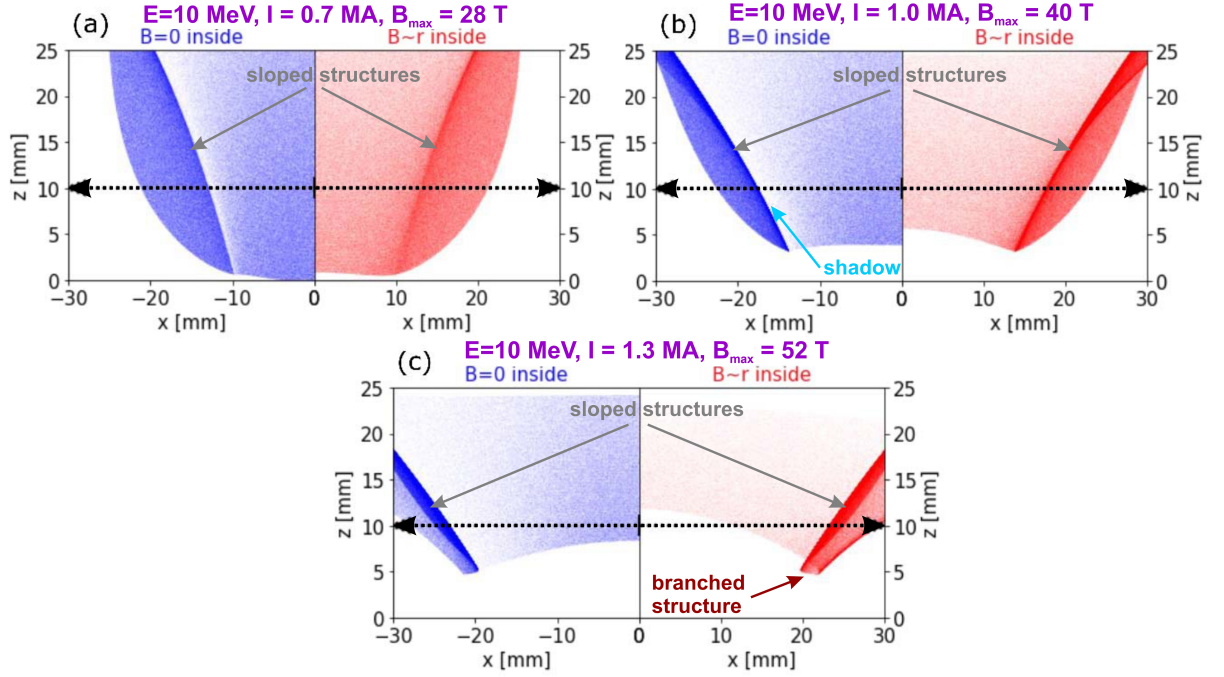


Figure 3.2: Synthetic proton images of the radial deflectometry of the skin-current z-pinch (blue) and the constant-current-density z-pinch (red) for (a) 0.7, (b) 1, and (c) 1.3 MA currents flowing within the 5-mm radius.

we axially extend the B-field region to infinity and permit protons to pass through the virtual electrodes. In addition, we increase the proton divergence up to 40° to probe the B-field area at different angles. As a result, we can analyze the distorted image of the whole proton beam for the 1.3-MA z-pinch in Fig. 3.4a. If the electrodes were not transparent, the realistic deflectograms would show only an area delimited by the dashed lines, which corresponds to Fig. 3.2c. Fig. 3.4a shows that the proton beam, which initially had a circular cross-section, is vertically elongated upstream to the z-pinch axial current due to proton deflections. Interestingly, the branched sloped structures are a part of larger “wing” features that overlap the other deflectogram’s areas. Comparing the two halves of the deflectogram, we observe that even the complete image of the distorted proton beam cannot distinguish the current profile.

Based on our simulations, Fig. 3.4b displays a map of proton displacements $\Delta \mathbf{r}$, which helps us elucidate the structure of the synthetic deflectograms. We see that B-fields force protons in the beam to rotate in the poloidal direction (around the azimuthal B-fields). It is crucial that the spatial distribution of the “proton rotations” is not uniform, so specific protons are more deflected than others. In addition, the rotations on opposite sides of the z-pinch have opposite directions. As a result, the deflected proton beam unravels like a blossom due to proton deflections and creates a low-proton-fluence region near the axis bordered by the sloped high-proton-fluence structures. This rotation is generated by two basic proton deflections in azimuthal B-fields, demonstrated in Fig. 3.5a-b. As the proton beam with a predominant longitudinal (radial) velocity v_r approaches the z-pinch, the azimuthal B-fields B_ϕ cause a strong

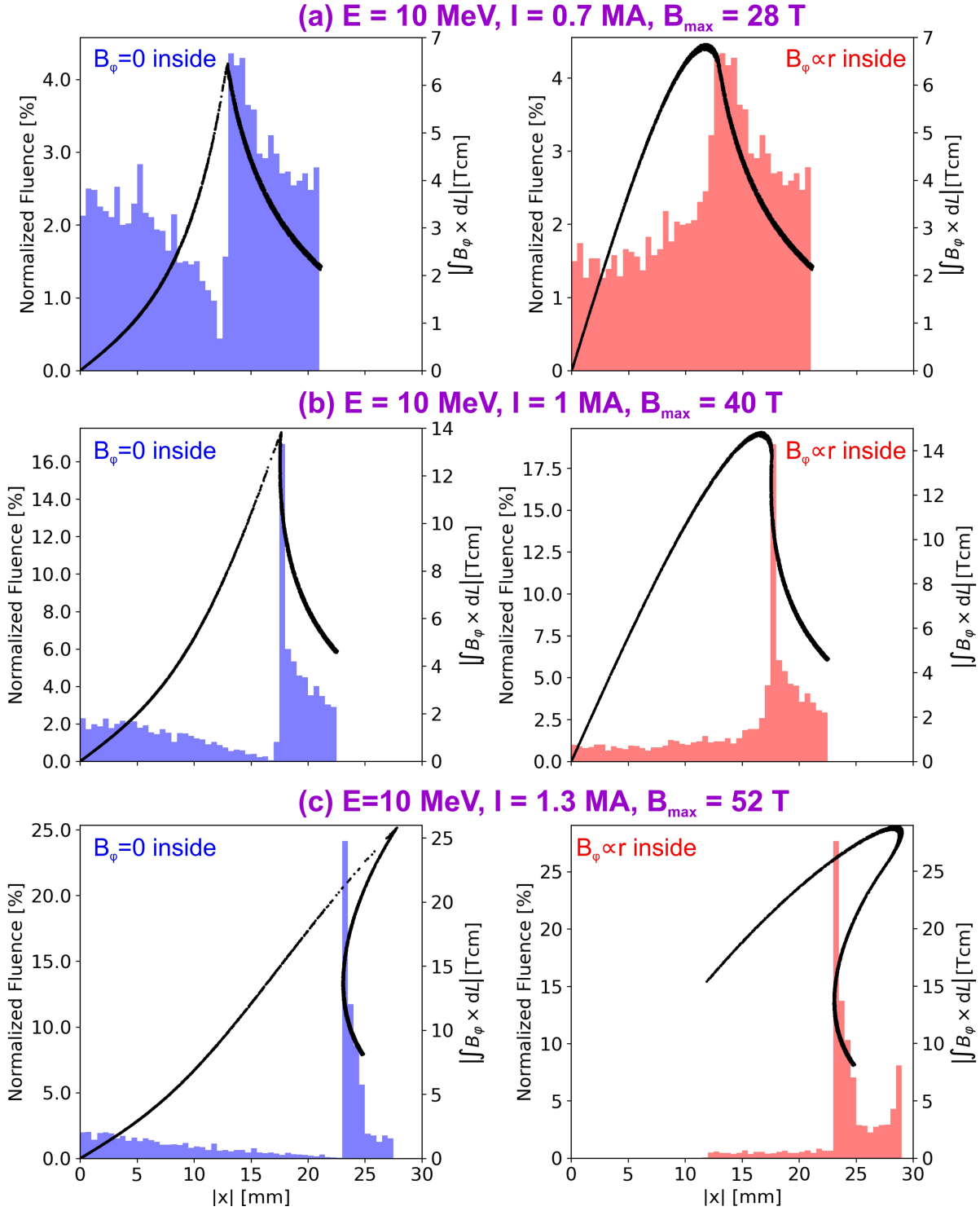


Figure 3.3: Radial cross-sections of fluence (bars) and the calculated path-integrated B-fields (black curves) for protons detected along the highlighted dotted lines in Fig. 3.2. Left: the skin-current z-pinch [$B_\phi(r < R_p) = 0$]. Right: the constant-current-density z-pinch [$B_\phi(r < R_p) \propto r$].

axial force $F_z = Qv_r B_\phi$ (see Fig. 3.5a) in the opposite (upstream) direction to the z-pinch current. Moreover, an upstream axial velocity component $+v_z$, produced by this axial deflection or given by the initial beam divergence θ , generates with the azimuthal B-fields a radial force

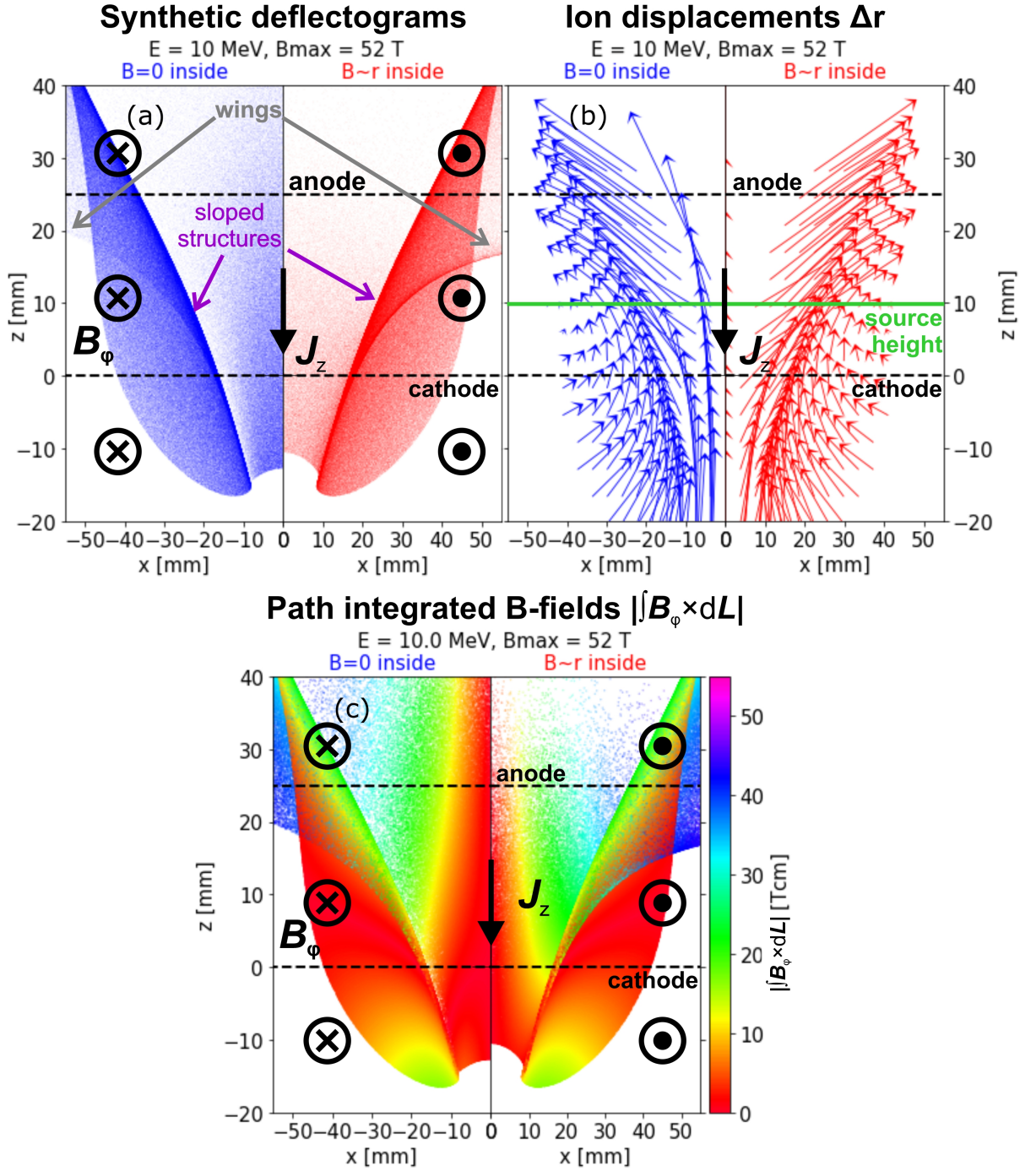


Figure 3.4: Comparison of the synthetic images for two B-field distributions inside the z-pinch: a skin-current profile [$B_{\phi}(r < R_p) = 0$] in blue color and a constant current-density profile [$B_{\phi}(r < R_p) \propto r$] in red color. (a) Synthetic proton deflectograms (i.e., proton fluence image). Maps of (b) proton displacements vectors $\Delta \mathbf{r}$ and (c) the path-integrated B-fields. Spatial scales correspond to the detector plane.

$F_r = -Qv_z B_{\phi}$, which deflects (defocuses) protons away from the z-pinch axis (see Fig. 3.5b). In contrast, protons initially emitted in the downstream direction with the axial velocity $-v_z$ are focused toward the z-pinch axis. Therefore, turning points of displacement vectors in Fig. 3.4b are situated at the height of the proton source, that is, 10 mm above the cathode. The combination

of the axial and radial deflections leads to the poloidal orientation of the proton displacements in Fig. 3.4b and the unfolding of the proton beam (see Fig. 3.5c). In addition, the strong deflections make it difficult for protons to penetrate into the interior of the z-pinch. Nevertheless, protons with a non-negligible azimuthal velocity v_ϕ are pushed by the radial deflections outwards (see Fig. 3.5b), and so they can pass around the z-pinch.

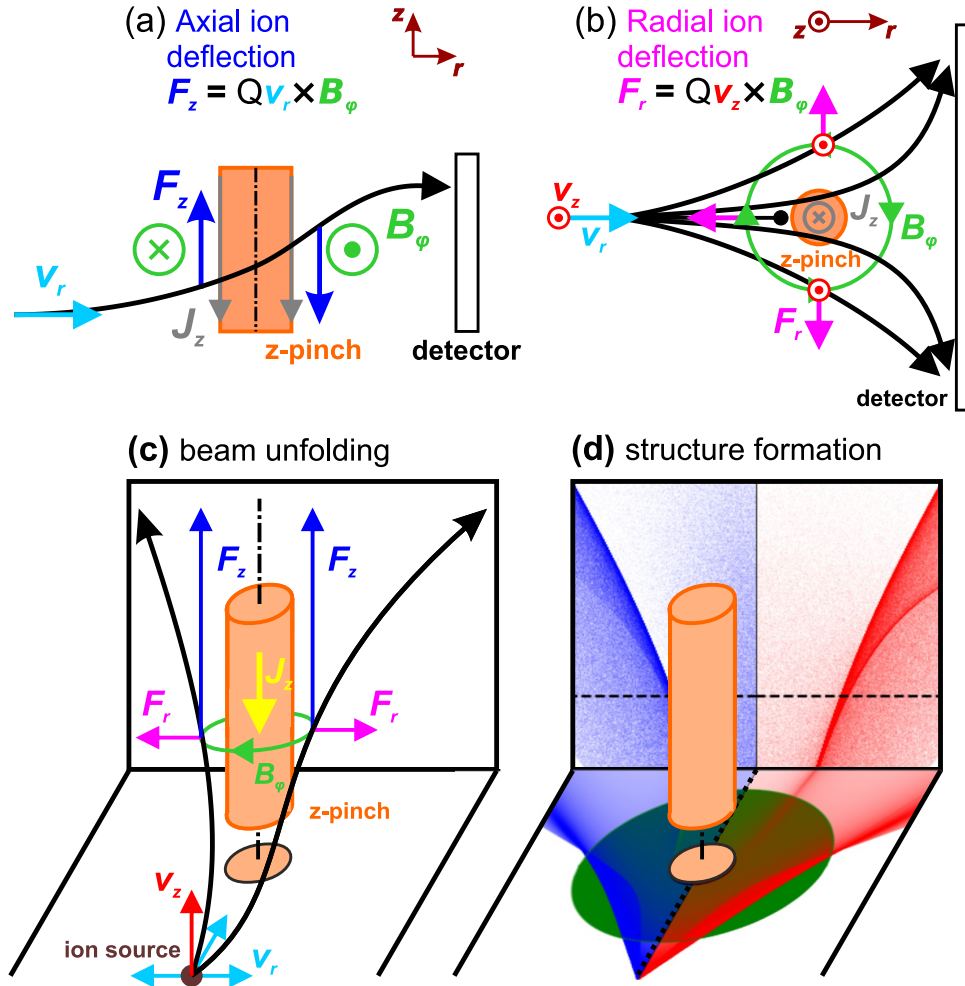


Figure 3.5: Fundamental deflections of radial proton beams in azimuthal B-fields B_ϕ : (a) A longitudinal (radial) proton velocity component v_r causes an axial force $F_z = Qv_r B_\phi$ deflecting protons upstream in the front side and downstream in the rear side of the z-pinch. (b) An upstream axial proton velocity component v_z causes a radial force $F_r = -Qv_z B_\phi$ deflecting protons outward from the z-pinch axis. (c) Due to the combination of the axial and radial proton deflection, protons are rotated in the poloidal direction and, the proton beam unravels. (d) Due to the inhomogeneity of the azimuthal B-fields, proton deflections are not uniform and modify the proton fluence creating the high-fluence sloped structures.

In addition to the velocity direction, the B-field distribution also significantly affects the synthetic deflectograms. Since most protons travel only in the B-field region outside the z-pinch, they are influenced by the B-field profile inversely proportional to the radius [$B_\phi(r \geq R_p) \propto 1/r$]. Due to the B-field's non-homogeneity, the proton displacements' strengths in Fig. 3.4b vary over the area of the synthetic deflectograms. Therefore, protons close to the z-pinch edge, where the B-fields are maximal, are deflected the most (the longest displacement vectors Fig. 3.4b) and

get closer to the less deflected ones (see Fig. 3.5b). The gradient in the proton displacements manifests itself in the gradient of the detected proton fluence and the creation of the sloped structures (see Fig. 3.5d). The strong proton deflections by maximum B-fields push out protons from the region near the z-pinch edge. In the case of the hollow skin-current z-pinch (blue image in Fig. 3.4a), evicted protons generate the shadow adjacent to the sloped structures. In the case of the constant-current-density z-pinch (red image in Fig. 3.4a), this shadow is filled by protons deflected within the z-pinch by the interior B-fields. Nonetheless, the high-fluence sloped structures are produced by protons deflected by peak B-fields and, thus, are mainly determined by the z-pinch current I and not the specific profile inside the z-pinch.

If the z-pinch current in the given setup reaches a critical value (in our case, ≈ 1 MA), protons start to cross each other, and their signals in the deflectograms overlap (see Fig. 3.4a). Fig. 3.4c shows that these 'wing' structures coupled with high path-integrated B-fields overlap the proton signal with lower path-integrated B-fields. This explains the non-injective relation between the path-integrated B-fields and the cross-sectional proton fluence in Fig. 3.3c. It is worth noting that the overlapping of the proton signal in the deflectogram is possible due to the radially decreasing B-field profile outside the z-pinch, which causes protons near the edge of the z-pinch to be displaced more than protons farther from the z-pinch (i.e., the radially decreasing proton-displacement profile). The overlapping 'wings' of the sloped structures manifest a difference between the skin-current (left images in Fig. 3.4a) and the constant-current-density (right images) profile. In the latter case, the interior B-fields intensify proton deflections and, thus, push the overlapping signal further.

Interestingly, there are regions of the synthetic deflectogram that indicate substantial proton displacements in Fig. 3.4b but almost zero path-integrated B-fields in Fig. 3.4c. This discrepancy originates in the fact that proton displacements correspond to the shift of the proton positions, but the path-integrated B-fields to the rotation of the proton velocities. Displaced protons may indicate zero path-integrated B-fields if their velocity vector is rotated to its initial direction by either proton deflections with alternating directions or completing a full proton turn. In our setup, the former possibility typically occurs for protons emitted in a plane between the z-pinch axis and the proton source. Suppose these protons have a velocity with the negligible azimuthal ($v_\varphi \approx 0$) and the non-zero downstream axial components $\mathbf{v} = (v_r, 0, -v_z)$. On the front side of the z-pinch, protons undergo purely upstream axial deflections. On its rear side, the relative orientation of the azimuthal B-fields to the proton velocity is reversed. Thus, when protons pass the z-pinch, they are deflected to the same degree but in the opposite direction due to the axisymmetry (see Fig. 3.5a). Therefore, the path-integrated B-fields $\int_0^{\mathcal{L}} \mathbf{B}_\varphi \times d\mathbf{L}$ averaging deflections of protons along their trajectories are zero. After exiting the B-field region, protons travel ballistically. If the detector were at the same distance from the z-axis as the proton source, protons would level their displacements completely. However, in our simulated setup (cf. Fig. 3.1a), the distance of the B-field region boundary to the detector is 5 mm, which is two times smaller than the 10-mm distance from the boundary on the other side of the z-pinch to the proton source. Therefore, the detector displays in Fig. 3.4b remnant displacements of these

protons.

We conclude that the most significant constraint of radial deflectometry is that, in order to reach the z-pinch, protons must traverse the peripheral B-fields, which strongly deflect them away from the z-pinch axis. To evaluate this issue, our paper [1] examines how many and how far protons can penetrate the B-field region with the 20-mm radius depending on their energy E and the current I and still manage to reach the detector in the setup shown in Fig. 3.1a. In particular, we are interested in how many protons can reach the z-pinch column. We find that a penetration depth is determined by the maximal proton deflections, which are proportional to a curvature (Larmor) radius $R_L(R_p) \propto I/\sqrt{E}$ at the z-pinch radius $R_p = 5$ mm. To estimate the required beam parameters for the penetration, we use our numerical simulations, where protons are fired into the z-pinch in the proposed setup with a half-angle divergence of 20° . After performing a large set of simulations for a broad spectrum of the beam energy E and total currents I (see Fig. 3.6), we estimate that protons must have the curvature radius $R_L(R_p)$ greater than $0.7 R_p$ to be detected. Moreover, to penetrate the z-pinch column and then reach the detector (see black dashed curves in Fig. 3.6a), protons require $R_L(R_p) \gtrsim 1.1 \cdot R_p$ (i.e., 2.4-MeV protons for 1-MA z-pinch) in the case of the skin-current z-pinch, and $R_L(R_p) \gtrsim 1.3 R_p$ (i.e., 3.5-MeV protons for 1-MA z-pinch) in the case of the constant-current-density z-pinch.

Nevertheless, these values do not show the percentage of protons capable of passing through the B-fields to the detector. Our simulations in Fig. 3.6b estimate that at least 10-MeV protons are required for 1-MA 5-mm-radius z-pinch to achieve 40% proton penetration. Such high proton energy and low sensitivity to the specific B-field profile led us to conclude that the radial deflectometry is favorable only for the measurements of the total z-pinch current.

To measure the B-field distribution inside the z-pinch, we investigate the axial configuration of the proton deflectometry (Fig. 3.1b). This configuration is comparable to the classical experimental setup (Fig. 2.9a) used in the proton radiography experiments in the laser-produced plasmas (e.g., [142], [181], [192]).

3.2.2 Axial deflectometry of the azimuthal B-fields

In the axial deflectometry configuration, shown in Fig. 3.1b, the proton beams are sent into the z-pinch from the proton source along the z-pinch axis. Therefore, they can directly access the interior of the z-pinch and map its B-field distribution. However, in this configuration, the electrodes must be transparent (for example, in a gas-puff z-pinch) or virtual (for example, in a plasma focus) because protons must enter and exit the z-pinch region through them. The proton detector is located on the opposite side of the z-pinch to the proton source. In our simulated setup, we locate the proton source on-axis at a 30-mm distance from the B-field region and set the divergence half-angle to 20° to map the whole cross-section of the z-pinch and the part of the peripheral vacuum B-fields.

Fig. 3.7 shows two possible orientations of the proton beam to the direction of the z-pinch

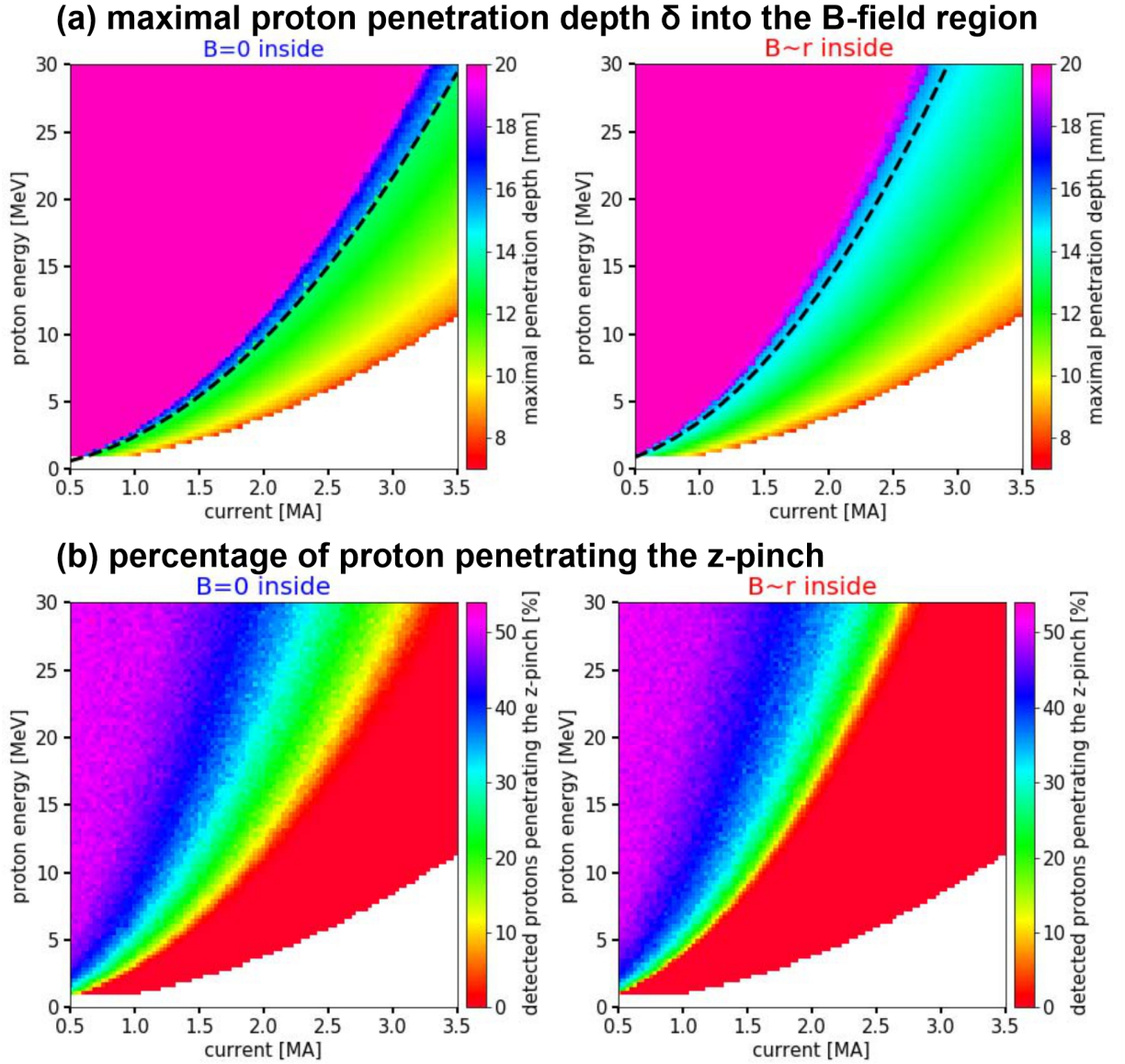


Figure 3.6: (a) Maximal penetrated depth δ into the B-field region by the subsequently detected protons according to the beam energy E and the current I of the z-pinch with the radius $R_p = 5$ mm. The dashed curves indicate $\delta = 15$ mm, which corresponds to the penetration the pinch column. (b) The fraction of the beam protons that can penetrate the z-pinch column and reach the detector depending on their energy E and the z-pinch current I .

current: downstream when B-fields are focusing proton beams and upstream when B-fields are defocusing. We exclude the focusing configuration (Fig. 3.7a) from our considerations because focusing proton beams would cross each other and produce an image that is difficult to analyze (compare distortion patterns of focusing and defocusing beams in the deflectogram in Fig. 2.14b). On the other hand, the B-fields in the defocusing configuration enhance the initial divergence of the proton beams and further divert protons away from the z-axis (see Fig. 3.7b). To avoid extreme proton displacements in our simulations, we increase the proton energy to 15-MeV, decrease the z-pinch current I , and place the detector at a 5-mm distance from the anode. Fig. 3.8 displays synthetic deflectograms of the skin-current (blue) and the constant-

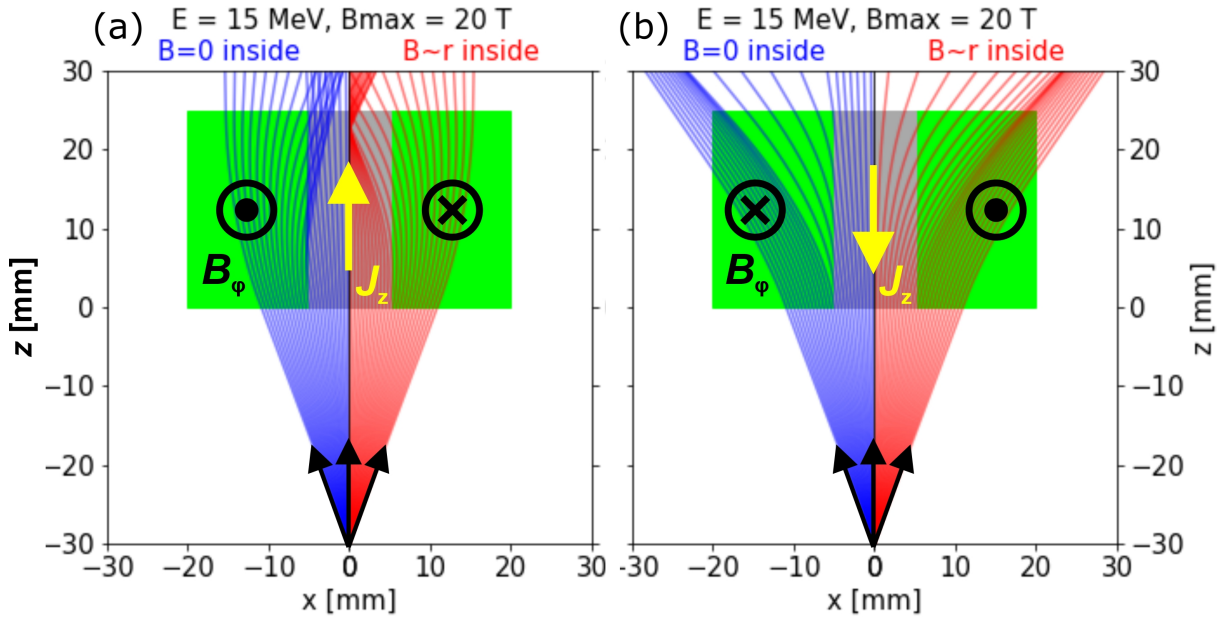


Figure 3.7: Two setups of the axial deflectometry configurations for two B-field distributions inside the z-pinch volume: (a) Protons are emitted (downstream) in the direction of the z-pinch current and are focused by the azimuthal B-fields. (b) Protons are emitted (downstream) in the direction of the z-pinch current and are focused by the azimuthal B-fields.

current-density (red) z-pinch for currents 0.1, 0.5, and 1 MA flowing within the 5-mm radius. The black circles in Fig. 3.8 highlight the cross-section area of the z-pinch column. In our simulations, protons pass through electrodes (meshes) with 1×1 -mm openings. The entrance electrode mesh, that is, the cathode, is situated between the proton source and the B-field's interaction region. Therefore, it acts as a deflectometry grid, and proton deflections distort its shadow. The synthetic deflectograms also show the shadow of the anode mesh, which appears finer than the cathode mesh. The anode mesh shadow is not distorted since protons are no further deflected after leaving the interaction region between the electrodes.

The synthetic deflectograms shown in Fig. 3.8 can easily distinguish between two B-field distributions inside the z-pinch. Inside the black circles in the skin-current-z-pinch deflectogram (in blue color), there is an undistorted image of the deflectometry (cathode) mesh. This part of the deflectogram is created by undeflected protons passing through the interior of the skin-current z-pinch with zero B-fields. In the case of the constant-current-density z-pinch with the linear B-field profile (in red color), the circular undistorted image of the cathode mesh disappears because the protons are deflected even close to the z-pinch axis. At low z-pinch currents, the proton displacements are moderate, and the pattern of the cathode shadow in the deflectogram in Fig. 3.8a is only slightly perturbed. At higher z-pinch currents (Fig. 3.8b and Fig. 3.8c), strong B-fields cause more significant proton displacements, which produce a decrease of proton fluence in the central region of the deflectograms outside the black circles. This low-proton-fluence region of the deflectograms consists of protons that have entered the z-pinch column but

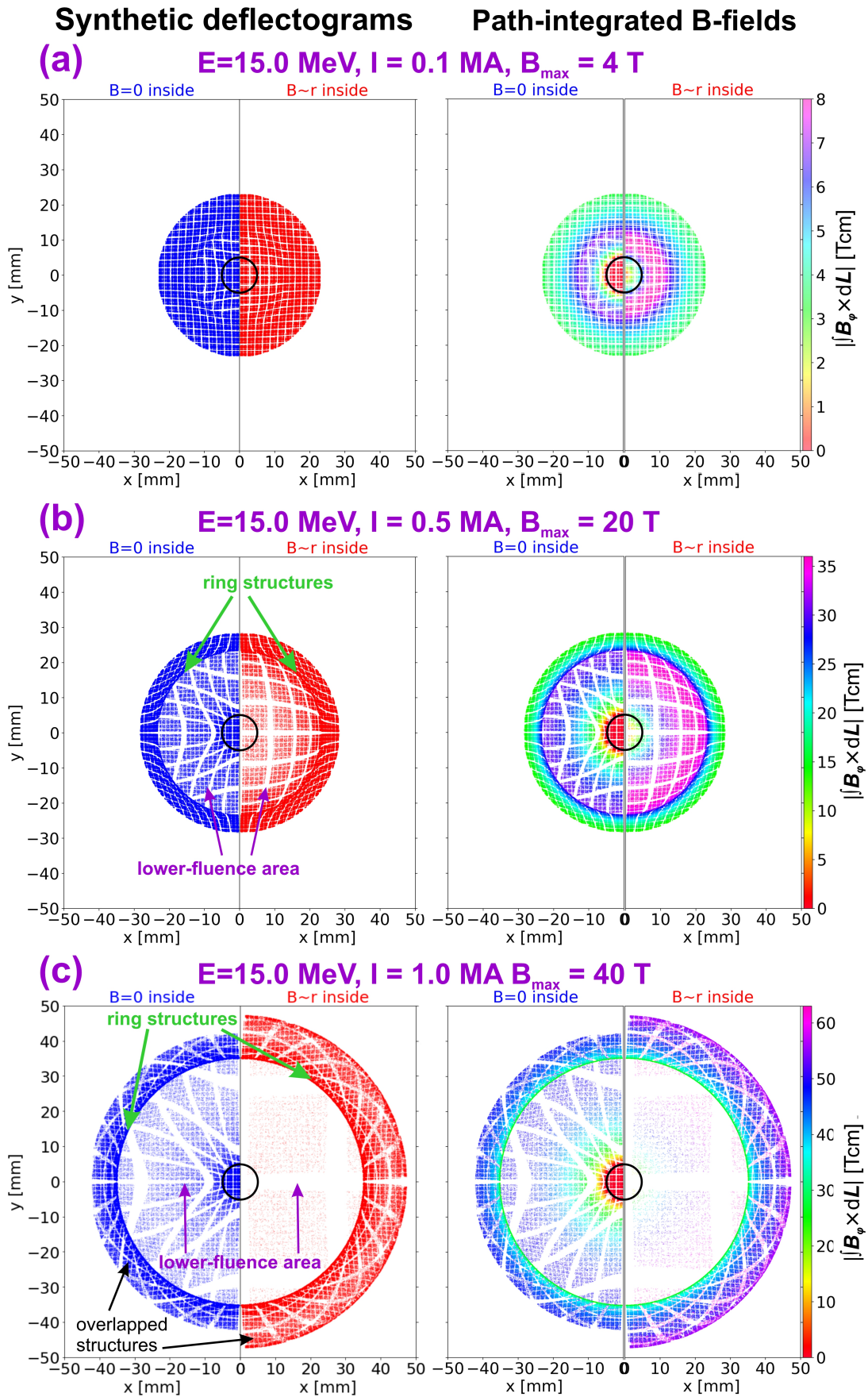


Figure 3.8: Synthetic proton deflectograms and path-integrated B-field maps in the defocusing axial deflectometry configuration for three values of the z-pinch current I : (a) 0.1, (b) 0.5, and (c) 1 MA at the 5-mm radius (black circles).

then, at a certain point, reached its edge and exited into the B-fields outside the z-pinch volume (see the representative proton trajectories in Fig. 3.7b). Therefore, this part of the deflectogram indicates the specific B-field distribution inside the z-pinch but, to some extent, it is also affected by the $1/r$ -distribution of the B-fields outside the z-pinch.

At the outer border of this lower-fluence region, proton displacements create a high-fluence ring-like structure whose radius for the given proton energy E is proportional to the z-pinch current I . Studying the individual simulated proton trajectories, we find that the ring structures consist of detected protons, which have entered the z-pinch near its edge where B-fields are maximal (see Fig. 3.7b) and were deflected more than those that entered the interaction region outside the z-pinch and were deflected by weaker (vacuum) B-fields. The difference in the proton deflections (their gradient) leads to the proton accumulation and the creation of the high-fluence ring-like structures.

With increasing z-pinch current, more protons are expelled from the high-B-field regions near the z-pinch edge. The low-fluence region is depleted, making the distorted pattern of the deflectometry mesh hardly noticeable. After exceeding a certain limit of the z-pinch current I (see Fig. 3.8c), these protons are so deflected (indicated by high values of path-integrated B-fields) that they cross the less deflected ones. Accordingly, the edge of the deflectogram “flips over” very similarly to the overlapping wing features in the radial deflectometry (cf. Fig. 3.4c). In the case of the constant-current-density profile (right sides of the synthetic deflectograms), the overflipped edge is even more pronounced because the B-fields inside the z-pinch further enhance proton deflections. Therefore, the ring structures in the axial deflectometry have a similar origin as the characteristic sloped structures in the radial deflectometry. After publishing our paper [1], the overlapping structures in the deflectograms, represented by sloped and ring structures, became known in the laser-plasma community as *caustics* (see Fig. 2.11).

There is a difference in the proton fluence of the overflipped deflectogram edges of the blue and red deflectograms in Fig. 3.4c, which distinguishes the individual B-field profiles. However, the strong proton displacements in these edges result in the non-injective profile of the path-integrated B-fields and make the experimental data difficult to analyze directly. This correlates with the caustic regime in the image analysis of the laser-plasma experiments (see Subsec. 2.4.3).

In the end of our paper [1], we suggest a simple method for estimation of the path-integrated B-field in the case of small proton deflections. Fig. 3.9a explains a basic principle of this method, which is similar to the paraxial approximation in the laser-plasma measurements (Subsec. 2.4.3). It requires the knowledge of the initial radial position r_0 of a proton ray in the cathode plane before entering the B-fields and its final (deflected) radial position R in the detector plane after exiting the B-field. The crucial assumption of this method is that an angle α' , given by a radial displacement $R - r_0$, approximates the actual deflection angle α , given by the angular difference between the initial and final proton directions (i.e., $\alpha \approx \alpha'$). Accordingly, the line segment AD in Fig. 3.9a approximates the line segment AE. In other words, we approximate the proton deflections in the B-field region by an abrupt change of proton directions in the cathode plane

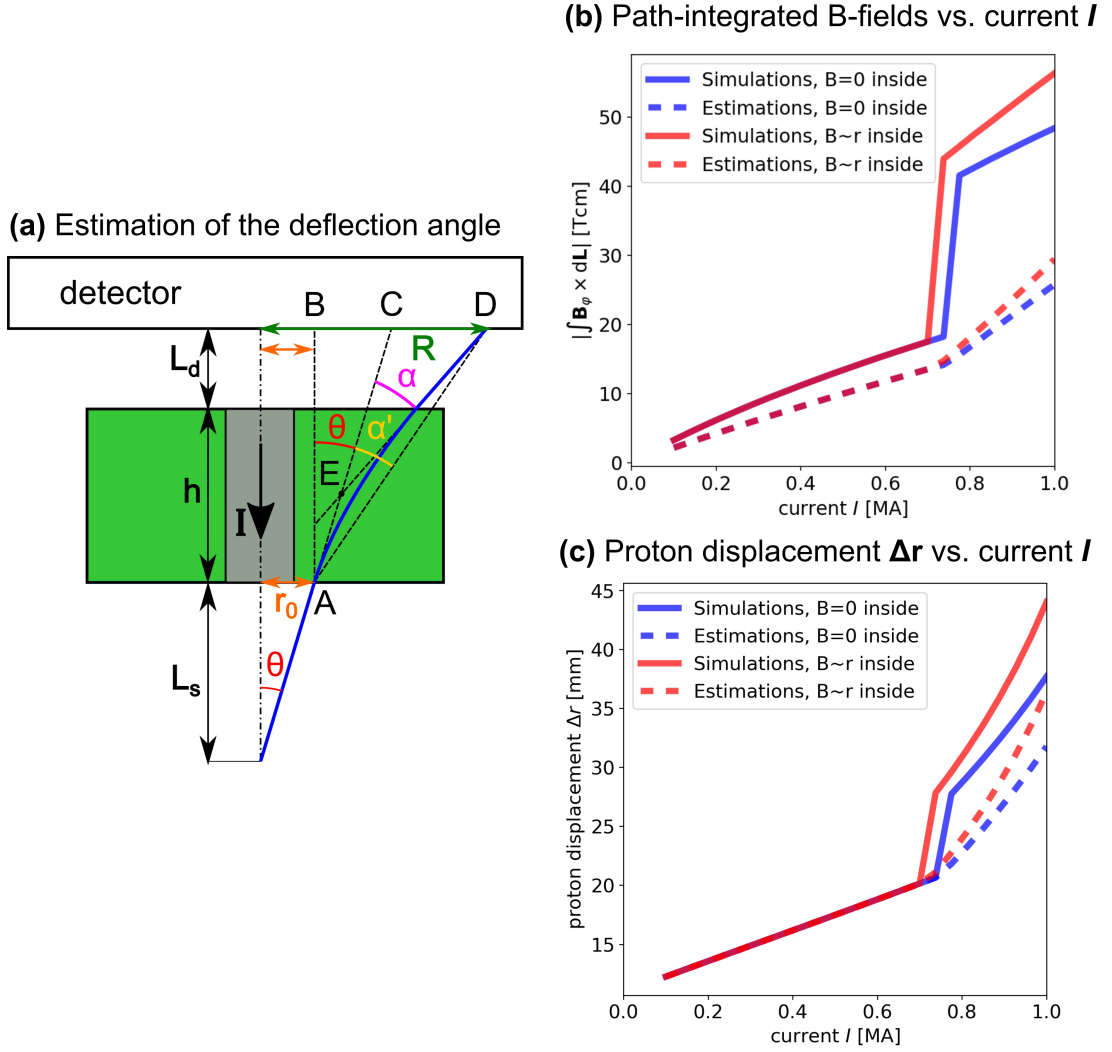


Figure 3.9: The paraxial approximation in the axial deflectometry of the z-pinch B-fields. (a) A schematic for estimating the actual deflection angle α from a measurable radial proton displacement $\Delta r = R - r_0$. Dependence of (b) the path-integrated B-fields $\|\int_0^L \mathbf{B}_\varphi \times d\mathbf{L}\|$, and (c) the proton displacements $\Delta r(I) = R(I) - r_0$ on the total pinch current I . Solid lines: calculated values using proton tracking simulations. Dashed lines: estimated values from the synthetic deflectograms using Eq. (3.1). Blue: the skin-current z-pinch. Red: the constant-current-density z-pinch.

at the point A in Fig. 3.9a. In the paraxial approximation in the laser-produced plasmas (see Fig. 2.10), this plane is referred to as the object plane.

The initial proton radius r_0 is determined by the deflectometry mesh (the cathode) and corresponds to the divergence angle θ of the proton ray ($r_0 = L_s \tan \theta$). Then, we estimate the deflection angle α according to the following equation

$$\tan(\alpha + \theta) \approx \tan(\alpha' + \theta) = \frac{R - r_0}{h + L_d}, \quad (3.1)$$

where $h = 25$ mm is the height of the B-field region (the anode-cathode distance), $L_d = 5$ mm is the distance of the detector from the exit electrode, i.e., the anode; and $L_s = 30$ mm is the distance from the entrance electrode, i.e., the cathode, to the ion source. By substituting the estimated deflection angle $\alpha'(r_0)$ from Eq. (3.1) into the deflection equation Eq. (2.17), we can estimate the path-integrated B-fields at the radius r_0 .

It would be highly beneficial to use the approximation based on Eq. (3.1) to measure the maximal deflection angles α and then the path-integrated B-fields $\|\int_0^{\mathcal{L}} \mathbf{B}_\varphi \times d\mathbf{L}\|$, which are coupled with the high-fluence ring structure. To achieve that, we need the initial and the final proton positions, R and r_0 , respectively. The ring structure is created by detected protons, which initially entered the B-field region near the pinch radius R_p . However, to determine the position and size of the z-pinch, we would require additional diagnostics (e.g., the side view of the z-pinch). Therefore, we cannot accurately assign the deflected position R of the ring structure to the specific initial proton position $r_0 \approx R_p$, and use Eq. (3.1) to calculate the deflection angle α .

Nevertheless, we can at least estimate the initial proton positions at the beam's edge corresponding to its size before entering the B-field region. We assume that the diameter of the proton beam at the cathode ("object") plane is equal to $2r_0$. Therefore, we can follow the expansion (deflection) of the whole emission cone and estimate the path-integrated fields near the initial position of the proton beam's boundary r_0 . For the analysis, it is beneficial to avoid proton trajectories through different B-field profiles inside and outside the z-pinch. Therefore, we set the beam divergence (in our setup, $\theta = 20^\circ$) so that protons at the beam edge are directed into vacuum B-fields outside the z-pinch radius R_p (in our setup, $R_p < r_0 \approx 11$ mm). Then, we can use Eq. (3.1) to measure the path integrals of these B-fields and estimate the total z-pinch current I .

Fig. 3.9b demonstrates how the path-integrated B-fields $\|\int \mathbf{B}_\varphi \times d\mathbf{L}\|(I)$ grow with the increasing pinch current I . This figure shows the actual path-integrated B-fields calculated using our proton-tracking simulations (solid lines). It compares them with the values estimated analytically from the synthetic data via the paraxial approximation using Eq. (3.1) (dashed lines). Fig. 3.9b also compares these values for two current-density profiles of the z-pinch. The blue plots refer to the skin-current z-pinch. The red plots refer to the z-pinch with the constant current density and the linear B-field profile. The estimated values approximate the actual path-integrated B-fields at lower currents coupled with weaker B-fields. However, when the

current I reaches a critical value I_C (in our setup, $I_C \approx 0.7$ MA), the trend of the actual path-integrated B-fields suddenly changes, which the estimated values do not reflect. This can be explained using Fig. 3.9c, comparing the values of the proton displacements $\Delta r = R - r_0$. The estimation of the proton displacements is accurate until the current I reaches the critical value I_C . Then, we observe a similar change in the profile of Δr , which means that the protons at the deflectogram's edge become suddenly more displaced. It is caused by proton deflections, which become so strong due to the current increase that a ring structure, coupled with the highest proton deflections, overlaps the less deflected proton beam's edge (see Fig. 3.8c). Then, the edge of the deflectogram no longer corresponds to the initial edge of the proton beam. Thus, we observe substantial discrepancies between the simulations and the estimations in Figs. 3.9b-c.

There is another important conclusion, which our paper did not mention but arises from its results. It concerns the trends of the plots in Fig. 3.9b and Fig. 3.9c. Interestingly, if the current does not reach the critical value $I < I_C$, the proton displacements $\Delta r(I)$ grow linearly with the increasing pinch current I and thus also with the path-integrated B-fields $\|\int \mathbf{B}_\varphi \times d\mathbf{L}\|$. This linear relation between the proton displacements and the path-integrated B-fields (and the deflection angle α) is analogous to the linear relation in Eq. (2.19), which corresponds to the *linear regime* discussed in the image analysis via the paraxial approximation (see Sec. 3.9) for the proton deflectometry in laser-produced plasmas¹. Therefore, the critical value of the pinch current I_C corresponds to the critical value of the contrast parameter μ_C .

In conclusion, we gained knowledge of the basics of ion deflectometry in the z-pinch geometry. Moreover, we proved that ion deflectometry could measure the z-pinch current in the radial configuration. However, the specific B-field distribution is evident in the deflectograms only in the axial configuration and assuming moderate proton deflections. Estimated B-fields can be retrieved by reproducing experimental data via the numerical ion-tracking simulations. In the case of the small deflections, we estimated the path-integrated B-fields at the edge of the initial proton beam. It is worth noting that these experiments would still require some laser system for accelerating multi-MeV protons.

3.2.3 Radial-axial deflectometry of the azimuthal B-fields

During our research, we came up with an idea for the third configuration, which was not included in the article's final version. It is a compromise between the radial configuration of proton emission, which is preferable for access to the z-pinch plasma, and the axial configuration, which we found preferable for the determination of the B-field distribution inside the z-pinch. We call this idea the radial-axial proton deflectometry. Its setup is illustrated in Fig. 3.10a. This method is similar to radial deflectometry, except that the detector is not situated on the

¹In the different (unconventional) deflectometry setup for measurements of z-pinch B-fields, Chap. 5 will discover another linear relation between the ion displacements Δr and the path-integrated fields $\int B_\varphi dz$ using the Larmor orbit approximation.

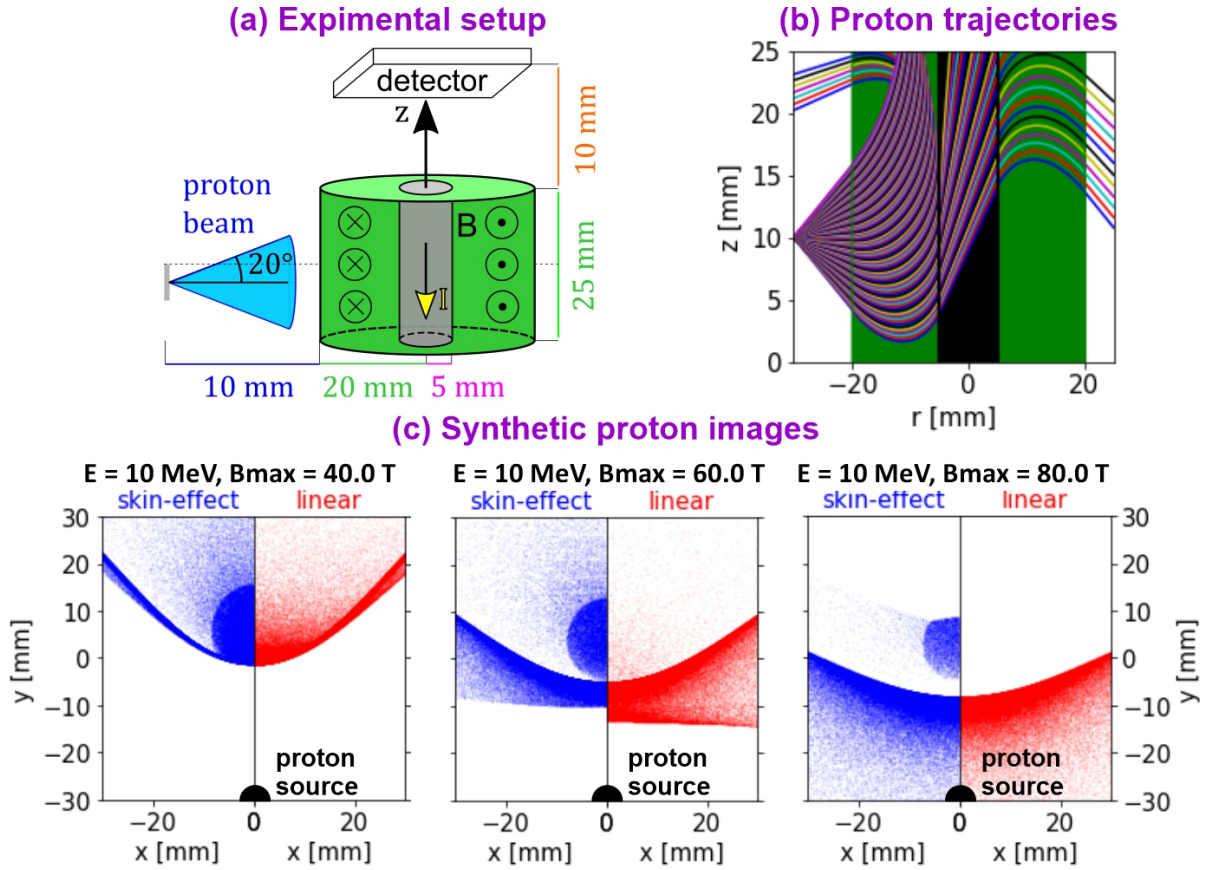


Figure 3.10: Advanced radial configuration of proton deflectometry. (a) Schematics of the experimental setup, where the detector is located above the anode mesh. (b) Demonstration side-on view of deflected proton trajectories. (c) Synthetic deflectograms comparing two profiles of the B-field for different values of the z-pinch current.

side of the z-pinch. However, it is above the anode mesh, similar to the axial configuration. The radial component of proton velocity, which is dominant, causes the strong axial deflection of proton beams upstream of the z-pinch current. The detector near the anode can capture strongly deflected protons (see Fig. 3.10b), and so the condition for the minimal energy of the proton beams is lower than in the classical radial deflectometry. As shown in Fig. 3.10c, synthetic images reveal similar sloped structures as in the radial deflectometry. Protons also create them due to their deflections predominantly in the vacuum B-fields, and thus, there is only a little difference between the two B-field profiles inside the z-pinch. There is another structure between the sloped structures, and its form depends on the B-fields distribution inside the z-pinch. In the case of the hollow z-pinch, the deflected protons fill the B-field cavity inside, and this structure has a circular shape. In the case of the z-pinch with the constant current density, these protons are further deflected, so the contours of this structure are smeared out. Therefore, the radial-axial deflectometry can provide rather qualitative information about the B-field distribution of the z-pinch.

Chapter 4

Characterization of MeV ion sources in z-pinches

In the previous Chapter, we studied the feasibility of the proton deflectometry in z-pinch plasmas but we still assumed a proton source driven by a high-intensity short-pulse laser pulse. The required beam energy for mapping MA-z-pinch plasmas was in terms of MeV for protons as diagnostic ions. However, an adequate laser system necessary for accelerating multi-MeV protons (or different ions with a comparable momentum) is unavailable for the vast majority of the z-pinch facilities. Therefore, the greater development of the deflectometry on z-pinch plasma requires a different and more accessible source of diagnostic charged particles. In particular, light ions, such as protons or deuterons, can be accelerated the most effectively. The z-pinches operating with a deuterium load can produce intense hydrogen ion emissions. However, most recent experiments with the deuterium load have aimed for the high-neutron-yield emission via fusion reactions, which mainly employ deuterons with <1 -MeV energies. Nevertheless, a few z-pinch facilities reported protons and deuterons with energies 1 – 10 MeV [25], [26].

Our group also investigated emissions of hydrogen ions with energies in tens of MeV on a 3-MA pulsed-power generator GIT-12. Initially, we focused on optimizing the neutron yield for possible applications and only indirectly studied the hydrogen ion beams. We used a hybrid gas-puff configuration of the z-pinch employing so-called cable guns. This configuration has proved to be very beneficial because it led to higher yields and multi-MeV energies of not only neutrons but also hydrogen ions [22], [23], [252]. Our group first measured deuteron and proton beams with energies reaching up to 28 MeV in 2013 [22]. Afterwards, our interest has shifted to investigating ion sources and associated ion accelerating mechanisms in z-pinches [253], [254]. This Chapter focuses on the characterization of the source of hydrogen ions based on ion images, which are observed not only in our gas-puff z-pinch on GIT-12 but also on plasma foci.

First, Sec. 4.1 describes the typical evolution of the imploding z-pinch plasmas on GIT-12, which results in the acceleration of hydrogen ion beams. Then, we introduce our experimental ion diagnostics (Sec. 4.2) and key features in the experimental ion images, which are *radial lines* and *ring structures* (Sec. 4.3). The second generation of our numerical ion-tracking code, which we

developed based on the code used in Chap. 3, allows us to create synthetic ion images of selected shots and reproduce the typical experimental structures. Found parameters of our simulations help us investigate the properties of the z-pinch-driven multi-MeV ion source and the z-pinch azimuthal B-fields. Our two papers, [253] and [2], review the most important results of these simulations. The paper [253] lays the foundations for our ideas about the MeV-ion accelerating mechanism in z-pinches. We discuss the selected results of this paper in Sec. 4.4. Nonetheless, most of the results relevant to the ion deflectometry originate from the investigation of the ion source's spatial distribution and the ion-beam divergence estimation, which is described in our paper [2]. These results are presented and further discussed in Sec. 4.5. Moreover, we include the full version of the paper [2] in the Appendix (see App. G.2).

4.1 Hybrid gas-puff z-pinch driven by the GIT-12 generator

Our experiments are carried out on the GIT-12 generator at the Institute of High Current Electronics (IHCE) in Tomsk, Russia [255], [256]. The peak current in a short-circuit load is ~ 4.7 MA with the ~ 1.7 - μs rise time. The output voltage of 0.6 MV is provided by 12-staged Marx generators charged at 50 kV. Fig. 4.1a illustrates the experimental arrangement. The electrodes formed by two planar meshes with the 70%-transparency are separated by a 20 – 25-mm gap. The experimental z-pinch configuration in Fig. 4.1a is a hybrid deuterium gas puff. In this configuration, an inner shell, a deuterium gas with a linear density $\sim 100 \mu\text{gcm}^{-1}$, is ejected at a 40-mm radius by supersonic nozzles 3 ms before the generator trigger. Afterwards, $\sim 1.7 \mu\text{s}$ before the onset of the primary current, 48 cable off-axis guns exhaust a carbon-hydrogen (CH) plasma shell ($\sim 5 \mu\text{gcm}^{-1}$) into the anode-cathode gap at a ~ 175 -mm radius, where they create a homogeneously conducting layer. After the generator is triggered, and the electric current starts to flow through the CH-plasma shell, the plasma starts to implode radially due to the $\mathbf{J} \times \mathbf{B}$ force. The velocity of the shell implosion can reach up to ~ 600 km/s [253]. Through the ionization and compression of the dense deuterium gas, the imploding shell generates hot dense z-pinch plasmas. A z-pinch stagnation occurs ~ 700 ns after the current onset. At that time, the circuit current usually reaches ≈ 2.7 MA.

Fig. 4.1b shows the typical evolution of the z-pinch plasma shell in recorded soft x-ray images before and during the z-pinch stagnation. The current breakdown of the neutral gas that fills the electrode gap is usually a random process in nature, which may create asymmetries in the imploding layer and give rise to its instabilities. In our hybrid configuration, the plasma injection by the off-axis cable guns results in the smooth and symmetrical imploding plasma shell. This is crucial for delivering high-density current close to the axis and generating strong azimuthal B-fields storing a large amount of the magnetic energy. As seen in Fig. 4.1b, the imploding shell is perturbed by low- k MRT instability compressing the plasma in the middle of the z-pinch to a smaller diameter. At stagnation, an MHD $m = 0$ instability usually develops close to the anode (starting at -1 ns in Fig. 4.1b) and creates a plasma neck. Interestingly, the necking instability appears preferably close to the anode, which can be explained by the Hall effect [257].

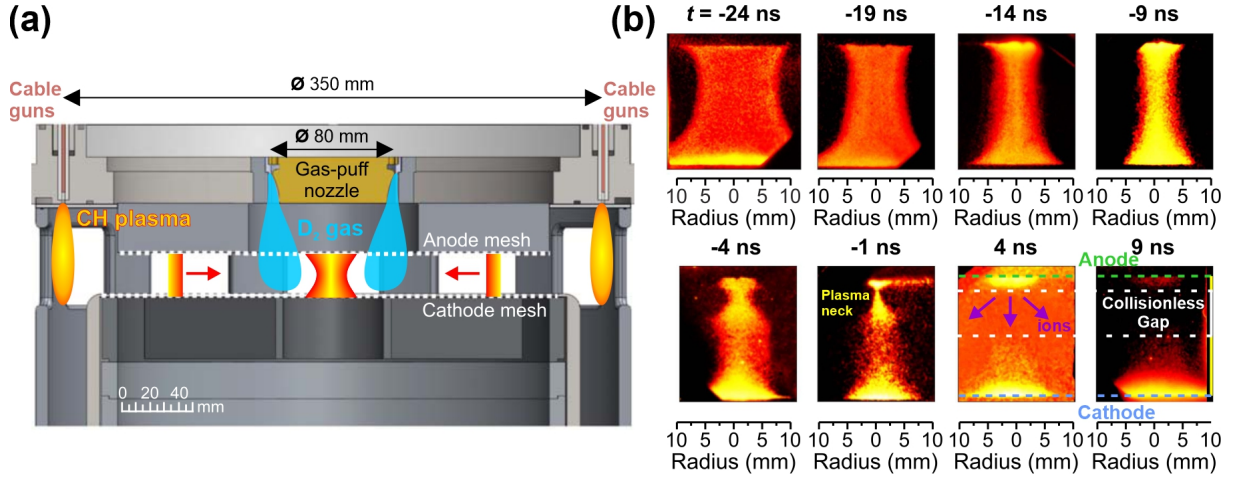


Figure 4.1: (a) Arrangement of the experimental hybrid gas-puff z-pinch load on the device GIT-12. (b) Typical evolution of the imploding plasma shell captured in soft x-ray images [253]. Time $t = 0$ corresponds to the sharp onset of >2 -MeV gamma emission.

The instability pushes the plasma mass out of the necked region, so its linear density starts to drop. Consequently, the electron drift velocity increases, and electrons in the narrowing plasma neck, which would otherwise carry the conductive current through the z-pinch plasma via their collisions, might become collisionless. According to a mechanism explained in [253], the low electron collisionality might lead to a space-charge-limited flow and the magnetic self-insulation of the electrons. Subsequently, the plasma impedance and the voltage might escalate and disrupt the conducting current. In Fig. 4.1b, it occurs approximately at $t = 0$ ns.

As a result, the low-impedance current-carrying plasma neck transforms into a high-impedance E-field-inducting gap (between -1 ns to 4 ns in Fig. 4.1b). Within ~ 1 ns after the current disruption, the high voltage caused by the impedance of the collisionless gap accelerates a burst of hydrogen ion beams (protons and deuterons) up to energies of tens MeV along the current direction [24], [253]. While accelerated protons originate from the pre-ionized low-density CH-plasma shell and surface impurities on the electrodes, deuterons are accelerated from the dense D_2 gas-puff load, and we assume they predominate over the accelerated protons. Electrons are accelerated in the opposite direction to ions and produce >2 -MeV bremsstrahlung gamma emission by collisions with metal surfaces of the experimental chamber. The sharp onset of gamma emission, corresponding to the time $t = 0$ ns in Fig. 4.1b, marks roughly the time of the current disruption and the subsequent ion emission. Interestingly, the plasma below the collisionless gap (closer to the cathode) is relatively unaffected by the current disruption (see images at -1 , 4 , and 9 ns in Fig. 4.1b). In this unaffected plasma, conductive currents may persist, powering the azimuthal B-fields that may deflect hydrogen ion beams accelerated in the gap. Nevertheless, this plasma region cannot be sustained for long, and shortly after the ion emission, the z-pinch is completely disrupted.

A detailed discussion of this and other ion acceleration mechanisms in z-pinzches with additional information about the emission of multi-MeV hydrogen ions on GIT-12 are presented in

[253]. Interestingly, the ion acceleration powered by the transition from a low-impedance plasma to a high-impedance collisionless gap is also studied in ion diodes and plasma-filled diodes [258]–[261], which represent different types of pulsed-power devices.

This Chapter examines the z-pinch-driven source of multi-MeV deuterons on GIT-12 to evaluate its possible employment in z-pinch B-field ion deflectometry. One of the important quantities for the ion imaging is the duration of the ion emission. It should be shorter than the B-field’s characteristic evolution time so that diagnostic ions take only a snapshot of the transient B-fields. Our paper [253] shows that the emission of >500 keV deuterons lasts for ≈ 10 ns, but the duration of the >1 MeV-deuteron emission can be much shorter. If we compare this temporal scale with the plasma implosion in Fig. 4.1b, we see that the z-pinch radius at the cathode during 5 ns (from $t = -1$ ns to $t = 4$ ns) does not change much and remains at 5 mm. Besides the energy and the temporal duration of the ion emission, our experiments further investigated the ion source using various ion diagnostics. The following section (Sec. 4.2) introduces two types of ion detectors, namely, the beam-profile detector and the ion pinhole cameras, which help us investigate the spatial distribution and the divergence of the ion source.

4.2 Ion diagnostics on GIT-12

This section presents two types of ion diagnostics, the beam-profile detector and the ion pinhole camera. Their experimental arrangement is illustrated in Fig. 4.2. Both these diagnostics are equipped with a stack of radiochromic films (RCFs) to record images of the ion source. The RCFs may be supplemented by particle-track detectors CR-39 to verify that the recorded signal is created by hydrogen ions (protons or deuterons) and not, for example, by x-ray irradiation. Each layer of the RCF stack is coupled with the Bragg peak of the ion stopping power and the narrow interval of ion energies, for which the RCF detector is most sensitive. Ions with energies above this interval may also contribute to the recorded ion signal, especially if the total number of high-energy ions is significant.

The beam-profile detector and the ion pinhole cameras are housed in an ion-detector assembly (see Fig. 4.3), a cylindrical metal container located on-axis ~ 110 mm below the cathode (i.e., downstream of the ion emission). The beam-profile detector is situated on the container’s top and directly faces ion beams incoming from the z-pinch. It consists of a stack of circular RCFs and CR-39s with a ~ 62.5 -mm diameter shielded by a ~ 1 -mm-thick duralumin (Al-Cu-alloy) absorber. The beam-profile detector provides information about the anisotropy of the ion beams, but, due to the heavy shielding, it captures only images of $\gtrsim 18$ -MeV hydrogen ions. The cylindrical metal container itself is a darkened room of the ion pinhole cameras. Below cutouts in the beam-profile detector and the container’s partition wall is one or more pinholes with the ~ 250 - μm diameter. Incoming ions are point-projected through these pinholes onto a stack of RCFs and CR39s (see red ion trajectories in Fig. 4.2).

Fig. 4.3 presents pinhole cameras in four configurations. There can be a single central pinhole (the *1-pinhole* camera) located on-axis (see Fig. 4.3a), or a triplet of pinholes (the *3-pinhole*

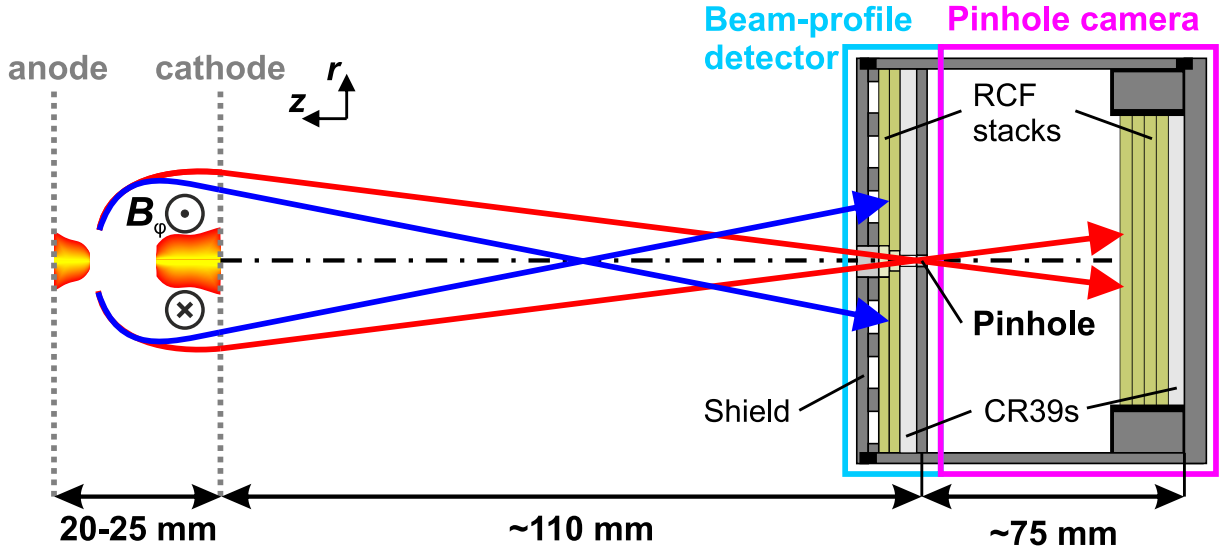


Figure 4.2: Experimental arrangement of the ion-detector assembly consisting of the beam-profile detector and the pinhole camera. The schematic is not to scale.

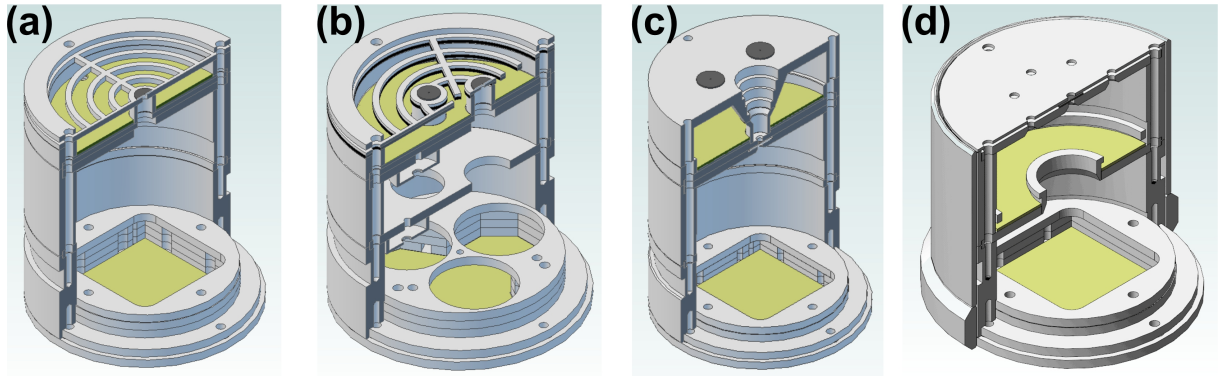


Figure 4.3: Four types of the ion pinhole assemblies used in the experimental arrangement on GIT-12: (a) the central 1-pinhole camera with the beam-profile detector, (b) the 3-pinhole camera with the beam-profile detector; (c-d) the multi-pinhole cameras, i.e., the central 1-pinhole camera with the 4- and 8-pinhole camera. The beam-profile detectors are displayed without the duralumin shield.

camera) arranged symmetrically at a 9.6-mm radial distance from the axis (see Fig. 4.3b). It is also possible to replace the beam-profile detector with another pinhole detector, the *multi-pinhole* camera, with four or eight pinholes symmetrically arranged at a 17-mm distance from the axis (see Figs. 4.3c-d). In that case, there are two RCF stacks at two different levels of the detector assembly to capture ion images of both multi- and 1-pinhole camera. The pinhole cameras select the incoming ion beams and pick an image of the ion source from the ion emission. Depending on the pinhole diameter and image magnification, the spatial resolution is 0.7 – 1.25 mm for the 1- and 3-pinhole cameras, and 2 – 3 mm for the multi-pinhole camera. Observing the ion emission from different angles and distances allows us to distinguish the effects caused by ion deflections in azimuthal B-fields from the ion source properties.

Sec. 4.3 investigates characteristic features, i.e., the radial lines and ring structures, in the experimental images recorded by the ion beam profile and pinhole diagnostics. Sec. 4.4 presents selected results from the paper [253], provided by the author of this thesis and, based on his ion-tracking simulations, examines the origin of the ring structures in the ion pinhole images. Our paper [2] investigates further properties of the ion source, namely, its spatial distribution and the divergence of emitted ion beams. These are essential conditions for the employment of the ion deflectometry. The author's most important results in the paper [2] are reviewed and discussed in Sec. 4.5. Then, Sec. 4.6 an alternative hypothesis explaining the origin of the ring structures in the ion pinhole images.

4.3 Experimental observations made with ion diagnostics on GIT-12

Fig. 4.4a depicts the experimental setup with the assembly of the beam-profile and the 3-pinhole detectors. The image in Fig. 4.4b shows a typical distribution of deuteron emission (>27 MeV) recorded by the beam-profile detector. The pinhole camera captures images of the ion source for wide spectrum of deuteron energies. The typical ion images are represented in Fig. 4.4c by two half images from two pinhole cameras for lower-energy (8 MeV) and higher-energy (18 MeV) deuterons. In following subsections (Subsec. 4.3.1 and Subsec. 4.3.2), we provide interpretations of these typical experimental observations and show they are influenced by properties of both the ion source and the global azimuthal B-fields of the z-pinch.

4.3.1 Characteristic radial lines captured by the beam-profile detector

On the one hand, the beam-profile detector provides information about the angular distribution of the detected deuteron emission. On the other hand, it must be heavily shielded, and thus, provides only images of deuterons with high energies. The example image of >27 deuterons in Fig. 4.4b shows that the angular distribution is anisotropic, and we observe characteristic *radial lines* in the fluence of detected deuterons. Since the signal is visible in the locations shielded by the protective mask, we can also partly observe radial lines produced by >44 -MeV deuterons. It is unlikely that the ion source would emit deuterons in discrete directions associated by these lines. Thus, we propose that the radial lines are created by strictly radial forces deflecting ion beams during the beam propagation through the plasma. We assume that ion beams are deflected by radial forces caused by time-dependent azimuthal magnetic fields $B_\varphi(t)$. Then, the crossing point of the radial lines in Fig. 4.4b, which we refer to as a beam center, is the intersection of the azimuthal B-field axis and the detector plane. Because the ion signal in the beam-profile detector is not entirely homogeneous but distributed into individual lines, we suggest that the ion source, at least during the emission of high-energy deuterons, is granular, i.e., it consists of numerous *micro-sources*. Then, each radial line corresponds to a

single deuteron beam (a *micro-beam*) emitted from a single micro-source. The results of the pinhole camera partly confirm this assumption. The high-energy deuteron image in Fig. 4.4c reveals ring structures consisting of individual dots, which we interpret as the ion signals of the individual micro-sources. These and other observations of the ion pinhole camera will be further discussed below in Subsec. 4.3.2.

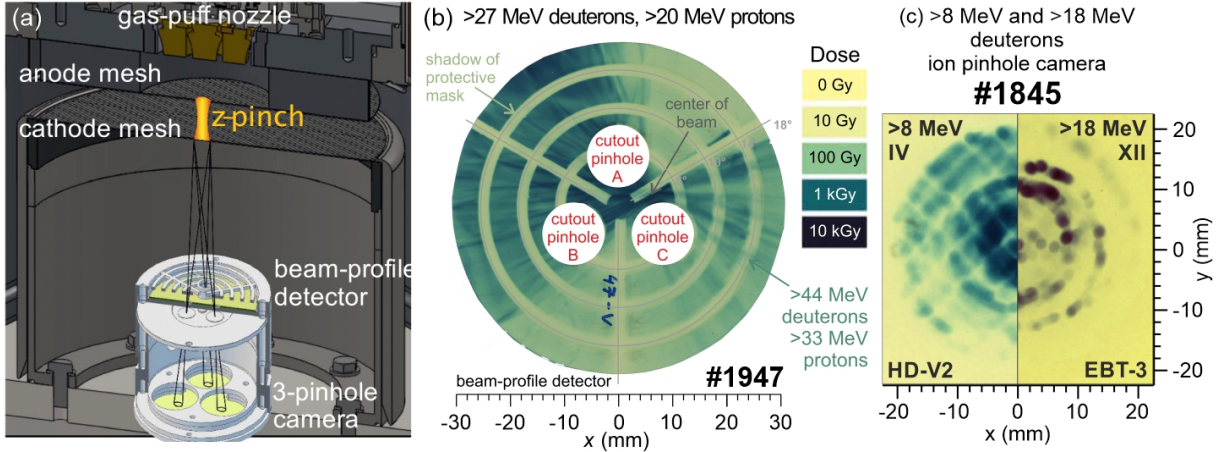


Figure 4.4: (a) Experimental setup on GIT-12 employing the beam-profile detector and the pinhole cameras. Experimental data show the characteristic observations by these detectors: (b) the radial lines created by high-energy (>27 MeV) deuterons in the ion beam profile detector, and (c) the ring structures captured by the ion pinhole detector in a wide spectrum of deuteron energies, represented by 8 MeV and 18 MeV. The spatial scales of the ion pinhole images correspond to the cathode plane.

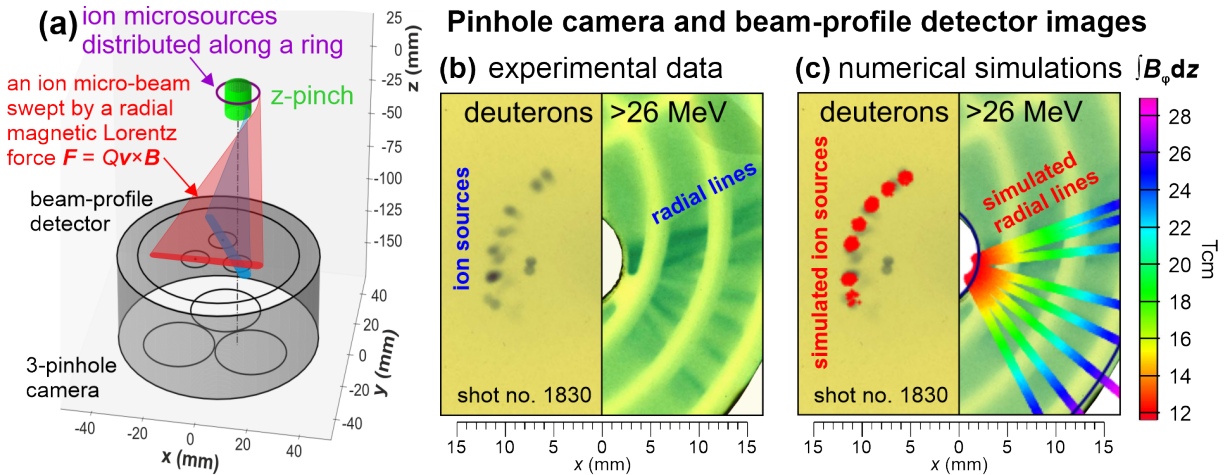


Figure 4.5: (a) The radial lines in the beam-profile detector are created when the microbeams emitted from the individual micro-sources arranged into a ring are radially swept by azimuthal B-fields. (b) Shot 1830 allows us to assign dots in the ion pinhole image (left), representing the ion micro-sources, with the radial lines in the beam profile detector (right). (c) Simulation of the radial lines (colorful line on the right) originating from the synthetic ion sources (red dots on the left). Colors of the lines indicate the range of the time-varying path-integrated B-fields, ranging from 10 to 30 Tcm [253].

Suppose the anisotropy of the beam profile is mainly caused by the radial Lorentz forces. In that case, it means that the ion emission in the azimuthal direction is unaffected by B-fields and provides information about the initial divergence of the micro-sources (*micro-divergence*). According to the small thickness of the radial lines in the beam-profile detector, this micro-divergence of high-energy ions must be low. In other words, the ion micro-beams at high energies are initially highly collimated and then deflected in the radial direction. To create continuous lines, the deflecting B-fields must vary continuously during the ion beam production, so they gradually move the collimated deuteron beams along the plane of the beam-profile detector (see Fig. 4.5a). We hypothesize that the temporal evolution of B-fields originates in the current disruption of the z-pinch in the plasma neck.

In the paper [253], we use our numerical simulations to estimate the range of time-varying path-integrated B-fields based on the length of the radial lines. Fig. 4.5b compares the >26 -MeV deuteron images captured by the pinhole camera and the beam-profile detector in shot 1830. The experimental data in this shot allow to assign the dots in the pinhole image, representing the micro-sources, to the individual radial lines in the beam-profile detector. We assume the deuteron microbeams are emitted initially along the axis from the micro-sources at the ≈ 10 -mm radius, related to the ring radius, and then swept (overfocused) by azimuthal B-fields towards the edge of the beam-profile detector. Then, we can associate the measured lengths of the radial lines to the deflection angles and the path-integrated B-fields $\int_0^Z B_\varphi dz$ according to Eq. (2.17). Fig. 4.5c displays that the measured path-integrated B-fields in shot 1830 range from 10 to 30 Tcm. In the presented shot, the upper limit of the measured range is given by the size of the beam-profile detector. In another shot employing a larger beam-profile detector, the estimated path-integrated B-fields reached up to 60 Tcm [253]. This analysis represents a basic use of the deflectometry method for B-field measurements.

Based on the information from the beam-profile detector, we conclude that the deuterons beams are emitted from the granular ion source and are radially deflected by strong time-varying azimuthal B-fields. The experimental data of the pinhole cameras showing characteristic ring structures provide further information about effects of the azimuthal B-fields, the spatial distribution of the ion source, and the divergence of micro-beams. These results will be discussed in the next subsection.

4.3.2 Characteristic rings captured by the pinhole cameras

Fig. 4.6a illustrates the experimental arrangement employing an on-axis 1-pinhole camera below the z-pinch. The pinhole camera projects incoming deuterons onto a stack of RCF and CR-39 detectors. It captures deuteron images for a wide range of energies. In Fig. 4.6b, the detector stack is represented by the selection of six deuteron images (one CR-39 and five RCF layers) from shot 1771. The images are sorted in descending order with respect to the deuteron energies (i.e., from the bottom to the top of the detector stack). At all presented deuteron energies, we observe characteristic rings (or their parts) with the central spots. At the highest deuteron energies of

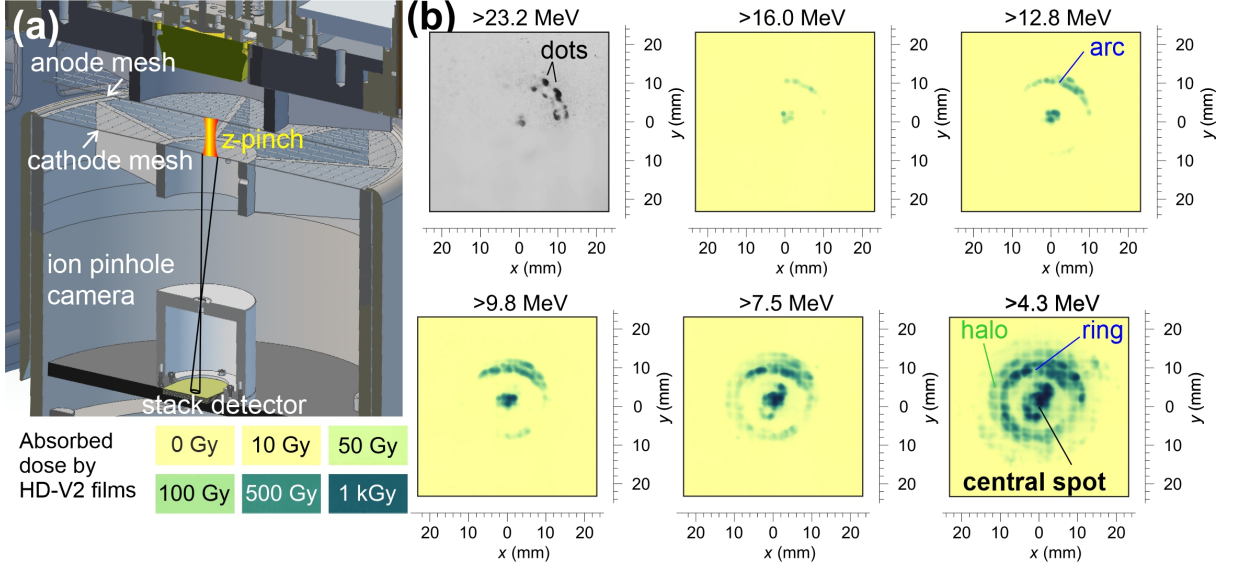


Figure 4.6: (a) Experimental setup on GIT-12 employing the 1-pinhole camera. (b) Selection of ion images obtained in the 1-pinhole camera in shot 1771 for six different deuteron energies. The spatial scales of these data correspond to the ion beam image in the cathode plane.

>23 MeV, the experimental data shows the individual dots arranged into parts of the concentric rings (arcs). Because the most energetic ions are the least influenced after their acceleration by the azimuthal B-field, we conclude that their image corresponds best to the real ion-source position and that the dots are coupled to the individual micro-sources of collimated ion micro-beams. This is in agreement with the discrete nature of the radial lines on the beam-profile detector discussed in Subsec. 4.3.1. With decreasing deuteron energy, the deuteron fluence in the pinhole images increases. The dots begin to merge into continuous arcs, and the central spots become larger. At lower deuteron energies ($\lesssim 10$ MeV), the deuteron signal starts to form complete concentric rings, which are often blurred or surrounded by a ‘halo’ (see Fig. 4.6b). At the lowest presented deuteron energy of >4.3 MeV, the deuteron signal is more extensive and has higher fluence. Due to a good contrast of this deuteron image, we can recognize a shadow of the cathode mesh, which deuterons must have passed through to leave the anode-cathode (A-K) gap. The shadow of this mesh is undeflected, which means that these deuterons have not been deflected after they left the cathode. Therefore, there can be no significant fields between the cathode and the detector. Deuterons are only deflected either during their acceleration in the collisionless gap or their travel through the plasma below. For future discussions, we consider all ion deflections in the necked plasma as a part of the ion acceleration process and include them in the term “ion source”.

Nonetheless, one of the most important information obtained by the 1-pinhole camera is that the radius of the observed rings in the cathode plane is almost the same (≈ 10 mm) for all deuteron energies. Interestingly, the azimuthal B-fields do not seem to influence the ring radius at any deuteron energy. Yet, the B-fields likely create radial lines in the beam-profile detector due to the strong deflections of high-energy deuterons. The constant ring radius is examined in

Sec. 4.4.

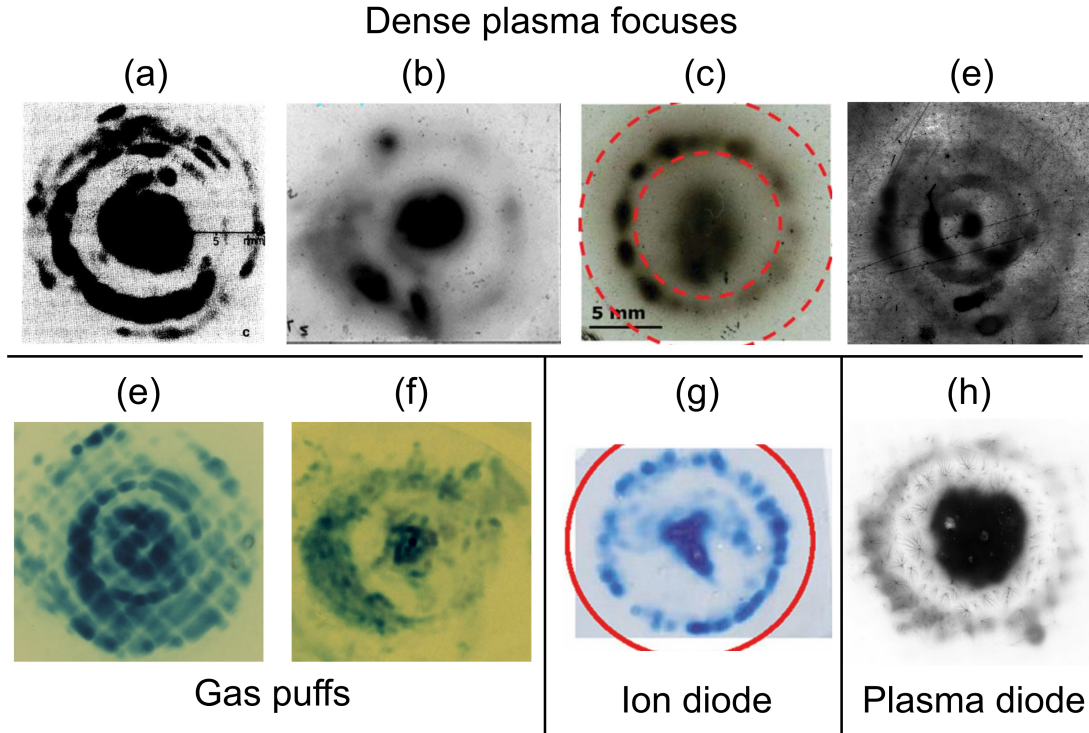


Figure 4.7: Selection of typical experimental data recorded by the ion pinhole cameras in various pulsed-power facilities. The rings (annuli) have been captured in dense plasma foci (a) DPF-78 [262], (b) SHOTGUN III [263], and (c-d) PF-1000 [264], [265]; but also in gas puffs: (e) GIT-12 [2] and (f) HAWK [266]. Interestingly, they have also been observed in (g) ion diodes [261] and (h) plasma-filled diodes [260].

Investigation of the origin of the ring structures is essential for a general understanding of multi-MeV ion acceleration in the z-pinch. Moreover, these rings have been observed in ion images of different z-pinch configurations (see Fig. 4.7). Besides the gas puffs, the rings appeared in ion images of the plasma foci and, interestingly, of ion diodes and plasma-filled diodes. Examining the multi-MeV ion source is also valuable from the point of view of the ion deflectometry development in z-pinch. We assume that the rings recorded by the pinhole camera are coupled to the actual ion sources, consisting of the many micro-sources. However, we assume ions are deflected, so the ring size may not equal the ion source's size simply magnified by the pinhole projection. Thus, the next section estimates how the size of the ion source depends on the ring radius and whether it is more extensive than the region of the plasma neck, where the ion acceleration subsequently occurs.

From a crude analysis of the experimental data, we cannot decide whether the rings originate in the structure of the actual ion source, associated with the ion acceleration and deflection in the high-impedance gap, or are formed after the ion acceleration via ion deflections in global B-fields. In the former case, the rings are dominated by the spatial distribution of the ion source, and in the latter case, by the distribution of the deflecting B-fields. This thesis will analyze both

hypotheses. Sec. 4.4 begins with the study of the origin dominated by the ion source, which is presented in [253]. Then, the size and the divergence of this ion source is evaluated in the paper Klir et al. 2020 [2], which is discussed in Sec. 4.5 and included in App. G.2. In contrast, the aspects of the B-field-dominated rings are then evaluated in Sec. 4.6.

4.4 Investigation of the origin of the ring structures observed by the pinhole camera

The size of the ion source is vital for the ion deflectometry, and, in the classical setup (see Fig. 2.7), it determines the spatial resolution of the B-field measurements. The source size should be considerably smaller than the typical spatial scales of the z-pinch, from a few mm up to several cm. Since the ion acceleration occurs right after the disruption of the plasma neck, we may suspect that the size of the ion source is coupled with the neck's thickness before the disruption ($\lesssim 1$ mm). Due to the spatial resolution of the pinhole diagnostics of 1 – 2 mm, we would consider such an ion source as point-like.

The observation of the central spots in ion images (cf. Fig. 4.6) suggests there is an on-axis ion source, but we must analyze whether this source can also produce the ion image of the ring structures. Fig. 4.8a illustrates that the on-axis point-like source must be highly divergent so that the ion image in the cathode plane is comparable in size to the observed ring image by the pinhole camera. However, the point-like ion source with the continuous divergence in the continuous B-fields would form a filled circle-shaped ion image. Thus, to produce the ring structure with the central spots, the source divergence must have a specific distribution so that only selected ion rays (blue trajectories in Fig. 4.8a) can reach the pinhole, which is improbable. The ion emission could be similarly selected by a specific (discontinuous) B-field distribution with a strong gradient, which characterizes the B-field-dominated ion source investigated in Sec. 4.6. However, the on-axis point-like ion source alone cannot explain all the experimental observations. Therefore, instead of the discontinuity in the distribution of the ion-beam divergence or the deflecting B-fields, we explain the ring formation by a discontinuity in the ion source's spatial distribution. Accordingly, we introduce an off-axis ring-like source with a radius larger than the plasma neck's thickness (see Fig. 4.8b). Because the ring source emits ions from many micro-sources at a significant radius (>2 mm), it is not required to be highly divergent for the ring-image production. Nevertheless, the initial ion direction, coupled with the divergence half-angle θ , is key for producing the ring images in the pinhole detector. If ions are emitted from the ring source radially outwards, they can be focused towards the axis by the azimuthal B-fields and reach the pinhole. In contrast, the ions emitted from the ring source inwards, i.e., in the direction of the deflecting force, are “overfocused” (gray trajectories in Fig. 4.8b), and their signal does not appear in the ion images captured by the on-axis pinhole camera. In this way, the ring-shaped ion image is created by the ring-shaped ion source and is not dominated by a specific B-field profile. Nonetheless, it does not explain the observation of the central spots

inside the ring ion images. Therefore, we assume there can be a small-scale on-axis ion source with lower divergence (the lime circle in Fig. 4.8b).

We have shown how the rings can be formed in the experimental data for the specific deuteron energy. Now, we explain why the ring radius could remain roughly the same for various deuteron energies.

In our paper [253], we bring an explanation illustrated in Fig. 4.9. It is based on the results of the beam-profile detector indicating that the deflecting B-fields vary in time during the ion imaging. Suppose that deuteron beams with two unequal energies, $E_1 > E_2$, are emitted from the ring source. Let us assume azimuthal B-fields B deflect deuterons with the higher energy E_1 into the central pinhole camera, where they create a ring-shaped ion image (see the blue curve in Fig. 4.9a). If deuterons with the lower energy E_2 are fired at the same or lower divergence half-angle θ , they cannot reach the pinhole because the given azimuthal B-field B deflects them away from the pinhole due to their smaller curvature radius $R_L \propto \sqrt{E}/B$ (the dotted red trajectory in Fig. 4.9a). The lower-energy deuterons can compensate for the focusing effect of the azimuthal B-fields and hit the pinhole if they are emitted radially outward with the higher divergence, that is, at the larger divergence half-angle θ . However, then, these deuterons reach the cathode plane at the larger radius (see the solid red curve in Fig. 4.9a) and, in the pinhole camera, produce a ring image with a larger radius $R'_{r2} > R'_{r1}$.

We see that the radius of the ring image R'_r , produced by the detected deuteron beams, is influenced by the initial radius of the ring source R_r and the curvature radius R_L of the deflected deuteron trajectories (see Eq. (2.14)). To create rings at different energies (E_1 and E_2) but with similar radii, deuterons must follow similar trajectories with the similar curvature ($R_{L1} \approx R_{L2}$). It is possible due to the magnitudes of azimuthal B-fields $B(t)$, which may vary during the deuteron emission as manifested by the radial lines in the beam-profile detector. We assume that the azimuthal B-fields may evolve in time during and after the z-pinch current disruption. Fig. 4.9b depicts two situations in separate time intervals, $t_1 \pm \Delta t$ and $t_2 \pm \Delta t$. In each one, deuteron beams are fired into the z-pinch B-fields from the ring source with the same divergence but with two different energies ($E_1 > E_2$). We assume that these azimuthal B-fields change slowly during each interval. Therefore, Fig. 4.9b displays deuteron trajectories in two azimuthal B-fields that are constant in time and have the same profile but different magnitudes $B_1 = B(t_1 \pm \Delta t)$ and $B_2 = B(t_2 \pm \Delta t)$, where $B_1 > B_2$. In the first situation, we set the B-field magnitude B_1 so that deuterons with the higher energy E_1 hit the on-axis pinhole and create a ring image with the radius R'_r . The shape of their trajectories is given by the profile of the curvature radius R_{L1} . The deuterons with the lower energy E_2 are strongly deflected away from the pinhole, cannot be captured by the pinhole camera, and do not create a ring image that would have a radius different from R'_r . In the second situation, we lower the B-field magnitude to the value B_2 so that the deuterons with the lower energy E_2 follow the path with the similar curvature ($R_{L2} \approx R_{L1}$). When captured by the pinhole camera, these deuterons create a ring

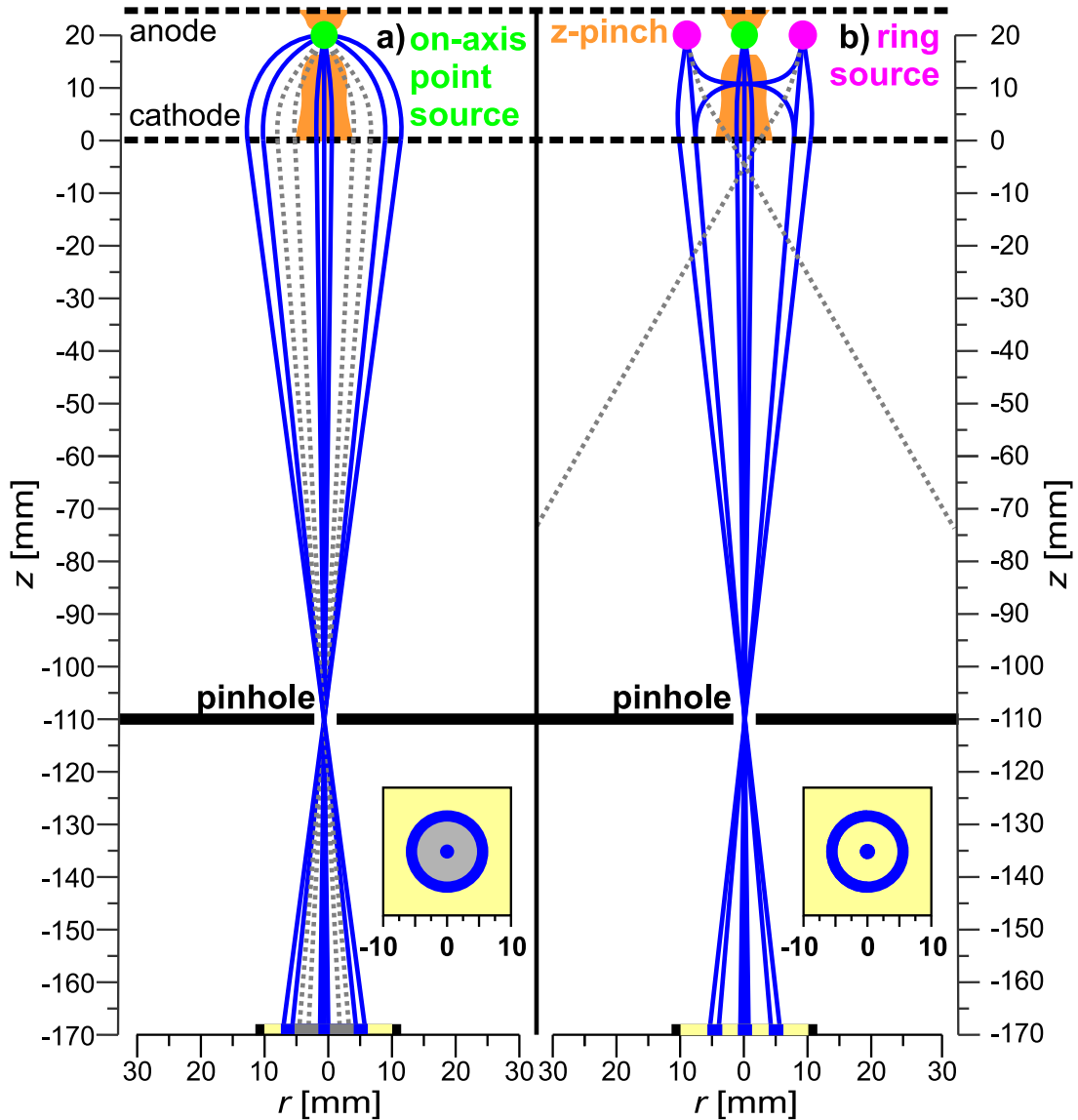


Figure 4.8: Two models of possible deuteron sources are proposed to produce ring structures in the pinhole detector’s data. (a) A point-like source with the high and continuous divergence create a filled circle-shaped ion image (a combination of gray and blue images in the inset). To produce ring structures, ion beams would need to be emitted in the specific directions (i.e., at the specific divergence angles along the blue trajectories). (b) Despite the high ion-beam divergence and time-varying B-fields, ions originating from the ring-shaped sources create ring structures in ion images. However, we still consider the point-like source with low divergence (the lime circle) to reproduce the circular image in the ring’s center (the central spot).

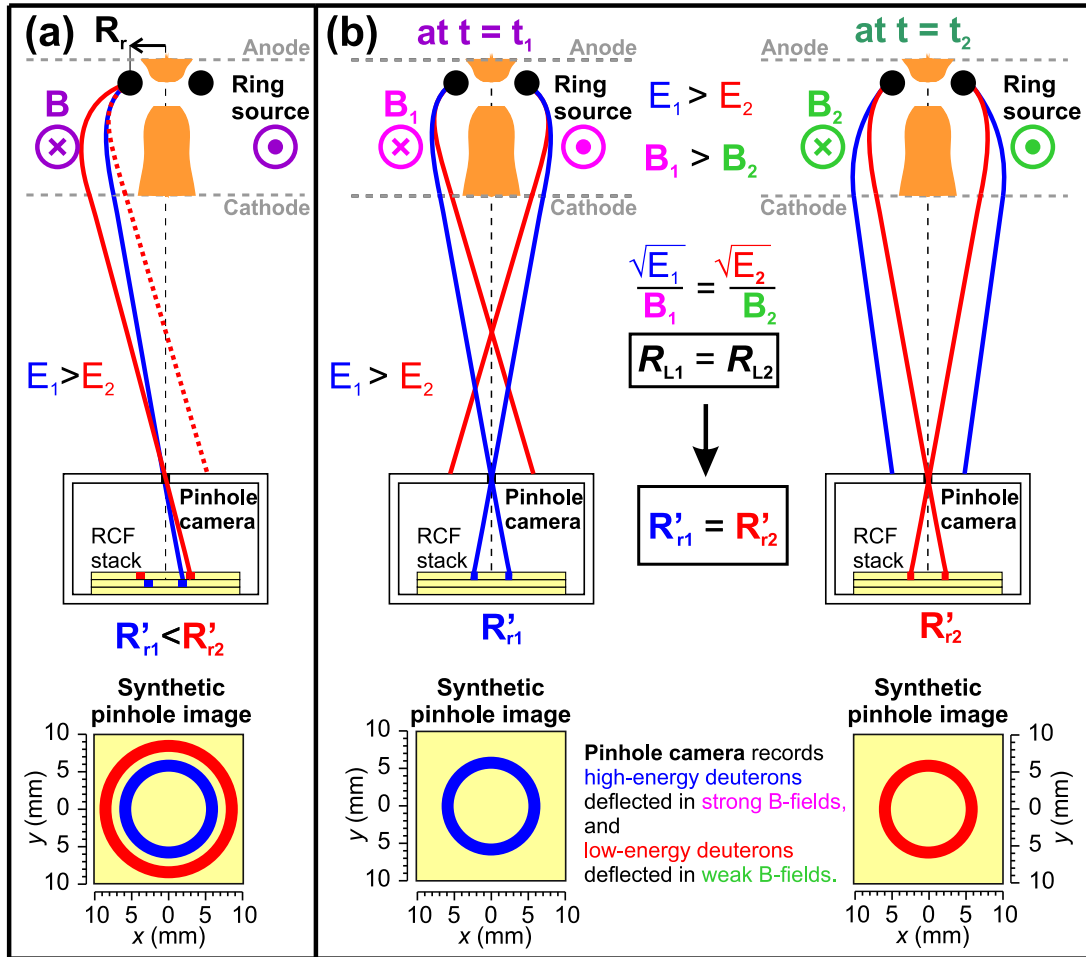


Figure 4.9: Formation of rings with different deuteron energy but the same radius in the central (on-axis) pinhole detector. (a) Deuterons with two energies E_1 and E_2 in B-fields with the same profile and magnitude B create rings with different radii ($R'_{r1} < R'_{r2}$). (b) To produce comparable rings with a similar radius R'_r ($R'_{r1} \approx R'_{r2}$) at different their energies, deuterons must follow specific trajectories given by a curvature radius R_L ($R_{L1} \approx R_{L2}$). Ring images with different energies E are produced at different times t when the magnitude of the time-dependent B-field $B(t)$ change by the ratio \sqrt{E}/B associated with the curvature radius R_L of the specific deuteron trajectory remains constant.

image with the same radius R'_r ($R'_{r1} \approx R'_{r2}$). In contrast, the deuterons with the higher energy E_1 are in this situation deflected insufficiently to hit the pinhole and thus do not create a ring image with a radius different from R'_r . It means that the pinhole camera captures the ion source at the specific times when the B-fields favorably deflect deuterons with the given energy to follow a similar path and hit the pinhole.

As a result, we obtain ring images with comparable radii created by the deuterons with different energies at different times. In general, the lower-energy deuterons can follow a broader range of trajectories due to various effects in their source that cause a broader range of the initial divergence angles θ . This might explain the secondary signal forming the halo in the lower-energy deuteron images (represented by 4.3 MeV deuteron image in Fig. 4.6b).

After explaining the formation of the ring structures in the experimental data of the 1-pinhole camera, we analyze the deuteron images even further. Via the investigation of the results from the multi-pinhole and 3-pinhole detectors, the next section (Sec. 4.5) provides additional information about the size and the divergence of the ion ring-shaped sources. These results are presented in our selected paper Klir et al. [2] that is included in the Appendix (App. G.2). In addition to his results in the paper [2], the author of this thesis uses his numerical ion-tracking simulations and the ion deflectometry principles to estimate the path integrals of the global B-fields in the z-pinch.

4.5 Selected results of our paper Klir et al., PPCF (2020) with additional comments

At the beginning of our paper [2], as in the previous sections of this Chapter, we introduce the experimental device GIT-12, employed ion diagnostics, and the typical experimental observations of the ring structures by the 1-pinhole camera.

We follow that up with results from multiple off-axis pinhole cameras capturing the ion beams from different sightlines to obtain information about the ring-like ion source. In particular, we analyze the results of the multi-pinhole detector consisting of one on-axis and four off-axis pinhole cameras. The experimental arrangement is illustrated in Fig. 4.10a.

4.5.1 Ion multi-pinhole images

Two sets of deuteron images for energies >4.3 MeV and >7.5 MeV from shot 1771 are shown in Figs. 4.11a-b. At the lower deuteron energy (Fig. 4.11a), the ring structures with the central spots appear not only in the on-axis images but also in the off-axis images recorded by the multi-pinhole camera. Although the off-axis cameras detect deuterons by an angle of $\approx 12^\circ$ from the setup axis, the ring radius is roughly the same in all images. This observation supports the hypothesis that the rings are coupled with the ring-shaped ion source. At higher deuteron energies, represented by 7.5 MeV in Fig. 4.11b, off-axis cameras show principally different pic-

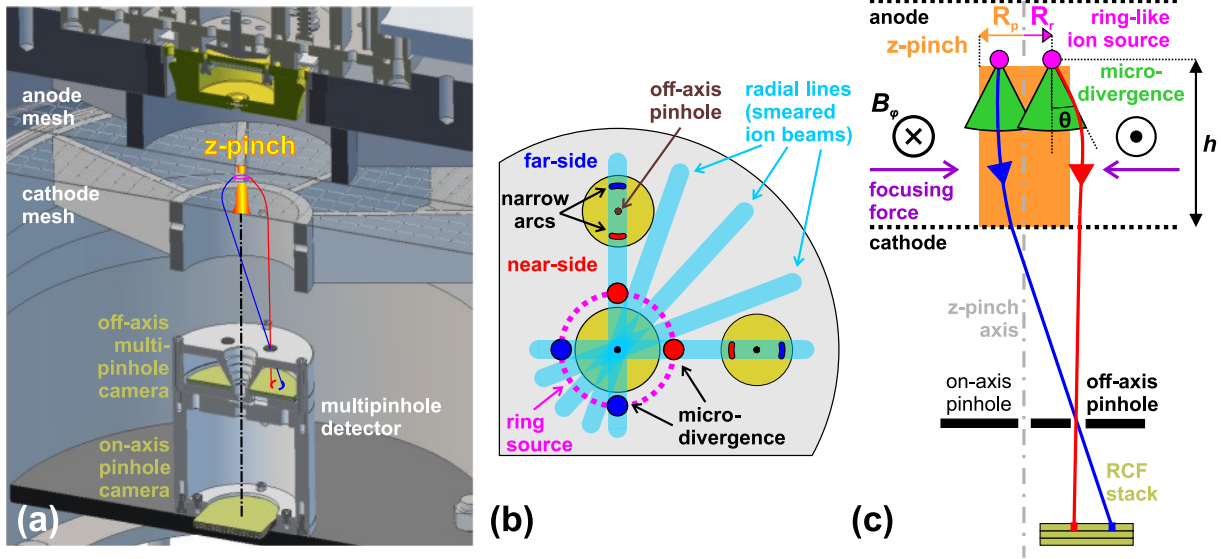


Figure 4.10: (a) Arrangement of the ion multi-pinhole camera. (b) Formation of the narrow arcs in off-axis ion pinhole detectors. (c) Geometry used for the simulation of deuterons detected by the multi-pinhole camera. For simplicity, the ion emission from the central spot is not shown. The schematics are not to scale.

tures than the central on-axis camera. The central spots remain but the rings transform into two narrow arcs, which are aligned into a straight stripe. The alignment axes of these arcs are determined by a plane set by an individual off-axis pinhole and the beam center.

Fig. 4.10b shows that the formation of these arcs in the off-axis pinhole images correlates with the observation of the radial lines in the beam-profile detector. These arcs appear in the off-axis pinhole images when the collimated deuteron micro-beams are swept radially by the azimuthal B-fields and hit pinholes in the 17-mm distance from the axis. Therefore, the arcs demonstrate the influence of the deflecting azimuthal B-fields on the deuteron emission. In contrast, the lengths of the arcs (the azimuthal sizes) are not affected by the B-fields because they are determined by the initial lateral (azimuthal) micro-divergence of micro-beams, which is perpendicular to the radial force deflecting ions. It means that the arc structures in the off-axis images at higher deuteron energies can provide information about both the B-fields and the initial micro-divergence of the ion source.

At lower deuteron energies, the micro-divergence increases, and the arc-shaped deuteron images grow until they form complete rings (see Fig. 4.11a). Therefore, the information about the B-fields and the initial micro-divergence cannot be acquired unambiguously. In addition, the ring and arc radii in the on-axis and off-axis images, respectively, are influenced by the size of the deuteron ring-shaped source.

To obtain these information, we use our numerical ion tracking code to reproduce the significant features of the experimental data, namely, rings in the on-axis and arcs in off-axis deuteron images. We implement the experimental setup with the multi-pinhole camera into our numerical model and simulate deuteron paths in the B-fields. This numerical code has evolved from the

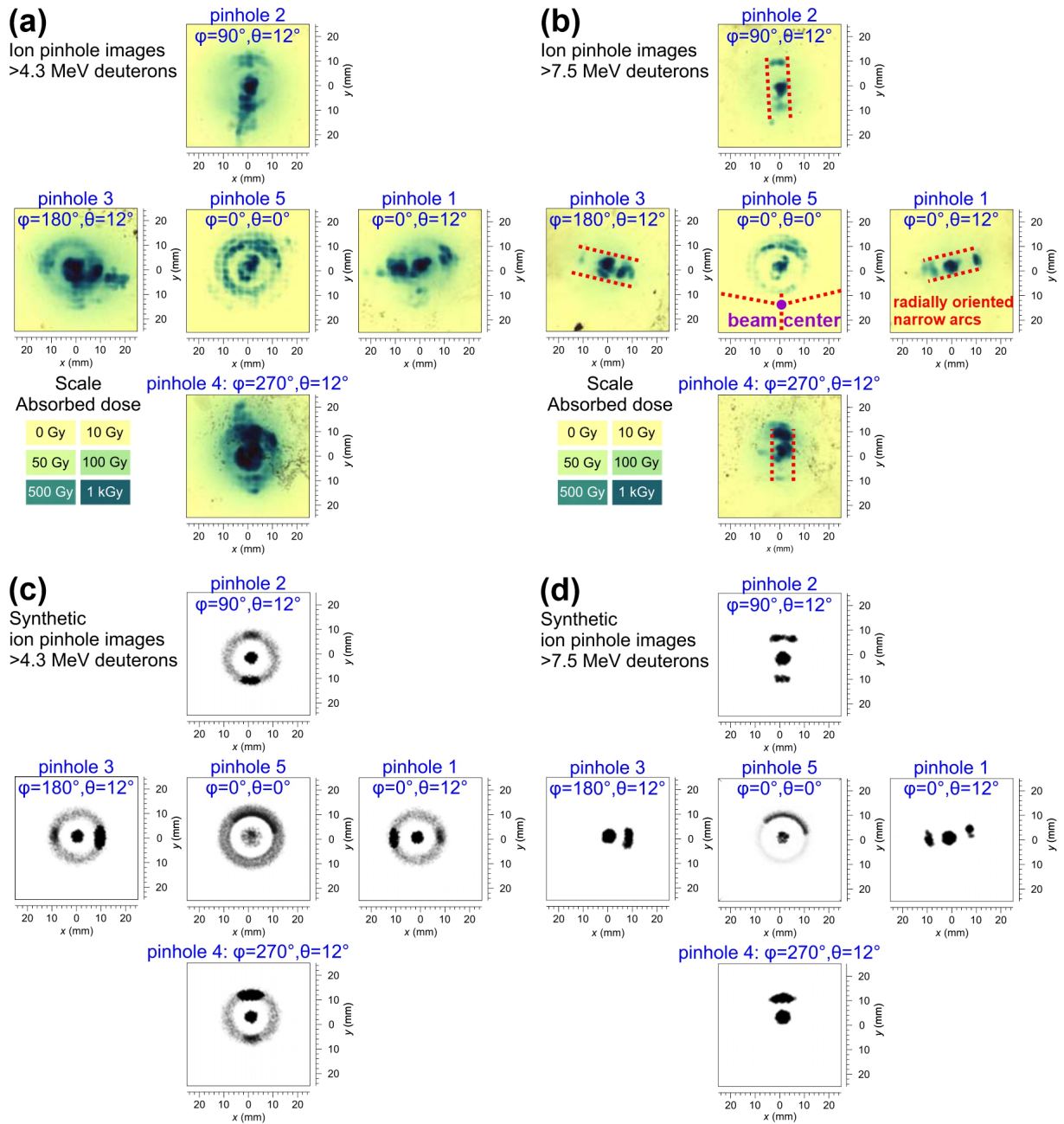


Figure 4.11: Experimental (*a-b*) and synthetic (*c-d*) sets of ion pinhole images (one on-axis and four off-axis) for 4.3 and 7.5 MeV deuteron energies in the shot 1771. Spatial scales correspond to the plane of the cathode mesh.

code used for simulations in Chap. 3. To best fit the experimental data at various deuteron energies, our second-generation numerical code defines numerous parameters of the modeled ion source, azimuthal B-fields, and the geometry of the pinhole diagnostics. Fig. 4.10c illustrates the geometry of the simulated setup. Our numerical simulations do not address the acceleration of the ions because detailed information about the parameters of the ion acceleration is the subject of another research and is beyond the scope of this thesis. Therefore, we assume that monoenergetic deuterons already reaching their final energy are emitted from many micro-sources arranged into an infinitely thin ring with the radius R_r . Each micro-source produces a symmetric emission cone with the divergence (micro-divergence) half-angle θ_{max} . Usually, we set the rings', emission cones' and z-pinch's axes parallel to each other and to the z-axis. In the experimental images (Figs. 4.11a-b), we see a specific anisotropy of the ring structures, which appear when the central pinhole lies slightly off the beam axis. In simulations, we model it by the unevenly distributed intensity of the ring-shaped ion source and by shifting the beam axis from the center by ~ 1 -mm. In our model, the ion source is a two-dimensional object situated in a plane defining from above the B-field region and the z-pinch, a symmetrical cylinder with a radius R_p and a height h . We assume the B-field does not vary during the path of the individual particles but changes during the ion emission, which we simulate by choice of the total z-pinch current I_C from the defined range in the specific B-field profile for each trajectory. We compare two current profiles $I(r)$, namely, the skin-current and the uniform current density inside the z-pinch. The boundary of the z-pinch defines its radius R_p where the current density falls to zero, and the B-fields have a $1/r$ profile.

To find the approximate fit of the experimental data, we must balance various parameters of our model, which have opposing effects to the synthetic data, in particular, for the 7.5-MeV deuteron images (Fig. 4.11a). For example, deuterons from the micro-source nearer to the off-axis pinhole (see the red circles in Fig. 4.10b) must be fired radially outwards at a large divergence half-angle θ to compensate for the focusing effect of the B-fields (see the red trajectory in Fig. 4.10c). However, the maximum micro-divergence half-angle θ_{max} of the emission cone, which we assume to be symmetric, is defined in the perpendicular (azimuthal) direction by the observed radial line width and the arc length (Fig. 4.10b). In contrast, deuterons fired from the micro-sources farther from the off-axis pinhole (see the blue circles in Fig. 4.10b) benefit from the focusing effect of the B-fields, and thus, they do not require such a high divergence to hit the off-axis pinhole (see the blue trajectory in Fig. 4.10c). Therefore, the numerical simulations must allow the azimuthal B-fields to vary for each ion trajectory. This way, micro-beams from the *near-side* micro-sources travel in slightly weaker B-fields and are not deflected away from the off-axis pinhole, whereas micro-beams from the *far-side* travel in slightly stronger B-fields and are focused toward the off-axis pinhole.

The synthetic images for the two deuteron energies, shown in Figs. 4.11c-d, represent a compromise between all effects while qualitatively capturing the main features of the experimental data. Found parameters of the simulations are interesting. From two considered B-field profiles, we find that the best fit is the profile, when the current flows in a skin layer at the 9-mm z-pinch

radius R_p . It means that inside the z-pinch there are almost no B-fields. Moreover, the found value of the total z-pinch current at this radius is rather low and reaches only to 1 MA, which is less than a half of the 2.7-MA circuit current during the z-pinch stagnation. The corresponding B-field magnitude is equal to 22 T. Nonetheless, these values are determined by the axial length h of the B-field region. The crucial and the most relevant result represents the estimated value of the maximum path-integrated B-fields $\int_0^h B_\varphi dz \approx B_\varphi h$, which is equal to 40 Tcm. In our model, we have assumed that the B-field region spreads from the cathode to the ion source, which we set in the approximate height of the collisionless gap, that is, $h = 18$ mm. However, the actual gap can expand during the ion acceleration due to the plasma disruption. The gap expansion reduces the height h of the B-field region. Therefore, if we would lower the effective height of the B-fields to $h = 10$ mm = 1 cm, the maximum of the B-field magnitude, given by their path-integral, and the total z-pinch current would be 40 T and 1.8 MA, respectively. Regardless of different numerical solutions for shot 1771, we have found that the radius of the modeled ion source is equal to (10 ± 1) mm for all energies, which is close to but outside the 9-mm-radius z-pinch. By reproducing other shots, we have found that the radius of the ion source varies between 6 and 10 mm [2]. Moreover, we have been able to estimate the maximum micro-divergence half-angle θ_{max} based on the azimuthal lengths of the arcs in the synthetic 7.5-MeV deuteron image (Fig. 4.11d). The emission cone of 7.5-MeV deuteron beams fired from the 10-mm ring has the half-angle θ_{max} of ≈ 100 mrad, and for those fired from the central spot, the half-angle is ≈ 250 mrad. It is worth noting that whereas the maximum estimated path-integrated B-fields are determined by the far-side arcs in the synthetic data, the maximum estimated micro-divergence is coupled with the near-side arcs.

4.5.2 Ion three-pinhole images

Due to the relatively large 17-mm distance of its off-axis pinholes from the center, the multi-pinhole detector provides valuable ion images with separated effects of the radially deflecting B-fields and the symmetrically emitting ion source. However, due to the low magnification ratio (a large reduction of the ion image at the cathode), the multi-pinhole detector has a low spatial resolution of 2 – 3 mm. Moreover, the assembly of this detector cannot house a stack of many RCFs, which would capture a broader spectrum of deuteron energies, because the off-axis cameras must share space inside the detector assembly with the central pinhole camera (see Fig. 4.10a). Therefore, instead of the multi-pinhole camera, we employ the 3-pinhole camera with three pinholes arranged closer to the axis at a 9.6-mm radius (see Fig. 4.12a). It can accommodate many more layers of RCFs, allowing us to further explore ion images over a wide range of deuteron energies.

Although the pinholes in this detector are situated symmetrically around the diagnostic center, the z-pinch axis in most shots usually aims closer to one of the pinholes. Then, this pinhole camera effectively becomes an ‘on-axis’. In the experimental data of the shot 1845,

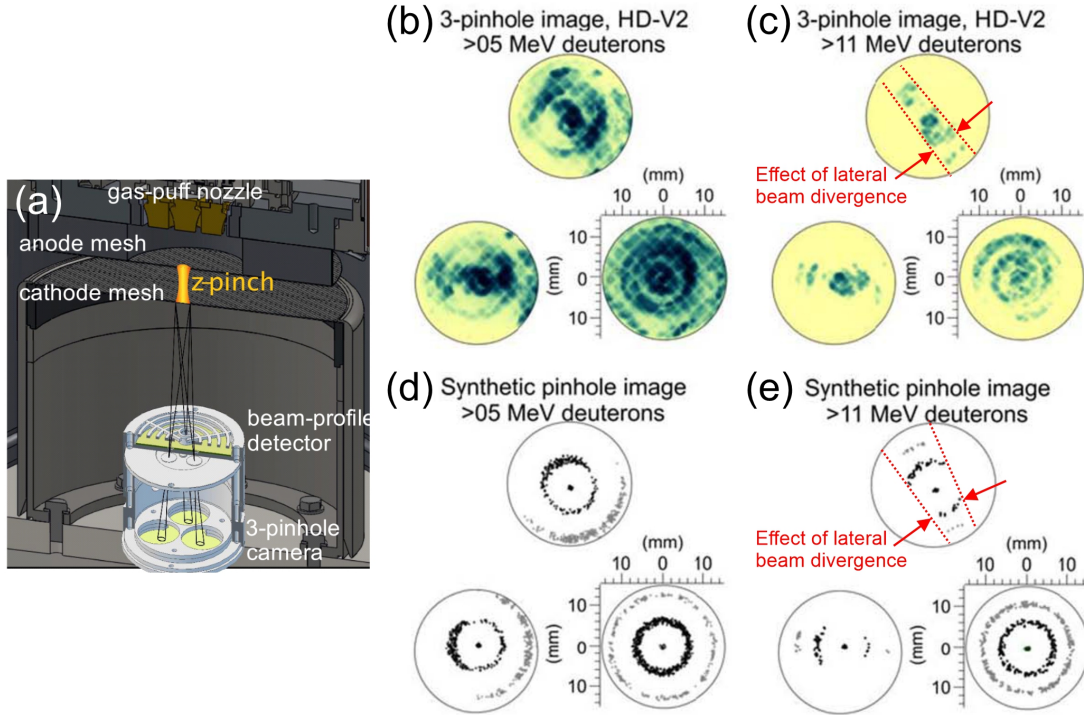


Figure 4.12: Measurement of the micro-beam divergence from three-pinhole images. (a) Arrangement of the ion 3-pinhole detector. Experimental (b–c) and synthetic (d–e) pinhole images of 5 and 11 MeV deuterons in shot 1845. The spatial scales correspond to the plane of the cathode mesh.

represented by 5-MeV and 11-MeV deuteron images in Figs. 4.12b-c, this ‘on-axis’ pinhole camera is the one on the right. However, according to the rings’ center and the spatial fiducials (cutouts) in the cathode mesh imprinted into the deuteron signal (see Fig. 4.12b), the sloped z-pinch is located close to the diagnostic axis. Interestingly, this ‘on-axis’ pinhole image captured more than one ring at the given deuteron energy. The inner ring keeps its radius with an increase of the deuteron energy, but the outer does not. The movement of the outer ring can be coupled with some temporal evolution of the ion source or the specific effect of the global B-fields, which is discussed in Sec. 4.6. The other two (‘off-axis’) pinhole cameras capture anisotropic ion signal, which forms somehow asymmetrical rings at the lower deuteron energies and narrow radially-oriented arcs at the higher energies.

To analyze the deuteron source’s size and micro-divergence, we employed our numerical model previously used on the experimental data from the multi-pinhole detector. However, we added more parameters for the positions and slopes of the deuteron source’s and azimuthal B-field’s axes. Therefore, deuterons were deflected (focused) towards the rightmost pinhole that acts as an ‘on-axis’ pinhole. As a result, we could reproduce synthetic images capturing features of experimental data from the 3-pinhole camera in shot 1845 for eight deuteron energies from 5 to 26 MeV. Synthetic images for deuteron energies of 5 and 11 MeV are in Figs. 4.12d-e. The lowest analyzed deuteron energy is 5 MeV because, at lower deuteron energies, the RCF detectors in this shot were mostly saturated by high irradiation. The image of 11-MeV deuterons illustrates higher-energy images. Using our numerical simulations, we estimate that the radius

of the inner ring source equals 7 mm at both energies. The radius of the outer ring source has shifted between presented energies from 10 to 13 mm. Since we aimed to reproduce deuteron images for a wide range of energies but for the identical distributions of the ion source and B-fields, synthetic images in Figs. 4.12d-e capture the positions of the rings and the central spots but only roughly display their detailed shape.

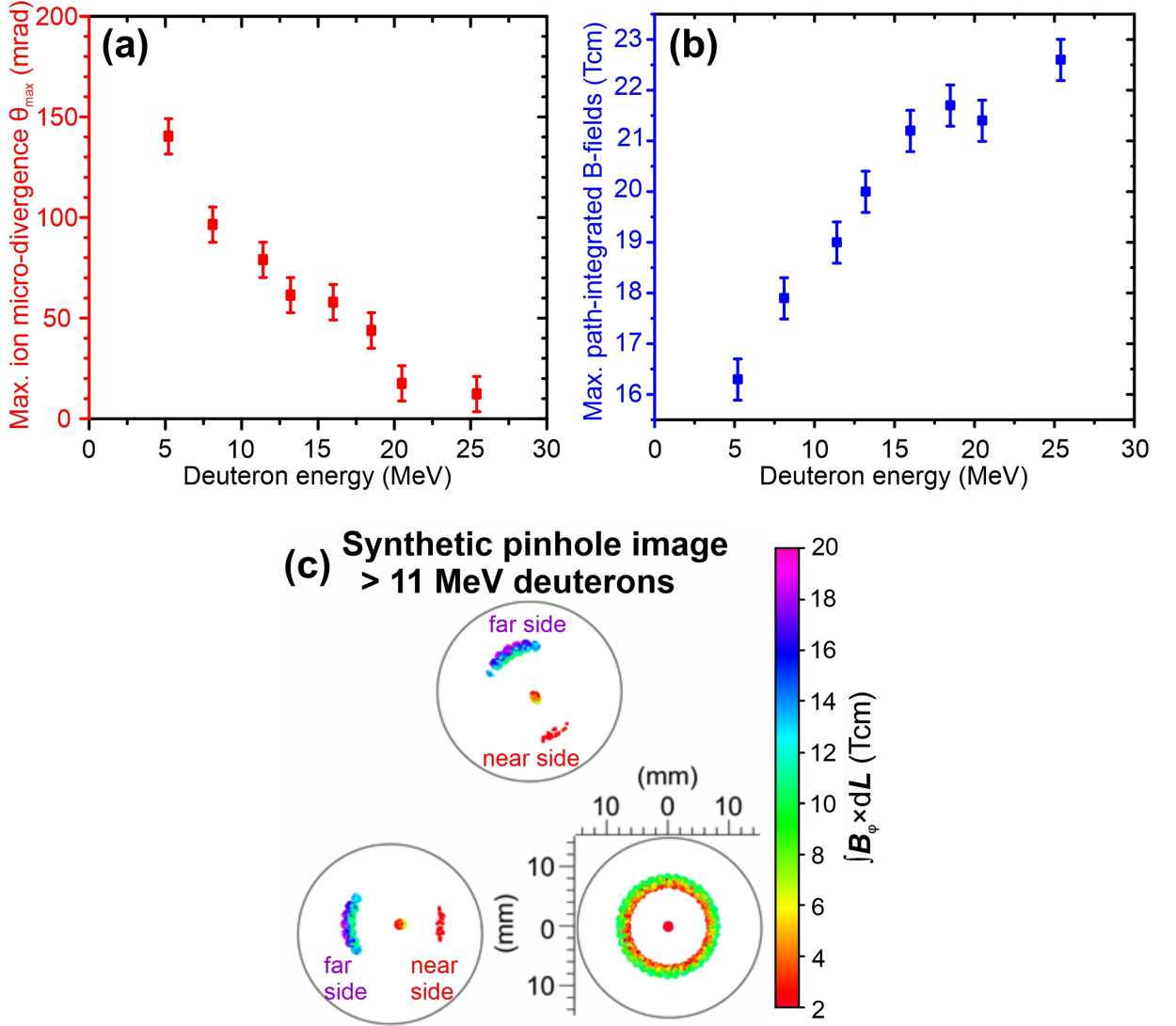


Figure 4.13: The estimated dependence of (a) the maximum ion-beam micro-divergence and (b) path-integrated B-fields on the deuteron energy in shot 1845. (c) The synthetic pinhole image of 11-MeV deuterons indicates the calculated path-integrated B-fields.

Based on the obtained synthetic data, Fig. 4.13a presents the crucial dependence of the maximum ion-beam micro-divergence half-angles θ_{\max} of the inner ring source on the deuteron energy. The micro-divergence half-angle decreases from ~ 140 mrad at 5 MeV to ~ 10 mrad at 26 MeV. At the highest deuteron energies, the micro-divergence, if assumed symmetric, corresponds to the thickness of the radial lines observed in the beam-profile detector in this shot. This indicates a correlation between the results of the beam-profile and the pinhole detectors.

In addition to the results published in our paper [2] and discussed in this Section, Fig. 4.13b also presents maximum values of the calculated path-integrated B-fields for each deuteron energy. The highest path-integrated B-field of 22.6 Tcm in shot 1845 is lower than the maximum value of synthetic data from the multi-pinhole detector of 40 Tcm in shot 1771. It is caused by the fact that the off-axis pinholes of the 3-pinhole camera, used in shot 1845, are closer to the axis than those of the multi-pinhole detector, used in shot 1771. Therefore, the 3-pinhole camera could not capture more deflected (radially outwards) deuterons. However, it is interesting that a ratio between the highest estimated path-integrated B-fields of these two detectors ($22.6/40 = 56.50\%$) used in these shots is comparable to a ratio of the radial distances of their pinholes from the axis ($9.6/17 \approx 56.47\%$). Therefore, the path-integrated B-fields seem to grow linearly with the radial ion displacements.

Furthermore, Fig. 4.13b shows that the calculated path-integrated B-fields grow with the detected deuteron energy. This agrees with the hypothesis that deuterons must follow similar trajectories to create rings with the fixed radius at the different deuteron energies (Sec. 4.4). However, note that the maximum micro-divergence θ_{max} in Fig. 4.13a is mainly determined by deuterons from the near-side arcs and the maximum path-integrated B-fields in Fig. 4.13b by deuterons from the far-side arcs.

Fig. 4.13c shows the difference in the path-integrated B-fields of the near- and far-side arcs. As shown by Fig. 4.10c, the near-side off-axis signal (arcs) requires high ion-beam divergence half-angles and low values of path-integrated B-fields (red and yellow colors), which tend to deflect deuterons in the radial direction away from the pinhole. The far-side off-axis signal (arcs) requires high path-integrated B-fields (blue and violet colors) to deflect deuterons toward the pinhole. Due to their stronger focusation, more deuterons from the far side of the ion source than those from its near side can hit the off-axis pinhole. Thus, these deuterons create longer arcs at the far sides of the synthetic ‘off-axis’ images in Fig. 4.10c.

4.5.3 Ion pinhole images on the HAWK generator at the Naval Research Laboratory

Until now, we have discussed our research on GIT-12. To confirm our conclusions, we have performed similar measurements of the hydrogen ion emission on another pulsed-power z-pinch device. Our paper [2] also presents results of the pinhole diagnostic in experiments on the HAWK generator in the Naval Research Laboratory (NRL) in Washington, D.C., USA. This device has similar architecture as GIT-12, but the z-pinch on HAWK is in the experimental configuration of the dense plasma focus, and the electrodes are not the a form of meshes. The charging and output voltages are 60 kV and 0.64 MV. The z-pinch load is driven by the current 0.7 MA with a 1.2- μ s rise time. Fig. 4.14a shows the experimental setup. Instead of the cable guns used on GIT-12, three Marshall guns situated symmetrically around the z-axis create a smooth preionized 1- μ gcm⁻¹ plasma shell. The main experimental load is a deuterium gas puff

injected from a valve situated inside the central conductor of the anode (see Fig. 4.14b). The cathode is a hollow structure created by coaxial metal rods and, therefore, does not limit the axial size of the imploding z-pinch plasmas. A detailed description of this device can be found in [267]. Our experiments on HAWK and GIT-12 devices are compared in [266]. To record ion

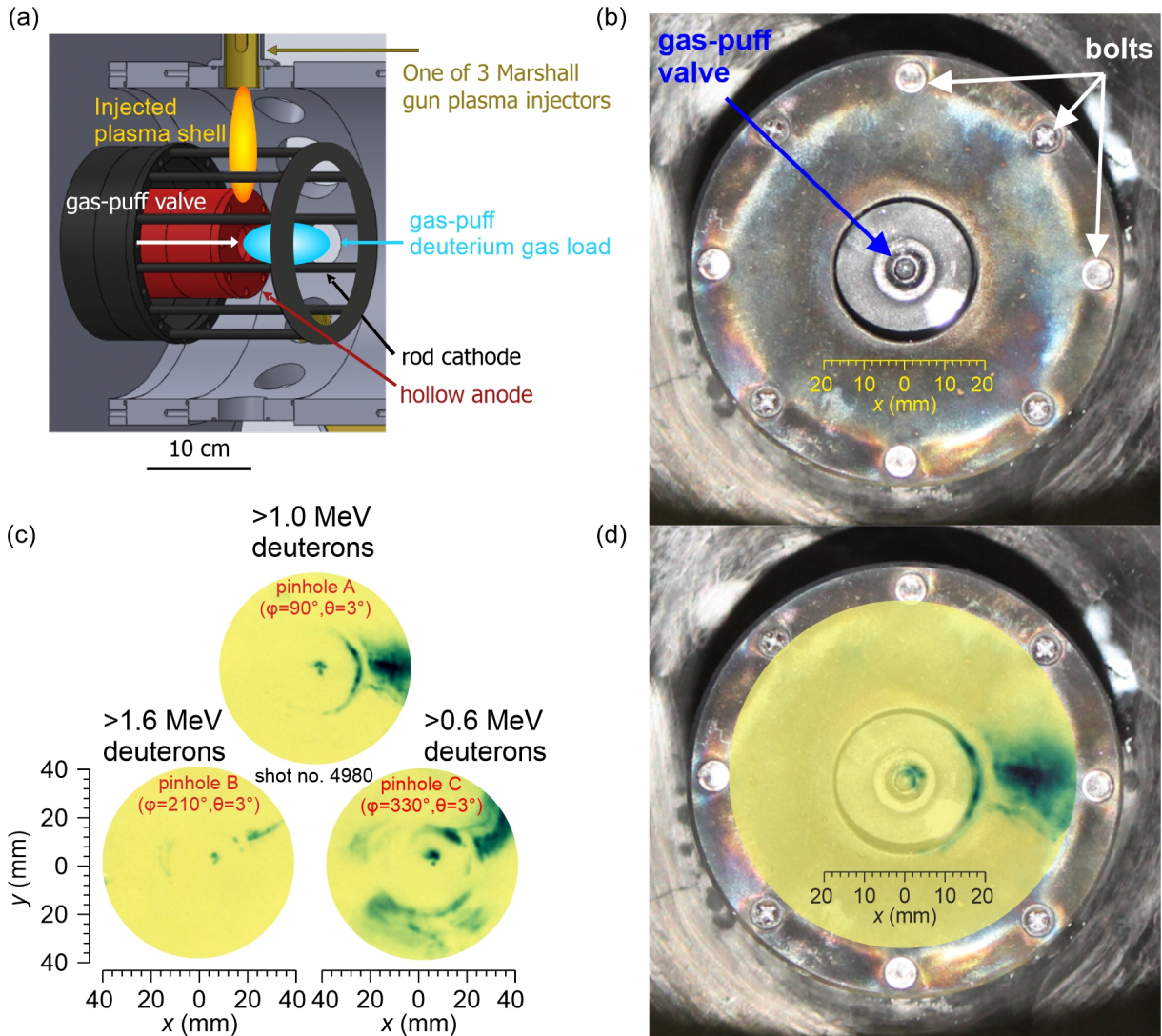


Figure 4.14: (a) Arrangement of the electrode system on the HAWK generator. (b) Top-view photo of the anode with the gas-puff valve inside the central conductor. (c) Deuteron images for three deuteron energies obtained by the 3-pinhole camera using three different Al absorbers. (d) Top-view of the anode overlaid by the scaled pinhole image of the >1-MeV deuterons. All spatial scales correspond to the plane of the anode end.

images in the experiments on HAWK, we have used the 3-pinhole camera, placed on-axis and ~ 200 mm from the anode. Typical examples of these experimental images are in Fig. 4.14c. Due to the use of three different absorbers (filters), we can observe ion signals at three deuteron energies, namely, 0.6, 1.0, and 1.6 MeV. The spatial scales correspond to the plane of the anode end. The radius of the employed pinholes is ~ 250 μm and the spatial resolution is ≈ 2 mm. The experimental images show parts of ring structures similar to the ring structures observed

on GIT-12 and others. We find that the radius of these ring parts is comparable for all three energies, similarly to the experiments on GIT-12. Interestingly, if we compare the top-view image of the anode with the experimental pinhole images, we can associate the ring structure with the spatial layout of the gas-puff hole inside the central anode (see Fig. 4.14d). Moreover, we can observe the ion emission aimed close to one of the anode screws (on the right-hand side of Fig. 4.14d). These observations indicate that the rings in the ion images correlate with the spatial layout of the experimental setup. We hypothesize that this layout determines the spatial distribution of the current density close to the anode wall before the current disruption. Therefore, the ion images may reflect the actual structure of the current density distribution in and around the necked plasma. According to the ion accelerating mechanism described in [253], the current-conducting plasma transforms into the collisionless gap due to the plasma disruption, and the current density is replaced by the transient E-fields accelerating ions. Therefore, the distributions of the initial current density and the E-fields creating the multi-MeV-ion source may be related.

In the next Section, we explore the possibility that even after the ion acceleration, the current density and B-field profile, this time below the ion source in the remnant plasma, have a crucial role in forming the ring structure in the ion images. Therefore, after the source-dominated origin of the rings, we discuss the B-field-dominated rings.

4.6 Ring formation in ion pinhole images dominated by the distribution of azimuthal B-fields

The formation of the ring structures in ion images is influenced by the properties of the ion source and the B-fields. So far, we have considered *the source-dominated origin* of the rings (see Fig. 4.15a), assuming that the rings somehow reflect the spatial distribution of the ion source. We have concluded that, at multi-MeV ion energies, the rings are produced by hydrogen ions accelerated from discrete micro-sources, which are already arranged into narrow ring-like structures. The effect of the azimuthal B-fields in this hypothesis is limited only to direct (focus) the diverging ion beams towards the axis, enabling their projection through the pinholes into the detector. The rings with the seemingly energy-invariant radius, observed by the pinhole camera, originate from a small set of possible ion trajectories leading to the ring structures. To achieve that, the B-fields must change during the ion emission to ensure similar ion deflections for various ion energies.

This section considers the possibility of an alternative hypothesis of the rings' origin, *the B-field-dominated ring formation*, assuming that the rings are related not to the ion source structure but the distribution of global B-fields deflecting already accelerated ion beams. In particular, we assume azimuthal B-fields with a sharp gradient and high magnitude caused by a thin current sheath with a high current density (see Fig. 4.15b). As a result, the sharp B-field

gradient creates a “magnetic mirror” that reflects ions in different directions. Due to its large distance (≈ 110 mm) from the cathode, the pinhole camera effectively selects ion beams reflected from the B-field gradient in the direction nearly perpendicular to the cathode plane ($\Omega \approx 0$). This way, the reflected beams produce a ring image at the cathode plane with the radius given by the current sheath’s position. Since the observed features in the experimental data, i.e., the rings, are mainly determined by the B-field’s characteristics, the ion source in this hypothesis can be more general than in the source-dominated hypothesis.

To evaluate the hypothesis of the B-field-dominated ring formation, we use our ion-tracking simulations and reproduce experimental ion images in shots 1771 (see Fig. 4.16) and 1845 (see Fig. 4.12). Because we focus on the ring structures, we base our simulations on the on-axis pinhole camera results. Although there was no on-axis pinhole in shot 1845, the beam axis was close to one of the pinholes of the 3-pinhole camera, so we can consider this pinhole to be ‘on-axis’.

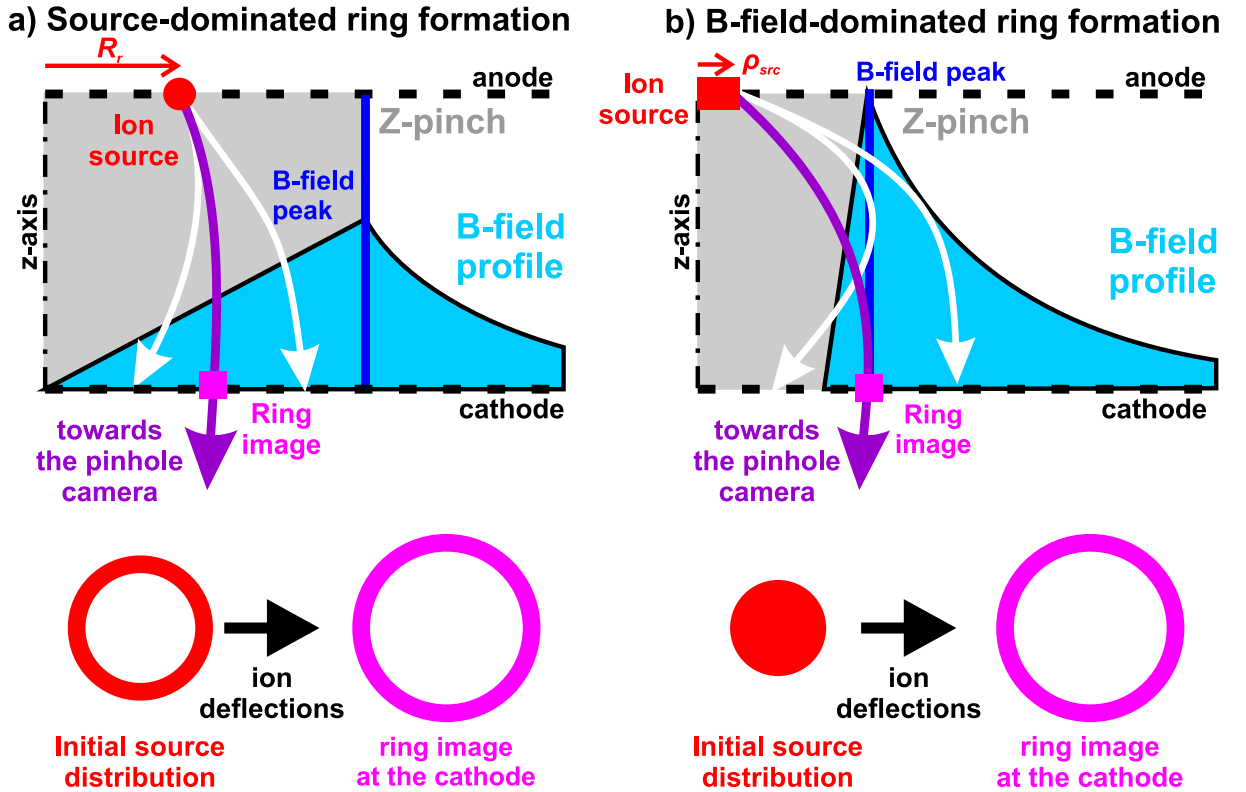


Figure 4.15: Two possible origins of the ring structures in the ion pinhole images. (a) Source-dominated rings are created by deuterons emitted from a specific ring-shaped source. (b) Deuteron beams producing source-dominated rings are emitted from a generic source but then selected by a specific B-field profile with a sharp gradient. Because the pinhole camera is selective, only certain ions (purple) can reach the pinhole and be recorded. Other ions (white) are deflected away.

Fig. 4.16 illustrates two experimental ion images from the central 1-pinhole camera in shot 1771 for deuteron energies 16.1 MeV and 4.3 MeV. We begin our analysis with the 16-MeV deuteron image. If the rings refer to the location of the thin current shell creating the z-pinch,

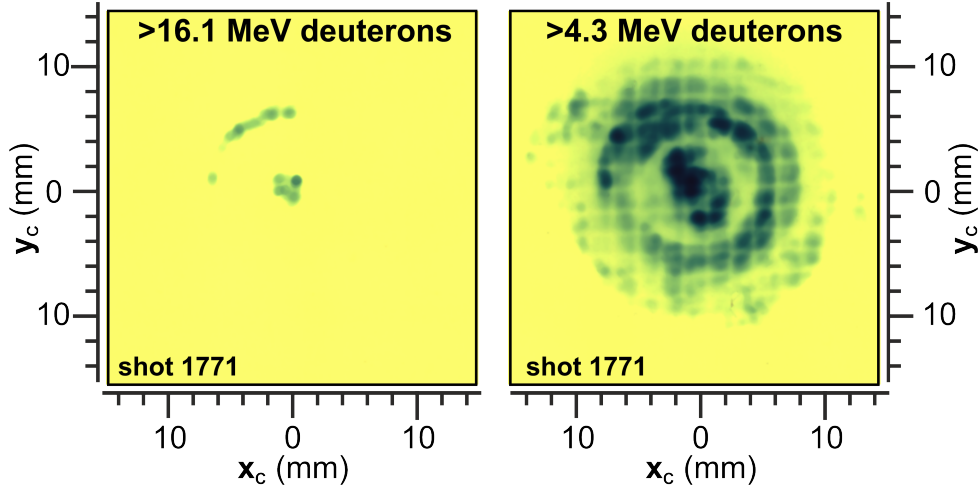


Figure 4.16: Experimental ion images for two deuteron energies (16.1 MeV and 4.3 MeV) recorded by the central on-axis pinhole camera in shot 1771. All spatial scales correspond to the cathode plane.

it means that within the z-pinch radius, there are no B-fields. Therefore, the central spots in the ion images are created by ions traveling ballistically and represent the actual ion source. Accordingly, the expected ion source has a circular cross-section with a diameter of $\approx 3 - 4$ mm, corresponding to the central spot size in Fig. 4.16a. Besides the source diameter, we impose no other conditions for the ion emission in our simulations. Thus, in our numerical model, 16-MeV deuteron beams are emitted from a cylinder with the 2-mm radius and a height of ~ 20 mm, stretched from the anode to the cathode. In addition, we set the maximal half-angle divergence of each microsource to $\theta_{max} = \pi/2$. Therefore, the specific B-field profile will be the only limitation in our simulated setup. We create the magnetic mirror by implementing the B-field profile with a steep gradient. We choose a gradient width of ≈ 2 mm, which roughly corresponds to the thickness of the ring in the experimental data of 16-MeV deuterons (see Figs. 4.17a-b). The location of the current sheath with the B-field peak correlates with the ring's position at the cathode plane. To achieve strong B-fields capable of reflecting 16-MeV deuterons, our numerical model assumes a high current of 2.2 – 2.5 MA flowing through the thin current sheath.

Although we set the simulated deuteron source highly divergent and uniform, only a ring with the central spot appears in the synthetic deuteron image at the projected location of the B-field peak (see Figs. 4.17c-d). The reason is that only the strongest B-field at the narrow peak of the current sheath can reflect the high-energy deuterons into the pinhole. Deuterons traveling closer to the axis cannot be deflected due to the B-fields absent inside the shell of the hollow z-pinch. Deuterons aiming farther from the axis are too deflected to hit the on-axis pinhole.

Now, we continue with the reproduction of the 4.3-MeV deuteron image in the same configuration of the simulated B-fields. Fig. 4.16b shows that the central spot in the image of 4.3-MeV deuterons is larger than for 16.1-MeV. Therefore, we increase the diameter of the synthetic source of 4.3-MeV deuterons to 8 mm. Fig. 4.18 presents the experimental and synthetic images of 4.3-MeV deuterons projected onto the cathode plane and compares them with the

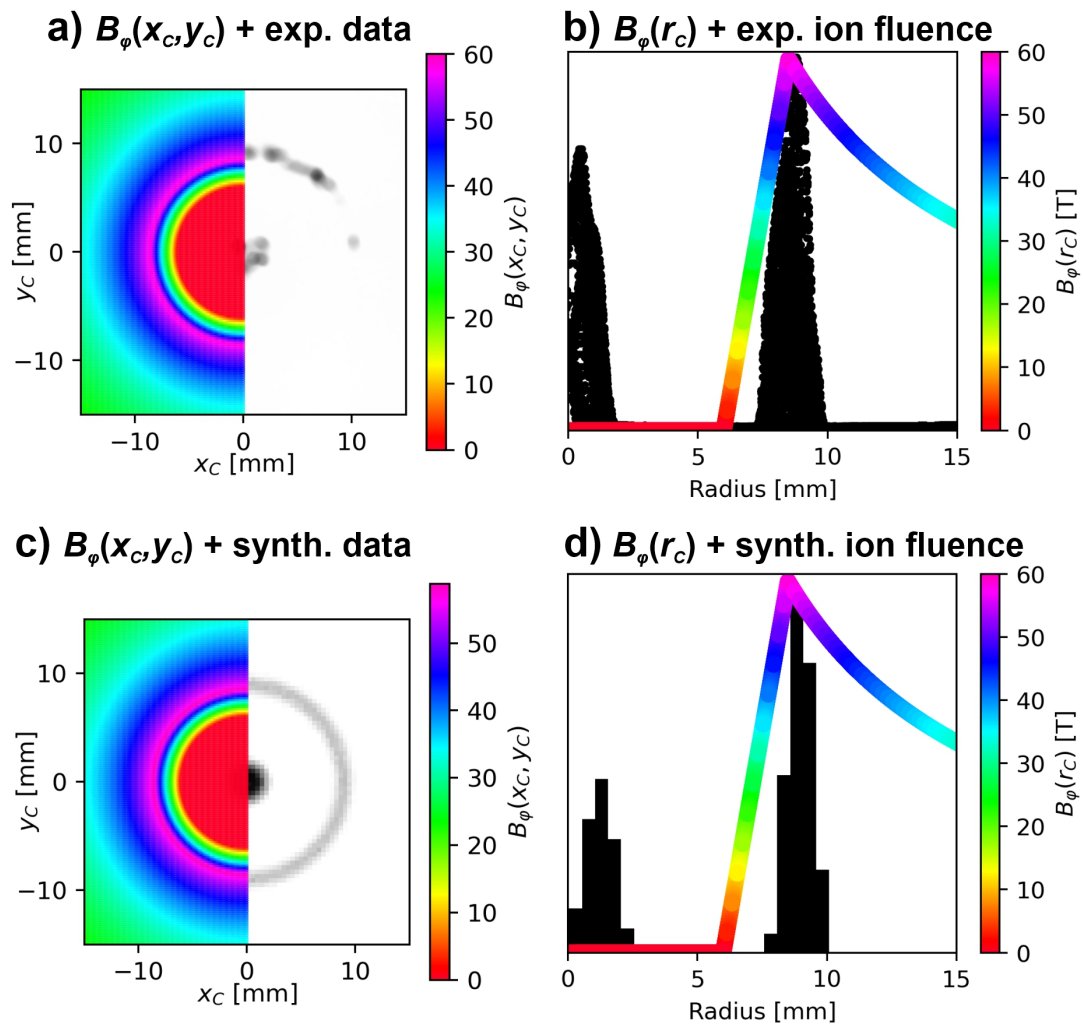
>16.1 MeV deuterons

Figure 4.17: Simulated azimuthal B-fields are fitted to (a) the experimental data of 16.1-MeV deuterons obtained by the central pinhole camera. (b) The input B-field profile corresponds to the averaged radial profile of the deuteron fluence. In the B-field-dominated ring formation, the B-fields and its profile determine (c) the synthetic deuteron images and (d) the cross-sectional deuteron fluence, respectively. All spatial scales correspond to the cathode plane.

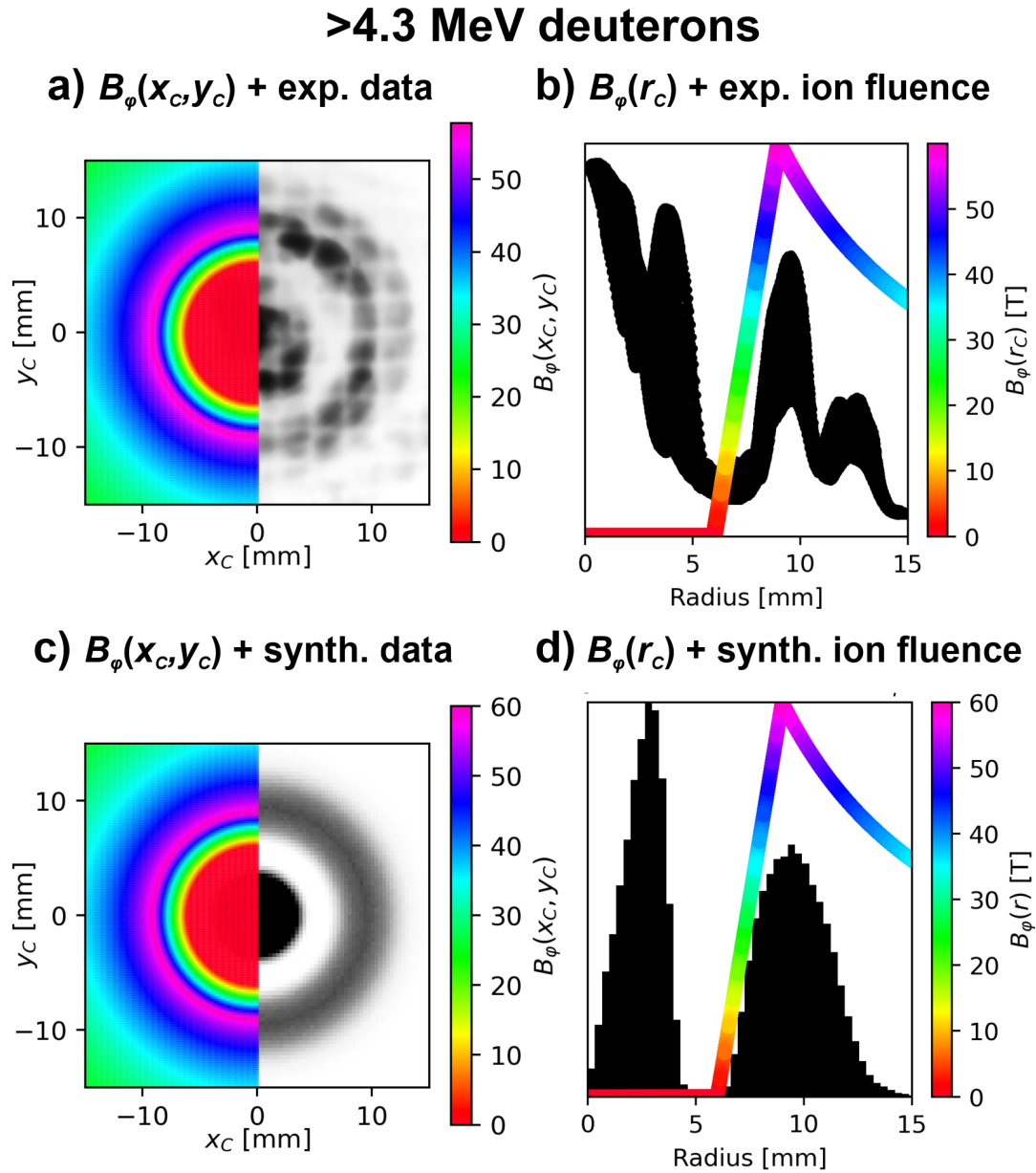


Figure 4.18: Simulated azimuthal B-fields correlate with (a) the experimental and (c) synthetic images of 4.3-MeV deuterons obtained by the central pinhole camera. The input B-field profile follows the averaged radial profile of the deuteron fluence of both (b) the experimental and (d) synthetic data. All spatial scales correspond to the cathode plane.

simulated B-field distribution. Due to the extensive ion source, deflected deuterons can reach B-field regions farther from the axis and create a broader ring in the synthetic deuteron image (see Figs. 4.18c-d). Interestingly, the ring radius in the synthetic image correlates with the experimental data and remains the same as for the 16.1 MeV deuterons. It may seem that the given B-field should reflect the deuterons with different energies at different distances leading to the shift of the ring. However, if deuterons are reflected close to the cathode by the magnetic mirror (the B-field gradient), their trajectories cannot noticeably diverge (see Fig. 4.15b). Thus, the ring radius in the synthetic deuteron images of different energies remains comparable.

In our simulations, the deuteron source was the 20-mm-high column stretched between the electrodes. However, for both deuteron energies (4.3 and 16.1 MeV), the vast majority of the detected deuterons originated from a region at the 16 – 20-mm distance from the cathode, which is an approximate location of the collisionless gap (see Fig. 4.1b). Therefore, we consider these simulations to be consistent with our theory of the multi-MeV ion acceleration mechanism.

We go further with our analysis and investigate the images of 5.2-MeV and 16.1-MeV deuterons in shot 1845, where more than one ring feature appears in images of the given deuteron energy (see Fig. 4.12b-c). In Sec. 4.5, we have reproduced two rings observed in the deuteron images by implementing two independent ring-shape deuteron sources with the different radii and micro-source divergence (see Fig. 4.12d-e). Now, we consider only one extensive and highly divergent deuteron source but implement the B-field profile with a strong gradient at the location of the inner ring (see Fig. 4.19).

Fig. 4.19a compares the experimental and synthetic images of 5.2-MeV and 16.1-MeV deuterons, projected onto the cathode plane, with the simulated B-field profile. In contrast to the simulations of shot 1771, the peak of the simulated B-field profile is not in the location of either ring, but we place it between them. This way, the strongest B-fields of the current sheath produce too strong deflections, so most deuterons cannot hit the pinhole. Deuterons can reach the pinhole camera only if deflected by a specific interval of B-field magnitudes. Therefore, suitable deuteron deflections are possible only in the regions on either side of the B-field peak, where B-fields decrease below a certain limit. Therefore, the B-field peak splits the deuteron beams and produces a shadow in the deuteron fluence between two rings in the synthetic images. The inner ring is created by deuterons deflected at the inner side of the current layer. Since the B-field profile is steep, the deuterons with different energies are reflected in different B-fields but from the approximately same location, and thus, recorded deuterons produce a ring radius similar for both energies. Notice that the outer ring at the 5.2-MeV image is slightly larger than at the 16.1-MeV image (cf. Figs. 4.19a-b). Outside the z-pinch, the simulated B-fields have a flatter profile given by $B_\varphi(r) \propto I/r$ than in the current sheath. Therefore, the limit B-fields for each deuteron energy are at a slightly different radial distance which causes the outer rings to have different radii.

These simulations demonstrate that the B-field distribution can strongly influence the synthetic deuteron images. However, we need to investigate how the ion source distribution affects

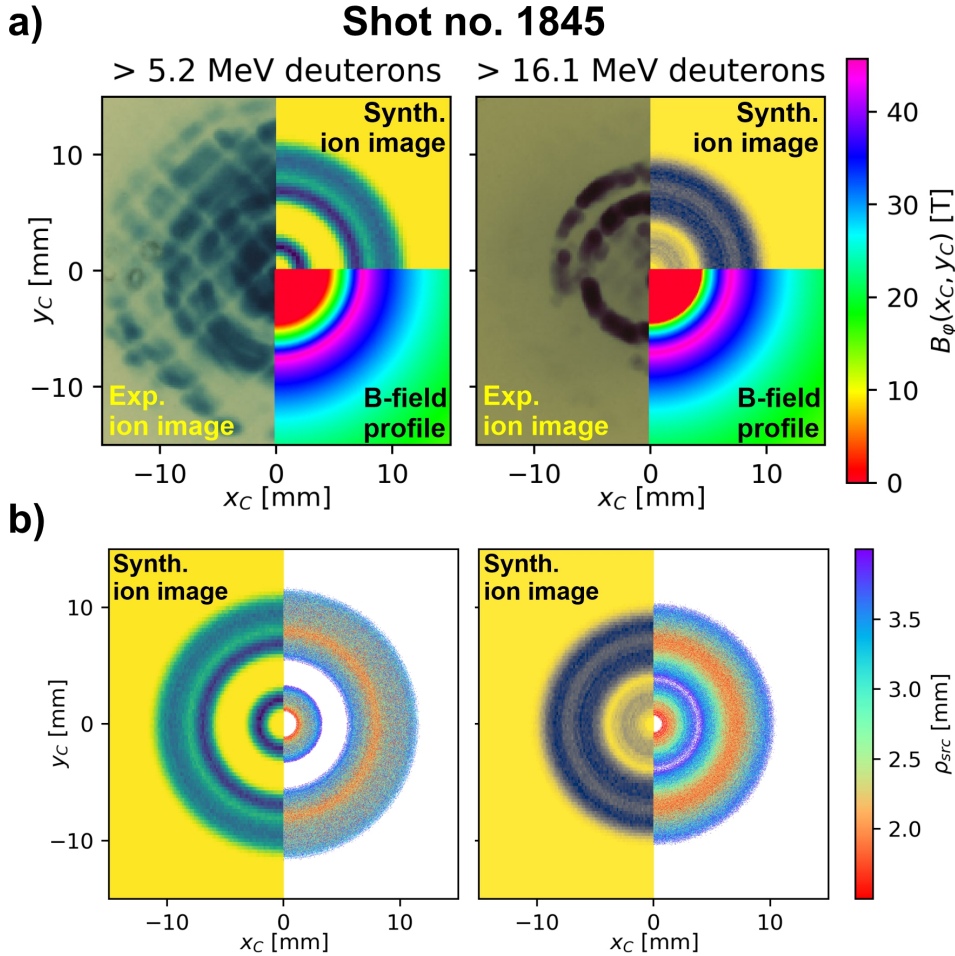


Figure 4.19: (a) Experimental and synthetic ion images in shot 1845 for deuteron energies >5.2 and >16.1 MeV are compared to the cross-sectional B-field profile. (b) The synthetic images for both deuteron energies with the indication of the initial radial positions ρ_{src} in the simulated ion source. All spatial scales correspond to the cathode plane. The axial distance of the simulated deuteron source from the cathode is 16-18-mm.

the ring formation in the B-field-dominated model. Fig. 4.19b shows the synthetic images in shot 1845 with highlighted values of the initial radial positions ρ_{src} in the cylindrical source of the captured deuterons. The axial distance of the simulated deuteron source from the cathode is 16-18-mm. Fig. 4.19b demonstrates that captured deuteron beams were fired from the micro-sources situated at the 2 – 4-mm radial distance from the axis. It means that the simulated ion source has a ring shape and is two times smaller than in the source-dominated model in Sec. 4.5. We excluded micro-sources situated close to the axis ($\rho_{src} \lesssim 2$ mm) from our simulations. Deuterons emitted from these sources reach the magnetic mirror at large angles, which can be balanced by strong ion deflection at the B-field peak just so that they can hit the pinhole. Such deuterons would fill the low-fluence region between the rings in Fig. 4.19b. Thus, the inner and outer rings in the synthetic images would merge. Due to a small source size, the maximum micro-beam divergence θ_{max} in these simulations must be high, namely 30° and 60° for 5.2-MeV and 16.1-MeV deuterons, respectively.

In conclusion, these simulations prove that the ion source partly determines the ring forma-

tion in the ion pinhole images even in the B-field-dominated regime. Without the measurements of the B-field distribution, we can exclude neither the source-dominated nor B-field-dominated ring formation hypothesis. However, the latter represents a rather extreme situation of high-magnitude B-fields with strong gradients and highly divergent ion sources. Nevertheless, it is crucial for ion deflectometry that the ion source cannot be solely point-like in neither hypothesis.

This Chapter demonstrated that the deuteron z-pinches can produce hydrogen ions (predominantly deuterons) with high yield and energies in multiple MeV per nucleon. Ion beams are predominantly emitted many micro-sources arranged into the ring structures. The divergence of each micro-source decreases with the ion energy. The crucial results are that the size of the deuteron source on GIT-12 is $\sim 1 - 2$ cm. Since the micro-sources in the extensive ion source are divergent, the emitted ion beams are not laminar. Since the beam laminarity is necessary for the unambiguous ion deflection measurements and the source size determines the spatial resolution of the ion deflectometry in the classical configuration described in Chap. 3, we conclude that the ion deflectometry using this ion source in this setup is not feasible. However, in the next Chapter, we use our ion pinhole diagnostics to develop a unique configuration employing a z-pinch-driven ion source and yet allowing the ion deflectometry measurements in the MA z-pinch B-fields.

Chapter 5

Z-pinch-driven ion deflectometry measurements

Ion emission measurements in the previous chapter (Chap. 4) provided essential information about the spatial distribution of the ion source and the magnitude of the global azimuthal B-fields in the z-pinch plasmas on GIT-12. However, these measurements could not unambiguously differentiate between the ion deflections occurring during ion acceleration in the ion source and after it in the global B-fields. Therefore, we must find a way to separate these effects and estimate azimuthal B-fields based on ion images independently of the properties of the ion source.

Ion deflectometry offers a solution for direct B-field measurements. The classical deflectometry setup (see Fig. 2.1) requires a point-like source of laminar ion beams for ion backlighting. Chap. 4 inspects the source of deuteron beams observed in several gas puffs and plasma foci (see Fig. 4.7). On the one hand, this source provides sufficient ion energies and yield for purposes of ion deflectometry. On the other hand, the z-pinch-driven ion source is too extensive to be employed in the classical configuration assuming a point-like ion backlighter. This Chapter (i.e., Chap. 5) finds an alternative experimental setup for ion deflectometry in z-pinch plasmas, which uses the z-pinch-driven ion source described in Chap. 4 and allows direct measurements of the azimuthal z-pinch B-fields using ion deflections on GIT-12.

Sec. 5.1 describes the development of the alternative method for the deflectometry measurements utilizing the pinhole detectors and the extensive and highly divergent source of hydrogen ions. This experimental setup allows not only deflectometry B-field measurements but also, for moderate ion deflections, the analytical retrieval of the path-integrated B-fields from the experimental ion images using the Larmor orbit approximation (Sec. 5.2). We have developed a high-performance numerical code capable of producing synthetic ion deflectograms with high contrast. Sec. 5.3 exploits these numerical simulations and presents the characteristic synthetic deflectograms of the various current density distributions in our alternative deflectometry configuration. Using our alternative setup, we have performed the first-ever z-pinch-driven ion deflectometry measurements of azimuthal B-fields and currents in the z-pinch plasmas. The results of these experiments were presented in our paper [3]. The paper, in its entirety, is included in the

Appendix (see App. G.3). This thesis in Sec. 5.4 summarizes the published results and provides further commentaries.

5.1 Development of the z-pinch-driven ion deflectometry in z-pinches

The development of ion deflectometry on the GIT-12 generator was based on five critical milestones in our research, partly described in the previous chapters of this thesis.

The first prerequisite was the theoretical analysis of the ion deflections in z-pinch B-fields (Sec. 2.4) and, particularly, the derivation of the general deflectometry equation Eq. (2.13) for an arbitrary ion deflection angle α , and related Eq. (2.17) for radial ion displacements. This analysis examined the relation between the deflection angle α and the path-integrated B-fields. Moreover, it showed that the estimation of the deflection angle α requires the knowledge of the initial θ and final angle Ω of diagnostic beams. In the classical setup (Fig. 2.9a), the laminar well-defined ion source allows us to determine the undistorted image of the ion beam and establish the divergence half-angle θ . Then, the deflection angle α is estimated by measuring the incident angle Ω of deflected ions in the detector plane. In contrast, if the ion backlighter is not laminar, we have no information about individual ion beams' divergence (micro-divergence) half-angle θ . In this case, we can estimate the deflection angle $\alpha = \Omega - \theta$ by determining the observation angle Ω via the projection of deflected ions through a well-defined focal point and then deducing the initial angle θ . To that end, we can use a small aperture of the pinhole camera. Its employment in ion diagnostics lead us to the second step.

The second step was our experience in measuring ion emissions using the pinhole camera. Based on ion pinhole images, we characterized the multi-MeV deuteron sources in the z-pinches (Chap. 4). In particular, we estimated the maximum beam micro-divergence θ_{max} for several deuteron energies E (see Fig. 4.13a), and proved that the ion source is extensive. If the observation angle Ω is known due to the pinhole projection, the micro-divergence θ of the ion source becomes crucial for measurements of deflection angles α and corresponding path-integrated B-fields $\int B_\varphi dz$. Suppose we put the pinhole camera at a large distance l_{pin} from the cathode so the observation angle is small ($\Omega \approx 0$). Then, the micro-divergence half-angle θ corresponds to the deflection angle magnitude α (i.e., $|\theta| \approx |\alpha|$), and we can simplify Eq. (2.17) as follows

$$|\sin \theta| \approx |\sin \alpha| = \frac{Q}{\sqrt{2m_i E}} \int B_\varphi dz = \int \frac{dz}{R_L} \quad (5.1)$$

where R_L is the Larmor radius corresponding to a local curvature of the ion trajectory. Eq. (5.1) demonstrates that the maximum micro-divergence θ_{max} for a given ion energy E determines the maximum measurable path-integrated B-fields. Moreover, Sec. 4.6 showed that pinhole projection may select deflected ions depending on their radial position in the ion source after the acceleration and the magnitude of the path-integrated B-fields. Ions emitted at the larger radii can reach B-fields further from the axis. Ions emitted at the smaller radii can reach a

specific region of the B-fields at larger (micro-divergence) angles coupled with the deflection angles. Therefore, in the setup with the pinhole camera, it is beneficial that the ion source is divergent and extensive.

The third step was the relatively reproducible regime of our experiments on GIT-12 producing accelerated hydrogen ions, mostly deuterons, with sufficient yield and energies in MeV [24], [266]. The number of detected ions must be high for a good contrast of the ion images (deflectograms), and sufficient ion energy is required to prevent interactions between the plasma and the diagnostic beam. Our ion-beam divergence measurements on GIT-12 (Fig. 4.13a) showed that the most divergent deuteron beams have the lowest MeV energies.

The fourth step, described in [253], was discovering that ions detected in our experiments are accelerated in the collisionless gap near the anode and that the plasma dynamics at the cathode were usually relatively slow and independent of the plasma neck disruption and the accelerating processes. To approximate ion source's axial position, we placed a pyramid wire structure onto the cathode mesh (see Fig. 5.1). In these experiments, we effectively disturbed the plasma near the cathode, yet the pinhole camera still recorded images of >2.1 -MeV deuteron emission. We concluded that the pyramid did not prevent forming the necked plasma near the anode and accelerating multi-MeV deuterons. Because a pyramid's shadow was visible in experimental ion images recorded by the pinhole camera, the source of the ion backlighting must have been above the pyramid, i.e., higher than 10 mm from the cathode. These results suggested that we could separate the ion source from the rest of the z-pinch plasma and use multi-MeV z-pinch-driven deuteron beams for ion-deflectometry measurements of the B-field in this plasma.

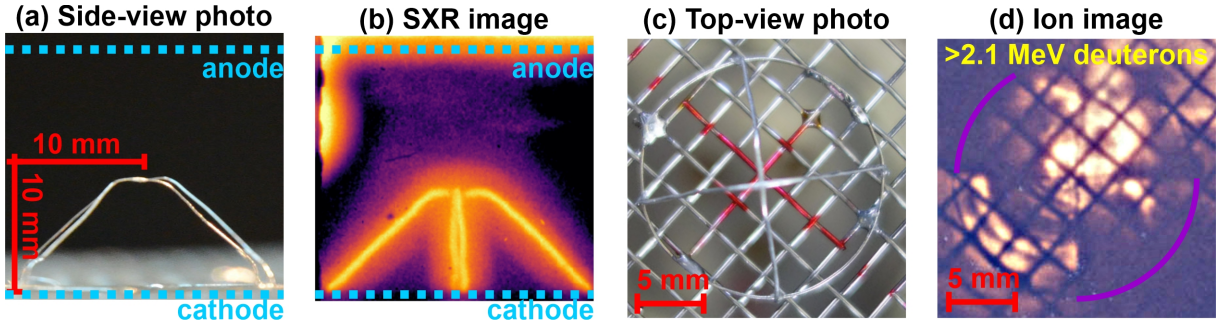


Figure 5.1: Experiments with a 10-mm-high pyramid structure placed on the cathode mesh. (a) Side-view photo of the pyramid. (b) Soft x-ray (SXR) image capturing imploding plasma. (c) Top-view photo of the pyramid standing on a circular base wire. (d) An ion image captured by the pinhole camera showing the pyramid shadow. For better clarity, purple arcs indicate those parts of the base-wire shadow that are not visible in the ion image.

Estimating the axial position of the ion source was important for introducing a crucial component in any deflectometry setup: the deflectometry grid (D-grid). The D-grid must be placed between the ion backlighter and the deflection region of investigated B-fields to set the diagnostic beams' initial state (the reference beam image). Thus, we propose an experimental setup where the D-grid is placed between the z-pinch-based ion source in the collisionless gap and the z-pinch B-fields in the remnant plasma close to the cathode. It means inserting the

D-grid between the electrodes. On the one hand, it might seem like the D-grid could severely influence the behavior of the imploding plasma and the ion-accelerating mechanism. On the other hand, the experiments with the inserted pyramid suggested that the plasmas downstream and below the ion source can be influenced without suppressing the ion emission.

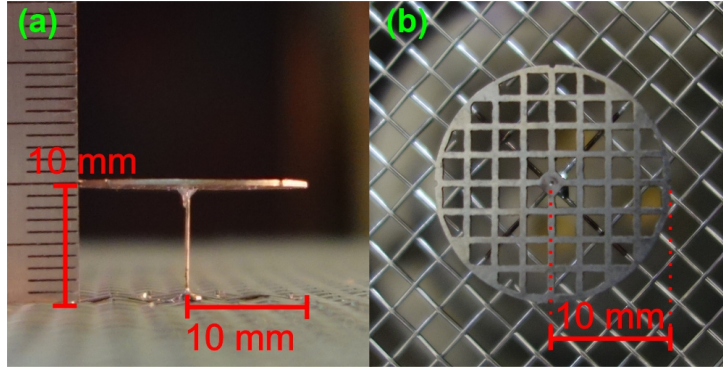


Figure 5.2: Side view (a) and top view (b) of a circular stainless-steel (SS) deflectometry grid (D-grid). Its diameter was 20 mm, and it was connected by the 10-mm-long and 300- μm -thick stalk SS wire to the cathode mesh.

Therefore, the last milestone was the successful performance of the D-grid in our experimental setup [24]. To test the performance of the D-grid experimentally, we inserted a circular stainless-steel (SS) deflectometry grid (D-grid) (see Fig. 5.2) in the 20 – 25-mm anode-cathode gap. The D-grid had a 20-mm diameter and 2-mm-wide square openings framed by 0.5-mm-thick wires. The D-grid was attached to the cathode mesh in its center by a standing-up 10-mm-long and 300- μm -thick SS stalk wire. A series of SXR images in Fig. 5.3 captures the evolution of the imploding plasma with the inserted D-grid in the experiment. The current sheath is vertically split by the D-grid and propagates above and below it, effectively creating two separated and partly independent z-pinchs. The plasma above the D-grid (closer to the anode) is disrupted and produces diagnostic deuterons. The plasma below the D-grid (closer to the cathode) is delayed by several ns. Thus, this plasma is still imploding toward the axis during the current

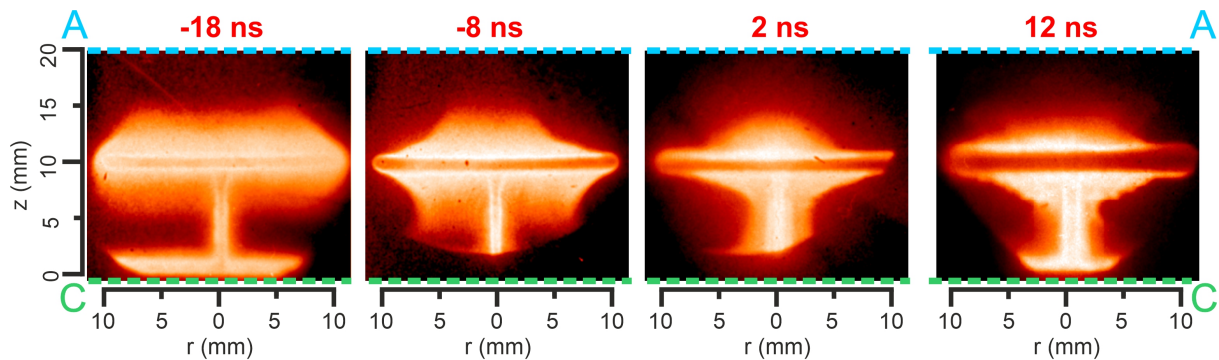


Figure 5.3: SXR images of the evolution of the imploding plasma with the inserted deflectometry grid obtained by a soft x-ray camera. The time $t = 0$ ns corresponds to the onset of the >2 MeV gamma, neutron, and ion emission.

disruption, quickly followed by the ion flash. We admit that the D-grid does influence the plasma implosion but only to the extent that it separates the ion source from the rest of the plasma. The stalk wire supporting the D-grid glows in the SXR images but carries only a negligible portion of the total current, which has been confirmed by subsequent measurements (see Sec. 5.4). The D-grid's axial position Z has proved to be an essential parameter for ion backlighting. If the D-grid is placed too close to the anode, it disrupts the acceleration mechanism and the ion emission. The ion acceleration is not affected if the D-grid is too close to the cathode, but in that case, the current remains at the D-grid edge and does not penetrate below it. For the 20-mm anode-cathode distance, the most advantageous D-grid's axial position from the cathode was $Z = 10$ mm. Interestingly, in one of these experiments with the inserted D-grid, we measured the record energy of hydrogen ions reaching up to 60-MeV [24]. In theory, ions could be accelerated not only above the D-grid, closer to the anode, but also below it, closer to the cathode. The secondary ion source below the D-grid would complicate the analysis of the deflectogram and the B-field measurements. Therefore, the additional role of the supporting stalk wire in the center of the D-grid is to prevent the plasma on-axis from depleting and forming the plasma neck and the ion-accelerating gap.

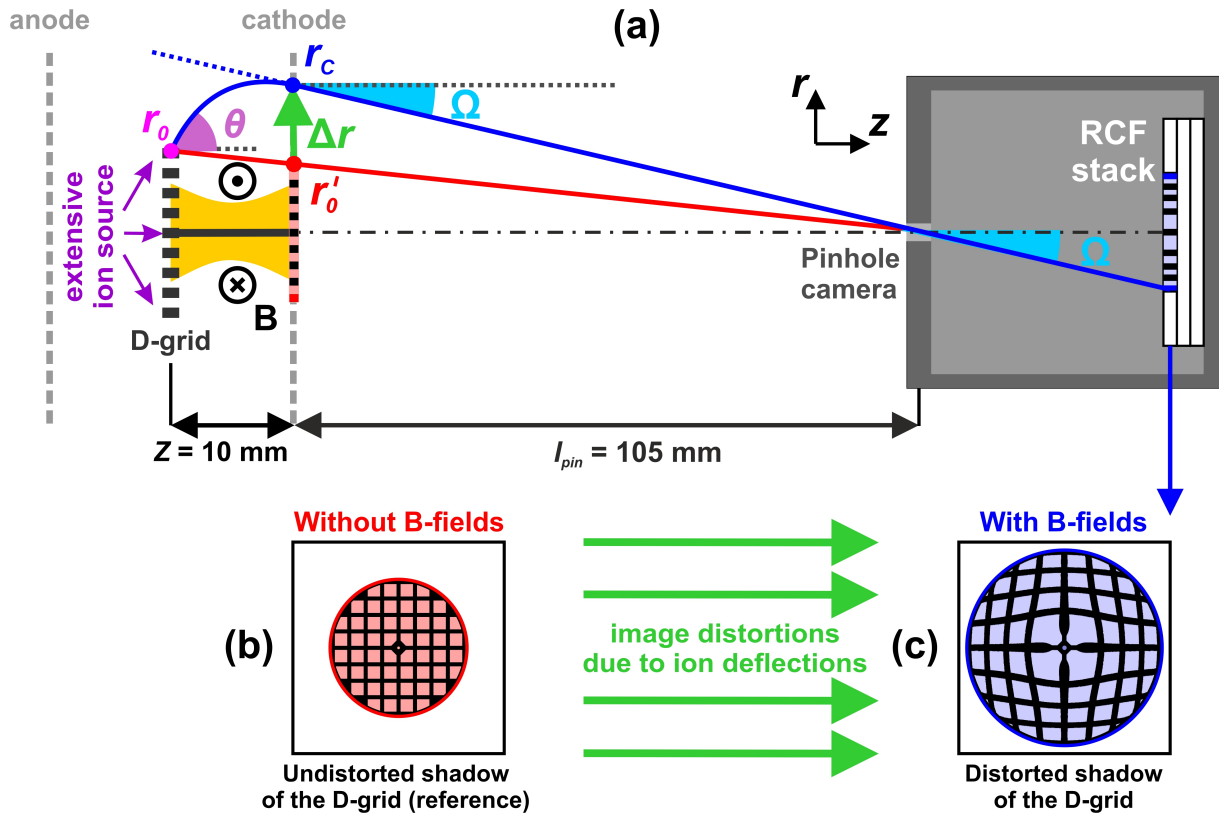


Figure 5.4: (a) Deflectometry setup on GIT-12 employing the pinhole camera and the D-grid inserted into the anode-cathode gap. To measure ion deflections, we compare images of the D-grid shadow imprinted into the deuteron beams (b) in the reference image of zero B-fields and (c) distorted deflectogram manifesting ion deflections in non-zero B-fields.

Based on the milestones of our research on GIT-12, we have proposed an experimental setup for the ion deflectometry measurements in z-pinches, shown in Fig. 5.4a. In this setup, diagnostic deuteron beams are fired from an extensive z-pinch-driven ion source downstream along the z-axis and intersect the D-grid at the initial radial positions $\mathbf{r}_0 = (x_0, y_0)$. The initial ion directions, given by the divergence angle θ , are unknown because the ion source is not point-like. When ion beams irradiate the D-grid, its shadow is imprinted into deuteron beams and creates the initial image of the D-grid shadow (Fig. 5.4b). Beyond the D-grid, deuterons are deflected (focused) by the azimuthal B-fields towards the axis, and the imprinted D-grid shadow becomes distorted (Fig. 5.4c). When deflected deuterons reach the cathode, their final radial positions in the cathode plane are $\mathbf{r}_C = (x_C, y_C)$. Afterward, ions continue towards the pinhole camera situated on the axis at a ≈ 105 -mm distance below the cathode mesh. We assume that deuterons travel between the cathode and the ion detector ballistically. Thus, the pinhole camera captures a scaled image of the distorted D-grid shadow representing the distribution of the deuteron deflections and path-integrated B-fields. Moreover, the pinhole camera provides information about the final ion directions after deflections, given by the observation angles Ω .

The D-grid provides the reference image of deuteron beams in the D-grid plane, and the pinhole camera reflects the distorted deflectogram in the cathode plane. To measure ion displacements, we need to compare both images in the same plane. Because we do not know the divergence angle θ , we cannot project the original (undistorted) D-grid image from the detector plane onto the cathode. However, due to the known final observation angle Ω , we can reconstruct a reference D-grid image, which would be created in the cathode plane by undeflected deuterons aiming into the pinhole camera in the case of zero B-field below the D-grid. By connecting the point of the pinhole with the initial deuteron positions \mathbf{r}_0 in the D-grid, we find the radial positions $\mathbf{r}'_0 = (x'_0, y'_0)$ of undeflected ions in the reference image at the cathode plane. Finally, we can calculate the ion displacements in the cathode plane $\Delta\mathbf{r} = \mathbf{r}_C - \mathbf{r}'_0$ and estimate the path-integrated B-fields $\int_0^Z B_\varphi dz$. Since the longitudinal (axial) size of the B-field region is determined by the D-grid with the fixed height of $Z = 10$ mm, we can characterize the path integrals of mapped B-fields by the averaged B-fields \overline{B}_φ , defined as $\overline{B}_\varphi = \int_0^Z B_\varphi dz / Z$.

Our deflectometry setup (Fig. 5.4a) contrasts in the evaluation of the ion displacements $\Delta\mathbf{r}$ to the classical arrangement (Fig. 2.9). We do not consider the ion deflections in our setup as modulations of the initial ion trajectories from the ion source but as modulations of the deflected ion trajectories coming from the pinhole camera. The point-like pinhole in our setup substitutes the point-like ion source and allows deflectometry measurements. The benefit of our experimental setup with the pinhole camera is that it imposes fewer requirements for the ion backlighter, which can be more general than in the classical setup. Its disadvantage is that we utilize only a small part of deuteron emission, which is deflected into and then captured by the pinhole camera.

To estimate the path-integrated B-fields, we must find how they depend on the measured ion displacements $\Delta\mathbf{r}$. In general, a relation between the measured ion displacements Δr and the actual B-fields is non-linear [see Eq. (2.4)], and thus, the path-integrated B-fields $\int B_\varphi dz$

are retrieved from the experimental data by reproducing the deflectograms via numerical ray-tracing simulations. The classical configuration in the specific cases allows the analytical analysis of experimental images using the paraxial approximation (Sec. 2.4.3). Analogously, Sec. 5.2 introduces the so-called *Larmor orbit approximation* that allows us to analytically estimate path-integrated B-fields in our deflectometry setup for the moderate B-fields directly from the experimental data.

5.2 Larmor orbit approximation

Using our numerical code calculating ion trajectories in model z-pinch B-fields, we explore the possibilities of our deflectometry setup. The azimuthal B-fields in these simulations are static and φz -symmetric. The B-field region is axially delimited by the D-grid and the cathode, separated by a distance of $Z = 10$ mm. In our model, highly divergent and monoenergetic deuteron beams are fired from many micro-sources situated in a large circular area (with the >20 -mm diameter) right above the D-grid. Because the observed deuteron fluence in the experimental data on GIT-12 and the estimated micro-divergence θ of detected deuterons decrease with the increasing deuteron energy E , we choose the lowest detected deuteron energy (the first RCF layer in the stack), i.e., 2.3 MeV. Our simulations have proved that the analytical retrieval of the path-integrated B-fields via the paraxial approximation, used in the classical setup, is not possible in our deflectometry setup because deflections of deuterons in realistic B-fields of a MA z-pinch are not sufficiently weak. However, if ion deflections are moderate ($\alpha < 60^\circ$) and azimuthal B-fields have no strong gradients, curved ion trajectories in our setup can be approximated by circular Larmor orbits for a wide range of B-field profiles and magnitudes. Fig. 5.5 demonstrates this so-called *Larmor orbit approximation* on simulated deuteron trajectories in model B-fields of the 1.5-MA z-pinch with the uniform current density and the 9-mm pinch radius R_p (see a grey profile in Fig. 5.5a). Radii \overline{R}_L of these Larmor orbits represent mean values of curvature radii R_L averaged along the ion paths. Therefore, we can associate each ion trajectory (dashed curves in Fig. 5.5a) with the mean value of the B-fields $\overline{B}_L = \sqrt{2m_i E}/Q\overline{R}_L$, which we call Larmor B-fields.

Our deflectometry setup, illustrated in Fig. 5.5b, allows finding the radius \overline{R}_L of these approximating Larmor orbits from the known initial ion position at the D-grid r_0 (from the reference D-grid image), the measured final ion position at the cathode r_C (from the recorded distorted image of the D-grid shadow), and the observation angle Ω that is set by the 105-mm distance of the pinhole camera from the cathode. Because the pinhole camera is distant, its line of sight is nearly parallel to the z-axis ($\Omega \leq 7^\circ \approx 0$), and the initial radial ion position r_0 in Fig. 5.5b is almost equal to the reference ion position at the cathode r'_0 (i.e., $r_0 - r'_0 < 1$ mm). Therefore, we can approximate the measured ion displacements in the cathode plane as $\Delta r \approx r_C - r_0$. Based on this information, we can establish the matching Larmor orbit with the

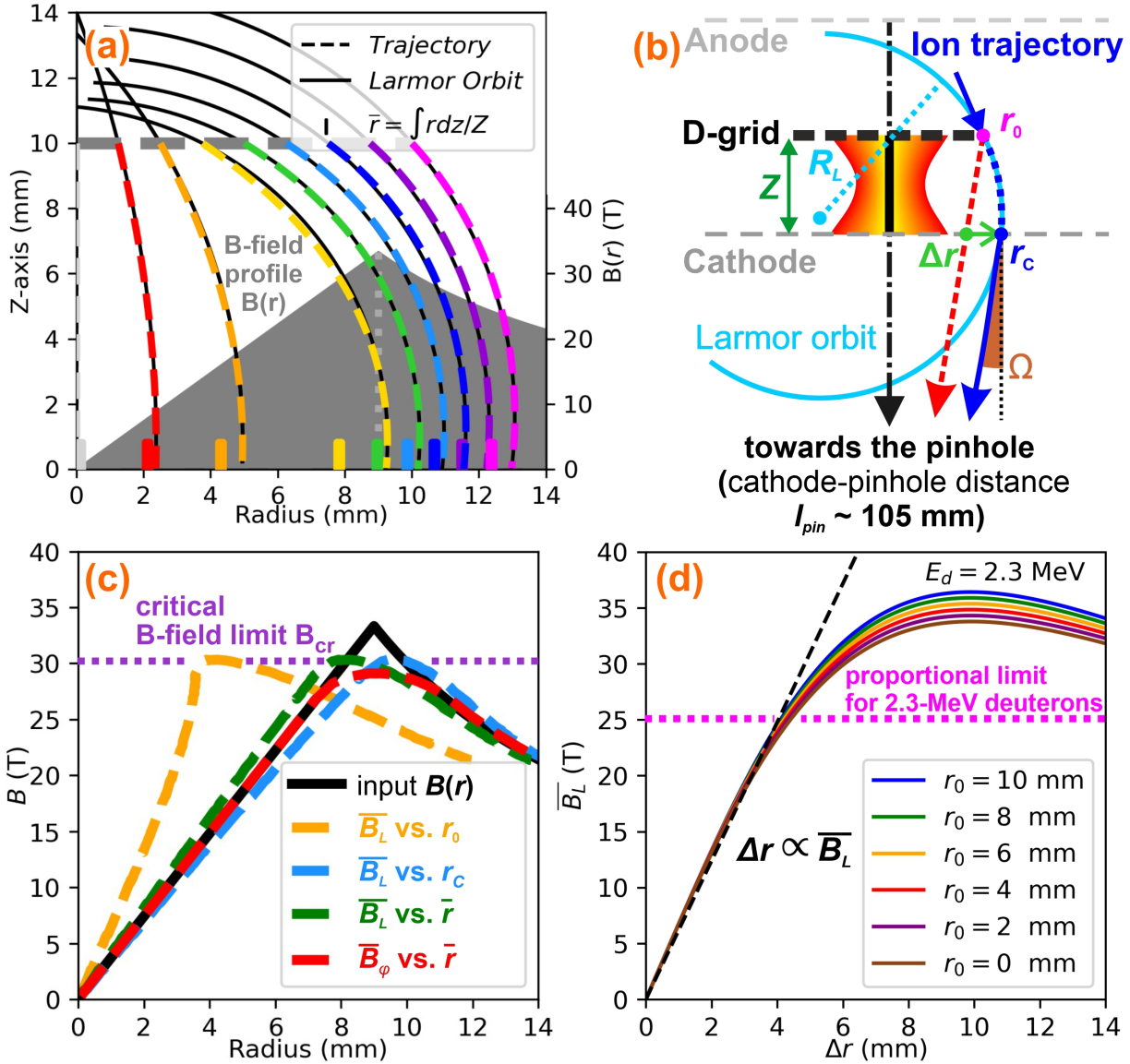


Figure 5.5: The Larmor orbit approximation is demonstrated on 2.3-MeV deuteron trajectories mapping symmetrical azimuthal B-fields of z-pinch with the 9-mm radius and the 1.5-MA current on GIT-12. (a) Simulated ion trajectories in the case of moderate deflections ($\alpha < 60^\circ$) can be approximated by circular orbits. (b) The deflectometry setup developed on GIT-12 allows us to analytically estimate the radius \bar{R}_L of approximating circular Larmor orbit for each ion trajectory using its two points and one tangential. Namely, these are the initial ion position at the D-grid r_0 , the final displaced ion position at the cathode r_c , and the ion beam direction at the cathode given by the observation angle of a pinhole camera Ω . (c) Larmor B-fields \bar{B}_L analytically estimated from \bar{R}_L assigned to the initial r_0 , final r_c , and averaged $\bar{r} = \int r dz / Z$ radii (yellow, blue, and green dashed curves, respectively) are compared to the numerically averaged B-fields $\bar{B}_\phi = \int B_\phi dz / Z$ at \bar{r} (the red dashed curve) and the distribution of the model B-fields (the black curve). The maximum of the model B-field of 33 T intentionally exceeds the moderate deflection limit for 2.3-MeV deuterons of 30 T. (d) The Larmor B-fields $\bar{B}_L(\Delta r, r_0)$ are estimated using Eq. (5.2) for a range of ion displacements $\Delta r = r_c - r_0$ and six specific initial ion positions r_0 at the D-grid.

radius \overline{R}_L (see Fig. 5.5b) and find an analytical relation for the approximated Larmor B-fields:

$$\overline{B}_L(\Delta r, r_0) = \frac{\sqrt{2m_i E}}{Q} \frac{2l_{pin}\Delta r + 2Z(\Delta r + r_0)}{[(\Delta r)^2 + Z^2] \sqrt{(\Delta r + r_0)^2 + l_{pin}^2}}. \quad (5.2)$$

The Larmor B-fields \overline{B}_L characterize the total curvature of the deflected ion trajectories $\int R_L^{-1}(z) dz$, which is given by Eq. (5.1) and relates to the path-integrated B-fields $\int_0^Z B_\varphi dz$. Because the circular orbits approximate ion trajectories in our model (see Fig. 5.5b), the Larmor B-fields \overline{B}_L approximate the averaged B-fields $\overline{B}_\varphi = \int_0^Z B_\varphi dz / Z$ ($\overline{B}_\varphi \approx \overline{B}_L$). It means that the Larmor orbit approximation can estimate the path-integrated B-fields from the experimental deflectograms analytically ($\int_0^Z B_\varphi dz = \overline{B}_\varphi Z \approx \overline{B}_L Z$). Both \overline{B}_φ and \overline{B}_L refer to an average of the B-fields probed by ions along their paths. Using our ion-tracking simulations, we investigate how they relate to the actual B-fields.

It follows from the mean value theorem for integration that if the B-field B_φ mapped by a particular ion along its trajectory is a continuous function on the closed interval between $[0, Z]$, the average B-field $\overline{B}_\varphi = \int_0^Z B_\varphi dz / Z$ corresponds to a B-field magnitude at a certain point ζ in this interval. Through the ion motion, the axial ion position ζ is associated with a radial ion position $\rho(\zeta)$. The point $(\rho(\zeta), \zeta)$, where the averaged B-fields \overline{B}_φ correspond to the local B-fields $B_\varphi(\rho, \zeta)$, can generally be anywhere along the ion trajectory, depending on the specific B-field profile. However, if we assume B-fields uniform along the z -axis, we can only inspect the B-field magnitude as a function of ρ .

Therefore, we use our simulations to investigate whether \overline{B}_L and \overline{B}_φ somehow reflect the distribution of axially uniform B-fields $B_\varphi(r)$ if we associate them to a certain radial position ρ between r_0 and r_C . In other words, whether averaged B-fields $\overline{B}_\varphi(\rho)$ and Larmor B-fields $\overline{B}_L(\rho)$ sampled over $\rho(\zeta)$ can describe the actual B-field distribution $B_\varphi(r)$. The best candidate for the radial point ρ , where the estimated B-fields would refer to the B-field profile, seems to be the averaged radius along the ion path $\bar{r} = \int_0^Z r dz / Z$. Our ion-tracking simulations in Fig. 5.5c demonstrate that the profile of the calculated averaged B-fields $\overline{B}_\varphi = \int_0^Z B_\varphi dz / Z$ at \bar{r} (the red dashed curve) is a relatively good fit of the input B-field distribution $B(r)$ of the constant-current-density 1.5-MA z -pinch (the black curve). To benchmark the Larmor orbit approximation, Fig. 5.5c also displays that the analytically estimated Larmor B-fields \overline{B}_L assigned to \bar{r} (the green dashed curve) fits the input B-fields to the similar extent as the averaged B-fields $\overline{B}_\varphi(\bar{r})$.

Notice that, in our example in Fig. 5.5c, neither analytically approximated \overline{B}_L nor numerically calculated \overline{B}_φ can fit the implemented B-fields $B(r)$ near its maximum of ≈ 35 T. This behavior is not primarily caused by the error of the simulations or the approximation and is not coupled with this specific B-field profile. It reveals the inherent integrating behavior of ion deflectometry. The discrepancy between the reconstructed and the input B-field profiles corresponds to a limit of our ion deflectometry technique when ion deflections are not moderate. In our setup, the threshold for moderate ion deflections is $\alpha \approx 60^\circ$. From Eq. (2.13), we find that

the critical B-field strength B_{cr} for 2.3-MeV deuterons and $Z = 10$ mm is in our setup equal to ≈ 30 T (see purple dotted line in Fig. 5.5c). The maximum of input B-fields in our example are intentionally beyond this threshold. In that case, the deuteron deflections are so strong that diagnostic deuteron beams map a too-wide B-field interval (see the most deflected trajectories in Fig. 5.5a) and lose the ability to measure B-field locally. The crucial discovery is that the Larmor orbit approximation reflects this behavior of deflecting ions and, thus, describes the properties of ion deflectometry just as well as the numerical analysis of simulated ion trajectories does.

Nevertheless, we cannot establish the averaged radius \bar{r} experimentally. The measurements provide only information about two points of the particular ion trajectory: the initial and final ion positions at the D-grid and the cathode, i.e., r_0 and r_C , respectively. Interestingly, the ideal averaged radius \bar{r} in our model simulation is close to the radial ion position at the cathode r_C (compare positions of the pins and ion trajectories near the cathode in Fig. 5.5a). Accordingly, Fig. 5.5c demonstrates that Larmor B-fields \overline{B}_L assigned to the measured ion position at the cathode r_C (the blue dashed curve) fits the input B-field distribution similarly to our estimations \overline{B}_φ and \overline{B}_L at \bar{r} . This result is fundamental and generally valid for B-field profiles with moderate magnitudes and gradients. It implies that we can use the Larmor orbital approximation to analytically reconstruct the distribution of axially uniform B-fields only from the initial and final ion positions r_0 and r_C that we obtain from experimental data.

The equivalence between \bar{r} and r_C originates from the design of our deflectometry setup. The distant pinhole camera detects only ions whose trajectories near the cathode are aligned parallelly to the z -axis (see Fig. 5.5a). In this way, the pinhole camera determines the shape of ion trajectories close to the cathode (near the radius r_C). The initial location of these ions r_0 at the D-grid and the micro-divergence θ are selected dependently on the strength of ion deflections.

In the case of weak or moderate ion deflections ($\overline{B}_L < B_{cr}$), ion displacements $\Delta r = r_C - r_0$ are small. So the divergence angle θ is set low according to Eq. (5.1). Assuming the extensive ion source right above the D-grid, the pinhole camera picks ions emitted from the radius r_0 situated close to the radius r_C . Hence, the averaged radius \bar{r} is also close to r_C (compare the orange and magenta ion trajectories with the corresponding pins in Fig. 5.5a).

In the case of strong ion deflections ($\overline{B}_L \gtrsim B_{cr}$), the distance between r_0 and r_C corresponding to the ion displacement $\Delta r = r_C - r_0$ is large. Accordingly, the deflection angle α is also large and, it follows from Eq. (5.1) that ions must leave the D-grid at large divergence half-angles θ . Therefore, the ion trajectory is radially elongated and the averaged radius \bar{r} shifts closer to r_0 (see the most deflected yellow ion trajectory and the corresponding pin at the cathode in Fig. 5.5a). As a result, Larmor B-fields B_L assigned to r_C no longer fit the B-field distribution $B(r)$. It means that the critical B-fields B_{cr} is the limit of the linear regime in Larmor orbit approximation, similarly to μ_C in the paraxial approximation.

To further investigate the Larmor orbit approximation, Fig. 5.5d displays graphs of the Larmor B-fields $\overline{B}_L(\Delta r, r_0)$ given by Eq. (5.2) for ion displacements Δr from 0 mm up to 14 mm and for six initial ion positions r_0 . We see that the estimated Larmor B-fields \overline{B}_L for 2.3-MeV

deuterons in our setup are almost independent of r_0 and have a maximum of ≈ 35 T. The most crucial feature of the plots in Fig. 5.5d is that \overline{B}_L below ≈ 25 T grow linearly with the radial ion displacements Δr . For larger ion displacements, the Larmor B-fields $\overline{B}_L(\Delta r)$ become non-linear. However, they are still injective until the critical B-field $B_{cr} \approx 30$ T.

By fitting the linear part of the curves in Fig. 5.5d, we approximate Eq. (5.2) and obtain a linear relation between Δr and \overline{B}_L as follows

$$\Delta r \approx \frac{Q}{\sqrt{2m_i E}} \frac{Z^2}{2} \overline{B}_L. \quad (5.3)$$

For 2.3-MeV deuteron beams and $Z = 10$ mm, we can write Δr [mm] $\approx 0.165 \cdot \overline{B}_L$ [T]. Eq. (5.3) demonstrates the linear relation between the ion displacements and estimated B-fields $\Delta r \propto \overline{B}_L$. This relation is analogous to Eq. (2.19) for the estimated deflection angle α in the paraxial approximation. In contrast with the paraxial approximation (see Subsec. 2.4.3), which estimates the path-integrated B-fields only for small deflection angles $\alpha \ll 1$, the Larmor orbit approximation is valid for $\alpha < 60^\circ$. Moreover, Larmor B-fields \overline{B}_L approximate the averaged B-fields $\overline{B}_\varphi = \int_0^Z B_\varphi dz / Z$. If we know the axial length Z of ion path in B-fields that are axially uniform, we can even estimate the actual B-field distribution $B_\varphi(r)$. Further investigation of the Larmor approximation using our numerical simulations showed that the relations $\Delta r \propto \int B_\varphi dz$ and $\overline{B}_L \approx \overline{B}_\varphi$ remain relatively accurate even for the axially non-uniform B-fields with moderate magnitudes and gradients (see Fig. 5.10a).

It follows from Eq. (5.3) that a displacement of each point in the deflectogram Δr increases linearly with the averaged B-fields \overline{B}_φ approximated by \overline{B}_L . It implies that the derivative of the radial displacements $\partial_r \Delta r \equiv \partial(r\Delta r)/(r\partial r)$, corresponding to the divergence of the radial displacement $\nabla \cdot \mathbf{\Delta r}$ in the polar coordinates, is directly proportional to a derivative of the averaged azimuthally symmetric B-fields $\partial(r\overline{B}_\varphi)/(\mu_0 r \partial r)$ coupled with an axial component $(\nabla \times \overline{\mathbf{B}}_\varphi)_z$ and an averaged current density $\overline{J}_z = \int J_z dz / Z$. Therefore, the Larmor approximation shows that, in the case of moderate ion deflections, the relative displacements of the D-grid pattern $\partial_r \Delta r$ correlate with the path-integrated current density \overline{J}_z . From Eq. (5.3), we obtain

$$\partial_r \Delta r \approx \frac{Q}{\sqrt{2m_i E}} \frac{Z^2}{2} \mu_0 \overline{J}_z \quad (5.4)$$

Eq. (5.4) implies that, for moderate B-fields, the current density determines the deflectogram shape. Interestingly, Graziani in [171] has come to a similar relation to Eq. (5.4) and the physical interpretation of the shape of the deflectograms in the linear regime of the paraxial approximation in the classical deflectometry setup.

In conclusion, the Larmor orbit approximation can estimate the distribution of the path-integrated B-fields $\int_0^Z B_\varphi dz$ in our setup directly from the deflectogram distortion profile, analogously to the paraxial approximation in the classical deflectometry setup. However, the Larmor orbit approximation requires a more easily implemented projection point, instead of the point-like ion source, and applies for larger deflection angles (up to $\alpha < 60^\circ$) than the paraxial

approximation. Assuming the B-field region fills the gap between the cathode and D-grid with a height of Z , we can approximate the averaged B-fields $\overline{B}_\varphi = \int_0^Z B_\varphi dz / Z$ by Larmor B-fields \overline{B}_L instead of only estimating the path-integrated B-field $\int_0^Z B_\varphi dz$. Because the Larmor orbits in the case of moderate ion deflections approximate the actual ion trajectories, the Larmor orbit approximation [Eq. (5.3)] allows us to analytically analyze the properties of the ion deflectometry technique in our setup for $\alpha < 60^\circ$ and identify its linear regime when $\Delta r \propto \int_0^Z B_\varphi dz$.

In the following section (Sec. 5.3), Eqs. (5.3) and (5.4) are demonstrated using our ion-tracking simulations on synthetic deflectograms of z-pinch for four fundamental current-density profiles. In addition, our simulations manifest that, in the case of the axially uniform B-fields and using the Larmor orbit approximation, the B-field distribution $B_\varphi(r)$ can be retrieved directly from the deflectograms.

5.3 Analysis of the synthetic deflectograms of characteristic B-fields profiles

For evaluation of the deflectometry results, it is beneficial to understand the morphology of the deflectograms and interpret their structure. To that end, we use our ion-tracking numerical code to produce synthetic deflectograms for the setup on GIT-12. In our numerical model, we implement our deflectometry setup where a φz -symmetric z-pinch has the height $Z = 10$ mm, the radius $R_p = 9$ mm, and the total current $I = 1$ MA. This way, the maximum B-field strength of 22 T is below the proportional limit of the Larmor approximation for 2.3-MeV deuterons in this setup (≈ 25 T) and lies in the linear part of the plot in Fig. 5.5d. Because the size of the z-pinch column is smaller than of the D-grid, we can examine ion deflections in azimuthal $B_\varphi(r)$ B-fields inside and outside the z-pinch. Outside the z-pinch volume (the red circle in Fig. 5.6), there are no currents and thus, $B_\varphi(r \geq R_p) = \mu_0 I / 2\pi r$. Inside the pinch volume, we inspect several radial distributions of $B_\varphi(r < R_p)$ given by a polynomial function:

$$B_\varphi(r < R_p) = \frac{\mu_0 I}{2\pi R_p} \left(\frac{r - R_{cs}}{R_p - R_{cs}} \right)^{n_B} \quad (5.5)$$

where I is the total pinch current at the pinch radius R_p . Our model permits the situation when the imploding layer of the z-pinch plasma has not yet reached the axis. Therefore, Eq. (5.5) includes an inner radius of the imploding current sheath R_{cs} within which we assume no B-fields.

Fig. 5.6 presents synthetic deflectograms of four simulated z-pinch with current density profiles $J_z(r)$ corresponding to four values of the polynomial exponent n_B :

- (a) $n_B = -\infty$: a thin skin-current sheath with no B-field inside [$B_\varphi(r < R_p) = 0$]
- (b) $n_B = 1$: a constant current density with the linear B-field profile [$B_\varphi(r < R_p) \propto r$]
- (c) $n_B > 1$: a radially increasing current density

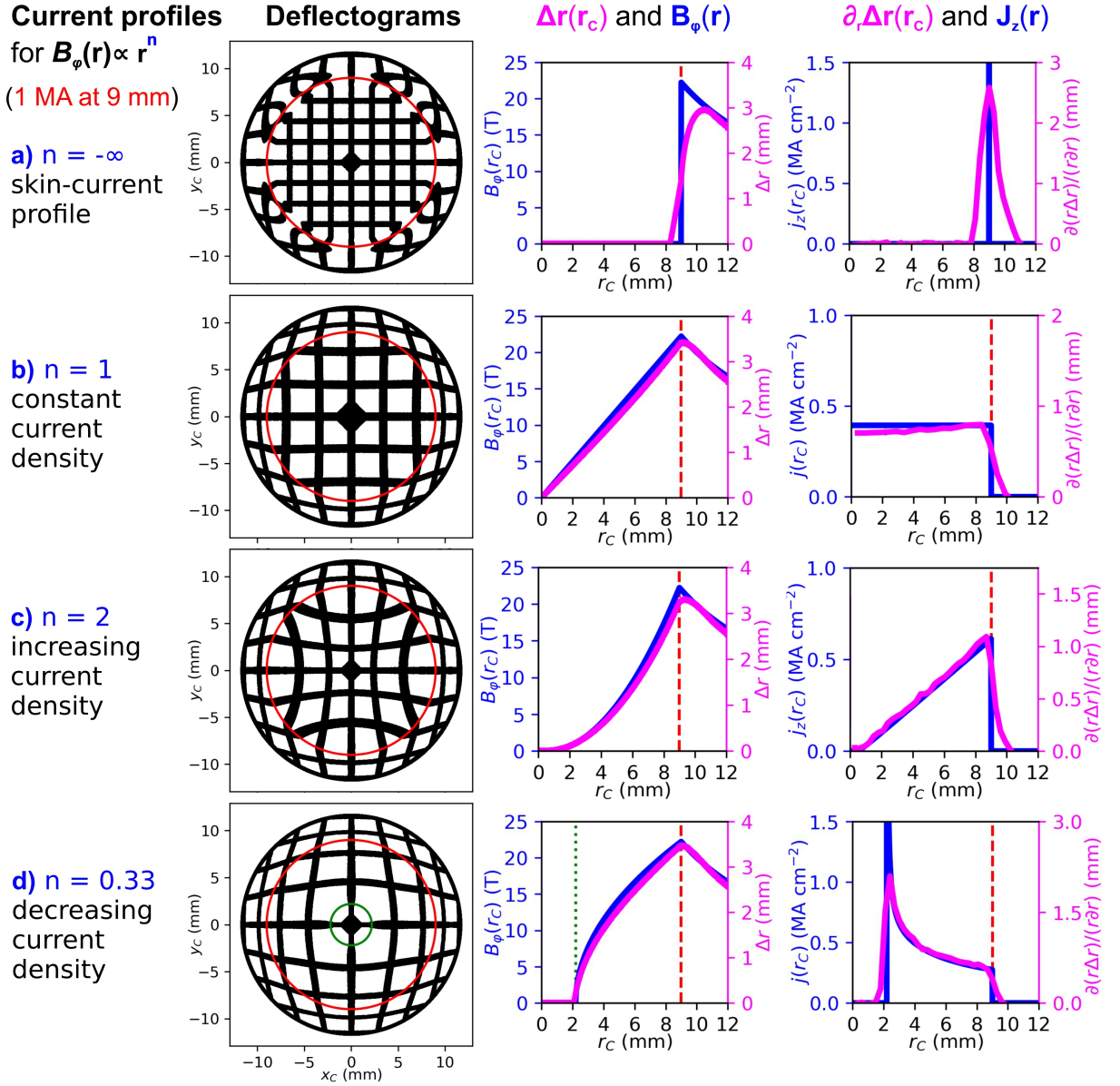


Figure 5.6: Demonstration of typical synthetic deflectograms of 2.3-MeV deuterons for four radial distributions of the axially uniform azimuthal B-field $B_\phi(r < R_p)$ inside the z-pinch with a radius $R_p = 9$ mm (red circle) and a total pinch current 1 MA. The z-pinch height equal to the axial position of the D-grid is $Z = 10$ mm. Within the pinch radius R_p , the tested B-fields are proportional to r^{n_B} . We consider four typical profiles of current densities $J_z(r < R_p)$, proportional to r^{n_B-1} and coupled to four values of the exponent n_B : (a) $n_B = -\infty$: no current density inside the z-pinch [$B_\phi(r < R_p) = 0$]; (b) $n_B = 1$: constant current density; (c) $n_B > 1$: radially increasing current density; (d) $0 < n_B < 1$: radially decreasing current density. In the last case, there is no B-field inside the radius $R_{cs} = 2.2$ mm (green circle). Outside the z-pinch volume in all cases, there are only vacuum B-fields $B_\phi(r \geq R_p) = \mu_0 I / 2\pi r$. The ion displacement profiles $\Delta r(r_C)$ and their derivatives $\partial_r \Delta r(r_C)$ (magenta graphs), retrieved from the synthetic deflectograms, are compared to radial distributions of the input B-fields $B_\phi(r_C)$ and current densities $J_z(r_C)$ (blue graphs). All spatial scales correspond to the cathode plane.

(d) $0 < n_B < 1$: a radially decreasing current density

Only in the last case we consider $R_{cs} \neq 0$ to avoid the B-field singularity at the z-axis. Here,

we set $R_{cs} = 2.2$ mm (the green circle in Fig. 5.6d), which agrees with the experimental data presented in Sec. 5.4. In addition, Fig. 5.6 compares distributions of ion displacements $\Delta r(r_C)$ and their derivatives $\partial_r \Delta r(r_C)$ (magenta graphs), obtained from the synthetic deflectograms, with the input B-field $B_\varphi(r)$ and current-density $J_z(r)$ profiles (blue graphs), respectively. All spatial scales of synthetic deflectograms in Fig. 5.6 correspond to the cathode plane, and all plotted quantities are situated in the final radial ion positions r_C at the cathode.

From Eqs. (5.3) and (5.4), it follows that moderate $\Delta r(r_C)$ and $\partial_r \Delta r(r_C)$ copy the profiles of the averaged B-fields $\overline{B_\varphi}(r_C)$ and averaged current densities $\overline{J_z}(r_C)$, respectively. Fig. 5.6 demonstrates that, for the B-fields uniform along the z-axis, these quantities can approximate the actual radial distributions of the B-field $B_\varphi(r)$ and current density $J_z(r)$.

Outside the z-pinch ($r_C \geq R_p$), the B-field distributions in all cases are the same, and thus, the distorted D-grid patterns of deflectograms in Figs. 5.6b-d outside the red circle have the same structure. The only exception is the synthetic deflectogram in Fig. 5.6a. In the case of the skin-current z-pinch, currents flow in a thin layer at the z-pinch radius R_p (the red circle) and create a steep B-field gradient. Due to their inertia, deflecting ions cannot reflect this abrupt change in the B-field profile into the ion beam image. Thus, they create a broad distorted transition in the deflectogram in Fig. 5.6a and the averaged B-field profile near the z-pinch edge at R_p . Accordingly, the profile of the relative displacements $\partial_r \Delta r(r_C)$ cannot duplicate a delta function of the skin-current distribution. This example demonstrates that the B-field retrieval via ion deflectometry requires both moderate B-field strengths and gradients coupled with the magnitudes and continuity of the current density profile, respectively. However, there is a discontinuity in all current density profiles near R_p because the current density must drop at the z-pinch's edge. Therefore, Figs. 5.6b-d show minor differences between plots of the relative displacements $\partial_r \Delta r = \partial(r \Delta r)/(r \partial r)$ and the current densities $J_z(r)$ near the pinch radius R_p .

Inside the z-pinch ($r_C < R_p$), the D-grid pattern distortion is determined by a specific profile of the current density $J_z(r_C < R_p)$. In Fig. 5.6c, the increasing current density produces the negative (*pincushion*) distortion of the deflectogram. In Fig. 5.6d, the decreasing current density creates the positive (*barrel*) distortion of the deflectogram. In this case, the current density near the 9-mm z-pinch radius R_p is so low that the deflectogram pattern within the red circle (the z-pinch interior) is similar to the pattern outside (the z-pinch exterior) where J_z is zero. As a result, the transition in a distortion of deflectogram at $r = R_p$ in Fig. 5.6d is hardly noticeable. In Figs. 5.6a-b, we observe a squared D-grid pattern in both deflectograms, because the constant current density profile results in a uniform (*rectilinear*) distortion. In these two cases, the current densities are zero and non-zero, respectively, but constant for both cases. Therefore, the synthetic deflectograms in Fig. 5.6a and Fig. 5.6b reveal an undistorted D-grid pattern in the former and a magnified squared D-grid pattern in the latter.

In conclusion, we demonstrated that the path-integrated B-fields $\int_0^Z B_\varphi dz$ and the averaged B-field $\overline{B_\varphi}$ influence the magnitude of ion displacements Δr , related to the spatial scales of the deflectogram, and that the path-integrated and averaged current densities $\int_0^Z J_z dz$ and $\overline{J_z}$

influence the derivative (divergence) of the ion displacements $\partial_r \Delta r$, related to the shape of the deflectogram pattern.

After analytical part of this Chapter, we continue with the first-ever z-pinch-driven ion deflectometry measurements, which have been performed on GIT-12. The following section contains experimental results of these measurements presented in our selected paper [3]. Besides the results of this paper, which is in its entirety in the Appendix (App. G.3), this thesis provides the additional analysis and comments.

5.4 Experimental results of our paper Munzar et al., POP (2021) with additional comments

Our paper [3] describes our ion deflectometry measurements of z-pinch B-fields on GIT-12. We have used our deflectometry setup presented in Fig. 5.4. We have employed the internal z-pinch-driven ion source, a D-grid inserted into the anode-cathode gap, and the pinhole diagnostics. Fig. 5.7 compares a reference (“undistorted”) photo of the original D-grid (Fig. 5.7a) with a selection of experimental deflectograms for the deuteron energy of 2.3-MeV with distorted D-grid shadows in shots 2402, 2404, 2408, 2418, and 2420 (Fig. 5.7b-f). All images are scaled to the cathode plane. These images represent the first-ever experimental data obtained via the z-pinch-driven ion deflectometry and the first deflectograms of the z-pinch using axially emitted ions. For better clarity, the deflectograms are presented with enhanced contrast and in inversed colors, where higher ion fluence is in brighter colors.

In our deflectometry setup (Fig. 5.4), diagnostic ions traverse both the D-grid and the cathode mesh. Shadows of them both are evident in the experimental deflectograms. The cathode mesh is rotated diagonally by the 45° angle relative to the D-grid for their better distinction. The undistorted cathode-mesh shadow in shot 2402 confirms that there are no ion deflections between the cathode and that the ion detector and the image distortions are determined only by z-pinch B-fields between the D-grid and the cathode.

Although the time evolution of the B-fields during the ion backlighting might partly contribute to the lower quality of some deflectograms (e.g., in shot 2418 presented in Fig. 5.7e), the visible D-grid shadow in the experimental data proves that the deuteron emission has been short enough to make only a snapshot of the “static” B-fields in the imploding plasma. We do not observe multiple shadows or visible discontinuities of the D-grid shadow caused by possible multiple exposures. The lowered image contrast may originate in ion scattering at the obstacle edges (i.e., D-grid or pinhole) or by the pinhole-camera resolution (≈ 0.8 mm). However, the most significant complication of the experiments arises from the deuteron energy estimation of the measured data. All the experimental data discussed in this section are obtained from the first RCF layers in the stack. A 30- μm -thick Al layer shields the first RCF, and hence, its signal corresponds to the deuteron energy threshold of 2.3 MeV. The detection probability of ions with

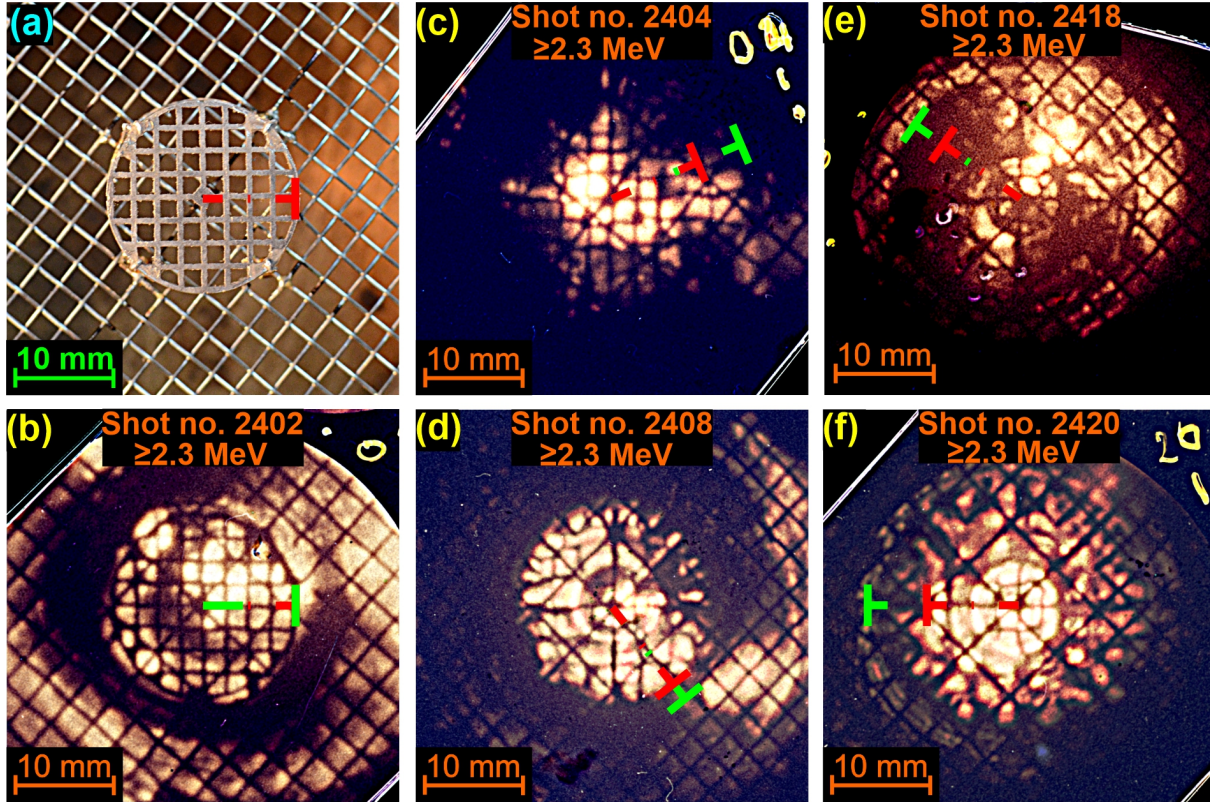


Figure 5.7: Comparison of (a) top-view photograph of the D-grid placed on the cathode mesh and (b)-(f) the experimental deflectograms obtained in shots 2402, 2404, 2408, 2418, and 2420. The deflectograms are shown in inversed colors, and so, brighter shades correspond to higher ion fluence. The D-grid distortions in the deflectogram are caused by deflections of 2.3-MeV deuterons, and are proportional to the path-integrated B-fields. Red and lime lines show the initial and displaced radius of the D-grid edge. The images are scaled to their corresponding size in the cathode plane.

higher energies in this layer is low but not negligible. Therefore, deuterons with higher energies might create parts of the deflectograms. Even if we perform the energy unfolding of the RCF detectors, there is uncertainty in the energy corresponding to the difference between the two following layers. The second RCF layer in the stack corresponds to the 4.7-MeV deuteron energy threshold. Thus, there is a relatively wide interval of possible deuteron energies from 2.3 to 4.7 MeV. The beam energy estimation is the biggest but removable source of uncertainty in our measurements. Since ion deflections grow with $\alpha \propto 1/\sqrt{E}$, measured path-integrated B-fields might differ by a coefficient $\sqrt{4.7/2.3} \approx 1.43$, that is, roughly 40%. Nonetheless, we will assume that most of the signal is created by monoenergetic 2.3-MeV deuterium beams and consider our results as lower estimates of the measured quantities.

Shot 2402 represents the first attempt to perform ion deflectometry on GIT-12. It was successful because the deflectogram in Fig. 5.7b shows the shadow of the D-grid. The size and shape of the D-grid shadow are nearly identical to its original undistorted image in Fig. 5.7a, which indicates almost no B-fields below the D-grid. A slight distortion near the D-grid edge represents weak but nonzero B-fields, where the current sheath went under the D-grid. Placing

the D-grid too close to the cathode (≈ 6 mm) probably prevented the current sheath below the D-grid from penetrating further to the axis. Moreover, in this shot, the D-grid was supported by four stalk wires at its edge. These wires might obstruct the imploding current sheath. In the other shots (Fig. 5.7c-f), the D-grid was located at ≈ 10 -mm distance from the cathode mesh and was supported by only one wire at the center. Therefore, the current sheath could propagate closer to the axis, and these deflectograms revealed the distorted D-grid shadows. Due to the non-uniform ion backlighting, parts of ion images are not visible. This absence of the ion signal in the deflectograms is probably caused by some asymmetry in the ion source or B-fields.

Although the quality of the experimental deflectograms, and hence, the amount of provided information, varied, most deflectograms provided some information about the z-pinch B-fields and currents.

5.4.1 Estimation of the enclosed pinch current from the D-grid edge's displacement

Low-quality deflectograms, where the pattern of the distorted D-grid shadow is unclear or missing, provide no information about the distribution of ion displacements coupled with the distribution of the path-integrated B-fields. However, if the D-grid edge is visible (e.g., deflectogram of the shot 2418 in Fig. 5.7e), we can estimate the value of the enclosed pinch current flowing within reach of ion deflections (within the radial ion position at the cathode r_C). Assuming the azimuthal symmetry of the measured B-fields, we approximate displacements of all visible parts of the D-grid edge shadow by a single radial displacement $\Delta r(r_C)$. Using the Larmor orbit approximation [Eq. (5.2)], we estimate the averaged B-fields \overline{B}_φ and an averaged enclosed current $\overline{I}(r_C) = \overline{B}_\varphi 2\pi r_C / \mu_0$.

Fig. 5.8 presents the measurements of path-integrated B-fields $\overline{B}_\varphi Z$ at the radius r_C and the averaged enclosed current $\overline{I}(r_C)$ within the radius r_C in seven shots. The estimated values of $\overline{B}_\varphi(r_C)$ and $\overline{I}(r_C)$ (black dots) are compared to $\int_0^Z B_\varphi dz$ calculated by numerical ion-tracking simulations (lines) for three distributions of the axially uniform B-fields, that is, $B_\varphi(r) \propto r$, $B_\varphi(r) = \text{const.}$, and $B_\varphi(r) = 1/r$. These distributions refer to B-fields of constant $J_z(r) = \text{const.}$, and the decreasing current density profile $J_z(r) \propto 1/r$, and to B-fields outside the z-pinch $J_z(r > R_p) = 0$, respectively. Because the displacement of the D-grid edge corresponds to the single averaged value of the B-fields, the simulated $\int_0^Z B_\varphi dz$ plots (green, red, and blue curves in Fig. 5.8) are similar and prove that we can use the Larmor orbit approximation to estimate the enclosed current $\overline{I}(r_C)$ from the D-grid's displacement regardless of the specific B-field distributions.

In shots 2404 and 2420, the estimated averaged enclosed currents $\overline{I}(r_C)$ reach up to ≈ 2.4 MA at the ≈ 15 -mm radius, which represents the majority of the total 2.7-MA circuit current during the stagnation. Error bars in the measured points are given by the uncertainty of radial displacements $\Delta r(r_C)$ of the D-grid edge in the selected deflectograms. The maximal deviation error of the D-grid edge localization is ≈ 1.1 mm, which corresponds to maximal uncertainty of

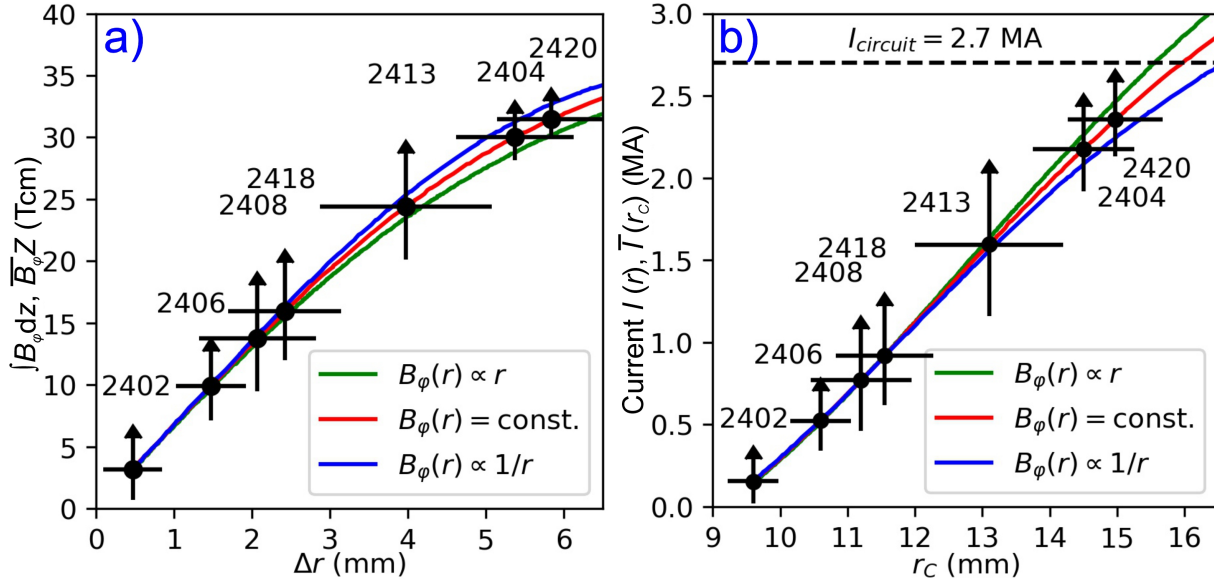


Figure 5.8: (a) Estimation of $\overline{B_\phi}Z$ using the Larmor approximation [see Eq. (5.3)] from the measured displacements Δr of the D-grid edge in the deflectograms (green lines in Fig. 5.7) of the selected shots (black dots). To determine the influence of a B-field profile on the estimates, plots of the simulated path-integrated fields $\int_0^Z B_\phi dz$ for three radial distributions of axially uniform azimuthal B-fields (green, red, and blue plots) are compared. (b) Calculated averaged enclosed current $\bar{I}(r_C) = \overline{B_\phi} 2\pi r_C / \mu_0$ (black dots) and the simulated plots of the enclosed currents $I(r)$ for three B-field distributions. Error bars in the measured points are given by uncertainty of estimating the average radial displacement of the D-grid edge in the selected deflectograms. Arrows from these points show that these results are lower estimates.

20%, according to Eq. (5.2). However, these values describe only the statistical errors that are still much smaller than the beam-energy uncertainty ($\approx 40\%$), which can lead to higher B-fields and currents. Therefore, the arrows in Fig. 5.8 remind us that these results are lower estimates.

5.4.2 Mapping xy profiles of the azimuthal B-fields employing the Larmor orbit approximation

The deflectograms in shots 2404, 2408, and 2420 (see Fig. 5.9a) reveal considerable parts of the D-grid shadows and thus, allow us to measure the xy distributions of the path-integrated B-fields in each shot.

However, the distortions of the D-grid shadow manifesting ion deflections do not capture the ion displacements at every point of the deflectogram. We estimate the ion displacements only in several *representative* points, namely, nodes and approximate wire midpoints of the D-grid pattern, which characterize the structure of the D-grid shadow and are recognizable in the deflectograms. Fig. 5.9b highlights the connected representative points of the D-grid shadow, which are visible in the experimental deflectograms. Inset figures illustrate parts of the D-grid that these points represent. Then, displacements of these points refer to averaged deflections of ions, which would pass through 1.25-mm-long and 0.5-mm-wide D-grid segments.

From the measured displacements ($\Delta x, \Delta y$) of the representative points (black arrows in

Fig. 5.9c), we establish corresponding averaged B-fields at the cathode from analytical Eq. (5.2) via the Larmor orbit approximation. Then, Fig. 5.9c shows continuous 2D (xy) maps of the averaged B-fields $\overline{B}_\varphi(x_C, y_C)$ obtained from estimated values of \overline{B}_φ by the cubic interpolation. For all three shots, the values at the edge of the maps correlate with the results in Fig. 5.8a. In shots 2404 and 2408, we observe significant asymmetry of $\overline{B}_\varphi(x_C, y_C)$, caused by errors in the localization and interpolation of the representative points.

To analyze the B-field maps, Fig. 5.10a illustrates distributions of the radial displacements $\Delta r = \sqrt{\Delta x^2 + \Delta y^2}$ of the representative points and associated averaged B-fields \overline{B}_φ for each selected shot. Interestingly, in all three shots, there are almost no B-fields near the z-pinch axis, i.e., roughly within the radius of $R_{cs} = 2 - 3$ mm. Starting with the radius R_{cs} , the averaged B-fields in shots 2404 and 2420 are increasing strictly monotonically with the radius (the left and right graphs in Fig. 5.10a). It means that the current sheath must be spread from R_{cs} to at least 13-mm radius. In shot 2408, the averaged B-fields $\overline{B}_\varphi(x_C, y_C)$ reach their peaks at 7–9 mm, and then at a greater distance, the calculated values fluctuate because the measured displacements become azimuthally asymmetric.

To further investigate these results, we fit the averaged B-fields $\overline{B}_\varphi(r_C)$ by the polynomial function $\mathcal{P}(r_C) \propto (r_C - R_{cs})^{n_B}$ from Eq. (5.5). In shot 2408, we consider only the undispersed data within the radius $r_C \leq 7$ mm. From the fitted data, we find the power-law exponents $n_B^{2404} = 2$, $n_B^{2408} = 0.8$, and $n_B^{2420} = 0.5$ for shots 2404, 2408, and 2420, respectively. Therefore, the averaged current density profiles $\overline{J}_z(r_C) \propto (r_C - R_{cs})^{n_B - 1}$ in these selected shots (see insets in Fig. 5.10b) are gradually increasing ($n_B^{2404} - 1 > 0$), quickly dropping to a constant ($n_B^{2408} - 1 \approx 0$), and decreasing ($n_B^{2420} - 1 < 0$). In the last two cases, the averaged current density $\overline{J}_z(r_C)$ peaks at the radius of the current sheath front R_{cs} . In the case of shot 2404, the $\overline{B}_\varphi(r_C)$ distribution differs from the other two shots. The different profile might have been caused by four wires placed at the edge of the D-grid to support it instead of only one wire in the center. The imploding current sheath probably interfered with these wires and became more diffuse. Nevertheless, the presented current density profiles are very sensitive to the experimental data and have poor spatial resolution. More robust but less detailed information is provided by distributions of the averaged enclosed current $\overline{I}(r_C) = \overline{B}_\varphi 2\pi r_C / \mu_0$ (main figures in Fig. 5.10b). Their values agree with results in Fig. 5.8b for the selected shots.

5.4.3 Mapping rz profile of the azimuthal B-fields in the shot 2420 using numerical simulations

Deflectograms reflect only the distribution of the averaged B-fields $\overline{B}_\varphi = \int B_\varphi dz / Z$ and thus, the information about the axial profile of azimuthal B-fields is integrated along the path of diagnostic ions. To estimate the “local” B-field distribution, we need to supplement the ion deflectometry with some additional information about the axial profile of B-fields using measurements from a radial line of sight.

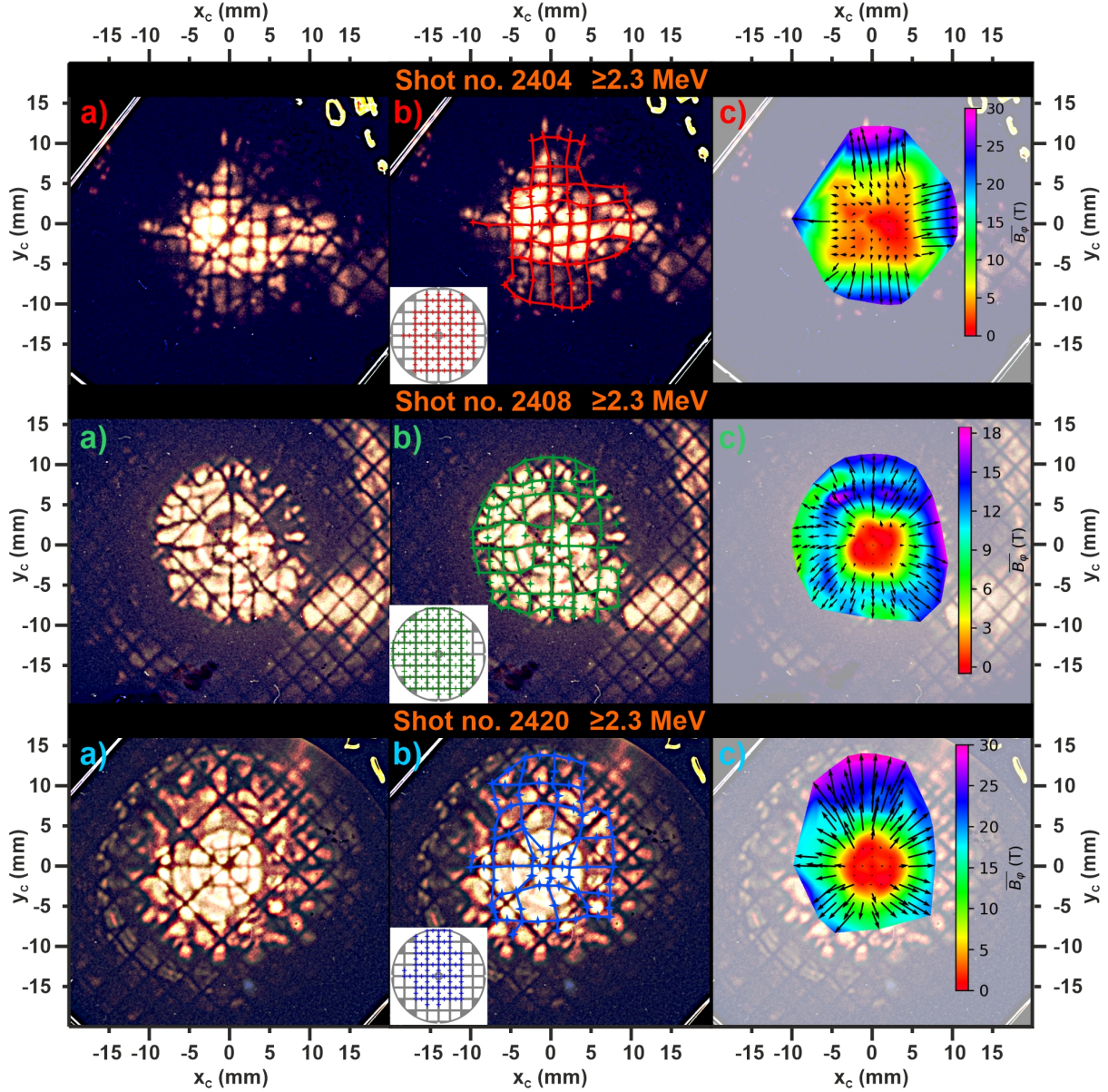


Figure 5.9: (a) Original experimental deflectograms in false colors from shots 2404, 2408, and 2420 showing shadows of both the distorted D-grid and the undistorted cathode mesh; (b) Deflectograms with retrieved representative points of the D-grid shadow. Corresponding sections of the original D-grid image are highlighted in the insets. (c) The (xy) maps of the averaged azimuthal B-fields $\int B_\phi dz/Z$, calculated via the Larmor orbit approximation. The black arrows indicate a field of measured displacements $(\Delta x, \Delta y)$ of the retrieved D-grid. Spatial scales of all images correspond to the plane of the cathode mesh.

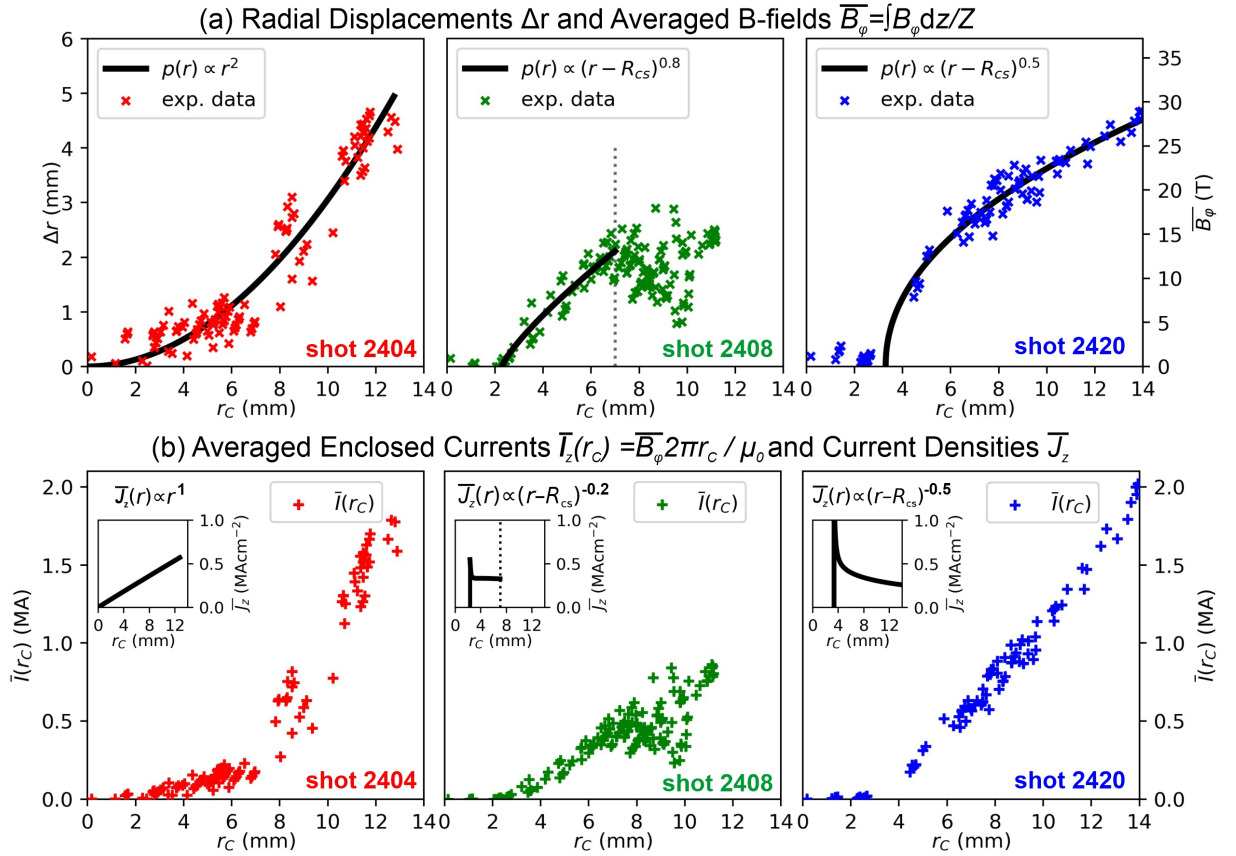


Figure 5.10: Radial distributions of (a) radial displacements $\Delta r(r_C)$ together with corresponding averaged B-fields $\overline{B}_\phi(r_C)$, and (b) averaged enclosed currents $\overline{I}(r_C) = \overline{B}_\phi(r_C) = 2\pi r_C / \mu_0$ within the radius r_C . Averaged B-fields \overline{B}_ϕ are calculated using Larmor orbit approximation [see Eq. (5.2)] from the radial displacements Δr of the retrieved points of the D-grid shadow in the deflectograms shown in Fig. 5.9. To approximate the radial profiles of the averaged current densities $\overline{J}_z(r_C)$ shown in insets, we fit the experimental data [$\Delta r(r_C)$ and $\overline{B}_\phi(r_C)$] by the power function $\mathcal{P}(r_C) \propto (r_C - R_{cs})^{n_B}$ from Eq. (5.5). The radii of the current sheath R_{cs} in shots 2404, 2408, and 2420 are 0 mm, 2.3 mm, and 3.3 mm, respectively.

In the case of shot 2420, we acquired this information by recording side-view SXR-emission images of the z-pinch plasma via the SXR camera. Fig. 5.11a shows an implosion of the curved z-pinch plasma layer during the ion imaging. Based on this image, we can make a crucial assumption that an inner boundary of the current sheath has a similar shape (the solid line curve) as the curved plasma perturbation, which we consider azimuthally symmetric. We approximate this almost parabolic boundary in Fig. 5.11b by a power function $r_{cs}(z) \propto (z - Z_{cs})^4$ with a turning point Z_{cs} at the 4.7-mm height above the cathode. Interestingly, the radial position of this point correlates with the onset of the measured D-grid displacements at $R_{cs} = 3.3$ mm in Fig. 5.10a. Thus, we presume that the boundary of the glowing plasma is also the inner boundary of the current sheath and that B-fields inside glowing plasmas (within the radius R_{cs}) are almost zero. Furthermore, we evaluate two possible current distributions inside the current sheath using our numerical ion-tracking simulations.

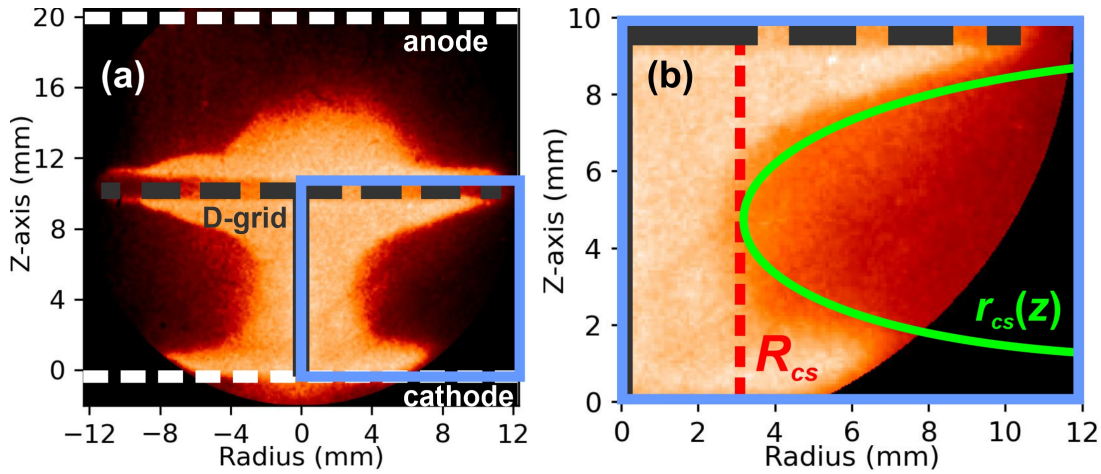


Figure 5.11: (a) SXR image of the imploding plasma recorded by the SXR camera in shot 2420 within the duration of ion imaging. (b) In the highlighter area, we set the shape of the imploding plasma $r_{cs}(z)$ as an input parameter to our numerical code to characterize the current sheath perturbation.

In the first model, z-pinch currents flow in a thin layer with a high current density close to the plasma edge $r_{cs}(z)$ (see Fig. 5.12a). The outer boundary of the current layer is characterized by a pinch radius $R_p(z)$, which is a function of z . Beyond the layer, they create a cavity with no currents [$J(r > R_p) = 0$]. Correspondingly, azimuthal B-fields in the cross-section of the layer rise quickly with the radius due to the high current density and fall as $B_\phi(r > R_p) \propto 1/r$ behind the layer due to zero currents in the cavity. Therefore, there is a small region of very high B-fields near the point (R_{cs}, Z_{cs}) . Probing ions are significantly deflected by the B-fields in this region which leads to a peak in the distribution of the path-integrated B-field $\int_0^Z B_\phi dz$. Therefore, the profile of the simulated ion displacements $\Delta r(r_C)$ (see Fig. 5.12b) also has a peak and decreases for $r_C \gtrsim 6.5$ mm. Thus, it contrasts with the measured D-grid displacements and makes the model with the magnetic cavity improbable. Nevertheless, this example proves that currents must fill a large part of the cavity to ensure the monotonic increase of the path-integrated B-fields at least up to 14 mm.

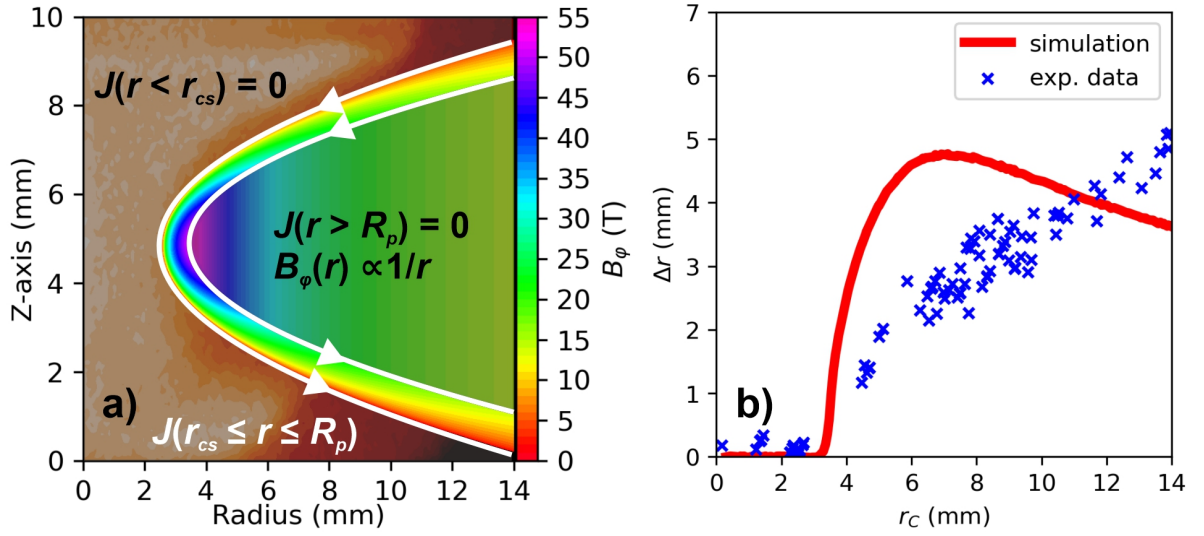


Figure 5.12: (a) B-field distribution $B_\phi(r, z)$ with a thin current sheath, considered for shot 2420. (b) Ion displacement profile for this B-field distribution obtained by numerical ion-tracking simulations does not correspond to the displacements of the D-grid obtained from the experimental data.

In the second model, the curved current sheath is spread and fills the area below the D-grid so that the integrated azimuthal B-fields grow monotonically with the radius. To fit the experimental data using the simulations, we propose the B-field distribution inside the current layer shown in Fig. 5.13a and given by

$$B_\phi(r < R_p, z) = \frac{\mu_0 I}{2\pi R_p} \left(\frac{r - r_{cs}(z)}{R_p - r_{cs}(z)} \right)^{m_B}, \quad (5.6)$$

where $r_{cs}(z)$ determines the current sheath's inner edge. In this example, we assume there is no current cavity and that the current layer's outer boundary is behind the D-grid displacements. Therefore, we set the pinch radius $R_p = 15$ mm as the most displaced radial position of the D-grid's edge, and the total current $I = 2.5$ MA in agreement with the current measurements in Fig. 5.10b for the shot 2420. To find the B-field distribution, we must estimate the last parameter of our proposed B-fields in Eq. (5.6), the power-law exponent m_B , describing the slope of the B-field distribution in the cross-section of the current sheath.

Fig. 5.10a showed that the path-integrated B-fields $\int_0^Z B_\phi dz$ rise with the polynomial $(r - R_{cs})^{n_B}$, where the power-law exponent $n_B \approx 0.5$. However, this profile represents the distribution of the local B-fields only if they are axially uniform. Due to the curved current sheath in Fig. 5.13a, the height of the actual B-fields $Z(r) = \int_0^{Z(r)} dz$ decreases towards the axis. To compensate for this effect and produce the $\int B_\phi dz$ profile given by the measured D-grid displacements, the cross-sectional profile of the actual B-fields $B_\phi(r, z = \text{const})$ in our simulations (along the dotted arrow in Fig. 5.13a) must grow from large radii towards R_{cs} steeper than the profile of $\int B_\phi dz$ (compare the black and red curve in Fig. 5.13b). Therefore, we find that the

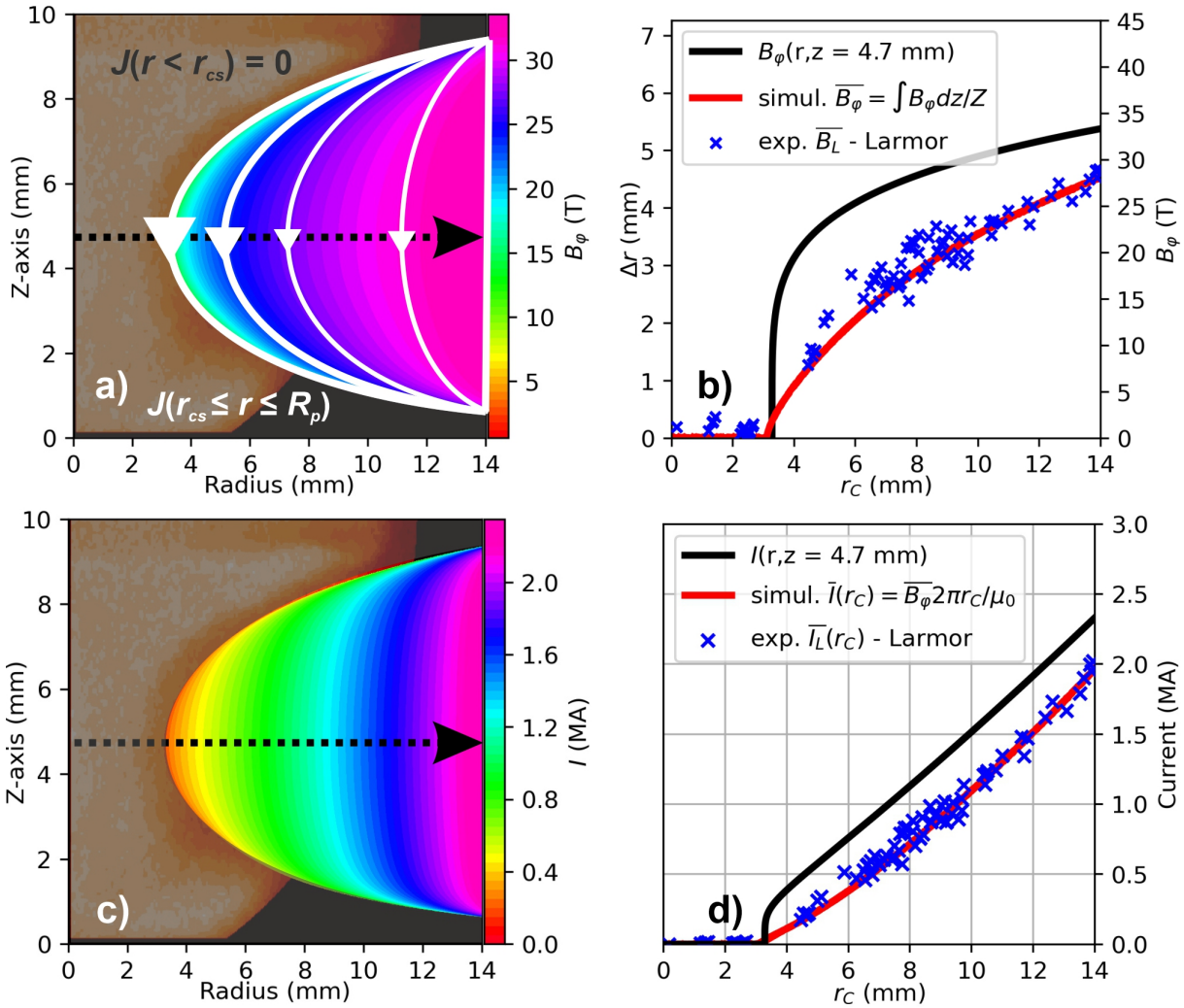


Figure 5.13: Tomographic 2D (rz) maps of (a) B-field $B_\varphi(r, z)$ and (c) current $\bar{I}(r, z)$, which we obtain as input distributions from the numerical simulations reconstructing the experimental deflectogram in shot 2420. Cross-sectional profiles of (b) the azimuthal B-fields $B_\varphi(r, z = 4.7 \text{ mm})$ and (d) the current $I(r, z = 4.7 \text{ mm})$ are compared to the averaged \bar{B}_φ and \bar{I} , respectively, which are obtained from the experimental data.

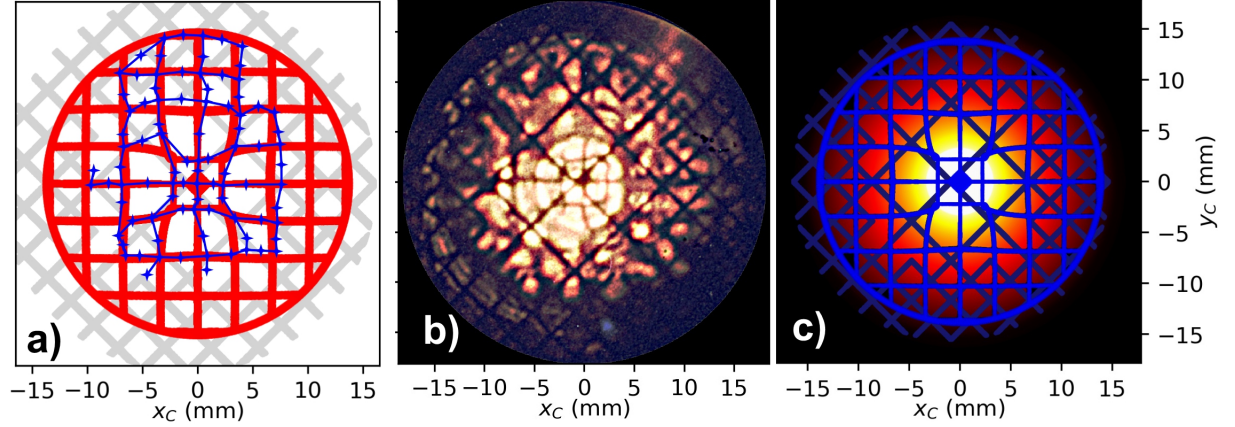


Figure 5.14: (a) Comparison of the simulated D-grid pattern (red) with the retrieved part of the distorted D-grid (blue) from the experimental data. (b) Experimental and (c) synthetic deflectograms of the distorted D-grid and the undistorted cathode mesh (rotated by 45°).

exponent value in the suggested B-field distribution given by Eq. (5.6) is $m_B = 0.2$. Fig. 5.13b shows that the proposed B-field distribution produces in our simulations ion displacements and the averaged B-fields that fit the radial D-grid displacements and calculated Larmor B-fields obtained from experimental data, respectively.

The found radial profile of the B-fields provides some information about the current density. Due to the abrupt increase of the cross-sectional B-fields $B_\varphi(r, z = 4.7 \text{ mm})$ near the radius $R_{cs} = 3.3 \text{ mm}$ in Fig. 5.13b, the current density must be high ($\geq 10^1 \text{ MAcm}^{-2}$) at the thin layer of the current sheath front (roughly $\approx 0.5 \text{ mm}$). With increasing radius (for $r \gtrsim 5 \text{ mm}$), the B-fields growth in Fig. 5.13b becomes linear, and thus, the estimated current density falls below $\approx 4 \cdot 10^{-1} \text{ MAcm}^{-2}$. However, detailed information about the current density is not possible to obtain because it relies heavily on a specific fit of the B-fields. The uncertainty of this fit is caused by the uncertainty determination of the radial position of the onset of the ion deflections (between 3 and 4 mm in Fig. 5.13b), which cannot be determined precisely from the experimental deflectogram of the shot 2420.

The graphs in Fig. 5.13 illustrate only radial profiles of the displacements and B-fields. To better evaluate our numerical solution, we must compare 2D (x - y) images of the experimental and synthetic deflectograms. Fig. 5.14a presents a solution of a synthetic D-grid pattern (red), which best fits not only the retrieved part of the D-grid shadow (blue) but also the experimental deflectogram in Fig. 5.14b as a whole. The synthetic D-grid shadow is in good agreement with the experimental data. Discrepancies between the synthetic and observed D-grid patterns are caused by the azimuthal asymmetry of measured B-fields. To better evaluate the fit by comparison with the experimental deflectogram, Fig. 5.14c shows a synthetic deflectogram with shadows of the distorted D-grid and the undistorted cathode mesh.

The good fit of the experimental and synthetic deflectograms proves that the input B-field distribution in Fig. 5.13a represents the actual tomographic 2D (r - z) map of local B-fields $B_\varphi(r, z)$ in the shot 2420. In addition, Fig. 5.13c presents the corresponding map of the enclosed currents

$I(r, z) = B_\varphi(r, z)2\pi r/\mu_0$. It is worth noting that the cross-sectional profile of these currents $I(r, z = 4.7 \text{ mm})$ in Fig. 5.13d is similar to the averaged currents $\bar{I} = \overline{B_\varphi}2\pi r/\mu_0$, and thus, it is less sensitive to the “local” B-field distribution. It is caused by the fact that the B-fields go with the power-law exponent $m_B = 0.2$, which is close to zero, and so, the currents $I(r, z = \text{const.}) \propto rB_\varphi(r, z = \text{const.})$ are rather determined by the radial positions r and grow linearly.

The found B-field distribution $B_\varphi(r, z)$ in Fig. 5.13a is the most important result of our deflectometry measurements. Interestingly, this B-field profile implies that the current flow outside the glowing part of the imploding plasma in the SXR image in Fig. 5.11b. This image relates to the intensity of the collisional Bremsstrahlung emission, which is non-linear with the plasma particle density $I_{Brems}(r, z) \propto n^2$. In contrast, the plasma pressure distribution linearly with the density $p(r, z) \propto n$. Therefore, there may be hot plasmas with low but not insignificant temperatures and densities even in places where the intensity of SXRs is low (cf. Fig. 5.11b), but where we measure the significant B-fields (cf. Fig. 5.13a).

In conclusion, we sum up the results of our ion deflectometry measurements in this section:

1. There is a region near the axis of the z-pinch with almost no B-field during the ion emission that simultaneously correlates with the region of the glowing plasma in the SXR image.
2. This hollow region is surrounded by the current sheath with a very steep B-field gradient and a thin current density peak at its front.
3. Beyond the current density peak, there is a relatively wide current layer ($\gtrsim 12 \text{ mm}$) where cross-sectional current density drops with the radius.
4. The spatial distribution of moderate ion deflections is related to the spatial distribution of averaged B-fields near the cathode [$\Delta r(r_C) \propto \overline{B_\varphi}(r_C)$].
5. Most of the 2.7-MA total current ($\gtrsim 80\%$) flowed within 15-mm radius.

The article is in its entirety included in Sec. G.3. It has been published in *Physics of Plasmas* and selected as “Editor’s Pick”. In addition, it has been chosen for a cover of the June issue of this journal and, in a few first weeks after its publication, it was the most read paper of this issue.

Chapter 6

Thesis summary and future prospects

6.1 Summary

This thesis focused on further developing ion deflectometry, a common diagnostic for measuring EM fields in laser-produced plasmas, for use in z-pinch plasmas. The presented work followed the results of three selected papers and brought additional insights and analysis.

Chapter 1 introduced the high-energy-density plasmas (HED), which can be found in many places in the Universe. In the laboratory, they are reproduced by the z-pinch and laser-produced plasmas using pulsed-power high-current devices and high-power laser facilities, respectively. On the one hand, both HED plasmas share several features since they create high-pressure environments. On the other hand, z-pinch plasmas contrast with the inertially-confined and strongly localized laser-generated plasmas because they are magnetically confined by strong B-fields and can be held for longer temporal durations and at larger spatial scales. The dense z-pinch plasmas and laser-produced plasmas are famously difficult to diagnose. In particular, the standard methods struggle to probe EM fields in HED plasmas due to the necessary interaction with the dense plasma or to map the spatial distributions of currents and B-fields since the measurements can be performed only at several specific points. Ion deflectometry or ion radiography, developed in the laser-plasma community, overcomes some of the obstacles of classical methods. It employs deflections of high-energy charged-particle beams, which can probe extensive areas of studied EM fields and do not require the plasma background for the measurements.

Chapter 2 examined the current employment of ion deflectometry in laser-produced plasmas. We discussed the classical deflectometry setup and its components to evaluate its implementation into the z-pinch plasmas. Ion detectors currently used for the ion deflectometry (i.e., RCFs and CR-39s) can measure the spatial distribution of the ion emission and, after post-shot analysis, provide ion images with the energy resolution crucial to the ion deflection strength estimation. The classical setup requires a short-pulse source of laminar and high-energy ion beams for backlighting the studied B-fields. The short exposition by the ion backlighter is necessary

for inspecting time-varying B-fields. The beam laminarity is essential for identifying individual ion rays. The high beam energy ensures negligible beam-beam and beam-plasma interaction and determines the range of measurable B-field magnitudes. To that end, the deflectometry experiments usually employ multi-MeV proton beams. However, suitable particle beam sources are currently generated exclusively using ultra-intense high-power lasers, which are inaccessible for most pulsed-power facilities. Furthermore, a theoretical study of the ion deflections is usually adapted to the experiments mapping laser-produced plasmas, where ion deflection angles α are usually presumed small due to the small spatial scales of the observed plasmas limiting the path-integrated effect of investigated fields. For employment in the z-pinch, Sec. 2.4 analyzed ion deflections by arbitrary angles in the cylindrical symmetrical setup and found the general deflection equations for radial electric and azimuthal magnetic fields. In contemporary laser-plasma deflectometry experiments with the classical setup, moderate magnitudes of ion deflections often allow describing the ion deflectometry analytically using the paraxial approximation. Sec. 2.4 reviewed this theoretical analysis and introduced the contrast parameter μ , which is coupled with the magnitudes and gradients of recorded ion deflections and characterizes the performance regimes of the ion deflectometry. In the linear regime ($\mu \ll 1$), the path integrals of investigated B-fields can be estimated analytically from the measured ion displacements from the experimental data using an analytical relation between these two quantities. When the parameter μ reaches a critical value μ_C , i.e., when the ion rays start to cross, the analytical relation is no longer valid. The ion mapping of B-fields becomes non-linear and non-injective and may lead to ambiguous results.

In Chapter 3, presenting results of our first selected paper, we developed a numerical ion-tracking code and used it to investigate the performance of the ion deflectometry of MA z-pinch B-fields in two fundamental arrangements of the classical experimental setup. In the first one, the radial deflectometry, synthetic deflectograms helped to understand the results of deflectometry measurements performed to date in z-pinch-like B-fields and similar setups. Our simulations demonstrated that in this setup, where probe ions are fired radially into the z-pinch, the ion deflections are dominantly influenced by the vacuum B-fields outside the z-pinch. Thus, the radial ion beams can be used to estimate the total z-pinch current but provide only indirect information about the current distribution inside the z-pinch. In the second arrangement, the axial deflectometry, ions approach the z-pinch axially and produce images comparable with recorded deflectograms of azimuthal B-fields in the laser-produced plasma bubbles. The axial arrangement allowed distinguishing the B-field distribution inside the simulated z-pinch but led to strong ion deflections limiting the possible use of the ion deflectometry. In addition, we demonstrated on synthetic deflectograms of the z-pinch in both configurations that there exist critical values of the z-pinch current signifying the non-injectivity regime of the ion deflectometry technique analogously to critical values μ_C in the laser-plasma measurements.

Chapter 4 followed our second selected paper inspecting the multi-MeV deuteron emissions on the gas-puff 3-MA z-pinch at the GIT-12 facility. We examined the source of these deuteron beams to understand high-energy ion acceleration mechanisms in the z-pinch and to investigate

a possible ion backlighter for ion deflectometry. To examine the deuteron sources, we analyzed experimental deuteron images obtained using the ion pinhole cameras. The experimental data were interpreted using our numerical ion-tracking code, which we modified for more versatile experimental setups in various configurations using numerous parameters characterizing the synthetic ion beams, azimuthal B-fields, and ion detectors. By producing comparable synthetic data, we reached several conclusions about the high-energy ion sources and the B-fields in the studied z-pinch. However, we could not separate the effects of these two phenomena. We proved that high-energy deuteron sources consist of many individual micro-sources forming a ring-like structure in the collisionless region created after the disruption of the compressed plasma neck. The most significant results were found by reproducing deuteron images at multiple energies, that is, in multiple RCFs of the same stack, using our numerical simulations. We concluded that the diameter of ion ring-like sources is larger than the size of the plasma necks. Moreover, we estimated the maximum values of path-integrated B-fields and divergence of individual micro-sources depending on the deuteron energy. Concerning their employment for ion deflectometry backlighting, these z-pinch-driven sources produce deuterons with sufficient energies and yields but are extensive and non-laminar. Therefore, we concluded that they cannot be used in the classical deflectometry setup employing a well-defined point-like ion backlighter.

Chapter 5 used the experience obtained in the previous chapters to perform the first-ever z-pinch-driven B-field measurements in an alternative deflectometry setup. This setup allowed deflectometry B-field measurements using the extensive z-pinch-driven ion source because it used the well-defined projection point of the pinhole camera's aperture instead of the well-defined point-like source. The pinhole selected the ion beams from the extensive and divergent ion source and picked the deflected ions aiming to the almost point-like aperture of the pinhole camera. This way, it effectively made the projected ion beams laminar and the ion deflectometry possible. Therefore, this experimental setup reduced the requirements for the ion source, which need not be point-like. However, any deflectometry setup requires separating the ion source and the investigated B-field region. In our case, it meant splitting the z-pinch plasma by the fiducial deflectometry grid (D-grid). Interestingly, introducing the D-grid into the electrode gap did not suppress the ion emission or severely influence the z-pinch's azimuthal B-fields. On the contrary, the D-grid's employment led to the record detected deuteron energy of nearly 60 MeV. However, for ion deflectometry, we used deuteron beams with lower deuteron energy of 2 MeV due to the much higher contrast in the pinhole image. We further modified our numerical code to be more straightforward, to have better efficiency due to parallel computing, and to be capable of producing synthetic deflectograms with good contrast. Our ion-tracking simulations discovered that our alternative setup allowed an analytical description of the deflectometry measurements by approximating moderately deflected ion trajectories using circular Larmor orbits. Most importantly, we discovered a linear equation between the measured ion displacements and the path-integrated B-fields, allowing analytic deflectometry measurements directly from the experimental data. In addition, we found the critical value of B-fields indicating stronger than moderate ion deflections and delimiting the applicability of the Larmor orbit

approximation. Furthermore, the analysis of the synthetic deflectograms of axially uniform B-fields demonstrated that the magnitude and shape of ion image distortions corresponded to the path-integrated B-field and the current densities, respectively. After theoretical and numerical study of our alternative deflectometry setup, we used it to perform the experimental deflectometry current and B-field measurements described in Sec. 5.4. Based on the quality (contrast) of the recorded experimental deuteron images, we obtained results from measurements with three degrees of the provided information: (i) For all performed shots, we estimated the total enclosed currents of the z-pinch. (ii) For three shots, we analytically estimated the spatial distribution of the axially averaged or path-integrated B-fields. (iii) In shot 2420, the experimental deflectogram was supplemented with the image of the z-pinch plasma at the time of ion exposition, allowing us to use our numerical simulations to retrieve the tomographic 2D (rz) map of the local azimuthal B-fields. Therefore, we have successfully developed and performed the ion deflectometry in the z-pinches.

6.2 Future prospects

We have several ideas for the future development of the ion deflectometry in the z-pinches. We divide them into three categories: experimental, analytical, and conceptual.

The first category includes improvements of previous experiments, which are feasible within the current state of the ion deflectometry in the z-pinches. Our measurements in Chap. 5 suffered from relatively low contrast of the experimental ion images and poor spatial resolution of the detected deuteron from 2.3-4.7 MeV forcing us to assume our current and B-field measurements as lower estimates. The lower contrast of the ion images originated from the fact that we analyzed the distorted shadow of the D-grid. Since our pinhole camera was the time-integrated ion diagnostic, the signal of the distorted D-grid shadow might be partly redrawn by ion emission in the later times of the z-pinch evolution. To enhance the contrast of the recorded ion signal, we proposed an *inverse D-grid* which is a SS plate with cutouts in the locations of the classical D-grid wires. To improve the energy resolution of the experimental data, we should change the composition of the detector stack or focus on images of higher deuteron energies. Finally, we might improve the temporal resolution given by the ion emission duration by further investigating the ion source and the ion accelerating mechanism.

In the second category, we might focus on the analytical description of the ion deflections and the investigation of the topology of the deflected ion trajectories. Due to the assumption of the small deflection angles, the paraxial approximation used in the laser plasmas and the classical setup considered the ion deflection in the plasma as an abrupt change of the ion trajectory and, thus, neglected its specific topology. In the case of moderate ion deflections and our alternative setup, the Larmor orbit approximation considered the deflected ion trajectories as circular Larmor orbits in the constant mean B-fields. Further investigation of the ion trajectories could provide other possible approximations allowing the analytical estimation of the studied

B-fields.

In the last category, we could pursue other concepts of ion deflectometry. We could examine other sources of ion backlighting that would be more available for sub-MA z-pinch devices than the ion beams accelerated due to the laser interactions or the rapid high-current disruption. For example, we might investigate sources of DD-fusion protons with MeV energies. In addition, we might investigate the feasibility of ion deflectometry measurements of axial B-fields. The axial B-fields can stabilize the z-pinch column in the thermonuclear-fusion experiments, but their distribution in the plasma is poorly investigated.

Appendix A

Own contributions of the author

The ultimate goal of this thesis was to develop a new diagnostic method, ion deflectometry, and to use it to characterize the azimuthal B-fields and the multi-MeV ion sources in MA z-pinch plasmas. This work was motivated by the considerable success of the rapidly developing proton radiography/deflectometry measurements in laser-produced plasmas. This thesis investigated the principles of this diagnostic to introduce it to z-pinch environments.

The role of the thesis's author (hereinafter referred to as "the author") in his team was developing numerical simulations, data interpretation, and hypothesis validation. To this extent, he developed a numerical code in Python tracking trajectories of many charged test particles deflected in various B-fields. The author analyzed the synthetic ion images in order to understand the behavior of the ion deflectometry in z-pinch plasmas and to interpret the experimental results. Moreover, he found and verified the generalized deflection equations and the relations for the paraxial approximation numerically and investigated their applicability.

This thesis presented the results of three most influential papers following the author's work during his doctoral studies. The author of this thesis is the first author of two articles [1] and [3] that described the development of the ion deflectometry B-field measurements in z-pinch plasmas. He is one of the main contributors to the third paper [2], which characterized the multi-MeV deuteron source that was subsequently employed as an ion backlighter for the z-pinch-driven ion deflectometry.

The first selected article [1], discussed in Chap. 3, was based solely on the results of the author's simulations. Besides developing the numerical code, one of the author's main contributions was the investigation of the basic principles of ion deflectometry in two fundamental experimental setups. In addition, the numerical simulations discovered that the deflection equations that are commonly presented in the laser-plasma papers could not be used in typical z-pinch B-fields producing large ion deflections. Therefore, another significant result of this paper was the finding of the generalized deflection equation that is valid for arbitrary deflection angles.

The second selected paper [2], discussed in Chap. 4, described measurements of ion emission and the characterization of the ion source in the experiments on the GIT-12 and HAWK generators. The main author's contribution was the numerical reproduction and interpretation of the

experimental ion images and the estimation of several parameters of the proposed model of the ion source and the z-pinch B-fields. Some of the author's results of the numerical simulations were also presented in the paper [253] and discussed in Sec. 4.4. In addition to the published results, in Sec. 4.6, the numerical simulations evaluated the alternative model of the ion source and the B-fields based on different assumptions.

The third selected paper [3], discussed in Chap. 5, presented the deflectometry measurements on GIT-12 employing the z-pinch-driven ion source examined in the previous chapter (Chap. 4). The author partly contributed on the designing the deflectometry setup. However, his main contribution was the numerical evaluation of the experimental data allowing the z-pinch current and B-field measurements. The numerical simulations demonstrated that our deflectometry setup on GIT-12 allows the Larmor orbit approximation and the analytical estimation of the path-integrated B-fields directly from the experimental ion images. Simultaneously, he identified the physical interpretation of ion images that, in the case of moderate ion deflections, the ion displacements and their spatial derivative manifest the path-integrated B-field and current densities, respectively.

Appendix B

Source codes of our numerical simulations

Our numerical code was developed to reconstruct the ion trajectories in various azimuthal B-fields. We wrote it in Python using Numpy, Scipy, Numba, Matplotlib, and other packages. We used the Numpy n -dimension arrays for their versatile compatibility, efficient data storage, and fast vectorized mathematical operations. Advanced data analysis and image processing were performed using the Scipy package. We utilized a Just-In-Time (JIT) compiler from the Numba package to optimize and parallelize our algorithm's critical parts, allowing us to compute millions of test particles' trajectories in a few seconds. A large number of computed test particle trajectories was required to produce synthetic ion images with sufficient contrast. This was crucial especially for reproducing images of the pinhole camera, because the transparency of the pinhole in our simulations was $\sim 10^{-6} - 10^{-4}$ depending on the simulated setup and the chosen range of the initial parameters of the ion source and B-field. High computation speed allowed us to quickly map the assumed ranges of the simulation parameters and understand their effects on the synthetic images. In addition, we used routines from the Matplotlib package to create readable synthetic images (deflectograms) and visualizations of B-fields crucial for comprehending the results of ion deflectometry. In this chapter, we present selected functions of our numerical code.

To fit the experimental data, we tested multiple models of the z-pinch B-fields with different distributions. Usually, we implemented only azimuthal B-fields because we assumed azimuthal symmetric and non-helical Z-pinch, where the currents symmetrically flow in the (rz) plane.

B.1 Models of the azimuthal magnetic fields

In our simulations, we separated the simulated B-field distribution into three sections: internal region before the current sheath (of the hollow Z-pinch) with no B-fields (i.e., $r \leq R_{cs}$), the Z-pinch region with specific B-field distributions where the current is flowing with the nonzero (i.e., $R_{cs} \leq r \leq R_p$), and the exterior of the Z-pinch with vacuum B-fields (i.e., $B_\varphi(r \geq R_p) =$

$\mu_0 I_p / 2\pi r$).

In the skin-current B-field profile model, the current should flow in the infinitely thin sheath, i.e., $R_{cs} = R_p$. However, it creates an infinite B-fields gradient which might cause problems in the simulations. When the spatial step size of the testing particles is too long, artificial “fringes” will appear in the ion images (for example, see Fig. 2.24b). To avoid these artifacts without the unnecessary increase of the computation time, we implement a very narrow current layer with a constant current density and a finite thickness D_{curr} not longer than a single spatial step of the particles (typically, $10\mu\text{m}$).

```

1 import numpy as np
2 from numba import njit
3 # B = np.zeros(Nparts, dtype = np.float64)
4 @njit(parallel=True)
5 def Beq_skin(qAlive, qR, qZ, qI, _Bnew, qR_pinch, qDcurr):
6     for ip in prange(len(qAlive)):
7         if qAlive[ip] == True:
8             if (0. < qZ[ip] < h_areaB):
9                 r_Sh = qR_pinch - qDcurr
10                dS = (qR[ip]**2 - r_Sh**2)/(qR_pinch**2 - r_Sh**2)
11                if abs(qR[ip]) < r_Sh:
12                    _Bnew[ip] = 0.0
13                elif abs(qR[ip]) < qR_pinch:
14                    _Bnew[ip] = 2e-7*qI[ip]/qR[ip]*dS
15                else:
16                    _Bnew[ip] = 2e-7*qI[ip] /qR[ip]
17    return _Bnew
18 # Beq_skin(Alive, r[0], r[1], B, r_p)
19 # %time Bnew3 = Beq_skin(Alive, r[0], r[1], B, r_p)

```

Furthermore, we simulated axially symmetric Z-pinch column and implemented B-field distributions according to a polynomial function in Eq. (5.5). In our simulations, we assumed that the current sheath might not reach the z-pinch axis, and thus, an inner radius of the current sheath R_{cs} defined the zero-B-field region inside the Z-pinch. It was an optional argument that was in default set to zero.

```

1 # B = np.zeros(Nparts, dtype = np.float64)
2 @njit(parallel=True)
3 def Beq_Rn(rN, qAlive, qR, qZ, qI, _Bnew, qR_pinch, qR_Sh=0.):
4     for ip in prange(len(qAlive)):
5         if qAlive[ip] == True:
6             if (0. < qZ[ip] < h_areaB):
7                 if abs(qR[ip]) <= qR_Sh:
8                     _Bnew[ip] = 0.
9                 elif qR_Sh < abs(qR[ip]) <= qR_pinch:
10                    _Bnew[ip] = 2e-7*qI[ip]/qR_pinch*((qR[ip]-qR_Sh)/(qR_pinch-qR_Sh))**rN
11                else:
12                    _Bnew[ip] = 2e-7*qI[ip] /qR[ip]

```

```

13     return _Bnew
14 # Beq_Rn(1,Alive,r[0],r[1],B,r_p)

```

In order to investigate axially perturbed B-fields by a low- k instability, we established another set of B-field profiles $B_\varphi(r, z)$. We assumed that the instability influenced the front of the current sheath, which we controlled by the inner radius of the current sheath $r_{cs}(z)$ at the given axial position z . The shape of its outer boundary could be also perturbed, which we set by the outer radius of the current sheath $r_p(z)$ (i.e., the pinch radius) at the given axial position. To control the shape of the inner and outer shape of the current sheath, we defined $r_{cs}(z)$ and $r_p(z)$ as even polynomial functions of the axial position z . The perturbed B-field distributions were given by Eq. (5.6). In our simulations, we implemented two functions representing two types of the perturbed B-field distributions. In the first one, we set the outer current-sheath boundary straight so that $r_p(z)$ is constant ($r_p(z) = R_p$). It represented the situation when the current sheath was stretched inwards to a broader region, but its rear side was unperturbed.

```

1 # B = np.zeros(Nparts, dtype = np.float64)
2 @jit(parallel=True)
3 def Beq_m0str8Rn(rN, qAlive, qR, qZ, qI, _Bnew, qRpa0, qRpa1, qR_pinch, qZ_peak=l_mriz/2):
4     for ip in prange(len(qAlive)):
5         if qAlive[ip] == True:
6             if (0. < qZ[ip] < h_areaB):
7                 R_sh = (qRpa1-qRpa0)/(qZ_peak)**2 *(qZ[ip]-qZ_peak)**2 + qRpa0
8                 if abs(qR[ip]) < R_sh:
9                     _Bnew[ip] = 0.
10                elif abs(qR[ip]) < qR_pinch:
11                    _Bnew[ip] = 2e-7*qI[ip]/qR_pinch * ((qR[ip]-R_sh) / (qR_pinch-R_sh) )**rN
12                else:
13                    _Bnew[ip] = 2e-7*qI[ip]/qR[ip]
14     return _Bnew

```

In the second B-field distribution, we assumed the current sheath was not stretched but bent inwards by the instability. Therefore, both the inner and outer boundary given by $r_{cs}(z)$ and $r_p(z)$, respectively, depended on the axial position z .

```

1 # B = np.zeros(Nparts, dtype = np.float64)
2 @jit(parallel=True)
3 def Beq_m0hoRn(rN, qAlive, qR, qZ, qI, _Bnew, qRpa0, qD_curr, qZ_peak=l_mriz/2, zN=2):
4     for ip in prange(len(qAlive)):
5         if qAlive[ip] == True:
6             if (0. < qZ[ip] < h_areaB):
7                 R_sh1 = (qD_curr)/(qZ_peak)**zN *(qZ[ip]-qZ_peak)**zN + qRpa0
8                 R_sh0 = R_sh1 - qD_curr
9                 dS = (qR[ip]**2 - R_sh0**2)/(R_sh1**2 - R_sh0**2)
10                if abs(qR[ip]) < R_sh0:
11                    _Bnew[ip] = 0.000
12                elif abs(qR[ip]) < R_sh1:
13                    _Bnew[ip] = 2e-7*qI[ip]/R_sh1*((qR[ip]-R_sh0)/(R_sh1-R_sh0))**rN

```

```

14         else:
15             _Bnew[ip] = 2e-7*qI[ip] /qR[ip]
16     return _Bnew

```

B.2 3D B-fields of the sloped z-pinch

The experimental data in our ion emission measurements discussed in Chap. 4 hints that the z-pinch might be sloped and directed into one of the pinholes. To reproduce comparable synthetic data for multiple deuteron energies, we implemented a model of the B-fields with a selectable axis determined by the current direction, represented by a unit vector \mathbf{di} . Thus, the direction of the sloped magnetic fields at a specific point was given by a cross product of the current vector \mathbf{di} and \mathbf{r}_\perp , a vector from the B-field axis to this point ($\mathbf{B} \parallel \mathbf{di} \times \mathbf{r}_\perp$).

```

1  @jit
2  def SLOPED_Bfield_LIN(R,I,r_pinch,h_areaB,di,R_center):
3      parts = len(R[0])
4      B = np.zeros((3,parts))
5      for i in range(parts):
6          x = R[0,i]-R_center[0]
7          y = R[1,i]-R_center[1]
8          z = R[2,i]-R_center[2]
9          Tx = di[1]*z - di[2]*y # (dI x r)_x
10         Ty = di[2]*x - di[0]*z # (dI x r)_y
11         Tz = di[0]*y - di[1]*x # (dI x r)_z
12
13         dist = np.sqrt(Tx**2 + Ty**2 + Tz**2)
14         if 0. <= R[2,i] <= h_areaB:
15             if r_pinch < dist: # out
16                 bx = 2e-7*I[i]*( Tx/dist**2 )
17                 by = 2e-7*I[i]*( Ty/dist**2 )
18                 bz = 2e-7*I[i]*( Tz/dist**2 )
19             elif dist <= r_pinch: # in
20                 bx = 2e-7*I[i]*( Tx/r_pinch**2 )
21                 by = 2e-7*I[i]*( Ty/r_pinch**2 )
22                 bz = 2e-7*I[i]*( Tz/r_pinch**2 )
23         else:
24             bx = 0.0
25             by = 0.0
26             bz = 0.0
27         if np.isnan(bx):
28             bx = 0.0
29         if np.isnan(by):
30             by = 0.0
31         if np.isnan(bz):
32             bz = 0.0
33         B[0,i] = bx
34         B[1,i] = by
35         B[2,i] = bz
36     return B

```

Besides the arbitrary current direction \mathbf{d}_i , we also implemented the arbitrary direction of the simulated ion emission. To that end, we generated ion velocities given by an emission cone directed along the z-axis and then rotated its axis using Rodrigues' rotation formula [268]. Then, the rotated ion velocity vectors \mathbf{v}_{rot} was given by

$$\mathbf{v}_{\text{rot}} = \mathbf{v} \cos \beta + (\hat{\mathbf{n}} \times \mathbf{v}) \sin \beta + \hat{\mathbf{n}}(\hat{\mathbf{n}} \cdot \mathbf{v})(1 - \cos \beta), \quad (\text{B.1})$$

where β is the angle of the right-hand rotation, $\hat{\mathbf{n}}$ is a unit vector that represents the rotation axis and is perpendicular to the axis of the ion emission cone.

```

1 def Rodrigues_Rot(V,k,theta):
2     ### Rotate "V" around the axis "k" by the angle "beta"
3     n = k/np.linalg.norm(k,axis=0)
4     Sin0 = np.sin(beta)
5     Cos0 = np.cos(beta)
6     V_rot = V*Cos0 + np.cross(k,V,axis=0)*Sin0 + k*(k[0]*V[0] + k[1]*V[1] + k[2]*V[2])*(1-Cos0)
7     return V_rot

```

B.3 Boris Pusher

In our simulations, we solved the motion equation (2.1) for test particles using the Boris method [166]. This method is de facto standard in plasma physics particle-in-cell simulations for its favorable properties. Although it is only a second-order-accuracy method it requires only one evaluation of acting fields per step (it is fast) which contrasts with four evaluations in the Runge-Kutta 4 (RK4) method that is forth order accurate. Unlike RK4, the Boris method preserves an energy of the particles over a large number of iterations and even large step sizes, which is crucial for simulations of B-field-dominated ion movements (it is stable).

Although the Boris method is commonly used to calculate the ion movements by both electric and magnetic fields, we used our simulations only to compute the magnetic deflections of the test particles. The Boris algorithm rotates the particle velocity from \mathbf{v}_n to \mathbf{v}_{n+1} in two steps by performing two $\mathbf{v} \times \mathbf{B}$ velocity shifts.

The first step is finding a vector \mathbf{w} that bisects the deflection angle α (and the temporal step Δt) in two and is given by $\mathbf{w} = \mathbf{v}_n + \mathbf{v}_n \times \mathbf{B}_t$ where $\mathbf{B}_t = (Q/m)(\Delta t/2)\mathbf{B}$. The second step is performing the cross product of the bisector vector \mathbf{w} with a vector $\mathbf{b}_t = 2\mathbf{B}_t/(1 + \|\mathbf{B}_t\|^2)$ corresponding to the vector \mathbf{B}_t but scaled down to satisfy the conservation of the velocity magnitude. Therefore, the numerical scheme of the Boris method is:

$$\mathbf{w} = \mathbf{v}_n + \mathbf{v}_n \times \mathbf{B}_t \quad (\text{B.2})$$

$$\mathbf{v}_{n+1} = \mathbf{v}_n + \mathbf{w} \times \mathbf{b}_t = \mathbf{v}_n + 2 \frac{(\mathbf{v}_n + \mathbf{v}_n \times \mathbf{B}_t) \times \mathbf{B}_t}{1 + \|\mathbf{B}_t\|^2} \quad (\text{B.3})$$

$$\mathbf{x}_{n+1} = \mathbf{x}_n + \mathbf{v}_{n+1}\Delta t \quad (\text{B.4})$$

Note that the updated particle position \mathbf{x}_{n+1} is evaluated from the previous position \mathbf{x}_n using the updated velocity \mathbf{v}_{n+1} . In the case of the relativistic velocities of the particles, we must modify the vectors of the velocity and the B-field by the Lorentz factor $\gamma_n = 1/\sqrt{1 - v_n^2/c^2}$. Then, the numerical scheme of the relativistic Boris method is as follows:

$$\tilde{\mathbf{B}}_t = \mathbf{B}_t/\gamma_n \quad (\text{B.5})$$

$$\tilde{\mathbf{v}}_n = \gamma_n \mathbf{v}_n \quad (\text{B.6})$$

$$\tilde{\mathbf{v}}_{n+1} = \tilde{\mathbf{v}}_n + 2 \frac{(\tilde{\mathbf{v}}_n + \tilde{\mathbf{v}}_n \times \tilde{\mathbf{B}}_t) \times \tilde{\mathbf{B}}_t}{1 + \|\tilde{\mathbf{B}}_t\|^2} \quad (\text{B.7})$$

$$\mathbf{v}_{n+1} = \frac{\tilde{\mathbf{v}}_{n+1}}{\sqrt{1 + \tilde{\mathbf{v}}_{n+1}^2/c^2}} \quad (\text{B.8})$$

$$\mathbf{x}_{n+1} = \mathbf{x}_n + \mathbf{v}_{n+1}\Delta t \quad (\text{B.9})$$

```

1 @njit(parallel = True)
2 def Boris(qAlive, _R, _V, qB, qdt):
3     c = 299792458.
4     for j in prange(len(qAlive)):
5         if qAlive[j]:
6             vx = _V[0, j]
7             vy = _V[1, j]
8             vz = _V[2, j]
9
10            btx = 0.5*qdt*Q/m*qB[0, j]
11            bty = 0.5*qdt*Q/m*qB[1, j]
12            btz = 0.5*qdt*Q/m*qB[2, j]
13
14            # gamma = 1/np.sqrt(1-(vx**2 + vy**2 + vz**2)/c**2)
15            # ux = gamma*vx
16            # uy = gamma*vy
17            # uz = gamma*vz
18            # btx /= gamma
19            # bty /= gamma
20            # btz /= gamma
21
22            bt2 = btx**2 + bty**2 + btz**2
23
24            # double cross product
25            KrossX = uy*btz+uz*btx*btz-ux*btx*btz-uz*bty-ux*bty*bty+uy*btx*bty
26            KrossY = uz*btx+ux*bty*btx-uy*btx*btz-ux*btz-uy*btz*btz+uz*bty*btz
27            KrossZ = ux*bty+uy*btz*bty-uz*bty*bty-uy*btx-uz*btx*btz+ux*btz*btz

```

```

28
29     uux = ux + 2*KrossX/(1+bt2)
30     uuy = uy + 2*KrossY/(1+bt2)
31     uuz = uz + 2*KrossZ/(1+bt2)
32
33     uu2 = uux**2 + uuy**2 + uuz**2
34
35     vnewx = uux/np.sqrt(1+uu2/c**2)
36     vnewy = uuy/np.sqrt(1+uu2/c**2)
37     vnewz = uuz/np.sqrt(1+uu2/c**2)
38
39     _R[0,j] += vnewx*qdt
40     _R[1,j] += vnewy*qdt
41     _R[2,j] += vnewz*qdt
42
43     _V[0,j] = vnewx
44     _V[1,j] = vnewy
45     _V[2,j] = vnewz
46     return _R,_V

```

If the B-fields are only azimuthal $\mathbf{B} = (0, B_\varphi, 0)$, we can simplify the triple vector cross product in the Boris algorithm.

```

1 @njit(parallel=True)
2 def Boris2D_nonRel(qAlive,_R,_V,qB,qdt):
3     for j in prange(len(qAlive)):
4         if qAlive[j] == True:
5             ur = _V[0,j]
6             uz = _V[1,j]
7
8             btu = qm*0.5*qdt*qB[j]
9
10            vr = ur + 2*(-uz*btu - ur*btu*btu)/(1.+btu**2)
11            vz = uz + 2*( ur*btu - uz*btu*btu)/(1.+btu**2)
12
13            _R[0,j] += vr*qdt
14            _R[1,j] += vz*qdt
15
16            _V[0,j] = vr
17            _V[1,j] = vz
18            return _R,_V

```

B.4 Grid filter

In the case of the azimuthally symmetric setup, we calculate the movements of the test particles only in the (r-z) plane to maximize the number of the particles that passed through the pinhole of the simulated ion detector. Therefore, these simulations provided only radial displacements of test particles in the detector plane. To produce the whole synthetic deflectogram, we needed

to spread particles over the xy plane and imprint the D-grid shadow into their image. To that extent, we implemented two functions that selected detected particles to those that passed through and those that hit the D-grid according to their initial radial positions in the D-grid plane, and returned arrays of their indices and angular positions in the xy plane. Then, we use these arrays to populate the whole synthetic image.

```

1 @njit
2 def GridLines(qR,dWire=0.25e-3):
3     # selects particles that hit the D-grid
4     xG = np.array([-9.6e-3,-7.2e-3,-4.8e-3,-2.4e-3,0.,2.4e-3,4.8e-3,7.2e-3,9.6e-3])
5     yG = np.copy(xG)
6
7     U = np.linspace(0,pi*2,1500)
8     UX = []
9     IDX = []
10    UY = []
11    IDY = []
12    for j,ri in enumerate(qR):
13        if ri <= 10e-3:
14            for ui in U:
15                xi = ri*np.cos(ui)
16                yi = ri*np.sin(ui)
17                if xG[-1]**2 <= (xi**2 + yi**2) or (np.abs(xi)+np.abs(yi))<=0.92e-3*np.sqrt(2):
18                    UX.append(ui)
19                    IDX.append(j)
20            else:
21                for xg in xG[4:]:
22                    if np.abs(np.abs(xi)-xg) < dWire:
23                        UX.append(ui)
24                        IDX.append(j)
25                    if np.abs(np.abs(yi)-xg) < dWire:
26                        UY.append(ui)
27                        IDY.append(j)
28    IDin = np.array(IDX)
29    Uin = np.array(UX)
30    IDY = np.array(IDY)
31    UY = np.array(UY)
32    return IDX,UX,IDY,UY

```

```

1 @jit
2 def GridSq(qR, aRib = 0.5e-3/2):
3     # selects particles that pass through the D-grid
4     xG = np.array([-9.6e-3,-7.2e-3,-4.8e-3,-2.4e-3,0.,2.4e-3,4.8e-3,7.2e-3,9.6e-3])
5     yG = np.copy(xG)
6     U = np.linspace(0,pi*2,1500)
7     Uin = []
8     IDin = []
9     for j,ri in enumerate(qR):
10        for ui in U:
11            if (ri>=10e-3):

```



```
12         Uin.append(ui)
13         IDin.append(j)
14         continue
15     xi = ri*np.cos(ui)
16     yi = ri*np.sin(ui)
17     if (ri <= xG[-1]) and (abs(xi)+abs(yi))>=0.92e-3*np.sqrt(2):
18         for xg in xG:
19             for yg in yG:
20                 ## Ruzky na okraji
21                 if (xg == xG[6] and yg == yG[7]) or (xg == xG[7] and yg == yG[6]) or\
22                     (xg == xG[0] and yg == yG[6]) or (xg == xG[1] and yg == yG[7]) or\
23                     (xg == xG[0] and yg == yG[1]) or (xg == xG[6] and yg == yG[0]) or\
24                     (xg == xG[1] and yg == yG[0]) or (xg == xG[7] and yg == yG[1]):
25                     continue
26                 elif (aRib<=(xi-xg)<=2.4e-3-aRib) and (aRib<=(yi-yg)<=2.4e-3-aRib):
27                     Uin.append(ui)
28                     IDin.append(j)
29     IDin = np.array(IDin)
30     Uin = np.array(Uin)
31     return IDin,Uin
```

Appendix C

Publications in Impacted Journals

Publications related to this thesis

- 1 **V. Munzar**, D. Klir, J. Cikhardt, B. Cikhardtova, J. Kravarik, P. Kubes, and K. Rezac, “Investigation of magnetic fields in z-pinches via multi-mev proton deflectometry”, *IEEE TRANSACTIONS ON PLASMA SCIENCE*, vol. 46, no. 11, 1, SI, pp. 3891–3900, Nov. 2018, ISSN: 0093-3813. DOI: 10.1109/TPS.2018.2874207.
- 2 **V. Munzar**, D. Klir, J. Cikhardt, J. Kravarik, P. Kubes, J. Malir, J. Novotny, K. Rezac, A. Shishlov V, V. A. Kokshenev, R. K. Cherdizov, and N. A. Ratakhin, “Mapping of azimuthal b-fields in z-pinch plasmas using z-pinch-driven ion deflectometry”, *PHYSICS OF PLASMAS*, vol. 28, no. 6, 062702, Jun. 2021, ISSN: 1070-664X. DOI: 10.1063/5.0040515.
- 3 D. Klir, A. Shishlov V, S. L. Jackson, V. A. Kokshenev, P. Kubes, K. Rezac, A. R. Beresnyak, R. K. Cherdizov, J. Cikhardt, B. Cikhardtova, G. N. Dudkin, J. T. Engelbrecht, F. Fursov I, J. Kaufman, J. Krasa, J. Kravarik, N. E. Kurmaev, **V. Munzar**, N. A. Ratakhin, K. Turek, and V. A. Varlachev, “Spatial distribution of ion emission in gas-puff z-pinches and dense plasma foci”, *PLASMA PHYSICS AND CONTROLLED FUSION*, vol. 62, no. 3, 035009, Mar. 2020, ISSN: 0741-3335. DOI: 10.1088/1361-6587/ab6902.
- 4 D. Klir, A. Shishlov V, V. A. Kokshenev, P. Kubes, K. Rezac, R. K. Cherdizov, J. Cikhardt, B. Cikhardtova, G. N. Dudkin, F. Fursov I, T. Hyhlik, J. Kaufman, B. M. Kovalchuk, J. Krasa, J. Kravarik, N. E. Kurmaev, A. Y. Labetsky, **V. Munzar**, H. Orcikova, V. N. Padalko, N. A. Ratakhin, O. Sila, J. Stodulka, K. Turek, V. A. Varlachev, and R. Wagner, “Ion acceleration mechanism in mega-ampere gas-puff z-pinches”, *NEW JOURNAL OF PHYSICS*, vol. 20, 053064, May 2018, ISSN: 1367-2630. DOI: 10.1088/1367-2630/aac545.
- 5 D. Klir, A. Shishlov V, V. A. Kokshenev, S. L. Jackson, K. Rezac, R. K. Cherdizov, J. Cikhardt, G. N. Dudkin, F. Fursov I, J. Krasa, J. Kravarik, P. Kubes, N. E. Kurmaev, **V. Munzar**, N. A. Ratakhin, K. Turek, and V. A. Varlachev, “Production of energetic protons, deuterons, and neutrons up to 60 mev via disruption of a current-carrying plasma

- column at 3 ma”, *NEW JOURNAL OF PHYSICS*, vol. 22, no. 10, 103036, Oct. 2020, ISSN: 1367-2630. DOI: 10.1088/1367-2630/abbab5.
- 6 D. Klir, A. Shishlov V, V. A. Kokshenev, P. Kubes, K. Rezac, S. Buryiskova, R. K. Cherdizov, J. Cikhardt, B. Cikhardtova, G. N. Dudkin, J. T. Engelbrecht, F. Fursov I, S. L. Jackson, J. Krasa, J. Kravarik, N. E. Kurmaev, **V. Munzar**, V. N. Padalko, N. A. Ratakhin, O. Sila, K. Turek, V. A. Varlachev, and R. Wagner, “Acceleration of protons and deuterons up to 35 mev and generation of 10(13) neutrons in a megaampere deuterium gas-puff z-pinch”, *PLASMA PHYSICS AND CONTROLLED FUSION*, vol. 61, no. 1, 014018, Jan. 2019, ISSN: 0741-3335. DOI: 10.1088/1361-6587/aadc99.
 - 7 D. Klir, S. L. Jackson, A. Shishlov V, V. A. Kokshenev, K. Rezac, A. R. Beresnyak, R. K. Cherdizov, J. Cikhardt, B. Cikhardtova, G. N. Dudkin, J. T. Engelbrecht, F. Fursov I, J. Krasa, J. Kravarik, P. Kubes, N. E. Kurmaev, **V. Munzar**, N. A. Ratakhin, K. Turek, and V. A. Varlachev, “Ion acceleration and neutron production in hybrid gas-puff z-pinches on the git-12 and hawk generators”, *MATTER AND RADIATION AT EXTREMES*, vol. 5, no. 2, 026401, Mar. 2020, ISSN: 2468-2047. DOI: 10.1063/1.5132845.

Other publications

- 1 P. Kubes, M. Paduch, M. J. Sadowski, J. Cikhardt, B. Cikhardtova, D. Klir, J. Kravarik, **V. Munzar**, K. Rezac, E. Zielinska, E. Skladnik-Sadowska, A. Szymaszek, K. Tomaszewski, and D. Zaloga, “Characterization of fast deuterons involved in the production of fusion neutrons in a dense plasma focus”, *PHYSICS OF PLASMAS*, vol. 25, no. 1, 012712, Jan. 2018, ISSN: 1070-664X. DOI: 10.1063/1.5012021.
- 2 P. Kubes, M. Paduch, M. J. Sadowski, J. Cikhardt, B. Cikhardtova, D. Klir, J. Kravarik, R. Kwiatkowski, **V. Munzar**, K. Rezac, A. Szymaszek, K. Tomaszewski, D. Zaloga, E. Zielinska, and M. Akel, “Characteristics of fast deuteron sources generated in a dense plasma focus”, *EUROPEAN PHYSICAL JOURNAL PLUS*, vol. 136, no. 8, 810, Aug. 2021, ISSN: 2190-5444. DOI: 10.1140/epjp/s13360-021-01799-w.
- 3 P. Kubes, M. Paduch, M. J. Sadowski, J. Cikhardt, B. Cikhardtova, D. Klir, J. Kravarik, **V. Munzar**, K. Rezac, E. Skladnik-Sadowska, A. Szymaszek, K. Tomaszewski, D. Zaloga, and E. Zielinska, “Evolution of a pinch column during the acceleration of fast electrons and deuterons in a plasma-focus discharge”, *IEEE TRANSACTIONS ON PLASMA SCIENCE*, vol. 47, no. 1, 3, pp. 339–345, Jan. 2019, ISSN: 0093-3813. DOI: 10.1109/TPS.2018.2874288.
- 4 P. Kubes, M. Paduch, M. J. Sadowski, J. Cikhardt, B. Cikhardtova, D. Klir, J. Kravarik, R. Kwiatkowski, **V. Munzar**, K. Rezac, E. Skladnik-Sadowska, A. Szymaszek, K. Tomaszewski, D. Zaloga, and E. Zielinska, “Features of fast deuterons emitted from plasma focus dis-

- charges”, *PHYSICS OF PLASMAS*, vol. 26, no. 3, 032702, Mar. 2019, ISSN: 1070-664X. DOI: 10.1063/1.5080974.
- 5 P. Kubes, M. Paduch, M. J. Sadowski, J. Cikhardt, B. Cikhardtova, D. Klir, J. Kravarik, **V. Munzar**, K. Rezac, E. Zielinska, E. Skladnik-Sadowska, A. Szymaszek, K. Tomaszewski, and D. Zaloga, “Evolution of the pinched column during hard x-ray and neutron emission in a dense plasma focus”, *JOURNAL OF FUSION ENERGY*, vol. 38, no. 3-4, SI, pp. 490–498, Aug. 2019, ISSN: 0164-0313. DOI: 10.1007/s10894-018-0194-x.
 - 6 J. Malir, D. Klir, J. Cikhardt, J. Kravarik, P. Kubes, **V. Munzar**, J. Novotny, K. Rezac, and M. Paduch, “Dynamics of implosion phase of modified plasma focus studied via laser interferometry and electrical measurements”, *PHYSICS OF PLASMAS*, vol. 29, no. 9, Sep. 2022, ISSN: 1070-664X. DOI: 10.1063/5.0098124.
 - 7 P. Kubes, M. Paduch, M. J. Sadowski, B. Cikhardtova, J. Cikhardt, D. Klir, J. Kravarik, R. Kwiatkowski, **V. Munzar**, K. Rezac, A. Szymaszek, K. Tomaszewski, E. Zielinska, D. Zaloga, and M. Akel, “Characteristics of closed currents and magnetic fields outside the dense pinch column in a plasma focus discharge”, *PHYSICS OF PLASMAS*, vol. 27, no. 9, 092702, Sep. 2020, ISSN: 1070-664X. DOI: 10.1063/5.0010249.
 - 8 P. Kubes, M. Paduch, M. J. Sadowski, J. Cikhardt, D. Klir, J. Kravarik, R. Kwiatkowski, **V. Munzar**, K. Rezac, A. Szymaszek, K. Tomaszewski, E. Zielinska, M. Akel, and B. Cikhardtova, “Scenario of a magnetic dynamo and magnetic reconnection in a plasma focus discharge”, *MATTER AND RADIATION AT EXTREMES*, vol. 5, no. 4, 046401, Jul. 2020, ISSN: 2468-2047. DOI: 10.1063/1.5133103.
 - 9 P. Kubes, M. Paduch, M. J. Sadowski, J. Cikhardt, B. Cikhardtova, D. Klir, J. Kravarik, R. Kwiatkowski, **V. Munzar**, K. Rezac, E. Skladnik-Sadowska, A. Szymaszek, K. Tomaszewski, D. Zaloga, and E. Zielinska, “Influence of an external additional magnetic field on the formation of a plasma column in a dense plasma focus”, *PHYSICS OF PLASMAS*, vol. 26, no. 10, 102701, Oct. 2019, ISSN: 1070-664X. DOI: 10.1063/1.5094568.
 - 10 P. Kubes, M. Paduch, M. J. Sadowski, J. Cikhardt, B. Cikhardtova, D. Klir, J. Kravarik, **V. Munzar**, K. Rezac, E. Zielinska, E. Skladnik-Sadowska, A. Szymaszek, K. Tomaszewski, and D. Zaloga, “Axial compression of plasma structures in a plasma focus discharge”, *PHYSICS OF PLASMAS*, vol. 25, no. 6, 062712, Jun. 2018, ISSN: 1070-664X. DOI: 10.1063/1.5033997.
 - 11 P. Kubes, M. Paduch, K. Tomaszewski, M. J. Sadowski, J. Cikhardt, D. Klir, J. Kravarik, J. Malir, **V. Munzar**, J. Novotny, K. Rezac, and A. Szymaszek, “Temporal behavior of hard x-ray and neutron production in plasma focus discharges”, *PHYSICS OF PLASMAS*, vol. 29, no. 6, 062709, Jun. 2022, ISSN: 1070-664X. DOI: 10.1063/5.0085351.
 - 12 D. Klir, A. V. Shishlov, V. A. Kokshenev, R. K. Cherdizov, J. Cikhardt, F. I. Fursov, J. Kravarik, P. Kubes, N. E. Kurmaev, J. Malir, **V. Munzar**, J. Novotny, N. A. Ratakhin, and K. Rezac, “K-shell radiation and neutron emission from z-pinch plasmas generated

- by hybrid gas-puff implosions onto on-axis wires”, *PHYSICS OF PLASMAS*, vol. 28, no. 6, 062708, Jun. 2021, ISSN: 1070-664X. DOI: 10.1063/5.0054683.
- 13 J. Novotny, J. Cikhardt, J. Kravarik, D. Klir, P. Kubes, **V. Munzar**, and K. Rezac, “Optimizing of experimental load of pfz-200 plasma focus”, *IEEE TRANSACTIONS ON PLASMA SCIENCE*, vol. 49, no. 1, pp. 450–454, Jan. 2021, ISSN: 0093-3813. DOI: 10.1109/TPS.2020.3041329.
- 14 J. Cikhardt, D. Klir, A. Shishlov V, V. A. Kokshenev, K. Rezac, R. K. Cherdizov, G. N. Dudkin, F. Fursov I, J. Kravarik, P. Kubes, N. E. Kurmaev, **V. Munzar**, J. Novotny, N. A. Ratakhin, K. Turek, and V. A. Varlachev, “Neutron fluence distribution in experiments with 3 ma deuterium gas-puff z-pinch”, *PHYSICS OF PLASMAS*, vol. 27, no. 7, 072705, Jul. 2020, ISSN: 1070-664X. DOI: 10.1063/5.0008108.

Appendix D

List of presentations

D.1 International conference

D.1.1 Oral presentations

- **Invited presentation:** “First Measurements of Magnetic Fields in Z-pinch Plasmas by the Ion Deflectometry on GIT-12”: **V. Munzar**, D. Klir, J. Cikhardt, B. Cikhardtova, J. Kravarik, P. Kubes, K. Rezac, A. V. Shishlov, V. A. Kokshenev, R.K. Cherdizov, N. A. Ratakhin, K. Turek; *21st International Symposium on High-Current Electronics (SHCE) at 7th International Congress Energy Fluxes and Radiation Effects (EFRE)*, September 14-25 2020, Tomsk, Russia, [Online].
- “Study of Z-pinch Magnetic Field via Proton Deflectometry”: **V. Munzar**, D. Klir, J. Cikhardt, B. Cikhardtova, J. Kravarik, P. Kubes, K. Rezac, *Workshop and Expert Meeting On Dense Magnetised Plasmas (ICDMP)*, October 14-15 2017, Warsaw, Poland.
- “Study of Magnetic Fields and MeV Hydrogen Ions in Z-pinch plasmas via Ion Deflectometry”: **V. Munzar**, D. Klir, J. Cikhardt, B. Cikhardtova, J. Kravarik, P. Kubes, K. Rezac, A. V. Shishlov, V. A. Kokshenev, R.K. Cherdizov, F. I. Fursov, N.E. Kurmaev, N. A. Ratakhin, H. Orcikova, K. Turek, R. Wagner, *28th Symposium on Plasma Physics and Technology (SPPT), Prague*, June 18-21 2018, Prague, Czech Republic.
- “Study of Z-pinch Magnetic Fields and Sources of MeV Ions via Ion Deflectometry”: **V. Munzar**, D. Klir, J. Cikhardt, B. Cikhardtova, J. Kravarik, P. Kubes, K. Rezac, A. V. Shishlov, V. A. Kokshenev, R. K. Cherdizov, F. I. Fursov, N.E. Kurmaev, N. A. Ratakhin, H. Orcikova, K. Turek, R. Wagner; *60rd Annual Meeting of the APS Division of Plasma Physics (APS DPP)*, November 5-9 2018, Portland, Oregon, USA.
- “First Use of Z-pinch-driven Ion Deflectometry for Azimuthal Magnetic Field Measurements”: **V. Munzar**, D. Klir, J. Cikhardt B. Cikhardtova, J. Kravarik, P. Kubes, K. Rezac, A. V. Shishlov, V. A. Kokshenev, R.K. Cherdizov, N. A. Ratakhin, K. Turek;

62rd Annual Meeting of the APS Division of Plasma Physics (APS DPP), November 9-13 2020,[Online], Memphis, Tennessee, USA.

D.1.2 Poster presentations

- “Study of Magnetic Fields and Ion Beams In Z-pinch Plasmas via Ion Deflectometry”: **V. Munzar**, D. Klir, J. Cikhardt, B. Cikhardtova, J. Kravarik, P. Kubes, K. Rezac, A. V. Shishlov, N. A. Ratakhin, V. A. Kokshenev, R.K. Cherdizov, F. I. Fursov, N.E. Kurmaev, H. Orcikova, K. Turek; *PLASMA 2017 – International Conference on Research and Application of Plasmas*, September 18-22 2017, Warsaw, Poland
- “Proof-of-principle of the ion deflectometry for B-field measurements in Z-pinch Plasmas”: **V. Munzar**, D. Klir, J. Cikhardt, B. Cikhardtova, J. Kravarik, P. Kubes, K. Rezac, A. V. Shishlov, V. A. Kokshenev, R. K. Cherdizov, N. A. Ratakhin, K. Turek, J. Krasa; *61rd Annual Meeting of the APS Division of Plasma Physics (APS DPP)*, September 19-28 2019, Fort Lauderdale, Florida, USA.
- “Influence of the azimuthal B-field distribution on the formation of ring structures in the ion images on GIT-12”: **V. Munzar**, D. Klir, J. Cikhardt, J. Kravarik, P. Kubes, K. Rezac, J. Novotny, J. Malir, A. V. Shishlov, V. A. Kokshenev, R.K. Cherdizov, N. A. Ratakhin; *63rd Annual Meeting of the APS Division of Plasma Physics (APS DPP)*, November 6-15 2021, Pittsburgh, Pennsylvania, USA [Online].

D.2 Student conferences

D.2.1 Oral presentations

- **Award-winning presentation:** “Ion Beams and Magnetic Fields in a Deuterium Z-pinch”: **V. Munzar**, D. Klir, J. Cikhardt, B. Cikhardtova, J. Kravarik, P. Kubes, K. Rezac, A. V. Shishlov, V. A. Kokshenev, R. K. Cherdizov, F. I. Fursov, N. E. Kurmaev, N. A. Ratakhin, H. Orcikova, K. Turek, R. Wagner; *PhDiaFusion 2017 - Summer School of Plasma Diagnostics*, September 11-15 2017, Podlesice, Poland;
- “Investigation of Z-pinch Magnetic Fields via Ion Deflectometry”: **V. Munzar**, D. Klir, J. Cikhardt, B. Cikhardtova, J. Kravarik, P. Kubes, K. Rezac, A. V. Shishlov, V. A. Kokshenev, R. K. Cherdizov, F. I. Fursov, N. E. Kurmaev, N. A. Ratakhin, H. Orcikova, K. Turek, R. Wagner; *14th Kudowa Zdroj Summer School - "Towards Fusion Energy"*, June 4-9 2018, Kudowa Zdroj, Poland.
- “Ion Deflectometry Measurements of the Magnetic Fields and Currents in Z-pinch Plasmas”: **V. Munzar**, D. Klir, J. Cikhardt, B. Cikhardtova, J. Kravarik, P. Kubes, K. Rezac, A. V. Shishlov, V. A. Kokshenev, R.K. Cherdizov, N. A. Ratakhin, K. Turek, J. Krasa; *15th Kudowa Zdroj Summer School - "Towards fusion energy"*, June 29 - July 3 2020, Kudowa Zdroj, Poland [Virtual].

D.3 Seminars at foreign institutions

- “Study of Z-pinch Magnetic Fields and Sources of MeV Ions via Ion Deflectometry”: **V. Munzar**, at Naval Research Laboratory (NRL) - Plasma Physics Division, Washington, D.C., USA, November 14, 2018.
- “Ion deflectometry for B-field measurements in the Z-pinch plasmas”: **V. Munzar**, at Institute of Nuclear Physics, Polish Academy of Sciences, Krakow, Poland, December 2 2019.

Appendix E

List of international internships

- Internship at Institute of Plasma Physics and Laser Microfusion (IPPLM), August 31 - October 1 2018, Warsaw, Poland (31 days).
- Internship at Naval Research Laboratory (NRL), November 11-18, 2018, Washington, D.C., USA (8 days).

Appendix F

List of international experimental campaigns

- Institute of Plasma Physics and Laser Microfusion (IPPLM), February 5-16 2018, Warsaw, Poland (12 days).
- Institute of Plasma Physics and Laser Microfusion (IPPLM), September 16-28 2018, Warsaw, Poland (13 days).
- Institute of Plasma Physics and Laser Microfusion (IPPLM), February 11-23 2019, Warsaw, Poland (13 days).
- Institute of Plasma Physics and Laser Microfusion (IPPLM), September 19-27 2019, Warsaw, Poland (9 days).
- Institute of Nuclear Physics, Polish Academy of Sciences, November 24 - December 1 2019, Krakow, Poland (8 days).
- Institute of Plasma Physics and Laser Microfusion (IPPLM), February 9-22 2021, Warsaw, Poland (14 days).
- Institute of Plasma Physics and Laser Microfusion (IPPLM), October 18-30 2021, Warsaw, Poland (13 days).
- Institute of Plasma Physics and Laser Microfusion (IPPLM), July 11-22 2021, Warsaw, Poland (13 days).

Appendix G

Selected papers

G.1 Article: Munzar et al., IEEE Trans. Plasma Sci. (2018)

Investigation of Magnetic Fields in Z-Pinches via Multi-MeV Proton Deflectometry

V. Munzar¹, D. Klir, J. Cikhardt¹, B. Cikhardtova, J. Kravarik, P. Kubes¹, and K. Rezac

Abstract—Proton deflectometry is a promising way for mapping electric and magnetic fields in high-density and high-temperature plasmas, where an application of the classical methods (B-dot probes, Faraday rotation, and Zeeman splitting) is limited. It is based on the detection of a multi-MeV proton beam deflected in examined B-fields. In the past years, it has been successfully utilized in laser-generated plasmas for E-field and B-field measurements. Using our numerical code, we investigate the capabilities of proton deflectometry as a diagnostic method of MA Z-pinches. We simulate proton trajectories propagating through typical Z-pinch B-fields in two fundamental experimental setups (radial and axial) in order to study synthetic images (deflectograms). We demonstrate where proton deflectometry might be beneficial for the Z-pinch research. We explain a formation of the key features of deflectograms, which give us information about a profile and strength of the Z-pinch B-fields. We introduce a B_L parameter, denoting an effective B-field averaged along the deflected proton orbit and show its importance for the proton deflectometry.

Index Terms—Magnetic fields, plasma pinch, proton beams, proton deflectometry, simulations, Z-pinches.

I. INTRODUCTION

FOR years, there has been a significant effort to study the B-field in Z-pinch experiments. Effects of the current and magnetic fields are crucial for various phenomena in Z-pinch plasmas. Until now, classical measurement methods have been used, that is: 1) Faraday rotation; 2) B-dot probes; and 3) Zeeman splitting. Nevertheless, these methods have some drawbacks and limitations. A proper determination of an averaged B-field using the Faraday rotation relies on the knowledge of electron density profile and suffers from low contrast (signal-to-noise ratio). In high-temperature and high-density plasmas of a Z-pinch, B-dot probes cannot be placed near the Z-pinch axis, and hence, B-field can only be measured at peripheral regions or at the time of the beginning of the discharge. Due to the poor spatial resolution of a single B-dot probe, a set of the B-dot probes is needed to measure the

distribution of the B-field. A large number of B-dot probes can also affect measurements. Finally, the results of the Zeeman splitting method might be influenced by the effects of the Doppler splitting of dynamic high-temperature high-Z plasmas of the Z-pinch. With the development of proton acceleration via laser-target interactions, target normal sheath acceleration (TNSA) mechanism, and a new B-field diagnostic method appeared, i.e., proton deflectometry.

The proton deflectometry, as a diagnostic method, was developed for E-field and B-field measurements in laser-generated plasma experiments at the beginning of the millennium. It is based on the detection of a MeV proton beam, which is deflected in B-fields of the Z-pinch plasma. Trajectories of charged particles passing through the B-field are bent by the magnetic force. Magnitude and profile of the B-field can be estimated by comparing the synthetic images of the detected proton beam (i.e., deflectograms) with experimental results. For measurement purposes, MeV protons are commonly achieved via laser-target acceleration (usually by TNSA) with broad energy spectrum (see [1]–[7]) or via D³He fusion reactions with a monoenergetic spectrum (see [8]–[16]). The laser-accelerated proton beam is highly laminar and collimated with angular divergence decreasing with beam energy, and it is emitted from a pointlike source. High-energy MeV protons undergo almost no collisions even in high-density plasmas and interact only with electric and magnetic fields. A low divergence of the beam is convenient for more detailed mapping (pinpointing) of B-field regions.

In Z-pinch plasmas, the proton deflectometry is a rather new technique, and only a few experiments and simulations were performed [17]–[21]. The goal of this paper is to give a better understanding of this diagnostic method for its application in Z-pinch plasma experiments. For this purpose, a simple numerical code, simulating proton trajectories, deflected by Lorentz force in the Z-pinch, has been developed. The synthetic deflectograms of the Z-pinch B-fields show typical results of the proton deflectometry in the radial and axial configurations. Analyzing the images, we elucidate the origin of key features of the deflectograms and estimate the B_L parameter, which defines the averaged B-field along the proton trajectory.

II. PARAMETERS OF OUR MODEL

Since the problem of proton tracking through the B-fields is simple enough and well documented, the code is written in Python, using Numpy, Numba, and Matplotlib packages. The particles are pushed by the Lorentz force using a relativistic

Manuscript received December 31, 2017; revised August 20, 2018 and September 24, 2018; accepted September 26, 2018. Date of publication October 25, 2018; date of current version November 8, 2018. This work was supported in part by the Grant Agency of the Czech Republic under Grant 16-07036S, in part by the Czech Ministry of Education under Grant LTT17015, Grant LTAUSA17084, and Grant CZ.02.1.01/0.0/0.0/16_019/0000778, and in part by the CTU in Prague under Grant SGS 16/223/OHK3/3T/13. The review of this paper was arranged by Senior Editor F. Beg. (Corresponding author: V. Munzar.)

The authors are with the Faculty of Electrical Engineering, Czech Technical University in Prague, 16627 Prague, Czech Republic (e-mail: munzarvoj@fel.cvut.cz).

Color versions of one or more of the figures in this paper are available online at <http://ieeexplore.ieee.org>.

Digital Object Identifier 10.1109/TPS.2018.2874207

0093-3813 © 2018 IEEE. Personal use is permitted, but republication/redistribution requires IEEE permission. See http://www.ieee.org/publications_standards/publications/rights/index.html for more information.

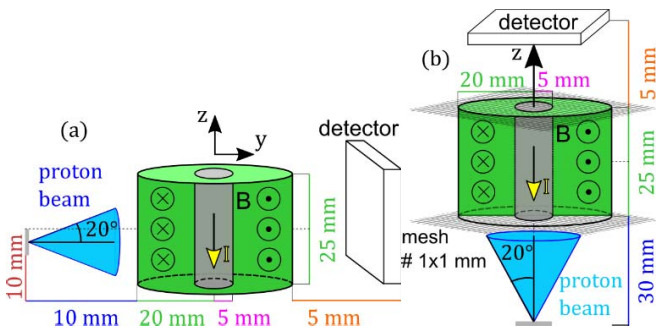


Fig. 1. Experimental setup for the (a) radial and (b) axial deflectometry (not in scale).

Boris particle pusher [22]. The simulated experimental setup is similar to the one in experiments with the ZEBRA device at the Nevada Terawatt Facility [18]–[20]. In our simple model, we presuppose the Z-pinch as a finite-column conductor, with two basic B -field profiles inside a Z-pinch column, namely: 1) a hollow pinch without B -field inside, due to skin effect and 2) a full Z-pinch with a linear profile of the B -field, due to constant current density. Moreover, we neglect boundary conditions near the electrodes. The simulated Z-pinch has a 5 mm radius, where current flows in the negative direction of the z -axis with a constant value in the range of 0.5–2 MA and generates symmetric azimuthal B -field. The B -field region is delimited radially by return-current conductors at the distance of 20 mm from the Z-pinch axis and axially by the electrodes with a 25-mm gap. Outside of this area, there is no field. Due to a very short duration (\sim ps) of the proton pulse compared to the time of a Z-pinch evolution (\sim ns), the simulated B -field is time invariant. Effects of the electric field in the Z-pinch are assumed to be negligible. The simulated proton beam has 20° half-cone divergence, uniformly distributed over the solid angle and emitted from a point source. Due to cylindrical symmetry, there are principally only two configurations of the proton source with respect to the Z-pinch current. Protons, in our simulations, are at first emitted from the side of the Z-pinch, i.e., radial deflectometry [Fig. 1(a)], and then from beneath, the Z-pinch along its axis, i.e., axial deflectometry [Fig. 1(b)]. Previous proton deflectometry experiments in Z-pinch plasmas have been carried out in the radial configuration [17]–[21]. However, the axial configuration of proton deflectometry in Z-pinch plasmas is also feasible, and analogous experiments were performed with laser-generated plasma [3]–[7], [11], [12], [14]. Chosen parameters of the experimental configurations and the proton beam are typical for proton deflectometry experiments with Z-pinch and laser-generated plasmas. The collisional stopping/scattering effects of MeV protons in Z-pinch plasma can also be neglected in our model. The stopping power of 10-MeV protons in the typical Z-pinch plasma (with the electron density $n_e = 10^{19}\text{cm}^{-3}$ and the temperature $T = 100\text{ eV}$) is $dE/dx \sim 1\text{ keV/cm}$ [23], [24].

The synthetic images, generated by our code, show a single-layer image of CR-39 or radiochromic films (RCFs) detectors, which are commonly used for the proton deflectometry. The

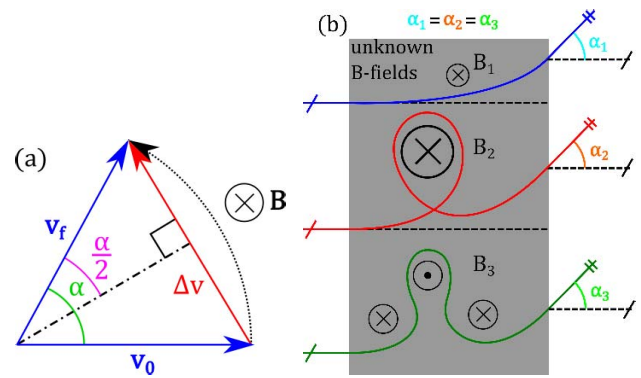


Fig. 2. (a) Deflections in magnetic field \mathbf{B} change a direction of the proton velocity from \mathbf{v}_0 into \mathbf{v}_f . The deflection angle α is the angle between \mathbf{v}_0 and \mathbf{v}_f . (b) Deflection angle α of a proton does not depend on the specific profile of unknown B -field but only on the value of the $B_L \equiv \|\int \mathbf{B} \times d\mathbf{L}\|$ parameter given by the deflection equation (2). B_L is periodic so the same value of B_L and the deflection angle α can be achieved by a proton following either the blue or the red trajectory. The green trajectory with conflicting proton deflections caused by a change of a B -field orientation also results in the same B_L . Therefore, B_L is coupled only with the effective proton deflection.

CR-39 detector is a type of a solid-state nuclear track detector, which interacts dominantly with ions and neutrons. The RCF detector contains an active layer, which changes color according to the exposed radiation dose. In reality, they are used in a detector stack, where each layer of the detector acts as a filter for others and is sensitive only to a narrow range of beam energies with energy cutoff, due to the Bragg peak profile of beam–target interaction. Therefore, the simulated proton beam is monochromatic.

III. DEFLECTION EQUATION

The proton deflectometry is based on detecting protons deflected by the magnetic Lorentz force. These deflections determine a distorted image of a proton beam on the detector (i.e., a deflectogram). Rygg [8], Séguin [9] introduced a formula $\sin(\alpha) = (Q/\sqrt{2mE})\|\int \mathbf{B} \times d\mathbf{L}\|$. Here, Q , m , and E are the charge, the mass, and the energy of a proton, respectively, the deflection angle α is defined as an angle between the initial and deflected proton directions, \mathbf{B} is a magnetic field, and $d\mathbf{L}$ is an element of the proton path. This formula is valid only for small deflections, but a generalized deflection equation can be found.

Let \mathbf{v}_0 and \mathbf{v}_f be proton velocities before and after arbitrary deflections by magnetic field \mathbf{B} , respectively. Of course, $\mathbf{v}_0 = \mathbf{v}_f \equiv \mathbf{v}$ since the B -field does not change the proton energy, but it rotates the proton by adding displacement velocity vector $\Delta\mathbf{v}$ [see Fig. 2(a)]. It can be obtained by integrating of the Lorentz force law $m(d\Delta\mathbf{v}/dt) = Q\mathbf{v} \times \mathbf{B}$ into a relationship

$$\Delta\mathbf{v} = - \int \frac{Q}{m} \mathbf{B} \times \mathbf{v} dt = - \int \frac{Q}{m} \mathbf{B} \times d\mathbf{L}. \quad (1)$$

The deflection angle α is defined as an angle between \mathbf{v}_0 and \mathbf{v}_f . If we split the angle α and $\Delta\mathbf{v}$, we get a right triangle with a hypotenuse v and one cathetus $\Delta\mathbf{v}/2$. Using a relationship $\sin(\alpha/2) = \Delta v/(2v)$ and (1), we get the generalized deflection

equation

$$\sin\left(\frac{\alpha}{2}\right) = \frac{Q}{2mv} \left\| \int \mathbf{B} \times d\mathbf{L} \right\| = \frac{Q}{2\sqrt{2mE}} \left\| \int \mathbf{B} \times d\mathbf{L} \right\|. \quad (2)$$

We denote the term $\left\| \int \mathbf{B} \times d\mathbf{L} \right\|$ a B_L parameter, which measures the magnetization of a proton. Its major benefit is that it does not depend on the specific profile of the B -field. The conflicting deflections of the proton balance out, so B_L indicates only the effective value of the B -field. Moreover, greater deflections $\alpha > \pi$ lead to an ambiguous determination of B_L , due to the periodicity of the sine [Fig. 2(b)]. Therefore, the deflection equation (2) gives a maximum limit of B_L for a certain energy, given by $\alpha = \pi$. For proton energy $E = 10$ MeV, the maximum B_L is $91 \text{ T} \cdot \text{cm}$, and for $E = 15$ MeV, the maximum B_L is $112 \text{ T} \cdot \text{cm}$. Larger deflections result in smaller angles between the initial and final directions, and thus, in smaller B_L values [Fig. 2(b)]. B_L is related to the magnetic field-radius product BR used to quantitatively measure the magnetization of the fuel for the MagLIF device [25].

IV. RADIAL PROTON DEFLECTOMETRY

Fig. 1(a) shows a schematic of the radial configuration with described spatial scales. The Z-pinch current flows in the negative direction of the z -axis. Protons, emitted perpendicularly to the Z-pinch, undergo several types of deflections in the B -field region. Fig. 3 illustrates a 10-MeV proton beam, penetrating the B -field of Z-pinch with 1-MA current at 5 mm radius. The dominant radial component of proton velocity causes a strong axial upstream lift [see Fig. 3(a)]. Due to this effect and upstream divergence of the beam (with positive z -velocity component), the protons bounce off radially from the Z-pinch. On the other hand, the protons with downstream divergence (with negative z -velocity component) are focused toward the Z-pinch axis and penetrate deeper into the B -field region toward the Z-pinch. On the other side of the B -field region, the direction of the B -field changes and the axial deflections are inverted, and thus, the protons are pulled downstream. Due to nonhomogeneity of the B -field, the proton beam is not diverted uniformly. Protons, which penetrate deep into the high B -field region, are deflected more than the rest of the beam. Fig. 4 shows typical deflectograms for the radial configuration. Here, we present synthetic deflectograms of the hollow Z-pinch (no B -field inside) in blue, and deflectograms of the full one (linear B -field profile) in red. The results exhibit mirror symmetry by the Z-pinch axis, and thus, deflectograms of the opposite sides of each B -field profile are put together for comparison.

The axial shift and distortions of the deflectograms visibly grow with the increasing B -field magnitude and reveal characteristic sloped structures of higher proton fluence, observed in Z-pinch experiments [17]–[21], together with the low-fluence region in the center of the deflectogram. The sectional histograms of the deflectograms (dotted arrows) in Fig. 5 show that the high-fluence sections are coupled with high B_L values and, thus, are most affected by B -fields. The next section of this paper explains the formation of deflectograms and the high-fluence structures.

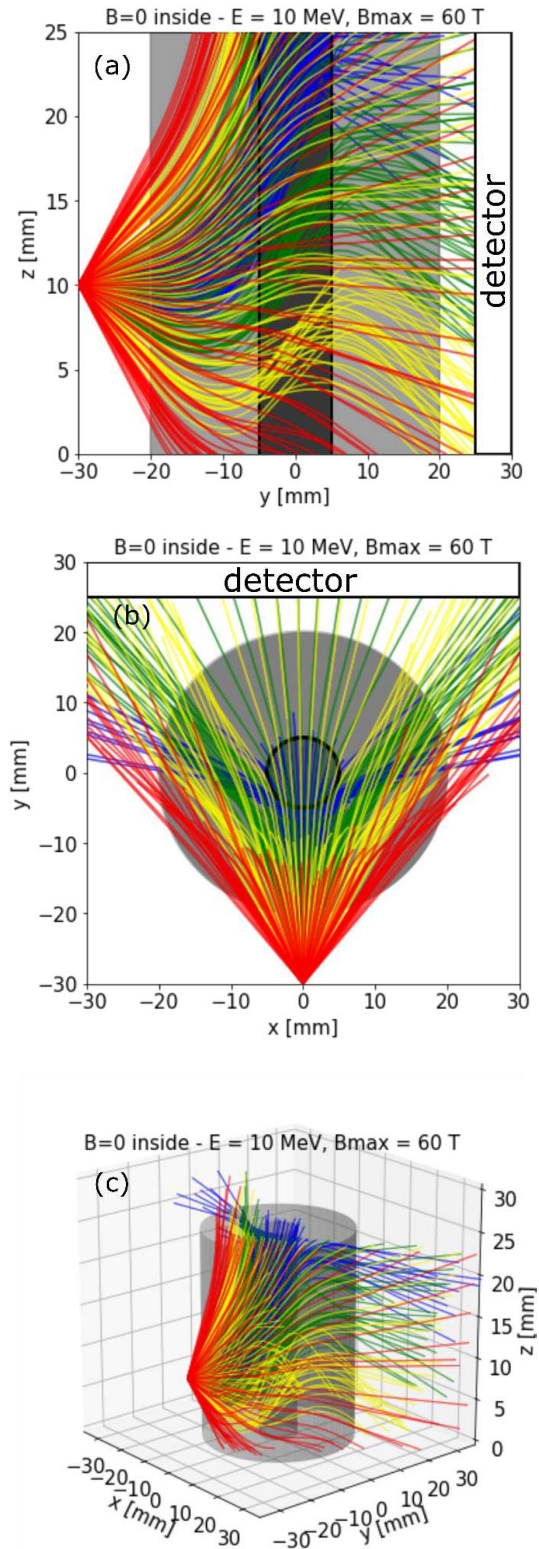


Fig. 3. (a) Side view, (b) top view, and (c) 3-D view of the computed trajectories of the 10-MeV proton beam with 40° divergence in the radial deflectometry. The pinch radius is 5 mm, where 1.5-MA skin current flows.

A. Origin of the Sloped Structures

The sloped structures are very important for the radial proton deflectometry because they are the most noticeable

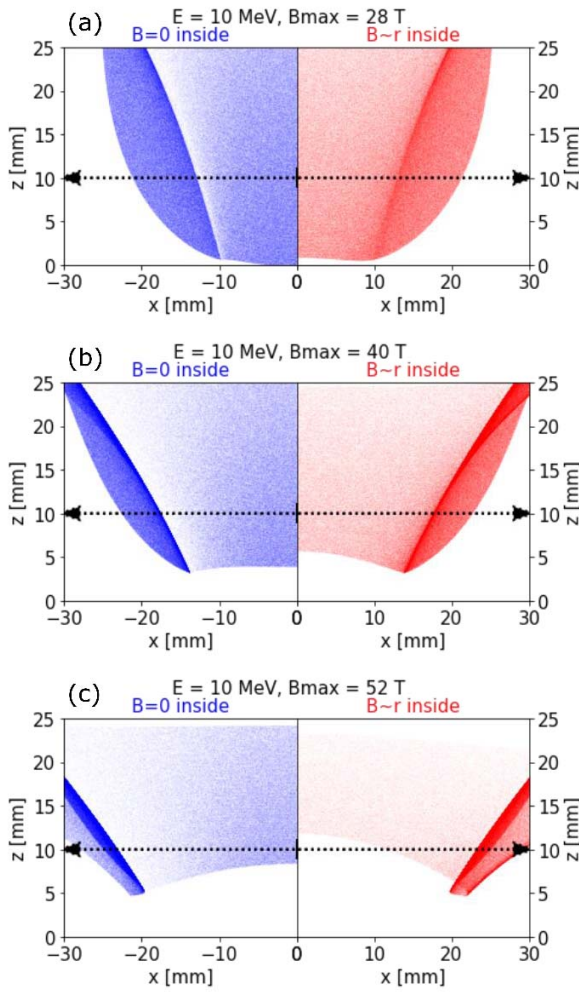


Fig. 4. Synthetic deflectograms of the radial deflectometry of a hollow Z-pinch. Blue: with no B -field inside. Red: a full Z-pinch with a linear profile of the B -field. Pinch currents (a) 0.7, (b) 1, and (c) 1.3 MA at 5-mm radius. The distorted image of the proton beam in the detector creates characteristic sloped high-fluence structures.

manifestation of the azimuthal B -field. The magnitude and distribution of the magnetic fields can be estimated by the correlation of experimental and numerical data, similar to the laser-generated experiments. It is, therefore, crucial to understand the formation of the deflectograms and the sloped structures. First, we discuss how certain parameters influence the shape of the deflectogram.

It has been shown in [18]–[20] that for a given experimental setup, a tilt of the structures is dependent on the magnitude B of the B -field, beam energy E , and radius of the Z-pinch. Too high beam energy E results in small deflections and inherently low signal-to-noise ratio. In consequence of too high B -field, the protons are largely deflected or even reflected, and hence cannot be detected and analyzed. The relationship between these effects is given by (2), and thus, identical deflections occur when $(\int \mathbf{B} \times d\mathbf{L})/\sqrt{E}$ is kept constant. Furthermore, every part of the beam trajectory $d\mathbf{L}$ is coupled with the local condition of the proton gyroradius $r_c(r) = (mv_{\perp}/QB(r)) \propto (\sqrt{E}/B(r))$. The simulations confirm that for constant ratio $(\sqrt{E}/B(r))$ and nonrelativistic energies, the proton deflecto-

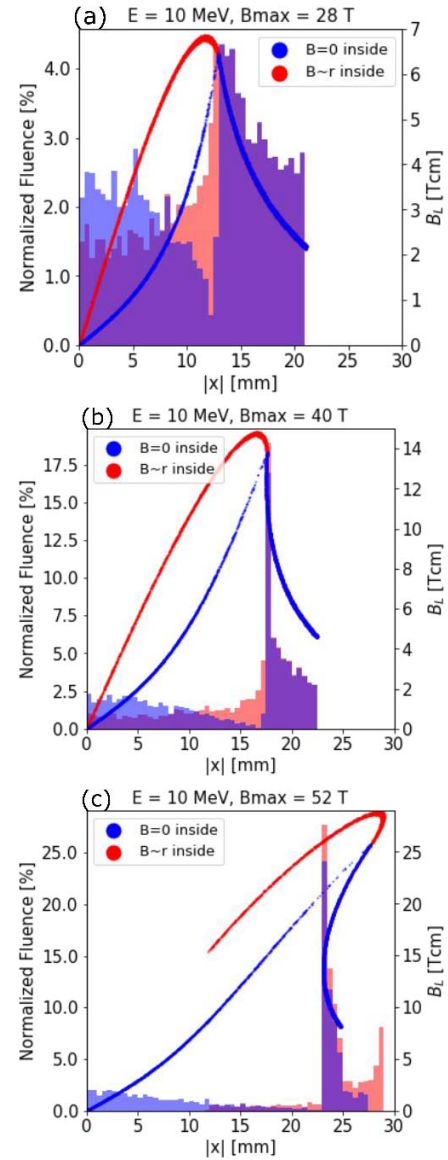


Fig. 5. Histograms of detected protons (bars) in the radial deflectometry with their B_L parameter values (lines) for both B -field profiles along the dotted line in Fig. 4. Purple in histograms: shared values for both profiles. Pinch currents (a) 0.7, (b) 1, and (c) 1.3 MA at 5-mm radius.

grams are identical. This fact might be used for scaling of proton deflectometry experiments. However, for low proton energies, the assumption of insignificant beam–plasma collisions becomes invalid. There is also a limitation on other side of spectrum because (2) does not apply for relativistic protons. Nonetheless, the dependence of beam energy on the B -field implies the requirement of a wide range of proton energies for a range of typical Z-pinch B -field magnitudes. The Z-pinch radius determines the size of the current volume, and therefore, the distance between sloped structures, the position of the maximal B -field magnitude, and also the tilt of the structures. With the increasing beam divergence, protons map larger B -field region, but the shape of the deflectogram does not change.

To further investigate the formation of the radial deflectograms, we vertically extended the B -field region in our model to the infinity. In other words, we excluded the electrodes from our simulations, so they no longer obstruct the path of deflected protons. Also, we increased half-cone beam divergence to 40° . Now, we see the whole picture of the distorted beam in the detector [Fig. 6(a)]. The grid of displacement vectors in Fig. 6(b) allows us to compare the locations of the deflected protons with the locations of the protons as if there has been no B -field. From this point of view, we can elucidate the origin of characteristic sloped structures. Via magnetic deflections by the azimuthal B -field, the protons perform cyclotron rotations. Since the direction of the proton orbits on the one side of the Z-pinch is opposite to the orbits on the other side, the proton beam is unfolded by the magnetic force like a blossom [see Fig. 6(b)]. The protons are pushed away from the high B -field region near the Z-pinch radius, and they create the low proton fluence region in the center of the deflectograms. The particles, which penetrate the closest to the pinch radius, are deflected more than the rest of the beam and pass them. This explains the connection between high density and high B_L in histograms (Fig. 5). When the most deflected protons overlap the less deflected ones, the high-fluence structures, sloped by the cyclotron rotation, are formed. Eventually, these protons might cross the ones at the edge of the beam [see Figs. 4(c) and 6(a)]. In the case of the hollow Z-pinch, there is a narrow region of no proton fluence on the inner side of deflectogram [Fig. 6(a)], which is typical for deflectograms of skin current profile B -field. In case of the Z-pinch with a constant current density, the deflectogram has larger overlap regions and the second density peak in histograms (Fig. 5), due to the additional deflections of the protons by the B -field inside the Z-pinch. However, the orbits of the protons are complicated, so it is difficult to find a clear relationship between the tilt of the structures and the experimental parameters.

It is interesting to study the deflectograms with an indication of the B_L parameter [Fig. 6(c)]. The protons, creating the overlap regions of the deflectogram, have high B_L since these are strongly deflected to the side, and thus, their displacements are not compensated at the rear side of the B -field region. These strongly deflected protons carry the information about the maximum B -field and, to some extent, about the current distribution. The penetration depth and an amount of these protons are discussed in the next section. On the other hand, the protons, directed into the Z-pinch column, have very low B_L ; hence, the overall deflection angle is very low. The direction of these protons is almost perpendicular to the azimuthal B -field. Therefore, the protons are not deflected radially, but they undergo deflections at the front side which are similar to the ones at the rear side of the B -field region [see Fig. 3(a)], due to front–rear symmetry. As a result, these exit the B -field region at roughly the same angle as the initial one (the divergence angle) but with a significant axial shift.

Finally, the overall appearance of the deflectograms for both B -field topologies is quite similar. This indicates that sloped features of the deflectograms are predominantly formed by

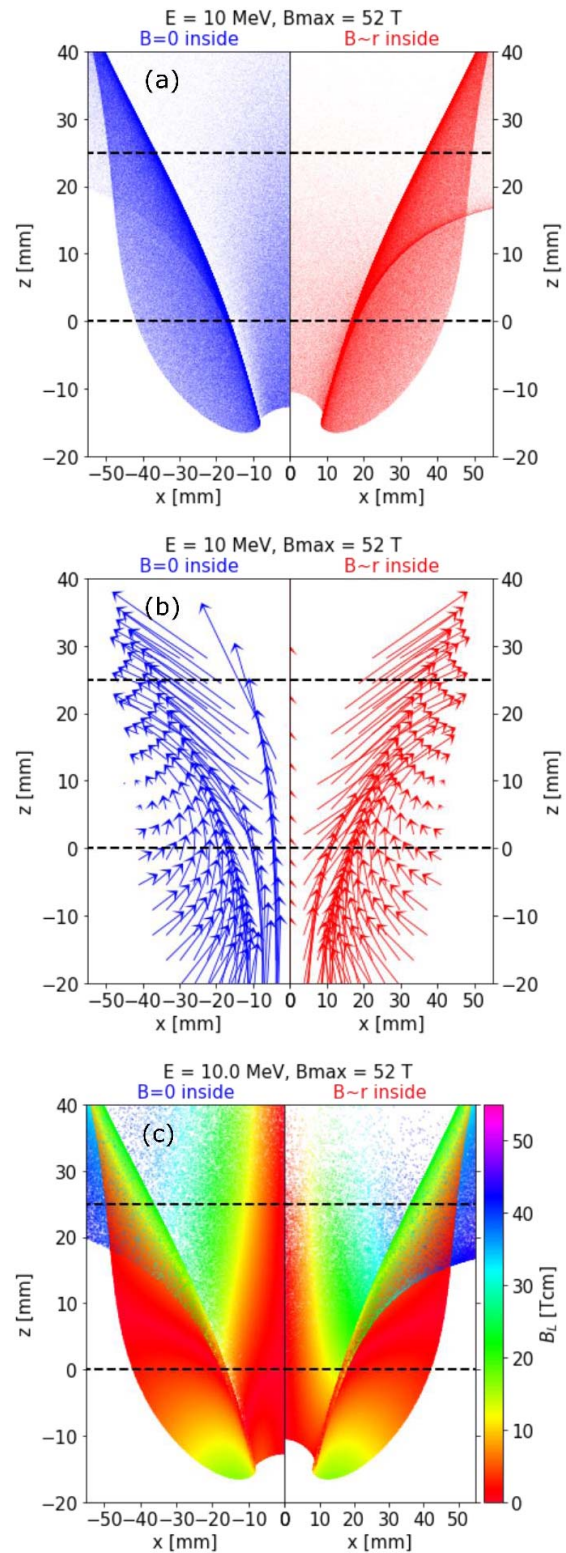


Fig. 6. (a) Deflectograms of the 10-MeV proton beam with increased divergence of 40° , distorted by the B -field of the infinite 1.3-MA Z-pinch with 5 mm radius. Black dashed lines: vertical positions of the absent electrodes. (b) Displacement vectors of the several protons on the detector plane show that the shape of the deflectogram is formed by the cyclotron rotation. (c) Deflectograms with B_L indication show the deflection angles of the protons.

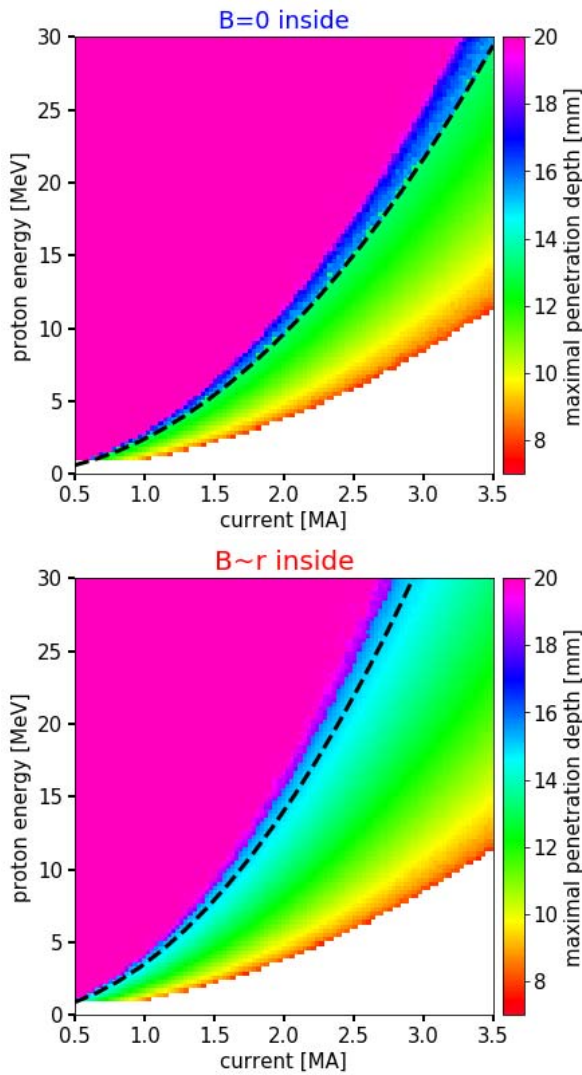


Fig. 7. Maximal penetrated depth δ into the B -field region by the subsequently detected protons according to the beam energy E and the current of the Z-pinch with 5 mm radius. Dashed curve: δ equal to the pinch radius (given by E [MeV] $\cong 2.4I^2$ [MA] for the hollow Z-pinch, and E [MeV] $\cong 3.5I^2$ [MA] for the full Z-pinch).

deflections in the B -field regions, outside of the Z-pinch. Therefore, through analyzing and simulating the sloped structures in the radial configuration of the proton deflectometry, it is possible to conclusively estimate only the B -field magnitude but not its distribution.

B. Penetration Depth of Protons

As seen before, protons are strongly deflected away from the axis in the B -field region outside the Z-pinch column. Only some protons penetrate the B -field enough to reach the interior of the Z-pinch and still be detected on the other side of the B -field region. Another simulation shows how a penetration depth (Fig. 7) depends on the beam energy E and the current I of the Z-pinch with 5 mm radius. The experimental setup is still the same as in the last paragraph. Fig. 7(a) shows a mesh of 100×100 points, where each

point represents a simulation of the situation with certain parameters (i.e., the beam energy and the Z-pinch current). The color of the points indicates a maximal penetrated depth δ into the B -field region (with 20 mm radius) reached by subsequently detected protons. The dashed line indicates the boundary of the penetrated radius, which equals the pinch radius. Points of the same color (i.e., the same penetration depth) form parabolic curves, given by E [MeV] = λI^2 [MA] in accordance with (2). White points imply that no protons are detected by a $100 \text{ mm} \times 25 \text{ mm}$ detector. A boundary of this region determines the minimal energy necessary for protons to be detected in a given experimental configuration. The boundary depends on the constant λ , dimensions of the B -field region, and the position of the proton source, but it does not depend on the pinch radius R_p . Therefore, we can connect λ with a ratio of the gyroradius r_c , coupled with the maximal B -field B_m , and the pinch radius R_p

$$\frac{r_c}{R_p} = \frac{\sqrt{2mE}}{QB_m R_p} = \frac{2\pi\sqrt{2mQE} [\text{eV}]}{Q\mu_0 I} \cong A \frac{\sqrt{E} [\text{MeV}]}{I [\text{MA}]} = A\sqrt{\lambda} \quad (3)$$

where $A = \sqrt{8\pi^2 m}/Q\mu_0^2 10^6 \cong 0.7 \text{ kg}^{1/2} \text{C}^{-1/2} \text{mH}^{-1}$. For our experimental setup, the boundary for the detectable region is given by a relationship E [MeV] $\cong I^2$ [MA], thus $\lambda \cong 1 \text{ eV/A}^2$ and $r_c \cong 0.7R_p \cong 3.5 \text{ mm}$. Strongly magnetized protons have an insufficient energy to go through the B -field region. A criterion for penetrating the Z-pinch radius is roughly $\lambda \cong 2.4 \text{ eV/A}^2$ (i.e., 2.4-MeV protons for 1-MA current) and $r_c \cong 1.1R_p \cong 5.5 \text{ mm}$ for the hollow Z-pinch, and $\lambda \cong 3.5 \text{ eV/A}^2$ (i.e., 3.5-MeV protons for 1-MA current) and $r_c \cong 1.3R_p \cong 6.6 \text{ mm}$ for the full Z-pinch with the constant current profile.

However, Fig. 7(a) does not show how many protons reach the maximum penetration depth δ . In theory, the penetration value can be achieved by a single proton. Therefore, the percentage of protons, which penetrate deeper than the pinch radius ($\delta > 15 \text{ mm}$) and are still detectable, is illustrated in Fig. 8. Due to the beam divergence, some protons in the beam cone are not directed toward the Z-pinch. Thus, they cannot penetrate the Z-pinch even for the highest beam energies, and therefore, the maximum value is not 100%. In order to achieve at least 40% proton penetration, λ must be at least equal to 10 eV/A^2 , and thus, $r_c \cong 2.2R_p \cong 11 \text{ mm}$. In other words, for 1-MA 5-mm-radius Z-pinch, it is recommended to use ≥ 10 -MeV proton source. This justifies the choice of beam energy in our simulations. Nevertheless, these are very rough estimates using a simple model in the given configuration, and therefore, a further investigation is needed, which will be conducted in the future.

V. AXIAL PROTON DEFLECTOMETRY

The experimental setup for the axial deflectometry is illustrated in Fig. 1(b). The proton beam is emitted axially along the Z-pinch axis from a source, located at a 30-mm distance below the lower electrode. The beam divergence is again 20° . The detector is at a 5-mm distance above the B -field region, which has the same dimensions as for the radial deflectometry.

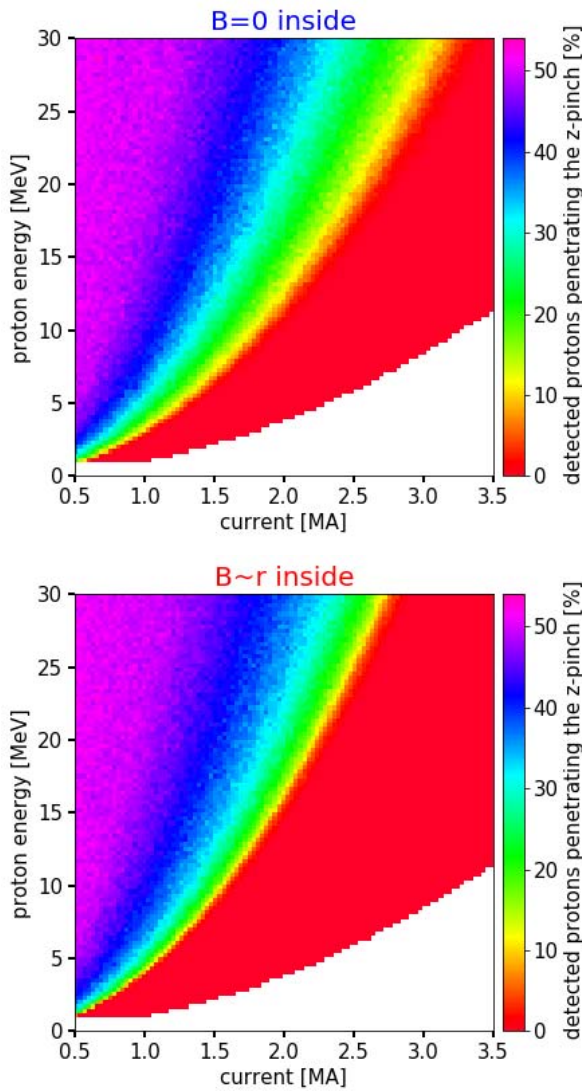


Fig. 8. Percentage of the protons that penetrated the Z-pinch ($\delta > 15$ mm) and reached the detector.

In the axial experimental setup, the electrodes are required to be passable for the proton beam. Accordingly, in our simulations, each electrode is in the form of a $100 \text{ mm} \times 100 \text{ mm}$ regular mesh with 1-mm openings; therefore, one can observe the distortion of the mesh shadow in the detector. Our goal is to simulate the synthetic data similar to the proton radiography experiments of laser-generated plasma (e.g., [3]–[7], [11], [12], [14]). Here, megagauss azimuthal B -fields are generated via nonparallel electron density and temperature gradients ($\nabla n_e \times \nabla T$) at the surface of hemispherical bubbles of laser-generated plasma.

Due to the azimuthal symmetry, there are two fundamental configurations of the direction of the Z-pinch current according to the direction of the proton beam, which determines an orientation of proton deflections. If the protons are passing the B -field region downstream (in the direction of the current), their rotation is directed toward the Z-pinch axis, and the proton beam is focused. If the proton source is located on the

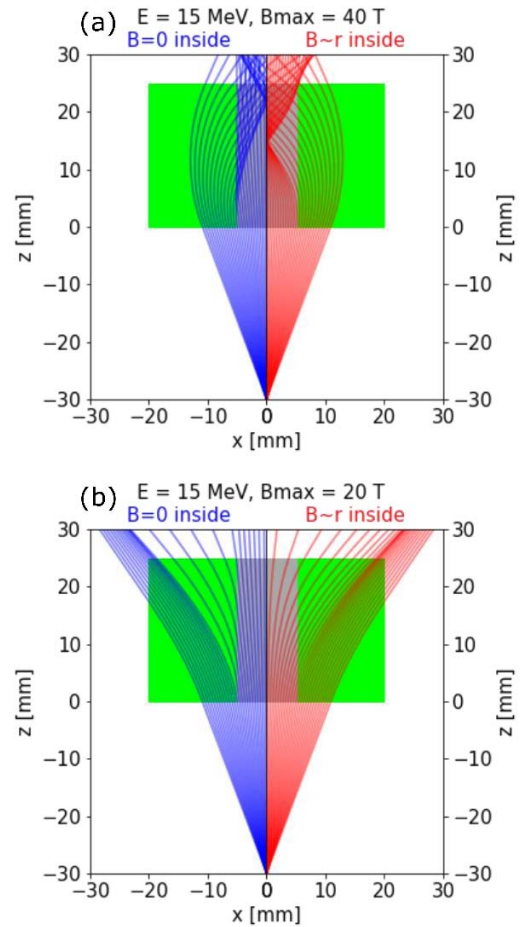


Fig. 9. 2-D scheme of (a) focusing and (b) defocusing proton trajectories in the B -field of the hollow and the full Z-pinch.

Z-pinch axis, the focusing is undesirable for the imaging of the B -fields. In this configuration, the dimensions of the observed features in the deflectograms decrease with the strength of B -field for weak B -fields, but they may increase for strong B -fields, due to overfocusing of the proton trajectories [see Fig. 9(a)]. Analysis of the focusing deflectometry might be ambiguous. Therefore, we consider the protons that penetrate the B -field upstream (in the opposite direction of the current). Their orbits diverge, and the proton beam is defocused away from the Z-pinch axis. Fig. 9(b) shows several defocusing proton trajectories. The direction of the proton orbits stays the same along its path. The deflections are not equalized, so the deflection angles and, hence, dimensions of deflectograms are larger than those in the radial case. For the better illustration of all aspects of this method, we increased the proton energy to 15 MeV in our model.

A. Origin of the Ring Structure

The great advantage of the axial deflectometry compared to the radial deflectometry is that the proton beam does not penetrate the outer B -field regions in order to map the B -field topology inside of the Z-pinch. Protons, passing through the inside of the hollow Z-pinch (no B -field inside),

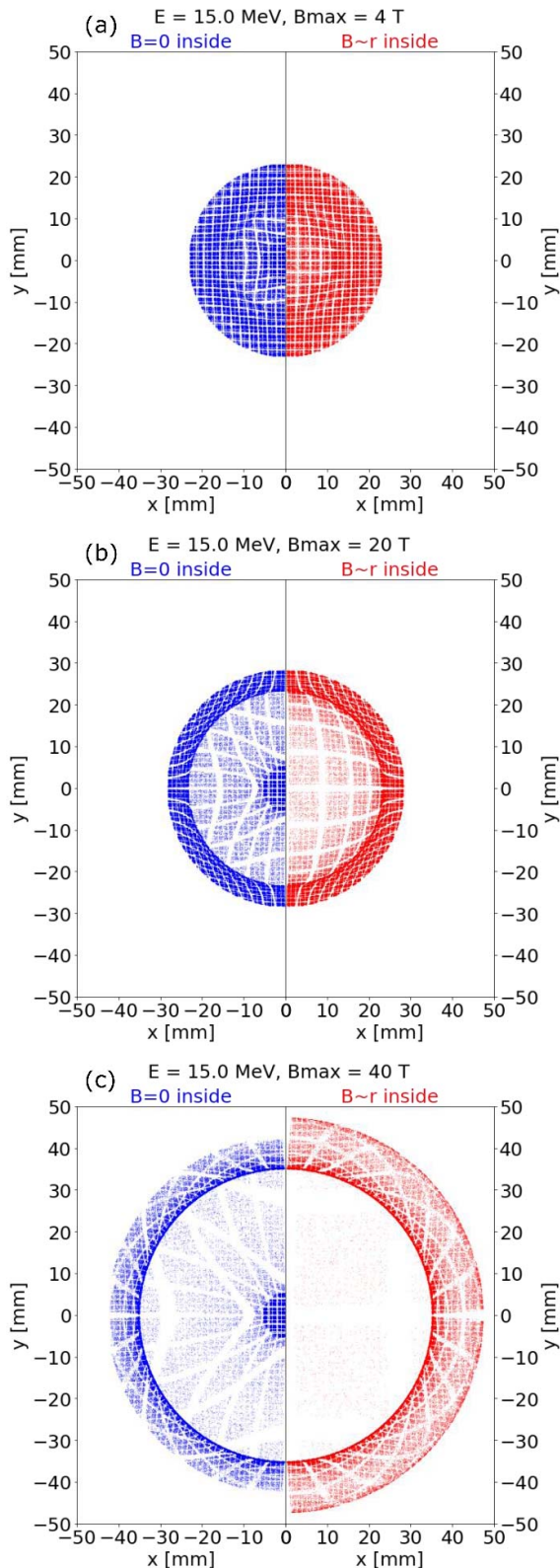


Fig. 10. Synthetic radiographs of the defocused 15-MeV proton beam in the B -fields of hollow and full Z-pinches. Pinch currents (a) 0.1, (b) 0.5, and (c) 1 MA at 5-mm radius. Protons pass first through a cathode mesh and then an anode mesh. Deflections of the protons in the B -field create a distorted shadow of the cathode mesh. The anode mesh casts an undistorted shadow since there is no B -field above it.

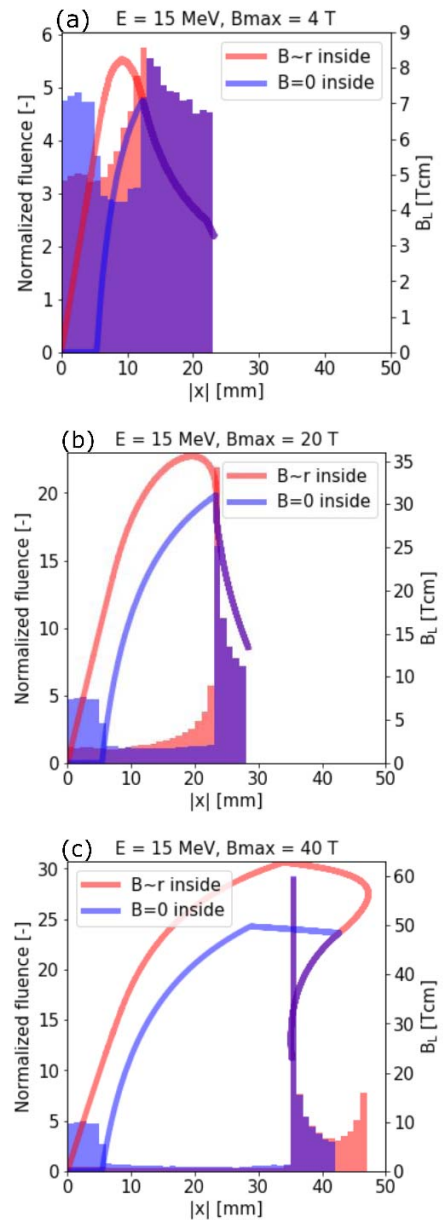


Fig. 11. Histograms of detected protons (bars) in the axial deflectometry with their B_L parameter values (lines) for both B -field profiles according to their locations in the deflectograms. Purple in histograms: shared values for both profiles. Pinch currents (a) 0.1, (b) 0.5, and (c) 1 MA at 5-mm radius.

are not deflected and create an undistorted shadow of the cathode mesh in the center of the deflectogram in Fig. 10. This contrasts with proton trajectories inside the full Z-pinch with constant current density. The dimensions of the Z-pinch determine the size of the undistorted shadow. The magnetic force defocuses all protons; however, due to the nonhomogeneity of the B -field, the deflection angles are not equal. Protons, emitted into the high B -field region near the pinch radius, are deflected more than the rest of the beam and create a high-fluence ring in the deflectograms of both B -field profiles

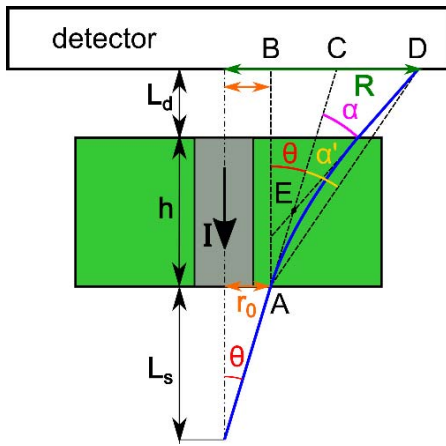


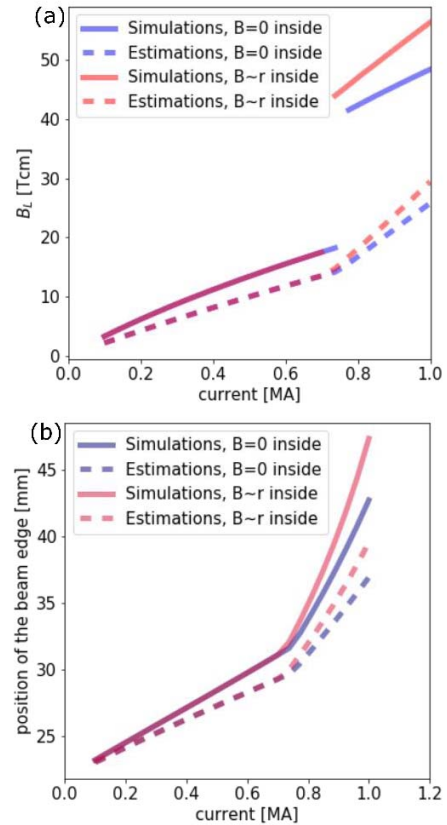
Fig. 12. Scheme for the estimation of the deflection angle.

(see Figs. 10 and 11). The ring is equivalent to the sloped structures for radial deflectometry. Due to the shift of strongly deflected protons, a depleted region develops inside the ring. The histograms with a B_L indication (Fig. 11) show the shift of the high-fluence ring with the increasing B -field magnitude. The ring is coupled with the maximum deflections, hence, with the maximum B_L values. Eventually, protons of the ring surpass the ones in the edge of the beam and the deflectogram flips over, which can be observed by the inverted pattern of the mesh shadow [Fig. 10(c)]. For the linear B -field profile, a second peak appears in the proton fluence [Fig. 11(c)], due to additional deflections inside the Z-pinch. Analogously to the radial deflectometry, the outer regions of the deflectograms are similar for both profiles, because the majority of the protons goes only through the B -field regions outside the Z-pinch. Due to significant differences between deflectograms, it is possible to determine both the strength and the profile of the B -field by comparing the simulations and experimental data. Unlike in the radial deflectometry, the orbits of the protons are simple, until deflection angles $\alpha < \pi/2$. Therefore, we can study the B -fields directly and estimate B_L by measuring the dimensions of the deflectograms. We demonstrate this method by analyzing our synthetic data.

B. Estimation of the B_L Parameter

The B_L parameter ($B_L \equiv \int \mathbf{B} \times d\mathbf{L}$) is crucial for the proton deflectometry since it is connected with deflections by (2). It can be estimated, provided the curvature of the proton trajectories is small. Fig. 12 shows the geometry of the problem. For small deflections, the deflection angle α of the triangle CDE becomes the angle α' of the right triangle ABD, because the curved trajectory becomes the AD line segment. To evaluate the B_L parameter of a proton, we must know the position of a proton's image in the detector R and the position of the proton entering the B -field r_0 .

The most interesting structure of the deflectogram is surely the high-fluence ring, which is coupled with the maximum B -field. However, the ring is created by protons entering the B -field near the pinch radius ($r_0 \cong R_p$), which is usually unknown. On the other hand, the entering position of the edge


 Fig. 13. (a) Comparison of the B_L values. Solid lines: calculated during the simulations. Dashed lines: ones estimated by measurements of the dimensions of the synthetic deflectograms. (b) Position of the beam edge in the deflectogram according to the pinch current.

of the beam is known because it is determined by the beam divergence θ . Therefore, we can calculate the B_L parameter of the beam border if we assume deflection angle $\alpha \approx \alpha'$, use (2) and

$$\tan(\alpha' + \theta) = \frac{R - r_0}{h + L_d}. \quad (4)$$

where h is the height of the B -field region, L_d is the distance of the detector, L_s is the distance of the proton source from the B -field region, and finally, $r_0 = L_s \tan(\theta)$. In Fig. 13(a), there is a comparison of two graphs, where the B_L parameter is first calculated directly by the simulations along the proton trajectories, and then estimated by measuring of the displacement of the proton beam in the synthetic deflectograms. The values are comparable only as long as the magnetic field is weak enough. Then, the curvature of the trajectory is no longer negligible, but more importantly, the deflectogram image turns over [see Fig. 10(c)], and its edge is connected to the high-fluence ring instead of the initial beam edge. This is also evident in Fig. 13(b), since the high B_L of the protons in the ring causes their stronger deflections and displacements at the detector. With increasing the distance of the detector, the error caused by the curvature of the trajectories decreases, but at the same time, the shift of the ring increases. Finding the favorable parameters will be the subject of the future research.

A highly collimated beam covers only a small area of the B -field, thus there is a small difference between the deflections of the protons, and the turning over is no longer a problem. Moreover, it allows the pinpoint measurements of the certain area of the B -fields. Of course, if the Z -pinch is hollow and there is no B -field inside, the placing of the collimated proton beam on the Z -pinch axis is undesirable. This seems promising and, in fact, we have already used this method for similar B_L measurements of deflections of highly collimated multi-MeV deuteron beams in MA deuterium gas-puff Z -pinch, published in [26].

VI. CONCLUSION

Using our numerical code, we studied a promising diagnostic method for investigating B -fields in dense Z -pinch plasmas, i.e., proton deflectometry. In this method, a proton beam is emitted into unknown B -fields, and then, its distorted image (a deflectogram) at the detector is studied. Only a few experiments were performed by this method in Z -pinch plasmas, therefore, we intended to show typical examples of results for radial and axial configurations. We showed that information about the B -field strength and profile is embedded in the deflectograms. Moreover, we elucidated a formation of important features of the experimental data, i.e., the sloped structures for the radial configuration and the ring for the axial configuration. We explained that these structures are created by highly deflected protons in nonhomogeneous B -fields of the Z -pinch. We characterized the magnetic deflections by the B_L parameter, coupled with an effective average B -field along the proton path. Analyzing the synthetic deflectograms for the axial configuration, we were able to estimate a value of this parameter, and thus to measure the strength of the deflections.





REFERENCES

- [1] M. Borghesi *et al.*, "Proton imaging: A diagnostic for inertial confinement fusion/fast ignitor studies," *Plasma Phys. Controlled Fusion*, vol. 43, no. 12A, p. A267, 2001.
- [2] M. Borghesi *et al.*, "Laser-produced protons and their application as a particle probe," *Laser Part. Beams*, vol. 20, no. 2, pp. 269–275, 2002.
- [3] A. J. Mackinnon *et al.*, "Proton radiography as an electromagnetic field and density perturbation diagnostic (invited)," *Rev. Sci. Instrum.*, vol. 75, no. 10, pp. 3531–3536, 2004.
- [4] C. A. Cecchetti *et al.*, "Magnetic field measurements in laser-produced plasmas via proton deflectometry," *Phys. Plasmas*, vol. 16, no. 4, p. 043102, 2009.
- [5] L. Romagnani *et al.*, "Dynamics of electric fields driving the laser acceleration of multi-MeV protons," *Phys. Rev. Lett.*, vol. 95, no. 19, p. 195001, 2005.
- [6] L. Romagnani *et al.*, "Proton probing measurement of electric and magnetic fields generated by ns and ps laser-matter interactions," *Laser Part. Beams*, vol. 26, no. 2, pp. 241–248, 2008.
- [7] A. Macchi, M. Borghesi, and M. Passoni, "Ion acceleration by superintense laser-plasma interaction," *Rev. Mod. Phys.*, vol. 85, no. 2, p. 751, 2013.
- [8] J. R. Rygg *et al.*, "Proton radiography of inertial fusion implosions," *Science*, vol. 319, no. 5867, pp. 1223–1225, 2008.
- [9] F. H. Séguin *et al.*, "Time evolution of filamentation and self-generated fields in the coronae of directly driven inertial-confinement fusion capsules," *Phys. Plasmas*, vol. 19, no. 1, p. 012701, 2012.
- [10] C. K. Li *et al.*, " D^{-3} He proton spectra for diagnosing shell ρR and fuel T_i of imploded capsules at OMEGA," *Phys. Plasmas*, vol. 7, no. 6, pp. 2578–2584, 2000.
- [11] C. K. Li *et al.*, "Monoenergetic proton backlighter for measuring E and B fields and for radiographing implosions and high-energy density plasmas (invited)," *Rev. Sci. Instrum.*, vol. 77, no. 10, p. 10E725, 2006.
- [12] C. K. Li *et al.*, "Observation of megagauss-field topology changes due to magnetic reconnection in laser-produced plasmas," *Phys. Rev. Lett.*, vol. 99, no. 5, p. 055001, 2007.
- [13] C. K. Li *et al.*, "Monoenergetic-proton-radiography measurements of implosion dynamics in direct-drive inertial-confinement fusion," *Phys. Rev. Lett.*, vol. 100, no. 22, p. 225001, 2008.
- [14] C. K. Li *et al.*, "Proton radiography of dynamic electric and magnetic fields in laser-produced high-energy-density plasmas," *Phys. Plasmas*, vol. 16, no. 5, p. 056304, 2009.
- [15] C. K. Li *et al.*, "Charged-particle probing of X-ray-driven inertial-fusion implosions," *Science*, vol. 327, no. 5970, pp. 1231–1235, 2010.
- [16] M. J.-E. Manuel *et al.*, "Source characterization and modeling development for monoenergetic-proton radiography experiments on OMEGA," *Rev. Sci. Instrum.*, vol. 83, no. 6, p. 063506, 2012.
- [17] M. J.-E. Manuel *et al.*, "Mapping return currents in laser-generated Z -pinch plasmas using proton deflectometry," *Appl. Phys. Lett.*, vol. 100, no. 20, p. 203505, 2012.
- [18] D. Mariscal *et al.*, "Measurement of pulsed-power-driven magnetic fields via proton deflectometry," *Appl. Phys. Lett.*, vol. 105, no. 22, p. 224103, 2014.
- [19] D. A. Mariscal, "Investigation of magnetic field and current topology in Z -pinch plasmas," Ph.D. dissertation, Center Energy Res., Univ. California, San Diego, San Diego, CA, USA, 2015.
- [20] F. N. Beg, "Assessment of proton deflectometry for exploding wire experiments," Center Energy Res., Univ. California, San Diego, San Diego, CA, USA, Tech. Rep. UCSD 2009-0512, Sep. 2013.
- [21] M. S. Schollmeier, A. B. Sefkow, M. Geissel, P. K. Rambo, and J. Schwarz, " Z -petawatt driven ion beam radiography development," Sandia Nat. Laboratories (SNL-NM), Albuquerque, NM, USA, Tech. Rep. SAND2013-7201, 2013.
- [22] C. K. Birdsall and A. B. Langdon, *Plasma Physics via Computer Simulation*. Boca Raton, FL, USA: CRC Press, 2004.
- [23] J. D. Huba, "NRL (Naval Research Laboratory) plasma formulary, revised," Naval Res. Lab., Washington, DC, USA, Tech. Rep. NRL/PU/6790-16-614, 2016.
- [24] S. Karsh, "High-intensity laser generated neutrons," Ph.D. dissertation, Faculty Phys., LMU, Munich, Germany, 2002.
- [25] P. F. Schmit *et al.*, "Understanding fuel magnetization and mix using secondary nuclear reactions in magneto-inertial fusion," *Phys. Rev. Lett.*, vol. 113, no. 15, p. 155004, 2014.
- [26] D. Klir *et al.*, "Ion acceleration mechanism in mega-ampere gas-puff z -pinches," *New J. Phys.*, vol. 20, no. 5, p. 053064, 2018.

Authors' photographs and biographies not available at the time of publication.

G.2 Article: Klir et al., PPCF (2020)

Spatial distribution of ion emission in gas-puff z-pinches and dense plasma foci

D Klir^{1,7} , A V Shishlov², S L Jackson³, V A Kokshenev², P Kubes¹ , K Rezac¹, A R Beresnyak³, R K Cherdizov², J Cikhardt¹ , B Cikhardtova¹, G N Dudkin⁴, J T Engelbrecht³, F I Fursov², J Kaufman⁵, J Krasa⁵ , J Kravarik¹, N E Kurmaev², V Munzar¹, N A Ratakhin^{2,4}, K Turek⁶ and V A Varlachev⁴

¹ Czech Technical University in Prague, Faculty of Electrical Engineering, 16627 Prague 6, Czech Republic

² Institute of High Current Electronics SB RAS, Tomsk, 634055, Russia

³ Plasma Physics Division, U.S. Naval Research Laboratory, Washington, DC 20375 United States of America

⁴ National Research Tomsk Polytechnic University, Tomsk, 634050, Russia

⁵ Institute of Physics, Academy of Sciences of Czech Republic, 18221 Prague 8, Czech Republic

⁶ Nuclear Physics Institute, Academy of Sciences of Czech Republic, 18086 Prague, Czech Republic

E-mail: klirdani@fel.cvut.cz

Received 25 September 2019, revised 15 November 2019

Accepted for publication 8 January 2020

Published 29 January 2020



CrossMark

Abstract

Mega-ampere dense plasma foci and deuterium gas-puff z-pinches can accelerate deuterons to multi-MeV energies. Diagnostic measurements of the properties of these ions provide information about ion acceleration in z-pinch plasmas. In particular, the results from ion pinhole cameras seem to be useful for the discussion of ion acceleration mechanisms. Recently, we have used various configurations of ion pinhole cameras in deuterium gas-puff experiments on the GIT-12 generator at the Institute of High Current Electronics in Tomsk and on the HAWK generator at the US Naval Research Laboratory in Washington. The stack of radiochromic films and CR-39 solid-state nuclear track detectors recorded deuterons with energies up to 30 MeV. From our ion diagnostics, we obtained the spatial distribution of the ion source and the ion-beam divergence during the ion emission. This ion-beam divergence was found to decrease with increasing deuteron energy. At 20 MeV, the divergence of each of the individual micro-beams that composed the ion source was on the order of 10 mrad. The deflection of each micro-beam due to the azimuthal magnetic and/or radial electric fields resulted in radial stripes observed by the beam-profile detectors. By analyzing the ion pinhole images, we found that the deuterons were emitted both from a central spot and from a ring-shaped region with a rather large diameter, on the order of 1 cm. The origin and particular diameter of this ring is attributed to the geometry of the electrodes and to the distribution of the current density before the disruption.

Keywords: z-pinch, dense plasma focus, multi-MeV deuterons, acceleration mechanism, plasma diagnostics

(Some figures may appear in colour only in the online journal)

1. Introduction

Deuterium z-pinches and dense plasma foci (DPFs) have been researched as efficient sources of fast neutrons [1–5]. A large number of neutrons originating from the $D(d,n)^3\text{He}$ reaction

were observed in linear deuterium pinches in the 1950s [6–8]. However, these neutrons were not of thermonuclear origin (see [9, 10]), i.e. they were not produced by the fusion of deuterons accelerated by elastic collisions in high-temperature plasmas. At the very beginning of fusion research, the dominant fraction of neutrons observed in z-pinches was explained as arising from deuterons that were accelerated to fusion-inducing energies by

⁷ Author to whom any correspondence should be addressed.

transient electric fields [6, 8]. Since then, many experiments with various diagnostic tools have been performed [1, 11, 12], and many hypotheses have been proposed to explain the acceleration of deuterons in z-pinches and DPF [13, 14]. Recently, state-of-the-art numerical codes have been used to solve this very old problem in plasma physics [15–17]. Despite these efforts, the exact acceleration mechanism has still not been resolved [14].

One of the unexplained results was the observation of ring-like structures in ion pinhole images. We suppose that a better understanding of the intriguing ion pinhole images and the correct answer to the question of where ions are accelerated could help with identification of the acceleration mechanism. Interestingly, characteristic annuli were observed by ion pinhole cameras both in dense-plasma foci [18–25] and in gas-puff z-pinches [26–28]. This is an important result, since it indicates that the acceleration of high-energy ions can take place in an analogous way in both devices. Taking into account other similarities, such as the correlation of ion and neutron emission with an $m = 0$ disruption [14], the acceleration mechanism seems to be quite general and might occur in various current-carrying plasmas. From this point of view, the explanation of the ring-like structures in pinhole images is of great importance.

40 years ago, Filippov *et al* [18] suggested that the annuli were created by deuterons which were emitted from an on-axis source and then bent towards the pinhole by the magnetic fields of the current sheath. The second hypothesis was proposed by Bertalot with his colleagues [19], who claimed that ions originated from ‘many point sources localized off-axis, possibly on the surface of the plasma region’. In other words, Bertalot was of the opinion that the rings in the pinhole images reflected the spatial distribution of the original ion source. Both research groups did not prove their hypotheses. Unambiguous interpretation of the ring-shaped patterns has not been provided, even in other DPF experiments with single or multi-pinhole cameras [20–25]. The main difficulty was that the study of ion emission was inevitably connected to the knowledge of the electric and magnetic fields in z-pinches or DPF. Since the effect of the magnetic fields on the ion trajectories was not known, the experimental results were not sufficient to distinguish even between the two completely different hypotheses mentioned above. To solve this issue, it is necessary to obtain comprehensive information about the ion emission. For this purpose, we have carried out deuterium gas-puff experiments on the GIT-12 and HAWK microsecond generators at 3 MA and 0.7 MA current, respectively. GIT-12 is unique in the acceleration of deuterons to unprecedented high energies up to 40 MeV [26, 27, 29, 30]. The high deuteron energies enable us to diagnose the ions by several novel (to z-pinches) techniques (nuclear methods [30], radiochromic film (RCF) stack spectroscopy [31, 32], etc) and, therefore, to obtain comprehensive information about the spatial, spectral, and temporal properties of the accelerated ions.

In this paper, we will present results from various configurations of ion pinhole cameras. Section 2 describes the z-pinch load used in our experiment on GIT-12. Section 3 introduces characteristic results from the ion pinhole cameras. Ion pinhole images with spectral resolution are presented in section 4. Section 5 brings forward results from a multi-

pinhole camera which provided some conclusions about the anisotropy of the ion emission. These conclusions about the anisotropy were confirmed by three-pinhole cameras with beam-profile detectors which are described in section 6. Section 7 correlates pinhole images with neutron yields. Section 8 deals with the origin of ion rings of a particular diameter and presents the results from a pinhole camera on the HAWK generator. Finally, section 9 summarizes the most important points of this paper with respect to ion acceleration mechanisms.

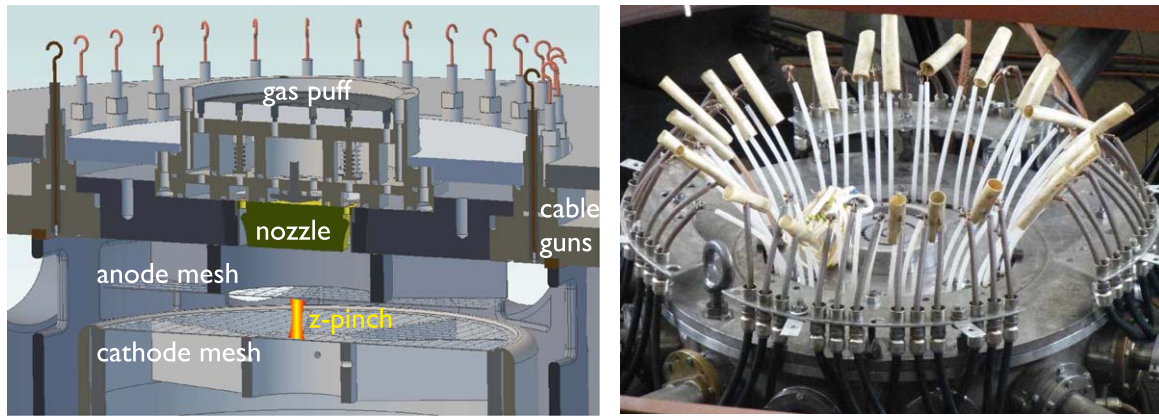
2. Experimental set-up and diagnostics on GIT-12 and HAWK

2.1. GIT-12 generator at the Institute of High Current Electronics in Tomsk

Z-pinch experiments with deuterium gas puffs have been carried out on the GIT-12 generator at a 3 MA current and microsecond rise-time [33]. In order to form a homogeneous, uniformly conducting layer at a large initial radius, an inner 8 cm diameter deuterium gas puff was surrounded by an outer hollow cylindrical plasma shell [5, 29]. The plasma shell, consisting of hydrogen and carbon ions, was formed at a diameter of 35 cm by 48 cable guns (see figure 1). When the plasma guns were triggered 1.7–1.8 μs before the onset of the main current, the linear mass of the plasma shell was estimated to be $5 \mu\text{g cm}^{-1}$.

As shown in figure 1, the nozzle was placed on the anode side 3.0–3.6 cm from the anode mesh. The anode–cathode gap varied between 2.0 and 2.8 cm for most of the shots. The diameter of the cathode was 32 cm, and the inner diameter of the return-current conductor was approximately 37 cm. Both the anode and cathode were formed by a stainless-steel mesh with a transparency of about 70%. The optimal time delay between the valve opening and the triggering of the generator varied between 250 and 330 μs . Due to the relatively long injection time and multiple reflections of the gas from the mesh electrodes, the gas was spread over a large area and the gas-density profile was expected to be quite smooth (see also the 2D ANSYS FLUENT CFD simulation in figure 1 in [26]). The total linear mass of deuterium in the single shell (annular) gas puffs was usually between 80 and 120 $\mu\text{g cm}^{-1}$. During implosion, it is assumed that some mass is lost through the meshes.

The initial parameters mentioned above led to a deuterium gas-puff implosion that lasted about 700 ns (measured from the time at which the load current reached 100 kA). Soft x-ray images showed a DPF-like (smooth and curved) imploding layer that was stable until it reached a radius of 4 mm (see figure 2(a)). The z-pinch column stagnated at a current of 2.7 MA. During stagnation, $m = 0$ instabilities became more pronounced near the anode (see figure 2(b)). At $t = 0$, the disruption of an $m = 0$ neck occurred [26], and a bright spot was detected by the radial streak camera between 0 and 10 ns (see figure 2(d)). The moment of the z-pinch disruption corresponded to the time of emission of high



(a) Schematic diagram of the experimental arrangement with electrodes, gas-puff hardware, and cable guns. (b) Photograph of the experimental chamber with 48 cable guns.

Figure 1. Experimental arrangement of the electrode system, gas-puff hardware, and cable guns on GIT-12.

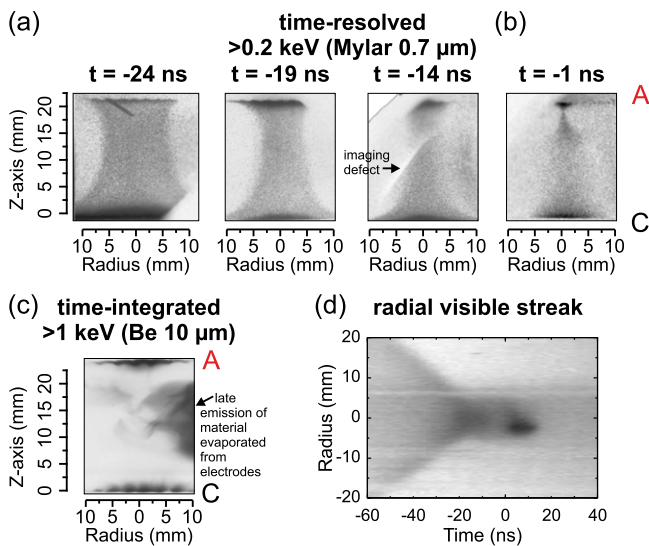


Figure 2. Time-resolved soft x-ray images of a deuterium gas-puff z-pinch on shots (a) 1771 and (b) 1764. The anode is at the top and the cathode is at the bottom. Note: The x-ray pinhole framing camera did not have a full view of the anode mesh at the z-pinch axis. (c) Time-integrated soft x-ray image and (d) radial streak-camera image of a deuterium gas-puff z-pinch on shot 1771. The time $t = 0$ corresponds to the sharp onset of a γ -ray pulse and a bright spot in the streak camera image. Shot 1771 with $(2.0 \pm 0.4) \times 10^{12}$ neutrons.

energy (>2 MeV) bremsstrahlung radiation and the main neutron pulse [5, 26]. The average neutron yield was 2×10^{12} per shot.

The implosion, stagnation, and disruption of the deuterium gas-puff z-pinch were observed by a comprehensive set of diagnostics. The electrical, optical, x-ray, gamma, and neutron detectors were described in [5], and ion diagnostics were presented in [26, 30]. Several new ion detectors will be introduced later in this article.

2.2. HAWK generator at the Naval Research Laboratory in Washington

HAWK is a high-inductance (607 nH) generator located at the US Naval Research Laboratory in Washington [34]. The pulsed-power architecture of the HAWK generator is similar to that of GIT-12. At an 80 kV charging voltage, HAWK stores an energy of 0.22 MJ and delivers a 0.64 MV, 0.7 MA pulse to a load within a 1.2 μ s rise time. Since 2017, the HAWK generator has been used to drive a DPF. The arrangement of the electrode system is presented in figure 10(a) in section 8. The anode and cathode diameters were 10.5 and 17.3 cm, respectively. In the DPF configuration on HAWK, 3 Marshall guns injected a deuterium plasma shell radially between coaxial electrodes. The total plasma shell mass was $1 \mu\text{g cm}^{-1}$. The additional mass of neutral deuterium gas was puffed by an on-axis, 3.8 or 4.45 cm diameter valve placed inside the central anode [35]. In a recent experimental campaign with reproducible high neutron yields of about 3×10^{10} , the mass per unit length was about $30 \mu\text{g cm}^{-1}$. Unlike the experimental set-up on GIT-12, there was no cathode mesh on HAWK. Therefore the initial set-up of the HAWK load might be considered similar to the radial implosion phase of a dense plasma focus where the length of the imploding plasma column is not fixed [36]. A detailed description of the experimental set-up is the subject of an upcoming paper [37]. Preliminary results were published in [27, 38]. Recent data from an ion pinhole camera on HAWK will be presented at the end of this paper in section 8. In the following sections 3–7, we will present the results from ion diagnostics on GIT-12.

3. Characteristic annuli in ion pinhole images

Multi-MeV deuterons were observed in the GIT-12 z-pinch experiments first in 2013 [29]. Since then, a large number of

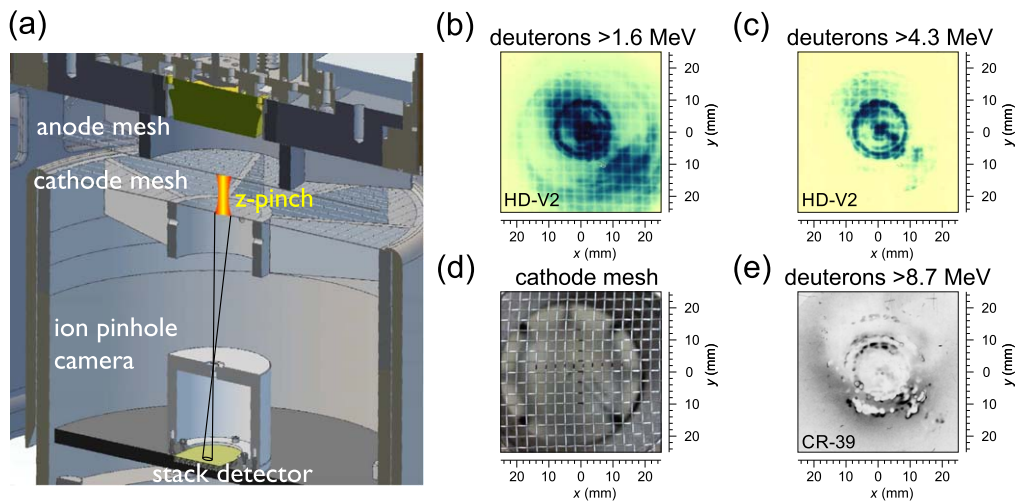


Figure 3. Measurement of the spatial distribution of the ion source. (a) Schematic showing the arrangement of the axial ion pinhole camera with a magnification of 0.6, a pinhole diameter of 0.5 mm, and a spatial resolution of 1.3 mm. (b)–(c) Axial ion pinhole images recorded by the first and second HD-V2 GafChromic films in the stack. (d) On-axis view of the cathode mesh. (e) Axial ion pinhole image recorded by a CR-39 TasTrak detector. Shot no. 1750 with $(1.2 \pm 0.3) \times 10^{12}$ neutrons. Spatial scales correspond to the plane of the cathode mesh. The detector darkness is proportional to the ion flux.

ion detectors have been used to characterize the ion emission and to investigate the ion acceleration mechanism. Among these diagnostic measurements, a characteristic structure was observed in the ion pinhole images obtained. Although the origin of this structure was not clear, we supposed it was connected to the ion acceleration mechanism and that an ion pinhole camera would be helpful in identifying that mechanism. In most of the shots, we placed the ion pinhole camera on the z-pinch axis below the cathode mesh. The arrangement of the experimental set-up and typical results are shown in figure 3. The ion pinhole camera used a stack consisting of absorbers, RCFs, and solid-state nuclear track detectors. Deuterons with different energies were stopped in different layers. Ions with lower energies were stopped at the beginning of the stack, whereas deuterons with higher energies penetrated the first detectors and got stopped in the deeper layers of the stack. The minimum deuteron energy required for each layer was evaluated by the stopping and range of ions in matter (SRIM) code [39]. This minimum energy value is shown along with each ion image presented in this paper. The signal in a particular ion detector layer within the stack was mainly due to ions near their Bragg peak. But more energetic deuterons that largely passed through the layer also contribute to the total dose absorbed in that layer. As ion detectors, we used FWT-60 RCFs, HD-V2 and EBT-3 GafChromic films, and CR-39 TasTrak solid-state nuclear track detectors. Each of these detectors has different properties. Therefore it proves beneficial to use them simultaneously to obtain complementary information. The advantage of RCFs is that they are relatively thin and can provide a high dynamic range for radiation dose detection, namely 0.1–20 Gy (EBT-3), 10–1000 Gy (HD-V2), and 0.5–200 kGy (FWT-60). As for CR-39 detectors, an important property is that they are insensitive to x-rays and electrons [40]. In addition to that, CR-39 detectors enable us to detect individual ions and distinguish different ion species. Therefore, we used CR-39

detector layers mainly at the bottom end of each detector stack (see e.g. figure 4(a)). In our experiment, CR-39 detectors were usually etched for 2 h in 30% KOH at 70 °C. At higher ion fluences detected by CR-39, we needed to be mindful of saturation effects and consequent artifacts (see [41] and compare figures 3(c) with (e)). The data from the CR-39 detectors, particularly the agreement between the signals on CR-39 and on adjacent RCFs, indicated that we could safely neglect the contribution of x-rays and electrons to the doses measured in HD-V2 GafChromic films fielded in ion pinhole cameras placed below the cathode.

As shown in figures 3(b)–(c), the characteristic feature recorded by the pinhole images was ion emission from both a central spot and ring-like structures of a relatively large diameter. At low deuteron energies, i.e. below 3 MeV, these rings were blurred. The unperturbed shadow of the cathode mesh is apparent in the pinhole images, indicating that the ions are transported ballistically below the cathode mesh. The images in figure 3 then represent the distribution of ions at the plane of the cathode mesh whose direction of travel and energy allow them to pass through the pinhole and deposit their energy within a particular layer of the camera.

As mentioned in the introduction, the circular structures in the ion pinhole images are not unique to these experiments and have been observed in DPF since 1980 [18, 19, 20–25]. However, the experimental results obtained in those experiments did not allow researchers to unambiguously determine whether the ring-shaped patterns reflected the real spatial distribution of the ion source or whether they were created by magnetic fields focusing ions from one divergent point source.

In our opinion, it was necessary to obtain additional experimental data to elucidate the origin of the patterns recorded by the ion pinhole cameras. In working towards that goal, we used various ion detectors. Results relevant to

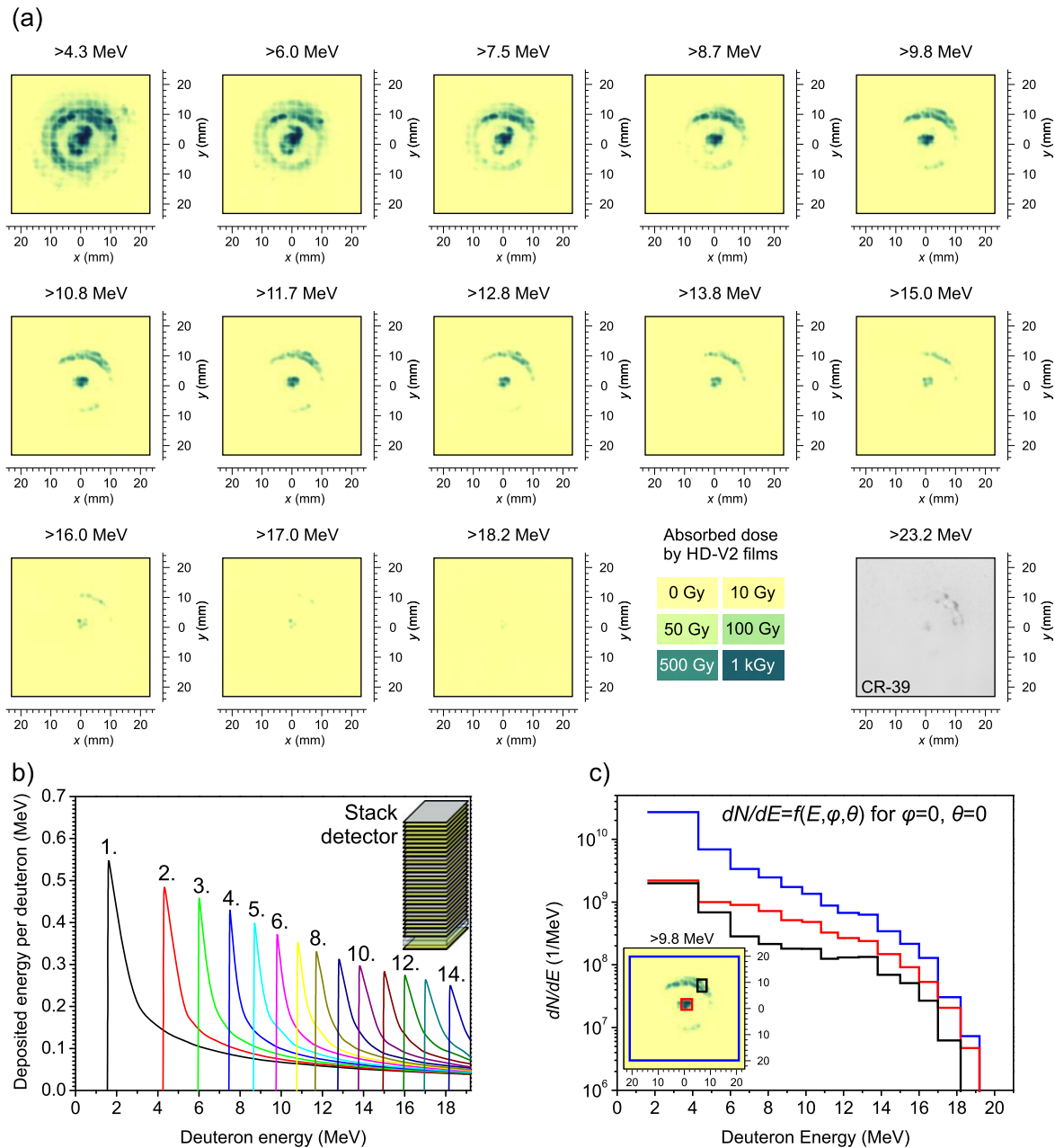


Figure 4. (a) Images from the ion pinhole camera recorded by the stack of HD-V2 films and a CR-39 detector with a spatial resolution of 1.2 mm. The energy refers to deuterons. The contribution of protons to RCF doses is expected to be significant mainly at the highest energies. (b) Spectral response of RCFs in the stack calculated with the SRIM/TRIM code [39]. (c) Deuteron energy distribution functions unfolded from the stack of RCF films. Three spectra (black, red, and blue) correspond to three regions selected in the ion pinhole image at a >9.8 MeV deuteron energy. Shot no. 1771 with $(2.0 \pm 0.4) \times 10^{12}$ neutrons.

understanding the structure in the ion pinhole images will be presented in the following sections 4–6.

4. Ion pinhole images with spectral resolution

In order to obtain additional information about the patterns in the ion pinhole camera images, we took advantage of the multi-MeV ion energies produced on GIT-12. High-energy deuterons generated in our experiment enabled us to record images on multiple detectors placed in the stack of the pinhole camera. If there is a sufficient number of detectors in the

stack, as in the shot presented in figure 4(a), it is possible to unfold the depth-dose distribution to obtain a deuteron spectrum through so-called RCF stack spectroscopy [31, 32]. This method is based on the fact that each RCF in the stack has a different sensitivity to deuterons (see figure 4(b)). We used a numerical code to process the images, and the unfolded spectra are shown in figure 4(c). The spectrum obtained depended on the region selected for analysis within the exposed area of the detector. The spectrum from a small part of the ring is plotted in black. This region is highlighted by the black square in the accompanying detector image. A significant result is that this ring of nearly constant diameter

through the film stack was formed by ions with various energies ranging from ~ 1 MeV up to 20 MeV. Consequently, we can rule out the hypothesis from [18] that the ring was produced by magnetic fields focusing ions from one divergent central point source towards a pinhole. In the case of a divergent point source, the ring diameter in pinhole images would strongly depend on the ion energy, since the Lorentz force depends on the deuteron velocity. To produce a nearly constant diameter ring spanning such a wide range of energies, ions of a specific energy would require either that their trajectory be bent by a specific magnetic field or that they be accelerated at a specific initial angle with respect to the axis. It is not likely that such specific conditions reliably occurred over so many shots with different initial parameters during various experimental campaigns. Therefore, in our previous paper [26], we arrived at the conclusion that the ring in the pinhole images somehow reflected the spatial distribution of the ion source. The relationship between the diameter of the circular source at its origin and that observed in the plane of the cathode mesh depends on the parameters of the ion source above the cathode mesh and on the strength of the electric and magnetic fields inside the z-pinch. Taking into account the complexity of the electric and magnetic fields during the ion acceleration in z-pinch, we admit that there are other possible explanations for the formation of a nearly constant diameter ring by ions of various energies. We are not able to make definite conclusions based on images recorded by only one ion pinhole camera with spectral resolution. Therefore we present additional results in the following sections 5 and 6.

5. Ion multi-pinhole images

It has been shown in the previous section that the annuli observed by the ion pinhole camera somehow represent the real spatial distribution of the ion source. To study the real diameter and other parameters of the ion source at its origin, it seems desirable to detect ions using many pinholes distributed at different distances from the cathode mesh that observe the z-pinch along different lines of sight. For this purpose, a multi-pinhole camera was added to the top of the detector shown in figure 3. This addition allowed us to obtain results from one on-axis and four off-axis pinhole cameras (see figures 5(a)–(c)). The absorber and the first five layers in the stack of the off-axis pinhole cameras were the same as the layers in the on-axis camera presented in figure 4. The series of pinhole images at >4.3 MeV and >7.5 MeV from shot no. 1771 (i.e. the same shot as presented in figures 2 and 4) are shown in figures 5(b)–(c).

A significant result is that, at the 4.3 MeV deuteron energy, the ring was observed by all pinhole cameras regardless of the line of sight and the distance of the pinholes from the cathode mesh. It supports the hypothesis that the ring was real. However, it does not mean that magnetic fields played no role. The magnetic field likely manifested itself in a blurring of the concentric ring at lower ion energies (see figure 5(b)) and in the ion emission anisotropy observed by the pinhole camera along different lines of sight at higher energies (see differences between images in figure 5(c)).

To find out the real diameter of the ion source, we tried to reproduce the most important features observed in the multi-pinhole images by numerical simulations. Our numerical simulation did not address the acceleration of the ions. In our charged-particle tracking code, we assumed that ions were already accelerated to their final energy. Then we simulated trajectories of these ions in azimuthal magnetic fields generated by the z-pinch current. By comparing simulated and experimental multi-pinhole images at many ion energies, it was possible to study both the real diameter of the ion source and the influence of magnetic fields on ions detected by the multi-pinhole camera. The geometry of the numerical simulation and the simulated pinhole images are shown in figures 5(d)–(f). The set-up of the simulations was as follows. In our simulations, we placed the source of accelerated ions 18 mm above the cathode mesh. The anode–cathode gap was 25 mm. The ion source consisted of two parts, namely a central spot and a ring. As shown in figure 5(d), the free parameters of our simulations were the radius of the ring-shaped source, the (energy-dependent) angular divergence of the ion micro-beams from the z-axis, and the current at a specified radius (skin or uniform current density). The azimuthal asymmetry was reproduced by the variable intensity of the ion source along the ring and by a slight (~ 1 mm) displacement of the multi-pinhole camera from the z-axis. The pinhole diameters and the geometry of the pinhole camera were the same as in the experiment. The quantitative agreement of the numerical simulation with our experiment was obtained with the skin current distributed at a 9 mm radius. The current was time-varying and was decreasing from a relatively low peak value of ~ 1 MA. However, we should note that this value would be higher if the source were placed at a lower height above the cathode mesh or if the initial directions of the ion micro-beams were not oriented along the z-axis. Despite this ambiguity, the initial radius of the ring-shaped source was (10 ± 1) mm in all our simulations of shot no. 1771. By analyzing other shots, we estimated the initial radius of the ion source to be between 6 and 10 mm.

The radius of the ring-shaped ion source is not the only important result encoded in the ion pinhole images. The multi-pinhole camera could also provide information about the ion-beam divergence. At deuteron energies above 5 MeV, the characteristic feature was that each ion pinhole camera detected mainly those localized spots which lie in the plane determined by the z-pinch axis and that particular pinhole (see figure 5(f)). This observation can be explained by localized sources and collimated ion emission which is deflected by azimuthal magnetic (or radial electric fields) as shown in figure 5(d) (see also figure 6 in [26]). This forms radial lines at the beam-profile detector (see figure 7(b)). Each individual source can be detected by a pinhole camera if the radial line hits a pinhole (see figure 6 in [26]). As a result, the central (on-axis) pinhole near the center of the beam (the cross-section of many of the radial lines) sees the largest number of localized ion sources. The off-axis pinholes can detect sources which lie in the plane determined by the pinhole and the z-pinch axis. Other sources can be seen only if the initial micro-beam divergence is sufficiently large. This caused us to consider investigating the ion

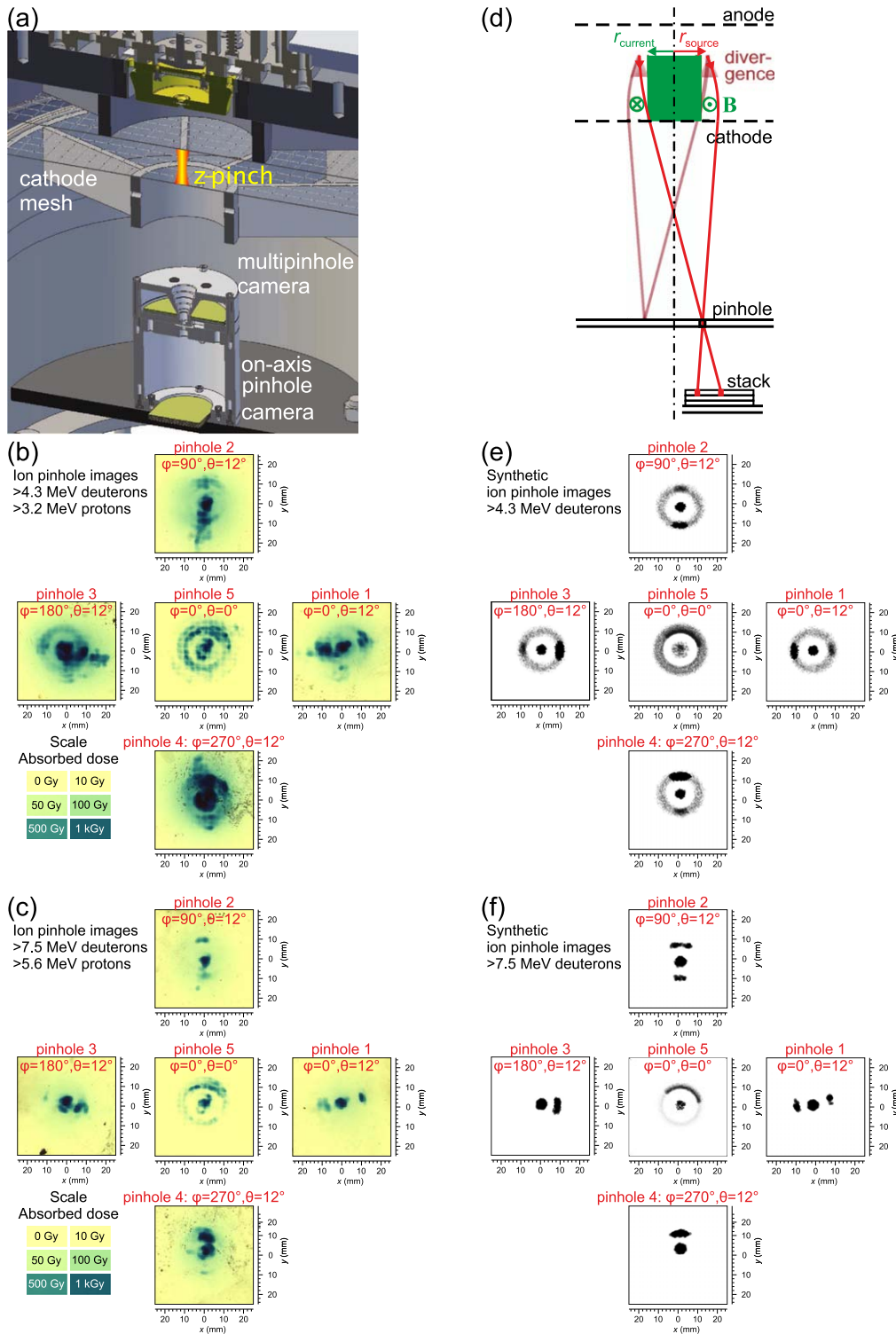


Figure 5. Measurement of the spatial distribution of the ion source. (a) Arrangement of the ion multi-pinhole camera with pinhole diameters of 0.5 mm, magnifications of 0.6 and 0.3, and spatial resolutions of 1.3 and 2.2 mm for the on-axis and off-axis pinholes, respectively. (b)–(c) Experimental (one on-axis and four off-axis) ion pinhole images at 4.3 and 7.5 MeV deuteron energies on shot no. 1771 with $(2.0 \pm 0.4) \times 10^{12}$ neutrons. Spatial scales correspond to the plane of the cathode mesh. (d) Geometry used for the simulation of deuterons detected by the multi-pinhole camera. For simplicity, the ion emission from the central spot is not shown. Not to scale. (e)–(f) Synthetic ion pinhole images at 4.3 and 7.5 MeV deuteron energies.

micro-beam divergence using off-axis pinhole images. For instance, at an 7.5 MeV energy, the synthetic images in figure 5(f) were simulated with ions emitted into 100 mrad and

250 mrad cones for the ring source and the central spot, respectively. The ion-beam divergence measured in a wider energy range will be presented in the following section 6.

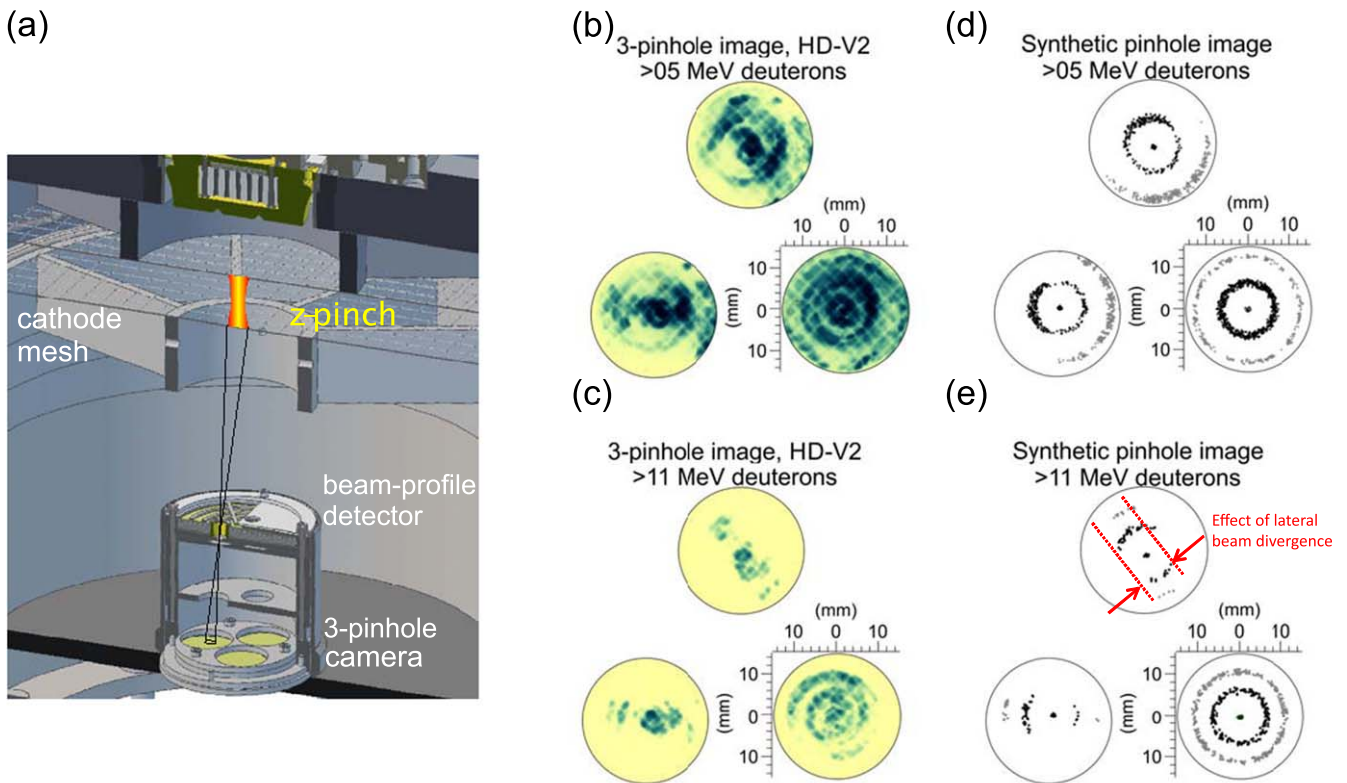


Figure 6. Measurement of the micro-beam divergence from three-pinhole images. (a) Arrangement of the ion three-pinhole detector with pinhole diameters of 0.45 mm, a magnification of 0.55, and a spatial resolution of 1.3 mm. (b)–(c) Experimental three pinhole images at 5 and 11 MeV deuteron energies on shot no. 1845 with $(3.4 \pm 0.6) \times 10^{12}$ neutrons. (d)–(e) Synthetic ion pinhole images at 5 and 11 MeV deuteron energies. Spatial scales correspond to the plane of the cathode mesh. Note: The pinhole images showed two ring-like structures. The radius of the outer ring seemed to depend on the deuteron energy. Therefore we will try to verify the hypothesis that both rings came from one original ring-shaped source in future simulations. Regardless of their origin, two rings helped us to measure the beam divergence with greater precision.

6. Ion three-pinhole images and ion beam-profile

We suggested in the previous section 5 that micro-beam divergence could be estimated from off-axis ion pinhole images. For this purpose, we used a three-pinhole camera with a better spatial and spectral resolution. The detector is shown in figure 6(a) and described in [26]. This detector measured angular, spatial, and spectral properties of ion emission. The angular distribution (ion-beam profile) was measured by using large pieces of ion detector materials (CR-39, GafChromic films) at about 10 cm below the cathode mesh. The effective area of the detectors was reduced by a shielding mask and 3 cutouts. At the center of each cutout, there was a pinhole, thereby providing the spatial distribution of the ion source. The pinhole diameters were chosen between 0.25 and 0.45 mm. Calculating with the image magnification of 0.55, the pinhole camera provided a spatial resolution between 0.7 and 1.25 mm. Three pinholes were used to estimate the anisotropy of the ion emission and consequently the ion microbeam divergence. On shot no. 1845 presented in figure 6, we used a stack of 21 GafChromic films (see also figure 5(a) in [26]). Figures 6(b) and (c) show typical pinhole images of deuterons with energies above 5 and 11 MeV, respectively. In the images, it is evident that the deuterons produced a radiograph of the cathode mesh. The marks in the cathode mesh (spatial fiducials) enabled us to compare the absolute radial position of the ion

emission seen along different lines of sight, i.e. seen by different off-axis pinholes. At low energies, the rings were blurred and visible in all images of the three-pinhole camera. Above 5 MeV, we can see differences between individual pinholes (see figure 6). Above 11 MeV, the whole ring was detected only in the bottom-right pinhole image which corresponded most closely to the center of the ion beam. The off-center pinhole images recorded only those parts of the rings which laid in the plane determined by the beam axis and a pinhole.

We tried to reproduce the characteristic features mentioned above in simulations. In a manner similar to the simulation in figure 5, the radius of the ring-shaped source, the current at a specified radius, and the divergence of the localized ion sources were free parameters whose values were chosen for the simulation. The divergence of ions emitted from the ring is connected to the width of arcs observed in off-center pinhole images. This width is marked by a red color in figure 6(e). The width and, therefore, the reconstructed ion micro-beam divergence decreased with increasing deuteron energy. The result obtained on shot no. 1845 is shown in figure 7(a). At 5 MeV, the lateral micro-beam divergence was 140 mrad whereas it decreased to 10 mrad at 26 MeV. The latter value is in agreement with the result from the beam-profile detector. At deuteron energies above 18 MeV, the beam-profile detector recorded distinguishable radial lines. The width of the radial stripes in figure 7(b)

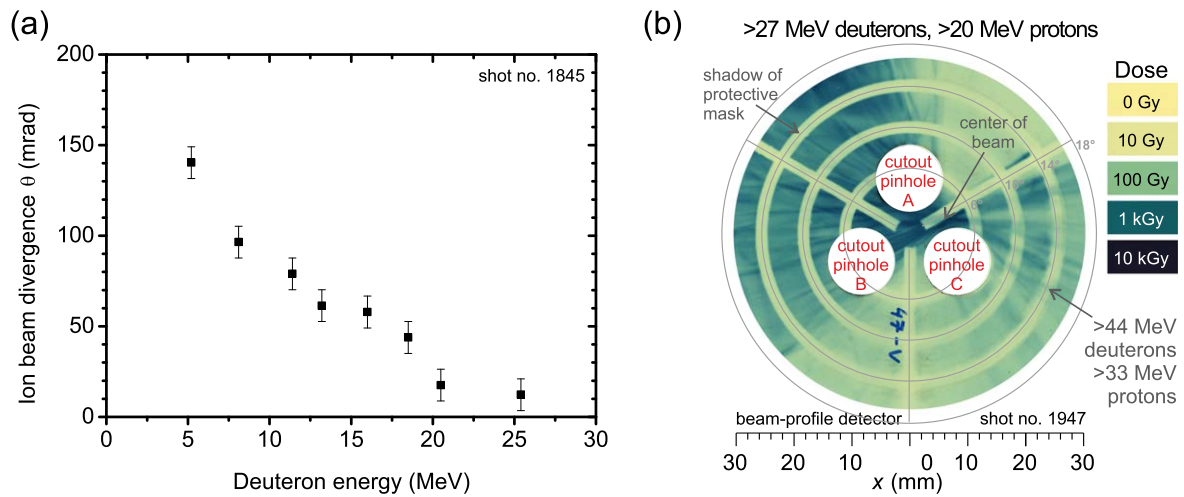


Figure 7. (a) Dependence of the ion-beam microdivergence on deuteron energy, estimated for shot no. 1845. (b) An image of the beam profile detected by HD-V2 GafChromic film at 10 cm on shot no. 1947.

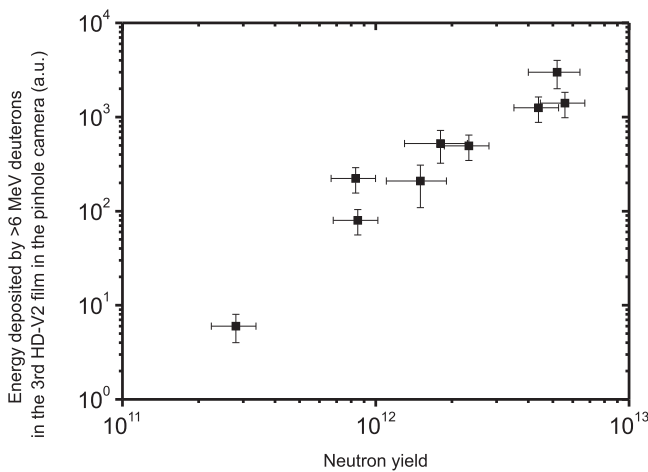


Figure 8. Correlation between the neutron yield and the energy deposited by >6 MeV deuterons in the third HD-V2 film in the on-axis pinhole camera. We intentionally selected shots with different neutron yields observed in 2016. The differences in neutron yields were caused by shot-to-shot variation or by non-ideal initial parameters (on shots with different aims than a high-neutron yield or on shots before the optimal conditions were set up).

implies a lateral divergence between 5 and 10 mrad at 27 MeV deuteron energy. This demonstrates the consistency of the pinhole images and the beam-profile patterns. In the next section, we will present the correlation of pinhole images with neutron yields.

7. Ion pinhole images and neutron yields

Deuterium z-pinch and DPF are researched primarily as neutron sources. From this point of view, it is interesting to determine if there is any correlation between the neutron yield and features of the ion pinhole images. In our experiments on GIT-12, the most obvious correlation was seen between the neutron yields and the dose absorbed in the GafChromic films fielded in our pinhole cameras. For example, figure 8 presents

the neutron-yield dependence of the energy deposited by >6 MeV deuterons in the GafChromic films placed in the on-axis pinhole camera.

At deuteron energies below 5 MeV, the HD-V2 GafChromic films were often saturated. In figure 8, we therefore show the doses produced by >6 MeV deuterons which correlated with neutron yields quite well. If the shape of the energy spectrum of fast deuterons is approximately the same from shot to shot, then the relative neutron yield from ${}^2\text{H}(d, n){}^3\text{He}$ fusion reactions is given by the numbers of accelerated and target deuterons. Therefore, the close connection of neutron yields with the doses produced by accelerated deuterons is not surprising.

We also looked for a correlation between the neutron yields and ring diameters but did not find any. In the following section 8, we will therefore present another attempt to identify the origin of a ring with a particular diameter.

8. Origin of the ring ion source

8.1. Anode pinhole camera

Various research groups have measured ring-like structures with ion pinhole cameras in DPF and z-pinch experiments since 1980. In our experiments on GIT-12, we also observed annuli along with the expected on-axis spots in pinhole camera images produced by multi-MeV deuterons. In the previous sections 4 and 5, we showed that the ring represented the real spatial distribution of an ion source with a radius of about 1 cm. This is an extremely important result to include in discussion of the ion acceleration mechanism (see e.g. [26]). Since the estimated diameter of the ion source was significantly larger than the diameter of the compressed necks observed shortly before the acceleration of the ions (see figure 2(b)), it is natural to ask what sets the diameter of the ring.

To explain a particular diameter in our experiment, we looked for any correlation between the estimated diameter of the ring and results from other diagnostics. We found out that 15–20 mm diameters were characteristic for the plasma

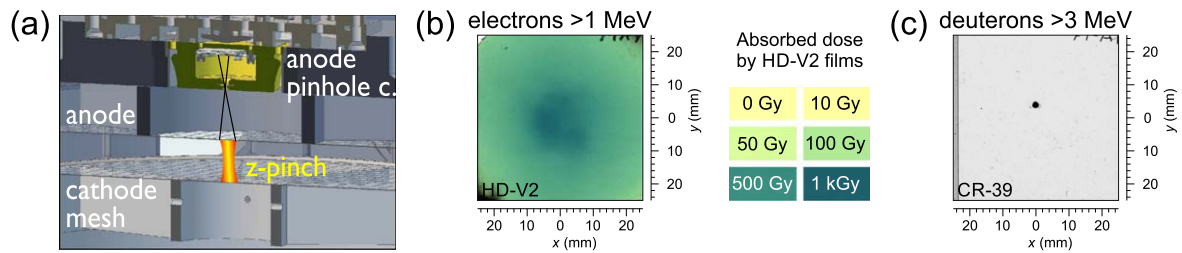


Figure 9. (a) Arrangement of the anode pinhole camera with a magnification of 0.55, a pinhole diameter of 0.6 mm, and a spatial resolution of 1.7 mm. (b) Anode pinhole image recorded by the third HD-V2 GafChromic film in the stack. (c) Pinhole image detected by the first CR-39 detector. Shot no. 1771. The stack consisted of a 50 μm aluminum absorber, a 0.65 mm CR-39 detector, the first HD-V2 film, a 0.55 mm CR-39 detector, the second HD-V2 film, a 1 mm aluminum absorber, the third HD-V2 film. Spatial scales correspond to the plane of the anode mesh.

emission near the anode (observed by a time-integrated x-ray pinhole camera as shown in figure 2(c)). We hypothesized that the plasma emission at the anode mesh could be a consequence of electron flow at stagnation or disruption. That is why we were interested in the spatial distribution of the electron beam at the anode. For this purpose, we decided to make an ‘anode’ pinhole camera inside the gas-puff hardware.

The arrangement of the anode pinhole camera is displayed in figure 9(a). Figures 9(b) and (c) then show the results obtained on shot no. 1771 (the same shot as presented in figures 2, 4, and 5). The electron beam was detected by the stack of HD-V2 GafChromic films. The third HD-V2 film in the stack recorded the pattern shown in figure 9(b), which is a circle that is not hollow. The stopping range of electrons in our stack was calculated by the ESTAR program provided by the National Institute of Standards and Technology (NIST) [42].

HD-V2 GafChromic films are sensitive also to ions and x-rays. The contribution of ions was studied by the CR-39 detector which was placed in front of the HD-V2 films. On shot no. 1771, the CR-39 detector behind a 50 μm Al absorber recorded only a small spot which was created by protons or deuterons with energies above 2.3 MeV or 3.0 MeV, respectively (see figure 9(c)). The etching and the visibility of tracks could be influenced by high dose x-ray and electron irradiation [43–45]. Nevertheless, it was clear that the total number of $>2\text{MeV}$ hydrogen ions emitted towards the anode was at least three orders of magnitude lower than towards the cathode. This is in agreement with the previous ‘upstream’ measurements in DPFs [23]. We suppose that some deuterons could be accelerated in the direction of an electron beam by a collective ion acceleration mechanism [46]. Another hypothesis is that fast protons from ${}^2\text{H}(d,p){}^3\text{H}$ fusion reactions escaped the z-pinch towards the anode along the z-axis. To estimate the number of $>8\text{MeV}$ hydrogen ions emitted towards the anode, we analyzed the rear side of the first CR-39 detector, which had a thickness of 0.65 mm. Even though we observed a few proton or deuteron tracks above the background (neutron) level, the contribution of ions to the dose detected by the HD-V2 films behind the CR-39 detector can be neglected. As far as the contribution of hard x-rays is concerned, the patterns in the HD-V2 films were shifted when magnets were placed inside the pinhole camera. We may,

therefore, conclude that the circular pattern of about 15–20 mm diameter in figure 9(b) was produced by fast electrons with energies above 1 MeV. It should be noted that the recorded image could be influenced by the transport of the high-current electron beam in the low-pressure gas (or plasma) between the anode mesh and the pinhole camera. Based on the shadow of the anode mesh in the pinhole images, the original electron beam diameter at the anode mesh could be 1.6 times smaller than the one shown in figure 9(b). Besides that, even if the recorded pattern is of a size similar to that of the rings in the ion pinhole images, it does not explain why the ion pinhole camera below the cathode mesh detected only individual annuli of a specific diameter. Consequently, we have to search for the origin of a particular diameter in a different way.

Another possible way to study the origin of the annuli in the (cathode) ion pinhole images is to change the initial parameters of the GIT-12 experiments. In previous experimental campaigns, we changed the length of the anode–cathode gap, or we placed cylindrical objects of various diameters on the anode or cathode meshes. We also tried to influence the ion emission by making a hole in the meshes. We believed that the rings in the pinhole images would be changed and we would see some correlation with the initial electrode configuration. Unfortunately different initial parameters usually had deleterious effects on the ion acceleration and neutron production. Therefore, the results from these experiments have not been conclusive so far. To study how the diameter of the ring in the ion pinhole images might change, we instead decided to make measurements with the ion pinhole camera on a different pulsed-power generator. Recently, we have had an opportunity to carry out dense-plasma focus experiments on the HAWK pulsed-power generator. The results from our ion pinhole camera are presented in the following subsection.

8.2. Ion pinhole images on HAWK at the Naval Research Laboratory

The experimental arrangement on HAWK is displayed in figure 10(a). Figure 10(b) shows an on-axis view with the valve inserted inside the central anode. Our ion detector was placed 20 cm from the anode. We used the same three-pinhole camera as on GIT-12 (see figure 6). With an image

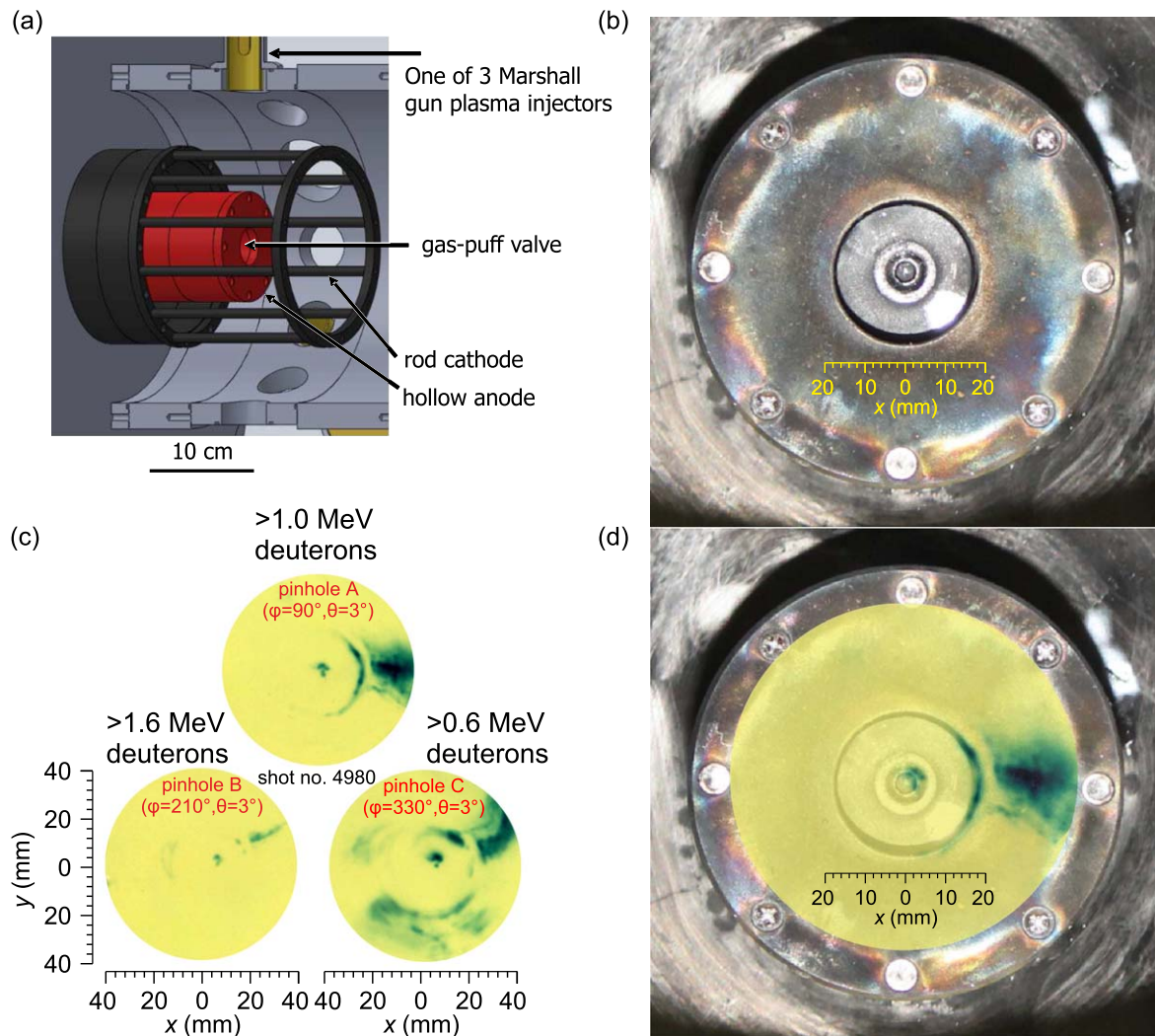


Figure 10. (a) Arrangement of the electrode system on the HAWK generator. (b) On-axis view of the anode with the gas-puff valve inside the central conductor. (c) Images from the three-pinhole camera (with magnification of 0.25, pinhole diameter of 0.4 mm, spatial resolution of 2 mm) recorded by the HD-V2 film behind three different absorbers ($6\ \mu\text{m}$ Kimfoil, $10\ \mu\text{m}$ Al, and $20\ \mu\text{m}$ Al). (d) On-axis view of the anode overlapped by the pinhole image at the >1.0 MeV deuteron energy. All spatial scales correspond to the plane of the anode end.

magnification of 0.25 and a pinhole diameter of 0.4 mm, the pinhole camera provided a spatial resolution of 2 mm. The detector stack consisted of a layer of HD-V2 GafChromic film followed by two EBT-3 films. In front of three individual parts of the first HD-V2 film, we placed three different absorbers, namely $6\ \mu\text{m}$ Kimfoil, $10\ \mu\text{m}$ Al, and $20\ \mu\text{m}$ Al. Pinhole images from a typical shot are shown in figure 10(c). Despite the 0.64 MV output voltage and relatively modest current of the HAWK generator, we recorded a high dose behind all three absorbers. The presence of signal behind the $20\ \mu\text{m}$ Al absorber implies deuteron energies above 1.6 MeV. Further, in figure 10(c) we can see that the diameter of the characteristic rings is the same in the three pinhole images, despite the fact that each of these images corresponds to a different deuteron energy and line of sight. As on GIT-12, we assume that the electric and magnetic fields inside the plasma could influence the trajectory of ions traveling between the anode and the pinholes. However, an important result that is apparent from figure 10(d) is that for HAWK, the diameter

of the rings in all of the pinhole images matches the diameter of the gas-puff hole inside the anode. This result indicates that the spatial distribution of the ion emission could be influenced by the geometry of the electrodes. Several implications of these findings will be discussed in the last section 9.

9. Discussion and conclusions

Mega-ampere DPF and deuterium gas-puff z-pinches can produce high-energy ions. Recently, we have accelerated deuterons to multi-MeV energies in deuterium gas-puff experiments on the GIT-12 and HAWK microsecond generators at 3 MA and 0.7 MA current, respectively. We used a large number of different detectors to characterize the ion emission and determine specific details about the nature of the ion source and acceleration mechanism. In particular, the results from ion pinhole cameras fielded during the

experiments seemed to be useful for the discussion of ion acceleration mechanisms.

In the ion pinhole images on GIT-12, we observed rings of nearly constant diameter at various deuteron energies ranging from ~ 1 MeV up to 20 MeV. Despite some anisotropy in the ion emission, these rings were observed by cameras with pinholes which were distributed at different distances from the z-pinch and which observed the z-pinch along different lines of sight. Based on measurements with one-, three-, and multi-pinhole cameras, we therefore concluded that the observed rings reflected both the spatial distribution of the ion source and the influence of magnetic fields. The estimated ion source diameter on the order of 1 cm was significantly larger than the width of the necks in the plasma observed before the disruption of the current (see figure 2(b)). This knowledge helped us to determine specific details about the acceleration mechanism. These details are consistent with the mechanism that we described in [26] which is based on the generation of GV m^{-1} electric fields during fast ($\sim \text{ns}$) disruption of the conduction current (see also [47, 48]). A significant current drop in our experiments is attributed to a transition from a low-impedance plasma to a space-charge-limited flow and/or self-magnetic insulation in a gap formed after the ejection of plasmas from $m = 0$ constrictions. Then the electric field is induced in regions where the conduction current was flowing before the disruption. We do not expect that the total current flows within the ~ 1 mm neck observed in framing camera images from GIT-12 (see also [49]). In addition to the current flowing outside the observed neck, the generated electromagnetic pulse can propagate throughout the whole inter-electrode region. Therefore, it is not surprising that ions were accelerated from the anode (plasma) region not only on the axis but also at a larger (~ 1 cm) diameter. We still need to explain why the ring-shaped portion of the ion source forms at a particular diameter. We hypothesize that the current density distribution plays a role in determining this diameter, but we do not know the current density distribution in the z-pinch on GIT-12 before the disruption.

A significant result explaining why a ring-shaped ion source might form at a particular diameter was achieved on the HAWK generator at the US Naval Research Laboratory in Washington. Despite differences in initial conditions, the experiment on HAWK exhibited many similarities to GIT-12. When the three-pinhole camera was placed on the axis, we saw characteristic rings behind different absorbers and along different lines of sight. The apparent correlation of the ion-ring diameter with the diameter of the gas-puff hole inside the anode demonstrated the importance of the electrode edge on the ion emission. The influence of the electrode geometry on the ion acceleration was also clearly visible in DPF experiments on PF-1000 [24]. Taking all the above considerations into account, the spatial profile of the original ion source seems to be determined both by the current density distribution before the disruption and by the geometry of the experiment. Then the properties of the ion emission are determined by the (secondary) breakdown in the anode–





cathode gap when the unstable plasma is unable to carry the total conduction current.

So far, our conclusions about the ion pinhole images have been drawn from experimental observations. It would be desirable to support our conclusions about the ion acceleration mechanism by reproducing the experimental results with state-of-the-art numerical codes. Unfortunately, we have not found any numerical code capable of simulating ion acceleration in z-pinches that could explain the experimentally-observed ion pinhole images. When a numerical code is developed that is able to simulate the most important experimental details, it will then be reasonable to move from researching the acceleration mechanism to learning how to intentionally influence the ion acceleration.

Acknowledgments

The authors acknowledge A Yu Labetsky and B J Sobocinski for their help with the experiments on GIT-12 and HAWK, respectively. This research has been supported by the Grant Agency of the Czech Republic (Grant No. 19-02545S), the Czech Ministry of Education (Grant Nos. LTT17015, LTAUSA17084 and CZ.02.1.01/0.0/0.0/16_019/0000778), the Czech Technical University in Prague (Grant No. SGS19/167/OHK3/3T/13), the Naval Research Laboratory Base Program, and TPU Competitiveness Enhancement Program grant.

ORCID iDs

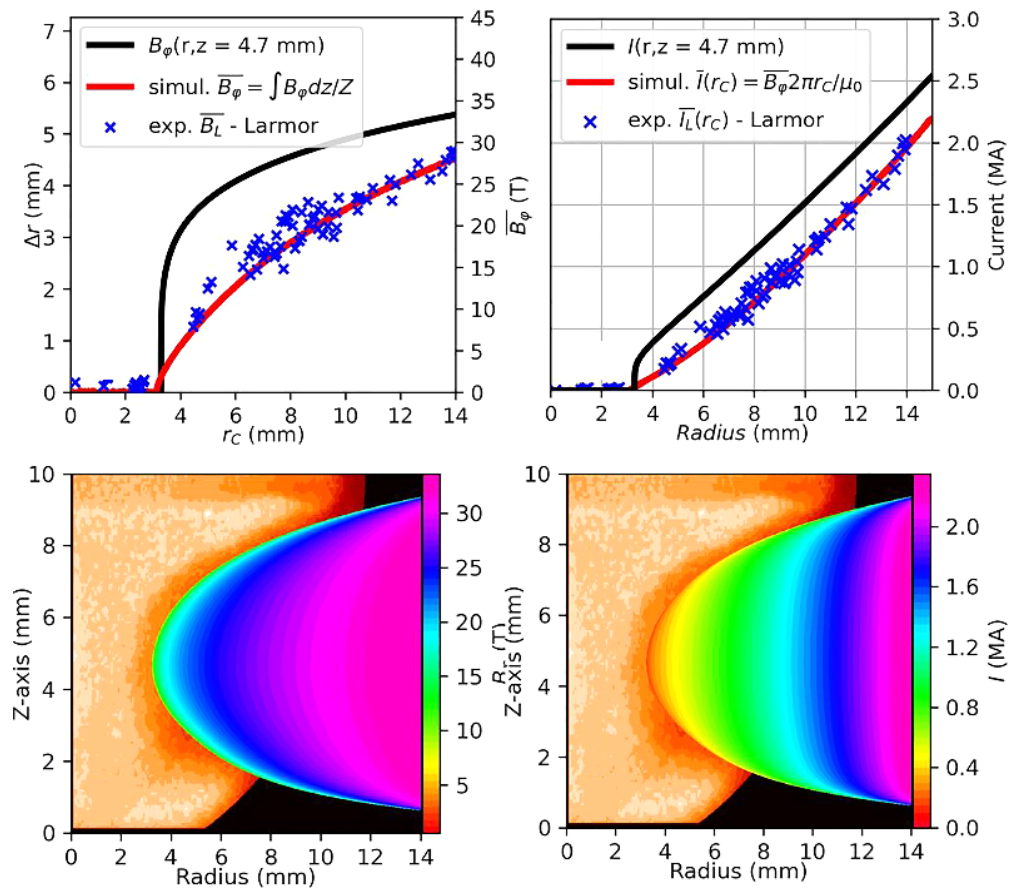
D Klir  <https://orcid.org/0000-0002-0510-3653>
 P Kubes  <https://orcid.org/0000-0003-1356-8765>
 J Cikhardt  <https://orcid.org/0000-0002-8222-8038>
 J Krasa  <https://orcid.org/0000-0002-3888-8370>

References

- [1] Bernard A *et al* 1998 *J. Mosc. Phys. Soc.* **8** 93–170
- [2] Coverdale C A *et al* 2007 *Phys. Plasmas* **14** 022706
- [3] Velikovich A L *et al* 2007 *Phys. Plasmas* **14** 022701
- [4] Krishnan M 2012 *IEEE Trans. Plasma Sci.* **40** 3189
- [5] Klir D *et al* 2015 *Plasma Phys. Control. Fusion* **57** 044005
- [6] Kurchatov I V 1956 *At. Energy* **1** 359
- [7] Andrianov A M *et al* 1958 *Proc. 2nd United Nations Int. Conf. on Peaceful Uses of Atomic Energy* (vol 31) (Geneva) ed J H Martens *et al* (Geneva, Switzerland: United Nations) p 348
- [8] Anderson O A, Baker W R, Colgate S A, Ise J and Pyle R V 1958 *Phys. Rev.* **110** 1375
- [9] Klir D *et al* 2011 *Appl. Phys. Lett.* **98** 071501
- [10] Klir D *et al* 2012 *Plasma Phys. Control. Fusion* **54** 015001
- [11] Vikhrev V V and Korolev V D 2007 *Plasma Phys. Rep.* **33** 356
- [12] Klir D *et al* 2008 *Phys. Plasmas* **15** 032701
- [13] Ryutov D D, Derzon M S and Matzen M K 2000 *Rev. Mod. Phys.* **72** 167
- [14] Haines M G 2011 *Plasma Phys. Control. Fusion* **53** 093001
- [15] Welch D R, Rose D V, Clark R E, Mostrom C B, Stygar W A and Leeper R J 2009 *Phys. Rev. Lett.* **103** 255002

- [16] Schmidt A, Tang V and Welch D 2012 *Phys. Rev. Lett.* **109** 205003
- [17] Appelbe B and Chittenden J 2015 *Phys. Plasmas* **22** 102703
- [18] Filippov N A 1980 *JETP Lett.* **31** 120
- [19] Bertalot L, Herold H, Jager U, Mozer A, Oppenlander T, Sadowski M and Schmidt H 1980 *Phys. Lett. A* **79** 389–92
- [20] Skladnik-Sadowska E, Baranowski J, Milanese M, Moroso R, Pouzo J, Sadowski M and Zebrowski J 2001 *Radiat. Meas.* **34** 315–8
- [21] Sadowski M J, Gribkov V A, Kubes P, Malinowski K, Skladnik-Sadowska E, Scholz M, Tsarenko A and Zebrowski J 2006 *Phys. Scr.* **T123** 66–78
- [22] Yousefi H R, Nakata Y, Ito H and Masugata K 2007 *Plasma Fusion Res.: Regular Artic.* **2** S1084
- [23] Kwiatkowski R *et al* 2011 *Nukleonika* **56** 119–23
- [24] Kwiatkowski R, Czaus K, Skladnik-Sadowska E, Sadowski M J, Zaloga D R, Paduch M and Zielinska E 2015 *Nukleonika* **60** 297–302
- [25] Kubes P *et al* 2018 *Phys. Plasmas* **25** 012712
- [26] Klir D *et al* 2018 *New J. Phys.* **20** 053064
- [27] Klir D *et al* 2019 *Plasma Phys. Control. Fusion* **61** 014018
- [28] Takasugi K, Iwata M and Nishio M 2016 *J. Phys.: Conf. Ser.* **688** 012120
- [29] Klir D *et al* 2014 *Phys. Rev. Lett.* **112** 095001
- [30] Klir D *et al* 2016 *Phys. Plasmas* **23** 032702
- [31] Nuernberg F, Schollmeier M, Brambrink E, Blazevic A, Carroll D C, Flippo K and Roth M 2009 *Rev. Sci. Instrum.* **80** 033301
- [32] Schollmeier M, Geissel M, Sefkow A B and Flippo K A 2014 *Rev. Sci. Instrum.* **85** 043305
- [33] Bugaev S P *et al* 1997 *Russ. Phys. J.* **40** 1154–61
- [34] Boller J, Commisso R, Goodrich P, Hinshelwood D, Kellogg J, Shipman J, Weber B and Young F 1991 *Design and performance of HAWK, a versatile pulsed power generator* NRL Memorandum Report 6748 US Naval Research Laboratory, Washington, DC
- [35] Commisso R, Apruzese J, Black D, Boller J, Moosman B, Mosher D, Stephanakis S, Weber B and Young F 1998 Results of radius scaling experiments and analysis of neon K-shell radiation data from an inductively driven Z-pinch *IEEE Trans. Plasma Sci.* **26** 1068–85
- [36] Beresnyak A, Giuliani J L, Jackson S L, Richardson A S, Swanekamp S, Schumer J, Weber B and Mosher D 2018 Simulations of a dense plasma focus on a high-impedance generato *X Dense Z-Pinch Conf. (Stateline, NV, August, 2017); IEEE Trans. Plasma Sci.* **46** 3881–5
- [37] Engelbrecht J T, Jackson S L, Mamonau A A, Beresnyak A R, Rezac K, Cikhart J, Klir D, Weber B V, Giuliani J L and Schumer J W 2019 Initial conditions in the HAWK dense plasma focus 2019 *IEEE Pulsed Power and Plasma Science Conf., (combined ICOPS 2019 and PPC 2019) (Orlando, FL, USA)* to be published in the Proc. of the XXII IEEE International Pulsed Power Conf. (PPC 2019)
- [38] Jackson S L *et al* 2018 Initial results from a dense plasma focus driven by a high-inductance generator *45th IEEE Int. Conf. on Plasma Science (ICOPS 2018) (Denver, CO, USA)* 6D–5
- [39] Ziegler J F 2004 *Nucl. Instrum. Methods B* **219–220** 1027
- [40] Knoll G F 1999 *Radiation Detection and Measurement* 3rd edn (New York: Wiley)
- [41] Gaillard S, Fuchs J, Renard-Le Galloudec N and Cowan T E 2007 *Rev. Sci. Instrum.* **78** 013304
- [42] National Institute of Standards and Technology (NIST): Stopping power, density effect parameters, range, and radiation yield tables for electrons in various materials. <http://physics.nist.gov/PhysRefData/Star/Text/ESTAR.html>
- [43] Charvat J and Spurny F 1988 *Nucl. Tracks Radiat. Meas.* **14** 451–5
- [44] Rinderknecht H G *et al* 2015 *Rev. Sci. Instrum.* **86** 123511
- [45] Sahoo G S, Tripathy S P, Joshi D S and Bandyopadhyay T 2016 *J. Appl. Phys.* **120** 025107
- [46] Graybill S E and Uglum J R 1970 *J. Appl. Phys.* **41** 236
- [47] Trubnikov B A 1958 *Plasma Physics and the Problem of Controlled Thermonuclear Reactions (Izd. Akad. Nauk SSSR, Moscow vol 4)* (New York: Pergamon) p 87 1960
- [48] Trubnikov B A 1986 *Sov. J. Plasma Phys.* **12** 271
- [49] Maron Y *et al* 2013 *Phys. Rev. Lett.* **111** 035001

G.3 Article: Munzar et al., POP (2021)



Volume 28, Issue 6, June 2021

Mapping of azimuthal B-fields in Z-pinch plasmas using Z-pinch-driven ion deflectometry

Phys. Plasmas **28**, 062702 (2021); doi.org/10.1063/5.0040515

V. Munzar, D. Klir, J. Cikhardt, J. Kravarik, P. Kubes, J. Malir, J. Novotny, K. Rezac, A. V. Shishlov, V. A. Kokshenev, R. K. Cherdizov, and N. A. Ratakhin



Mapping of azimuthal B-fields in Z-pinch plasmas using Z-pinch-driven ion deflectometry

Cite as: Phys. Plasmas **28**, 062702 (2021); doi: [10.1063/5.0040515](https://doi.org/10.1063/5.0040515)

Submitted: 14 December 2020 · Accepted: 1 May 2021 ·

Published Online: 2 June 2021








View Online



Export Citation



CrossMark

V. Munzar,^{1,a)}  D. Klir,¹  J. Cikhardt,¹  J. Kravarik,¹  P. Kubes,¹  J. Malir,¹  J. Novotny,¹  K. Rezac,¹ 
A. V. Shishlov,²  V. A. Kokshenev,²  R. K. Cherdizov,²  and N. A. Ratakhin²

AFFILIATIONS

¹Faculty of Electrical Engineering, Czech Technical University in Prague, 16627 Prague 6, Czech Republic

²Institute of High Current Electronics SB RAS, Tomsk 634055, Russia

^{a)} Author to whom correspondence should be addressed: munzavoj@fel.cvut.cz

ABSTRACT

B-field measurements are crucial for the study of high-temperature and high-energy-density plasmas. A successful diagnostic method, ion deflectometry (radiography), is commonly employed to measure MGauss magnetic fields in laser-produced plasmas. It is based on the detection of multi-MeV ions, which are deflected in B-fields and measure their path integral. Until now, protons accelerated via laser-target interactions from a point-like source have been utilized for the study of Z-pinch plasmas. In this paper, we present the results of the first Z-pinch-driven ion deflectometry experiments using MeV deuterium beams accelerated within a hybrid gas-puff Z-pinch plasma on the GIT-12 pulse power generator. In our experimental setup, an inserted fiducial deflectometry grid (D-grid) separates the imploding plasma into two regions of the deuteron source and the studied azimuthal B-fields. The D-grid is backlit by accelerated ions, and its shadow imprinted into the deuteron beams demonstrates ion deflections. In contrast to the employment of the conventional point-like ion source, in our configuration, the ions are emitted from the extensive and divergent source inside the Z-pinch. Instead of having the point ion source, deflected ions are selected via a point projection by a pinhole camera before their detection. Radial distribution of path-integrated B-fields near the axis (within a 15 mm radius) is obtained by analysis of experimental images (deflectograms). Moreover, we present a 2D topological map of local azimuthal B-fields $B(r,z)$ via numerical retrieval of the experimental deflectogram.

Published under an exclusive license by AIP Publishing. <https://doi.org/10.1063/5.0040515>

I. INTRODUCTION

Magnetic fields have a crucial role in the behavior of high-temperature and high-energy-density plasmas. In Z-pinch discharges, the B-field and current topology are essential for studying the dynamics of imploding plasmas and energy coupling to the plasma. Complex dynamics of the imploding plasma are investigated using numerical simulations, which must be verified against some experimental data. Conventionally, there are several methods for the measurements of the magnetic fields in Z-pinch plasmas. However, measurements of their spatial distribution are a difficult task for any of them. We are referring to these B-field measurement methods: (1) Faraday rotation; (2) B-dot probes; (3) Zeeman broadening, and all have some limitations.

In the first method, the Faraday rotation, a plane of polarization of an electromagnetic (EM) wave, rotates while propagating through the plasma parallelly to B-fields B_{\parallel} . An angle of the rotation β is proportional to $\int n_e(s)B_{\parallel}(s)ds$, where $n_e(s)$ and $B_{\parallel}(s)$ are the electron density and the parallel B-fields at each point s along the path. Due to the necessity of non-negligible electron density, this method cannot be

used in near-vacuum environments. A proper determination of an averaged B-field requires specific knowledge of the electron density profile $n_e(s)$. It can be obtained either by simultaneous interferometric measurements, which bring an additional source of error or by the employment of a magneto-optical fiber with known length and density,^{1,2} which must not be invasive to the measured plasmas. On the other hand, diagnostic beams can be used only in environments with densities lower than the critical density, which obstructs measurements in dense plasmas close to the Z-pinch axis during a stagnation. However, using ultraviolet laser diagnostics at the wavelength of 266 nm,¹ it has been possible to study plasmas up to densities of $\sim 10^{20} \text{ cm}^{-3}$.

B-dot probes measure the temporal derivative of the B-fields by a coil inserted into the plasma. For high-temperature and high-density plasmas of the Z-pinch, these probes may be intrusive. Thus, they are usually used to study B-fields at peripheral regions of the Z-pinch or placed in front of the imploding plasma. Measurements of B-fields in hot dense plasmas close to the Z-pinch axis are indirect. They require

estimating the B-field evolution or extrapolation via numerical simulations.^{3,4} To minimize the influence of the inserted probe, a micro-B-dot probe has been developed at Cornell.^{5,6} A set of B-dot probes is needed to measure the B-field distribution, which makes this method more perturbative.

In the presence of magnetic fields, the emission lines split due to the Zeeman effect. The shift of lines in the spectral emission profile is proportional to the magnetic strength. High temperature and high density of the plasma cause Stark and Doppler broadening, which smear out the fine structure of the Zeeman splitting. Therefore, the employment of different components of the same multiplet is required, then the exact spectral measurements rely on the line positions rather than their widths. Only certain lines of sight are possible for the measurements, and thus, the study of the spatial distribution of the magnetic field is difficult. However, the B-field profile has been measured for radius $r > 7 \text{ mm}$ ⁷ and, recently, using two-polarization method.^{8,9} The latter experiments have been performed in Z-pinch oxygen plasmas. Employment of the Zeeman method in low-Z plasma (e.g., hydrogen or deuterium) may be problematic.

Another alternative method of B-field measurements in hot dense plasmas has risen in the last two decades. It is an *ion deflectometry* (or more general name, an *ion radiography*). This diagnostic method is based on detecting ion beams deflected by either perpendicular electric or magnetic fields. As ions propagate through these fields, their trajectories bend due to the Lorentz force. When recorded by an ion detector, these deflected beams create a distorted image, a *deflectogram*. Ion displacements in the deflectogram are proportional to the path integral of these fields, that is, $\int \mathbf{E}_1 d\mathbf{L}$ for electric fields and $\int \mathbf{B} \times d\mathbf{L}$ for magnetic fields, which are main quantities inherently coupled to this diagnostics. This paper considers only ion deflections in the azimuthal magnetic fields B_ϕ of the Z-pinch. The path integral of B-fields $\int \mathbf{B} \times d\mathbf{L}$ will be discussed in Sec. II. The ion radiography has been developed in the laser-plasma community as methods for measurements in hot dense plasmas using multi-MeV protons.^{10,11} In the past years, the laser-accelerated proton beams allowed radiographic measurements of E- or B-fields in experiments related to plasma jets,^{12–15} laser-target interactions accelerating multi-MeV protons,^{16–18} laser-driven capacitor coils,^{19–22} Weibel instability,^{23,24} plasma flows in hohlraums,²⁵ imploding inertial confinement fusion (ICF) capsules,^{26–28} propagation of laser-driven EM pulses in metallic wires,^{29,30} magnetic reconnections,^{31–35} and self-generated B-fields in laser-produced plasma bubbles^{36–40} with excellent μm -spatial and ps -temporal resolution. Moreover, ion deflections can be also exploited for field measurements in other types of plasmas. In tokamak plasmas, the heavy ion beam probe (HIBP) diagnostic, commonly used for electron density and plasma potential measurements, utilizes deflections of heavy ions for the investigation of poloidal B-field fluctuations.^{41–46}

In Z-pinch plasmas, there were only a few experimental measurements of magnetic fields using proton beams. In 2012, dynamic electric fields and return currents were measured in laser-driven Z-pinch plasmas created by irradiation of a boron stalk at the Omega facility.⁴⁷ In 2014, the proton deflectometry was tested in azimuthal vacuum magnetic fields driven by Zebra, a MA pulsed-power Z-pinch device in Nevada Terawatt Facility (NTF).⁴⁸ Moreover, experiments with radial foil loads were performed to demonstrate the feasibility of the proton deflectometry in the pulse power plasmas. There were experiments with other loads in NTF,⁴⁹ including a hybrid X-pinch and

cylindrical wire array configuration. The proton deflectometry has also been considered for Z-machine.⁵⁰ However, numerical simulations showed that 4.5-GeV probe protons would be necessary to radially traverse the azimuthal magnetic fields near the axis of the imploding 20-MA liner, which is unrealistic. Instead, the deflectometry was suggested for fringe B-field measurements, but it would still necessitate at least 30 MeV protons. These simulations pointed out two main issues of employment of the ion deflectometry in azimuthal Z-pinch-like magnetic fields.

The first one is a source of ion beams with sufficient momentum, so the Larmor radius of ions is large enough compared to the size of the plasma, and hence, the ion deflections are manageable. It is convenient for experiments in dense plasmas to utilize light ions, for example, protons or deuterons, but then their necessary energy must be in terms of MeV. In all experiments mentioned in the last paragraph, multi-MeV protons were produced separately via laser-target interactions by either fusion reactions (DD or D²He) or the target normal sheath acceleration (TNSA) mechanism. Therefore, these experiments required a high-intensity short-pulse laser system connected to the Z-pinch assembly. However, such laser systems are only available at a few Z-pinch facilities. The second point in question is the direction of the probing ion beams. In all previous experiments, the proton beams were emitted into azimuthal B-fields radially.^{47,48} In this configuration, ions must traverse the peripheral B-fields, which dominantly affect ion trajectories, so the spatial B-field distribution measurements near the axis are nearly impossible. An axial deflectometry allows mapping of the B-fields near the axis. However, if ions travel upstream, in the opposite direction as the current, their initial divergence is extended by the defocusing deflections in azimuthal B-fields. In strong B-fields, the deflectograms may become large to be recorded in the plane detector located far from the plasma.⁵¹ If the ion focusing direction is chosen, the deflected ion trajectories may cross each other, which may cause problems for the deflectogram interpretation.

This paper introduces another approach to the deflectometric measurements of azimuthal B-field of the Z-pinch in an unconventional experimental setup. We studied an acceleration mechanism of multi-MeV hydrogen ions in Z-pinch plasma for a few past years in experiments on the 4.7-MA GIT-12 pulse generator in Tomsk, Russia. The maximum energy of these hydrogen ions (mostly deuterons) reaches up to 55 MeV.⁵² These multi-MeV deuteron beams are accelerated downstream inside the Z-pinch so that we can investigate the distribution of the azimuthal B-fields of the Z-pinch close to the axis (<15 mm) without a high-intensity laser system. Although the ion source region is extensive (i.e., not point-like) and its properties are still subject to our study, B-field measurements are possible because the point-like projection selects the deflected deuterons via a pinhole camera. We can avoid undesirable crossing of the ion trajectories in the azimuthal B-fields because the small pinhole on top of the ion detector acts as a well-defined crossing point of ion trajectories. Because the probing deuterons originate from within the Z-pinch itself, we call our method a *Z-pinch-driven ion deflectometry*.

This paper is structured into sections and subsections as follows: In Sec. II, we discuss the path integral of B-fields $\int \mathbf{B} \times d\mathbf{L}$ and its radial component $\int B_\phi dz$ along ion trajectories, which are crucial quantities for the ion deflectometry B-field measurements. In Sec. III, we describe experiments on GIT-12 and the analysis techniques for estimating averaged B-fields $\overline{B_\phi}$ from the measured ion displacements,

and for the examination of the deflectogram structure. This section introduces the three vital elements of our unique diagnostics that enable the deflectometric measurements of azimuthal B-fields in Z-pinch plasmas. In Subsection III A, we describe the first two, which are coupled to the Z-pinch. The first one is an alternative ion source for the backlighting by employment of the deuteron beams accelerated inside the Z-pinch. The second one is a fiducial deflectometry grid (*D-grid*), which we insert into the anode–cathode gap. It separates the ion source from the rest of the imploding plasma and its distorted shadow captures ion deflections in the azimuthal B-field below the D-grid. Conventional ion sources for the deflectometry are point-like, but in our experiments, deuterons are accelerated in a broad region above the D-grid. However, the deflectometric measurements are still possible if we detect the deflected ions via a point-like projection (e.g., through a small pinhole). In Subsection III B, we explain the deflectometry setup and introduce the last key component of our diagnostics, which is a distant pinhole camera for the detection of deflected deuteron beams. In Subsection III C, we propose an analytic method for the measurement of the averaged B-fields \overline{B}_ϕ , coupled to the path-integrated B-field $\int B_\phi dz$. In Subsection III D, we use our ion-tracking simulations and illustrate four types of characteristic distortions of synthetic deflectograms, which are coupled to four current density distributions.

In Sec. IV, we discuss our experimental results and analysis. In Subsection IV A, we present the first-ever experimental Z-pinch-driven deflectograms. The quality of these data varies, and thus, the deflectograms provide different amounts of information about the B-fields. In Subsection IV B, we show that even low-quality deflectograms without a distorted D-grid shadow allow us to estimate the total current in the Z-pinch during the ion imaging. In Subsection III D, we investigate the formation and the structure of the D-grid patterns in the synthetic deflectograms via our ion-tracking simulations. In Subsection IV C, we analyze three selected deflectograms with recognizable D-grid shadows and reconstruct 2D (x-y) maps of the averaged B-fields, assuming the axially uniform B-fields. In Subsection IV D, we carry our analysis of one experimental deflectogram even further. Using an experimental deflectogram and a side view, namely a soft x-ray (SXR) image, of the imploding plasma captured during the ion imaging, we numerically reconstruct a 2D (r,z) topological map of the local B-fields and the current. At the end of this paper (Sec. V), we conclude our experimental results and outline our plans to improve our future experiments employing ion deflectometry for B-field measurements in Z-pinch plasmas.

II. DEFLECTION EQUATION AND PATH-INTEGRATED MAGNETIC FIELD

Ion deflectometry is used for measurements of E- and B-fields. In this paper, we exclude electric fields, and we assume a highly conducting Z-pinch plasma with solely azimuthal magnetic fields B_ϕ , which are nearly stationary for the passing ions. Let the energy of ion beams be sufficiently high, so the collisional scattering and the stopping power are low even in high-density plasmas. Furthermore, let the ion beam has a space-charge potential negligible compared to the beam energy E so that the ions act as individual test particles.

A cartoon of the conventional experimental setup of the ion deflectometry is illustrated in Fig. 1. Ions are emitted axially toward the plasma from a divergent point-like source, so the ion beams are

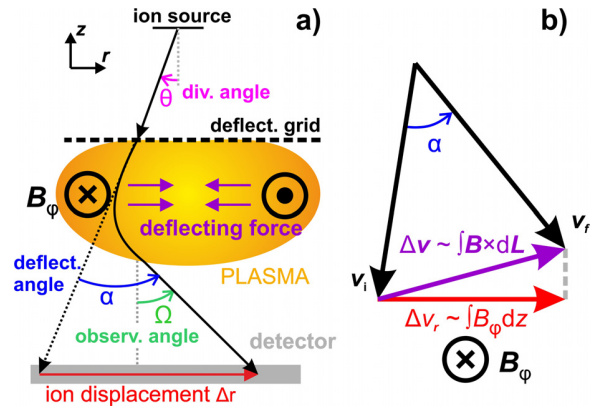


FIG. 1. (a) Scheme of a typical experimental setup of the ion deflectometry. Ions are emitted into the plasma through the deflectometry grid (D-grid), which splits the beams into the beamlets. An image of the ions deflected in the azimuthal B-field in the plasma is recorded by an ion detector. By measuring deflection angles α from ion displacements in the detector Δr , we estimate the path-integrated B-field. (b) Deflections of the ion in the perpendicular B-fields cause a rotation of the ion velocity vector, which can be characterized by a change of its direction Δv from its initial velocity v_i to its final velocity v_f by the deflection angle α . The vector Δv is proportional to the path-integrated B-fields $\int \mathbf{B} \times d\mathbf{L}$ and its radial component Δv_r to $\int B_\phi dz$. Because the ion energy is conserved during the motion in B-fields, the magnitude of the velocity remains the same, that is, $v = \|v_f\| = \|v_i\|$.

laminar. Before entering the plasma, the ions pass through a fiducial deflectometry grid (*D-grid*). A shadow of the grid is imprinted into the ion beams, which split into beamlets. In the plasma, the ions are deflected by a deflection angle α due to magnetic fields. Finally, the deflected ions reach an ion detector, usually a filtered stack of radiochromic films (RCF) or CR-39 track detectors, and create a distorted image of the D-grid shadow, a *deflectogram*.

When the ions are going through the magnetic fields, the Lorentz force changes directions of their velocity vectors. The initial velocity v_i is rotated to its final velocity v_f . We can characterize the rotation as a velocity shift by a vector $\Delta v = v_f - v_i$, for which we can write

$$\Delta v = -\frac{Q}{m} \int \mathbf{B} \times v dt = -\frac{Q}{m} \int \mathbf{B} \times d\mathbf{L}, \quad (1)$$

where Q and m are the ion charge and mass, and $v dt = d\mathbf{L}$ is an element of the ion path. During the magnetic deflections, the magnitude of the ion velocity vector remains the same $v = \|v_f\| = \|v_i\|$. The vector integral $\int \mathbf{B} \times d\mathbf{L}$ denotes the path-integrated B-field, which is a crucial quantity describing the cumulative effect of magnetic fields on deflecting ions along the ion path. It is inherently coupled with a deflection angle α by which the ions are deflected, and their velocities are rotated during their deflections. The deflection angle α is related to a strength of the path-integrated B-field $\|\int \mathbf{B} \times d\mathbf{L}\|$ by a deflection equation⁵¹

$$\left| \sin\left(\frac{\alpha}{2}\right) \right| = \frac{\|\Delta v\|}{2v} = \frac{Q}{2mv} \left\| \int \mathbf{B} \times d\mathbf{L} \right\|. \quad (2)$$

The path-integrated B-field $\int \mathbf{B} \times d\mathbf{L}$ and the deflection angle α have similar importance for the ion deflectometry as do the integral $\int n_e(s) B_\parallel(s) ds$ and the rotation angle β for the Faraday rotation.

However, the ion deflectometry does not require knowledge of the electron density distribution along the ion paths and it can be used in the vacuum environment.

The path-integrated field $\int \mathbf{B} \times d\mathbf{L}$ represents an effective sum of ion deflections along the ion path. Ion trajectories in topologically different but equivalent B-fields result in the same value of this integral. For example, suppose that an ion undergoes the same but opposite consecutive deflections or rotates by a multiple of the complete orbit. In that case, a contribution of this part of the ion trajectory to the path-integrated B-fields is zero because the velocity direction after deflections remains the same as before them ($\mathbf{v}_i = \mathbf{v}_f$). Given by the sine function in Eq. (2), there is a maximum of the measurable path-integrated B-field $|\int \mathbf{B} \times d\mathbf{L}|$, which corresponds to a half turn ($\alpha = \pi$). One orbit deflection of a 1-MeV proton means two half turns and ~ 100 Tcm.

Because we assume only azimuthal B-fields \mathbf{B} with the azimuthal symmetry, the components of $\int \mathbf{B} \times d\mathbf{L}$ are $\int (0, B_\phi, 0) \times (dr, rd\phi, dz) = (\int B_\phi dz, 0, -\int B_\phi dr)$, where dr and dz are not differentials of independent spatial coordinates but components of an ion path element $d\mathbf{L} = (dr, dz)$. Therefore, they depend on each other according to the motion equation due to the Lorentz force. A radial component of the velocity shift vector Δv_r is given by

$$\Delta v_r = v_{fr} - v_{ir} = v(\sin \Omega - \sin \theta) = -\frac{Q}{m} \int B_\phi dz. \quad (3)$$

The vectors \mathbf{v}_i and \mathbf{v}_f have radial components v_{ir} and v_{fr} , and make angles θ and Ω with the negative direction of the Z-axis, respectively, as illustrated in Fig. 1. Let these angles be left-handed about the B-field vector \mathbf{B}_ϕ . The angle θ is coupled with the initial velocity \mathbf{v}_i and the ion source's divergence, so we call it the *divergence angle*. The angle Ω relates to the final velocity \mathbf{v}_f and an incident angle at which ions are detected, so we call it the *observation angle*. We define the deflection angle α as a difference between the initial and final angles $\alpha = \Omega - \theta$. However, a sign of the divergence angle θ in Fig. 1 is opposite to the observation angle Ω , as it is set in our experimental configuration, and therefore, $|\alpha| = |\Omega| + |\theta|$. In reality, either the divergence angle θ or the observation angle Ω usually cannot be easily measured in the experiment, which complicates direct measurements of the deflection angle α and, hence, the path-integrated fields $\int \mathbf{B} \times d\mathbf{L}$. Therefore, numerical ray-tracing simulations are often necessary. By choosing the specific experimental setup, one can determine one of these angles. If the ions are emitted to the D-grid from a point, the divergence angle θ is set. If the ions are projected onto the detector through a point (e.g., a small pinhole), the observation angle Ω is established.

The recorded image in the detector displays a map of D-grid distortions (deflectometry) or simply the ion fluence (radiography), which represents the ion displacements. Because the ions are emitted along the Z-pinch axis, we record only radial displacements $\Delta r = \int \Delta v_r dt$. For the path-integrated B-field measurements from the experimental data, we need to find a relation between Δr and $\int \mathbf{B} \times d\mathbf{L}$. Typically, the estimation of the path-integrated B-fields from the measured ion displacements is provided by a paraxial approximation or a specific experimental setup.

In laser-produced plasma experiments, the dimensions of the observed plasmas a are small ($\sim \mu\text{m}$) compared to their distance to the detector A ($\sim \text{mm}$). For small proton deflections ($\sin \alpha \approx \alpha$), one can use the paraxial approximation and obtain the deflection angles

$\alpha = (Q/m_p v_p) \int B da$ from the proton displacements $\Delta r \propto \alpha A$, where m_p and v_p are the proton mass and velocity, respectively. In this approximation, deflections are small deviations of the laminar proton rays emitted from the well-defined point-like source. Because the laser-produced plasmas are usually expanding and highly dynamic, their spatial scale during ion probing may be difficult, and thus, only values of the path-integrated B-field are presented. They are calculated using numerical simulations⁵³ and can reach up to hundreds of $\text{MG} \mu\text{m}$ or a few Tcm (e.g., in Ref. 33), which correspond to deflection angles of a few degrees ($100 \text{ MG} \mu\text{m} \sim 3^\circ$, for 3-MeV protons).

In tokamak plasmas, the heavy ion beam probe (HIBP) diagnostic is used for the measurements of local fluctuations of the toroidal vector potential A_ϕ . It analyzes the toroidal shift $\Delta\phi$ of the probing heavy ions in the detector caused by a change in their gyroradius in a selected region of the plasma (sample volume) due to their additional ionization. The deflection angles are large because both the ion injector and the ion collector are located on the low-field side of the tokamak vessel. Again, only small fluctuations of predicted ion trajectories in the equilibrium magnetic fields are investigated.^{41,42,44} The experimental data by conventional measurements of equilibrium plasma parameters are required for the numerical reconstruction of these equilibrium magnetic fields and the ion trajectories.

In the Z-pinch plasmas, we can use neither of these two approaches. The expected path-integrated magnetic fields (tens of Tcm) are too strong to use the paraxial approximation, and the adequately small ion source requires a high-intensity laser system connected to the Z-pinch device. Compared to the tokamak plasmas, we have only limited information about the topology of ion trajectories. However, in Z-pinch plasmas, one may consider only azimuthal B-fields, which are weakly dependent on a z-variable. To employ the ion deflectometry in Z-pinch plasmas, we have developed our unique experimental setup. Its three key elements are: a source of multi-MeV deuterons, investigated in our previous research,^{54,55} a fiducial deflectometry grid, and, finally, a projection through a small and distant pinhole, which selects deflected deuteron beams with aligned trajectories. This experimental setup allows us to apply several approximations to estimate the path-integrated $\int B_\phi dz$ and will be discussed in Sec. III.

III. EXPERIMENTAL SETUP AND ANALYSIS TECHNIQUES

A. Experimental configuration

At present, ion sources used for ion deflectometry are usually external and well defined. For the ion beam probe diagnostics in tokamaks, ion beams are provided by an ion injector supply, which is already employed for plasma density and potential measurements. In the proton radiography of laser-generated plasmas, MeV protons are produced by the interaction of a high-intensity laser with a target⁵⁶ or a fusion capsule filled by D^3He gas.⁵⁸ In both cases, a virtual point-like source of laminar proton beams is created. Now, we introduce an alternative for the source of ions capable of probing Z-pinch B-fields. For a few past years, we have studied the acceleration of multi-MeV hydrogen ions in Z-pinch plasmas. The obtained experience enabled us to enhance both an average ion and neutron yield and better understand the ion acceleration mechanism.⁵⁴

The experimental results discussed in this paper come from the first-ever Z-pinch-driven ion deflectometry experiments performed on the GIT-12 generator in Tomsk, Russia. The peak current of this

pulsed power device is ~ 3.5 MA with ~ 1.7 μs rise time, and the circuit current during the stagnation of the Z-pinch is ~ 2.7 MA. The electrodes, planar meshes, are separated by the 20 – 25 mm distance. The experiments are carried out in a configuration with a hybrid gas-puff (see Refs. 54 and 57 for more details). A homogenous and uniformly conducting current sheath is created in preionized low-density (~ 5 $\mu\text{g cm}^{-1}$) carbon-hydrogen (CH) plasma shell injected by cable guns before the implosion. Deuterium gas load (~ 100 $\mu\text{g cm}^{-1}$) is puffed from supersonic nozzles and then heated and compressed by an imploding current sheath, resulting in a Z-pinch. Figure 2 illustrates a typical evolution of the imploding Z-pinch plasma. First, the plasma implodes toward the axis of the experimental setup. Afterward, a stagnation of the Z-pinch occurs, and a plasma neck is created due to plasma instabilities near the anode. The density of the perturbed plasma drops until the current is subsequently disrupted due to a rapid increase in the plasma impedance. Due to the loss of its quasineutrality, the plasma neck is depleted. Shortly after the disruption (~ 1 ns), a burst of the hydrogen ion beams, mostly deuterons, with energies up to tens of MeV⁵² is accelerated in the current direction in the depleted gap near the anode.⁵⁴ Some protons can also be accelerated since they are present as an impurity from the preionized low-density CH-plasma shell. However, the deuterons accelerated from the dense D₂ gas-puff load predominate. During the ion emission, the azimuthal magnetic fields in the plasma near the cathode remain relatively unaffected and deflect accelerated ions arriving downstream from the depleted gap. Even during their acceleration phase, the ions are deflected by both transient electric and magnetic fields, but we assign these effects to the acceleration processes in the depleted gap and assume no ion acceleration in the plasma near the cathode in the time of ion emission. The ion beams carry information about transient fields during their *acceleration stage* near the anode, and about global B-fields during their *deflection stage* in the rest of the Z-pinch plasma. Simultaneous and unambiguous analysis of magnetic fields in both stages during one shot is impossible. Thus, we study these two stages of the ion trajectories separately. The mechanism of the efficient ion acceleration due to Z-pinch plasma neck disruption is thoroughly discussed by Klir.⁵⁴ In the present paper, we focus on the measurements of the global magnetic fields using already accelerated deuterons. Therefore, we generalize the *ion source* as the region above the D-grid. We only demand that the ion beams passing the D-grid at any point have sufficient divergence to be focused into the pinhole even in the strong B-fields.

To avoid strong deflections and complicated ion paths, the energy of the probe ions should be sufficiently high. From Eq. (2), we see that for reasonable measurements of $B_p \sim 10 - 100$ T with dimensions $L \sim 1$ cm (i.e., with the path-integrated fields of $|\int \mathbf{B} \times d\mathbf{L}| \sim 10 - 100$ Tcm), the deuteron energies $\sim 1 - 10$ MeV are favorable. Other conditions for our measurements are the sufficient fluence and divergence of the ion beams. The former is needed for a good contrast of the deflectograms; the latter is to offset the ion focusing by the azimuthal magnetic field. The spectrum of the accelerated deuterium beams in our experiments is quite broad. However, both ion divergence and fluence decrease with the ion energy, and thus, for mapping the B-field distribution, we could only utilize deuterons with energies of 1 – 5 MeV. Achieving such ion energies is, in our opinion, within reach of current MA Z-pinch devices so that similar experiments may be considered in other MA Z-pinch facilities. In cooperation with the team working in Naval Research Laboratory in Washington, DC, on the HAWK generator, we have accelerated deuterons up to energies >7 MeV⁵⁵ with sufficient ion fluence. Moreover, $\sim 0.1 - 5$ MeV protons have been reported on the MAGPIE pulsed-power generator.⁵⁸

Conventionally, the ion deflections are manifested using a fiducial mesh located between a source of the ion backlighting and the region of interest. However, in our case, the ion source is internal, that is, located together with the studied magnetic fields inside the Z-pinch plasma. To separate the source and the B-fields and to measure the ion deflections in our experiments, we place a circular stainless-steel (SS) deflectometry grid (*D-grid*) in the anode–cathode gap (see Fig. 3). The diameter of the D-grid is 20 mm. The D-grid has 2-mm-wide square openings and 0.5-mm-thick wires, and it is attached to the cathode mesh by a 10-mm-high and 330- μm -thick stainless-steel stalk wire. Figure 4 shows a series of SXR images obtained by a multichannel plate (MCP) camera, which captures the evolution of the imploding plasma with the inserted D-grid. As seen, the plasma splits and propagates above and below the D-grid, effectively creating two separated and partly independent Z-pinches. The plasma below the D-grid is delayed by several ns, and so, at the time of the current disruption and the ion emission, it is still imploding toward the axis. Surprisingly, in these experiments with the inserted D-grid, we detected ion beams with very high energies, reaching up to at least 55 MeV.⁵² The height of the D-grid is an important parameter for the ion acceleration mechanism. If the D-grid is put too close to the anode, it disrupts the acceleration mechanism and the ion emission. On the other hand, if the D-grid is put too close to the cathode, the ion acceleration is not

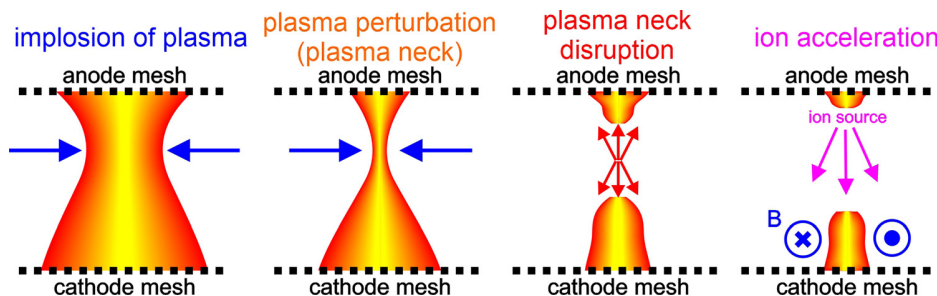


FIG. 2. Cartoon of a typical evolution of the Z-pinch plasma on GIT-12: plasma implodes toward the axis between the electrode meshes due to $\mathbf{J} \times \mathbf{B}$ force. A strangulated necked plasma appears near the anode due to the plasma instabilities, until it is disrupted. Shortly after, hydrogen ions (mostly deuterons) are accelerated in the depleted region after disrupted necked plasma and are deflected in azimuthal magnetic fields in the remaining plasma, which stay relatively unaffected by the disruption.

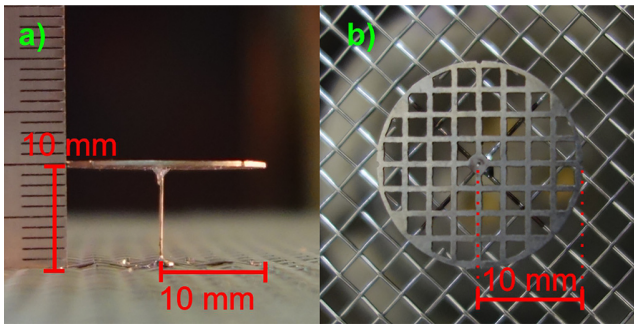


FIG. 3. Side view (a) and top view (b) of a circular stainless-steel (SS) deflectometry grid (D-grid). Its diameter is 20 mm, and it is connected by the 10-mm-high and 330- μm -thick stalk SS wire to the cathode mesh.

affected, but the current remains at the D-grid edge and does not penetrate below it. The D-grid does influence the plasma imploding but only to the extent that it separates the ion source from the rest of the plasma. The stalk wire supporting the D-grid may glow but carries only a small portion of the total current (see Sec. IV C). Because it prevents the depletion of the plasma on-axis, ions cannot be accelerated below the D-grid, which would complicate the analysis of the deflectogram and the B-field measurements.

B. Deflectometry setup

The setup of the ion deflectometry diagnostics is shown in Fig. 5. Probe deuterons are emitted downstream from the extensive and divergent source near the anode and intersect the D-grid plane at the initial radial positions r_0 . Here, their divergence is given by angle θ . A shadow of the D-grid is imprinted into the passing ions, and then, it becomes distorted when the ions are deflected in the azimuthal magnetic fields below the D-grid. When the ions reach the cathode plane, their radial positions are r_C . Because free electrons effectively neutralize a net charge of the ion beams in the plasma and the B-field are assumed negligible below the cathode mesh, the ions continue along the straight lines toward the pinhole camera, placed on the axis below the cathode mesh. The pinhole distance from the cathode is $l_{pin} = 105\text{ mm}$, and it determines the observation angle of the ions Ω at the radius r_C .

The pinhole camera is a metal container with one or a few tiny pinholes (250 – 500 μm in a diameter) bored in its top. The spacings between the pinholes are small compared to the distance between the cathode and the ion camera. Thus, we approximate these pinholes by only one pinhole located in the center of the setup. Inside the camera, there is a stack of radiochromic films (RCF) with Al filters. The ions are projected through a pinhole onto the detector stack and cause a measurable change of color in RCF, indicating a fluence of the detected ions. Here, the final image (deflectogram) of the distorted D-grid shadow is finally recorded. Distortions of the deflectogram created by ion displacements Δr are proportional to $\int B_\phi dz$. Each position of RCF detectors in the stack is coupled to a Bragg peak of the ion stopping power. We can estimate the lower energy threshold for the ion signal in each layer using Stopping and Range of Ions in Matter⁵⁹ (SRIM) simulations.

Suppose there would be no fields [see Fig. 5(a)], then, only ions directing right into the pinhole would be detected and the deflectogram would show a scaled original image of the undistorted D-grid shadow. We can use the corresponding ion positions in the cathode plane r'_0 as a reference for measuring the ion displacement Δr . We measure these displacements at the cathode because the experimental deflectograms show scaled images of the deflected ion beams in the cathode plane r_C due to the direct projection through the point-like pinhole between the cathode and the detector plane.

In the conventional setup, a fixed point of the virtual source is used to set the divergence angle θ . In contrast, we have the extensive ion source, but we use a fixed point of the pinhole to set the observation angle Ω [cf. Fig. 5(b)]. Due to the large cathode-pinhole distance l_{pin} compared to the ion radial position r_C at the cathode, the pinhole camera captures the ions at a very small observation angle ($\Omega \lesssim 7^\circ$). Then, the divergence angle θ is nearly equal and opposite to the deflection angle α . It means that, in strongly focusing magnetic fields, ion beams leaving the D-grid must be highly divergent (“defocused”) to be detected after their deflection. In other words, the source must emit ions far outwards from the axis, so they can be focused toward the axis into the pinhole by the azimuthal B-fields. If $\Omega \approx 0$, we can simplify Eq. (3) to

$$|\sin \theta| \approx |\sin \alpha| = \frac{Q}{mv} \int B_\phi dz = \int \frac{dz}{R_L}, \tag{4}$$

where R_L is an ion Larmor gyroradius. For each ion trajectory, we can study only the radial component of the path-integrated field

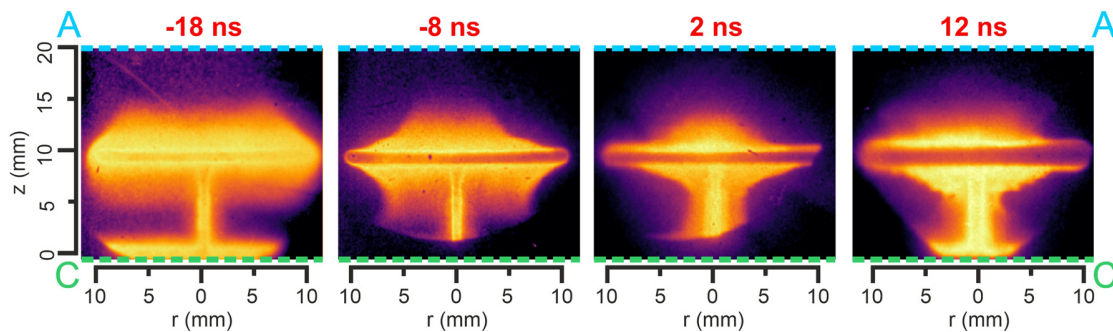


FIG. 4. SXR images of the evolution of the imploding plasma with the inserted deflectometry grid obtained by a multichannel plate (MCP) camera. The $t = 0\text{ ns}$ corresponds to the onset of $>2\text{ MeV}$ gamma, neutron, and ion emission.

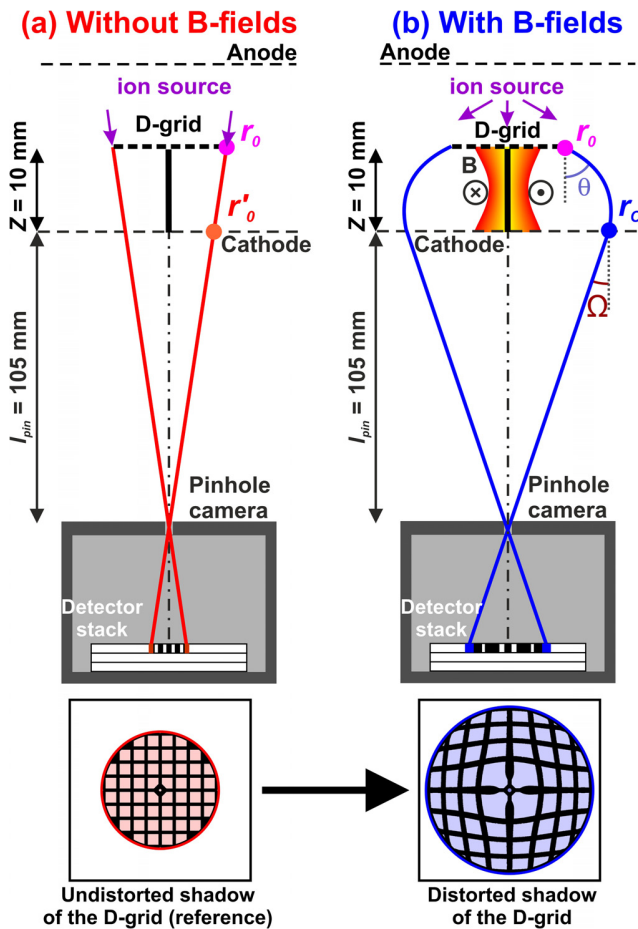


FIG. 5. Not-to-scale scheme of the deflectometry setup. Ions are accelerated downstream from the extensive and divergent source in the region above the D-grid. A pattern of the D-grid is imprinted into the passing beams and recorded by a distant pinhole camera. In the case of no fields below the D-grid (a), the ions must aim directly from the D-grid into the pinhole to be detected. The D-grid shadow is not distorted and shows us a reference image. In the case of non-zero azimuthal B-fields below the D-grid (b), the ions must leave the D-grid at a certain divergence angle θ because the focusing B-fields deflect them toward the axis and into the pinhole. Due to ion deflections, the D-grid shadow becomes expanded and distorted.

$(\int \mathbf{B} \times d\mathbf{L})_r = \int B_\phi dz$ instead of its strength $\|\int \mathbf{B} \times d\mathbf{L}\|$. This approximation holds as long as $\sin(\alpha) \approx 2 \sin(\alpha/2)$ [cf. Eqs. (2) and (4)], which can be applied to moderate ion deflections by deflection angles $\alpha < 50^\circ$. For every point in the measured distribution of a deflection field (a map of D-grid displacements in the deflectogram), we can find a corresponding value of an averaged azimuthal B-field $\overline{B_\phi} = \int B_\phi dz / Z$, where Z is the D-grid-cathode distance. Because we maximize the axial scale of the studied B-field region by $Z = 10$ mm, the averaged B-field is the low estimate of the actual B-fields, even if perturbed (see Sec. IV D). If deflection angles are not very small and one cannot use the paraxial approximation, the averaged B-fields $\overline{B_\phi}$ are usually estimated by reproducing the experimental data via numerical ray-tracing simulations. However, in our experiments, we can

approximate the ion trajectories by Larmor orbits and estimate $\overline{B_\phi}$ analytically using a Larmor orbit approximation.

C. Larmor orbit approximation

If the B-field strengths are moderate and the gradients are gentle, a curvature of an ion trajectory changes slowly along the ion path. In that case, we can approximate this ion trajectory by a Larmor orbit with an averaged radius $\overline{R_L}$ [see Fig. 6(a) and 6(b)] and calculate an averaged Larmor B-field $\overline{B_L}$.

The deflectometry setup provides enough information to find $\overline{R_L}$ for each ion trajectory from the measured quantities [see Fig. 6(a)]: the initial ion position r_0 at the D-grid, the final position of the deflected ion r_C at the cathode, and a tangent line of the ion trajectory at the cathode determined by the observation angle Ω . Because $\Omega \approx 0$, the initial radial ion position r_0 is almost equal to the reference ion position r'_0 at the cathode ($r_0 - r'_0 < 1$ mm). Therefore, we define the ion displacement in the cathode plane as $\Delta r \approx r_C - r_0$. By solving a simple geometric problem, we obtain a relation for Larmor B-fields $\overline{B_L}$

$$\overline{B_L} = \frac{mv}{Q} \frac{2l_{pin}\Delta r + 2Z(\Delta r + r_0)}{[(\Delta r)^2 + Z^2]\sqrt{(\Delta r + r_0)^2 + l_{pin}^2}}. \quad (5)$$

Figure 6(c) shows that $\overline{B_L}$ calculated by Eq. (5) is almost independent to the initial radial ion position r_0 . Moreover, the curves shown in Fig. 6(c) have a single maximum, which roughly corresponds to the maximum of the sine in Eq. (4), when the deflection angle $\alpha = \pi/2$ and $\Delta r \approx \overline{R_L} \approx Z$. For weaker (moderate) B-fields ($\overline{B_L} \lesssim 30$ T for 2.3-MeV deuterons), $\overline{B_L}$ grows linearly with increasing ion displacements Δr at the cathode. Because we assume that the Larmor orbits approximate the ion trajectories, then $\overline{B_L}$ approximates the averaged B-field $\overline{B_\phi} = \int B_\phi dz / Z$. Then, the linear part of the curves in Fig. 6(c) can be fitted by

$$\Delta r \approx \frac{Q}{2mv} \overline{B_L} Z^2 = \frac{Q}{2mv} Z \int B_\phi dz. \quad (6)$$

Therefore, we obtain a simple and linear relation between the ion displacements $\Delta r = \int \Delta v_r dt \propto \int \int B_\phi dz dt$ and the Larmor B-fields $\overline{B_L}$. We will demonstrate the Larmor orbit approximation on an example of the B-field profile [see Figs. 6(b) and 6(d)]. The azimuthal B-fields are axially uniform and linearly increasing with a radius up to $R_p = 9$ mm, where the total pinch current becomes 1.5 MA. The choice of the 9-mm-radius Z-pinch allows us to study B-fields both inside and outside the Z-pinch. In these simulations, a deuterium source is divergent, extensive (broad region above the D-grid), and monoenergetic (2.3 MeV).

To retrieve the averaged B-fields from the deflectograms, we need to assign the estimated B-fields $\overline{B_\phi}$ to some radial position between r_0 and r_C . It is reasonable to choose an averaged radial position \bar{r} integrated along the ion trajectory by the axial ion position z , that is, $\bar{r} = \int r dz / Z$, which characterizes the mean radius of the ion trajectory. In Fig. 6(b), our ion-tracing simulations show that for moderate deflections, this averaged radius \bar{r} is close to the measured radial position of the ions in the cathode plane ($\bar{r} \approx r_C$). Because the observation angle Ω of the detector is set low by the large pinhole-cathode distance l_{pin} , we detect only deflected ion beams that are aligned almost parallelly to the Z axis by the focusing B-field during their deflections and the ion trajectories have similar shape near the cathode.

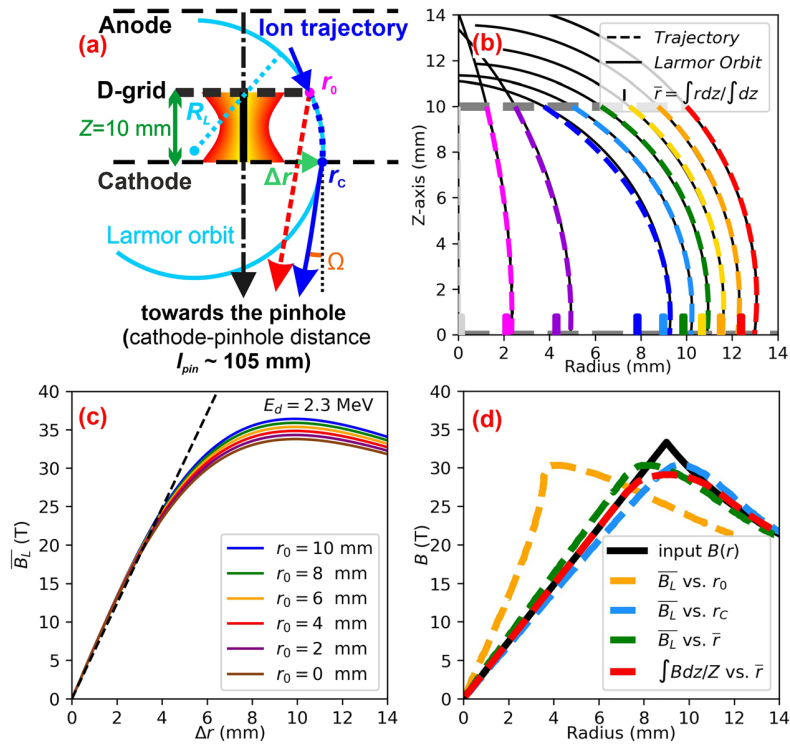


FIG. 6. (a) Moderate ion deflections can be approximated by a Larmor orbit approximation, which assumes small variations of the B-fields along the ion path. (b) Simulated trajectories of ions, deflected in azimuthal B-fields, can be quite well approximated by Larmor orbits. In this example, the synthetic B-field is axially uniform and grows linearly ($B_\phi(r) \propto r$) up to 9 mm radius, where the pinch current reaches $I = 1.5$ MA. These parameters are used for demonstration purposes of this approximation. (c) The Larmor-orbit B-field $\bar{B}_L(\Delta r, r_0)$ given by Eq. (5) depends weakly to the initial ion position r_0 at the D-grid. For moderate strengths, \bar{B}_L is linear with respect to the radial displacements Δr according to Eq. (6). (d) Reconstruction of the radial B-field profile $B_\phi(r)$ (black lines), which is the same as in a figure (b). First, it is reconstructed from the measured displacements using the Larmor orbit approximation (yellow, blue, green lines), where \bar{B}_L are assigned to the ion positions at the D-grid r_0 , at the cathode r_c , and then, to the averaged radius $\bar{r} = \int r dz / Z$, respectively, and finally by numerical ion-tracking simulations (red line), where $\int B_\phi dz / Z$ are assigned to averaged radius \bar{r} . The maximum of this B-field distribution is 33 T, which is slightly beyond the limit of the moderate B-fields for 2.3-MeV deuterons.

Therefore, the radii near r_c have greater weights in the integral $\int r dz$. Figure 6(d) illustrates how well the ion deflections can reproduce the radial profile of B-fields implemented in the simulations.

For B-fields up to $B \lesssim 30$ T, the deflections of the 2.3-MeV deuterons are moderate, and the averaged B-fields $\bar{B}_\phi = \int B dz / Z$ copy the input B-field very well. The best fit is if \bar{B}_ϕ is assigned to the averaged radius \bar{r} (red curve). However, even if \bar{B}_ϕ is assigned to the radial ion position at the cathode r_c (blue curve), the fit is still good.

For $B > 30$ T, the deuteron deflections are too strong, and ions lose the ability to measure B-field locally. Due to our choice of the current 1.5 MA at the 9 mm radius (~ 33 T) in our example, we show the performance of the ion deflectometry slightly beyond the B-field 30-T limit of the Larmor approximation for 2.3 MeV deuterons. Since the shape of the ion trajectories is set by Eq. (4), the divergence angle θ must grow with stronger B-fields and, hence, larger deflection angles α . Therefore, the ion trajectory becomes more curved close to the anode (near the initial radius r_0). Then, the distance between \bar{r} and r_c becomes relatively large [see blue indicator in Fig. 6(b)] and ion deflections stop reflecting the B-field distribution [see Fig. 6(d)]. Similar problems appear if the B-fields gradients are too steep. Comparing the red curve of simulated

averaged B-fields \bar{B}_ϕ to the Larmor B-fields in Fig. 6(d), we observe that the retrieved B-field profile smoothing does not originate from the Larmor orbit approximation. On the contrary, it shows the inherent integrating behavior of ion deflectometry if the B-field magnitudes or gradients are too strong.

In Subsection III D, we present typical patterns of synthetic deflectograms and reconstruct their corresponding radial distributions of the axially uniform B-fields within the limits of moderate deuteron deflections.

D. Analysis of the synthetic deflectogram patterns for characteristic radial profiles of azimuthal B-fields

The D-grid displacements in the deflectograms manifest the radial distribution of ion deflections and path-integrated B-fields. To understand the experimental deflectograms and interpret their structure, we present synthetic deflectograms generated by our ion-tracking numerical code using characteristic radial distributions of axially uniform azimuthal B-fields $B_\phi(r)$. The experimental setup is implemented in the simulations. The pinch radius is $R_p = 9$ mm, where the total pinch current reaches 1 MA. We use 2.3 MeV deuterons, and

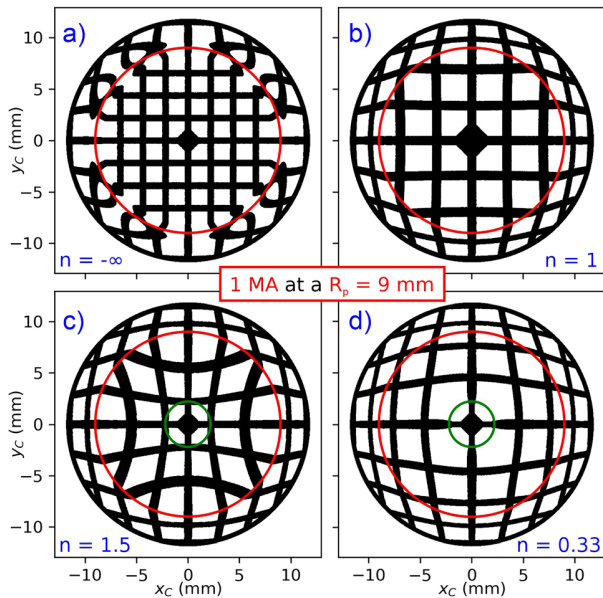


FIG. 7. Demonstration of typical synthetic deflectograms for four radial distribution of the B-field $B_\phi(r)$ inside the pinch with a radius $R_p = 9$ mm (red circle) where total pinch current reaches 1 MA. In the area within the pinch radius R_p , the B-fields are given by $B_\phi(r < R_p) = \mu_0 I r^n / 2\pi R_p^{n+1}$. Four typical profiles of current densities $j_z(r < R_p) \propto nr^{n-1}$ are coupled to four values of the exponent n : (a) $n = -\infty$: no current density inside the Z-pinch [$B_\phi(r < R_p) = 0$]; (b) $n = 1$: constant current density; (c) $n > 1$: radially increasing current density; (d) $0 < n < 1$: radially decreasing current density. In the last two cases, there is no B-field inside the radius $R_{cs} = 2.2$ mm (green circle). Outside the pinch volume (i.e., for $r > R_p$), there is no current density and so $B_\phi(r \geq R_p) = \mu_0 I / 2\pi r$. The images are scaled to the corresponding size at the cathode plane.

thus, the maximum B-field strength of ~ 22 T lies in the linear part of the curve in Fig. 6(c).

For a demonstration of the typical distortions of the D-grid shadow in the deflectograms, we present four synthetic deflectograms in Fig. 7. In the region within the pinch radius ($r < R_p$), delimited by a red circle, we compare four characteristic radial distributions of azimuthal magnetic fields $B_\phi(r < R_p) = \mu_0 I r^n / 2\pi R_p^{n+1}$ with current densities $j_z(r < R_p) \propto nr^{n-1}$ according to four cases of the exponent n :

(a) $n = -\infty$: a thin skin-current sheath with no B-field inside; (b) $n = 1$: uniform current density; (c) $n > 1$: increasing current density with a radius; (d) $0 < n < 1$: decreasing current density with a radius. In the two last cases, the current sheath is shifted and there is no B-field within the radius $R_{cs} = 2.2$ mm (green circle), which roughly agrees with the experimental data presented in Subsection IV C. Outside the pinch ($r > R_p$), there is zero current density and all B-field distributions are identically $B_\phi(r \geq R_p) = \mu_0 I / 2\pi r$.

For $r > R_p$, the distorted D-grid pattern has the same shape and structure for all examples, with the only exception of (a). In the case of the skin current, the B-field gradient is too steep, so the deflecting ions cannot quickly change their trajectories and accurately copy the jump in the B-field profile. Thus, the deflected ions create a broader distorted transition in the deflectogram near the Z-pinch radius of R_p .

For $r < R_p$, the D-grid shadows are substantially distinct. In general, the ion deflections cause an expansion of the D-grid shadow. The D-grid pattern structure in the deflectogram (b) keeps the squared but magnified shape and resembles the deflectogram with no B-field (a). The deflectogram (c) shows an increasing trend of ion displacements with an increasing radius. Because the D-grid pattern is more displaced in the corners of the square openings, the deflected ions create a concave pattern (*pincushion distortion*). In contrast, the ion displacements in the deflectogram (d) are decreasing with an increasing radius. The square D-grid openings are “inflated” outward, which results in a convex pattern (*barrel distortion*) of the D-grid shadow. Moreover, notice that in the deflectogram (d), the transition of the distortions near the radius R_p is very smooth.

These observations can be explained when we compare ion displacements Δr and the implemented distributions of the B-fields $B_\phi(r)$ (see Fig. 8). As seen, the distributions of the ion displacements in the cathode plane Δr follow the radial profile of the path-integrated B-fields $\int B_\phi dz$, according to Eq. (6). Because we input the axially uniform B-fields, the averaged B-fields $\bar{B}_\phi = \int B_\phi dz / Z$ approximate these B-fields B_ϕ . Due to the linear relation between Δr and B_ϕ , the derivative of the path-integrated B-fields and the distribution of the radial current density in the cylindrical coordinates $j_z(r < R_p) = \partial(rB_\phi) / (r\partial r) / \mu_0$ are proportional to displacement gradients $\partial(r_c \Delta r) / (r_c \partial r_c)$, which characterize the deflectogram structure. In both examples (a) and (b), the current density $j_z(r < R_p)$ is constant (in the former case, zero) and creates the regular squared grid pattern. In the other deflectograms (c) and (d), the current density profile $j_z(r)$ also dictates the distortion gradients. Near the pinch radius R_p in the B-field profile (d), the current density decreases so low that the pattern of the deflectogram within the red circle is similar to the outer region where j_z falls to zero, and hence, the transition in distortion at $r = R_p$ in Fig. 7(d) is hardly noticeable.

In conclusion, for moderate ion deflections and gradients of azimuthal B-fields, the magnitude of $\Delta r(r_c)$ is proportional to $\int B_\phi dz(r_c)$. If the B-fields are axially uniform, $\partial(r_c \Delta r) / (r_c \partial r_c)$ and

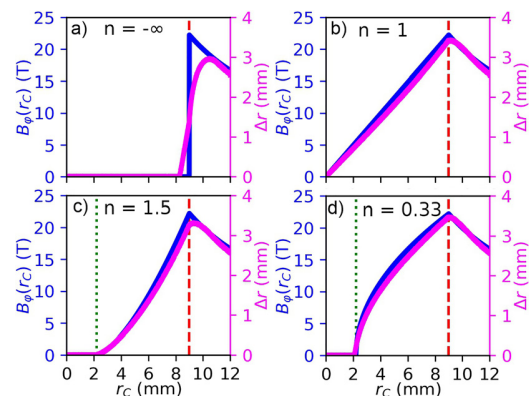


FIG. 8. Comparison of plots of the radial distributions of the input B-fields (blue curves) and displacements Δr of the D-grid (magenta curves), measured from the synthetic deflectograms in Fig. 7, according to the radial ion position in the cathode plane r_c . The total pinch current of 1 MA flows within the pinch radius $R_p = 9$ mm (red dashed line). In the deflectograms (c) and (d), we set no B-field within a radius $R_{cs} = 2.2$ mm (green dotted line).

the structure of the deflectogram (barrel, pincushion, etc.) are coupled to the current density profile j_z , mapped by the deflecting ions.

IV. EXPERIMENTAL RESULTS SUPPORTED BY OUR NUMERICAL SIMULATIONS

A. Experimental deflectograms

In Fig. 9, we present selected experimental deflectograms with distorted D-grid shadows and compare them to reference (“undistorted”) photographs of the original D-grids in the shots Nos. 2402, 2404, 2408, 2418, and 2420. The images are scaled to their corresponding size in the cathode plane. These are first-ever experimental data obtained via the Z-pinch-driven ion deflectometry and the first deflectograms of the Z-pinch using axially emitted ions. For better clarity, the deflectograms are presented in false colors with enhanced contrast. Parts of the detector irradiated by ions are bright, and the D-grid shadows are dark. The ions must traverse both the D-grid and the cathode mesh (cf. Fig. 5), and thus, shadows of them both are evident in the deflectograms. The meshes are rotated by the 45° angle relative to each other for a better distinction between them. Partially cut out the cathode mesh center helps a better, more unobstructed view of the D-grid center. The cathode-mesh shadow is not distorted because, below the cathode, ion trajectories are undeflected. Ion back-lighting in the images is not uniform. The absence of the ion signal in the deflectograms is caused by either a nonuniform ion source or ion beams deflected somewhere outside the pinhole (i.e., by not satisfying projection conditions).

Nevertheless, some parts or at least the edge of the distorted D-grid shadow are apparent on all shots in Fig. 9.

In the deflectogram of the shot No. 2402, the size and shape of the D-grid shadow are nearly identical to its original undistorted image. In this shot, the D-grid was placed closer to the cathode (~ 6 mm), which apparently prevented the current sheath below the D-grid from penetrating closer to the axis. Only a slight distortion near the D-grid edge indicates nonzero magnetic fields. In the other shots, the D-grid was located in ~ 10 mm distance from the cathode mesh. The current sheath propagated closer to the axis, and these deflectograms show the deformed D-grid shadows.

The deflectograms provide different amount of information according to their quality due to their clarity, which vary shot-to-shot due to the imperfect backlighting or blurry features of the D-grid shadow. In some shots, the D-grid shadow is not clear enough for retrieval of a B-field distribution. The expansion of the D-grid edge caused by the ion deflections allow us to estimate the total current flowing within reach of ion deflections, and it will be discussed in Sec. IV B.

Because the deflectograms show time-integrated images of ion beams deflected in the imploding plasma below the D-grid, the studied B-fields could vary during the ion probing (≈ 10 ns). According to the maximum implosion speed of the plasma, $\sim 4 \times 10^5$ m/s, the current sheath can move by ~ 4 mm during the 10-ns ion emission. However, if it were true, then the D-grid shadow would completely disappear. Although it might partly contribute to the low quality of some deflectograms (demonstrated by the shot No. 2418 in Fig. 9, for example), it is not a severe problem if the D-grid shadow is visible. Therefore, the emission of ions with the specific energy is much shorter or the plasma does not move much during this period. Moreover, we do not even observe multiple shadows or significant discontinuities of the D-grid caused by multiple exposures. On the other

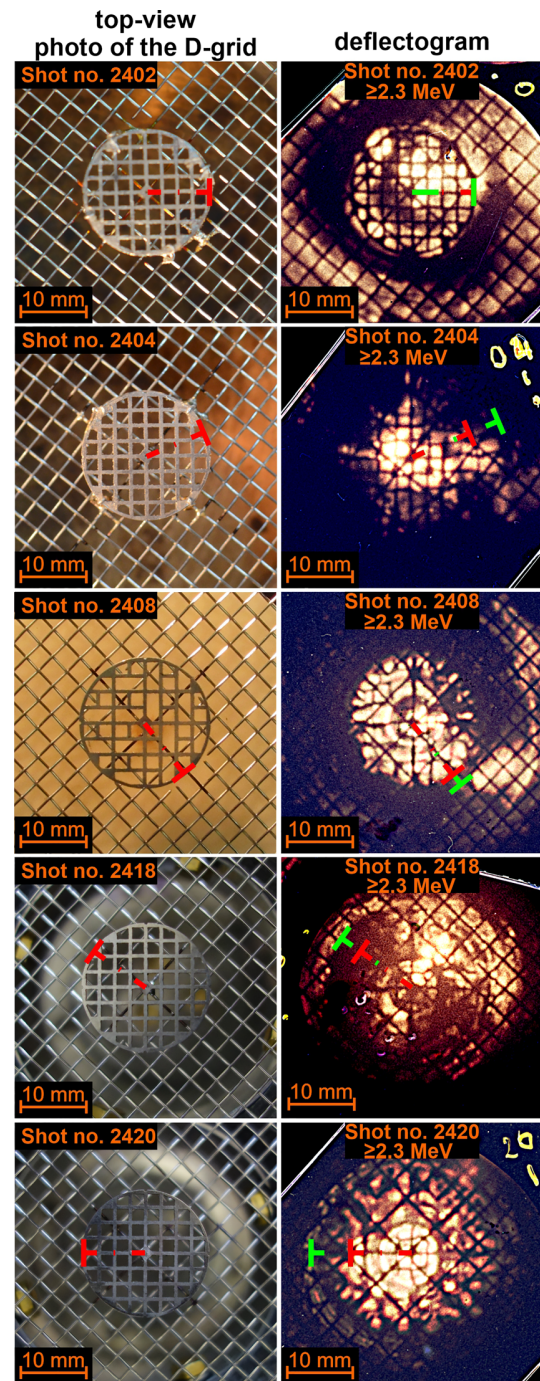


FIG. 9. Comparison of top-view photographs of the D-grid connected to the cathode mesh and the experimental deflectograms obtained in shot Nos. 2402, 2404, 2408, 2418, and 2420. Bright colors correspond to high ion fluence. The enlargement and distortion of the D-grid in the deflectogram are caused by ion deflections proportional to measured magnetic fields. Red and lime lines show the initial and displaced radius of the D-grid edge. The energy of the detected deuterons is ≥ 2.3 MeV. The images are scaled to their corresponding size in the cathode plane.

hand, the low image contrast may originate in ion scattering at the obstacle edges (i.e., D-grid or pinhole) or by the pinhole-camera resolution ($\delta \sim 0.8$ mm). However, larger complications arise from the deuteron energy estimation. All the experimental data discussed in this paper are recorded in the first RCF layers in the stack. They are shielded by a 30- μm -thick Al layer, and hence, their signals correspond to the deuteron energy threshold of 2.3 MeV. The detection probability of ions with higher energies is lower but not negligible. The second detector layer in the stack corresponds to 4.7-MeV deuterons, and thus, there is a relatively wide interval of possible deuteron energies. The beam energy estimation is the biggest but removable source of uncertainty in our measurements, and it will be addressed in future campaigns. Since the ion deflections grow with $\alpha \propto 1/\sqrt{E}$ according to Eq. (2), in theory, the path-integrated B-fields might be larger by a coefficient $\sqrt{4.7\text{-MeV}/2.3} \simeq 1.43$, that is, roughly 40%. Nevertheless, we will assume that most of the signal is created by monoenergetic 2.3-MeV deuterium beams but consider our results as low estimates of the measured quantities.

B. Estimation of the pinch current from the displacement of the circular D-grid edge

Displacements of the D-grid edge shadow provide undemanding measurements even from low-quality deflectograms, where the pattern of the distorted D-grid shadow is unclear or missing (see deflectogram of the shot No. 2418 in Fig. 9). Without the D-grid pattern, we have no information about distributions of the path-integrated B-fields, but we can estimate the value of the pinch current flowing within reach of ion deflections. To analyze the effects of the B-field distribution on the current measurements, we compare the results of several possible distributions in our ion-tracking simulations in Fig. 10.

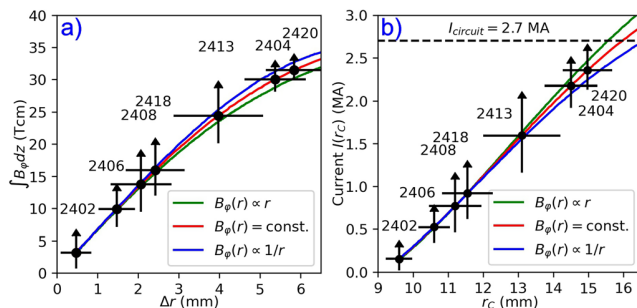


FIG. 10. (a) Estimation of $\overline{B_\phi Z}$ using the Larmor approximation [Eq. (5)] from the measured displacements Δr of the D-grid edge in the deflectograms of the selected shots (black dots). Plots of the simulated path-integrated fields $\int B_\phi dz$ for three radial distributions of axially uniform azimuthal B-fields $B_\phi(r)$ according to the edge displacements are close to each other. Therefore, from the single-point measurements of the averaged radius of the D-grid edge in the deflectograms, we can only estimate a single value of path-integrated or averaged B-fields $\overline{B_\phi}$. (b) Calculated averaged enclosed current $\overline{I}(r_C) = \overline{B_\phi} 2\pi r_C / \mu_0$ (black dots) and simulated currents $I(r_C)$ (lines) flowing within the radius r_C for these three B-field profiles are similar. The results show most of the 2.7-MA stagnation current flowing within the ~ 15 mm distance from the axis during ion probing in the shots Nos. 2404 and 2420. Error bars in the measured points are given by uncertainty of estimating the averaged radial displacement of the D-grid edge in the selected deflectograms. Arrows from these points show that these results are low estimates of the current.

We study three axially uniform azimuthal B-fields $B_\phi(r)$ with three different radial profiles: linear B-fields [$B_\phi(r) \propto r$], uniform B-fields [$B_\phi(r) = \text{const.}$], and decreasing B-fields [$B_\phi(r) \propto 1/r$]. The first B-field profile corresponds to a constant current density, the second to a decreasing current density with radius as $1/r$, and the last B-field profile is outside the Z-pinch. In these simulations, an extensive and divergent source of monoenergetic 2.3 MeV deuterons backlights the D-grid. Figure 10(a) shows plots of simulated path-integrated B-fields $\int B_\phi dz$ for these three distributions according to a radial shift Δr of the D-grid edge shadow in the cathode plane. The plots are very close to the uniform B-field curve, which corresponds to the Larmor orbit approximation. Since we utilize the displacement of a single deflection point (D-grid edge) from each experimental deflectogram, the measurements are rather insensitive to the radial distribution of $\int B_\phi dz$ and the axially uniform B-fields, and follow the relation in Eq. (5). Therefore, we can use the Larmor approximation for the evaluation of path-integrated B-fields $\overline{B_\phi Z}$ in the selected shots [black dots in Fig. 10(a)]. We consider the symmetric azimuthal displacement Δr of the averaged radius of the D-grid edge, highlighted in Fig. 9. For shot Nos. 2404 and 2420, the measured path-integrated B-fields reach up to ~ 31.5 Tcm, which is at the limit of the Larmor approximation for the given deuteron energy. In addition, we compare the currents $I(r_C)$ flowing within the reach of deflected ions, in Fig. 10(b). Again, the curves are close to the uniform B-field curve, which shows that the Larmor orbit approximation is a useful estimation for our measurements. In shot Nos. 2404 and 2420, the estimated averaged enclosed currents $\overline{I}(r_C) = \overline{B_\phi} 2\pi r_C / \mu_0$ reached up to ~ 2.4 MA at the ~ 15 -mm radius, which represents the majority of the total 2.7 MA circuit current during the stagnation. Error bars in the measured points are given by uncertainty of estimating the averaged radial displacement of the D-grid edge in the selected deflectograms. The maximal deviation error of the D-grid edge localization can be ~ 1.1 mm, which corresponds to maximal uncertainty of $\sim 20\%$, according to Eq. (5). However, these values describe only the statistical errors that are still much smaller than the uncertainty of the beam energy determination ($\sim 40\%$), which can lead to higher B-fields and currents. Therefore, the arrows in Fig. 10 remind us that these results are low estimates.

In Subsections IV C and IV D, we will investigate deflectograms, which provided information about the displacement field of many points representing the distorted D-grid pattern, which manifests the radial distribution of the path-integrated B-fields.

C. Mapping (x-y) profile of the azimuthal B-fields using the distorted D-grid pattern

If the deflectograms reveal a substantial part of the D-grid shadow, we can measure (x-y) distributions of the ion displacements and path-integrated B-fields. Now, we focus on the experimental data in the featured shots with numbers 2404, 2408, and 2420 [see Fig. 11(a)]. Highlighted parts of the distorted D-grid shadow in Fig. 11(b) correspond to representative points of the original D-grid, that is, nodes and midpoints of the D-grid pattern, which are recognizable in the deflectograms. Displacements of these points represent averaged ion deflections in ~ 1.25 -mm-long and ~ 0.5 -mm-wide D-grid segments, as if these ions would go through the D-grid structure. From the measured positions and displacements of these points, we establish a displacement field [black arrows in Fig. 11(c)], to which we assign averaged B-fields $\overline{B_\phi} = \int B_\phi dz / Z$ using the Larmor approximation.

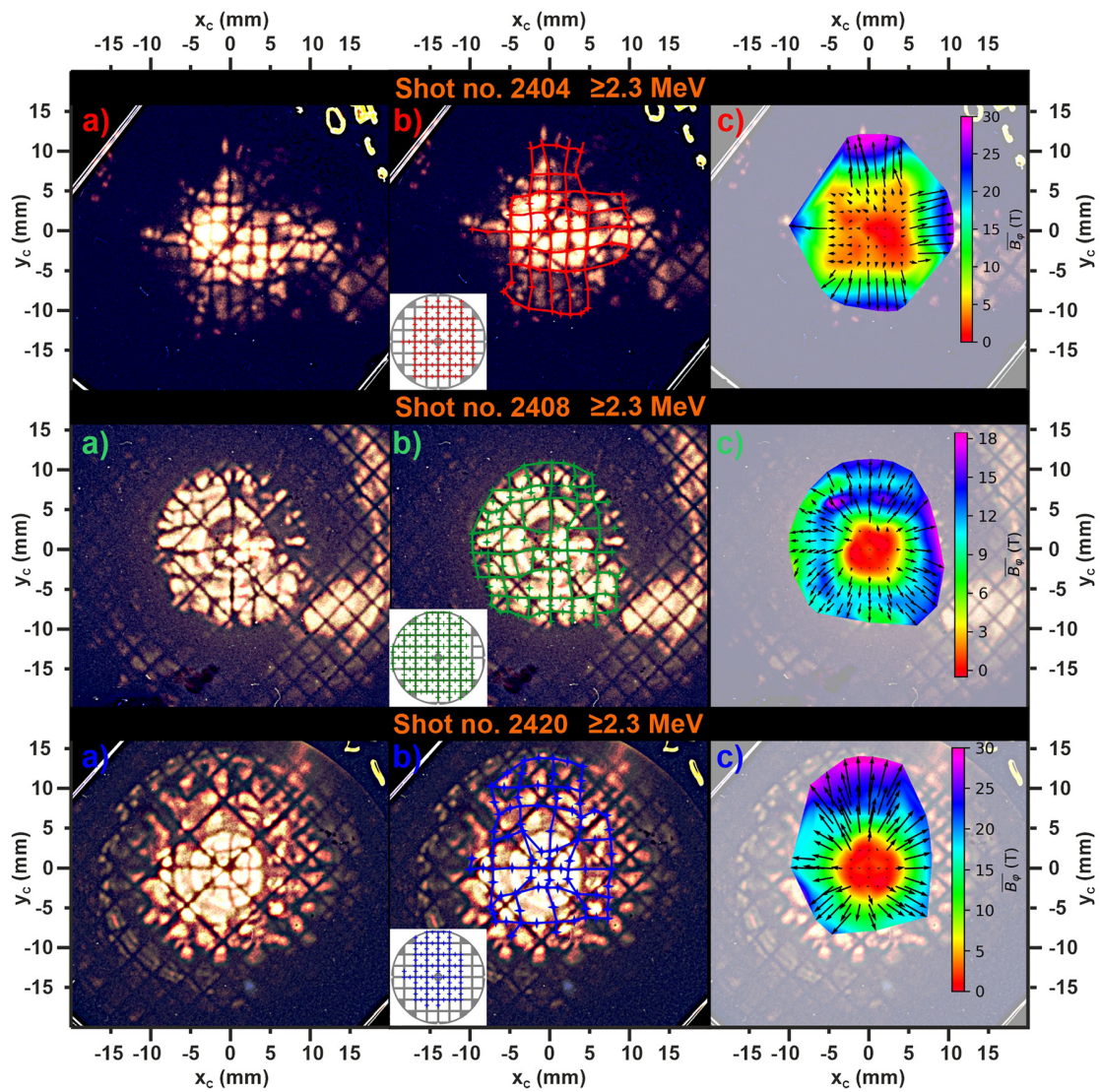


FIG. 11. (a) Original experimental deflectograms in shot Nos. 2404, 2408, and 2420 showing shadows of both the distorted D-grid and the undistorted cathode; (b) Deflectograms with retrieved representative points of the D-grid. Corresponding sections of the original D-grid image are highlighted in the insets. (c) The $(x-y)$ maps of the averaged azimuthal B-fields $\overline{B}_\phi = \int B_\phi dz / Z$, calculated via the Larmor orbit approximation. The black arrows indicate a field of measured displacements $(\Delta x, \Delta y)$ of the retrieved D-grid. Spatial scales of all images correspond to the plane of the cathode mesh.

Via a cubic interpolation, we obtain 2D $(x-y)$ maps of $\overline{B}_\phi(x_C, y_C)$ for all three selected shots [color maps in Fig. 11(c)]. The values at the edge of the maps correlate with the results in Fig. 10. In the shot Nos. 2404 and 2408, we observe a significant anisotropy of the calculated maps. They are caused by errors in the localization and interpolation of the representative points.

To analyze the B-field maps, we present distributions of the radial displacements Δr of the representative points and associated averaged B-fields \overline{B}_ϕ for each selected shot [see Fig. 12(a)]. We observe weak or no deflections within the ~ 3 mm radius R_{cs} for all three shots, which means that there are almost no magnetic fields near the axis. In shot

Nos. 2404 and 2420, the averaged B-fields are monotonically increasing with the radius r_C , and so, interestingly, the current sheath must be quite broad and spread under the D-grid from 3 to at least 13 mm radius. In shot No. 2408 [cf. Fig. 11(c)], the averaged B-field has a peak at the ~ 7 mm radius, which is followed by a spread of points at a greater distance because the displacements become asymmetric. The maximal deviation error of the point localization in the deflectograms is ~ 0.75 mm, which corresponds to the $\sim 15\%$ uncertainty by Eq. (6). It is comparable to the error due to the asymmetry of the B-fields and due to the position of the pinhole, which is in shot Nos. 2404 and 2408 located slightly off-axis. However, the presented values of the averaged

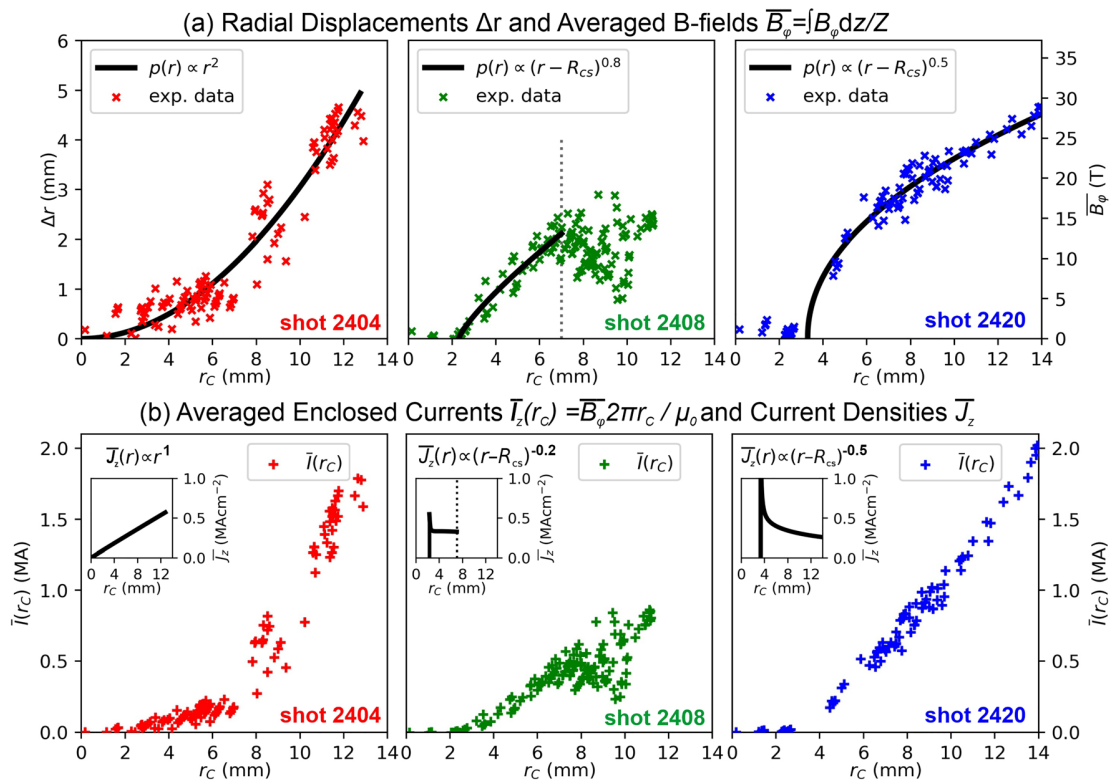


FIG. 12. Radial distributions of (a) radial displacements Δr together with corresponding averaged B-fields $\bar{B}_\phi(r_C) = \bar{B}_\phi(r_C)2\pi r_C / \mu_0$ vs r_C . Averaged B-fields \bar{B}_ϕ are calculated using Larmor orbit approximation and Eq. (5) from the radial displacements Δr of the retrieved points of the D-grid shadow in the deflectograms shown in Fig. 11. To approximate the radial profiles of the averaged current densities $\bar{J}_z(r_C)$, we fit the experimental data by a power function $p(r) \propto (r - R_{cs})^n$, similarly to the analysis in Sec. III D. The radius R_{cs} is 0, 2.3, and 3.3 mm for shot Nos. 2404, 2408, and 2420, respectively.

B-field can be even higher (by $\sim 40\%$) because deuterons with higher energies may contribute to some parts of the deflectogram.

Moreover, we can fit the experimental data by a power function $p(r) \propto (r - R_{cs})^{n_B}$ and discuss the exponent n_B , similarly to the analysis in Sec. III D. We assume that R_{cs} is equal to 0, 2.3, and 3.3 mm for shot Nos. 2404, 2408, and 2420, respectively. In shot No. 2408, we consider only the undispersed data within the radius $r_C \leq 7$ mm. The estimated exponents n_B of the averaged B-fields in the shots are $n_B^{2404} = 2$, $n_B^{2408} = 0.8$, and $n_B^{2420} = 0.5$.

For better comprehension of a role of these exponents, we outline the averaged current density profiles \bar{J}_z [insets in Fig. 12(b)] using the Ampere's law in cylindrical coordinates $\bar{J}_z = (\partial r \bar{B}_\phi(r)) / (\mu_0 r \partial r)$, where we characterize the averaged B-fields $\bar{B}_\phi(r)$ by their fits. We see that the power-law exponents n_B for the selected shots represent an increasing ($n_B^{2404} - 1 > 0$), almost constant ($n_B^{2408} - 1 \approx 0$), and decreasing ($n_B^{2420} - 1 < 0$) averaged current density profiles with respect to the radius r_C . Interestingly, only in shot 2404, the averaged current density is gradually increasing. Unlike in the other two, in this shot, the D-grid was supported by 4 wires at its edge instead of a single wire in the center. These wires interfered with the imploding plasma and so influenced the current sheath. Nevertheless, the presented experimental data do not have sufficient spatial resolution for more detailed study of the averaged current densities. While such

measurements are among our future goals, the outlined profiles should rather provide qualitative information about $\bar{J}_z(r_C)$. For example, because of the decreasing gradients of the B-field profiles in shot Nos. 2408 and 2420, the averaged current density $\bar{J}_z(r_C)$ must be decreasing and have a maximum near the current sheath radius R_{cs} . However, it is difficult to correctly estimate its position and height.

In contrast, we can quite easily derive the radial distributions of the averaged currents $\bar{I}(r_C)$ enclosed within the radius r_C [see main figures in Fig. 12(b)] from the measured experimental data by a relation $\bar{I}(r_C) = \bar{B}_\phi(r_C)2\pi r_C / \mu_0$. Maximal values of $\bar{I}(r_C)$ in the featured shots are in agreement with the results in Sec. IV B. While the averaged current density $\bar{J}_z(r_C)$ is coupled with detailed current structure, the averaged enclosed current $\bar{I}(r_C)$ is inherently cumulative and provides less detailed information.

D. Mapping (r-z) profile of the azimuthal B-fields in shot 2420 using numerical simulations

Deflectograms reflect only the radial distribution of path-integrated B-fields $\int B_\phi dz$, but provide no information about the axial profile of the B-fields. To estimate the actual B-field distribution, we need some knowledge of the complementary axial profile from a radial line of sight.

In the case of shot 2420, we have obtained this information by recording side-view SXR-emission images of the Z-pinch plasma via a multichannel plate (MCP) detector. Figure 13(a) shows an imploding Z-pinch plasma during the ion imaging. We suppose that an inner boundary of the current sheath has a similar parabolic shape as the depicted plasma instability, which we consider azimuthally symmetric. We set this the parabolic shape (but not the radial position) of the plasma boundary $r_{cs}(z)$ as an input parameter into the ion-tracking code.

We have tested various distributions of azimuthal B-fields $B_\phi(r, z)$ and compared the simulated ion displacements from simulations with the measured D-grid displacements. In Fig. 13(b), we present a simulated D-grid pattern (red), which best fits not only the retrieved part of the D-grid shadow (blue) but the whole deflectogram of shot No. 2420 in Fig. 13(c). The artificial D-grid shadow is in good agreement with the experimental data. Discrepancies between the synthetic and observed D-grid pattern are given by the azimuthal asymmetry of B-fields in the experiment. For a better comparison of the whole picture, a complete synthetic deflectograms is illustrated in Fig. 13(d) revealing both the distorted D-grid shadow and an undistorted shadow of the cathode.

We propose numerical solution for $B_\phi(r, z)$ given by a relation

$$B_\phi(r < R_p, z) = \frac{\mu_0 I_p}{2\pi R_p} \left(\frac{r - r_{cs}(z)}{R_p - r_{cs}(z)} \right)^{m_B}, \quad (7)$$

where the I_p is total pinch current at the pinch radius R_p . From Sec. IV C, we know that the distribution of the averaged B-fields $\overline{B_\phi}(r_C) = \int B_\phi dz / Z$ is proportional to $(r - R_{cs})^{m_B}$, where the exponent $n_B \approx 0.5$. While calculating $\overline{B_\phi}$ from the path integral $\int B_\phi dz$, we assume a constant B-field height $Z = 10$ mm. However, if the B-fields are axially perturbed, the height of the actual B-fields depends on the radius. According to Fig. 13(a), it becomes smaller than the D-grid-cathode distance Z closer to the axis. To compensate this effect while keeping the $\int B dz$ profile given by the measured displacements, the cross-sectional profile of the actual B-fields $B_\phi(r, z = \text{const.})$ must be steeper than the averaged B-field profile [cf. Fig. 14(a)]. Therefore, we estimate the exponent of m_B in Eq. (7) to be ≈ 0.2 .

As seen from Fig. 14(a), the retrieved part of the D-grid pattern displays the distortions ranging from the radius of $R_{cs} = r_{cs}(z = 4.7 \text{ mm}) \approx 3.3$ up to ~ 14 mm. The pinch radius R_p cannot be smaller than 14 mm, because in that case there would be a peak in the averaged B-field profile, which we do not observe. However, the low estimate of the pinch radius R_p in Sec. IV B is 1 mm farther, that is, at 15 mm. It is caused by the ~ 0.4 mm thickness of the D-grid edge because the retrieved points of the D-grid pattern refer only to its square openings, but the synthetic deflectogram also manifests the displacements around the circular D-grid edge shadow. Therefore, we determine a minimal pinch radius of $R_p = 15$ mm, which results in the low estimate of the 2.5-MA pinch current I_p and agrees with the displacement of the D-grid edge, measured in Subsection IV B.

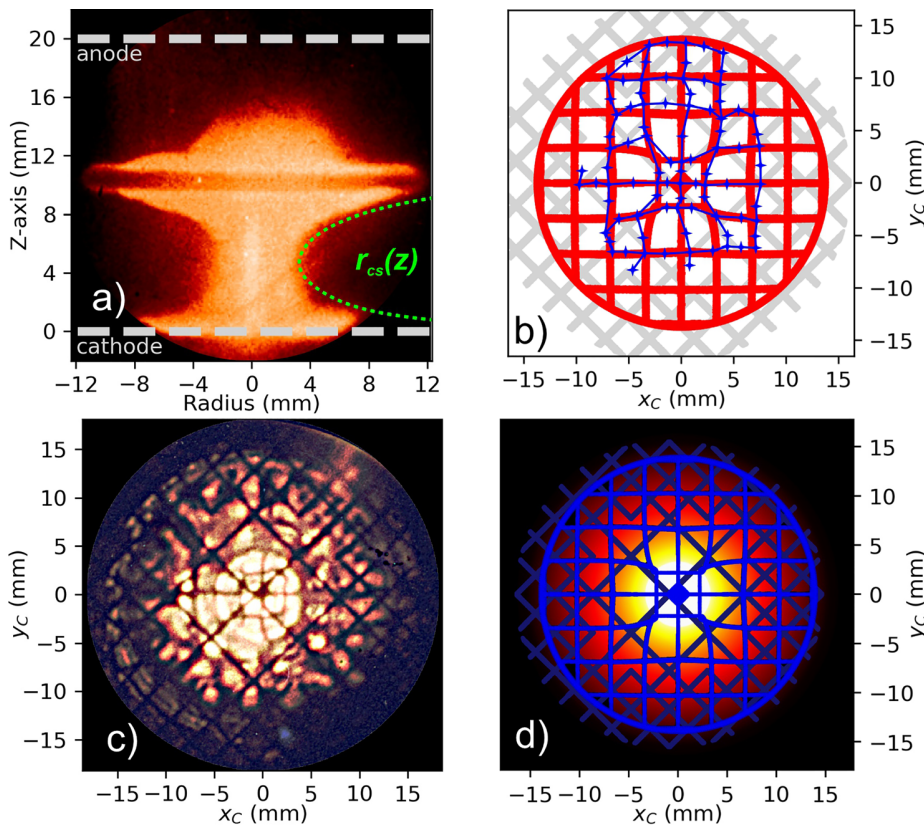


FIG. 13. (a) SXR image of the imploding plasma recorded by a multichannel plate (MCP) detector in the shot No. 2420 during ion imaging. We set the shape of the imploding plasma $r_{cs}(z)$ as an input parameter to our numerical code to characterize the current sheath perturbation. (b) Comparison of the simulated D-grid pattern with the retrieved part of the distorted D-grid from the experimental data; (c) experimental and (d) synthetic deflectograms of the distorted D-grid and the undistorted cathode mesh with the representative points.

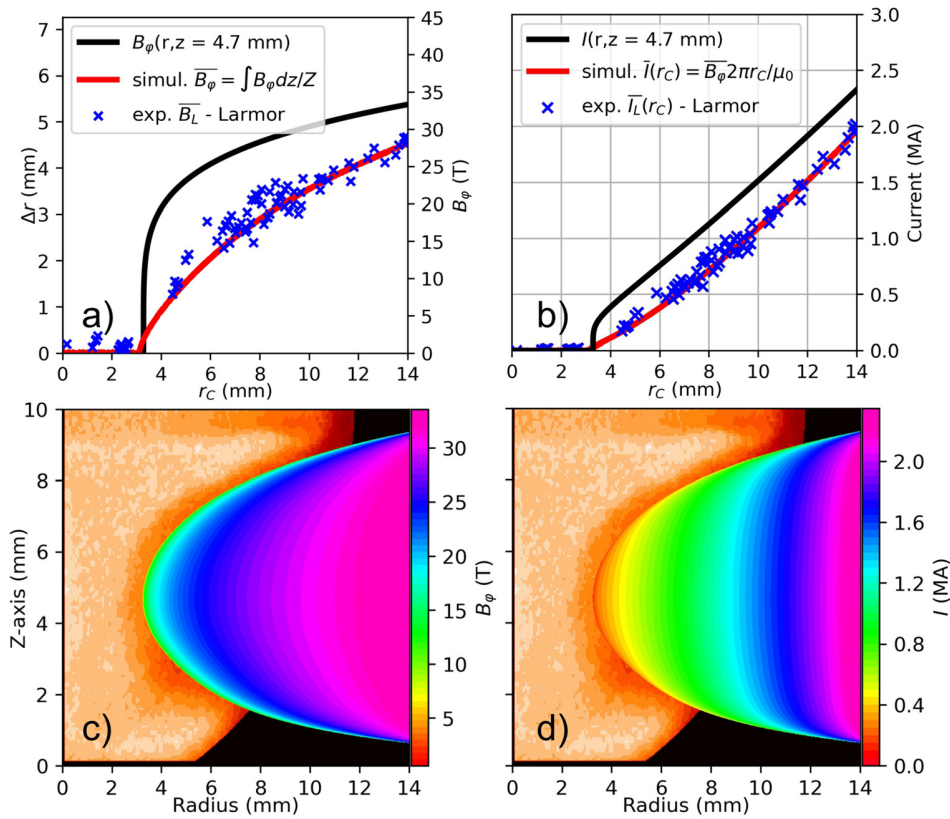


FIG. 14. Cross-sectional profiles of (a) the azimuthal B-fields $B_\phi(r, z = 4.7 \text{ mm})$ and (b) the current $I(r, z = 4.7 \text{ mm})$ are compared to the averaged $\overline{B_\phi}(r_c)$ and $\overline{I}(r_c)$. Topological (r - z) maps of (c) B-field $B_\phi(r, z)$ and (d) current $I(r, z)$, which we obtain as a fitting input distributions from the numerical simulations reconstructing the experimental deflectogram in shot No. 2420.

Due to the abrupt increase in the current profile near the radius $R_{cs} \sim 3.3 \text{ mm}$ in Fig. 14(b), the current density must be high ($\geq 10^1 \text{ MA cm}^{-2}$) at the thin layer of the current sheath front (roughly $\sim 0.5 \text{ mm}$). With increasing radius, the B-fields slope become more steady, and thus, the estimated current density falls to $10^{-1} \text{ MA cm}^{-2}$. However, detailed information about the current density is not possible because it relies heavily on a specific fit of the B-fields. The uncertainty of this fit is caused by the uncertainty determination of the radial position of the onset of the ion deflections [see Fig. 14(a) between 3 and 4 mm], which cannot be determined precisely from the experimental deflectogram of the shot No. 2420.

From our simulations, we obtain 2D (r - z) distributions of the local B-field $\overline{B_\phi}(r, z)$ and the corresponding current $\overline{I}(r, z)$, which we set as the input to our simulations [see Figs. 14(a) and 14(b)]. As seen, the current sheath is not only perturbed but also stretched along the whole interval from R_{cs} to R_p (3.3 – 15 mm). Therefore, the both B-field and current in the cross section of the current layer are monotonically increasing [see Figs. 14(c) and 14(d)]. If we would consider $R_p = R_p(z)$, then the strengths of the path-integrated B-fields would decrease from the minimal $R_p(z)$ and synthetic deflectogram would not reflect the ion displacements. Therefore, we set the outer boundary of the current sheath as a straight line and the pinch radius R_p

= 15 mm applies for all z . We conclude the current sheath must be wide, stretched and situated in the region of the plasma with lower temperature (not glowing in SXR).

V. CONCLUSIONS AND FUTURE PLANS

We proved that ion deflectometry is a feasible diagnostic method for measuring the magnetic fields in Z-pinch plasmas. We have found a novel method for ion backlighting of the deflectometry grid. For our B-fields measurements, we have employed multi-MeV deuteron beams accelerated after disrupting the Z-pinch current in the unstable plasma neck. Thus, we performed the first Z-pinch-driven ion deflectometry experiments. We have developed the unique experimental setup with a fiducial deflectometry grid (D-grid) inserted in-between the electrodes. The D-grid did not suppress the ion emission near the anode while not severely affecting the plasma implosion below the D-grid. On the other hand, the D-grid stalk prevented deuterons to be accelerated between the D-grid and the cathode. Otherwise, they would not pass the D-grid, blur the deflectogram, and lower its contrast. Therefore, we could utilize these ions to map the azimuthal B-fields in the plasma below the D-grid, which manifested their deflections.

We obtained images of the D-grid shadow imprinted in the deflected ion beams, which displayed the radial profile of the path-integrated B-field $\|\int \mathbf{B} \times d\mathbf{L}\|$ in an area within a 15 mm radius from

the axis. The experimental setup with a distant pinhole camera set a minimal observation angle of the detected ions. It allowed us to estimate the path-integrated B-fields $\int B_\phi dz$ using the Larmor orbit approximation.

We presented the experimental data from several shots with the different quality of the obtained information. Even from the low-quality deflectograms, we estimated the minimal value of the total pinch current within a 15 mm radius from the axis. It reached up to 2.5 MA for a few shots, which was close to the 2.7-MA total circuit current during the stagnation.

Using our numerical path-tracking simulations for various azimuthal B-fields, we have investigated how the deflectogram structure reflects specific B-field profiles. In three selected shots, where the distorted D-grid pattern was recognizable, we retrieved the (x-y) maps of the averaged B-fields. They revealed that, within the 3 mm distance from the axis, there were almost no B-fields at the time of ion imaging. Moreover, we were able to estimate the profile of the averaged current density for these selected shots.

In shot No. 2420, we captured the SXR image of the imploding Z-pinch plasma during the ion emission and utilized it to infer the axial shape of the current sheath. Using our numerical simulations, we found the fit for the experimental data and, as a result, reconstructed a topological (r-z) map of the local B-fields. It implies from our results that the current sheath is quite broad (~ 12 mm) and that the majority of the current was flowing in the peripheral plasma, which does not glow in the SXR spectrum.

All these experimental data have been obtained during our first experimental campaign while testing the concept of the ion deflectometry measurements. We determined that beam energy estimation and the deflectogram contrast are critical elements of our topics that need improvement. Due to the high uncertainty in energy of the detected deuterons (between 2.3 and 4.7 MeV), we report only low estimates of the measured B-fields. In the future, we will solve this problem by using improved detector stack with optimized filters. Moreover, we are planning experiments employing D-grids with larger diameters to map B-fields farther from the axis and with lower supporting stalk to measure larger deflections. We will test the D-grids with different sizes of openings for better contrast and to investigate further the role of the D-grid transparency and the D-grid stalk for the ion acceleration mechanism. We will test several inverse D-grids with very low transparency, where the spacings are in the place of the connecting wires of the classical D-grid. Therefore, we can analyze the high-fluence structures in the low-fluence background instead of vice versa. We also plan to shorten the time of ion emission compared to the plasma implosion below the D-grid by manipulating the initial parameters of the experiment and the structure of the D-grid. Nevertheless, it will always be essential that we must not drastically suppress the emission of ions for the backlighting in any of these experiments.

ACKNOWLEDGMENTS

This research has been supported by the Grant Agency of the Czech Republic (Grant No. 19-02545S), the Ministry of Education, Youth, and Sports of the Czech Republic (Grant Nos. LTAUSA17084, LTT17015, 8JPL19014, and CZ.02.1.01/0.0/0.0/16_019/0000778), and the Czech Technical University (Grant No. SGS19/167/OHK3/3T/13).

DATA AVAILABILITY

The data that support the findings of this study are available from the corresponding author upon reasonable request.

REFERENCES

- ¹V. V. Ivanov, A. A. Anderson, D. Papp, A. Astanovitskiy, V. Nalajala, and O. Dmitriev, "Study of magnetic fields and current in the z pinch at stagnation," *Phys. Plasmas* **22**, 092710 (2015).
- ²A. Anderson, V. Ivanov, and D. Papp, "Visualization of the magnetic field and current path in z-pinch and x-pinch plasmas," *High Energy Density Phys.* **15**, 1–3 (2015).
- ³K. Mitrofanov, V. Krauz, V. Myalton, E. Velikhov, V. Vinogradov, and Y. V. Vinogradova, "Magnetic field distribution in the plasma flow generated by a plasma focus discharge," *J. Exp. Theor. Phys.* **119**, 910–923 (2014).
- ⁴K. Mitrofanov, V. Krauz, E. Grabovski, V. Myalton, M. Paduch, and A. Gritsuk, "Features of the application of the magnetic-probe method for diagnostics of high-temperature plasma," *Instrum. Exp. Tech.* **61**, 239–259 (2018).
- ⁵J. Greenly, M. Martin, I. Blesener, D. Chalenski, P. Knapp, and R. McBride, "The role of flux advection in the development of the ablation streams and precursors of wire array z-pinches," *AIP Conf. Proc.* **1088**, 53–56 (2009).
- ⁶P.-A. Gourdain, I. Blesener, J. Greenly, D. Hammer, P. Knapp, B. Kusse, and P. Schrafel, "Initial experiments using radial foils on the Cornell beam research accelerator pulsed power generator," *Phys. Plasmas* **17**, 012706 (2010).
- ⁷G. Davara, L. Gregorian, E. Kroupp, and Y. Maron, "Spectroscopic determination of the magnetic-field distribution in an imploding plasma," *Phys. Plasmas* **5**, 1068–1075 (1998).
- ⁸G. Rosenzweig, E. Kroupp, A. Fisher, and Y. Maron, "Measurements of the spatial magnetic field distribution in a z-pinch plasma throughout the stagnation process," *J. Instrum.* **12**, P09004 (2017).
- ⁹G. Rosenzweig, E. Kroupp, T. Queller, A. Starobinets, Y. Maron, V. Tangri, J. Giuliani, and A. Fruchtman, "Local measurements of the spatial magnetic field distribution in a z-pinch plasma during and near stagnation using polarization spectroscopy," *Phys. Plasmas* **27**, 022705 (2020).
- ¹⁰M. Borghesi, A. Schiavi, D. Campbell, M. Haines, O. Willi, A. MacKinnon, L. Gizzi, M. Galimberti, R. Clarke, and H. Ruhl, "Proton imaging: A diagnostic for inertial confinement fusion/fast ignitor studies," *Plasma Phys. Controlled Fusion* **43**, A267 (2001).
- ¹¹M. Borghesi, D. Campbell, A. Schiavi, O. Willi, A. Mackinnon, D. Hicks, P. Patel, L. Gizzi, M. Galimberti, and R. Clarke, "Laser-produced protons and their application as a particle probe," *Laser Part. Beams* **20**, 269 (2002).
- ¹²N. Kugland, D. Ryutov, P.-Y. Chang, R. Drake, G. Fiksel, D. Froula, S. Glenzer, G. Gregori, M. Grosskopf, M. Koenig *et al.*, "Self-organized electromagnetic field structures in laser-produced counter-streaming plasmas," *Nat. Phys.* **8**, 809–812 (2012).
- ¹³C. Li, D. Ryutov, S. Hu, M. Rosenberg, A. Zylstra, F. Séguin, J. Frenje, D. Casey, M. G. Johnson, M.-E. Manuel *et al.*, "Structure and dynamics of colliding plasma jets," *Phys. Rev. Lett.* **111**, 235003 (2013).
- ¹⁴C. Li, P. Tzeferacos, D. Lamb, G. Gregori, P. Norreys, M. Rosenberg, R. Follett, D. Froula, M. Koenig, F. Seguin *et al.*, "Scaled laboratory experiments explain the kink behaviour of the crab nebula jet," *Nat. Commun.* **7**, 1–8 (2016).
- ¹⁵L. Gao, E. Liang, Y. Lu, R. Follett, H. Sio, P. Tzeferacos, D. Froula, A. Birkel, C. Li, D. Lamb *et al.*, "Mega-gauss plasma jet creation using a ring of laser beams," *Astrophys. J., Lett.* **873**, L11 (2019).
- ¹⁶L. Romagnani, J. Fuchs, P. Audebert, P. Antici, M. Borghesi, S. Kar, O. Willi, G. Pretzler, T. Toncian, F. Ceccherini *et al.*, "Dynamics of electric fields driving the laser acceleration of multi-mev protons," *Phys. Rev. Lett.* **95**, 195001 (2005).
- ¹⁷L. Romagnani, M. Borghesi, C. Cecchetti, S. Kar, P. Antici, P. Audebert, S. Bandhoupadajay, F. Ceccherini, T. Cowan, J. Fuchs *et al.*, "Proton probing measurement of electric and magnetic fields generated by ns and ps laser-matter interactions," *Laser Part. Beams* **26**, 241 (2008).
- ¹⁸T. Sokollik, M. Schnürer, S. Ter-Avetisyan, P. Nickles, E. Risse, M. Kalashnikov, W. Sandner, G. Priebe, M. Amin, T. Toncian *et al.*, "Transient electric fields in laser plasmas observed by proton streak deflectometry," *Appl. Phys. Lett.* **92**, 091503 (2008).

- ¹⁹K. Law, M. Bailly-Grandvaux, A. Morace, S. Sakata, K. Matsuo, S. Kojima, S. Lee, X. Vaisseau, Y. Arikawa, A. Yogo *et al.*, "Direct measurement of kilo-tesla level magnetic field generated with laser-driven capacitor-coil target by proton deflectometry," *Appl. Phys. Lett.* **108**, 091104 (2016).
- ²⁰J. J. Santos, M. Bailly-Grandvaux, M. Ehret, A. Arefiev, D. Batani, F. Beg, A. Calisti, S. Ferri, R. Florido, P. Forestier-Colleoni *et al.*, "Laser-driven strong magnetostatic fields with applications to charged beam transport and magnetized high energy-density physics," *Phys. Plasmas* **25**, 056705 (2018).
- ²¹P. Bradford, M. Read, M. Ehret, L. Antonelli, M. Khan, N. Booth, K. Glize, D. Carroll, R. Clarke, R. Heathcote *et al.*, "Proton deflectometry of a capacitor coil target along two axes," *High Power Laser Sci. Eng.* **8**, e11 (2020).
- ²²J. Peebles, J. Davies, D. Barnak, T. Cracium, M. Bonino, and R. Betti, "Axial proton probing of magnetic and electric fields inside laser-driven coils," *Phys. Plasmas* **27**, 063109 (2020).
- ²³W. Fox, G. Fiksel, A. Bhattacherjee, P.-Y. Chang, K. Germaschewski, S. Hu, and P. Nilson, "Filamentation instability of counterstreaming laser-driven plasmas," *Phys. Rev. Lett.* **111**, 225002 (2013).
- ²⁴C. Huntington, F. Fiuza, J. Ross, A. Zylstra, R. Drake, D. Froula, G. Gregori, N. Kugland, C. Kuranz, M. Levy *et al.*, "Observation of magnetic field generation via the Weibel instability in interpenetrating plasma flows," *Nat. Phys.* **11**, 173–176 (2015).
- ²⁵C. Li, F. Séguin, J. Frenje, R. Petrasso, P. Amendt, R. Town, O. Landen, J. Rygg, R. Betti, J. Knauer *et al.*, "Observations of electromagnetic fields and plasma flow in hohlraums with proton radiography," *Phys. Rev. Lett.* **102**, 205001 (2009).
- ²⁶J. Rygg, F. Séguin, C. Li, J. Frenje, M.-E. Manuel, R. Petrasso, R. Betti, J. Delettrez, O. Gotchev, J. Knauer *et al.*, "Proton radiography of inertial fusion implosions," *Science* **319**, 1223–1225 (2008).
- ²⁷C. Li, F. Séguin, J. Frenje, M. Rosenberg, R. Petrasso, P. Amendt, J. Koch, O. Landen, H. Park, H. Robey *et al.*, "Charged-particle probing of x-ray-driven inertial-fusion implosions," *Science* **327**, 1231–1235 (2010).
- ²⁸F. Séguin, C. Li, M.-E. Manuel, H. Rinderknecht, N. Sinenian, J. Frenje, J. Rygg, D. Hicks, R. Petrasso, J. Delettrez *et al.*, "Time evolution of filamentation and self-generated fields in the coronae of directly driven inertial-confinement fusion capsules," *Phys. Plasmas* **19**, 012701 (2012).
- ²⁹S. Kar, H. Ahmed, R. Prasad, M. Cerchez, S. Brauckmann, B. Aurand, G. Cantono, P. Hadjisolomou, C. L. Lewis, A. Macchi *et al.*, "Guided post-acceleration of laser-driven ions by a miniature modular structure," *Nat. Commun.* **7**, 1–7 (2016).
- ³⁰H. Ahmed, S. Kar, A. Giesecke, D. Doria, G. Nersisyan, O. Willi, C. L. Lewis, and M. Borghesi, "Proton probing of laser-driven em pulses travelling in helical coils," *High Power Laser Sci. Eng.* **5**, e4 (2017).
- ³¹P. Nilson, L. Willingale, M. Kaluza, C. Kamperidis, S. Minardi, M. Wei, P. Fernandes, M. Notley, S. Bandyopadhyay, M. Sherlock *et al.*, "Magnetic reconnection and plasma dynamics in two-beam laser-solid interactions," *Phys. Rev. Lett.* **97**, 255001 (2006).
- ³²L. Willingale, P. Nilson, M. Kaluza, A. Dangor, R. Evans, P. Fernandes, M. Haines, C. Kamperidis, R. Kingham, C. Ridgers *et al.*, "Proton deflectometry of a magnetic reconnection geometry," *Phys. Plasmas* **17**, 043104 (2010).
- ³³C. Palmer, P. Campbell, Y. Ma, L. Antonelli, A. Bott, G. Gregori, J. Halliday, Y. Katzir, P. Kordell, K. Krushelnick *et al.*, "Field reconstruction from proton radiography of intense laser driven magnetic reconnection," *Phys. Plasmas* **26**, 083109 (2019).
- ³⁴A. Chien, L. Gao, H. Ji, X. Yuan, E. G. Blackman, H. Chen, P. C. Efthimion, G. Fiksel, D. H. Froula, K. W. Hill *et al.*, "Study of a magnetically driven reconnection platform using ultrafast proton radiography," *Phys. Plasmas* **26**, 062113 (2019).
- ³⁵W. Fox, D. Schaeffer, M. Rosenberg, G. Fiksel, J. Matteucci, H.-S. Park, A. Bott, K. Lezhnin, A. Bhattacherjee, D. Kalantar *et al.*, "Fast magnetic reconnection in highly-extended current sheets at the national ignition facility," *arXiv:2003.06351* (2020).
- ³⁶A. Mackinnon, P. Patel, R. Town, M. Edwards, T. Phillips, S. Lerner, D. Price, D. Hicks, M. Key, S. Hatchett *et al.*, "Proton radiography as an electromagnetic field and density perturbation diagnostic," *Rev. Sci. Instrum.* **75**, 3531–3536 (2004).
- ³⁷C. Li, F. Séguin, J. Frenje, J. Rygg, R. Petrasso, R. Town, P. Amendt, S. Hatchett, O. Landen, A. Mackinnon *et al.*, "Measuring e and b fields in laser-produced plasmas with monoenergetic proton radiography," *Phys. Rev. Lett.* **97**, 135003 (2006).
- ³⁸C. Li, F. Séguin, J. Frenje, M. Manuel, D. Casey, N. Sinenian, R. Petrasso, P. Amendt, O. Landen, J. Rygg *et al.*, "Proton radiography of dynamic electric and magnetic fields in laser-produced high-energy-density plasmas," *Phys. Plasmas* **16**, 056304 (2009).
- ³⁹C. Cecchetti, M. Borghesi, J. Fuchs, G. Schurtz, S. Kar, A. Macchi, L. Romagnani, P. Wilson, P. Antici, R. Jung *et al.*, "Magnetic field measurements in laser-produced plasmas via proton deflectometry," *Phys. Plasmas* **16**, 043102 (2009).
- ⁴⁰G. Sarri, A. Macchi, C. Cecchetti, S. Kar, T. Liseykina, X. Yang, M. E. Dieckmann, J. Fuchs, M. Galimberti, L. Gizzi *et al.*, "Dynamics of self-generated, large amplitude magnetic fields following high-intensity laser matter interaction," *Phys. Rev. Lett.* **109**, 205002 (2012).
- ⁴¹V. Simcik, T. Crowley, P. Schoch, A. Aydemir, X. Yang, K. Connor, R. Hickok, A. Wootton, and S. McCool, "Internal magnetic and electrostatic fluctuation measurements of magnetohydrodynamic modes in the Texas experimental tokamak (text)," *Phys. Fluids B* **5**, 1576–1580 (1993).
- ⁴²J. Schwelberger, T. Crowley, K. Connor, and P. Schoch, "Current density profile measurement on the Texas experimental tokamak using a heavy ion beam probe," *Rev. Sci. Instrum.* **69**, 3828–3834 (1998).
- ⁴³A. Malaquias, I. Nedzelsky, B. Gonçalves, C. Varandas, J. Cabral, A. Melnikov, L. Eliseev, S. Perfilov, O. Yudina, and L. Krupnik, "Comparative study design of a heavy ion and neutral beam diagnostic for the international tokamak experiment reactor," *Rev. Sci. Instrum.* **74**, 1857–1860 (2003).
- ⁴⁴A. Fujisawa, A. Shimizu, H. Nakano, and S. Ohshima, "Evaluation of local magnetic field fluctuation in a toroidal plasma with heavy ion beam probe," *Plasma Phys. Controlled Fusion* **49**, 845 (2007).
- ⁴⁵Y. Hamada, T. Watari, A. Nishizawa, O. Yamagishi, K. Narihara, K. Ida, Y. Kawasumi, T. Ido, M. Kojima, K. Toi *et al.*, "Microtearing mode (mtm) turbulence in jippt-iii tokamak plasmas," *Nucl. Fusion* **55**, 043008 (2015).
- ⁴⁶A. Melnikov, M. Drabinskiy, L. Eliseev, P. Khabanov, N. Kharchev, L. Krupnik, J. De Pablos, A. Kozachek, S. Lysenko, A. Molinero *et al.*, "Heavy ion beam probe design and operation on the t-10 tokamak," *Fusion Eng. Des.* **146**, 850–853 (2019).
- ⁴⁷M.-E. Manuel, N. Sinenian, F. Séguin, C. Li, J. Frenje, H. Rinderknecht, D. Casey, A. Zylstra, R. Petrasso, and F. Beg, "Mapping return currents in laser-generated z-pinch plasmas using proton deflectometry," *Appl. Phys. Lett.* **100**, 203505 (2012).
- ⁴⁸D. Mariscal, C. McGuffey, J. Valenzuela, M. Wei, J. Chittenden, N. Niasse, R. Presura, S. Haque, M. Wallace, A. Arias *et al.*, "Measurement of pulsed-power-driven magnetic fields via proton deflectometry," *Appl. Phys. Lett.* **105**, 224103 (2014).
- ⁴⁹F. N. Beg, "Assessment of proton deflectometry for exploding wire experiments," Report No. UCSD 2009-0512, 2013.
- ⁵⁰M. S. Schollmeier, A. B. Sefkow, M. Geissel, P. K. Rambo, and J. Schwarz, "Z-petawatt driven ion beam radiography development," Sandia Report No. SAND2013-7201, 2013.
- ⁵¹V. Munzar, D. Klir, J. Cikhart, B. Cikhartova, J. Kravarik, P. Kubes, and K. Rezac, "Investigation of magnetic fields in z-pinch plasmas via multi-mev proton deflectometry," *IEEE Trans. Plasma Sci.* **46**, 3891–3900 (2018).
- ⁵²D. Klir, A. Shishlov, V. A. Kokshenev, S. L. Jackson, K. Rezac, R. K. Cherdizov, J. Cikhart, G. N. Dudkin, F. I. Fursov, J. Krasa *et al.*, "Production of energetic protons, deuterons, and neutrons up to 60 mev via disruption of a current-carrying plasma column at 3 megaamperes," *New J. Phys.* **22**, 103036 (2020).
- ⁵³A. Bott, C. Graziani, P. Tzeferacos, T. White, D. Lamb, G. Gregori, and A. Schekochihin, "Proton imaging of stochastic magnetic fields," *J. Plasma Phys.* **83**, 905830614 (2017).
- ⁵⁴D. Klir, A. Shishlov, V. Kokshenev, P. Kubes, K. Rezac, R. Cherdizov, J. Cikhart, B. Cikhartova, G. Dudkin, F. Fursov *et al.*, "Ion acceleration mechanism in mega-ampere gas-puff z-pinch," *New J. Phys.* **20**, 053064 (2018).
- ⁵⁵D. Klir, S. Jackson, A. Shishlov, V. Kokshenev, K. Rezac, A. Beresnyak, R. Cherdizov, J. Cikhart, B. Cikhartova, G. Dudkin *et al.*, "Ion acceleration and neutron production in hybrid gas-puff z-pinch on the git-12 and hawk generators," *Matter Radiat. Extremes* **5**, 026401 (2020).

- ⁵⁶A. Macchi, M. Borghesi, and M. Passoni, "Ion acceleration by superintense laser-plasma interaction," *Rev. Mod. Phys.* **85**, 751 (2013).
- ⁵⁷D. Klir, A. V. Shishlov, V. Kokshenev, P. Kubes, A. Y. Labetsky, K. Rezac, R. Cherdizov, J. Cikhardt, B. Cikhardtova, G. N. Dudkin *et al.*, "Efficient generation of fast neutrons by magnetized deuterons in an optimized deuterium gas-puff z-pinch," *Plasma Phys. Controlled Fusion* **57**, 044005 (2015).
- ⁵⁸F. Suzuki-Vidal, S. Patankar, S. Lebedev, S. Bland, H. Doyle, D. Bigourd, G. Burdiak, P. De Grouchy, G. Hall, A. Harvey-Thompson *et al.*, "Observation of energetic protons trapped in laboratory magnetic-tower jets," *New J. Phys.* **15**, 125008 (2013).
- ⁵⁹J. F. Ziegler, M. D. Ziegler, and J. P. Biersack, "SRIM—the stopping and range of ions in matter (2010)," *Nucl. Instrum. Methods Phys. Res., Sect. B* **268**, 1818–1823 (2010).

Bibliography

- [1] Munzar, V, D. Klir, J. Cikhardt, B. Cikhardtova, J. Kravarik, P. Kubes, and K. Rezac, “Investigation of magnetic fields in z-pinchs via multi-mev proton deflectometry”, *IEEE Transactions on Plasma Science*, vol. 46, no. 11, pp. 3891–3900, 2018.
- [2] D. Klir, A. Shishlov, S. Jackson, V. Kokshenev, P. Kubes, K. Rezac, A. Beresnyak, R. Cherdizov, J. Cikhardt, B. Cikhardtova, *et al.*, “Spatial distribution of ion emission in gas-puff z-pinchs and dense plasma foci”, *Plasma Physics and Controlled Fusion*, vol. 62, no. 3, p. 035 009, 2020.
- [3] Munzar, V, D. Klir, J. Cikhardt, J. Kravarik, P. Kubes, J. Malir, J. Novotny, K. Rezac, A. Shishlov, V. Kokshenev, *et al.*, “Mapping of azimuthal b-fields in z-pinch plasmas using z-pinch-driven ion deflectometry”, *Physics of Plasmas*, vol. 28, no. 6, p. 062 702, 2021.
- [4] R. P. Drake, “High-energy-density physics”, *Phys. Today*, vol. 63, no. 6, p. 28, 2010.
- [5] J. Colvin and J. Larsen, *Extreme physics: properties and behavior of matter at extreme conditions*. Cambridge University Press, 2013.
- [6] J. Larsen, *Foundations of high-energy-density physics: Physical processes of matter at extreme conditions*. Cambridge University Press, 2017.
- [7] A. Macchi, M. Borghesi, and M. Passoni, “Ion acceleration by superintense laser-plasma interaction”, *Reviews of Modern Physics*, vol. 85, no. 2, p. 751, 2013.
- [8] H. Daido, M. Nishiuchi, and A. S. Pirozhkov, “Review of laser-driven ion sources and their applications”, *Reports on progress in physics*, vol. 75, no. 5, p. 056 401, 2012.
- [9] M. Borghesi, “Ion acceleration: Tnsa and beyond”, *Laser-Driven Sources of High Energy Particles and Radiation*, pp. 143–164, 2019.
- [10] P. Bolton, K. Parodi, and J. Schreiber, *Applications of laser-driven particle acceleration*. CRC Press, 2018.
- [11] M. Roth, T. Cowan, M. Key, S. Hatchett, C. Brown, W. Fountain, J. Johnson, D. Pennington, R. Snavely, S. Wilks, *et al.*, “Fast ignition by intense laser-accelerated proton beams”, *Physical review letters*, vol. 86, no. 3, p. 436, 2001.
- [12] J. Fernández, B. Albright, F. N. Beg, M. E. Foord, B. M. Hegelich, J. Honrubia, M. Roth, R. B. Stephens, and L. Yin, “Fast ignition with laser-driven proton and ion beams”, *Nuclear fusion*, vol. 54, no. 5, p. 054 006, 2014.
- [13] J. Bin, K. Allinger, W. Assmann, G. Dollinger, G. A. Drexler, A. A. Friedl, D. Habs, P. Hilz, R. Hoerlein, N. Humble, *et al.*, “A laser-driven nanosecond proton source for radiobiological studies”, *Applied Physics Letters*, vol. 101, no. 24, p. 243 701, 2012.
- [14] F. Kroll, F.-E. Brack, C. Bernert, S. Bock, E. Bodenstern, K. Brüchner, T. E. Cowan, L. Gaus, R. Gebhardt, U. Helbig, *et al.*, “Tumour irradiation in mice with a laser-accelerated proton beam”, *Nature Physics*, vol. 18, no. 3, pp. 316–322, 2022.

- [15] P. Chaudhary, G. Milluzzo, H. Ahmed, B. Odlozilik, A. McMurray, K. M. Prise, and M. Borghesi, “Radiobiology experiments with ultra-high dose rate laser-driven protons: Methodology and state-of-the-art”, *Frontiers in Physics*, vol. 9, p. 624963, 2021.
- [16] P. Patel, A. Mackinnon, M. Key, T. Cowan, M. Foord, M. Allen, D. Price, H. Ruhl, P. Springer, and R. Stephens, “Isochoric heating of solid-density matter with an ultrafast proton beam”, *Physical review letters*, vol. 91, no. 12, p. 125004, 2003.
- [17] A. McKelvey, G. Kemp, P. Sterne, A. Fernandez-Panella, R. Shepherd, M. Marinak, A. Link, G. Collins, H. Sio, J. King, *et al.*, “Thermal conductivity measurements of proton-heated warm dense aluminum”, *Scientific reports*, vol. 7, no. 1, pp. 1–10, 2017.
- [18] A. Mancic, J. Robiche, P. Antici, P. Audebert, C. Blancard, P. Combis, F. Dorchies, G. Faussurier, S. Fourmaux, M. Harmand, *et al.*, “Isochoric heating of solids by laser-accelerated protons: Experimental characterization and self-consistent hydrodynamic modeling”, *High Energy Density Physics*, vol. 6, no. 1, pp. 21–28, 2010.
- [19] M. Cuneo, M. Herrmann, D. Sinars, S. Slutz, W. Stygar, R. Vesey, A. Sefkow, G. Rochau, G. Chandler, J. Bailey, *et al.*, “Magnetically driven implosions for inertial confinement fusion at sandia national laboratories”, *IEEE Transactions on Plasma Science*, vol. 40, no. 12, pp. 3222–3245, 2012.
- [20] R. Spielman, C. Deeney, G. Chandler, M. Douglas, D. Fehl, M. Matzen, D. McDaniel, T. Nash, J. Porter, T. Sanford, *et al.*, “Tungsten wire-array z-pinch experiments at 200 tw and 2 mj”, *Physics of Plasmas*, vol. 5, no. 5, pp. 2105–2111, 1998.
- [21] C. Deeney, C. Coverdale, and M. Douglas, “A review of long-implosion-time z pinches as efficient and high-power radiation sources”, *Laser and Particle Beams*, vol. 19, no. 3, pp. 497–506, 2001.
- [22] D. Klir, P. Kubes, K. Rezac, J. Cikhardt, J. Kravarik, O. Sila, A. V. Shishlov, B. M. Kovalchuk, N. A. Ratakhin, V. Kokshenev, *et al.*, “Efficient neutron production from a novel configuration of deuterium gas-puff z-pinch”, *Physical review letters*, vol. 112, no. 9, p. 095001, 2014.
- [23] D. Klir, A. V. Shishlov, V. Kokshenev, P. Kubes, A. Y. Labetsky, K. Rezac, R. Cherdizov, J. Cikhardt, B. Cikhardtova, G. N. Dudkin, *et al.*, “Efficient generation of fast neutrons by magnetized deuterons in an optimized deuterium gas-puff z-pinch”, *Plasma Physics and Controlled Fusion*, vol. 57, no. 4, p. 044005, 2015.
- [24] D. Klir, A. Shishlov, V. A. Kokshenev, S. L. Jackson, K. Rezac, R. K. Cherdizov, J. Cikhardt, G. N. Dudkin, F. I. Fursov, J. Krasa, *et al.*, “Production of energetic protons, deuterons, and neutrons up to 60 mev via disruption of a current-carrying plasma column at 3 megaamperes”, *New Journal of Physics*, 2020.
- [25] F. Suzuki-Vidal, S. Patankar, S. Lebedev, S. Bland, H. Doyle, D. Bigourd, G. Burdiak, P. De Grouchy, G. Hall, A. Harvey-Thompson, *et al.*, “Observation of energetic protons trapped in laboratory magnetic-tower jets”, *New Journal of Physics*, vol. 15, no. 12, p. 125008, 2013.
- [26] R. Gullickson and H. Sahlin, “Measurements of high-energy deuterons in the plasma-focus device”, *Journal of Applied Physics*, vol. 49, no. 3, pp. 1099–1105, 1978.
- [27] W. Bostick, H. Kilic, V. Nardi, and C. Powell, “Time resolved energy spectrum of the axial ion beam generated in plasma focus discharges”, *Nuclear fusion*, vol. 33, no. 3, p. 413, 1993.
- [28] L. Jakubowski, M. Sadowski, and J. Zebrowski, “Measurements of charged particle beams from plasma focus discharges”, *Nuclear fusion*, vol. 41, no. 6, p. 755, 2001.

- [29] J. Pouzo, H. Acuna, M. Milanese, and R. Moroso, “Relativistic electron beams detection in a dense plasma focus”, *The European Physical Journal D-Atomic, Molecular, Optical and Plasma Physics*, vol. 21, no. 1, pp. 97–100, 2002.
- [30] P. Choi, C. Deeney, H. Herold, and C. Wong, “Characterization of self-generated intense electron beams in a plasma focus”, *Laser and Particle Beams*, vol. 8, no. 3, pp. 469–476, 1990.
- [31] R. Fitzpatrick, *Plasma physics: an introduction*. Crc Press, 2014.
- [32] K. Miyamoto, *Plasma physics and controlled nuclear fusion*. Springer Science & Business Media, 2005, vol. 38.
- [33] A. Piel, *Plasma physics: an introduction to laboratory, space, and fusion plasmas*. Springer, 2017.
- [34] G. Belmont, L. Rezeau, C. Riconda, and A. Zaslavsky, *Introduction to plasma physics*. Elsevier, 2019.
- [35] N. R. Council, P. S. Committee, *et al.*, *Frontiers in high energy density physics: the X-games of contemporary science*. National Academies Press, 2003.
- [36] E. National Academies of Sciences, Medicine, *et al.*, *Plasma science: enabling technology, sustainability, security, and exploration*. National Academies Press, 2021.
- [37] R. Morrow, “The origin of ball and bead lightning from an expanded lightning channel”, *Journal of Atmospheric and Solar-Terrestrial Physics*, vol. 195, p. 105 116, 2019.
- [38] A. Srivastava, R. Erdélyi, D. Tripathi, V. Fedun, N. Joshi, and P. Kayshap, “Observational evidence of sausage-pinch instability in solar corona by sdo/aia”, *The Astrophysical Journal Letters*, vol. 765, no. 2, p. L42, 2013.
- [39] R. Lovelace, H. Li, A. Koldoba, G. Ustyugova, and M. Romanova, “Poynting jets from accretion disks”, *The Astrophysical Journal*, vol. 572, no. 1, p. 445, 2002.
- [40] D. Gabuzda, “Evidence for helical magnetic fields associated with agn jets and the action of a cosmic battery”, *Galaxies*, vol. 7, no. 1, p. 5, 2019.
- [41] W. H. Bennett, “Self-focusing streams”, *Physical Review*, vol. 98, no. 6, p. 1584, 1955.
- [42] S. Sadouni, “Fluid modeling of transport and instabilities in magnetized low-temperature plasma sources”, Ph.D. dissertation, Université Paul Sabatier-Toulouse III, 2020.
- [43] M. Haines, “A review of the dense z-pinch”, *Plasma Physics and Controlled Fusion*, vol. 53, no. 9, p. 093 001, 2011.
- [44] B. Kadomtsev, “Hydromagnetic stability of a plasma”, *Reviews of plasma physics*, vol. 2, pp. 153–199, 1966.
- [45] M. A. Liberman, J. S. De Groot, A. Toor, and R. B. Spielman, “Physics of high-density z-pinch plasmas”, 2012.
- [46] M. D. Kruskal and M. Schwarzschild, “Some instabilities of a completely ionized plasma”, *Proceedings of the Royal Society of London. Series A. Mathematical and Physical Sciences*, vol. 223, no. 1154, pp. 348–360, 1954.
- [47] R. Tayler, “Hydromagnetic instabilities of an ideally conducting fluid”, *Proceedings of the Physical Society. Section B*, vol. 70, no. 1, p. 31, 1957.
- [48] S. Katsuki, A. Kimura, Y. Kondo, H. Horita, T. Namihira, T. Sakugawa, and H. Akiyama, “Effects of an axial magnetic field on z-pinch plasmas for extreme ultraviolet sources”, *Journal of applied physics*, vol. 99, no. 1, p. 013 305, 2006.

- [49] F. Conti, N. Aybar, J. Narkis, J. Valenzuela, H. Rahman, E. Ruskov, E. Dutra, S. Haque, A. Covington, and F. Beg, “Study of stability in a liner-on-target gas puff z-pinch as a function of pre-embedded axial magnetic field”, *Physics of Plasmas*, vol. 27, no. 1, p. 012 702, 2020.
- [50] J. Narkis, F. Conti, A. Velikovich, and F. Beg, “Mitigation of magneto-rayleigh-taylor instability growth in a triple-nozzle, neutron-producing gas-puff z pinch”, *Physical Review E*, vol. 104, no. 2, p. L023201, 2021.
- [51] S. Slutz, M. Herrmann, R. Vesey, A. Sefkow, D. Sinars, D. Rovang, K. Peterson, and M. Cuneo, “Pulsed-power-driven cylindrical liner implosions of laser preheated fuel magnetized with an axial field”, *Physics of Plasmas*, vol. 17, no. 5, p. 056 303, 2010.
- [52] S. A. Slutz and R. A. Vesey, “High-gain magnetized inertial fusion”, *Physical review letters*, vol. 108, no. 2, p. 025 003, 2012.
- [53] D. Sinars, M. Sweeney, C. Alexander, D. Ampleford, T. Ao, J. Apruzese, C. Aragon, D. Armstrong, K. Austin, T. Awe, *et al.*, “Review of pulsed power-driven high energy density physics research on z at sandia”, *Physics of Plasmas*, vol. 27, no. 7, p. 070 501, 2020.
- [54] U. Shumlak and C. Hartman, “Sheared flow stabilization of the $m=1$ kink mode in z pinches”, *Physical review letters*, vol. 75, no. 18, p. 3285, 1995.
- [55] U. Shumlak, B. Nelson, R. Golingo, S. Jackson, E. Crawford, and D. Den Hartog, “Sheared flow stabilization experiments in the zap flow z pinch”, *Physics of Plasmas*, vol. 10, no. 5, pp. 1683–1690, 2003.
- [56] U. Shumlak, “Z-pinch fusion”, *Journal of Applied Physics*, vol. 127, no. 20, p. 200 901, 2020.
- [57] D. Ryutov, M. S. Derzon, and M. K. Matzen, “The physics of fast z pinches”, *Reviews of Modern Physics*, vol. 72, no. 1, p. 167, 2000.
- [58] I. Kurchatov, “The possibility of producing thermonuclear reactions in a gaseous discharge”, *The Soviet Journal of Atomic Energy*, vol. 1, no. 3, pp. 359–366, 1956.
- [59] N. Bennett, M. Blasco, K. Breeding, D. Constantino, V. DiPuccio, J. Friedman, B. Gall, S. Gardner, J. Gatling, A. Luttmann, *et al.*, “Source and diagnostic development for a neutron diagnosed subcritical experiment”, Nevada National Security Site/Mission Support and Test Services LLC; Las . . . , Tech. Rep., 2016.
- [60] T. Beller, M. Boswell, T. Cutler, A. DeYoung, D. Dinwiddie, T. Dugan, M. Fowler, J. Gomez, S. Gonzales, J. Goorley, *et al.*, “Primary assessment technologies fy2017 milestone report: Ndse development using dpf”, Los Alamos National Lab.(LANL), Los Alamos, NM (United States), Tech. Rep., 2018.
- [61] A. L. Cooper, J. Winkelbauer, P. Koehler, G. Rusev, R. Olson, P. Pazuchanics, J. Tinsley, R. Buckles, I. Garza, J. A. Green, *et al.*, “Development and validation of a gamma-ray detection response model for neutron-diagnosed subcritical experiments”, *Nuclear Instruments and Methods in Physics Research Section A: Accelerators, Spectrometers, Detectors and Associated Equipment*, vol. 1014, p. 165 755, 2021.
- [62] S. Saw, V. Damideh, J. Ali, R. Rawat, P. Lee, and S. Lee, “Damage study of irradiated tungsten using fast focus mode of a 2.2 kj plasma focus”, *Vacuum*, vol. 144, pp. 14–20, 2017.
- [63] E. Demina, A. Dubrovsky, V. Gribkov, S. Maslyaev, V. Pimenov, I. Sasinovskaya, R. Miklaszewski, and M. Scholz, “Application of a plasma accelerator of the dense plasma focus type in simulation of radiation damage and testing of materials for nuclear systems”.

- [64] S. Javadi, B. Ouyang, Z. Zhang, M. Ghoranneviss, A. S. Elahi, and R. Rawat, “Effects of fusion relevant transient energetic radiation, plasma and thermal load on plansee double forged tungsten samples in a low-energy plasma focus device”, *Applied Surface Science*, vol. 443, pp. 311–320, 2018.
- [65] R. Rawat, “Dense plasma focus-from alternative fusion source to versatile high energy density plasma source for plasma nanotechnology”, in *Journal of Physics: Conference Series*, IOP Publishing, vol. 591, 2015, p. 012021.
- [66] J. V. Vas, J. Pan, N. Wang, J. Xu, R. Medwal, M. Mishra, J. Y. Pae, M. V. Matham, L. Paul, and R. S. Rawat, “Plasma processed tungsten for fusion reactor first-wall material”, *Journal of Materials Science*, vol. 56, no. 17, pp. 10494–10509, 2021.
- [67] J. Feugeas, L. Rico, L. Nosei, B. Gómez, E. Bemporad, J. Lesage, and J. Ferrón, “Austenite modification of aisi 316l ss by pulsed nitrogen ion beams generated in dense plasma focus discharges”, *Surface and Coatings Technology*, vol. 204, no. 8, pp. 1193–1199, 2010.
- [68] Z. Wang, H. Yousefi, Y. Nishino, H. Ito, and K. Masugata, “Fabrication of dlc films by pulsed ion beam ablation in a dense plasma focus device”, *Physics Letters A*, vol. 373, no. 45, pp. 4169–4173, 2009.
- [69] T. Zhang, J. Lin, A. Patran, D. Wong, S. Hassan, S. Mahmood, T. White, T. Tan, S. Springham, S. Lee, *et al.*, “Optimization of a plasma focus device as an electron beam source for thin film deposition”, *Plasma Sources Science and Technology*, vol. 16, no. 2, p. 250, 2007.
- [70] S. Mohanty, N. Neog, R. Rawat, P. Lee, B. Nayak, and B. Acharya, “Self-organized transformation to polyaniline nanowires by pulsed energetic electron irradiation in a plasma focus device”, *Physics Letters A*, vol. 373, no. 22, pp. 1962–1966, 2009.
- [71] M. Shirazi, M. Ghasemloo, G. R. Etaati, M. T. Hosseinnejad, and M. R. Toroghinejad, “Plasma focus method for growth of molybdenum nitride thin films: Synthesis and thin film characterization”, *Journal of Alloys and Compounds*, vol. 727, pp. 978–985, 2017.
- [72] S. M. Ahmad, T. Hussain, R. Ahmad, J. Siddiqui, and D. Ali, “Synthesis and characterization of magnesium aluminate (mgal₂o₄) spinel (mas) thin films”, *Materials Research Express*, vol. 5, no. 1, p. 016415, 2018.
- [73] K. S. Tan, R. J. Mah, and R. S. Rawat, “Dense plasma focus device based high growth rate room temperature synthesis of nanostructured zinc oxide thin films”, *IEEE Transactions on Plasma Science*, vol. 43, no. 8, pp. 2539–2546, 2015.
- [74] R. Rawat, P. Lee, T. White, L. Ying, and S. Lee, “Room temperature deposition of titanium carbide thin films using dense plasma focus device”, *Surface and Coatings Technology*, vol. 138, no. 2-3, pp. 159–165, 2001.
- [75] M. Hosseinnejad, M. Ghoranneviss, G. Etaati, M. Shirazi, and Z. Ghorannevis, “Deposition of tungsten nitride thin films by plasma focus device at different axial and angular positions”, *Applied surface science*, vol. 257, no. 17, pp. 7653–7658, 2011.
- [76] M. Hassan, A. Qayyum, R. Ahmad, R. Rawat, P. Lee, S. Hassan, G. Murtaza, and M. Zakaullah, “Dense plasma focus ion-based titanium nitride coating on titanium”, *Nuclear Instruments and Methods in Physics Research Section B: Beam Interactions with Materials and Atoms*, vol. 267, no. 11, pp. 1911–1917, 2009.
- [77] K. M. Agah, M. Ghoranneviss, M. Salem, A. S. Elahi, S. Mohammadi, and R. Arvin, “Increase of diagnostic mirror lifetime using tin coated stainless steel by using a plasma focus device”, *Plasma Science and Technology*, vol. 15, no. 5, p. 485, 2013.
- [78] S. Kenawy, U. Rashed, and S. Hassaballah, “Synthesis and characterization of alumina-zirconia ceramic thin film deposited using a dense plasma focus (dpf) device”, *Interceram-International Ceramic Review*, vol. 68, no. 1, pp. 22–29, 2019.

- [79] Z. Umar, R. Rawat, R. Ahmad, Z. Chen, Z. Zhang, J. Siddiqui, A. Hussnain, T. Hus-sain, and M. Baig, “Structural, compositional and hardness properties of hydrogenated amorphous carbon nitride thin films synthesized by dense plasma focus device”, *Surface and Interface Analysis*, vol. 49, no. 6, pp. 548–553, 2017.
- [80] A. Srivastava, R. Nahar, C. K. Sarkar, W. Singh, and Y. Malhotra, “Study of hafnium oxide deposited using dense plasma focus machine for film structure and electrical prop-erties as a mos device”, *Microelectronics Reliability*, vol. 51, no. 4, pp. 751–755, 2011.
- [81] R. Rawat, “High energy density pulsed plasmas in plasma focus: Novel plasma processing tool for nanophase hard magnetic material synthesis”, *Nanoscience and Nanotechnology Letters*, vol. 4, no. 3, pp. 251–274, 2012.
- [82] R. Rawat, “High-energy-density pinch plasma a unique nonconventional tool for plasma nanotechnology”, *IEEE Transactions on Plasma Science*, vol. 41, no. 4, pp. 701–715, 2013.
- [83] F. Di Lorenzo, V. Raspa, P. Knoblauch, A. Lazarte, C. Moreno, and A. Clause, “Hard x-ray source for flash radiography based on a 2.5 kj plasma focus”, *Journal of Applied Physics*, vol. 102, no. 3, p. 033 304, 2007.
- [84] R. Verma, R. Rawat, P. Lee, M. Krishnan, S. V. Springham, and T. Tan, “Miniature plasma focus device as a compact hard x-ray source for fast radiography applications”, *IEEE transactions on plasma science*, vol. 38, no. 4, pp. 652–657, 2010.
- [85] C. Pavez, J. Pedreros, M. Zambra, F. Veloso, J. Moreno, T.-S. Ariel, and L. Soto, “Po-tentiality of a small and fast dense plasma focus as hard x-ray source for radiographic applications”, *Plasma Physics and Controlled Fusion*, vol. 54, no. 10, p. 105 018, 2012.
- [86] P. Knoblauch, V. Raspa, F. Di Lorenzo, A. Clause, and C. Moreno, “Hard x-ray dosime-try of a plasma focus suitable for industrial radiography”, *Radiation Physics and Chem-istry*, vol. 145, pp. 39–42, 2018.
- [87] S. Lebedev, A. Frank, and D. Ryutov, “Exploring astrophysics-relevant magnetohydro-dynamics with pulsed-power laboratory facilities”, *Reviews of Modern Physics*, vol. 91, no. 2, p. 025 002, 2019.
- [88] B. A. Remington, R. P. Drake, and D. D. Ryutov, “Experimental astrophysics with high power lasers and z pinches”, *Reviews of Modern Physics*, vol. 78, no. 3, p. 755, 2006.
- [89] S. Lebedev, J. Chittenden, F. Beg, S. Bland, A. Ciardi, D. Ampleford, S. Hughes, M. Haines, A. Frank, E. Blackman, *et al.*, “Laboratory astrophysics and collimated stellar outflows: The production of radiatively cooled hypersonic plasma jets”, *The Astrophysical Journal*, vol. 564, no. 1, p. 113, 2002.
- [90] S. Lebedev, A. Ciardi, D. Ampleford, S. Bland, S. Bott, J. Chittenden, G. Hall, J. Rapley, C. Jennings, M. Sherlock, *et al.*, “Production of radiatively cooled hypersonic plasma jets and links to astrophysical jets”, *Plasma Physics and Controlled Fusion*, vol. 47, no. 12B, B465, 2005.
- [91] V. Krauz, V. Myalton, V. Vinogradov, E. Velikhov, S. Ananyev, S. Dan’ko, Y. G. Kalinin, A. Kharrasov, Y. V. Vinogradova, K. Mitrofanov, *et al.*, “Laboratory simulations of astrophysical jets: Results from experiments at the pf-3, pf-1000u, and kpf-4 facilities”, in *Journal of Physics: Conference Series*, IOP Publishing, vol. 907, 2017, p. 012 026.
- [92] K. Mitrofanov, V. Krauz, V. Myalton, V. Vinogradov, A. Kharrasov, and Y. V. Vino-gradova, “Properties of the distribution of azimuthal magnetic field in a plasma flow during laboratory simulations of astrophysical jets in a plasma-focus installation”, *Astronomy Reports*, vol. 61, no. 2, pp. 138–152, 2017.

- [93] K. Mitrofanov, V. Krauz, V. Myalton, E. Velikhov, V. Vinogradov, and Y. V. Vinogradova, “Magnetic field distribution in the plasma flow generated by a plasma focus discharge”, *Journal of Experimental and Theoretical Physics*, vol. 119, no. 5, pp. 910–923, 2014.
- [94] S. Lebedev, A. Ciardi, D. Ampleford, S. Bland, S. Bott, J. Chittenden, G. Hall, J. Rapley, C. Jennings, A. Frank, *et al.*, “Magnetic tower outflows from a radial wire array z-pinch”, *Monthly Notices of the Royal Astronomical Society*, vol. 361, no. 1, pp. 97–108, 2005.
- [95] A. Ciardi, S. Lebedev, A. Frank, E. Blackman, J. Chittenden, C. Jennings, D. Ampleford, S. Bland, S. Bott, J. Rapley, *et al.*, “The evolution of magnetic tower jets in the laboratory”, *Physics of Plasmas*, vol. 14, no. 5, p. 056 501, 2007.
- [96] D. Mourenas, J. Vierne, F. Simonet, V. Krauz, S. Nikulin, V. Mialton, and M. Karakin, “Laboratory and computer simulations of super-alfvénic shocks in a weakly ionized medium”, *Physics of Plasmas*, vol. 10, no. 3, pp. 605–613, 2003.
- [97] A. Ciardi, D. J. Ampleford, S. V. Lebedev, and C. Stehle, “Curved herbig-haro jets: Simulations and experiments”, *The Astrophysical Journal*, vol. 678, no. 2, p. 968, 2008.
- [98] F. Suzuki-Vidal, S. Lebedev, A. Ciardi, L. Pickworth, R. Rodriguez, J. Gil, G. Espinosa, P. Hartigan, G. Swadling, J. Skidmore, *et al.*, “Bow shock fragmentation driven by a thermal instability in laboratory astrophysics experiments”, *The Astrophysical Journal*, vol. 815, no. 2, p. 96, 2015.
- [99] T. Clayson, S. Lebedev, F. Suzuki-Vidal, G. Burdiak, J. Halliday, J. Hare, J. Ma, L. Suttle, and E. Tubman, “Inverse liner z-pinch: An experimental pulsed power platform for studying radiative shocks”, *IEEE Transactions on Plasma Science*, vol. 46, no. 11, pp. 3734–3740, 2018.
- [100] L. Suttle, J. Hare, S. Lebedev, A. Ciardi, N. Loureiro, G. Burdiak, J. Chittenden, T. Clayson, J. Halliday, N. Niasse, *et al.*, “Ion heating and magnetic flux pile-up in a magnetic reconnection experiment with super-alfvénic plasma inflows”, *Physics of Plasmas*, vol. 25, no. 4, p. 042 108, 2018.
- [101] L. Suttle, J. Hare, S. Lebedev, G. Swadling, G. Burdiak, A. Ciardi, J. Chittenden, N. Loureiro, N. Niasse, F. Suzuki-Vidal, *et al.*, “Structure of a magnetic flux annihilation layer formed by the collision of supersonic, magnetized plasma flows”, *Physical review letters*, vol. 116, no. 22, p. 225 001, 2016.
- [102] J. Hare, L. Suttle, S. Lebedev, N. Loureiro, A. Ciardi, G. Burdiak, J. Chittenden, T. Clayson, C. Garcia, N. Niasse, *et al.*, “Anomalous heating and plasmoid formation in a driven magnetic reconnection experiment”, *Physical review letters*, vol. 118, no. 8, p. 085 001, 2017.
- [103] R. Lemke, M. Knudson, C. Hall, T. Hail, P. Desjarlais, J. Asay, and T. Mehlhorn, “Characterization of magnetically accelerated flyer plates”, *Physics of Plasmas*, vol. 10, no. 4, pp. 1092–1099, 2003.
- [104] M. D. Knudson, “Megaamps, megagauss, and megabars: Using the sandia z machine to perform extreme material dynamics experiments”, in *AIP Conference Proceedings*, American Institute of Physics, vol. 1426, 2012, pp. 35–42.
- [105] M. D. Knudson, D. L. Hanson, J. E. Bailey, C. A. Hall, J. R. Asay, and W. Anderson, “Equation of state measurements in liquid deuterium to 70 gpa”, *Physical Review Letters*, vol. 87, no. 22, p. 225 501, 2001.
- [106] M. Knudson, D. Hanson, J. Bailey, C. Hall, J. Asay, and C. Deeney, “Principal hgoniot, reverberating wave, and mechanical reshock measurements of liquid deuterium to 400 gpa using plate impact techniques”, *Physical Review B*, vol. 69, no. 14, p. 144 209, 2004.

- [107] D. Reisman, A. Toor, R. Cauble, C. Hall, J. Asay, M. Knudson, and M. Furnish, “Magnetically driven isentropic compression experiments on the z accelerator”, *Journal of Applied Physics*, vol. 89, no. 3, pp. 1625–1633, 2001.
- [108] R. G. Kraus, S. Root, R. W. Lemke, S. T. Stewart, S. B. Jacobsen, and T. R. Mattsson, “Impact vaporization of planetesimal cores in the late stages of planet formation”, *Nature Geoscience*, vol. 8, no. 4, pp. 269–272, 2015.
- [109] K. Cochrane, R. Lemke, Z. Riford, and J. Carpenter, “Magnetically launched flyer plate technique for probing electrical conductivity of compressed copper”, *Journal of Applied Physics*, vol. 119, no. 10, p. 105 902, 2016.
- [110] J. Bailey, G. Chandler, D. Cohen, M. Cuneo, M. Foord, R. Heeter, D. Jobe, P. Lake, J. MacFarlane, T. Nash, *et al.*, “Radiation science using z-pinch x rays”, *Physics of Plasmas*, vol. 9, no. 5, pp. 2186–2194, 2002.
- [111] J. E. Bailey, G. A. Rochau, C. Iglesias, J. Abdallah Jr, J. MacFarlane, I. Golovkin, P. Wang, R. Mancini, P. Lake, T. Moore, *et al.*, “Iron-plasma transmission measurements at temperatures above 150 ev”, *Physical review letters*, vol. 99, no. 26, p. 265 002, 2007.
- [112] J. E. Bailey, T. Nagayama, G. P. Loisel, G. A. Rochau, C. Blancard, J. Colgan, P. Cosse, G. Faussurier, C. Fontes, F. Gilleron, *et al.*, “A higher-than-predicted measurement of iron opacity at solar interior temperatures”, *Nature*, vol. 517, no. 7532, pp. 56–59, 2015.
- [113] V. V. Ivanov, A. A. Anderson, D. Papp, A. Astanovitskiy, V. Nalajala, and O. Dmitriev, “Study of magnetic fields and current in the z pinch at stagnation”, *Physics of Plasmas*, vol. 22, no. 9, p. 092 710, 2015.
- [114] A. Anderson, V. Ivanov, and D. Papp, “Visualization of the magnetic field and current path in z-pinch and x-pinch plasmas”, *High Energy Density Physics*, vol. 15, pp. 1–3, 2015.
- [115] K. Mitrofanov, V. Krauz, E. Grabovski, V. Myalton, M. Paduch, and A. Gritsuk, “Features of the application of the magnetic-probe method for diagnostics of high-temperature plasma”, *Instruments and Experimental Techniques*, vol. 61, no. 2, pp. 239–259, 2018.
- [116] J. Greenly, M. Martin, I. Blesener, D. Chalenski, P. Knapp, and R. McBride, “The role of flux advection in the development of the ablation streams and precursors of wire array z-pinch”, in *AIP Conference Proceedings*, American Institute of Physics, 2009, pp. 53–56.
- [117] P.-A. Gourdain, I. Blesener, J. Greenly, D. Hammer, P. Knapp, B. Kusse, and P. Schrafel, “Initial experiments using radial foils on the cornell beam research accelerator pulsed power generator”, *Physics of Plasmas*, vol. 17, no. 1, p. 012 706, 2010.
- [118] G. Davara, L. Gregorian, E. Kroupp, and Y. Maron, “Spectroscopic determination of the magnetic-field distribution in an imploding plasma”, *Physics of Plasmas*, vol. 5, no. 4, pp. 1068–1075, 1998.
- [119] E. Stambulchik, K. Tsigutkin, and Y. Maron, “Spectroscopic method for measuring plasma magnetic fields having arbitrary distributions of direction and amplitude”, *Physical review letters*, vol. 98, no. 22, p. 225 001, 2007.
- [120] R. Doron, D. Mikitchuk, C. Stollberg, G. Rosenzweig, E. Stambulchik, E. Kroupp, Y. Maron, and D. Hammer, “Determination of magnetic fields based on the zeeman effect in regimes inaccessible by zeeman-splitting spectroscopy”, *High Energy Density Physics*, vol. 10, pp. 56–60, 2014.
- [121] G. Rosenzweig, E. Kroupp, A. Fisher, and Y. Maron, “Measurements of the spatial magnetic field distribution in a z-pinch plasma throughout the stagnation process”, *Journal of Instrumentation*, vol. 12, no. 09, P09004, 2017.

- [122] G. Rosenzweig, E. Kroupp, T. Queller, A. Starobinets, Y. Maron, V. Tangri, J. Giuliani, and A. Fruchtman, “Local measurements of the spatial magnetic field distribution in a z-pinch plasma during and near stagnation using polarization spectroscopy”, *Physics of Plasmas*, vol. 27, no. 2, p. 022 705, 2020.
- [123] R. Snavely, M. Key, S. Hatchett, T. Cowan, M. Roth, T. Phillips, M. Stoyer, E. Henry, T. Sangster, M. Singh, *et al.*, “Intense high-energy proton beams from petawatt-laser irradiation of solids”, *Physical review letters*, vol. 85, no. 14, p. 2945, 2000.
- [124] S. Wilks, A. Langdon, T. Cowan, M. Roth, M. Singh, S. Hatchett, M. Key, D. Pennington, A. MacKinnon, and R. Snavely, “Energetic proton generation in ultra-intense laser–solid interactions”, *Physics of plasmas*, vol. 8, no. 2, pp. 542–549, 2001.
- [125] M. Passoni, L. Bertagna, and A. Zani, “Target normal sheath acceleration: Theory, comparison with experiments and future perspectives”, *New Journal of Physics*, vol. 12, no. 4, p. 045 012, 2010.
- [126] M. Borghesi, A. Schiavi, D. Campbell, M. Haines, O. Willi, A. MacKinnon, L. Gizzi, M. Galimberti, R. Clarke, and H. Ruhl, “Proton imaging: A diagnostic for inertial confinement fusion/fast ignitor studies”, *Plasma physics and controlled fusion*, vol. 43, no. 12A, A267, 2001.
- [127] M. Borghesi, D. Campbell, A. Schiavi, O. Willi, A. Mackinnon, D. Hicks, P. Patel, L. Gizzi, M. Galimberti, and R. Clarke, “Laser-produced protons and their application as a particle probe”, *Laser and Particle Beams*, vol. 20, no. 2, p. 269, 2002.
- [128] C. Li, F. Séguin, J. Frenje, J. Rygg, R. Petrasso, R. Town, P. Amendt, S. Hatchett, O. Landen, A. Mackinnon, *et al.*, “Monoenergetic proton backlighter for measuring e and b fields and for radiographing implosions and high-energy density plasmas”, *Review of scientific instruments*, vol. 77, no. 10, 10E725, 2006.
- [129] C. Li, P. Tzeferacos, D. Lamb, G. Gregori, P. Norreys, M. Rosenberg, R. Follett, D. Froula, M. Koenig, F. Seguin, *et al.*, “Scaled laboratory experiments explain the kink behaviour of the crab nebula jet”, *Nature communications*, vol. 7, no. 1, pp. 1–8, 2016.
- [130] A. Higginson, R. Gray, M. King, R. Dance, S. Williamson, N. Butler, R. Wilson, R. Capdessus, C. Armstrong, J. Green, *et al.*, “Near-100 mev protons via a laser-driven transparency-enhanced hybrid acceleration scheme”, *Nature communications*, vol. 9, no. 1, pp. 1–9, 2018.
- [131] M. Roth and M. Schollmeier, “Ion acceleration-target normal sheath acceleration”, *arXiv preprint arXiv:1705.10569*, 2017.
- [132] M. Rosen and J. Nuckolls, “Exploding pusher performance- a theoretical model”, *The Physics of Fluids*, vol. 22, no. 7, pp. 1393–1396, 1979.
- [133] M.-E. Manuel, A. Zylstra, H. Rinderknecht, D. Casey, M. Rosenberg, N. Sinenian, C. Li, J. Frenje, F. Séguin, and R. Petrasso, “Source characterization and modeling development for monoenergetic-proton radiography experiments on omega”, *Review of scientific instruments*, vol. 83, no. 6, p. 063 506, 2012.
- [134] C. Yeaman, G. Kemp, Z. Walters, H. Whitley, P. McKenty, E. Garcia, Y. Yang, R. Craxton, and B. Blue, “High yield polar direct drive fusion neutron sources at the national ignition facility”, *Nuclear Fusion*, vol. 61, no. 4, p. 046 031, 2021.
- [135] M. Rosenberg, A. Zylstra, F. Séguin, H. Rinderknecht, J. Frenje, M. Gatu Johnson, H. Sio, C. Waugh, N. Sinenian, C. Li, *et al.*, “Investigation of ion kinetic effects in direct-drive exploding-pusher implosions at the nif”, *Physics of Plasmas*, vol. 21, no. 12, p. 122 712, 2014.

- [136] C. Li, F. Séguin, J. Frenje, M. Rosenberg, R. Petrasso, P. Amendt, J. Koch, O. Landen, H. Park, H. Robey, *et al.*, “Charged-particle probing of x-ray–driven inertial-fusion implosions”, *Science*, vol. 327, no. 5970, pp. 1231–1235, 2010.
- [137] J. Rygg, F. Séguin, C. Li, J. Frenje, M.-E. Manuel, R. Petrasso, R. Betti, J. Delettrez, O. Gotchev, J. Knauer, *et al.*, “Proton radiography of inertial fusion implosions”, *Science*, vol. 319, no. 5867, pp. 1223–1225, 2008.
- [138] C. Li, F. Séguin, J. Frenje, J. Rygg, R. Petrasso, R. Town, O. Landen, J. Knauer, and V. Smalyuk, “Observation of megagauss-field topology changes due to magnetic reconnection in laser-produced plasmas”, *Physical review letters*, vol. 99, no. 5, p. 055 001, 2007.
- [139] F. Séguin, C. Li, M.-E. Manuel, H. Rinderknecht, N. Sinenian, J. Frenje, J. Rygg, D. Hicks, R. Petrasso, J. Delettrez, *et al.*, “Time evolution of filamentation and self-generated fields in the coronae of directly driven inertial-confinement fusion capsules”, *Physics of Plasmas*, vol. 19, no. 1, p. 012 701, 2012.
- [140] A. Zylstra, C. Li, H. Rinderknecht, F. Séguin, R. Petrasso, C. Stoeckl, D. Meyerhofer, P. Nilson, T. Sangster, S. Le Pape, *et al.*, “Using high-intensity laser-generated energetic protons to radiograph directly driven implosions”, *Review of scientific instruments*, vol. 83, no. 1, p. 013 511, 2012.
- [141] C. Li, F. Séguin, J. Frenje, J. Rygg, R. Petrasso, R. Town, P. Amendt, S. Hatchett, O. Landen, A. Mackinnon, *et al.*, “Measuring e and b fields in laser-produced plasmas with monoenergetic proton radiography”, *Physical review letters*, vol. 97, no. 13, p. 135 003, 2006.
- [142] R. Petrasso, C. Li, F. Seguin, J. Rygg, J. Frenje, R. Betti, J. Knauer, D. Meyerhofer, P. Amendt, D. Froula, *et al.*, “Lorentz mapping of magnetic fields in hot dense plasmas”, *Physical review letters*, vol. 103, no. 8, p. 085 001, 2009.
- [143] A. Zylstra, J. Frenje, P. Grabowski, C. Li, G. Collins, P. Fitzsimmons, S. Glenzer, F. Graziani, S. Hansen, S. Hu, *et al.*, “Measurement of charged-particle stopping in warm dense plasma”, *Physical review letters*, vol. 114, no. 21, p. 215 002, 2015.
- [144] A. Mančić, J. Fuchs, P. Antici, S. Gaillard, and P. Audebert, “Absolute calibration of photostimulable image plate detectors used as (0.5–20 mev) high-energy proton detectors”, *Review of Scientific Instruments*, vol. 79, no. 7, p. 073 301, 2008.
- [145] H. Schwoerer, S. Pfoth, O. Jäckel, K.-U. Amthor, B. Liesfeld, W. Ziegler, R. Sauerbrey, K. Ledingham, and T. Esirkepov, “Laser-plasma acceleration of quasi-monoenergetic protons from microstructured targets”, *Nature*, vol. 439, no. 7075, pp. 445–448, 2006.
- [146] M. Huault, D. De Luis, J. Apiñaniz, M. De Marco, C. Salgado, N. Gordillo, C. G. Neira, J. Perez-Hernandez, R. Fedosejevs, G. Gatti, *et al.*, “A 2d scintillator-based proton detector for high repetition rate experiments”, *High Power Laser Science and Engineering*, vol. 7, 2019.
- [147] F. Séguin, J. Frenje, C. Li, D. Hicks, S. Kurebayashi, J. Rygg, B.-E. Schwartz, R. Petrasso, S. Roberts, J. Soures, *et al.*, “Spectrometry of charged particles from inertial-confinement-fusion plasmas”, *Review of Scientific Instruments*, vol. 74, no. 2, pp. 975–995, 2003.
- [148] D. Hey, M. Key, A. Mackinnon, A. MacPhee, P. Patel, R. Freeman, L. Van Woerkom, and C. Castaneda, “Use of gafchromic film to diagnose laser generated proton beams”, *Review of Scientific Instruments*, vol. 79, no. 5, p. 053 501, 2008.
- [149] B. G. Cartwright, E. Shirk, and P. Price, “A nuclear-track-recording polymer of unique sensitivity and resolution”, *Nuclear Instruments and Methods*, vol. 153, no. 2-3, pp. 457–460, 1978.
- [150] R. Cassou and E. Benton, “Properties and applications of cr-39 polymeric nuclear track detector”, *Nuclear Track Detection*, vol. 2, no. 3, pp. 173–179, 1978.

- [151] D. O'Sullivan, D. Zhou, E. Semones, W. Heinrich, and E. Flood, "Dose equivalent, absorbed dose and charge spectrum investigation in low earth orbit", *Advances in Space Research*, vol. 34, no. 6, pp. 1420–1423, 2004.
- [152] G. Sahoo, S. Tripathy, S. Paul, S. Sharma, S. Sharma, D. Joshi, and T. Bandyopadhyay, "Neutron dose estimation via let spectrometry using cr-39 detector for the reaction $9\text{Be}(p, n)$ ", *Journal of Medical Physics/Association of Medical Physicists of India*, vol. 39, no. 4, p. 225, 2014.
- [153] M. Seimetz, P. Bellido, P. Garcíea, P. Mur, A. Iborra, A. Soriano, T. Hülber, J. Garcíea López, M. d. C. Jiménez-Ramos, R. Lera, *et al.*, "Spectral characterization of laser-accelerated protons with cr-39 nuclear track detector", *Review of Scientific Instruments*, vol. 89, no. 2, p. 023 302, 2018.
- [154] N. Sinenian, M. Rosenberg, M. Manuel, S. McDuffee, D. Casey, A. Zylstra, H. Rinderknecht, M. Gatu Johnson, F. Séguin, J. Frenje, *et al.*, "The response of cr-39 nuclear track detector to 1–9 mev protons", *Review of Scientific Instruments*, vol. 82, no. 10, p. 103 303, 2011.
- [155] Y. Zhang, H.-W. Wang, Y.-G. Ma, L.-X. Liu, X.-G. Cao, G.-T. Fan, G.-Q. Zhang, and D.-Q. Fang, "Energy calibration of a cr-39 nuclear-track detector irradiated by charged particles", *Nuclear Science and Techniques*, vol. 30, no. 6, pp. 1–9, 2019.
- [156] J. Frenje, C. Li, F. Séguin, D. Hicks, S. Kurebayashi, R. Petrasso, S. Roberts, V. Y. Glebov, D. Meyerhofer, T. Sangster, *et al.*, "Absolute measurements of neutron yields from dd and dt implosions at the omega laser facility using cr-39 track detectors", *Review of scientific instruments*, vol. 73, no. 7, pp. 2597–2605, 2002.
- [157] S. Gaillard, J. Fuchs, N. Renard-Le Galloudec, and T. Cowan, "Study of saturation of cr39 nuclear track detectors at high ion fluence and of associated artifact patterns", *Review of scientific instruments*, vol. 78, no. 1, p. 013 304, 2007.
- [158] S. Devic, N. Tomic, and D. Lewis, "Reference radiochromic film dosimetry: Review of technical aspects", *Physica Medica*, vol. 32, no. 4, pp. 541–556, 2016.
- [159] M. J. Butson, K. Peter, T. Cheung, and P. Metcalfe, "Radiochromic film for medical radiation dosimetry", *Materials Science and Engineering: R: Reports*, vol. 41, no. 3-5, pp. 61–120, 2003.
- [160] S. Devic, "Radiochromic film dosimetry: Past, present, and future", *Physica medica*, vol. 27, no. 3, pp. 122–134, 2011.
- [161] I. J. Das, *Radiochromic film: role and applications in radiation dosimetry*. CRC Press, 2017.
- [162] F. Nürnberg, M. Schollmeier, E. Brambrink, A. Blažević, D. Carroll, K. Flippo, D. Gautier, M. Geissel, K. Harres, B. Hegelich, *et al.*, "Radiochromic film imaging spectroscopy of laser-accelerated proton beams", *Review of scientific instruments*, vol. 80, no. 3, p. 033 301, 2009.
- [163] J. Kaufman, D. Margarone, G. Candiano, I. J. Kim, T. M. Jeong, J. Pšikal, F. Romano, P. Cirrone, V. Scuderi, and G. Korn, "Radiochromic film diagnostics for laser-driven ion beams", in *Research Using Extreme Light: Entering New Frontiers with Petawatt-Class Lasers II*, International Society for Optics and Photonics, vol. 9515, 2015, 95151J.
- [164] J. F. Ziegler, M. D. Ziegler, and J. P. Biersack, "Srim—the stopping and range of ions in matter (2010)", *Nuclear Instruments and Methods in Physics Research Section B: Beam Interactions with Materials and Atoms*, vol. 268, no. 11-12, pp. 1818–1823, 2010. [Online]. Available: <http://www.srim.org/>.
- [165] J. F. Ziegler, *The stopping and ranges of ions in matter*. Elsevier, 2013.

- [166] C. K. Birdsall and A. B. Langdon, *Plasma physics via computer simulation*. CRC press, 2004.
- [167] P. Schmit, P. Knapp, S. Hansen, M. Gomez, K. Hahn, D. Sinars, K. Peterson, S. Slutz, A. Sefkow, T. Awe, *et al.*, “Understanding fuel magnetization and mix using secondary nuclear reactions in magneto-inertial fusion”, *Physical review letters*, vol. 113, no. 15, p. 155 004, 2014.
- [168] N. Kugland, D. Ryutov, C. Plechaty, J. Ross, and H.-S. Park, “Invited article: Relation between electric and magnetic field structures and their proton-beam images”, *Review of Scientific Instruments*, vol. 83, no. 10, p. 101 301, 2012.
- [169] M. M. Sulman, J. Williams, and R. D. Russell, “An efficient approach for the numerical solution of the monge–ampère equation”, *Applied Numerical Mathematics*, vol. 61, no. 3, pp. 298–307, 2011.
- [170] M. F. Kasim, L. Ceurvorst, N. Ratan, J. Sadler, N. Chen, A. Sävert, R. Trines, R. Bingham, P. N. Burrows, M. C. Kaluza, *et al.*, “Quantitative shadowgraphy and proton radiography for large intensity modulations”, *Physical Review E*, vol. 95, no. 2, p. 023 306, 2017.
- [171] C. Graziani, P. Tzeferacos, D. Q. Lamb, and C. Li, “Inferring morphology and strength of magnetic fields from proton radiographs”, *Review of Scientific Instruments*, vol. 88, no. 12, p. 123 507, 2017.
- [172] A. Bott, C. Graziani, P. Tzeferacos, T. White, D. Lamb, G. Gregori, and A. Schekochihin, “Proton imaging of stochastic magnetic fields”, *Journal of Plasma Physics*, vol. 83, no. 6, 2017.
- [173] M. Kasim, A. Bott, P. Tzeferacos, D. Lamb, G. Gregori, and S. Vinko, “Retrieving fields from proton radiography without source profiles”, *Physical Review E*, vol. 100, no. 3, p. 033 208, 2019.
- [174] W. Fox, D. Schaeffer, M. Rosenberg, G. Fiksel, J. Matteucci, H.-S. Park, A. Bott, K. Lezhnin, A. Bhattacharjee, D. Kalantar, *et al.*, “Fast magnetic reconnection in highly-extended current sheets at the national ignition facility”, *arXiv preprint arXiv:2003.06351*, 2020.
- [175] N. F. Chen, M. F. Kasim, L. Ceurvorst, N. Ratan, J. Sadler, M. C. Levy, R. Trines, R. Bingham, and P. Norreys, “Machine learning applied to proton radiography of high-energy-density plasmas”, *Physical Review E*, vol. 95, no. 4, p. 043 305, 2017.
- [176] M. Levy, D. Ryutov, S. Wilks, J. Ross, C. Huntington, F. Fiuza, D. Martinez, N. Kugland, M. Baring, and H.-S. Park, “Development of an interpretive simulation tool for the proton radiography technique”, *Review of Scientific Instruments*, vol. 86, no. 3, p. 033 302, 2015.
- [177] B. Du, H.-B. Cai, W.-S. Zhang, S.-Y. Zou, J. Chen, and S.-P. Zhu, “A demonstration of extracting the strength and wavelength of the magnetic field generated by the weibel instability from proton radiography”, *High Power Laser Science and Engineering*, vol. 7, 2019.
- [178] B. Du, H.-B. Cai, W.-S. Zhang, J.-M. Tian, E.-H. Zhang, S.-Y. Zou, J. Chen, and S.-P. Zhu, “Distinguishing and diagnosing the spontaneous electric and magnetic fields of weibel instability through proton radiography”, *Plasma Physics and Controlled Fusion*, vol. 62, no. 2, p. 025 017, 2019.
- [179] J. Levesque, C. Kuranz, T. Handy, M. Manuel, and F. Fiuza, “Characterizing filamentary magnetic structures in counter-streaming plasmas by fourier analysis of proton images”, *Physics of Plasmas*, vol. 26, no. 10, p. 102 303, 2019.

- [180] N. Kugland, J. Ross, P.-Y. Chang, R. Drake, G. Fiksel, D. Froula, S. Glenzer, G. Gregori, M. Grosskopf, C. Huntington, *et al.*, “Visualizing electromagnetic fields in laser-produced counter-streaming plasma experiments for collisionless shock laboratory astrophysics”, *Physics of Plasmas*, vol. 20, no. 5, p. 056 313, 2013.
- [181] C. Palmer, P. Campbell, Y. Ma, L. Antonelli, A. Bott, G. Gregori, J. Halliday, Y. Katzir, P. Kordell, K. Krushelnick, *et al.*, “Field reconstruction from proton radiography of intense laser driven magnetic reconnection”, *Physics of Plasmas*, vol. 26, no. 8, p. 083 109, 2019.
- [182] E. Tubman, A. Joglekar, A. Bott, M. Borghesi, B. Coleman, G. Cooper, C. Danson, P. Durey, J. Foster, P. Graham, *et al.*, “Observations of pressure anisotropy effects within semi-collisional magnetized plasma bubbles”, *Nature Communications*, vol. 12, no. 1, pp. 1–9, 2021.
- [183] P. Tzeferacos, A. Rigby, A. Bott, A. Bell, R. Bingham, A. Casner, F. Cattaneo, E. Churazov, J. Emig, F. Fiuza, *et al.*, “Laboratory evidence of dynamo amplification of magnetic fields in a turbulent plasma”, *Nature communications*, vol. 9, no. 1, pp. 1–8, 2018.
- [184] P. Tzeferacos, A. Rigby, A. Bott, A. Bell, R. Bingham, A. Casner, F. Cattaneo, E. Churazov, J. Emig, N. Flocke, *et al.*, “Numerical modeling of laser-driven experiments aiming to demonstrate magnetic field amplification via turbulent dynamo”, *Physics of Plasmas*, vol. 24, no. 4, p. 041 404, 2017.
- [185] L. Romagnani, J. Fuchs, M. Borghesi, P. Antici, P. Audebert, F. Ceccherini, T. Cowan, T. Grismayer, S. Kar, A. Macchi, *et al.*, “Dynamics of electric fields driving the laser acceleration of multi-mev protons”, *Physical review letters*, vol. 95, no. 19, p. 195 001, 2005.
- [186] L. Romagnani, M. Borghesi, C. Cecchetti, S. Kar, P. Antici, P. Audebert, S. Bandhoupad-jay, F. Ceccherini, T. Cowan, J. Fuchs, *et al.*, “Proton probing measurement of electric and magnetic fields generated by ns and ps laser-matter interactions”, *Laser and Particle Beams*, vol. 26, no. 2, p. 241, 2008.
- [187] T. Sokollik, M. Schnürer, S. Ter-Avetisyan, P. Nickles, E. Risse, M. Kalashnikov, W. Sandner, G. Priebe, M. Amin, T. Toncian, *et al.*, “Transient electric fields in laser plasmas observed by proton streak deflectometry”, *Applied Physics Letters*, vol. 92, no. 9, p. 091 503, 2008.
- [188] M. Borghesi, S. Kar, L. Romagnani, T. Toncian, P. Antici, P. Audebert, E. Brambrink, F. Ceccherini, C. Cecchetti, J. Fuchs, *et al.*, “Impulsive electric fields driven by high-intensity laser matter interactions”, *Laser and Particle Beams*, vol. 25, no. 1, pp. 161–167, 2007.
- [189] S. Kar, H. Ahmed, R. Prasad, M. Cerchez, S. Brauckmann, B. Aurand, G. Cantono, P. Hadjisolomou, C. L. Lewis, A. Macchi, *et al.*, “Guided post-acceleration of laser-driven ions by a miniature modular structure”, *Nature communications*, vol. 7, no. 1, pp. 1–7, 2016.
- [190] H. Ahmed, S. Kar, A. Giesecke, D. Doria, G. Nersisyan, O. Willi, C. L. Lewis, and M. Borghesi, “Proton probing of laser-driven em pulses travelling in helical coils”, *High Power Laser Science and Engineering*, vol. 5, 2017.
- [191] C. Li, F. Séguin, J. Frenje, M. Manuel, D. Casey, N. Sinenian, R. Petrasso, P. Amendt, O. Landen, J. Rygg, *et al.*, “Proton radiography of dynamic electric and magnetic fields in laser-produced high-energy-density plasmas”, *Physics of Plasmas*, vol. 16, no. 5, p. 056 304, 2009.

- [192] C. Cecchetti, M. Borghesi, J. Fuchs, G. Schurtz, S. Kar, A. Macchi, L. Romagnani, P. Wilson, P. Antici, R. Jung, *et al.*, “Magnetic field measurements in laser-produced plasmas via proton deflectometry”, *Physics of Plasmas*, vol. 16, no. 4, p. 043 102, 2009.
- [193] G. Sarri, A. Macchi, C. Cecchetti, S. Kar, T. Liseykina, X. Yang, M. E. Dieckmann, J. Fuchs, M. Galimberti, L. Gizzi, *et al.*, “Dynamics of self-generated, large amplitude magnetic fields following high-intensity laser matter interaction”, *Physical review letters*, vol. 109, no. 20, p. 205 002, 2012.
- [194] L. Willingale, A. Thomas, P. Nilson, M. Kaluza, S. Bandyopadhyay, A. Dangor, R. Evans, P. Fernandes, M. Haines, C. Kamperidis, *et al.*, “Proton probe measurement of fast advection of magnetic fields by hot electrons”, *Plasma Physics and Controlled Fusion*, vol. 53, no. 12, p. 124 026, 2011.
- [195] M.-E. Manuel, C. Li, F. Séguin, J. Frenje, D. Casey, R. Petrasso, S. Hu, R. Betti, J. Hager, D. Meyerhofer, *et al.*, “First measurements of rayleigh-taylor-induced magnetic fields in laser-produced plasmas”, *Physical review letters*, vol. 108, no. 25, p. 255 006, 2012.
- [196] S. Le Pape, P. Patel, S. Chen, R. Town, and A. Mackinnon, “Proton radiography of magnetic field in laser produced plasma”, *The European Physical Journal Special Topics*, vol. 175, no. 1, pp. 61–64, 2009.
- [197] L. Lancia, B. Albertazzi, C. Boniface, A. Grisollet, R. Riquier, F. Chaland, K.-C. Le Thanh, P. Mellor, P. Antici, S. Buffechoux, *et al.*, “Topology of megagauss magnetic fields and of heat-carrying electrons produced in a high-power laser-solid interaction”, *Physical review letters*, vol. 113, no. 23, p. 235 001, 2014.
- [198] P. Nilson, L. Willingale, M. Kaluza, C. Kamperidis, S. Minardi, M. Wei, P. Fernandes, M. Notley, S. Bandyopadhyay, M. Sherlock, *et al.*, “Magnetic reconnection and plasma dynamics in two-beam laser-solid interactions”, *Physical review letters*, vol. 97, no. 25, p. 255 001, 2006.
- [199] L. Willingale, P. Nilson, M. Kaluza, A. Dangor, R. Evans, P. Fernandes, M. Haines, C. Kamperidis, R. Kingham, C. Ridgers, *et al.*, “Proton deflectometry of a magnetic reconnection geometry”, *Physics of Plasmas*, vol. 17, no. 4, p. 043 104, 2010.
- [200] M. Rosenberg, C. Li, W. Fox, A. Zylstra, C. Stoeckl, F. Séguin, J. Frenje, and R. Petrasso, “Slowing of magnetic reconnection concurrent with weakening plasma inflows and increasing collisionality in strongly driven laser-plasma experiments”, *Physical review letters*, vol. 114, no. 20, p. 205 004, 2015.
- [201] M. Rosenberg, C. Li, W. Fox, I. Igumenshchev, F. Séguin, R. Town, J. Frenje, C. Stoeckl, V. Glebov, and R. Petrasso, “First experiments probing the collision of parallel magnetic fields using laser-produced plasmas”, *Physics of Plasmas*, vol. 22, no. 4, p. 042 703, 2015.
- [202] A. Chien, L. Gao, H. Ji, X. Yuan, E. G. Blackman, H. Chen, P. C. Efthimion, G. Fiksel, D. H. Froula, K. W. Hill, *et al.*, “Study of a magnetically driven reconnection platform using ultrafast proton radiography”, *Physics of Plasmas*, vol. 26, no. 6, p. 062 113, 2019.
- [203] K. Law, Y. Abe, A. Morace, Y. Arikawa, S. Sakata, S. Lee, K. Matsuo, H. Morita, Y. Ochiai, C. Liu, *et al.*, “Relativistic magnetic reconnection in laser laboratory for testing an emission mechanism of hard-state black hole system”, *Physical Review E*, vol. 102, no. 3, p. 033 202, 2020.
- [204] G. Fiksel, W. Fox, A. Bhattacharjee, D. Barnak, P.-Y. Chang, K. Germaschewski, S. Hu, and P. Nilson, “Magnetic reconnection between colliding magnetized laser-produced plasma plumes”, *Physical review letters*, vol. 113, no. 10, p. 105 003, 2014.

- [205] L. Gao, E. Liang, Y. Lu, R. Follet, H. Sio, P. Tzeferacos, D. Froula, A. Birkel, C. Li, D. Lamb, *et al.*, “Mega-gauss plasma jet creation using a ring of laser beams”, *The Astrophysical Journal Letters*, vol. 873, no. 2, p. L11, 2019.
- [206] K. Law, M. Bailly-Grandvaux, A. Morace, S. Sakata, K. Matsuo, S. Kojima, S. Lee, X. Vaisseau, Y. Arikawa, A. Yogo, *et al.*, “Direct measurement of kilo-tesla level magnetic field generated with laser-driven capacitor-coil target by proton deflectometry”, *Applied Physics Letters*, vol. 108, no. 9, p. 091104, 2016.
- [207] J. J. Santos, M. Bailly-Grandvaux, M. Ehret, A. Arefiev, D. Batani, F. Beg, A. Calisti, S. Ferri, R. Florido, P. Forestier-Colleoni, *et al.*, “Laser-driven strong magnetostatic fields with applications to charged beam transport and magnetized high energy-density physics”, *Physics of Plasmas*, vol. 25, no. 5, p. 056705, 2018.
- [208] P. Bradford, M. Read, M. Ehret, L. Antonelli, M. Khan, N. Booth, K. Glize, D. Carroll, R. Clarke, R. Heathcote, *et al.*, “Proton deflectometry of a capacitor coil target along two axes”, *High Power Laser Science and Engineering*, vol. 8, 2020.
- [209] J. Peebles, J. Davies, D. Barnak, T. Cracium, M. Bonino, and R. Betti, “Axial proton probing of magnetic and electric fields inside laser-driven coils”, *Physics of Plasmas*, vol. 27, no. 6, p. 063109, 2020.
- [210] C. Goyon, B. Pollock, D. Turnbull, A. Hazi, L. Divol, W. Farmer, D. Haberberger, J. Javedani, A. Johnson, A. Kemp, *et al.*, “Ultrafast probing of magnetic field growth inside a laser-driven solenoid”, *Physical Review E*, vol. 95, no. 3, p. 033208, 2017.
- [211] S. Fujioka, Z. Zhang, K. Ishihara, K. Shigemori, Y. Hironaka, T. Johzaki, A. Sunahara, N. Yamamoto, H. Nakashima, T. Watanabe, *et al.*, “Kilotesla magnetic field due to a capacitor-coil target driven by high power laser”, *Scientific reports*, vol. 3, no. 1, pp. 1–7, 2013.
- [212] G. Liao, Y. Li, B. Zhu, Y. Li, F. Li, M. Li, X. Wang, Z. Zhang, S. He, W. Wang, *et al.*, “Proton radiography of magnetic fields generated with an open-ended coil driven by high power laser pulses”, *Matter and Radiation at Extremes*, vol. 1, no. 4, pp. 187–191, 2016.
- [213] H. Morita, B. B. Pollock, C. S. Goyon, G. J. Williams, K. F. F. Law, S. Fujioka, and J. D. Moody, “Dynamics of laser-generated magnetic fields using long laser pulses”, *Physical Review E*, vol. 103, no. 3, p. 033201, 2021.
- [214] Z. Zhang, B. Zhu, Y. Li, W. Jiang, D. Yuan, H. Wei, G. Liang, F. Wang, G. Zhao, J. Zhong, *et al.*, “Generation of strong magnetic fields with a laser-driven coil”, *High Power Laser Science and Engineering*, vol. 6, 2018.
- [215] X. Yuan, C. Zhou, H. Zhang, J. Zhong, B. Han, W. Sun, J. Wang, W. Zhou, B. Zhang, F. Lu, *et al.*, “Full treatment of the proton radiography technique for laser-driven capacitor-coil targets”, *Plasma Physics and Controlled Fusion*, vol. 63, no. 12, p. 125024, 2021.
- [216] W. Fox, G. Fiksel, A. Bhattacharjee, P.-Y. Chang, K. Germaschewski, S. Hu, and P. Nilson, “Filamentation instability of counterstreaming laser-driven plasmas”, *Physical review letters*, vol. 111, no. 22, p. 225002, 2013.
- [217] H.-S. Park, J. Ross, C. Huntington, F. Fiuza, D. Ryutov, D. Casey, R. Drake, G. Fiksel, D. Froula, G. Gregori, *et al.*, “Laboratory astrophysical collisionless shock experiments on omega and nif”, in *Journal of Physics: Conference Series*, IOP Publishing, vol. 688, 2016, p. 012084.
- [218] K. Quinn, L. Romagnani, B. Ramakrishna, G. Sarri, M. E. Dieckmann, P. Wilson, J. Fuchs, L. Lancia, A. Pipahl, T. Toncian, *et al.*, “Weibel-induced filamentation during an ultrafast laser-driven plasma expansion”, *Physical review letters*, vol. 108, no. 13, p. 135001, 2012.

- [219] C. Huntington, F. Fiuza, J. Ross, A. Zylstra, R. Drake, D. Froula, G. Gregori, N. Kugland, C. Kuranz, M. Levy, *et al.*, “Observation of magnetic field generation via the weibel instability in interpenetrating plasma flows”, *Nature Physics*, vol. 11, no. 2, pp. 173–176, 2015.
- [220] G. Scott, C. Brenner, V. Bagnoud, R. Clarke, B. Gonzalez-Izquierdo, J. Green, R. Heathcote, H. Powell, D. Rusby, B. Zielbauer, *et al.*, “Diagnosis of weibel instability evolution in the rear surface density scale lengths of laser solid interactions via proton acceleration”, *New Journal of Physics*, vol. 19, no. 4, p. 043 010, 2017.
- [221] H.-S. Park, C. Huntington, F. Fiuza, R. Drake, D. Froula, G. Gregori, M. Koenig, N. Kugland, C. Kuranz, D. Lamb, *et al.*, “Collisionless shock experiments with lasers and observation of weibel instabilities”, *Physics of Plasmas*, vol. 22, no. 5, p. 056 311, 2015.
- [222] C. Ruyer, S. Bolaños, B. Albertazzi, S. Chen, P. Antici, J. Böker, V. Dervieux, L. Lancia, M. Nakatsutsumi, L. Romagnani, *et al.*, “Growth of concomitant laser-driven collisionless and resistive electron filamentation instabilities over large spatiotemporal scales”, *Nature Physics*, vol. 16, no. 9, pp. 983–988, 2020.
- [223] N. Kugland, D. Ryutov, P.-Y. Chang, R. Drake, G. Fiksel, D. Froula, S. Glenzer, G. Gregori, M. Grosskopf, M. Koenig, *et al.*, “Self-organized electromagnetic field structures in laser-produced counter-streaming plasmas”, *Nature Physics*, vol. 8, no. 11, pp. 809–812, 2012.
- [224] C. Zhang, J. Hua, Y. Wu, Y. Fang, Y. Ma, T. Zhang, S. Liu, B. Peng, Y. He, C.-K. Huang, *et al.*, “Measurements of the growth and saturation of electron weibel instability in optical-field ionized plasmas”, *Physical Review Letters*, vol. 125, no. 25, p. 255 001, 2020.
- [225] C. Li, F. Séguin, J. Frenje, M. Manuel, R. Petrasso, V. Smalyuk, R. Betti, J. Delettrez, J. Knauer, F. Marshall, *et al.*, “Study of direct-drive capsule implosions in inertial confinement fusion with proton radiography”, *Plasma Physics and Controlled Fusion*, vol. 51, no. 1, p. 014 003, 2008.
- [226] A. Mackinnon, P. Patel, R. Town, M. Edwards, T. Phillips, S. Lerner, D. Price, D. Hicks, M. Key, S. Hatchett, *et al.*, “Proton radiography as an electromagnetic field and density perturbation diagnostic”, *Review of Scientific Instruments*, vol. 75, no. 10, pp. 3531–3536, 2004.
- [227] C. Li, F. Séguin, J. Rygg, J. Frenje, M. Manuel, R. Petrasso, R. Betti, J. Delettrez, J. Knauer, F. Marshall, *et al.*, “Monoenergetic-proton-radiography measurements of implosion dynamics in direct-drive inertial-confinement fusion”, *Physical review letters*, vol. 100, no. 22, p. 225 001, 2008.
- [228] C. Li, F. Séguin, J. Frenje, R. Petrasso, P. Amendt, R. Town, O. Landen, J. Rygg, R. Betti, J. Knauer, *et al.*, “Observations of electromagnetic fields and plasma flow in hohlraums with proton radiography”, *Physical review letters*, vol. 102, no. 20, p. 205 001, 2009.
- [229] C. Li, A. B. Zylstra, J. A. Frenje, F. H. Séguin, N. Sinenian, R. D. Petrasso, P. Amendt, R. Bionta, S. Friedrich, G. Collins, *et al.*, “Observation of strong electromagnetic fields around laser-entrance holes of ignition-scale hohlraums in inertial-confinement fusion experiments at the national ignition facility”, *New Journal of Physics*, vol. 15, no. 2, p. 025 040, 2013.
- [230] D. Mariscal, T. Ma, S. Wilks, A. Kemp, G. Williams, P. Michel, H. Chen, P. Patel, B. Remington, M. Bowers, *et al.*, “First demonstration of arc-accelerated proton beams at the national ignition facility”, *Physics of Plasmas*, vol. 26, no. 4, p. 043 110, 2019.

- [231] R. Simpson, D. Mariscal, J. Kim, G. Scott, G. Williams, E. Grace, C. McGuffey, S. Wilks, A. Kemp, N. Lemos, *et al.*, “Demonstration of tnsa proton radiography on the national ignition facility advanced radiographic capability (nif-arc) laser”, *Plasma Physics and Controlled Fusion*, vol. 63, no. 12, p. 124 006, 2021.
- [232] A. Ravasio, L. Romagnani, S. Le Pape, A. Benuzzi-Mounaix, C. Cecchetti, D. Batani, T. Boehly, M. Borghesi, R. Dezulian, L. Gremillet, *et al.*, “Proton radiography of a shock-compressed target”, *Physical Review E*, vol. 82, no. 1, p. 016 407, 2010.
- [233] D. Schaeffer, W. Fox, D. Haberberger, G. Fiksel, A. Bhattacharjee, D. Barnak, S. Hu, and K. Germaschewski, “Generation and evolution of high-mach-number laser-driven magnetized collisionless shocks in the laboratory”, *Physical review letters*, vol. 119, no. 2, p. 025 001, 2017.
- [234] Y. Sakawa, T. Morita, Y. Kuramitsu, and H. Takabe, “Collisionless electrostatic shock generation using high-energy laser systems”, *Advances in Physics: X*, vol. 1, no. 3, pp. 425–443, 2016.
- [235] R. Hua, H. Sio, S. Wilks, F. Beg, C. McGuffey, M. Bailly-Grandvaux, G. Collins, and Y. Ping, “Study of self-generated fields in strongly-shocked, low-density systems using broadband proton radiography”, *Applied Physics Letters*, vol. 111, no. 3, p. 034 102, 2017.
- [236] R. Hua, J. Kim, M. Sherlock, M. Bailly-Grandvaux, F. Beg, C. McGuffey, S. Wilks, H. Wen, A. Joglekar, W. Mori, *et al.*, “Self-generated magnetic and electric fields at a mach-6 shock front in a low density helium gas by dual-angle proton radiography”, *Physical review letters*, vol. 123, no. 21, p. 215 001, 2019.
- [237] C. Li, V. Tikhonchuk, Q. Moreno, H. Sio, E. D’Humières, X. Ribeyre, P. Korneev, S. Atzeni, R. Betti, A. Birkel, *et al.*, “Collisionless shocks driven by supersonic plasma flows with self-generated magnetic fields”, *Physical review letters*, vol. 123, no. 5, p. 055 002, 2019.
- [238] T. Morita, N. Kugland, W. Wan, R. Crowston, R. Drake, F. Fiúza, G. Gregori, C. Huntington, T. Ishikawa, M. Koenig, *et al.*, “Proton imaging of an electrostatic field structure formed in laser-produced counter-streaming plasmas”, in *Journal of Physics: Conference Series*, IOP Publishing, vol. 688, 2016, p. 012 071.
- [239] H. Sio, R. Hua, Y. Ping, C. McGuffey, F. Beg, R. Heeter, C. Li, R. Petrasso, and G. Collins, “A broadband proton backlighting platform to probe shock propagation in low-density systems”, *Review of Scientific Instruments*, vol. 88, no. 1, p. 013 503, 2017.
- [240] Y. Kuramitsu, Y. Sakawa, S. Dono, C. Gregory, S. Pikuz, B. Loupias, M. Koenig, J. Waugh, N. Woolsey, T. Morita, *et al.*, “Kelvin-helmholtz turbulence associated with collisionless shocks in laser produced plasmas”, *Physical review letters*, vol. 108, no. 19, p. 195 004, 2012.
- [241] H. Ahmed, M. E. Dieckmann, L. Romagnani, D. Doria, G. Sarri, M. Cerchez, E. Ianni, I. Kourakis, A. L. Giesecke, M. Notley, *et al.*, “Time-resolved characterization of the formation of a collisionless shock”, *Physical Review Letters*, vol. 110, no. 20, p. 205 001, 2013.
- [242] J. M. Levesque, A. S. Liao, P. Hartigan, R. P. Young, M. Trantham, S. Klein, W. Gray, M. Manuel, G. Fiksel, J. Katz, *et al.*, “Experimental observations of detached bow shock formation in the interaction of a laser-produced plasma with a magnetized obstacle”, *Physics of Plasmas*, vol. 29, no. 1, p. 012 106, 2022.
- [243] W. Schumaker, N. Nakanii, C. McGuffey, C. Zulick, V. Chyvkov, F. Dollar, H. Habara, G. Kalintchenko, A. Maksimchuk, K. Tanaka, *et al.*, “Ultrafast electron radiography of magnetic fields in high-intensity laser-solid interactions”, *Physical review letters*, vol. 110, no. 1, p. 015 003, 2013.

- [244] C. Zhang, J. Hua, X. Xu, F. Li, C.-H. Pai, Y. Wan, Y. Wu, Y. Gu, W. Mori, C. Joshi, *et al.*, “Capturing relativistic wakefield structures in plasmas using ultrashort high-energy electrons as a probe”, *Scientific reports*, vol. 6, no. 1, pp. 1–9, 2016.
- [245] C. Zhang, J. Hua, Y. Wan, C.-H. Pai, B. Guo, J. Zhang, Y. Ma, F. Li, Y. Wu, H.-H. Chu, *et al.*, “Femtosecond probing of plasma wakefields and observation of the plasma wake reversal using a relativistic electron bunch”, *Physical review letters*, vol. 119, no. 6, p. 064 801, 2017.
- [246] C. Zhang, Y. Wan, B. Guo, J. Hua, C. Pai, F. Li, J. Zhang, Y. Ma, Y. Wu, X. Xu, *et al.*, “Probing plasma wakefields using electron bunches generated from a laser wakefield accelerator”, *Plasma Physics and Controlled Fusion*, vol. 60, no. 4, p. 044 013, 2018.
- [247] M.-E. Manuel, N. Sinenian, F. Séguin, C. Li, J. Frenje, H. Rinderknecht, D. Casey, A. Zylstra, R. Petrasso, and F. Beg, “Mapping return currents in laser-generated z-pinch plasmas using proton deflectometry”, *Applied Physics Letters*, vol. 100, no. 20, p. 203 505, 2012.
- [248] D. Hicks, C. Li, F. Séguin, A. Ram, J. Frenje, R. Petrasso, J. Soures, V. Y. Glebov, D. Meyerhofer, S. Roberts, *et al.*, “Charged-particle acceleration and energy loss in laser-produced plasmas”, *Physics of Plasmas*, vol. 7, no. 12, pp. 5106–5117, 2000.
- [249] F. N. Beg, “Assessment of proton deflectometry for exploding wire experiments”, Sep. 2013. DOI: 10.2172/1093880.
- [250] D. Mariscal, C. McGuffey, J. Valenzuela, M. Wei, J. Chittenden, N. Niasse, R. Presura, S. Haque, M. Wallace, A. Arias, *et al.*, “Measurement of pulsed-power-driven magnetic fields via proton deflectometry”, *Applied Physics Letters*, vol. 105, no. 22, p. 224 103, 2014.
- [251] M. S. Schollmeier, A. B. Sefkow, M. Geissel, P. K. Rambo, and J. Schwarz, “Z-petawatt driven ion beam radiography development”, *Sandia Report SAND2013-7201*, 2013.
- [252] D. Klir, A. V. Shishlov, V. Kokshenev, P. Kubes, A. Y. Labetsky, K. Rezac, R. Cherdizov, J. Cikhardt, B. Cikhardtova, G. N. Dudkin, *et al.*, “Deuterium z-pinch as a powerful source of multi-mev ions and neutrons for advanced applications”, *Physics of Plasmas*, vol. 23, no. 3, p. 032 702, 2016.
- [253] D. Klir, A. Shishlov, V. Kokshenev, P. Kubes, K. Rezac, R. Cherdizov, J. Cikhardt, B. Cikhardtova, G. Dudkin, F. Fursov, *et al.*, “Ion acceleration mechanism in mega-ampere gas-puff z-pinch”, *New Journal of Physics*, vol. 20, no. 5, p. 053 064, 2018.
- [254] D. Klir, A. Shishlov, V. Kokshenev, P. Kubes, K. Rezac, S. Buryškova, R. Cherdizov, J. Cikhardt, B. Cikhardtova, G. Dudkin, *et al.*, “Acceleration of protons and deuterons up to 35 mev and generation of 1013 neutrons in a megaampere deuterium gas-puff z-pinch”, *Plasma Physics and Controlled Fusion*, vol. 61, no. 1, p. 014 018, 2018.
- [255] S. Bugaev, A. Volkov, A. A. Kim, V. Kiselev, B. M. Koval’chuk, N. Kovsharov, V. Kokshenev, N. Kurmaev, S. Loginov, G. Mesyats, *et al.*, “Git16: A megajoule pulse generator with plasma switch for a z-pinch load”, *Russian physics journal*, vol. 40, no. 12, pp. 1154–1161, 1997.
- [256] D. Klir, A. Shishlov, P. Kubes, K. Rezac, F. Fursov, V. Kokshenev, B. Kovalchuk, J. Kravarik, N. Kurmaev, A. Y. Labetsky, *et al.*, “Deuterium gas puff z-pinch at currents of 2 to 3 mega-ampere”, *Physics of Plasmas*, vol. 19, no. 3, p. 032 706, 2012.
- [257] A. Beresnyak, J. L. Giuliani, S. L. Jackson, A. S. Richardson, S. Swanekamp, J. Schumer, B. Weber, and D. Mosher, “Simulations of a dense plasma focus on a high-impedance generator”, *IEEE Transactions on Plasma Science*, vol. 46, no. 11, pp. 3881–3885, 2018.

- [258] J. Grossmann, S. Swanekamp, P. Ottinger, R. Commisso, D. Hinshelwood, and B. Weber, “Gap formation processes in a high-density plasma opening switch”, *Physics of Plasmas*, vol. 2, no. 1, pp. 299–309, 1995.
- [259] B. Weber, R. Commisso, G. Cooperstein, D. Hinshelwood, D. Mosher, P. Ottinger, D. Ponce, J. Schumer, S. Stephanakis, S. Strasburg, *et al.*, “Ultra-high electron beam power and energy densities using a plasma-filled rod-pinch diode”, *Physics of Plasmas*, vol. 11, no. 5, pp. 2916–2927, 2004.
- [260] B. Kovalchuk, A. Zherlitsyn, and N. Pedin, “Plasma-filled diode in the electron accelerator on base of a pulsed linear transformer”, *Laser and Particle Beams*, vol. 28, no. 4, pp. 547–552, 2010.
- [261] D. Hinshelwood, P. Ottinger, J. Schumer, R. Allen, J. Apruzese, R. Commisso, G. Cooperstein, S. Jackson, D. Murphy, D. Phipps, *et al.*, “Ion diode performance on a positive polarity inductive voltage adder with layered magnetically insulated transmission line flow”, *Physics of Plasmas*, vol. 18, no. 5, p. 053106, 2011.
- [262] L. Bertalot, H. Herold, U. Jäger, A. Mozer, T. Oppenländer, M. Sadowski, and H. Schmidt, “Mass and energy analysis and space-resolved measurements of ions from plasma focus devices”, *Physics Letters A*, vol. 79, no. 5-6, pp. 389–392, 1980.
- [263] K. TAKASUGI, M. IWATA, and M. NISHIO, “Emission of high-energy ions in the shotgun iii divergent gas-puff z-pinch experiment”, in *Journal of Physics: Conference Series*, IOP Publishing, vol. 688, 2016, p. 012120.
- [264] R. Kwiatkowski, E. Skladnik-Sadowska, K. Malinowski, M. J. Sadowski, K. Czaus, J. Zebrowski, L. Karpinski, M. Paduch, M. Scholz, I. E. Garkusha, *et al.*, “Measurements of electron and ion beams emitted from the pf-1000 device in the upstream and downstream direction”, *Nukleonika*, vol. 56, pp. 119–123, 2011.
- [265] P. Kubes, M. Paduch, M. Sadowski, J. Cikhardt, B. Cikhardtova, D. Klir, J. Kravarik, V. Munzar, K. Rezac, E. Zielinska, *et al.*, “Characterization of fast deuterons involved in the production of fusion neutrons in a dense plasma focus”, *Physics of Plasmas*, vol. 25, no. 1, p. 012712, 2018.
- [266] D. Klir, S. Jackson, A. Shishlov, V. Kokshenev, K. Rezac, A. Beresnyak, R. Cherdizov, J. Cikhardt, B. Cikhardtova, G. Dudkin, *et al.*, “Ion acceleration and neutron production in hybrid gas-puff z-pinch on the git-12 and hawk generators”, *Matter and Radiation at Extremes*, vol. 5, no. 2, p. 026401, 2020.
- [267] J. Engelbrecht, S. Jackson, A. Mamonau, A. Beresnyak, K. Rezac, J. Cikhardt, D. Klir, B. Weber, J. Giuliani, and J. Schumer, “Initial conditions in the hawk dense plasma focus”, in *2019 IEEE Pulsed Power & Plasma Science (PPPS)*, IEEE, 2019, pp. 1–5.
- [268] O. Rodrigues, “On the geometrical laws that govern the displacements of a solid system in space, and on the change of coordinates resulting from these displacements considered independently of the causes that can produce them”, *J Math Pures Appl*, vol. 5, pp. 380–440, 1840.